How mouse microbiomes can mess with experiments *p. 741*

Political turmoil threatens Brazil's environment *p. 746*

Zebra finch song prepares eggs for warming *p. 812*

Science

$15
19 AUGUST 2016
sciencemag.org

AAAS

SPECIAL ISSUE

IMMUNE CELLS AND THE BRAIN

CONTENTS

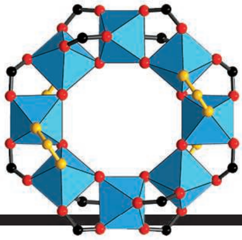

754 & 808

Better-ordered structures

19 AUGUST 2016 • VOLUME 353 • ISSUE 6301

NEWS

IN BRIEF

IN DEPTH

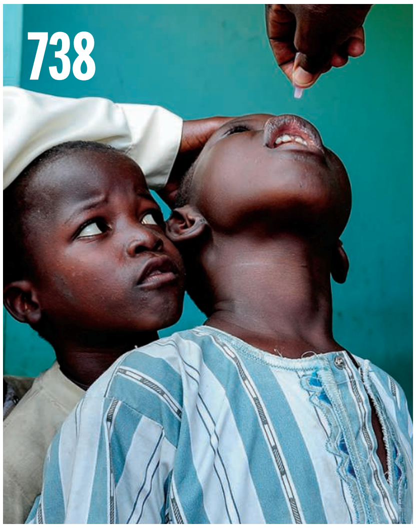

738

SPECIAL SECTION

Neuroimmunology

ON THE COVER

Resident immune cells in the brain, called microglia (purple), interact with neurons (yellow). The field of neuroimmunology has captivated a growing number of researchers as connections emerge between the body's defenses and the central nervous system. Immune cells in the brain play a role in many diseases but are also increasingly seen as central to normal brain development and function. See page 760. *Illustration: Valerie Altounian/*Science

FEATURES

INSIGHTS

POLICY FORUM

PERSPECTIVES

CONTENTS

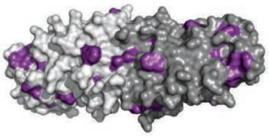

750 & 823

Analyzing antibodies against Zika virus

19 AUGUST 2016 • VOLUME 353 • ISSUE 6301

753 FIGHTING POVERTY WITH DATA

Machine learning algorithms measure and target poverty

By J. E. Blumenstock

▸ RESEARCH ARTICLE P. 790

754 NOW YOU SEE ME TOO

Attaching chiral molecules to a chiral framework allows their molecular structures to be determined

By L. Öhrström

▸ REPORT P. 808

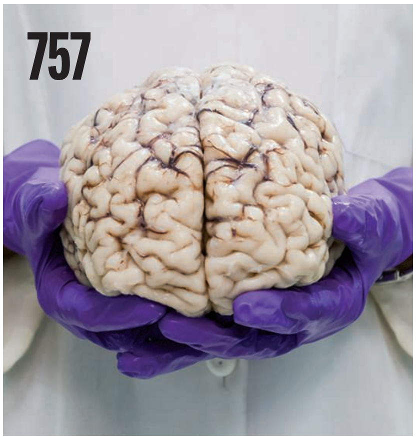

757

BOOKS *ET AL.*

756 TOUGH LOVE FOR TECHNOLOGY

A legal scholar probes how new technologies are raising risks, accentuating inequality, and affecting human nature *By C. Selin*

757 MEMORY LANE

An intimate portrait of a famous amnesiac is also a tale of personal grievances *By L. Stark*

LETTERS

758 PROTECTING INDIA'S CONSERVATION OFFSETS

By D. Narain and M. Maron

758 OPEN-ACCESS POLICIES: A LEGAL QUAGMIRE

By I. Kapovich

759 PASSPORT INITIATIVE FOSTERS APPLIED SCIENCE

By T. Krabacher and P. Flatt

759 TECHNICAL COMMENT ABSTRACTS

RESEARCH

IN BRIEF

786 From *Science* and other journals

RESEARCH ARTICLES

789 IMMUNOGENOMICS

Microglia development follows a stepwise program to regulate brain homeostasis *O. Matcovitch-Natan* et al.

RESEARCH ARTICLE SUMMARY; FOR FULL TEXT: dx.doi.org/10.1126/science.aad8670

▸ NEUROIMMUNOLOGY SECTION P. 760

790 ECONOMICS

Combining satellite imagery and machine learning to predict poverty

N. Jean et al.

▸ PERSPECTIVE P. 753

794 STATISTICAL PHYSICS

Quantum thermalization through entanglement in an isolated many-body system *A. M. Kaufman* et al.

▸ PERSPECTIVE P. 752

REPORTS

800 GEOMORPHOLOGY

Northward migration of the eastern Himalayan syntaxis revealed by OSL thermochronometry *G. E. King* et al.

804 SEPARATION MEMBRANES

Reverse osmosis molecular differentiation of organic liquids using carbon molecular sieve membranes

D.-Y. Koh et al.

808 CRYSTALLOGRAPHY

Coordinative alignment of molecules in chiral metal-organic frameworks *S. Lee* et al.

▸ PERSPECTIVE P. 754

812 BEHAVIORAL ECOLOGY

Prenatal acoustic communication programs offspring for high posthatching temperatures in a songbird

M. M. Mariette and K. L. Buchanan

▸ VIDEO

814 GENE REGULATION

Integration of omic networks in a developmental atlas of maize

J. W. Walley et al.

819 SYNTHETIC GENOMICS

Design, synthesis, and testing toward a 57-codon genome *N. Ostrov* et al.

▸ NEWS STORY P. 739

823 ZIKA VIRUS

Specificity, cross-reactivity, and function of antibodies elicited by Zika virus infection *K. Stettler* et al.

▸ PERSPECTIVE P. 750

827 HUMAN GENETICS

Cardiometabolic risk loci share downstream cis- and trans-gene regulation across tissues and diseases

O. Franzén et al.

812

DEPARTMENTS

731 EDITORIAL

Progress lies in precision

By Sue Desmond-Hellmann

838 WORKING LIFE

Choosing the nontenure track

By Amar M. Singh

PHOTO (RIGHT): CHRIS TZAROS

SCIENCE (ISSN 0036-8075) is published weekly on Friday, except the last week in December, by the American Association for the Advancement of Science, 1200 New York Avenue, NW, Washington, DC 20005. Periodicals mail postage (publication No. 484460) paid at Washington, DC, and additional mailing offices. Copyright © 2016 by the American Association for the Advancement of Science. The title SCIENCE is a registered trademark of the AAAS. Domestic individual membership and subscription (51 issues): $165 ($74 allocated to subscription). Domestic institutional subscription (51 issues): $1522; Foreign postage extra: Mexico, Caribbean (surface mail) $55; other countries (air assist delivery) $89. First class, airmail, student, and emeritus rates on request. Canadian rates with GST available upon request, GST #1254 88122. Publications Mail Agreement Number 1069624. **Printed in the U.S.A.**

Change of address: Allow 4 weeks, giving old and new addresses and 8-digit account number. **Postmaster:** Send change of address to AAAS, P.O. Box 96178, Washington, DC 20090–6178. **Single-copy sales:** $15.00 current issue, $20.00 back issue prepaid includes surface postage; bulk rates on request. **Authorization to photocopy** material for internal or personal use under circumstances not falling within the fair use provisions of the Copyright Act is granted by AAAS to libraries and other users registered with the Copyright Clearance Center (CCC) Transactional Reporting Service, provided that $35.00 per article is paid directly to CCC, 222 Rosewood Drive, Danvers, MA 01923. The identification code for *Science* is 0036-8075. *Science* is indexed in the *Reader's Guide to Periodical Literature* and in several specialized indexes.

Science

1200 New York Avenue, NW, Washington, DC 20005
Clarendon House, Clarendon Road, Cambridge, UK CB2 8FH

AAAS

Editor-in-Chief Jeremy Berg

Executive Editor Monica M. Bradford **News Editor** Tim Appenzeller

Deputy Editors Lisa D. Chong, Andrew M. Sugden(UK), Valda J. Vinson, Jake S. Yeston

Research and Insights

DEPUTY EDITOR, EMERITUS Barbara R. Jasny **SR. EDITORS** Caroline Ash(UK), Gilbert J. Chin, Julia Fahrenkamp-Uppenbrink(UK), Pamela J. Hines, Stella M. Hurtley(UK), Paula A. Kiberstis, Marc S. Lavine(Canada), Kristen L. Mueller, Ian S. Osborne(UK), Beverly A. Purnell, L. Bryan Ray, Guy Riddihough, H. Jesse Smith, Jelena Stajic, Peter Stern(UK), Phillip D. Szuromi, Sacha Vignieri, Brad Wible, Nicholas S. Wigginton, Laura M. Zahn **ASSOCIATE EDITORS** Brent Grocholski, Keith T. Smith **ASSOCIATE BOOK REVIEW EDITOR** Valerie B. Thompson **LETTERS EDITOR** Jennifer Sills **LEAD CONTENT PRODUCTION EDITORS** Harry Jach, Lauren Kmec **CONTENT PRODUCTION EDITORS** Jeffrey E. Cook, Chris Filiatreau, Cynthia Howe, Barbara P. Ordway, Catherine Wolner **SR. EDITORIAL COORDINATORS** Carolyn Kyle, Beverly Shields **EDITORIAL COORDINATORS** Aneera Dobbins, Joi S. Granger, Jeffrey Hearn, Lisa Johnson, Maryrose Madrid, Anita Wynn **PUBLICATIONS ASSISTANTS** Nida Masiulis, Dona Mathieu, Le-Toya Mayne Flood, Shannon McMahon, Scott Miller, Jerry Richardson, Alice Whaley(UK), Brian White **EXECUTIVE ASSISTANT** Anna Bashkirova **ADMINISTRATIVE SUPPORT** Janet Clements(UK), Lizanne Newton(UK)

News

NEWS MANAGING EDITOR John Travis **INTERNATIONAL EDITOR** Richard Stone **DEPUTY NEWS EDITORS** Elizabeth Culotta, David Grimm, Eric Hand David Malakoff, Leslie Roberts **CONTRIBUING EDITOR** Martin Enserink(Europe) **SR. CORRESPONDENTS** Daniel Clery(UK), Jeffrey Mervis, Elizabeth Pennisi **NEWS WRITERS** Adrian Cho, Jon Cohen, Jennifer Couzin-Frankel, Carolyn Gramling, Jocelyn Kaiser, Catherine Matacic, Kelly Servick, Robert F. Service, Erik Stokstad(Cambridge, UK) **INTERNS** Jessica Boddy, Ben Panko **CONTRIBUTING CORRESPONDENTS** John Bohannon, Warren Cornwall, Ann Gibbons, Mara Hvistendahl, Sam Kean, Eli Kintisch, Kai Kupferschmidt(Berlin), Andrew Lawler, Mitch Leslie, Charles C. Mann, Eliot Marshall, Virginia Morell, Dennis Normile(Shanghai), Heather Pringle, Tania Rabesandratana(London), Emily Underwood, Gretchen Vogel(Berlin), Lizzie Wade(Mexico City) **CAREERS** Donisha Adams, Rachel Bernstein(Editor), Maggie Kuo **COPY EDITORS** Julia Cole, Dorie Chevlen, Jennifer Levin (Chief) **ADMINISTRATIVE SUPPORT** Jessica Adams

Executive Publisher Rush D. Holt

Publisher Bill Moran **Chief Digital Media Officer** Rob Covey

BUSINESS OPERATIONS AND PORTFOLIO MANAGEMENT DIRECTOR Sarah Whalen **PRODUCT DEVELOPMENT DIRECTOR** Will Schweitzer **PRODUCT DEVELOPMENT ASSOCIATE** Hannah Heckner **BUSINESS SYSTEMS AND FINANCIAL ANALYSIS DIRECTOR** Randy Yi **MANAGER OF FULFILLMENT SYSTEMS** Neal Hawkins **SYSTEMS ANALYST** Nicole Mehmedovich **DIRECTOR, BUSINESS OPERATIONS & ANALYSIS** Eric Knott **MANAGER, BUSINESS OPERATIONS** Jessica Tierney **SENIOR BUSINESS ANALYST** Cory Lipman **BUSINESS ANALYSTS** David Garrison, Michael Hardesty Meron Kebede, Sandy Kim **FINANCIAL ANALYST** Drew Sher **DIRECTOR, COPYRIGHTS LICENSING SPECIAL PROJECTS** Emilie David **PERMISSIONS ASSOCIATE** Elizabeth Sandler **RIGHTS, CONTRACTS, AND LICENSING ASSOCIATE** Lili Kiser **RIGHTS & PERMISSIONS ASSISTANT** Alexander Lee

MARKETING DIRECTOR Elise Swinehart **ASSOCIATE MARKETING DIRECTOR** Stacey Burke Bowers **MARKETING ASSOCIATE** Steven Goodman **CREATIVE DIRECTOR** Scott Rodgerson **SENIOR ART ASSOCIATES** Paula Fry **ART ASSOCIATE** Kim Huynh

FULFILLMENT SYSTEMS AND OPERATIONS membership@aaas.org **MANAGER, MEMBER SERVICES** Pat Butler **SPECIALISTS** Terrance Morrison, Latasha Russell **MANAGER, DATA ENTRY** Mickie Napoleoni **DATA ENTRY SPECIALISTS** Brenden Aquilino, Fiona Giblin **MARKETING ASSOCIATE** Isa Sesay-Bah

PUBLISHER RELATIONS, EASTERN REGION Keith Layson **PUBLISHER RELATIONS, WESTERN REGION** Ryan Rexroth **SALES RESEARCH COORDINATOR** Aiesha Marshall **MANAGER, SITE LICENSE OPERATIONS** Iquo Edim **SENIOR OPERATIONS ANALYST** Lana Guz **FULFILLMENT ANALYST** Judy Lillibridge

WEB TECHNOLOGIES PORTFOLIO MANAGER Trista Smith **TECHNICAL MANAGER** Chris Coleman **PROJECT MANAGER** Nick Fletcher **DEVELOPERS** Ryan Jensen, Jimmy Marks, Brandon Morrison **BUSINESS ANALYST** Christina Wofford

DIGITAL MEDIA DIRECTOR OF ANALYTICS Enrique Gonzales **DIGITAL REPORTING ANALYST** Eric Hossinger **SR. MULTIMEDIA PRODUCER** Sarah Crespi **MANAGING DIGITAL PRODUCER** Alison Crawford **PRODUCER** Liana Birke **VIDEO PRODUCER** Chris Burns, Nguyên Khôi Nguyễn **DIGITAL SOCIAL MEDIA PRODUCER** Brice Russ

DIRECTOR OF OPERATIONS PRINT AND ONLINE Lizabeth Harman **DIGITAL/PRINT STRATEGY MANAGER** Jason Hillman **QUALITY TECHNICAL MANAGER** Marcus Spiegler **PROJECT ACCOUNT MANAGER** Tara Kelly **DIGITAL PRODUCTION MANAGER** Lisa Stanford **ASSISTANT MANAGER DIGITAL/PRINT** Rebecca Doshi **SENIOR CONTENT SPECIALISTS** Steve Forrester, Antoinette Hodal, Lori Murphy, Anthony Rosen **CONTENT SPECIALISTS** Jacob Hedrick, Kimberley Oster

DESIGN DIRECTOR Beth Rakouskas **DESIGN EDITOR** Marcy Atarod **SENIOR DESIGNERS** Garvin Grullón, Chrystal Smith **GRAPHICS MANAGING EDITOR** Alberto Cuadra **SENIOR SCIENTIFIC ILLUSTRATORS** Chris Bickel, Katharine Sutliff **SCIENTIFIC ILLUSTRATOR** Valerie Altounian **INTERACTIVE GRAPHICS EDITOR** Jia You **SENIOR GRAPHICS SPECIALISTS** Holly Bishop, Nathalie Cary **PHOTOGRAPHY MANAGING EDITOR** William Douthitt **SENIOR PHOTO EDITOR** Christy Steele **PHOTO EDITOR** Emily Petersen

DIRECTOR, GLOBAL COLLABORATION, CUSTOM PUBLICATIONS, ADVERTISING Bill Moran **EDITOR, CUSTOM PUBLISHING** Sean Sanders: 202-326-6430 **ADVERTISING MARKETING MANAGER** Justin Sawyers: 202-326-7061 science_advertising@aaas.org **ADVERTISING SUPPORT MANAGER** Karen Foote: 202-326-6740 **ADVERTISING PRODUCTION OPERATIONS MANAGER** Deborah Tompkins **SR. PRODUCTION SPECIALIST/GRAPHIC DESIGNER** Amy Hardcastle **SR. TRAFFIC ASSOCIATE** Christine Hall **SALES COORDINATOR** Shirley Young **ASSOCIATE DIRECTOR, COLLABORATION, CUSTOM PUBLICATIONS/CHINA/TAIWAN/KOREA/SINGAPORE** Ruolei Wu: +86-186 0082 9345, rwu@aaas.org **COLLABORATION/CUSTOM PUBLICATIONS/JAPAN** Adarsh Sandhu + 81532-81-5142 asandhu@aaas.org **EAST COAST/E. CANADA** Laurie Faraday: 508-747-9395, FAX 617-507-8189 **WEST COAST/W. CANADA** Lynne Stickrod: 415-931-9782, FAX 415-520-6940 **MIDWEST** Jeffrey Dembksi: 847-498-4520 x3005, Steven Loerch: 847-498-4520 x3006 **UK EUROPE/ASIA** Roger Goncalves: TEL/FAX +41 43 243 1358 **JAPAN** Katsuyoshi Fukamizu(Tokyo): +81-3-3219-5777 kfukamizu@aaas.org **CHINA/TAIWAN** Ruolei Wu: +86-186 0082 9345, rwu@aaas.org

WORLDWIDE ASSOCIATE DIRECTOR OF SCIENCE CAREERS Tracy Holmes: +44 (0) 1223 326525, FAX +44 (0) 1223 326532 tholmes@science-int. co.uk **CLASSIFIED** advertise@sciencecareers.org **U.S. SALES** Tina Burks: 202-326-6577, Nancy Toema: 202-326-6578 **EUROPE/ROW SALES** Sarah Lelarge **SALES ASSISTANT** Kelly Grace **JAPAN** Hiroyuki Mashiki(Kyoto): +81-75-823-1109 hmashiki@aaas.org **CHINA/TAIWAN** Ruolei Wu: +86-186 0082 9345 rwu@aaas.org **MARKETING MANAGER** Allison Pritchard **MARKETING ASSOCIATE** Aimee Aponte

AAAS BOARD OF DIRECTORS, CHAIR Geraldine L. Richmond **PRESIDENT** Barbara A. Schaal **PRESIDENT-ELECT** Susan Hockfield **TREASURER** David Evans Shaw **CHIEF EXECUTIVE OFFICER** Rush D. Holt **BOARD** Cynthia M. Beall, May R. Berenbaum, Carlos J. Bustamante, Stephen P.A. Fodor, Claire M. Fraser, Michael S. Gazzaniga, Laura H. Greene, Elizabeth Loftus, Mercedes Pascual

SUBSCRIPTION SERVICES For change of address, missing issues, new orders and renewals, and payment questions: 866-434-AAAS (2227) or 202-326-6417, FAX 202-842-1065. Mailing addresses: AAAS, P.O. Box 96178, Washington, DC 20090-6178 or AAAS Member Services, 1200 New York Avenue, NW, Washington, DC 20005

INSTITUTIONAL SITE LICENSES 202-326-6730 **REPRINTS:** Author Inquiries 800-635-7181 **COMMERCIAL INQUIRIES** 803-359-4578 **PERMISSIONS** 202-326-6765, permissions@aaas.org **AAAS Member Services** 202-326-6417 or http://membercentral.aaas.org/discounts

Science serves as a forum for discussion of important issues related to the advancement of science by publishing material on which a consensus has been reached as well as including the presentation of minority of conflicting points of view. Accordingly, all articles published in *Science*—including editorials, news and comment, and book reviews—are signed and reflect the individual views of the authors and not official points of view adopted by AAAS or the institutions with which the authors are affiliated.

INFORMATION FOR AUTHORS See pages 624 and 625 of the 5 February 2016 issue or access www.sciencemag.org/authors/science-information-authors

EDITORIAL

Progress lies in precision

Too often, I feel as though I live in two worlds. One is populated by scientists working on advanced tools, such as big data, sequencing, and data-based disease surveillance. The other is populated by public health professionals working on the demanding challenges of combating infectious diseases, empowering women and girls, and ensuring that more children survive and thrive. If we want to achieve the ambitions set out by the United Nations for global health and development by 2030, we need to bring these two worlds closer together through a new concept—precision public health.

The idea of precision public health has its roots in the precision medicine revolution, particularly in cancer treatment. By harnessing more effective tools—from big data to predictive analytics—oncologists are making more informed therapy decisions, applying specific agents to subtypes of tumors in ways that minimize side effects and maximize optimal clinical outcomes. This approach is starting to transform the way physicians think about treating other diseases, enabling different strategies, for different patients, at different times. Can we take the principles of precision medicine a step further, from individuals to populations?

Today, public health strategies involve epidemiologists examining geography, medical histories, biomarkers, and physical and demographic characteristics; and measuring exposures, behaviors, and susceptibility. General policies and programs are then developed. But a one-size-fits-all process does not always bring desired results. By more accurately detecting, identifying, and tracking unique traits in subpopulations, subgroups, or even communities, we can respond with greater precision.

Precision public health is already happening in a limited way, with big impact. Worldwide, around 17 million women are living with HIV. If an infected individual gets pregnant, she can pass the virus to her baby. Half those babies will die before their second birthday. Antiretroviral therapy almost guarantees that mothers will not pass on the virus. However, it has not been possible to test every pregnant woman everywhere for HIV, and then treat those who test positive. Instead, testing and treatment are focused on the areas of sub-Saharan Africa where enhanced data collection and analysis have revealed that HIV among women is most prevalent. This more exact approach to a public health problem has cut HIV transmission to babies by almost half in 5 years.

"Precision public health is already happening..."

Although technological and scientific advances are changing the way some diseases and conditions are tracked and treated, there has been too little focus on how scientific tools used in high-resource areas can help people in low-resource areas. Take, for example, the lack of specificity around the 2.6 million neonatal deaths every year, most of which occur in the world's poorest countries. Much of what we know about them relies on "verbal autopsies" and model data. The Bill & Melinda Gates Foundation is now working with partners on a program that takes tissue samples from the newborn to determine causes of death more definitively. The goal is to identify trends in a particular region, and then deliver specific interventions to help reduce infant mortality. Ultimately, I believe this approach could help save 1 million babies every year.

Imagine what more could be achieved. More children will survive and thrive if we know more about the causes of malnutrition in different populations with different diets and cultural practices. More women will avoid cervical cancer, the leading cause of cancer deaths in low-resource countries, if we know more about different risks in different populations. Fewer people will contract malaria if we know more about how it spreads differently among populations, and how the parasite and mosquito become resistant to remedies.

We have the tools to bring the right interventions, to the right people, in the right places to save lives. Now, we just need the will.

–Sue Desmond-Hellmann

Sue Desmond-Hellmann is the chief executive officer of the Bill & Melinda Gates Foundation, Seattle, WA, USA, and a former president at Genentech, Inc., San Francisco, CA, USA.

PHOTOS: (INSET) ©BILL & MELINDA GATES FOUNDATION/RICCARDO GANGALE; (TOP RIGHT) ©BILL & MELINDA GATES FOUNDATION/STEVEN DEWALL

10.1126/science.aai7598

NEWS

72% Increase in malaria cases in Venezuela in the first 6 months of 2016, *The New York Times* reports. Economic collapse and job losses have driven tens of thousands of people to seek work in the country's mosquito-infested, open-pit gold mines.

IN BRIEF

Marijuana verdict has highs and lows

Since 1970, a University of Mississippi farm was the only legal source of marijuana for research.

Marijuana will remain a Schedule I drug, the most tightly regulated class of drugs in the United States, the Drug Enforcement Administration (DEA) announced on 11 August. The decision, which keeps marijuana in the same class as heroin and LSD, frustrates researchers wishing to study its potential to treat conditions from chronic pain to brain tumors to childhood epilepsy. By ruling that there is not enough evidence of "currently accepted medical use"—a key distinction between Schedule I and the less restrictive Schedule II classification—the administration "is setting a standard that can't be met," says David Bradford, a health economist at the University of Georgia in Athens. "That level of proof … requires doing a really extensive clinical trial series, and given that a pharmaceutical company can't patent whole plant marijuana, it's in no company's interest to do that." However, the DEA announcement holds a glimmer of good news for scientists: DEA said it will amend a policy that had restricted them to a single source of marijuana for research studies, a federally funded farm at the University of Mississippi. That could allow researchers to investigate a wider variety of strains, including strains closer to those used in states where medical marijuana is legal. http://scim.ag/DEAmarijuana

AROUND THE WORLD

White House diverts funds to Zika

WASHINGTON, D.C. | To keep Zika vaccine development on track, the Obama administration has poached $81 million from the U.S. National Institutes of Health (NIH), money that was designated for other projects. In an 11 August letter to Congress, Secretary of Health and Human Services Sylvia Burwell explained that NIH and the Biomedical Advanced Research and Development Authority, which are jointly developing Zika vaccines, would "exhaust" their funding by the end of the month. Burwell blamed the funding shortfall on Congress, which did not heed President Barack Obama's request for $1.9 billion in funding to respond to the Zika virus. The virus has now moved beyond Latin America and is being spread by mosquitoes in Florida. "The failure to pass a Zika emergency supplemental has forced the administration to choose between delaying critical vaccine development work and raiding other worthy government programs," Burwell wrote.

Some Brexit relief for scientists

LONDON | The U.K. government announced this week that it will guarantee funding for research grants awarded by the European Union between now and an eventual Brexit. The decision could boost confidence for international collaborations that apply to Horizon 2020, the European Union's main competitive grants program. It has been welcomed by scientists, who have worried about the future of research funding after the United Kingdom voted in a June referendum to leave the European Union. The grant guarantee provides "much-needed reassurance to researchers in the U.K. and across Europe that the U.K. is still in the game as a reliable player in research funding bids," Sarah Main of the Campaign for Science and Engineering, an advocacy group based in London, said in a statement. "This is a great first step." But other research advocates said the move falls short of the full assurances that scientists need. Scientists for EU, an advocacy group based in London, called the announcement "decidedly underwhelming" because the government has not said what

PHOTO: ROBERT JORDAN/ASSOCIATED PRESS

will happen if U.K. scientists can no longer apply for EU money once the divorce from Europe is complete.

Cancer drug under suspicion

BRÜGGEN, GERMANY | A new type of cancer drug developed at Johns Hopkins University in Baltimore, Maryland, but not yet tested in clinical trials may have triggered the deaths of three patients who underwent an alternative cancer treatment by a nonmedical practitioner in Germany. A preliminary assessment by health authorities has found that Klaus Ross, who operates the Biological Cancer Centre in the German town of Brüggen, gave his patients the unapproved drug; prosecutors are investigating whether the case constitutes involuntary manslaughter. The drug, 3-Bromopyruvate, is believed to "starve" tumor cells to death by inhibiting glycolysis, the breakdown of glucose molecules. So far, human efficacy data are anecdotal; a U.S. company named PreScience Labs has received approval from the U.S. Food and Drug Administration for a phase I clinical trial, but that study has yet to begin. **http://scim.ag/cancersusp**

China builds cosmic ray array

SICHUAN PROVINCE, IN CHINA | Construction has begun on a new $180 million array of cosmic ray detectors in southern China. Situated on Haizi Mountain, the Large High Altitude Air Shower Observatory (LHAASO) will study cosmic rays that originate mainly within our galaxy. The observatory, to be completed in 2020, will cover 100 hectares with 6366 particle detectors to snare the avalanches of subatomic particles triggered when a high-energy cosmic ray crashes into the atmosphere. The LHAASO will also contain a core of 3000 so-called water Cherenkov detectors, which excel in telling one type of charged particle from another, as well as 12 telescopes to look for light generated by the particles passing through the night air. Compared with competing instruments, such as the High-Altitude Water Cherenkov Gamma-Ray Observatory near Puebla, Mexico, the LHAASO should have better sensitivity at high energies, enabling it to probe the crossover from galactic cosmic rays to even more energetic extragalactic cosmic rays, which are studied with far bigger arrays.

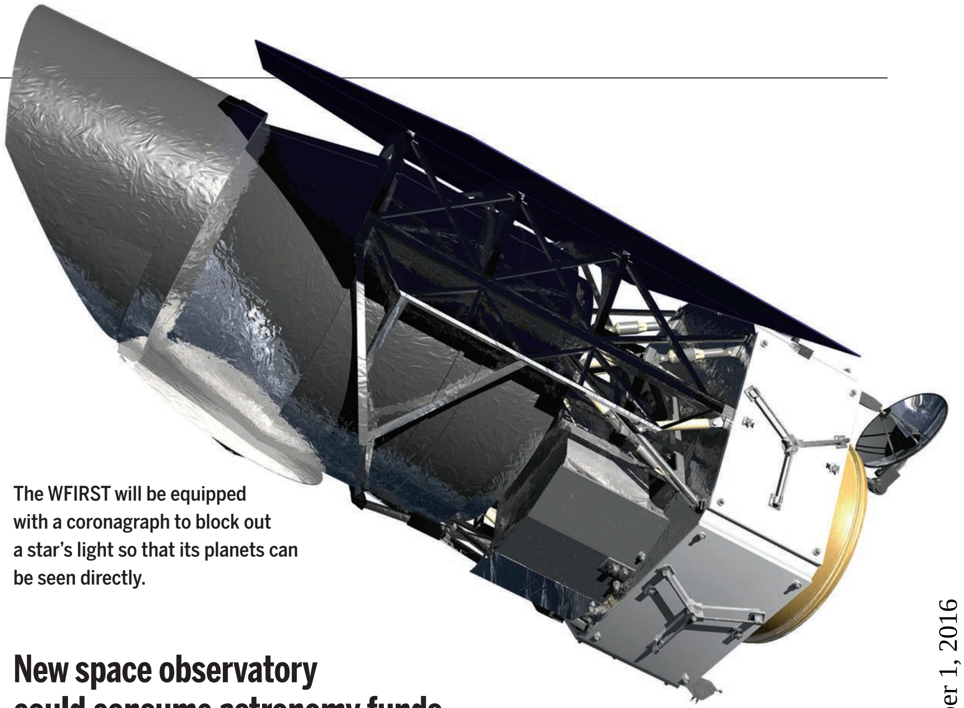

The WFIRST will be equipped with a coronagraph to block out a star's light so that its planets can be seen directly.

New space observatory could consume astronomy funds

Astronomers in the United States are wary that the Wide Field Infrared Survey Telescope (WFIRST), a mission to study cosmic acceleration, exoplanets, and other things, could balloon in cost and scope like the budget-busting $8 billion James Webb Space Telescope (JWST). So says a 14-member panel tasked by the National Academies of Sciences, Engineering, and Medicine with reviewing progress in the priorities set by the 2010 decadal survey of the field, known as *New Worlds, New Horizons in Astronomy and Astrophysics*. Overall, the panel was pleased with the progress made on a variety of scientific fronts, particularly in the study of exoplanets and gravitational waves. But they worried that large projects, combined with stagnant budgets at the National Science Foundation and NASA, may siphon away money from midsized projects and grants to individual investigators. The JWST's budget problems have also produced delays in the WFIRST project, the top-ranked space priority in the decadal survey; it is now set for a 2025 launch, 5 years later than expected. **http://scim.ag/astrosurvey**

FINDINGS

Mediterranean's ancient sea floor

Most of the ocean crust now found on Earth's surface is less than 200 million years old; anything older was long ago dragged into the mantle by the subduction of tectonic plates. But beneath a stretch of the eastern Mediterranean Sea between Cyprus, Crete, and Egypt known as the Herodotus Basin, there are patches of sea floor dating to about 340 million years old—the oldest ocean crust on Earth that remains under the sea (rather than outcropped on land), researchers reported online this week in *Nature Geoscience*. In 2012 and 2014, researchers aboard the *RV Mediterranean Explorer* dragged a magnetometer in parallel tracks along this patch of sea. The magnetometer recorded seafloor signatures resembling the striped

The world's oldest sea floor lies beneath the eastern Mediterranean Sea.

IMAGES: (TOP TO BOTTOM) NASA WFIRST PROJECT/DOMINIC BENFORD FROM BROOKE HSU/WIKIMEDIA COMMONS; GOOGLE EARTH

patterns seen at midocean spreading centers, where alternating magnetic orientations are imprinted on solidifying oceanic crust as Earth's magnetic field flip-flops over time. From these patterns, the researchers estimate that the Herodotus Basin is 315 million to 365 million years old—and was likely part of the Tethys Ocean, an ancient sea that once bordered the supercontinent Pangaea.

Studying Iceman's style

Two decades ago, a pair of tourists discovered a 5300-year-old mummy preserved in an alpine glacier. The so-called Iceman, nicknamed Ötzi, was unearthed wearing leather clothing, carrying a leather quiver, and sporting a fur hat to top it all off. Now, a team of researchers from the European Academy of Bozen/Bolzano in Italy and University College Dublin has taken a close look at those garments to determine what animals they were made from, in hopes of learning more about how the ancient man lived. The researchers sequenced the mitochondrial DNA of nine samples from the clothes and quiver. As detailed in *Scientific Reports*, the sequences showed that Iceman's getup represented five different species: goat leather leggings, a sheep hide loincloth, a roe deer quiver, cattle hide shoelaces, a brown bear fur hat, and a heavy coat made of goat and sheep hides haphazardly stitched together. Leather made of livestock skins wasn't a surprise (people from Ötzi's era were thought to be farmers), but the bear and deer garments were—they suggest Iceman and his people also hunted wild animals.

Ötzi's shoes had an inner grass netting layer (right), an outer deerskin layer, and a bearskin sole.

Olga Vyatkina visits the grave of her son, who was killed by anthrax in the 1979 outbreak.

Anthrax genome reveals secrets of 'biological Chernobyl'

On 2 April 1979, a plume of anthrax spores was accidentally released from a secret bioweapons facility in the Soviet city of Sverdlovsk. The cloud of spores drifted southeast on the wind for 50 kilometers, killing at least 66 people in one of the deadliest human anthrax outbreaks ever. Now, scientists have isolated the pathogen's DNA from the bodies of two human victims and pieced together its entire genome. This answered a lingering question: Soviet scientists didn't tinker with the anthrax strain to make it more resistant to antibiotics or vaccines, the team reports in the study, which is under review at the journal *mBio* and was released this week on the preprint server bioRxiv. Such tinkering would have made the bioweapons even more lethal. Many other questions linger about the outbreak in Sverdlovsk (today called Yekaterinburg, in modern Russia), however, such as how the cloud was released from the facility and whether Russia has fully ended the program, as it officially agreed to do in 1992. But the new study should help scientists determine whether any future anthrax outbreak is from a leftover Soviet weapon.

NEWSMAKERS

Three Qs

The Amazon faces a new wave of deforestation as Brazil, Peru, and other Amazonian countries plan hundreds of infrastructure projects—dams, roads, railroads, and more. Deforestation threatens biodiversity as well as the Amazon's role as the world's largest terrestrial carbon sink. Biologist **Thomas Lovejoy** of George Mason University, Fairfax, in Virginia, one of five new U.S. science envoys appointed jointly by the White House and the Department of State to promote scientific collaboration between the United States and other countries, spoke with *Science* about his role, which he plans to use to improve understanding of the Amazon's climate dynamics. http://scim.ag/LovejoyQA

Q: What do you consider the greatest threat to the Amazon?

A: The intersection between uncoordinated infrastructure and the hydrological cycle. The Amazon makes half of its own rainfall [through evapotranspiration], and the water recycles five or six times as it crosses the basin. [Deforestation disrupts] the hydrological cycle [and] is going to have effects on the weather system within the continent and perhaps even beyond. With the droughts of 2005, 2010, and the current one … I think we're seeing flickers of the potential tipping point [from carbon sink to source].

Q: Do we know where the tipping point will be?

A: One estimate is at about 40% deforestation. But that doesn't include other impacts on the hydrological cycle from climate change itself and the widespread use of fire.

Q: What do you see as research priorities?

A: How to design sustainable infrastructure. Also, a better understanding of biodiversity distribution patterns. At least in the eastern two-thirds of the Amazon, we're finding that there's a lot of undiscovered biodiversity … that needs to be looked at.

PHOTOS: (TOP TO BOTTOM) INSTITUTE FOR MUMMIES AND THE ICEMAN; LYNN JOHNSON/NATIONAL GEOGRAPHIC CREATIVE

A breach of Spirit Lake's debris dam (middle right) could in minutes or hours launch a flood five times the flow of the Columbia River.

PHOTO: BARRY MAAS/FLICKR

NATURAL HAZARDS

A debris-dammed lake threatens a flood

Engineers ponder fixes to Spirit Lake, bottled up 36 years ago by Mount St. Helens

By **Robert F. Service**, *in Kelso, Washington*

Mount St. Helens blew its top 36 years ago, but one of the hazards it spawned is again posing a threat.

In January, emergency crews raced to save an engineered tunnel built 3 decades ago to keep nearby Spirit Lake from breaching a natural dam of volcanic debris. A rupture could send a wall of water and mud downstream that would likely wipe out several towns and kill tens of thousands of people. The 2.6-kilometer-long tunnel, which had begun to collapse, was closed for 10 weeks so engineers could rebore a 10-meter-long section and bolster it with steel ribs. During the closure, Spirit Lake rose 6 meters, about halfway to a dangerous level where water could start cutting through the soft top of the dam.

In March, the tunnel reopened and lake levels soon dropped to normal. But the fix is a stopgap, sure to fail again. Earlier this month, a panel of experts set up by the U.S. National Academy of Sciences (NAS) gathered here to explore better ways to avoid devastation. The panel's report, due in June 2017, will help federal land management agencies navigate the pros and cons of more permanent fixes. Any decision will be controversial; one option—cutting a surface channel through the debris to drain the lake—could improve downstream fish habitat but would also allow more sediment to spill into the river, threatening farms and a major river port. "There is not going to be one answer that makes everyone happy," says Gina Owens, forest supervisor for the Gifford Pinchot National Forest in Vancouver, Washington.

When Mount St. Helens exploded in 1980, the blast not only blew ash nearly 20 kilometers high, but also sent an avalanche of rock, sand, and gravel barreling down the mountain's north slope. Some of that debris slammed into Spirit Lake, raising the lake bottom 64 meters and plugging the north fork of the Toutle River, Spirit Lake's previous outlet.

> ***"It would cause a flood so big you just don't want to know."***
>
> **Thomas Dunne**, University of California, Santa Barbara

With no outlet, rain and snowmelt swelled Spirit Lake, raising fears of a breach that would launch, in hours or minutes, a surge of water five times the average flow of the mighty Columbia River. "It would cause a flood so big you just don't want to know," says Thomas Dunne, a panel member and geomorphologist at the University of California, Santa Barbara.

In fact, it has happened before. Spirit Lake has repeatedly punctured debris dams from earlier eruptions, says Jon Major, a hydrologist with the U.S. Geological Survey in Vancouver, Washington. One such event some 3350 years ago appears to have inundated the area where the towns of Kelso, Castle Rock, and Longview now sit, more than 60 kilometers away in the Cowlitz River valley, under 20 meters of water and mud.

Hoping to avoid a similar disaster, the U.S. Forest Service (USFS), which oversees federal management of Mount St. Helens, contracted with the U.S. Army Corps of Engineers soon after the eruption to come up with a solution. In 1984, corps engineers bored a tunnel from Spirit Lake through a ridge to the north into south Coldwater Creek, a neighboring tributary.

The problem is that the ridge's bedrock is interrupted by squishier rocks and by faults, where the earth slips during the frequent small earthquakes that rattle the flanks of the volcano. In one 100-meter-long tunnel section, where the stout basalt bedrock meets a much softer volcanic tuff, a routine maintenance check in 2015 revealed that earthquakes had pushed the ground upward by nearly 1 meter in spots, blocking one-quarter of the tunnel's normal diameter.

This year's emergency repairs, together with two other past fixes for similar problems, have run up a cost of about $7 million. Each time, USFS has raided its budget to come up with the funds. So after this year's go-around, the forest agency asked NAS whether it could offer suggestions for a more permanent solution.

One idea discussed at the meeting would be to completely rehab the problematic 100-meter section of the tunnel, adding the reinforced steel ribs throughout. But that would likely cost tens of millions of dollars and force extended shutdowns of the tunnel over a period of years, Major says. Another option would be to add a second tunnel, creating a backup outlet. Many favor a third option, which would be the most controversial: cutting a channel through the debris field and either lining it with concrete or allowing the water to craft a new river channel over time.

That's what the corps did at nearby Coldwater Lake, when it was also hemmed in by debris from the eruption. Owens says that today its engineered channel is beginning to look like a natural river channel. Nicole Budine favors a similar solution for Spirit Lake. "We'd like natural processes to be restored as much as possible with respect to public safety," says Budine, the policy and campaign manager for the Gifford Pinchot Task Force in Portland, Oregon, an environmental group that works on the national forest that contains Mount St. Helens. Others add that a more natural stream flow off the mountain might help restore fish habitat that was wiped out by the eruption and subsequent rerouting of streams.

The tradeoff, however, is that an open stream would almost assuredly increase the amount of sediment washing down the valley from the debris dam. Already, sediment levels in nearby rivers are 10- to 50-fold higher than pre-eruption levels because of loose debris washing downhill, which models suggest is likely to continue for decades, if not centuries. "This is the new normal," says Youssef Hashash, an NAS committee member and geotechnical engineer at the University of Illinois, Urbana-Champaign.

Much of the sediment settles out in the Toutle and Cowlitz rivers. The Cowlitz is surrounded by fertile farmland and lined with levees to prevent routine winter storms from sending floodwaters over the banks. Increased sediment in the Cowlitz would raise the riverbed, increasing the chances of flooding and levee failure. Farther downstream is the Port of Longview, at the confluence of the Cowlitz and Columbia rivers. Corps engineers already spend millions of dollars every other year to dredge the rivers, which makes the prospect of more sediment unwelcome.

Sediment loads are already a big enough problem that the corps built a 56-meter-high dam to trap them, on the north fork of the Toutle River 30 kilometers downstream from the possible new Spirit Lake outlet channel. The dam is already near capacity, and the corps is considering raising the lip of the dam to trap additional sediment. But the runoff from the mountain keeps coming.

"These aren't problems that are going to go away," says Gordon Grant, a hydrologist with USFS's Pacific Northwest Research Station in Corvallis, Oregon. Living in the shadow of Mount St. Helens will never be easy. ■

In March, engineers reopened a tunnel that drains Spirit Lake after completing repairs to a 10-meter section.

PHOTO: PORTLAND CORPS/FLICKR

ARCHAEOLOGY

Bones record demise of Andean state

Violent death surged as drought and political turmoil doomed the Wari

By **Lizzie Wade***, in Lima*

When the end came for the first Andean empire, it wasn't pretty. The Wari state controlled most of the Peruvian highlands and coast, integrating disparate cultures and building a network of roads that the Inca would later repurpose for their own empire. But its collapse around 1000 C.E. amid a severe drought unleashed centuries of violence and deprivation, according to new research presented here last week at the World Congress on Mummy Studies.

The work, by Tiffiny Tung, a bioarchaeologist at Vanderbilt University in Nashville, traces violence and hardship so intense that they left a vivid record in people's bones. It combines cutting-edge methods to paint a detailed picture of a centuries-long social breakdown, and how state collapse can lead to indiscriminate violence. "When the state declined, novel ideas emerged regarding who could engage in violence, who could be targeted in violent acts, and how deadly those attacks might be," Tung reported.

"I was really impressed" by the work, said Maricarmen Vega, a bioarchaeologist at the Pontifical Catholic University of Peru here, who studies violence in pre-Columbian societies along the Peruvian coast. Tung's analysis of skeletons from during and after the collapse, in which she tallied injuries and tracked changes in bone chemistry, "goes beyond the traditional studies of trauma."

Beginning around 600 C.E.—800 years before the rise of the Inca—the Wari swept out of their capital of Huari in Peru's southern highlands and conquered nearly the entire Peruvian Andes and coast. Sometimes they used force and took captives; other times they expanded peacefully by building irrigation canals in dry regions and extending the benefits of agriculture to the people there. But by 1000, political infighting, perhaps abetted by the intensifying drought, had cracked apart the Wari state.

Excavating Huari, Tung found grisly clues

In their heyday, the Wari honored their dead with fabric wrappings and funerary masks.

Tung found grisly clues to what life was like for Wari's former subjects during and after the empire's fall. She compared skulls found at two sites in the city. The bones at one site were radiocarbon dated to between 897 and 1150, around the tail end of the Wari empire. The bones at the other dated from 1270 to 1390, several centuries after the Wari collapse.

Even in their heyday, the Wari were no strangers to violence. In earlier work, Tung had studied their practice of decapitating captives from conquered communities to create mummified trophy heads. But as long as the empire was strong, the violence was ritualized and limited. From previous excavations, Tung found that in imperial Huari, only 20% of adult skulls had healed skull fractures, which are evidence of nonlethal head injuries, and barely any had suffered fatal wounds. During and immediately after the collapse, however, nearly 60% of adults of both sexes and 38% of children showed signs of nonlethal head injury.

Centuries later, life in Huari had gone from bad to worse. Rates of nonlethal head trauma hadn't changed much, but fatal injuries had skyrocketed. At the time of the collapse, only 10% of adults had died of a head injury, but now the rate of fatal head injury had risen to 40% among adults and 44% in children. "Violence becomes much more deadly," Tung said in her talk. "These violent deaths aren't from random outbreaks of community brawls. This is much more systematic, lethal violence, but it's unclear at this time if it's from civil war or warfare with those perceived as outsiders."

Diets also seem to have deteriorated in the generations after the collapse, reported Theresa Miller, a chemical engineering student at Vanderbilt who worked with Tung. The mainstay of the Wari diet had been maize, which left a signature ratio of carbon isotopes in their bones. They also ate meat from domesticated camelids like alpacas and llamas, which left a distinctive ratio of nitrogen isotopes. Analysis of the carbon isotopes in bone collagen showed that immediately after the collapse, men, women, and children continued to eat a diet rich in maize, and their protein consumption also held steady.

Several hundred years later, Miller found, men and children were still eating plenty of maize—but women's carbon isotopes had changed drastically, indicating that for them, the staple crop was off the menu. At the same time, the whole population's nitrogen levels shot up. That could mean that they were eating more fish, possibly from increased trade with the coast, or were fertilizing their crops with guano or manure, Miller said. But high nitrogen levels can also be a sign of starvation, generated as the body burns through its own fat and muscle for fuel. By this time, core samples from Andean glaciers and lakebeds show, the drought had been going on for centuries, with what was probably a devastating impact on agriculture.

The social breakdown extended to the treatment of the dead, Tung reported. Many pre-Columbian Peruvian cultures, including the Wari, carefully bundled their dead in layers of textiles and buried them with offerings. In contrast, Tung said, the post-Wari skeletons were discovered jumbled in a ditch along the outside wall of what was once a ritual space. Many bones showed cut marks, indicating that their flesh had been stripped off. It's possible that "part of the attack on the individuals includes the desecration of their bodies," Tung said.

Rick Smith, a doctoral student in anthropology at the University of Texas, Austin, is now looking for other molecular indicators of stress in the bones from Huari. In modern people, chronic stress and violence are known to boost chemical changes in DNA known as methylation, and Smith is looking for the same pattern in ancient genetic material recovered from Tung's skeletons. He is hoping for new insights into life and health during the Wari collapse, such as whether the effects of stress were passed down through generations.

In her talk, Tung pointed out that violence hadn't always been Wari's answer to environmental stress. In fact, the Wari built their empire during a previous drought, thanks in part to their mastery of complex irrigation techniques. But she speculates that once the political system broke apart, the Wari could no longer cope with the increasingly harsh climate. "It's a one-two punch," she said. "The drought is layered on top of these other really intense changes."

Tung now hopes to find skeletons from other times during and after the Wari collapse to pinpoint the moment when the residents of Huari tipped from social cooperation into indiscriminate violence—and perhaps link it to a specific environmental or social shift. "It's the type of research we need," said bioarchaeologist Kenneth Nystrom of the State University of New York at New Paltz, who has worked in Peru and studies the bones of marginalized populations. "Looking at the varying human response to environmental change. … What could be more relevant?" ■

Holding the high ground

The Wari expanded from their capital to dominate much of Peru's mountains and coast.

CREDITS: (PHOTO) AP PHOTO/KAREL NAVARRO; (MAP) G. GRULLÓN/SCIENCE

Corrected 24 August 2016; see full text.

Massive vaccination campaigns like this one in 2010 beat back polio in Nigeria but did not eliminate it.

PHOTO: ZUMA PRESS INC./ALAMY STOCK PHOTO

INFECTIOUS DISEASE

New polio cases in Nigeria spur massive response

Country's hopes for polio-free status are dashed

By **Leslie Roberts**

The world reeled last week when Nigeria reported that, after a 2-year absence, polio had resurfaced in the northern state of Borno. The news of the two new cases hit just as Nigeria and the global community were celebrating 2 years without a wild-type polio case in a country that until recently accounted for half of all cases in the world. The setback has triggered massive emergency vaccination campaigns in Nigeria and neighboring countries.

The outbreak didn't come as much of a surprise to those who have long been trying to eradicate the virus, however. Much of Borno is under control of the ruthless terrorist group Boko Haram, vaccinators have been unable to reach hundreds of thousands of children, and the insurgency has disrupted surveillance for the virus, which appears to have been circulating undetected for years. "This is what keeps people in polio eradication up at night—the worry that polio virus could be lurking in the insecure parts of Borno and Somalia," says Steve Cochi, the point person for polio eradication at the U.S. Centers for Disease Control and Prevention (CDC) in Atlanta.

Cochi mentions another factor: complacency. With Nigeria off the list of endemic countries—only Afghanistan and Pakistan remain—eradication leaders have been optimistic they would stop transmission worldwide in 2016, bringing them tantalizingly close to the end of the 28-year, $14 billion eradication effort. But there were signs that, after its hard-won success, the government of Nigeria was letting down its guard. "It is not surprising that attention would slip after 2 years without a case," says Michel Zaffran, the new director of polio eradication at the World Health Organization (WHO) in Geneva, Switzerland. "You lose political commitment very quickly when a disease appears to have disappeared," Cochi agrees.

A 4-and-a-half-year-old girl named Aisha in Jere district was the first new case. In May, her extended family had escaped from Boko Haram–controlled territory and trekked 2 days to the Muna camp for internally displaced persons in Jere, according to Zaffran. The girl, who became paralyzed on 6 July, has recovered "and now walks without a limp," he says. Health officials are still investigating the second case, a 12-month-old boy who was paralyzed on 13 July in Gwoza district, not far from Chibok, where Boko Haram abducted more than 200 schoolgirls in 2014.

CDC scientists quickly sequenced viral isolates from the two cases. Both viruses are closely related to one last seen in Borno in 2011, suggesting that polio has persisted there for 5 years. Cochi and others fear the virus has spread widely throughout the countries of the Lake Chad region. "The borders are all insecure," he says.

Because of the 2-year respite, many of the government experts who led the battle to wipe out the virus in Nigeria have moved on. "New people will have to come to grips with the problem," says Muhammad Pate, the former minister of state for health who headed the country's polio effort (*Science*, 4 October 2013, p. 28) and who is now an adjunct professor at Duke University in Durham, North Carolina. The presidential task force on polio eradication he used to chair hasn't convened in at least a year. Although the central government has budgeted money for polio eradication this year, it has not yet released it, and interest among some local government officials had been waning.

Pate worries that people will attribute the outbreak to insecurity alone and "might miss the significance of this as a wake-up call to be more diligent when there are no cases." That means making sure that each campaign is meticulously executed, monitoring every vaccinator, and using real-time data from one vaccination round to plan the next.

Vaccination campaigns began on 15 August in Borno. A second campaign is scheduled to launch 27 August across four northern states, with the goal of reaching 4 million to 4.5 million children under 5. Chad, northern Cameroon, southern Niger, and parts of the Central African Republic will synchronize campaigns. Already helicopters are flying vaccine into hard-to-access areas like Gwoza, and "the next step is to airlift vaccinators because the road is not safe," says Alhaji Samaila Muhammad Mera, the emir of Argungu in Kebbi state and the deputy chairman of the Northern Traditional Leaders Committee on Primary Health Care. In one bit of good news, the military recently wrested control of large swaths of Borno from the insurgents, which may enable vaccinators to reach what were previously "no-go" zones.

Traditional and religious leaders, who have been pivotal in convincing suspicious populations to accept polio vaccination, are mobilizing quickly, Mera says. Because the camp where the girl was diagnosed is close to Maiduguri, Borno's densely populated capital, "we need to do something there very quickly," he says. "There is so much at risk."

WHO's Zaffran says the speed and magnitude of the response bode well for quashing the outbreak quickly. "I personally believe we can still interrupt transmission worldwide in 2016." Bruce Aylward, the longtime leader of the global initiative who more recently ran WHO's Ebola response, says program leaders should be ready for more setbacks. "You are dealing with the tail end of a huge eradication effort … this is when the virus will do everything to depress, demoralize, and derail you," he says. "Are we as committed to its extinction as it is to surviving?" ■

Published by AAAS

SYNTHETIC BIOLOGY

Mission possible: Rewriting the genetic code

A research team is making steady progress at overhauling a bacterium's genome

By **John Bohannon**

The term "life hacking" usually refers to clever tweaks that make your life more productive. But on p. 819, a team of scientists comes a step closer to the literal meaning: hacking the machinery of life itself. They have designed—though not completely assembled—a synthetic *Escherichia coli* genome that could use a protein-coding scheme different from the one employed by all known life. Requiring a staggering 62,000 DNA changes, the finished genome would be the most complicated genetic engineering feat so far. *E. coli* running this rewritten genome could become a new workhorse for laboratory experiments and a factory for new industrial chemicals, its creators predict.


Biologists are transforming the proteinmaking instructions of *Escherichia coli*.

ILLUSTRATION: C. BICKEL/SCIENCE

Such a large-scale genomic hack once seemed impossible, but no longer, says Peter Carr, a bioengineer at the Massachusetts Institute of Technology Lincoln Laboratory in Lexington who is not involved with the project. "It's not easy, but we *can* engineer life at profound scales, even something as fundamental as the genetic code."

The genome hacking is underway in the lab of George Church at Harvard University, the DNA-sequencing pioneer who has become the most high-profile, and at times controversial, name in synthetic biology (*Science*, 2 September 2011, p. 1236). The work takes advantage of the redundancy of life's genetic code, the language that DNA uses to instruct the cell's protein-synthesizing machinery. To produce proteins, cells "read" DNA's four-letter alphabet in clusters of three called codons. The 64 possible triplets are more than enough to encode the 20 amino acids that exist in nature, as well as the "stop" codons that mark the ends of genes. As a result, the genetic code has multiple codons for the same amino acid: the codons CCC and CCG both encode the amino acid proline, for example.

Church and others hypothesized that redundant codons could be eliminated—by swapping out every CCC for a CCG in every gene, for instance—without harming the cell. The gene that enables CCC to be translated into proline could then be deleted entirely. "There are a number of 'killer apps'" of such a "recoded" cell, says Farren Isaacs, a bioengineer at Yale University, who, with Church and colleagues, showed a stop codon can be swapped out entirely from *E. coli* (*Science*, 18 October 2013, p. 357).

The cells could be immune to viruses that impair bioreactors, for example, if crucial viral genes include now untranslatable codons. The changes could also allow synthetic biologists to repurpose the freed redundant codons for an entirely different function, such as coding for a new, synthetic amino acid.

For this study, Church's team decided to eliminate seven of the microbe's 64 codons. That target seemed like "a good balance" between the number of changes that appeared technically achievable and the number that might be too many for a cell to survive, says Matthieu Landon, one of Church's Ph.D. students. And the seven spare codons could eventually be repurposed to code up to four different unnatural amino acids.

But making so many changes, even with the latest DNA editing techniques such as CRISPR, still appeared impossible. Luckily, the cost of synthesizing DNA has plummeted over the past decade. So instead of editing the genome one site at a time, Church's team used machines to synthesize long stretches of the recoded genome from scratch, each chunk containing multiple changes.

The team has now turned to the laborious job of inserting these chunks into *E. coli* one by one and making sure that none of the genomic changes is lethal to the cells. The researchers have only tested 63% of the recoded genes so far, but remarkably few of the changes have caused trouble, they say.

Does this progress report from Church's lab put biologists on the doorstep of a new era of virus-free bioengineered cells? "More likely on the driveway than the doorstep," Isaacs says. Carr agrees. "The upcoming phases of synthesis, testing, and assembly are likely to take several years," he says. "The toughest 5% of the design may end up requiring 95% of the effort."

In the meantime, another issue is likely to dominate discussions: safety. One concern is that many of the "unnatural" proteins that the recoded *E. coli* could be engineered to produce may be toxic, and the cells' resistance to viruses would give them a competitive edge if they escaped into the environment—or into our own guts. "As we get closer to full multivirus resistance, this becomes more critical," Church acknowledges.

The failsafe that Church plans to build into the microbes is superficially similar to the one used to control the bioengineered dinosaurs in the film *Jurassic Park*. Those resurrected creatures couldn't survive without a special nutrient supplied by their human masters—that is, until they found a source of the nutrient in the wild. In a study published in *Nature* last year, Church demonstrated a failsafe system for engineered microbes that should be far more robust. Not only does the required nutrient not occur naturally, but it appears to be virtually impossible for the cells to overcome the barrier through mutation or mating with normal cells in the wild.

Whether others will agree with Church that his failsafe is unbeatable remains to be seen. "The term 'safe' needs a lot more scrutiny," Carr says. "Instead of the all-or-nothing connotations of 'safe' or 'not safe,' it is more useful to describe degrees of risk." ■

Published by AAAS

OPEN ACCESS

Chemists to get preprint server of their own

American Chemical Society launches ChemRxiv despite dubious precedents

By **Paul Voosen**

Call it a chain reaction. Following the leads of the physics, mathematics, social science, and biology communities, the American Chemical Society (ACS) announced on 10 August that it will start a preprint server for chemistry papers, tentatively titled ChemRxiv.

The site will be modeled after arXiv, the decades-old server that has provided a home for preliminary research in physics, mathematics, and computer science, and bioRxiv, which began to do the same for biology 3 years ago. But it will be the first preprint server begun by a professional scientific society, groups that have historically been concerned about the impact of free preprint servers on the revenue they derive from traditional journal publishing. ACS is chemistry's dominant professional organization and one of its leading publishers.

The emergence this year of ASAPbio, a loose coalition of high-profile biologists who have embraced preprints, drove the society to action, says Kevin Davies, vice president of the society's publications division in Washington, D.C. There was also an element of disciplinary peer pressure: "It would be somewhat bizarre," he says, "if chemistry was left too much longer as the sole major scientific field that lacked a major preprint server." ACS has invited other organizations to become co-organizers or sponsors of the new service, which will likely be a prime topic of conversation at the society's fall meeting later this month in Philadelphia, Pennsylvania.

Chemistry has long had a culture that prizes the close holding of data and scientific results until peer review and final publication. Many editors would reject papers that had appeared as preprints, counting that appearance as prior publication. That culture helped doom an effort by Elsevier, the for-profit publishing giant and a major rival to ACS, which 16 years ago tried to start its own chemistry preprint server through its ChemWeb subsidiary (*Science*, 1 September 2000, p. 1445). (Elsevier hasn't given up: In May, it bought the Social Science Research Network, the leading site for social science discussion papers.)

> ***"It's always heartening to see other disciplines belatedly joining the late 20th century."***
> **Paul Ginsparg**, arXiv founder

Davies believes a professional organization provides a natural fit for a preprint server. Although ACS has not formally polled its membership, he adds, most of its advisers and journal editors support ChemRxiv. The initiative was first proposed by Laura Kiessling, a chemistry professor at the University of Wisconsin, Madison, and editor-in-chief of *ACS Chemical Biology*, during a society retreat in January.

Twenty of ACS's 50 journals now routinely accept papers that first appeared as preprints, whereas another dozen require the authors to discuss the fact with an editor. The rest still reject such studies. Each journal will have the authority to decide whether to participate in the preprint service, says Davies, who predicts that some areas of chemistry will be slower than others to embrace the idea. (*Science* and *Nature*, among many others, now publish papers that first appeared as preprints.)

"It's always heartening to see other disciplines belatedly joining the late 20th century," says Paul Ginsparg, arXiv's founder and a physicist at Cornell University. "And it's refreshing to see more experimentation in this space."

Ginsparg worries that the imprimatur of ACS on the new service could make some chemists with papers intended for non-ACS journals less likely to participate, fearing that their papers' appearance on the service would bias other editors against their work. That dynamic may be one reason why Nature Precedings, intended as a preprint server for the life sciences, struggled for 5 years and finally closed in 2012.

In biology, many authors still avoid preprints out of the fear that editors would consider their study previously published and reject it, says John Inglis, executive director of Cold Spring Harbor Laboratory Press in New York, which founded bioRxiv. But bioRxiv has grown steadily, he notes, fueled by the rising emphasis on transparency combined with the creeping pace of peer review.

ChemRxiv's success will hinge on recruiting prominent members of subdisciplines and avoiding competition, Ginsparg says. ACS does not expect to derive revenue from ChemRxiv, Davies says, and the society is optimistic that the server can be supported without adding staff.

Beyond ChemRxiv, 2016 has seen the start of engrXiv and SocArXiv, for engineering and social science, respectively, supported by the Center for Open Science, the team behind the Reproducibility Project, an effort to replicate 100 psychology experiments. There are hints that a server for psychology, PsyArXiv, is also on the way. Ginsparg notes that, unlike ChemRxiv, these servers will properly imitate arXiv's name, where "X" marks the Greek letter chi. ■

The American Chemical Society is starting a preprint service despite an earlier failed Elsevier effort.

PHOTO: NORDRODEN/ISTOCKPHOTO

OF MICE AND MICROBES

The zoo of bacteria and viruses each lab animal harbors may confound experiments

By **Kelly Servick**

In the first experiment, Laura McCabe's lab seemed to hit a home run. The physiologist and her team at Michigan State University (MSU) in East Lansing were testing how a certain drug affects bone density, and they found that treated lab mice lost bone compared with controls. "I was thinking, 'Hey, great! Let's repeat it one more time to be certain,'" McCabe recalls.

They ordered a seemingly identical batch of mice—same strain, same vendor—and kept them under the same conditions: same type of cage, same bedding, same room. This time, however, treated mice gained bone density. "Maybe one was a fluke," McCabe thought. They did a third run—and saw no effect at all. She was baffled.

She knew that signals from the gut can affect how bone forms and gets reabsorbed, so her team took fecal samples from control mice in each of the three experiments and analyzed their gut microbes. They found something unexpected: Each group had a different microbial makeup to begin with.

McCabe has no idea where the mice acquired their distinct gut bacteria—from the containers that ferried them from the vendor? From a technician's clothing? But how the drug affected her subjects clearly depended on what already lived inside them.

It's easy to see how such effects could make it difficult to replicate experiments, a concern that has roiled fields from psychology to cancer. A few years ago, two pharmaceutical companies reported that they could not replicate the vast majority of academic findings in preclinical experiments (*Science*, 26 June 2015, p. 1411). Pressure to publish and a bias against negative results account for some replication problems. But other failures to replicate likely have "practical explanations: different animal strains, different lab environments or subtle changes in protocol," as Francis Collins and Lawrence Tabak, director and principal deputy director, respectively, of the U.S. National Institutes of Health (NIH) in Bethesda, Maryland, wrote in *Nature* in 2014. In other words, sometimes a study doesn't hold up because the replicator is unknowingly performing a slightly different experiment.

Increasingly, experimenters are questioning the potential research impact of the microbiome—a term often used to refer to commensal gut bacteria, but which also includes resident viruses, fungi, protozoa, and single-celled archaea species. Rarely even discussed a few years ago, this potential source of variability attracts growing attention at lab animal care conferences, says MSU's attending veterinarian, Claire Hankenson. "We didn't know to look for it before," she says.

ILLUSTRATION: DAVIDE BONAZZI/@SALZMANART

Yet a mouse's microbes can be maddeningly hard to pin down. The species living in a mouse are always changing, impossible to fully standardize, and for the most part unmeasured. Adding to the challenge, researchers are realizing that it may be a bad idea to simply wipe out lab mice's microbial guests, some of which are critical for health and immune responses and help make the animals into robust, meaningful research subjects. How, many researchers wonder, can this variable ever be controlled?


Housing for lab animals is meticulously standardized, but even so, variations in their resident microbes persist.

PHOTO: ANNEDDE/ISTOCKPHOTO

MICE ARE STIRRING on a quiet summer afternoon at Stanford University in Palo Alto, California. Roused from their daytime sleep by human visitors, they fill their room at the Veterinary Service Center with the faint rustle of shredded paper. Their clear, shoebox-sized cages, lining ceiling-high racks arranged like library shelves, represent investigators' best efforts to control every variable that might skew the outcome of studies. These little worlds are meticulously standardized: equal volumes of sterile bedding, steady cycles of light and dark, even a consistent flow of temperature-controlled air. Every cage is attached to two pressurized vents, as if these mice occupied the cabins of their own personal airplanes.

But are these environments as identical as they look? Researchers surprised by inconsistent results wonder what hidden variables may lurk in these cages (see graphic, p. 743). "I think what this [reproducibility] conversation is doing is expanding the variables for investigators to think about," says J.R. Haywood, MSU's assistant vice president of regulatory affairs.

And mice's resident microbes are an emerging concern. The zoo of organisms on and inside each animal can shift for all kinds of reasons, including a change in the formulation of mouse chow, or in the sources of grain or protein within a brand. Cagemates share microbes, thanks to their penchant for eating one another's feces. Some researchers suspect that even stress, such as an early separation from the mother, can also change a mouse's microbial ecosystem.

An explosion of recent studies in both animals and people suggests that resident microbes can influence susceptibility to diseases from HIV to asthma, predispose to obesity across generations, and tinker with how the body responds to drugs. Tying such effects to experimental results is challenging, but some hints have cropped up. In one early example, more than a decade ago, a research team at Pfizer detected an odd change in rats' urine: a sudden shift in the relative concentrations of two compounds produced when the body breaks down food. The change could muddy toxicology studies that rely on urine metabolites to measure how a drug gets broken down in the body. Researchers traced the unusual rat colony to a single room at the vendor's facility, and they restored the original urine composition in a few weeks by cohousing the rats with animals from other rooms. Although back then no one was sequencing rodent microbiomes, the Pfizer team suspected that microbes were responsible.

In a more recent example, last year scientists at the University of Missouri (MU), Columbia, working with a mouse model of multiple sclerosis accidentally reversed the symptoms by adding a common antibiotic to the animals' water. They restored symptoms simply by cohousing their mice with a microbially richer strain, suggesting that the traits they had come to rely on in their research hinged on a delicate balance of mouse microbes.

Veterinary pathologists Craig Franklin and Aaron Ericsson, also at MU Columbia, are trying to account for such effects by measuring and manipulating those microbes. "Even 5 years ago, most people considered doing microbiota analysis untouchable, unless that was the expertise in their lab," Franklin says. But today, more labs are sequencing fecal samples in search of bacterial genes or paying others to do so, he says. His own team offers such analysis for $125 a sample through the NIH-funded Mutant Mouse Resource and Research Center.

Last year, as a first step in defining a "normal" lab mouse microbiome, they analyzed feces from mice from two major vendors. Like all mammal poop, the samples were dominated by bacteria of two phyla: Firmicutes, thought to play a role in the absorption of dietary fats, and Bacteroidetes, associated with high-fiber diets. But the richness of species in a mouse varied between the vendors, as did the abundance of certain microbes.

Mice from one vendor, for example, were notably lacking segmented filamentous bacteria (SFB), a commensal lineage recently shown to help mice produce key antibodies and immune cells in their intestines. This is "a normal symbiont that can have dramatic effects," Franklin says, and its presence or absence could alter studies of inflammatory response. "We don't think that SFB is the lone soldier out there," he adds.

SFB is the dominant microbe of concern for researchers, says Jennifer Phelan, product manager at the commercial mouse supplier Taconic Biosciences in Germantown, New York. But she adds that she fields all kinds of study-specific questions about the contents of mouse guts. "It went from one query per month to … sometimes several per week." In 2014, the company began including the presence of SFB in health reports to customers, and mice are now available with or without it. Phelan also advises scientists to request mice from the same room when they reorder for an ongoing study.

A SOLITARY WHITE MOUSE sits at the bottom of every rack of cages at the Stanford mouse facility. This "sentinel" is another window into the mouse microbial world. Its sole job is to scratch around in its neighbors' filth. Caretakers periodically dump in a tablespoon of soiled bedding from other cages on the rack, then test the sentinel for disease.

The devilish details of rodent husbandry

Variation in an animal's microbiome is just one of a dizzying array of subtle factors that can affect the outcome of mouse experiments.

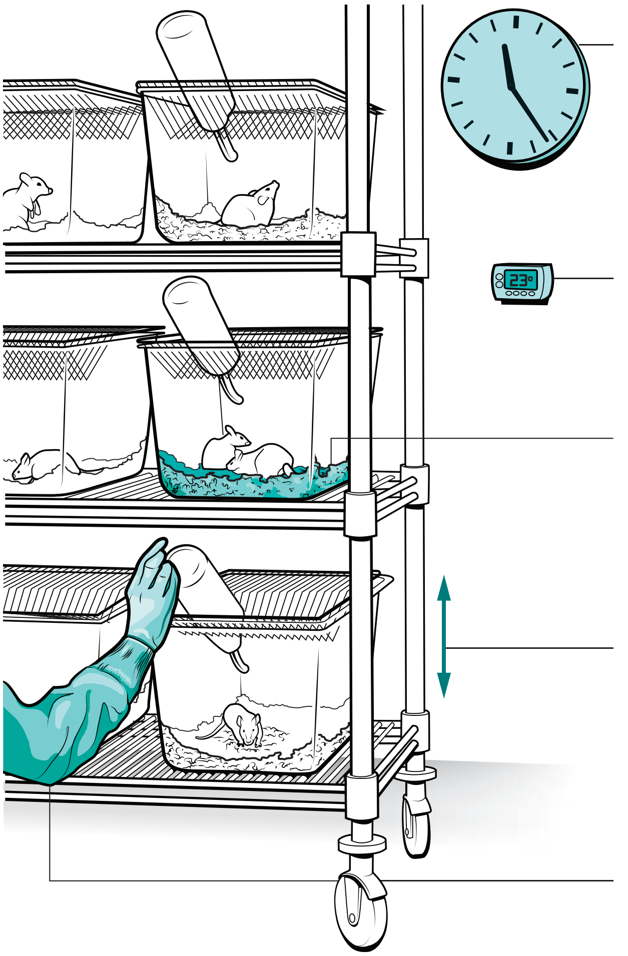

Timing
Circadian rhythms influence how a mouse's immune system responds. Mice exposed to bacteria in the morning versus the evening might have different levels of inflammation.

Temperature
The typical 20°C–26°C in a lab puts mice into a state of mild cold stress, in which they ramp up their metabolism, making them more prone to inflammation and fostering the growth of tumors.

Bedding
Rodent cages are filled with bits of wood, corncob, or paper. But corncob can inhibit estrogen signaling, and some types of wood may boost the activity of a drug-metabolizing enzyme in rats.

Shelf level
Mice on the top shelf were more prone than their downstairs neighbors to develop degeneration of the retina in one study, and slower to develop certain tumors in another.

Experimenter
Mice can distinguish their human visitors by smell. Mice given a painful injection in the presence of men rather than women had higher levels of stress hormones and a milder pain response.

GRAPHIC: V. ALTOUNIAN/*SCIENCE*

A mainstay of lab animal facilities, sentinels can pick up the major pathogens already known to sicken mice or skew results. When infectious agents are detected, facilities like Stanford's scramble to sterilize them away. But Franklin and others suspect that in their zeal to clean up, facilities may have wiped out some of the microbial complexity that makes mice useful models for human disease. Variations in the microbiome may skew results, but a diverse microbiome and exposure to microbes may be critical for some studies.

Earlier this year, a team led by immunologist David Masopust of the University of Minnesota, Twin Cities, tried cohousing lab mice with mice purchased from pet stores. The "dirty" visitors harbored diseases long eradicated from most labs, such as hepatitis and pneumonia. The sudden exposure to these disease-ridden cagemates killed nearly a quarter of the colony, but the survivors began producing a subset of the memory T cells key to fighting infection. They became, the authors argued, a more realistic model of the human immune system.

For immunology studies, the approach may be catching on. "My lab is incredibly excited about this," says Stephen McSorley, an immunologist at the University of California, Davis, School of Veterinary Medicine. Earlier this year, his lab brought in its own "dirty" colony from a company that sells mice as food for zoo animals. He hopes the animals will help him create more realistic mouse models of human chlamydia and salmonella infections.

In ongoing work, Franklin and Ericsson are finding that pet store mice also have highly rich intestinal flora. The prospect that they may offer a better approximation of the human gut than standard lab mice is enticing to some investigators. But introducing untold diseases into animal facilities runs counter to a hard-won culture of cleanliness and to the notion that tightly controlled mice make for more reproducible research. MSU's Hankenson, for one, isn't ready to embrace the pet store model. "To have this proposal, 'Hey don't keep them quite as clean, it's okay if you add a dabble of this and a bit of that back into the mouse.' … It's a little alarming," she says. "We've worked so hard to have very healthy animals for everyone to use."

Short of reimagining the lab mouse, others say, investigators need strategies for monitoring how microbes might be influencing their small research subjects. A first step is to design studies that separate the effects of microbial genes from the genes of their animal host, says Herbert Virgin, an immunologist at the Washington University School of Medicine in St. Louis in Missouri. In June, he and his colleague Thaddeus Stappenbeck argued in *Nature* that all mouse studies should use littermate controls: When studying the activity of a particular gene, breed mice with and without that gene by starting with heterozygous parents. The two groups of offspring will differ only in whether they carry that gene, not in their resident microbes, allowing the influence of the host gene and the microbes to be disentangled.

Virgin also argues that papers should note important details that could affect the microbiome, such as diet and exposure to antibiotics. Franklin predicts that authors will be asked to include fecal microbiome analysis in the material and methods sections of their papers in the next 20 years. But so far, genetic analysis can identify only a fraction of the species in an animal.

For now, adding multiple types of microbiomes to a study—more complexity, more unknown variables—may be the best way to know whether results are likely to hold up across diverse microbial makeups. Franklin's group has created four mouse colonies with different complex microbiota, based on the compositions found in four major vendors. For a few thousand dollars per procedure, they can transfer mouse embryos from other labs into females from each colony, so that the mouse pups pick up the new microbiomes and can be compared to the original strains. So far, no one has taken them up on the offer.

Teasing out messy, microbe-confounded results can not only make a result more reproducible; it may also end up yielding scientific spoils. For MSU's McCabe, the conflicting findings have led her into a whole new study of how microbes help regulate bone density. The mice that lost bone density in her experiment had started with more bacteria associated with inflammation, a clue she's following up. "What seemed a very negative result," she says, "we're going to use as a powerful finding." ■

Biologist Feng Limin—here on his way to check camera traps—helped persuade China to set up the park.

TIGER LAND

China's first national parks include a refuge for the world's largest cat

By **Kathleen McLaughlin**, *in Huangnihe, China*

Feng Limin follows the lives of China's scarcest wild cats like a soap opera fan. He has never encountered one, but thanks to a network of motion-sensing cameras in the forests along China's borders with Russia and North Korea, the biologist has glimpsed a total of 27 Siberian tigers and 42 Amur leopards as they breed and prey on deer and wild boar. The spying has paid off for the big cats. What Feng and his colleagues at Beijing Normal University (BNU) have learned has helped convince the central government to create a 15,000-square-kilometer national park—60% larger than Yellowstone—that could save the cats from extinction.

Feng's studies have indicated that both the Siberian tiger—the world's largest cat, with males weighing up to 300 kilograms—and the Amur leopard face dire threats from poaching, logging, and development. By easing those threats, the park "is likely to be one of the great tiger success stories" in a decade or two, says Dale Miquelle, a world authority on Siberian tigers and director of the Wildlife Conservation Society's Russia Program in Vladivostok.

The big cat park—still unnamed and not yet formally announced—also signals a change in China's attitude toward conservation, often slighted as the country rushed to develop economically. With little fanfare, China is creating its first system of national parks, a major step up in management and funding from the current mishmash of national reserves, semiprotected forests, and provincial parks. About two dozen national parks are planned, and the first four mentioned by state media aim to protect charismatic mammals: Asian elephants, giant pandas, Tibetan antelopes, and, here in the northeast, tigers and leopards. "China now has enough money," Feng says. "We can pay atten-

A motion-sensing camera captured a sight rarely seen: one of the 27 Siberian tigers known to range into northeastern China.

PHOTOS: (TOP TO BOTTOM) YUYANG LIU; BEIJING NORMAL UNIVERSITY

tion to environmental conservation."

Creating parks faces much the same obstacles in China as elsewhere. The central government has to convince local authorities that the parks will not undermine their economies, and locals who made their living by logging or poaching will need help to find other livelihoods. But Rose Niu, chief conservation officer at the Paulson Institute, a Chicago, Illinois–based think tank that is helping design the park system, hopes the Chinese public will embrace the idea. The parks, she hopes, will offer "spiritual healing" to Chinese who have had to endure worsening environmental degradation in recent years.

DEEP IN A MAPLE FOREST in China's Jilin province, Feng's team is scrambling over rough terrain to reach cameras and download photos from one of the 2000 motion-sensing cameras—one of hundreds of such visits they have to make every year. He crouches to unlock the metal frame bolting one camera to the base of a tree and scrolls rapidly through the images. "Pig, pig, deer. No tigers," he says with a shrug and a grin. He stands up, checks under his shirt for ticks, and moves on to the next camera.

China's wild tigers and leopards have long been on the ropes, suffering from hunting and habitat loss. Scientists believe that 20 years ago, both populations were nearing a genetic bottleneck. Numbers have ticked up recently with expanded habitat protection and antipoaching efforts in Russia and China, as the BNU group, led by ecosystem expert Ge Jianping, reported in June 2015 in the journal *Landscape Ecology*. Of the 27 tigers the team is tracking, a handful range entirely in China; a decade ago, it was unclear whether a single big cat remained exclusively on Chinese soil. The Amur leopards' plight is even more precarious, with fewer than 100 left in a tiny boundary-straddling patch of China and Russia.

Siberia has been a lifeline for the big cats. Surveys indicate that Russia's wild tiger population has increased from 40 in the 1940s to 540 today. That number is stable, but has just about maxed out the available habitat in Russia, Feng says. "If they're going to save this population, it's really going to be the Chinese, not the Russians. All the potential land for expansion is on the China side," says David Smith, a tiger expert at the University of Minnesota, Twin Cities, who has worked with Ge's team and visited the proposed park area. "This is really a chance for China to shine in tiger recovery."

China's central government has moved aggressively to help. Since the Communist Party signaled its intention to create a national park system in a 2013 planning document, the government has banned logging in Jilin and Heilongjiang provinces, canceled a highway project that would have bisected big cat habitat, and rerouted a high-speed railway connecting China to Vladivostok, a city on Russia's Pacific coast. In the next few years, the government will consolidate and expand protection across 15,000 square kilometers of prime cat habitat and conservation areas. And local police cleared 80,000 snares set by poachers to catch deer and boar—and incidentally, tigers—during a sweep last year, Feng says.

A last refuge

The dwindling range of China's big cats has spurred the government to create a national park to protect part of the Changbaishan Mountain ecosystem, once a stronghold of the Siberian tiger.

Assisting locals who lose their livelihoods or homes because of the park is critical to its success, planners say. Big cats are finicky about their habitat, he notes, so even seemingly minor intrusions such as gathering pine nuts and frog farming can alter their behavior. "The devil will be in the details," says Miquelle, who will meet with Chinese scientists and officials in August to discuss the park.

At the big cat park alone, planners hope to turn 30,000 former forest workers—loggers, hunters, and even poachers—into park rangers and conservation workers. In the Huangnihe conservation district, a patchwork of old growth forest and reforested former logging areas adjacent to Jilin's two main tiger habitat reserves, Huangnihe forest reserve director Li Cheng is working with scientists and conservation groups to find alternative jobs for locals, for example by training loggers and poachers as organic honey farmers.

One of Li's success stories is Xu Fu, a 42-year-old former logger. In a lush field surrounded by new growth forest, Xu pulls a rack of bees from a hive and describes how he collects honey. Beekeeping is safer and more lucrative than his former profession, he says. "The work and the income from bees are much better, more steady."

Starting around 2002, tigers vanished here in Huangnihe. Then, 2 years ago, locals saw footprints, scratch marks on trees, and the carcasses of prey. By the end of 2014, the BNU team's cameras had confirmed that for the first time in 14 years, a young male had moved back into the Huangnihe forest corridor, more than 200 kilometers inland of current confirmed Siberian tiger habitat.

Farther west, in Wangqing, near what will be the heart of the national park, foresters hope to convert a near-empty logging town into an ecotourism destination. The workers' former gymnasium and entertainment hall will be converted into a history museum, and the town's focus will be on preserving the forest, rather than razing it.

In a promising sign, the emptied village has already attracted a feline denizen. An Amur leopard these days is often spotted basking on a rock jutting from a hill overlooking the town, presiding over its new domain. ■

CREDITS: (GRAPHIC) A. CUADRA/SCIENCE; (DATA) TIGRIS FOUNDATION/WWF

INSIGHTS

POLICY FORUM

CONSERVATION

Brazilian politics threaten environmental policies

The country's environmental licensing system is threatened

By **Philip M. Fearnside**

The tumultuous political situation in Brazil carries risks for the environment in the most biologically diverse country in the world, home to the world's largest tropical forests and rivers. Among the threats is a proposed one-sentence constitutional amendment (PEC-65) that would revoke 40 years of progress in building a licensing system to evaluate and mitigate environmental impacts of development projects (*1*). Under PEC-65, the mere submission of an environmental impact assessment (EIA), regardless of its content, would allow any project to go unstoppably forward to completion. The scientific community contributed greatly to Brazil's environmental licensing system and now must redouble its efforts to communicate its importance.

Despite its limitations [e.g., (*2*)], Brazil's environmental licensing system, which began requiring EIAs in 1986, is vital in restraining infrastructure projects with exceptionally high impacts. The scientific community has documented services provided by Amazonian ecosystems to Brazil and to the world and has increased understanding of how services are lost when ecosystems are destroyed. Large infrastructure

---

National Institute for Research in Amazonia (INPA), 69067-375 Manaus, Amazonas, Brazil. Email: pmfearn@inpa.gov.br

PHOTO: PULSAR IMAGES/ALAMY STOCK PHOTO

The Santarém-Cuiabá (BR-163), slated for reconstruction to transport soybeans from Mato Grosso to Amazon River ports (*15*), is a major corridor for deforestation and logging. Building or upgrading a road unleashes population migration with far-reaching impacts on the environment and traditional population.

projects, such as highways and dams, are key drivers of these losses.

Yet proponents of PEC-65 claim that licensing procedures imply "waste of much time and of large quantities of government funds in flagrant disrespect for the will of the population" (*1*). The amendment reads: "Submission of the preliminary environmental impact study corresponds to authorization to execute the project, which may not be suspended or cancelled for the same reasons [i.e., environmental reasons] except in the face of additional unexpected facts." (*1*). In April 2016, a Senate committee approved PEC-65, clearing it for a full Senate vote. Senators opposed to PEC-65 were able to delay by returning it to committee, although the committee has the same makeup, Amendments require only a 60% majority in each house of the National Congress, after which they automatically take effect with no need for presidential sanction. Brazil's October 1988 constitution had been amended 90 times by December 2015 (*3*).

A spokesperson for the nongovernmental Brazilian Institute of Environmental Protection compared PEC-65 with allowing a student who passes the entry exam for an undergraduate medical program to immediately begin performing surgery (*4*). The Federal Council of Biology, which represents Brazil's biologists, has expressed indignation and has petitioned leaders in both houses of Congress (*5*). The Federal Public Ministry (charged with defending the interests of the people) has prepared a legal opinion (*6*) contesting the proposed amendment. Constitutional conflicts can potentially be judged by the Supreme Court.

This threat is added to a proposed law (654/2015) (*7*) awaiting a full Senate vote. This would allow any "strategic" project, such as a hydroelectric dam, to have simplified "fast-track" environmental approval. The normal sequence of three licenses (preliminary, installation, and operational) would be condensed to one license, with a virtually impossible deadline of 8 months for the environmental agency to approve the license, which normally takes 4 to 5 years. After the deadline, the project would be automatically authorized to proceed.

Brazil's vast plans for dams and highways (*8*) make the potential consequences enormous (see the figures, left and below). The government's most complete list of planned dams called for 79 large dams in Brazil's Amazon region flooding 10 million hectares (*9*). Planned highways would connect inaccessible areas in the central and western parts of the region to the "arc of deforestation" where clearing has been concentrated along the southern edge of the forest.

The makeup of Congress and their potential to respond to corporate development influences on environmental issues (*10*) heighten the chances of sudden approval of environmentally damaging measures. The politicians involved are some of the most powerful in Brazil, with histories that suggest a willingness to exploit and degrade the environment [e.g., (*11*)]. Aggravating the situation is the impeachment trial of President Dilma Rousseff, initiated 11 May 2016, resulting in her being replaced by Vice President Michel Temer for up to 180 days while the trial proceeds and, if one presumes that the same majority in favor of impeachment remains unchanged, until the presidential term ends in January 2019.

Frenetic activities surrounding impeachment proceedings led to an emptying out of normal Senate functions, such as committee sessions. This presented an opportunity for those interested in approving "sleeping" proposals to reverse environmental progress (PEC-65 had been pending since 2012), which can seemingly spring from nowhere to become full-blown threats. With collaboration of most of Brazil's political parties in approving the impeachment proceedings, the mood among

The Jirau Dam on Brazil's Madeira River has enormous impacts, as will planned dams, in displacing human populations; blocking fish migrations; and provoking biodiversity loss, greenhouse-gas emissions, and so on.

PHOTO: NOAH FRIEDMAN-RUDOVSKY/POLARIS/NEWSCOM

politicians is one of unusual unity to approve measures proposed by the interim government to stimulate the country's economy, e.g., freeing development projects from environmental restrictions.

Brazil's environmental governance, including licensing, was plagued by problems before the recent political tumult [e.g., (*12*)], particularly with a legislature dominated by "ruralists" (congressional representatives of large landholders). The power of this group was demonstrated by the 2011 vote by a seven-to-one margin to greatly reduce environmental protections in Brazil's Forest Code [e.g., (*13*)], despite the opposition of 80% of the Brazilian population to any change in the code (*14*).

A leader of the ruralists, also Brazil's largest soy planter, has been appointed Minister of Agriculture, which suggests higher priority for infrastructure projects for transporting soybeans (*15*). The ruralists have requested Interim President Temer to revisit executive-branch decisions from the final days of the previous administration on creating indigenous lands and protected areas called "conservation units." The new Minister of Justice has stated that all decisions from the end of the previous administration will be "reevaluated" (*16*). The previous administration declared seven indigenous lands totaling 14.8 million hectares in its last month in office (*17*). Indigenous lands are particularly important because they protect a greater area than do conservation units and they have a better record of resisting deforestation (*18*). Representatives of the state of Amazonas in the National Congress, together with a delegation from the state legislature, have made a direct appeal to the interim president to repeal five newly created conservation units in the Amazon region's largest state (*19*).

Also awaiting approval is PEC-215, a proposed constitutional amendment that has long been on the ruralists' agenda (*20*). This would transfer authority for creating indigenous lands and conservation units from the executive to the legislative branch, effectively ending creation of new protected areas so long as control of the legislature remains with the ruralists. Other legislation awaiting approval would open indigenous lands to mining (*21*). A proposal by state governments to weaken the licensing system by allowing "self-licensing" is progressing through the National Council on the Environment (*22*).

There are no easy solutions to these problems. Making the legislature more responsive to the impacts of unfettered infrastructure construction and less responsive to special interests is necessary. The ongoing "Lava Jato" ("Car Wash") corruption probe may help [e.g., (*23*)]. Communication by scientists and other experts with decision-makers is essential, despite a history of such information being ignored, as in the case of the Forest Code revision [e.g., (*24*)].

The executive branch is also key, despite its frequently ignoring scientific advice [as in the case of licensing the Belo Monte Dam (*25*)]. The Ministry of the Environment and the National Foundation of the Indian (under the Ministry of Justice) originated the substantial expansion of conservation units and officially recognized indigenous lands over past decades, despite opposition from more powerful ministries, such as mines and energy, transport, and agriculture.

A constant risk is that scientists and others working on the environment in Amazonia succumb to fatalism by assuming that avoiding regional destruction is a lost cause. Continued input from the scientific community is critical to guide environmental policy toward a better future in Brazil.

REFERENCES AND NOTES

1. Senado Federal, Proposta de Emenda à Constituição no. ___, de 2012 (2016); www.senado.leg.br/atividade/rotinas/materia/getTexto.asp?t=120446&c=RTF&tp=1.
2. P. M. Fearnside, *Water Altern.* **7**, 156 (2014).
3. G. de Moura Rocha Lima, Ph.D. thesis (2016); http://bit.ly/LimaThesis.
4. A. Borges, *O Estado de São Paulo*, 29 April 2016, p. 27.
5. CFBio (Conselho Federal de Biologia), CFBio entrega ofícios ao relator da PEC 65 e ao presidente da CCJ (CFBio, Brasília, Brazil, 2016).
6. Grupo de Trabalho Intercameral, Ministério Público Federal, Nota Técnica- A PEC 65/2012 e as clausulas pétreas (MPF, Brasília, DF, Brazil, 2016).
7. Senado Federal, Texto Final Projeto de Lei do Senado no. 654, de 2015 (Senado Federal, Brasília, DF, Brazil, 2015).
8. P. M. Fearnside, *Global Land Proj. News* **12**, 22 (2015).
9. P. M. Fearnside, *Environ. Conserv.* **22**, 7 (1995).
10. C. Zucco Jr., B. Lauderdale, *Legis. Stud. Q.* **36**, 363 (2011).
11. "Senador eleito mais rico tem quase R$ 400 milhões; veja onde eles investem," *Infomoney*, 9 October 2014; http://bit.ly/WealthElectedSenators.
12. J. Ferreira *et al.*, *Science* **346**, 706 (2014).
13. B. Soares-Filho *et al.*, *Science* **344**, 363 (2014).
14. R. J. Lopes, *Folha de São Paulo*, 13 June 2011; http://bit.ly/KeepForestProtection.
15. P. M. Fearnside, *Environ. Manage.* **39**, 601 (2007).
16. M. Bergamon, *Folha de São Paulo*, 16 May 2016, p. A-14.
17. Instituto Socioambiental (ISA), Ministério da Justiça declara mais três Terras Indígenas (ISA, Brasília, Brazil, 2016).
18. D. Nepstad *et al.*, *Conserv. Biol.* **20**, 65 (2006).
19. "Bancada tenta reverter decretos," *Amazonas em Tempo*, 16 June 2016, p. A-8.
20. OEco, "Ruralistas não desistirão da PEC das terras indígenas," *OEco*, 5 February 2015; http://bit.ly/Amendment2block-new-indigenouslands.
21. C. Barros, I. Barcelos, *Folha de São Paulo*, 16 June 2016, p. B-10.
22. ISA, Nota técnico-jurídica: Minuta de resolução CONAMA sobre licenciamento ambiental (ISA, Brasília, Brazil, 2016).
23. M. Baquero, *Revista Debates* **9**, 139 (2015).
24. J.-P. Metzger *et al.*, *Science* **329**, 276 (2010).
25. F. M. Hernandez, S. B. M. dos Santos, *Nov. Cadernos NAEA* **14** (1), 79 (2011).

ACKNOWLEDGMENTS

The author acknowledges support from the Ministry of Science, Technology, and Innovation (CNPq) (575853/2008-5 and 311103/2015-4), Fundação de Amparo à Pesquisa do Estado do Amazonas (FAPEAM) (708565), and National Institute of Amazonian Research (INPA) (PRJ15.125). P. M. Lima de Alencastro Graça and two reviewers provided comments.

10.1126/science.aag0254

METABOLISM

The quest to burn fat, effortlessly and safely

An enzyme steps up to BAT as a potential mitochondrial uncoupler

By **Weiwei Fan** *and* **Ronald Evans**

Treatment of obesity and obesity-associated diseases has been challenging, with the first potential cure claimed in 1934 with the protonophore 2,4-dinitrophenol (DNP). This chemical dissipates mitochondrial membrane potential into heat production and is extremely effective in boosting metabolic rate and promoting weight loss (*1*). However, severe side effects, including cataract formation, cardiotoxicity, overheating, and death, prevented its further use (*2*). In a recent study, Long *et al.* (*3*) report that a secreted enzyme called peptidase M20 domain containing 1 (PM20D1) converts fatty acids and amino acids into *N*-acyl amino acids, which directly uncouple mitochondrial membrane potential in a way similar to that of DNP, to increase energy expenditure without physical movement. Might these endogenous metabolites be a safe alternative to chemical uncouplers, facilitating effortless fat burning without a fatal consequence?

Mitochondrial uncoupling and thermogenesis

N-Acyl amino acids are generated from free fatty acids and amino acids by the enzyme PM20D1, which is secreted by adipocytes in fat tissue. The *N*-acyl amino acids act as mitochondrial uncouplers, thereby boosting energy expenditure, but it is not yet clear in which tissues this occurs.

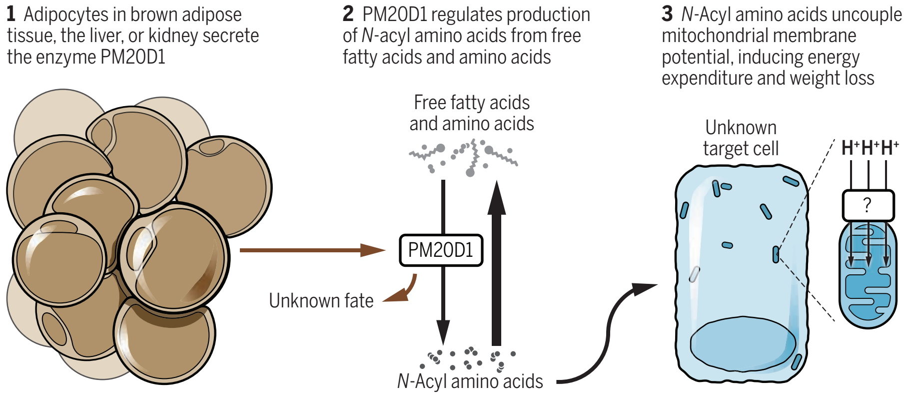

GRAPHIC: V. ALTOUNIAN/*SCIENCE*

Gene Expression Laboratory, The Salk Institute for Biological Studies, 10010 North Torrey Pines Road, La Jolla, CA 92037, USA. Email: evans@salk.edu

Mammals develop brown adipose tissue (BAT) and beige adipose tissue that are specialized in thermogenesis by their high expression of uncoupling protein 1 (UCP1), an endogenous mitochondrial uncoupler (*4*). To discover new proteins that contribute to thermogenesis, Long *et al.* conducted a combinatorial genomic and proteomic study and identified PM20D1, whose expression is highly enriched in UCP1-positive adipocytes. In mice, systemic delivery of PM20D1 (via an adeno-associated viral vector) boosted energy expenditure and reduced diet-induced obesity. Metabolomic and enzymologic analyses further revealed that PM20D1 catalyzes the conversion of fatty acids and amino acids into *N*-acyl amino acids, which directly uncouple mitochondrial membrane potential. When administered in mice, PM20D1 increased metabolic rate and promoted weight loss.

Although UCP1-mediated mitochondrial uncoupling in brown and beige fat is a critical component of heat production, other nonshivering thermogenic processes have been demonstrated in mice lacking UCP1 including the uncoupling of adenosine triphosphate (ATP) hydrolysis from Ca^{2+} transport by sarcolipin in muscle (*5*), and a compensatory creatine futile cycle in beige fat (*6*). The study of Long *et al.* suggests the possibility of an additional UCP1-independent thermogenic mechanism, but additional work is needed to elucidate the roles of PM20D1 and *N*-acyl amino acids. Although preferentially expressed in UCP1-positive adipocytes in brown and beige fat, the secreted enzyme PM20D1 and its products, *N*-acyl amino acids, have the potential to function in a paracrine or endocrine manner to promote heat production in other cells and tissues. Furthermore, PM20D1 is most highly expressed in liver and kidney, which are generally not considered to contribute to thermogenesis. Cold exposure induced the expression of many species of *N*-acyl amino acids in blood. However, the expression of PM20D1 in brown fat, as well as its circulating protein concentration, is not affected. This suggests the existence of other enzymes that catalyze the synthesis of *N*-acyl amino acids, which could also contribute to their elevation in mice that overexpress PM20D1. Indeed, the synthase activity of PM20D1 is much lower than its hydrolase activity, which is consistent with the previously reported hydrolase activities in other PM20D1 members, including aminoacylase, carboxypeptidase, dipeptidase, and aminopeptidase activities (*7*). More important, although the overexpression of PM20D1 increases the plasma concentration of *N*-acyl amino acids, it is not clear whether this rise directly contributes to energy expenditure and thermogenesis, because their physiological amounts are much lower than what is required to stimulate mitochondrial uncoupling. Therefore, whether the weight-loss phenotype observed in PM20D1-overexpressing mice is indeed mediated by *N*-acyl amino acids or by other targets or products of PM20D1 needs further exploration. In addition, although Long *et al.* suggest a paracrine mechanism for PM20D1 and *N*-acyl amino acid-induced thermogenesis in brown and beige fat, this idea requires further demonstration that physiological concentrations of PM20D1 and *N*-acyl amino acids within these tissues are high enough to affect mitochondrial membrane potential.

The study of Long *et al.* reawakens the promise of chemical-based mitochondrial uncoupling as a therapeutic strategy for obesity and obesity-associated diseases. Recent progress has been made toward developing liver-specific DNP derivatives or milder mitochondrial uncouplers that are effective in treating obesity and obesity-associated diseases but with minimal side effects (*8*–*10*). The identification of *N*-acyl amino acids as endogenous mitochondrial uncouplers would not only advance our understanding of adaptive thermogenesis, but also might present safer alternatives to chemical uncouplers if a direct role of *N*-acyl amino acids as mitochondrial uncouplers can be established. This may require the development of *N*-acyl amino acid mimetics, given the higher hydrolase over synthase activity of PM20D1. An immediate question that should be addressed is that in cell culture, *N*-acyl amino acids take 20 to 40 min to initiate uncoupling, which is much longer than the time taken by known chemical uncouplers such as DNP. In addition, *N*-acyl amino acids such as *N*-arachidonyl glycine (C20:4-Gly) have a wide range of biological functions via their interactions with G protein–coupled receptors and ion channels in brain and other tissues (*11*), which in vivo could contribute appreciably to the food suppression and weight-loss phenotypes observed in the treated mice. Furthermore, because the uncoupling effect of *N*-acyl amino acids is UCP1-independent and thus not limited to brown and beige fat, their role in mitochondrial ATP production in highly energetic tissues such as heart, brain, and kidney needs to be explored.

The findings of Long *et al.* open a door on a new class of endogenous mitochondrial uncouplers and present a new mechanism of adaptive thermogenesis via a secreted enzyme and its products. However, every open door reveals more questions than it answers, and follow-up studies are required. We are left to ponder the hope of a magic pill offering effortless and consequence-free fat burning. ■

REFERENCES AND NOTES

1. M. L. Tainter *et al.*, *Am. J. Public Health Nations Health* **10**, 1045 (1934).
2. E. Colman, *Regul. Toxicol. Pharmacol.* **48**, 115 (2007).
3. J. Z. Long *et al.*, *Cell* **166**, 424 (2016).
4. M. Harms, P. Seale, *Nat. Med.* **19**, 1252 (2003).
5. N. C. Bal *et al.*, *Nat. Med.* **10**, 1575 (2012).
6. L. Kazak *et al.*, *Cell* **163**, 643 (2015).
7. S. N. Jamdar *et al.*, *Arch. Biochem. Biophys.* **587**, 18 (2015).
8. R. J. Perry *et al.*, *Cell Metab.* **18**, 740 (2013).
9. H. Tao *et al.*, *Nat. Med.* **11**, 1263 (2014).
10. R. J. Perry *et al.*, *Science* **347**, 1253 (2015).
11. A. T. Deak *et al.*, *J. Cell Sci.* **126**, 879 (2013).

ACKNOWLEDGMENTS

We thank C. S. Lin for help with this manuscript.

10.1126/science.aah6189

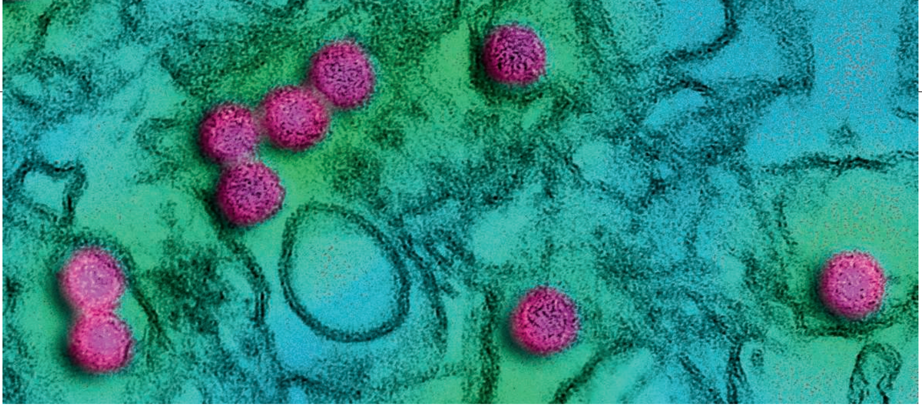

Well-characterized antibodies to ZIKV (pink; transmission electron micrograph shown) are needed.

PHOTO: CYNTHIA GOLDSMITH/VISUALS UNLIMITED, INC.

VIROLOGY

Diagnostics for Zika virus on the horizon

The immune response to Zika virus informs antibody-based diagnostics and therapeutics

By **Scott D. Speer** *and* **Theodore C. Pierson**

Zika virus (ZIKV) is a mosquito-transmitted flavivirus that is related to other pathogens of clinical importance, including yellow fever and dengue (DENV) viruses. Although once infrequently associated with human disease, ZIKV has emerged as a global health threat with its introduction into South America during 2014 and 2015. Of concern, recent ZIKV outbreaks are linked to severe neurodevelopmental complications in the children of women infected while pregnant, as well as Guillain-Barré syndrome in adults (*1*). Management of this epidemic has been complicated by extensive serological cross-reactivity among flaviviruses and the cocirculation of ZIKV and DENV in regions experiencing the greatest disease burden. Current serological diagnostics have a limited capacity to distinguish between DENV and ZIKV. On page 823 of this issue, Stettler *et al.* (*2*) characterize monoclonal antibodies (mAbs) isolated from ZIKV-infected humans that hold promise as diagnostics or therapeutics, and advance our understanding of the repertoire of antibodies elicited by ZIKV infection.

Flaviviruses are assembled from three viral structural proteins [capsid, premembrane (prM), and envelope (E)], a host-derived lipid envelope, and the genomic viral RNA (*3*). Flavivirus-infected cells also secrete a nonstructural protein 1 (NS1), which has multiple roles in viral replication and pathogenesis in vivo (*4*). Both NS1 and the structural proteins are immunogenic. Virus-neutralizing antibodies most commonly target the E protein, may be highly protective in vivo, and are a correlate of protection for many flavivirus vaccines (*5*). NS1 antibodies are non-neutralizing, yet they contribute to protection via antibody heavy chain–mediated effector functions (*6*). Whereas the functional characteristics of antibodies in ZIKV-immune individuals have been studied (*7*), human ZIKV mAbs have not been reported.

Accordingly, Stettler *et al.* have now isolated a panel of 119 human mAbs from the memory B cells of four ZIKV-infected donors; two of these subjects had been infected previously by DENV (*2*). Roughly two-thirds of the mAbs produced bound epitopes within the E protein. Antibodies specific for the immunoglobulin (Ig)–like domain III (DIII) had considerable neutralizing activity and were largely specific for either ZIKV or DENV. Numerous cross-reactive mAbs with modest neutralization capacity mapped to E protein domains I or II. Domain II is the location of the highly conserved fusion loop frequently targeted by antibodies elicited by other flaviviruses. Although more study is required, cross-reactive fusion loop–specific antibodies may also be common in ZIKV-immune individuals. Of considerable interest, Stettler *et al.* found that the most potent neutralizing mAbs bound efficiently to intact virions but not to soluble forms of the E protein, which suggests that antibodies that bind quaternary epitopes composed of more than a single ZIKV E protein may be desirable. In agreement, three recent studies detail the recognition and functional properties of neutralizing mAbs that bind a quaternary epitope shared by ZIKV and DENV (*8*–*10*). E protein antigens

---

Viral Pathogenesis Section, National Institute of Allergy and Infectious Diseases (NIAID), Bethesda, MD 20892, USA. Email: piersontc@niaid.nih.gov

and immunogens that include the antiparallel dimers found on virions may be required to capture the full complexity of the humoral immune response when used as diagnostics and vaccines, respectively.

Neutralizing mAbs have potential as therapeutics capable of preventing or limiting disease, when administered after infection. Stettler *et al.* demonstrated that at least one neutralizing ZIKV type–specific DIII-reactive mAb, genetically modified to prevent antibody-FcγR interactions, was protective when administered 1 day before or after lethal challenge of immune-compromised mice. Similar murine ZIKV DIII–specific mAbs with therapeutic potential were also recently reported (*11*). In this second study, mAbs were produced from mice immunized with ZIKV and recombinant DIII. Structural studies revealed that the two most potent mAbs were specific for a DIII lateral ridge (DIII-LR) epitope on the surface of intact mature virions. Strikingly, this same DIII-LR epitope is also the target of a potent neutralizing West Nile virus–specific antibody that was developed as a potential therapeutic (*12*). Whether robustly neutralizing mAbs will have utility for limiting infection and disease in the unborn requires further study in recently developed animal models.

NS1-reactive mAbs were also present in the panel of mAbs described by Stettler *et al.* Binding studies with recombinant NS1 from ZIKV and the four DENV serotypes revealed that most of these mAbs were virus type–specific. Antibody competition studies identified two sites on NS1 recognized by ZIKV-specific mAbs. While cross-reactive antibodies that target NS1 exist (*2*), the use of NS1 as a more specific antigen in diagnostics has been proposed (*13*).

The extensive serologic cross-reactivity among flaviviruses, and especially with DENV, poses an obstacle for the specific diagnosis of infection and management of disease, particularly in pregnant women. Existing diagnostic assays have limitations. Multiple commercial real-time reverse transcription–polymerase chain reaction assays for the detection of ZIKV RNA are now in use but are only effective during the brief window when viral RNA is detectable in blood, urine, or other fluids. Serological assays, such as the IgM-capture enzyme-linked immunosorbent assay (MAC-ELISA, with virus particles as antigen) and the plaque reduction neutralization test, have the potential to detect prior infection over longer intervals, but the specificity of these techniques is uncertain (*14*).

> ***"...serologic cross-reactivity among flaviviruses...poses an obstacle for the specific diagnosis..."***

A detailed understanding of epitopes recognized by ZIKV-specific and cross-reactive antibodies has the potential to improve the specificity of diagnostics in multiple ways. For example, recent structural insights into ZIKV type–specific and cross-reactive epitopes on the E protein may inform the design of novel antigens in which cross-reactive determinants are destroyed (*9, 11, 15*). More detailed mapping of the E and NS1 epitopes bound by members of the large panel of mAbs described here will advance such efforts considerably (*2*). The availability of ZIKV-specific mAbs may be used directly to enhance the specificity of diagnostic tests. Here, Stettler *et al.* provide proof-of-principle for the utility of ZIKV NS1–specific mAbs in a competition ELISA format to more stringently detect virus-specific patterns of recognition in the polyclonal antibodies of ZIKV- and DENV-exposed individuals. Thus, beyond their therapeutic potential, well-characterized mAbs will accelerate the development of approaches to decipher the complex serology of flaviviruses that limits our ability to diagnose and study infection in the field. ■

REFERENCES AND NOTES

1. J. Lessler *et al.*, *Science* **353**, aaf8160 (2016).
2. K. Stettler *et al.*, *Science* **353**, 823 (2016).
3. D. Sirohi *et al.*, *Science* **352**, 467 (2016).
4. D. Watterson, N. Modhiran, P. R. Young, *Antiviral Res.* **130**, 7 (2016).
5. G. Screaton, J. Mongkolsapaya, S. Yacoub, C. Roberts, *Nat. Rev. Immunol.* **15**, 745 (2015).
6. K. M. Chung *et al.*, *J. Virol.* **80**, 1340 (2006).
7. K. A. Dowd *et al.*, *Cell Rep.* 10.1016/j.celrep.2016.07.049 (2016).
8. W. Dejnirattisai *et al.*, *Nat. Immunol.* 10.1038/ni.3515 (2016).
9. G. Barba-Spaeth *et al.*, *Nature* 10.1038/nature18938 (2016).
10. J. A. Swanstrom *et al.*, *MBio* **7**, e01123 (2016).
11. H. Zhao *et al.*, *Cell* 10.1016/j.cell.2016.07.020 (2016).
12. T. Oliphant *et al.*, *Nat. Med.* **11**, 522 (2005).
13. D. Huzly, I. Hanselmann, J. Schmidt-Chanasit, M. Panning, *Euro. Surveill.* 10.2807/1560-7917.ES.2016.21.16.30203 (2016).
14. I. B. Rabe *et al.*, *Morb. Mortal. Wkly. Rep.* **65**, 543 (2016).
15. L. Dai *et al.*, *Cell Host Microbe* **19**, 696 (2016).

ACKNOWLEDGMENTS

Supported by the intramural program of NIAID.

10.1126/science.aah6187

The complex serology of ZIKV virus infection

The envelope proteins of ZIKV and DENV share a considerable degree of amino acid homology. Both ZIKV and DENV infection result in the production of antibodies specific for only one of these two viruses [type-specific (TS) antibody] as well as cross-reactive (CR) antibodies capable of binding both viruses to varying degrees. The presence of CR antibody complicates the development of specific and sensitive serological tests to diagnose ZIKV infection in populations frequently exposed to other flaviviruses such as DENV.

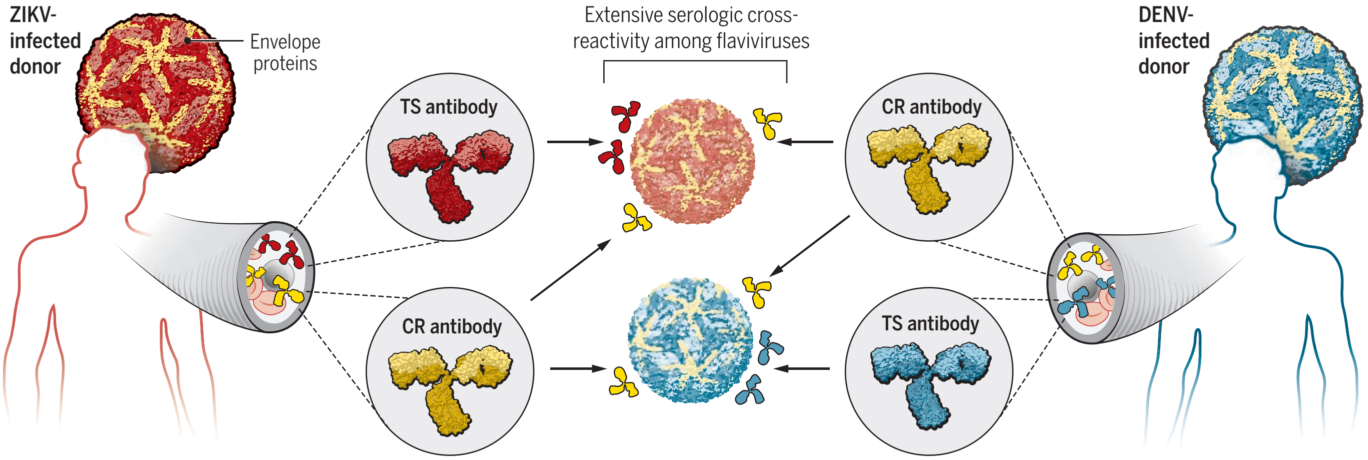

GRAPHIC: K. SUTLIFF/*SCIENCE*

PHYSICS

Thermalization in small quantum systems

A small closed quantum many-body system shows evidence of thermalization

By **Anatoli Polkovnikov** *and* **Dries Sels**

Department of Physics, Boston University, Boston, MA 02215, USA. Email: asp@buphy.bu.edu

Chaos and ergodicity are the cornerstones of statistical physics and thermodynamics. Although classically, even small systems such as a particle in a two-dimensional cavity can exhibit chaotic behavior and thereby relax to a microcanonical ensemble, quantum systems formally cannot. However, recent theoretical work and, in particular, the eigenstate thermalization hypothesis (ETH), indicate that quantum systems can also thermalize. Indeed, ETH provides a framework connecting microscopic models and macroscopic phenomena, based on the notion of highly entangled quantum states. On page 794 of this issue, Kaufman *et al.* (*1*) demonstrate such thermalization in the relaxation dynamics of a small lattice system of interacting bosonic particles. By directly measuring the entanglement entropy of subsystems, as well as other observables, they show that after the initial transient time, the system locally relaxes to a thermal ensemble while globally maintaining a zero-entropy pure state.

The laws of thermodynamics are fundamental in nature as they do not rely on any specific microscopic theory. In particular, the second law postulates that any isolated system will reach an equilibrium state characterized by the maximum entropy under given macroscopic constraints such as total energy, number of particles, and volume. Apart from these constraints, all memory of the initial state is lost. This law is intrinsically irreversible as once a higher-entropy state is reached, there is no way to go back. At the same time, microscopic laws of nature are reversible. This apparent inconsistency has been a topic of controversy for over a century. In classical systems, it was partially resolved through chaotic motion occurring in generic nonlinear systems, which implies that after a transient time, any initial configuration reaches a typical state, on average occupying available phase space points with equal probabilities. However, there are still open questions: What is this transient time, and which configurations are typical?

Quantum mechanically, the situation looks even more confusing as the Schrödinger equation, which governs time evolution of the system, is linear and conserves the probabilities of occupying stationary (eigen-) states (*1, 2*). Therefore, the density matrix cannot relax to any statistical ensemble, but always retains information about the initial state even when allowing for time averaging. As a way out of this puzzling observation, von Neumann formulated ideas of typicality (*3, 4*), where quantum complexity of macroscopic systems should be hidden in an exponentially large number of quantum states. For example, the number of states describing a small 7 × 7 × 7 system of spins is 2^{343}, far exceeding the number of particles in the universe. The physical information extractable from various observables is far less than what can be encoded in these many states. Consequently, most states have to be physically indistinguishable.

This observation, together with random matrix theory, developed and later applied to quantum chaotic systems (*5*), laid the foundations for the solution. In the 1990s the role of quantum chaos in the emergence of statistical mechanics was finally understood (*6, 7*), and the ETH was formulated. The ETH states that a single quantum eigenstate is equivalent to a microcanonical ensemble, in that they make identical predictions about physical observables. These ideas largely went unnoticed and were initially met with skepticism until they were confirmed numerically (*2*). The ETH elucidates the connections between microscopic laws and macroscopic phenomena, allowing precise and verifiable predictions to be made about chaotic systems (*8*). Yet ETH is only a conjecture, and there is no known rigorous way to derive it from first principles.

One of the most striking implications of ETH is that thermalization can occur even in relatively small systems. It is only sufficient to have a large Hilbert space, which scales exponentially with the system size. Thus, in the system experimentally realized by Kaufman *et al.* that consists of only six bosons confined to six lattice sites, the Hilbert space is already 462-dimensional. This

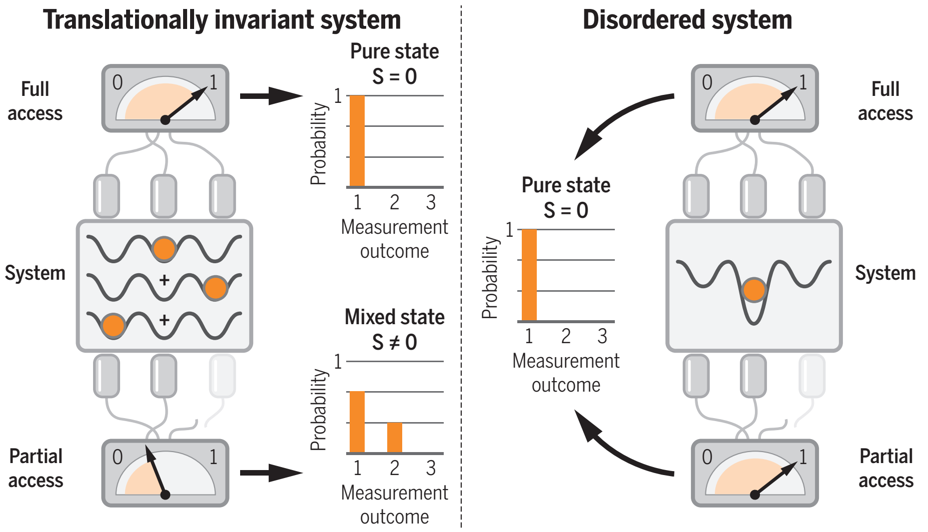

Entanglement in small quantum systems. (**Left**) An eigenstate of a particle in a translationally invariant system is a coherent superposition of three localized orbitals. An observer having access to the whole system can make a deterministic measurement giving reproducible identical results in each experimental realization. Conversely, an observer who can access only sites one and two can only see a statistical mixture of a particle in the state $(|01\rangle + |10\rangle)/\sqrt{2}$ with probability ⅔ and the state with no particles $|00\rangle$ with probability ⅓, and cannot make any deterministic measurement. According to ETH, in large chaotic systems, the reduced density matrices of stationary states describing small subsystems are maximally mixed, exactly as in a thermal ensemble. The level of mixing is encoded in the entanglement Rényi entropy S measured by Kaufman *et al.* (**Right**) In disordered systems, stationary states are localized; an observer having access to only a subsystem can still identify pure states with low entanglement. The many-body localization phenomenon (*12, 13*) implies that, surprisingly, such nonthermal states can be robust against interactions, preventing thermalization even in macroscopic systems.

GRAPHIC: C. BICKEL/*SCIENCE*

large dimensionality allows them to directly verify ETH predictions experimentally. Specifically, Kaufman *et al.* prepare two copies of the same system, with exactly one boson on every site. After a quantum quench, which allows particles to hop, correlations grow and the system becomes entangled. By performing a many-body interference experiment on the two copies, as suggested in (*9*) and tested experimentally in (*10*), the entanglement entropy of different subsystems as well as the entropy of the full state was measured (see the figure). Although the system as a whole remains pure, small subsystems are found to become mixed after a short transient time. Indeed, the reduced density matrices of one- and two-site subsystems become indistinguishable from those of a thermal ensemble. This equivalence is verified by direct observation of the particle occupation distribution and by comparing it with the equilibrium predictions. A recent experiment in a smaller system of three superconducting qubits (*11*) verified that the full time-averaged density matrix becomes thermal in chaotic regimes; another direct consequence of ETH (*8*).

Not only does ETH validate the use of statistical mechanics; there are also many important implications of these ideas to future science and technology. Understanding the microscopic structure of complex systems can provide the necessary tools and intuition for designing systems with similar or better performance than those found in nature, which often operate efficiently in far from ideal conditions. Understanding the conditions leading to the breakdown of ETH could be important for developing new technologies not suffering from the usual thermodynamic limitations. Remarkably, what first appeared to be an issue of controversy in quantum mechanics has provided an elegant solution to the problem of thermalization. It is the existence of individual highly entangled eigenstates that allows the somewhat ambiguous coarse-graining required in standard classical arguments to be dropped. Interestingly, ETH can be applied to systems near the classical limit, providing a simple mathematical framework to understand unanswered questions in classical chaotic systems. ■

REFERENCES

1. A. M. Kaufman *et al.*, *Science* **353**, 794 (2016).
2. M. Rigol, V. Dunjko, M. Olshanii, *Nature* **452**, 854 (2008).
3. J. Eisert, M. Friesdorf, C. Gogolin, *Nat. Phys.* **11**, 124 (2015).
4. S. Goldstein *et al.*, *Proc. R. Soc. A* **466**, 3203 (2010).
5. F. Borgonovi *et al.*, *Phys. Rep.* **626**, 1 (2016).
6. J. M. Deutsch, *Phys. Rev. A* **43**, 2046 (1991).
7. M. Srednicki, *Phys. Rev. E* **50**, 888 (1994).
8. L. D'Alessio *et al.*, *Adv. Phys.* **65**, 239 (2016).
9. A. J. Daley *et al.*, *Phys. Rev. Lett.* **109**, 020505 (2012).
10. R. Islam *et al.*, *Nature* **528**, 77 (2015).
11. C. Neill *et al.*; https://arxiv.org/abs/1601.00600 (2016).
12. M. Schreiber *et al.*, *Science* **349**, 842 (2015).
13. J.-Y. Choi *et al.*, *Science* **352**, 1547 (2016).

10.1126/science.aah5776

ECONOMICS

Fighting poverty with data

Machine learning algorithms measure and target poverty

By **Joshua Evan Blumenstock**

Policy-makers in the world's poorest countries are often forced to make decisions based on limited data. Consider Angola, which recently conducted its first postcolonial census. In the 44 years that elapsed between the prior census and the recent one, the country's population grew from 5.6 million to 24.3 million, and the country experienced a protracted civil war that displaced millions of citizens. In situations where reliable survey data are missing or out of date, a novel line of research offers promising alternatives. On page 790 of this issue, Jean *et al.* (*1*) apply recent advances in machine learning to high-resolution satellite imagery to accurately measure regional poverty in Africa.

Traditionally, wealth and poverty are measured through surveys of household income and consumption (*2*). These data provide a critical input to the world's most prominent antipoverty programs, from basic cash transfer programs to multifaceted aid programs designed to target the extreme poor (*3*). However, nationally representative surveys cost tens to hundreds of millions of dollars to collect, and many developing countries go for decades without updating their estimates.

> ***"...there is exciting potential for adapting machine learning to fight poverty."***

Over the past few decades, researchers have begun to develop different techniques for estimating poverty remotely. Initial work explored the potential of "nightlights" data: satellite photographs taken at night that capture light emitted from Earth's surface. Since such imagery first became available in the early 1970s, it was evident that wealthy regions tended to shine brightest (*4*). Recent studies have found a strong correlation between nightlight luminosity and traditional measures of economic productivity and growth (*5*, *6*). Nightlight-based measures are now frequently used by researchers, for instance to study the impact of sanctions on the economy of North Korea (*7*), where official statistics are dubious.

A series of studies in wealthy nations explore how data from the internet and social media can provide proxies for economic activity (*8*, *9*). Mining the tweets and search queries of millions of individuals promises real-time alternatives to more traditional methods of data collection. However, these approaches are less relevant to remote and developing regions, where internet infrastructure is limited and few people use social media.

In developing countries, researchers have found ways to measure wealth and poverty using the digital footprints left behind in the transaction logs of mobile phones, which are increasingly ubiquitous even in very poor regions. Regional patterns of mobile phone use correlate with the regional distribution of wealth (*10*). This relationship persists at the individual level, such that machine learning algorithms can infer an individual subscriber's socioeconomic status directly from his or her history of mobile phone use. The individual predictions can be aggregated into regional measures of wealth that are about as accurate as a 5-year-old household survey (*11*). Phone-based proxies for wealth are beginning to be used in research, e.g., to understand how new technologies differentially benefit the wealthy and the poor (*12*) and to assess the creditworthiness of would-be borrowers (*13*).

Although promising, these nontraditional methods have caveats. As Jean *et al.* show, nightlights data are less effective at differentiating between regions at the bottom end of the income distribution, where satellite images appear uniformly dark. And mobile phone data are owned by mobile phone operators and are generally not available to policy-makers. By contrast, Jean *et al.* use only publicly available data.

Taking nightlights as their starting point, the authors have devised a clever technique to also extract information from daytime satellite imagery. Daytime imagery is taken at much higher resolution than nighttime imagery. It thus contains visible features—such as paved roads and metal roofs—that make it possible to differentiate between poor and ultrapoor regions. Jean *et al.*'s insight was to apply state-of-the-art deep learning algorithms to the daytime imagery to extract these features. When given large quantities of data with labeled patterns, these algorithms

---

School of Information, University of California, Berkeley, CA 94720, USA. Email: jblumenstock@berkeley.edu

excel at generalizing those patterns to new data. For instance, search engines use this technology to automatically label the contents of billions of internet photos.

The authors use a convolutional neural network to learn the relationship between millions of daytime satellite images (which are rich in detail) and nighttime images (where light areas are assumed to be wealthy). In this way, the network learns which features in the daytime imagery are indicative of economic activity (see the figure). Knowledge of those features enabled the authors to accurately reconstruct survey-based indicators of regional poverty, improving on results from simpler models that relied solely on nightlights or mobile phone data.

How might these results change the way that we measure and target poverty? Perhaps the most immediate application is as a source of inexpensive, interim national statistics. Jean *et al.*'s results indicate that a model trained in one country can be used in another, creating options for countries where no recent survey data exist. For social welfare programs, some of which already use satellite imagery to identify eligible recipients (*14*), higher-fidelity estimates of poverty can help to ensure that resources get to those with the greatest need.

Other applications are on the horizon. Remotely sourced satellite and mobile phone data are updated frequently and can be used to generate nearly real-time estimates of regional vulnerability. Once it is possible to estimate short-term changes in wealth and poverty, new approaches to program monitoring and impact evaluation will follow.

Considerable validation and calibration are required before proof-of-concept studies such as that of Jean *et al.* can be used in practice. However, as their study illustrates, there is exciting potential for adapting machine learning to fight poverty. As the economist Sendhil Mullainathan has asked, "Why should the financial services industry, where mere dollars are at stake, be using more advanced technologies than the aid industry, where human life is at stake" (*15*)? ■

REFERENCES

1. N. Jean *et al.*, *Science* **353**, 790 (2016).
2. A. Deaton, *The Analysis of Household Surveys: A Microeconometric Approach to Development Policy* (World Bank Publications, 1997).
3. A. Banerjee *et al.*, *Science* **348**, 1260799 (2015).
4. D. Donaldson, A. Storeygard, "Big Grids: Applications of Remote Sensing in Economics," working paper, 2016; https://dl.dropboxusercontent.com/u/2734209/Donaldson_Storeygard_JEP.pdf.
5. J. V. Henderson *et al.*, *Am. Econ. Rev.* **102**, 994 (2012).
6. X. Chen, W. D. Nordhaus, *Proc. Natl. Acad. Sci. U.S.A.* **108**, 8589 (2011).
7. Y. S. Lee, "International Isolation and Regional Inequality: Evidence from Sanctions on North Korea," working paper, 2016; https://web.stanford.edu/~yongslee/NKsanctions_030216.pdf.
8. H. Choi, H. Varian, *Econ. Rec.* **88**, 2 (2012).
9. A. Llorente *et al.*, *PLOS ONE* **10**, e0128692 (2015).
10. N. Eagle *et al.*, *Science* **328**, 1029 (2010).
11. J. E. Blumenstock *et al.*, *Science* **350**, 1073 (2015).
12. J. E. Blumenstock *et al.*, *J. Dev. Econ.* **120**, 157 (2016).
13. D. Björkegren, D. Grissen, "Behavior Revealed in Mobile Phone Usage Predicts Loan Repayment," working paper, 2015; http://dan.bjorkegren.com/files/danbjork_creditscoring.pdf.
14. J. Haushofer, J. Shapiro, *Q. J. Econ.* 10.1093/qje/qjw025 (2016).
15. S. Mullainathan, "Satellite images can pinpoint poverty where surveys can't," *New York Times*, 1 April 2016; www.nytimes.com/2016/04/03/upshot/satellite-images-can-pinpoint-poverty-where-surveys-cant.html?_r=0.

10.1126/science.aah5217

Predicting poverty

Satellite images can be used to estimate wealth in remote regions.

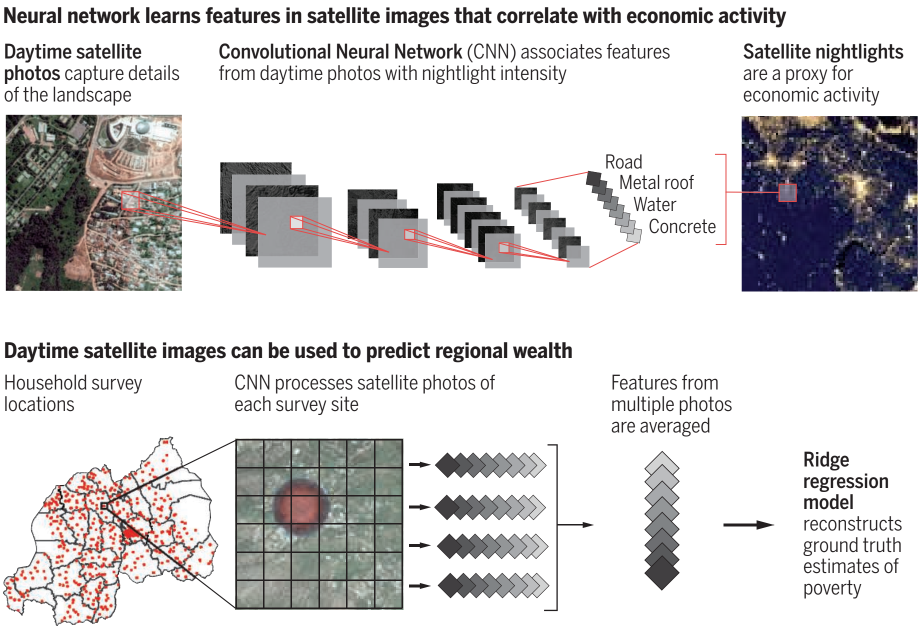

Neural network learns features in satellite images that correlate with economic activity

Daytime satellite images can be used to predict regional wealth

GRAPHIC: IMAGES COURTESY OF GOOGLE EARTH, NASA, AND J. E. BLUMENSTOCK; ADAPTED BY N.CARY/SCIENCE

CRYSTALLOGRAPHY

Now you see me too

Attaching chiral molecules to a chiral framework allows their molecular structures to be determined

By **Lars Öhrström**

Knowledge of three-dimensional (3D) molecular structures is crucial for scientific advances in fields ranging from materials chemistry to medicine. For solar cell materials, human proteins, or new drugs, the revelation of the exact arrangement of atoms and bonds vastly advances understanding of their properties. On page 808 of this issue, Lee *et al.* (*1*) report an approach that allows better structural data to be obtained for large, complex organic molecules that are difficult to crystallize on their own.

The method of choice to obtain structure information is single-crystal x-ray diffraction, a method so important that UNESCO declared 2014 the International Year of Crystallography. However, this method requires not only a pure substance, but also the ability to grow crystals of it—no crystals, no crystal structure data. The main complementary method, nuclear magnetic resonance, mainly provides structures of compounds in solution, often at great detail, but sometimes with inherent uncertainty, especially for chiral (handed) molecules with complicated stereochemistry.

Although long hours in the lab may produce crystals, some substances are notoriously difficult to crystallize or yield crystals with defects and disorder that prevent a complete structure determination. On the other hand, the molecular structures of small solvent molecules, trapped between the larger molecules that are the principal constituents of a specific crystal, are determined over and over again; for example, 1989 molecular structures of pyridine, C_5H_5N, are reported in the Cambridge Crystallographic Database (*2*). This occurs because the form and intermolecular interactions of the larger molecules sometimes generate voids in the crystal. Scientists

---

Department of Chemistry and Chemical Engineering, Chalmers University of Technology, Gothenburg, Sweden. Email: ohrstrom@chalmers.se

have therefore been exploring the idea that difficult-to-crystallize molecules could benefit from a similar approach if large enough voids could be deliberately engineered to trap the target molecules in.

An early example of such void engineering is the use of resorcinarenes and related substances (bowl-shaped molecules that assemble into hollow dimers) to encapsulate compounds and determine their structures (*3*). However, it was not until the discovery of coordination polymers and metal-organic frameworks (MOFs) (*4*) that a general protocol could be developed for the inclusion and structure determination of difficult-to-crystallize molecules.

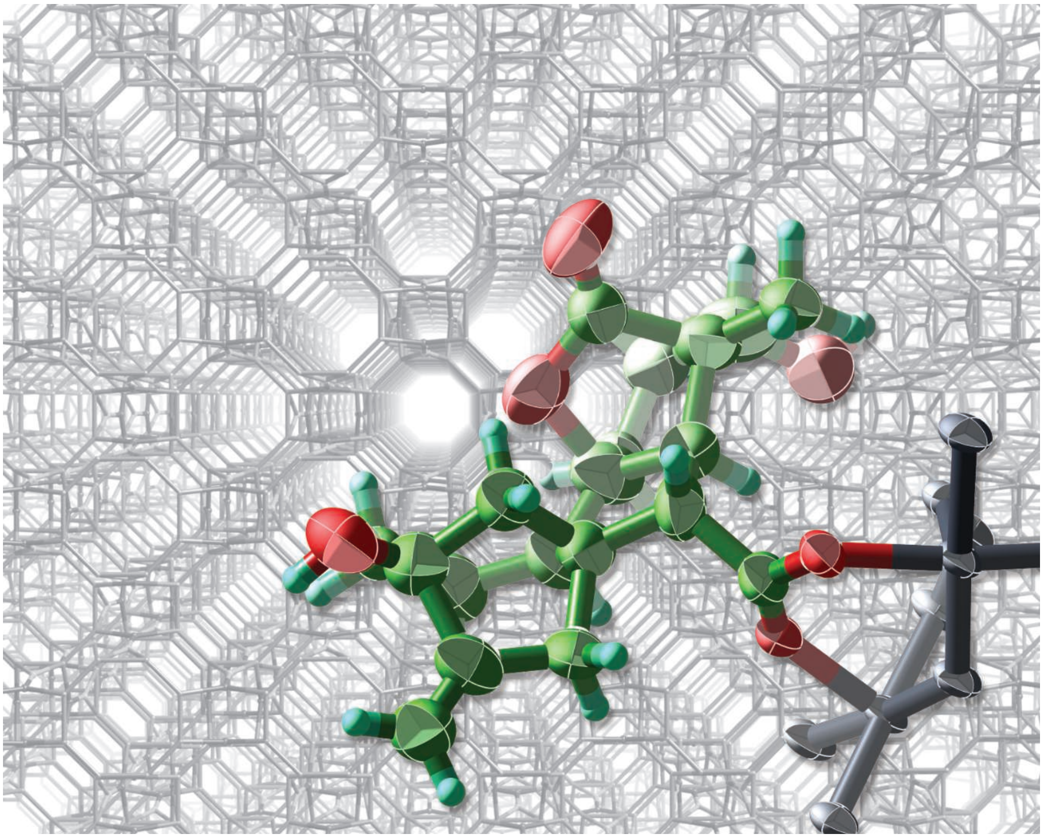

Lee *et al*. determined the structure of the plant hormone gibberellin A1 [carbon (green), hydrogen (light green), oxygen (red)] by trapping it inside MOF-520 (gray). The hormone is attached to aluminum ions (slate blue) in the MOF. The shapes of the atoms reflect data quality, with smaller and more spherical atoms indicating better precision (closer to attachment points to the MOF).

GRAPHIC: LARS OHRSTRÖM/CHALMERS UNIVERSITY OF TECHNOLOGY

MOFs consist of metal ions or clusters bridged by organic molecules (ligands) to form crystalline 3D networks with large potential voids and channels. First-generation MOF-based structure determination matrices were based solely on the void properties and are known as crystalline sponges (*5*). They work by soaking up the desired molecules from a solution. Information on molecular chirality has been obtained from molecules trapped in crystalline sponges (*6*), but the crystalline sponges themselves are nonchiral. They therefore do not provide a frame of reference (like a system of left hands could easily distinguish between right- and left-handed gloves) for absolute chirality assignment. Also, the probed molecules are only weakly attached to the framework. This can result in large thermal motions in the crystal and thus less precise data.

Lee *et al.* present a substantial improvement in data quality by using MOF-520. The bridging ligand in this MOF, 1,3,5-benzenetribenzoate, has a propeller-like handedness. The MOF forms separate crystals of either chirality, even though the 3D network in itself, assigned the topology symbol "sum," is not intrinsically chiral (*7*, *8*) (a well-known achiral topology is that of diamond; a chiral topology is that of quartz). The chiral framework makes it much easier to determine the stereochemistry of the trapped molecule; this information is crucial for understanding its potential biological activity.

To create the crystals, the authors first impregnated MOF-520 with fresh solvent and then soaked it in a saturated solution of the target molecule. The latter substitutes the small formate ions ($HCOO^-$) that are part of the original framework. The target molecule is thus firmly attached to the framework, reducing thermal motion and improving the precision of the data. However, it requires the probed substances to have a functional group that can be coordinated to a metal site. Fortunately, such functional groups are common in the molecules of interest.

"The approach...is an important advance, especially for difficult-to-crystallize natural products."

The approach reported by Lee *et al.* is an important advance, especially for difficult-to-crystallize natural products. However, having the molecular structure does not solve all crystallographic problems associated with a potential drug molecule. For legislation and patent reasons, a crystal structure of the pure compound or any of its pharmaceutically acceptable salts or co-crystals are also needed.

Beyond structure determination, Lee *et al.* show that MOFs could be used to exactly position molecular components. Such crystal engineering is, for example, of interest for solar energy applications (*9*), where it may reduce the need for costly covalent organic synthesis (*10*). Indeed, an early idea was that MOFs could be used to hang molecules on. Lee *et al.* show that MOF-520 provides both good hangers and a chiral wardrobe for complex molecular structures. ■

REFERENCES

1. S. Lee, E. A. Kapustin, O. M. Yaghi, *Science* **353**, 808 (2016).
2. C. R. Groom, I. J. Bruno, M. P. Lightfoot, S. C. Ward, *Acta Crystallogr. B* **72**, 171 (2016).
3. A. Scarso, A. Shivanyuk, J. Rebek Jr., *J. Am. Chem. Soc.* **125**, 13981 (2003).
4. S. R. Batten *et al.*, *Pure Appl. Chem.* **85**, 1715 (2013).
5. Y. Inokuma *et al.*, *Nature* **495**, 461 (2013).
6. S. Yoshioka, Y. Inokuma, M. Hoshino, T. Sato, M. Fujita, *Chem. Sci.* **6**, 3765 (2015).
7. M. O'Keeffe, M. A. Peskov, S. Ramsden, O. M. Yaghi, *Acc. Chem. Res.* **41**, 1782 (2008).
8. F. Gándara, H. Furukawa, S. Lee, O. M. Yaghi, *J. Am. Chem. Soc.* **136**, 5271 (2014).
9. P. Mahato *et al.*, *J. Am. Chem. Soc.* **138**, 6541 (2016).
10. M. Ghazzali, V. Langer, K. Larsson, L. Öhrström, *CrystEngComm* **13**, 5813 (2011).

10.1126/science.aah5367

The genetically engineered Suntory Applause is still a far cry from the "blue" rose hoped for by botanical enthusiasts.

SCIENCE AND SOCIETY

Tough love for technology

A legal scholar probes how new technologies are raising risks, accentuating inequality, and affecting human nature

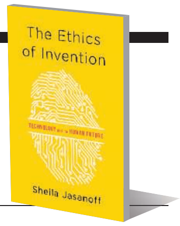

The Ethics of Invention
Technology and the Human Future
Sheila Jasanoff
Norton, 2016, 318 pp.

By **Cynthia Selin**

The imperfection of a genetically engineered blue rose, the self-driving car crash, the orphan drug, the ever-presence of smart phones: The shortcomings and unforeseen uses of technology are knitted into the fabric of our lives in extraordinary and mundane ways. In *The Ethics of Invention: Technology and the Human Future*, Sheila Jasanoff—legal scholar and revered matriarch in the field of science and technology studies—invites us to consider technology not as a mere tool but as a constellation of norms, machines, and regimes that form interlocking and evolving new relationships. Searching the middle ground between "unbridled enthusiasm and anachronistic Luddism," Jasanoff urges us to be more ambitious in the care and tending of these relationships.

Impressively spanning advances in biomedicine, information technology, and green biotechnology, Jasanoff deftly draws out the social and political dramas of technological systems in a series of case studies, revealing how we attempt to steer new science and technology to create more equitable, sustainable, and prosperous societies. Jasanoff's engaging prose brings essential and thoughtful attention to questions of justice, the limits of expert prediction, and the unwieldiness of responsibility in the 21st century.

Those familiar with Jasanoff's work will recognize her astute treatment of the Bhopal disaster—a 1984 gas leak at a pesticide plant in India, widely regarded as the world's worst industrial accident—as "a parable for modern human overreaching and neglect." Her chapter on "Tinkering with humans" offers a sweeping social and political history of revolutions in human genetic engineering that have led to 5 million babies born as a result of in vitro fertilization, bans on human cloning, and commercially motivated biobanks. She moves on to explore how our digital selves bear new vulnerabilities and confound a legal system designed for an analog world.

Through these and other stories, Jasanoff seeks to disrupt the myth of technological determinism, the powerful but incorrect notion that technology follows its own path, devoid of influence by culture, capital, and politics. She demonstrates how people and society do, and always have, set limits on technology, ranging from seat belts to police procedures for DNA testing and surveillance.

And yet Jasanoff seems unimpressed by the ad hoc, muddling, and, at times, negligent ways that we govern emerging technologies. In her view, existing risk frameworks and policy levers do not do enough to protect the vulnerable and disenfranchised, and they ignore deeper moral questions.

While mostly focused on diagnosing this struggle, she considers some concrete efforts to govern technologies more democratically and ethically. Examining instances of ethical analysis and technology assessment that engage the public in dialogue, she laments the loss of the U.S. Office of Technology Assessment and bemoans the impotence of "GM Nation," a large exercise that sought to engage citizens in debate about genetically modified food in the United Kingdom.

Yet, restricting her analysis to such formal modes of deliberation obscures the visibility and import of the plethora of ways that people and organizations strive to reimagine and reclaim technology futures. Through activism, advocacy, and art—and in making a dizzying array of consumer, patient, and parenting choices about technology use—there are a variety of informal ways to take control over technology. Considering *The Ethics of Invention*'s elegant foregrounding of the spirited and tenacious ways that a rich variety of social actors have sought to shape the directions of science and technology, it is odd that Jasanoff seems to prefer to turn governance over to more authorized mechanisms.

Neglected as well by this narrow gaze are enduring practices of foresight used by corporations, nonprofit organizations, and governments to make hard choices in ambiguous and turbulent times, fixing attention on trade-offs and alternatives before the next technological genie is out of the bottle. Tools like scenario planning do not seek to predict the future but aim to clarify systems dynamics and create stories about radically different trajectories of change that can aid decision-making in the present. Such methods may lack the bite of the law that tethers Jasanoff's inquiries, but they signal the diversity of approaches that might support the development of a broadly distributed societal capacity to work toward better futures.

Which futures to create and how pragmatically to amplify efforts to nurture and guide emerging technologies are questions that urgently need more attention. In this way, the sequel to this important book needs to be written by all of us, as we strive, in our own lives and professions, to invent new ideas and mechanisms to provide some tough love, setting limits that enable our technologies to better contribute to human, economic, and environmental flourishing.

10.1126/science.aag2783

The reviewer is at the School for the Future of Innovation in Society and the School of Sustainability, Arizona State University, Tempe, AZ 85287, USA. Email: cynthia.selin@asu.edu

PHOTO: BLUE ROSE MAN/WIKICOMMONS

NEUROSCIENCE

Memory lane

An intimate portrait of a famous amnesiac is also a tale of personal grievances

By **Laura Stark**

Stories are made, not discovered, and journalist Luke Dittrich is a master of his craft. In *Patient H.M.*, Dittrich stitches a history of memory science with the golden thread of his own family drama—a thread that frays at the end into personal vendetta. The book is an intricately plotted story of "heroes and villains" orbiting around the patient known as "H.M."

Henry Molaison was born in 1926, was diagnosed with epilepsy as a child, and spent most of his life around Hartford, Connecticut—graduating from high school and working blue-collar jobs until age 27. In 1953, he and his parents decided he should undergo a treatment for epilepsy that was considered experimental but promising at the time: brain surgery. The neurosurgeon who operated on Molaison was Dittrich's grandfather, William Beecher Scoville, a man underlings called Wild Bill. During surgery, he had expected to pinpoint the area that caused Molaison's seizures but was unable to do so; he opted nonetheless to remove both of Molaison's medial temporal lobes. After the surgery, Molaison could not create new memories.

A researcher holds the brain of Henry Molaison, whose surgically induced amnesia led to important insights into the neural correlates of learning and memory.

PHOTO: SPENCER LOWELL

To his credit, Dittrich avoids the easy "villain" narrative. He can have a subtle moral imagination that appreciates the humanity even of people often cast as bad guys. "None of us are all light or all dark," he writes, "and most of us are both at once."

Scoville's impulse decision debilitated Molaison, but it also made him into "H.M."—an invaluable human subject for scientists, his brain an irreplicable natural experiment. Scoville partnered with leading neuroscientists at McGill University, and the team published path-breaking studies on memory and amnesia through the 1950s and 1960s, based on continued work with Molaison.

When, after two decades, interest in Molaison waned at McGill, Suzanne Corkin, then a graduate student in the lab, adopted the project as she began a new faculty position at MIT. Corkin built her career around research on Molaison, and when he died in 2008, she coordinated the donation of his brain to a tissue bank. In 2013, she published a well-received memoir of her career with Molaison, *Permanent Present Tense* (*1*,*2*).

As Dittrich recounts this history, he braids in adventure stories from generations of men in his family: his grandfather's stunt dive from the George Washington Bridge, his great-grandfather's dodge of a fatal bullet, his grandfather's grandfather's seductions from the pulpit, and his own hike to pyramids in Egypt, bullfight in Mexico, and paramour in Ecuador, to name a few. If these stories sound tangential, that is precisely Dittrich's point: "One of the things our brains do, constantly, unconsciously, whether we like it or not, is make connections." Stories are those crooked connections that people put into language and mold into narrative form.

Dittrich's adventure stories bustle with intrigue and derring-do. But the book's exhilarating moments really come when he stays on topic and stretches his perspective—amplifying Molaison's voice from study transcripts or inhabiting the mind of his own grandmother, slowly revealing that she is schizophrenic.

It seems inevitable that the book will be compared to the patient biography *The Immortal Life of Henrietta Lacks*. But, while Dittrich is an exceptional writer, he focuses his talents in the last half of his book on a takedown of rival author Suzanne Corkin, missing opportunities to turn his own family story into one of more universal scope.

In 2010, Dittrich published his first piece in *Esquire*. It was about his grandfather and H.M., and it reappears in this book. For the article, Dittrich contacted Corkin, who was an old friend of his mother and still at MIT, requesting to interview this yet-anonymous patient and asking her to share study records. She hedged, he persisted, and eventually MIT agreed to share materials but with restrictions on private health information and commercial use—terms that seem conventional in the context of modern medical law but that Dittrich found "bizarre and somewhat unsettling." Dittrich's forgivable looseness with historical detail in earlier sections takes its toll here and in other episodes as he struggles to extend his moral imagination to Corkin.

Patient H.M.
A Story of Memory, Madness, and Family Secrets
Luke Dittrich
Random House, 2016, 464 pp.

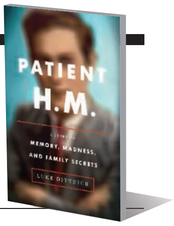

Dittrich only reveals at the end that Corkin was writing her own book on H.M., which recasts his story up to that point in a new light. It helps make sense of his eagerness to see her actions as personal slights, character flaws, and bad science rather than symptoms of broken systems. It is a pity, because his sense of personal grievance narrows him into a story about a uniquely menacing scientist rather than a universal story of the legal and institutional ties that bind even well-intentioned people (*3*).

Midway through this beguiling book, Dittrich learns that his grandfather may have done brain surgery on his schizophrenic grandmother. Dittrich closes the book with a transcript from his key source for this information, an elderly doctor who, Dittrich suggests, has amnesia himself. The book aims to show that memory is always selective, partial, and open to new interpretation—that all narrators are a bit unreliable. In the end, *Patient H.M.* is a story about how stories can never, finally, be trusted.

REFERENCES AND NOTES

1. S. Corkin, *Permanent Present Tense: The Unforgettable Life of the Amnesic Patient, H.M.* (Basic Books, New York, 2013).
2. N. Zeliadt, *Science*, **341**, 459 (2013).
3. An excerpt published in the New York Times Magazine on 7 August 2016 elicited a response from more than 200 members of the international scientific community disputing Dittrich's allegations (http://bcs.mit.edu/news-events/news/letter-editor-new-york-times-magazine).

10.1126/science.aag2904

The reviewer is at the Center for Medicine, Health, and Society, Vanderbilt University, Nashville, TN 37235, USA. Email: laura.stark@vanderbilt.edu

LETTERS

Edited by **Jennifer Sills**

PHOTO: NATIONAL GEOGRAPHIC CREATIVE / ALAMY STOCK PHOTO

Protecting India's conservation offsets

INDIA, A MEGADIVERSE country and fast-growing emerging economy (*1*, *2*), endures a constant tug-of-war between conservation and development. Biodiversity offsetting, an increasingly popular but controversial conservation tool, seeks to counterbalance biodiversity impacts associated with economic development (*3*). To provide a biodiversity offset, developers compensate for developed land by supporting conservation actions such as reforestation of degraded forests.

To be valid, biodiversity offsets must support conservation that would not otherwise be implemented, not conservation already planned or under way. This is the principle of "additionality": Only added conservation can counterbalance development (*3*). In violation of this widely accepted principle, the Indian government has sought to divert offset funds toward established conservation commitments. As a result, development remains uncompensated, and India suffers a net loss of biodiversity (*4*).

Biodiversity offsetting was codified in India's Forest Conservation Act (FCA), 1980, which requires projects that cause deforestation to pay for compensatory afforestation (*5*). Successive government administrations, however, have failed to implement this offsetting mechanism, leaving more than INR 38,000 crores (about USD 5.7 billion) sitting unused in a government account, even as deforestation continues. A proposed new law, the Compensatory Afforestation Fund (CAF) Bill, 2015, which is up for debate in the Indian parliament, seeks to resolve this inertia (*6*).

India's FCA, 1980, is explicit about the concept of additionality: "The compensatory afforestation should clearly be an additional plantation activity and not a diversion of part of the annual plantation programme" (*5*). The CAF Bill, 2015, proposes diverting compensatory afforestation funds to implement the Green India Mission (GIM), a separate afforestation program stipulated under India's National Action Plan on Climate Change to fulfill its international climate change mitigation commitments (*6*). This falls under the category of established conservation, and therefore does not qualify as compensation according to the principle of additionality.

Initially, INR 6000 crores (about USD 900 million) are proposed for diversion (*7*). This sum could be used to afforest about 1.2 mha (*8*). Thus, compensatory afforestation of 1.2 mha will be forgone, in effect, leaving an uncompensated net loss of almost all of the 1.48 mha deforested under FCA since 1980 (*9*). For effective mitigation of development impacts on India's forests and biodiversity, compensatory afforestation funds must not be diverted to the Green India Mission. The funds should be used strictly for compensatory afforestation, and the resulting forest cover gains should be measured and reported against a baseline that includes afforestation planned under the Green India Mission. To avoid double counting, there should be separate accounting for the spending on compensatory afforestation and that on the Green India Mission.

***Divya Narain*[1]* *and Martine Maron*[2]**

[1]Mumbai, 400050, India. [2]Landscape Ecology and Conservation Group and School of Geography, Planning and Environmental Management, The University of Queensland, Brisbane, QLD 4072, Australia.

*Corresponding author. Email: divyanarain01@gmail.com

REFERENCES

1. Ministry of Environment and Forests, Government of India, "National Biodiversity Action Plan" (2008); www.cbd.int/doc/world/in/in-nbsap-v2-p1-en.pdf.
2. International Monetary Fund, "World Economic Outlook Update" (2016); www.imf.org/external/pubs/ft/weo/2016/update/01/pdf/0116.pdf.
3. B. A. McKenney, J. M. Kiesecker, *Environ. Manage.* **45**, 165 (2010).
4. M. Maron, A. Gordon, B. G. Mackey, H. P. Possingham, J. E. M. Watson, *Nature* **523**, 401 (2015).
5. Ministry of Environment and Forests, Government of India, "Handbook of Forest (Conservation) Act, 1980 (With Amendments made in 1988) Forest (Conservation) Rules, 2003 (With Amendments made in 2004) Guidelines & Clarifications" (2004); http://wrd.bih.nic.in/guidelines/awadhesh02c.pdf.
6. "The Compensatory Afforestation Fund Bill, 2015" (as introduced in Lok Sabha) (2015); www.prsindia.org/uploads/media/Compensatory%20Afforestation/Compensatory%20afforestation%20fund%20bill,%202015.pdf.
7. Ministry of Environment and Forests, Government of India, "National Mission for a Green India (Under The National Action Plan on Climate Change)" (www.moef.gov.in/sites/default/files/GIM_Mission%20Document-1.pdf).
8. Ministry of Environment and Forests, Government of India, "Implementation Guidelines for National Mission for a Green India (GIM)" (2014); www.moef.gov.in/sites/default/files/GIM_Implementation_Guidelines.pdf.
9. Summary of FCA Projects, Website of e-Green Watch (http:// egreenwatch.nic.in/FCAProjects/Public/Rpt_State_Wise_Count_FCA_projects.aspx).

10.1126/science.aah3989

Open-access policies: A legal quagmire

MANY UNIVERSITY OPEN-ACCESS policies grant a shared copyright to the school for all faculty articles before publication. According to these policies, which are often based on Harvard's model language (*1*, *2*), faculty members deposit articles into an institutional open-access repository. Faculty can request a waiver from the policy for a particular article.

Once a publisher accepts an article for publication, the author signs a copyright agreement that transfers certain rights to the publisher and certifies that the author has unencumbered possession of those rights. However, if the author has not obtained a waiver to the school's open-access repository, it is unclear whether his or her rights to the article are encumbered by the previous grant to the school (*3*). The publisher copyright agreements are written

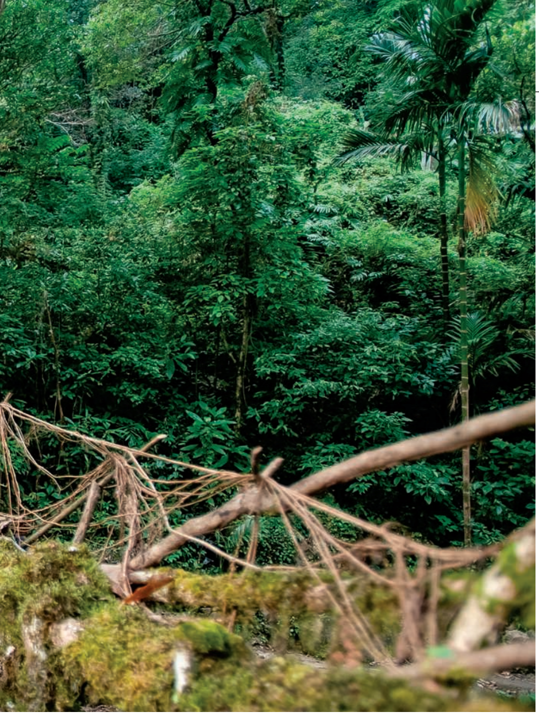

India's government is diverting funds intended for new conservation efforts.

using highly technical legal language (*3*) and vary greatly from publisher-to-publisher. Deciding whether the author still possesses sufficient rights to the article to transfer to the publisher becomes a complicated legal question. The faculty members are not qualified to answer these questions, and neither are the library staff usually charged by the schools with navigating the open-access policies.

As a result, unsustainable ethical and legal burdens are placed on the faculty in schools with Harvard-style open-access policies. These faculty are forced either to request waivers for almost every article they publish or to sign the copyright agreements without knowing whether they have the legal rights to do so. Faculty thus risk breaking the copyright law.

Online copyright law is an emerging field without clear rules or precedents. So far, there have been no lawsuits accusing journal authors of violations. However, by signing consents without a thorough understanding of the legal requirements, authors are leaving themselves vulnerable to unknown repercussions. We must look for better approaches to open-access policies.

Ilya Kapovich

Department of Mathematics, University of Illinois at Urbana-Champaign, Urbana, IL 61801, USA.
Email: kapovich@math.uiuc.edu

REFERENCES

1. E. Priest, *Northwest. J. Technol. Intell. Prop.* **10**, 377 (2012).
2. S. M. Shieber, "A model open-access policy" (2015); https://osc.hul.harvard.edu/modelpolicy/.
3. Secret Blogging Seminar, "Springer's copyright agreement is, according to Springer, compatible with posting your article on the arXiv under the CC-BY license" (https://sbseminar.wordpress.com/2016/04/26/springers-copyright-agreement-is-according-to-springer-compatible-with-posting-your-article-on-the-arxiv-under-the-cc-by-0-license/).

10.1126/science.aah4571

Passport Initiative fosters applied science

M. BALTZLEY'S LETTER "Institutionalizing creationism" (10 June, p. 1285) incorrectly argues that the Interstate Passport Initiative institutionalizes creationism in the undergraduate science curriculum. As members of the faculty team that developed the Passport's natural science content area, we strongly disagree.

The Interstate Passport Initiative is a mechanism for the transfer of lower-division general education, based not on specific courses but on the student's demonstrated competency in key subject areas. Students do so by satisfying content-specific learning outcomes through completion of class assignments (proficiency criteria) identified for that purpose.

The Passport's natural science learning outcomes and proficiency criteria were developed—independent of the Western Interstate Commission for Higher Education, in contrast to Baltzley's implication otherwise—by a multistate team of science faculty from accredited institutions. They center on scientific reasoning, literacy, and application in society. Students are expected to meet each of the learning outcomes. Baltzley's criticism stems from the inclusion of student analysis of the Ham-Nye debate among the coursework examples supporting the following learning outcome: "Students shall recognize the proper use of scientific data, principles, and theories to assess the quality of stated conclusions, and demonstrate an ability to gather, comprehend, apply and communicate credible information on scientific and technical topics" (*1*). Accompanying proficiency criteria address topics commonly misconstrued by the public, including the vaccination-autism controversy and climate change. One proficiency criterion makes use of the Ham-Nye evolution-creation debate as a tool by which students evaluate the proper use of scientific reasoning and data (*1*).

Analysis of the arguments presented by both sides in the debate does not validate creationism as a science, as implied by Baltzley's commentary. The Passport natural science team does not support the teaching of creationism or "creation science" within the science classroom. To the contrary, like the National Center for Science Education, we believe the classroom is where students should learn to challenge the false claims of ideas such as young earth creationism and intelligent design (*2*). Moreover, proficiency criteria such as the Ham-Nye debate are examples of coursework some faculty now use to meet the learning outcomes; they are not intended to be required assignments.

Thomas Krabacher[1]* and Patricia Flatt[2]

[1]Natural Sciences Faculty Team, Department of Geography, California State University, Sacramento, CA 95819-6003, USA. [2]Natural Sciences Faculty Team, Department of Chemistry, Western Oregon University, Monmouth, OR 97361, USA.

*Corresponding author. Email: krabacherts@csus.edu

REFERENCES

1. Interstate Passport, "Faculty handbook: Constructing your institution's Passport block" (2016); p. 43; www.wiche.edu/files/info/Faculty%20HB-CYIPB%20March%202016%20%28REV%204-08-16%29.pdf.
2. National Center for Science Education, The Creationism/Evolution Continuum (https://ncse.com/library-resource/creationevolution-continuum).

10.1126/science.aah4621

TECHNICAL COMMENT ABSTRACTS

Comment on "A bacterium that degrades and assimilates poly(ethylene terephthalate)"

Yu Yang, Jun Yang, Lei Jiang

Yoshida *et al.* (Report, 11 March 2016, p. 1196) reported that the bacterium *Ideonella sakaiensis* 201-F6 can degrade and assimilate poly(ethylene terephthalate) (PET). However, the authors exaggerated degradation efficiency using a low-crystallinity PET and presented no straightforward experiments to verify depolymerization and assimilation of PET. Thus, the authors' conclusions are rather misleading.

Full text at http://dx.doi.org/10.1126/science.aaf8305

Response to Comment on "A bacterium that degrades and assimilates poly(ethylene terephthalate)"

Shosuke Yoshida, Kazumi Hiraga, Toshihiko Takehana, Ikuo Taniguchi, Hironao Yamaji, Yasuhito Maeda, Kiyotsuna Toyohara, Kenji Miyamoto, Yoshiharu Kimura, Kohei Oda

Yang *et al.* suggest that the use of low-crystallinity poly(ethylene terephthalate) (PET) exaggerates our results. However, the primary focus of our study was identifying an organism capable of the biological degradation and assimilation of PET, regardless of its crystallinity. We provide additional PET depolymerization data that further support several other lines of data showing PET assimilation by growing cells of *Ideonella sakaiensis*.

Full text at http://dx.doi.org/10.1126/science.aaf8625

TECHNICAL COMMENT

BIODEGRADATION

Comment on "A bacterium that degrades and assimilates poly(ethylene terephthalate)"

Yu Yang, Jun Yang,* Lei Jiang*

Yoshida *et al*. (Report, 11 March 2016, p. 1196) reported that the bacterium *Ideonella sakaiensis* 201-F6 can degrade and assimilate poly(ethylene terephthalate) (PET). However, the authors exaggerated degradation efficiency using a low-crystallinity PET and presented no straightforward experiments to verify depolymerization and assimilation of PET. Thus, the authors' conclusions are rather misleading.

Yoshida *et al*. (*1*) reported that they found a novel poly(ethylene terephthalate) (PET)–degrading bacterium, *Ideonella sakaiensis* 201-F6. The authors claim that there are very few reports on the biological degradation of PET, except that a few fungal species or enzymes have been shown to be able to degrade PET (*1*). However, the authors did not cite three previous studies demonstrating that some bacteria or bacterial enzymes, such as cutinases, are also able to effectively degrade PET (*2*–*4*).

The authors used a low-crystallinity PET (1.9%) as a tested substrate to dramatically boost the degradation efficiency of PET by *I. sakaiensis* 201-F6. Because PET is a semicrystalline polyester, only the amorphous regions were demonstrated to be susceptible to enzymatic degradation rather than crystalline regions (*4*, *5*). Therefore, decreasing the crystallinity may substantially increase the degradability of PET. An earlier paper published by Vertommen *et al*. (*5*) indicates that the degradative activity of PET hydrolases (cutinase), from *Fusarium solanipisi*, for low-crystallinity PET (4.1%) is about 15 times as high as that of mid-crystallinity PET (13.7%) and 500 times as high as that of high-crystallinity PET (48.2%). Experimental data presented in the article by Yoshida *et al*. [figures 2D and 2E in (*1*)] also showed that the activity of PET hydrolases, from *I. sakaiensis* 201-F6, for low-crystallinity PET (1.9%) is about 20 times as high as that of commercial bottle-derived high-crystallinity PET (crystallinity was not specified in the article but often ranges from 30 to 40%). One might expect that if the commercial bottle-derived high-crystallinity PET was used as the tested substrate, then the degradation efficiency by *I. sakaiensis* 201-F6 would be very limited.

The information about the changes in molecular weight of PET film after cultivation with *I. sakaiensis* 201-F6 was not presented, although it is well known that the decrease in molecular weight is a major indication of depolymerization and degradation of polymers (*6*–*11*). In our earlier work, we reported that polyethylene (PE) and polystyrene (PS) could be degraded by plastic-eating insects or their associated gut bacteria and presented the evidence of decrease in molecular weight of PE or PS after degradation (*6*–*9*). Yoshida *et al*. did use gel permeation chromatography to analyze the molecular weight of PET film before and after cultivation with consortium no. 46 [figure S1C in (*1*)]; however, no changes have been observed. One may speculate whether the surface degradation of PET film resulted only from the mechanical destruction by the bacterial consortium without any cleavage of the long-chain molecules. Nevertheless, evidence for the degradation of PET by *I. sakaiensis* 201-F6 could have been more complete if data of molecular weight changes had been presented.

The assimilation of PET by *I. sakaiensis* 201-F6 as a carbon source for growth does not appear to be sufficiently supported by the data despite the adherence of *I. sakaiensis* 201-F6 to PET film, as shown in the presented scanning electronic micrograph images [figure 2, D to F, in (*1*)]. Carbon isotopic tracer experiments can verify assimilation of organic carbon in the biomass [e.g, (*7*)] but were not performed. The authors also could have easily measured changes in the number or the weight of *I. sakaiensis* 201-F6 cells grown in a medium with PET as a sole carbon source. Without such data, the authors' claim that the bacterium can assimilate PET is unconvincing.

Key Laboratory of Bio-Inspired Smart Interfacial Science and Technology of Ministry of Education, School of Chemistry and Environment, Beihang University, Beijing 100191, P.R. China.
*Corresponding author. Email: yangjun@buaa.edu.cn (J.Y.); jianglei@iccas.ac.cn (L.J.)

REFERENCES AND NOTES

1. S. Yoshida *et al*., *Science* **351**, 1196–1199 (2016).
2. C. Sharon, M. Sharon, *J. Microbiol. Biotech. Res.* **2**, 248–257 (2012).
3. R.-J. Müller, H. Schrader, J. Profe, K. Dresler, W. D. Deckwer, *Macromol. Rapid Commun.* **26**, 1400–1405 (2005).
4. Å. M. Ronkvist, W. Xie, W. Lu, R. A. Gross, *Macromolecules* **42**, 5128–5138 (2009).
5. M. A. M. E. Vertommen, V. A. Nierstrasz, M. Veer, M. M. C. G. Warmoeskerken, *J. Biotechnol.* **120**, 376–386 (2005).
6. J. Yang, Y. Yang, W.-M. Wu, J. Zhao, L. Jiang, *Environ. Sci. Technol.* **48**, 13776–13784 (2014).
7. Y. Yang *et al*., *Environ. Sci. Technol.* **49**, 12080–12086 (2015).
8. Y. Yang *et al*., *Environ. Sci. Technol.* **49**, 12087–12093 (2015).
9. "One way to get rid of Styrofoam: Feed it to mealworms," *Science*, 30 September 2015 (2016); www.sciencemag.org/news/sifter/one-way-get-rid-styrofoam-feed-it-mealworms
10. T. Deguchi, Y. Kitaoka, M. Kakezawa, T. Nishida, *Appl. Environ. Microbiol.* **64**, 1366–1371 (1998).
11. H. B. Bode, A. Zeeck, K. Plückhahn, D. Jendrossek, *Appl. Environ. Microbiol.* **66**, 3680–3685 (2000).

ACKNOWLEDGMENTS

This work was supported by the National Natural Science Foundation of China (grants 51373006 and 20477002) and the State Basic Research Program of China (grant 2014CB931800).

6 April 2016; accepted 14 July 2016
10.1126/science.aaf8305

TECHNICAL RESPONSE

BIODEGRADATION

Response to Comment on "A bacterium that degrades and assimilates poly(ethylene terephthalate)"

Shosuke Yoshida,[1,2]* Kazumi Hiraga,[1] Toshihiko Takehana,[3] Ikuo Taniguchi,[4] Hironao Yamaji,[1] Yasuhito Maeda,[5] Kiyotsuna Toyohara,[5] Kenji Miyamoto,[2]† Yoshiharu Kimura,[4] Kohei Oda[1]†

Yang *et al*. suggest that the use of low-crystallinity poly(ethylene terephthalate) (PET) exaggerates our results. However, the primary focus of our study was identifying an organism capable of the biological degradation and assimilation of PET, regardless of its crystallinity. We provide additional PET depolymerization data that further support several other lines of data showing PET assimilation by growing cells of *Ideonella sakaiensis*.

We appreciate the Comment by Yang *et al.* (*1*) and are grateful for this opportunity to explain the context of how our work builds on previous studies. The intent of our study was to isolate and describe a microorganism that can degrade and assimilate poly(ethylene terephthalate) (PET) (*2*). Therefore, we only cited the pioneering works that report specific microorganisms able to grow on PET (*3*, *4*). In a previous study, Sharon and Sharon (*5*) confirmed microbial PET degradation by semi-isolated microorganisms, where the involvement of *Nocardia* species was implied by microscopic observation. However, the contribution of other microorganisms was not ruled out, nor was the possibility that the PET was degraded by the resting cells harboring PET-hydrolyzable enzymes. We identified the PET hydrolase (PETase) gene based on amino acid sequence identity with a known hydrolase from *Thermobifida fusca* (TfH) that exhibited PET-hydrolyzing activity (*6*), similar to other PET-hydrolyzing enzymes (*7*–*10*). We further referred cutinase from *Humicola insolens* (HiC) (*11*) and seven other enzymes in the supplementary materials [table S2 in (*2*)]. The functions of these enzymes, particularly TfH, LCC (*9*), and FsC (*10*), greatly contributed to the understanding of PETase enzymology.

With the intention of isolating a specific microorganism that can use PET for growth, even if the PET is mostly in the amorphous form, the extent of crystallinity is of secondary importance. We described the motivation for using low-crystallinity (1.9%) PET and the observation that the structure of crystallized PET hampered the enzymatic hydrolysis of its ester linkages (*8*, *12*) in our Report.

Based on the proton nuclear magnetic resonance and gel permeation chromatography profiles of the degraded PET film, we concluded that the degradation by the consortium termed "no. 46" proceeded from the PET surface (*2*). To support this inference, we analyzed the surface of the PET film using x-ray photoelectron spectroscopy (XPS). The XPS spectrum for degraded PET film by no. 46 showed that a new peak appeared at 0.6 eV higher in binding energy than that observed for the O_{1s} peak of C–*O*–C linkage (532.5 eV), indicating the formation of the C–*O*–H linkage by hydrolysis of the ester linkage, which should either be of hydroxyl or carboxyl groups. To accurately determine the surface functional groups, each group was labeled with heptafluorobutyryl chloride (for –OH) and 1,1-carbonyldiimidazole (for –COOH) (*13*) and analyzed by XPS. Consequently, the peaks of F_{1S} (687.5 eV) and N_{1S} (398.5 eV) after degradation dramatically increased (Fig. 1A). The values of surface hydroxyl and carboxyl groups for the degraded film were calculated to be $1.09 \pm 0.03 \times 10^{14}$ and $7.11 \pm 0.92 \times 10^{14}$ groups per cm^2, respectively; those for the control film were

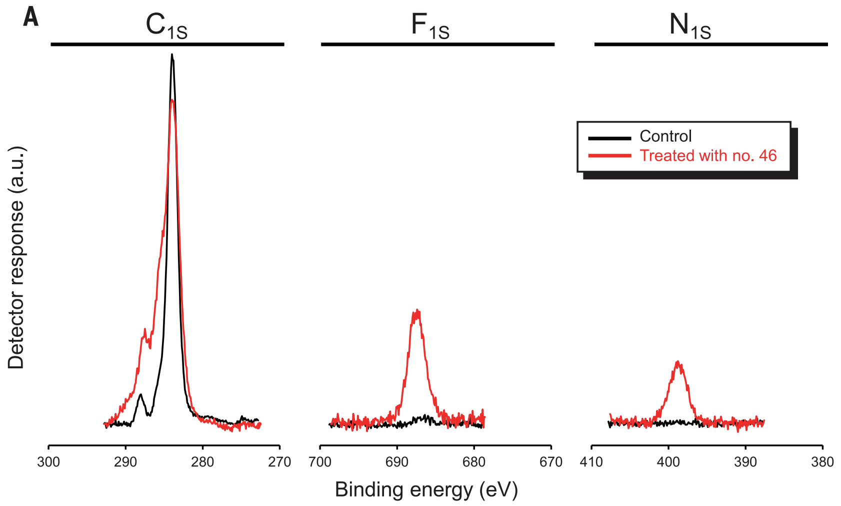

B

PET film	–OH (×10^{14} group/cm^2)	–COOH (×10^{14} group/cm^2)
Control	0.13 ± 0.01	0.36 ± 0.10
Treated with no. 46	1.09 ± 0.03	7.11 ± 0.92

Fig. 1. XPS analyses of PET films degraded by consortium no. 46. No. 46 was cultured with PET film (20 by 15 by 0.2 mm) in MLE (modified lettuce and egg) medium at 30°C for 22 days with a biweekly medium change. The degraded PET film was washed with 1% SDS, distilled water, and then ethanol, followed by air drying. The hydroxyl and carboxyl groups on the film surface were labeled with heptafluorobutyryl chloride and 1,1′-carbonyldiimidazole, respectively (*13*), and independently quantified by XPS on a JEOL JPS-9010MC/SP photoelectron spectrometer (Tokyo, Japan) with a 100 W MgKα x-ray source (λ 9.889 Å, 1253.5 eV) with take-off angle of 45°. (**A**) Narrow spectra of C_{1s}, N_{1s}, and F_{1s} regions. The spectra were obtained by accumulation of 15 scans at intervals of 0.1 eV. (**B**) Density of surface functional groups. The atomic compositions were calculated on the software equipped. At the take-off angle, photoelectrons ~3 nm in depth were assumed to be detected. The surface functional density (groups per cm^2) was calculated with PET density of 1.375 g/cm^3.

---

[1]Department of Applied Biology, Faculty of Textile Science, Kyoto Institute of Technology, Matsugasaki, Sakyo-ku, Kyoto 606-8585, Japan. [2]Department of Biosciences and Informatics, Keio University, 3-14-1 Hiyoshi, Kohoku-ku, Yokohama, Kanagawa 223-8522, Japan. [3]Life Science Materials Laboratory, ADEKA Corporation, 7-2-34 Higashiogu, Arakawa-ku, Tokyo 116-8553, Japan. [4]Department of Polymer Science, Faculty of Textile Science, Kyoto Institute of Technology, Matsugasaki, Sakyo-ku, Kyoto 606-8585, Japan. [5]Ecology-Related Material Group Innovation Research Institute, Teijin Ltd., Hinode-cho 2-1, Iwakuni, Yamaguchi 740-8511, Japan.
*Present address: Department of Polymer Chemistry, Graduate School of Engineering, Kyoto University, Nishikyo-ku, Kyoto 615-8530, Japan. †**Corresponding author. Email: kmiyamoto@bio.keio.ac.jp (K.M.); bika@kit.ac.jp (K.O.)**

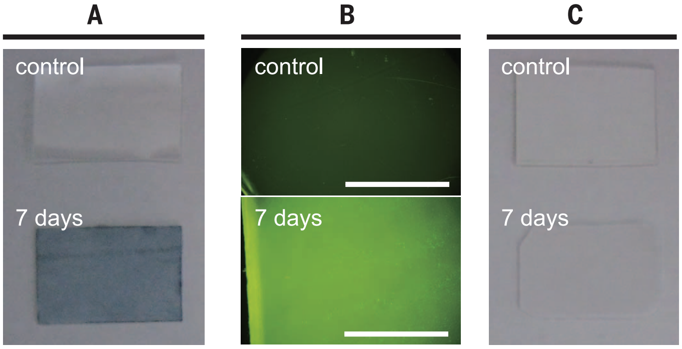

Fig. 2. Qualitative surface analyses of PET films degraded by *I. sakaiensis*. *I. sakaiensis* was cultured with PET film (20 by 15 by 0.2 mm) in YSV medium at 30°C for 7 days. Intact PET film (control) and PET film after cultivation (7 days) were washed with 1% SDS, distilled water, and then ethanol, followed by air drying. (**A**) Detection of the hydroxyl groups. The film was stained with Reactive Black 5 following the reported manuscript (*14*). (**B**) Detection of the carboxyl groups. The film was soaked in 0.18% (w/v) Alexa Fluor 488-hydrazide, and then 1-(3-dimethylaminopropyl)-3-ethylcarbodiimide was added to the solution (final concentration, 0.25% w/v) for activating carboxyl groups. After 24 hours in the dark, the film was washed with distilled water and then ethanol, followed by air drying. The surface was observed by fluorescence microscope at λ excitation = 493 nm, λ emission = 517 nm. Scale bar, 100 μm. (**C**) Detection of the proteins. The film was stained with 0.025% (w/v) Coomassie brilliant blue R250 in 20% (v/v) acetic acid and then destained with 10% (v/v) acetic acid.

$0.13 \pm 0.11 \times 10^{14}$ and $0.36 \pm 0.10 \times 10^{14}$ groups per cm^2, respectively (Fig. 1B). The increase in the surface functional groups strongly suggests an endo-type scission of the polymer chain. In addition, the surface of the PET film cultured with *Ideonella sakaiensis* was qualitatively analyzed. Reactive Black 5 staining (*14*) revealed an increased number of –OH groups (Fig. 2A), while Alexa Fluor 488-hydrazide labeling revealed an increased number of –COOH groups (Fig. 2B). The surface was not stained with Coomassie brilliant blue R250 (Fig. 2C). These results indicate that the increase in these functional groups was due to PET hydrolysis in an endo-type manner and not due to protein contamination.

The isotopic carbon tracing experiments are a direct method for tracing carbon among nutrients. We demonstrated PET assimilation using multiple approaches instead, because isotope-labeled PET was commercially unavailable. As shown in figure S9 in (*2*), the growth of *I. sakaiensis* in the PET film–fed YSV (yeast extract–sodium carbonate–vitamins) medium reached an average optical density of 0.88 at 600 nm for 151 hours (the rightmost panel), whereas that in the absence of PET stopped at ~0.06 (the leftmost panel). During this period of time, the weight loss of the PET film was clearly observed [figure 1H and figure S8 in (*2*)]. These results indicate that a part of the degraded PET was assimilated by *I. sakaiensis* cells. Furthermore, in the culture fluid, the amount of enzymatically released compounds from the PET film—such as terephthalic acid (TPA) and mono(2-hydroxyethyl) terephthalic acid (MHET)—was markedly lower than that of the TPA or MHET units in the degraded PET, indicating that they were incorporated into the cells for growth. By culturing *I. sakaiensis* cells with the PET film, the expression of genes for PETase, MHET hydrolase (MHETase), and TPA degradation pathway, involved in the PET degradation, was found to be dramatically up-regulated, indicating that PET was actively metabolized for energy acquisition and cell proliferation.

REFERENCES

1. Y. Yang, J. Yang, L. Jiang, *Science* **353**, 759 (2016).
2. S. Yoshida *et al.*, *Science* **351**, 1196–1199 (2016).
3. T. Nimchua, H. Punnapayak, W. Zimmermann, *Biotechnol. J.* **2**, 361–364 (2007).
4. T. Nimchua, D. E. Eveleigh, U. Sangwatanaroj, H. Punnapayak, *J. Ind. Microbiol. Biotechnol.* **35**, 843–850 (2008).
5. C. Sharon, M. Sharon, *J. Microbiol. Biotech. Res.* **2**, 248–257 (2012).
6. R. J. Müller, H. Schrader, J. Profe, K. Dresler, W. D. Deckwer, *Macromol. Rapid Commun.* **26**, 1400–1405 (2005).
7. D. Ribitsch *et al.*, *Biocatalysis Biotransform.* **30**, 2–9 (2012).
8. W. Zimmermann, S. Billig, *Adv. Biochem. Eng. Biotechnol.* **125**, 97–120 (2011).
9. S. Sulaiman *et al.*, *Appl. Environ. Microbiol.* **78**, 1556–1562 (2012).
10. C. M. Silva *et al.*, *J. Polym. Sci. A Polym. Chem.* **43**, 2448–2450 (2005).
11. Å. M. Ronkvist, W. C. Xie, W. H. Lu, R. A. Gross, *Macromolecules* **42**, 5128–5138 (2009).
12. M. A. M. E. Vertommen, V. A. Nierstrasz, M. Veer, M. M. C. G. Warmoeskerken, *J. Biotechnol.* **120**, 376–386 (2005).
13. W. Chen, T. J. McCarthy, *Macromolecules* **31**, 3648–3655 (1998).
14. A. O'Neill, R. Araújo, M. Casal, G. Guebitz, A. Cavaco-Paulo, *Enzyme Microb. Technol.* **40**, 1801–1805 (2007).

23 April 2016; accepted 14 July 2016
10.1126/science.aaf8625

NEUROIMMUNOLOGY

Immune cells on the brain

INSIDE

By **Kristen L. Mueller**, **Pamela J. Hines**, *and* **John Travis**

Until recently, many scientists viewed immune cells and the central nervous system (CNS) as a deadly mix. A classic example is multiple sclerosis, where T lymphocytes, together with other inflammatory mediators, damage the protective myelin sheath that encases nerve fibers in the brain and spinal cord. Decades of research on this autoimmune disorder opened a window into how the immune system and the CNS interact, but more recent research efforts have revealed the exceptionally broad scope of communication between the two. We now know that the immune system is very likely a key player in many neurological diseases and, surprisingly, that immune-CNS interactions may not all be bad.

The immune system's reach within the CNS is extensive, probably contributing to the initiation and pathogenesis of neurodegenerative diseases, neurodevelopmental disorders such as autism, and mental health disorders such as schizophrenia. Disease-driving mechanisms vary and include, among others, the pruning of neuronal synapses, effects on CNS development in utero, and inflammation. Although immune cells can clearly be a liability, they are likely also essential for normal brain development and function and for recovery from trauma.

These exciting revelations place neuroimmunology at the forefront of biomedical research priorities. With the potential to affect such a diverse array of neurological ailments, many of which have no known therapy, the hope is that an improved understanding of immune-CNS interactions will bring to light new paradigms for preventing and treating neurological disease.

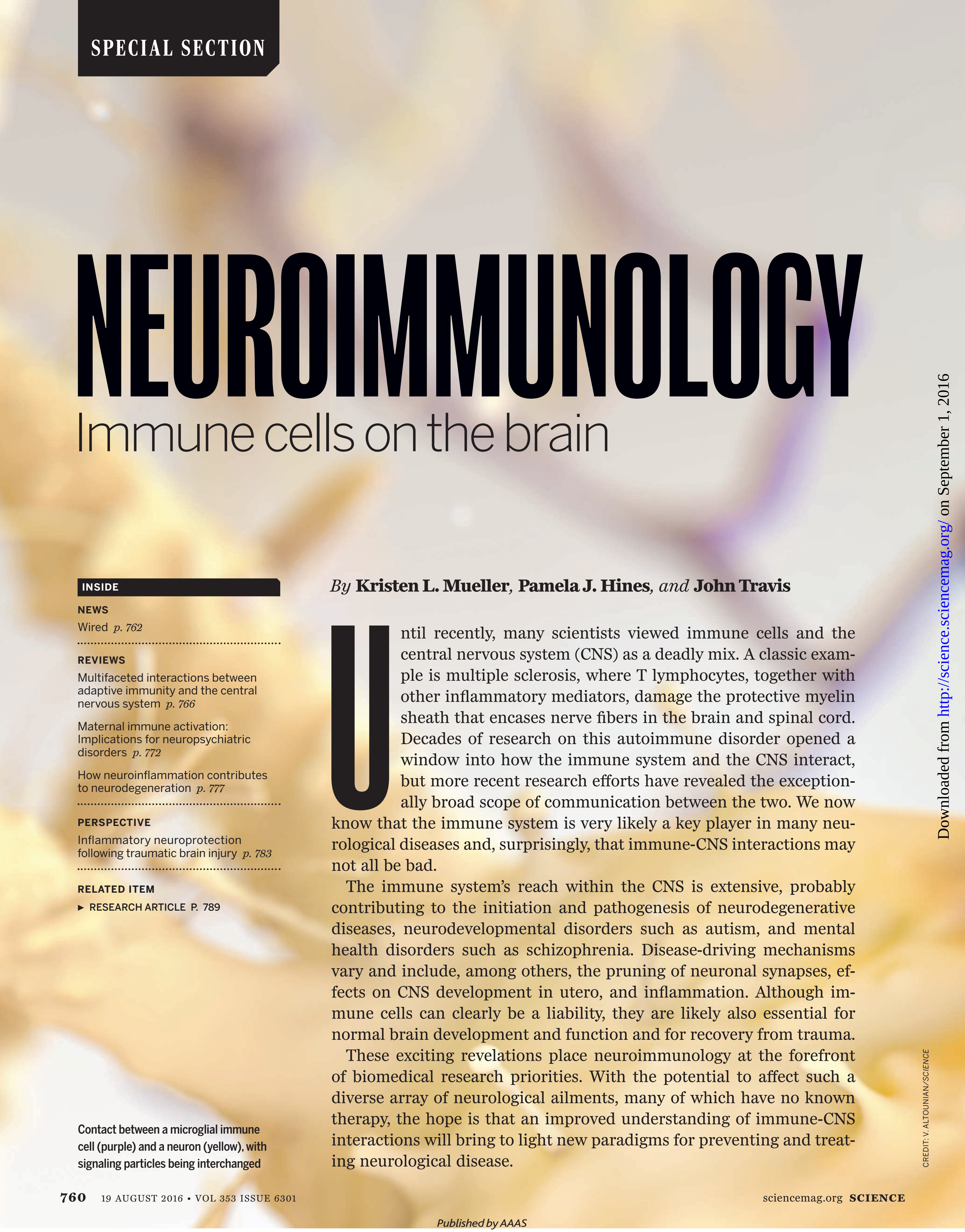

Contact between a microglial immune cell (purple) and a neuron (yellow), with signaling particles being interchanged

CREDIT: V. ALTOUNIAN/*SCIENCE*

WIRED

Beth Stevens and her network of collaborators are showing how immune cells sculpt connections in the brain

By **Emily Underwood**

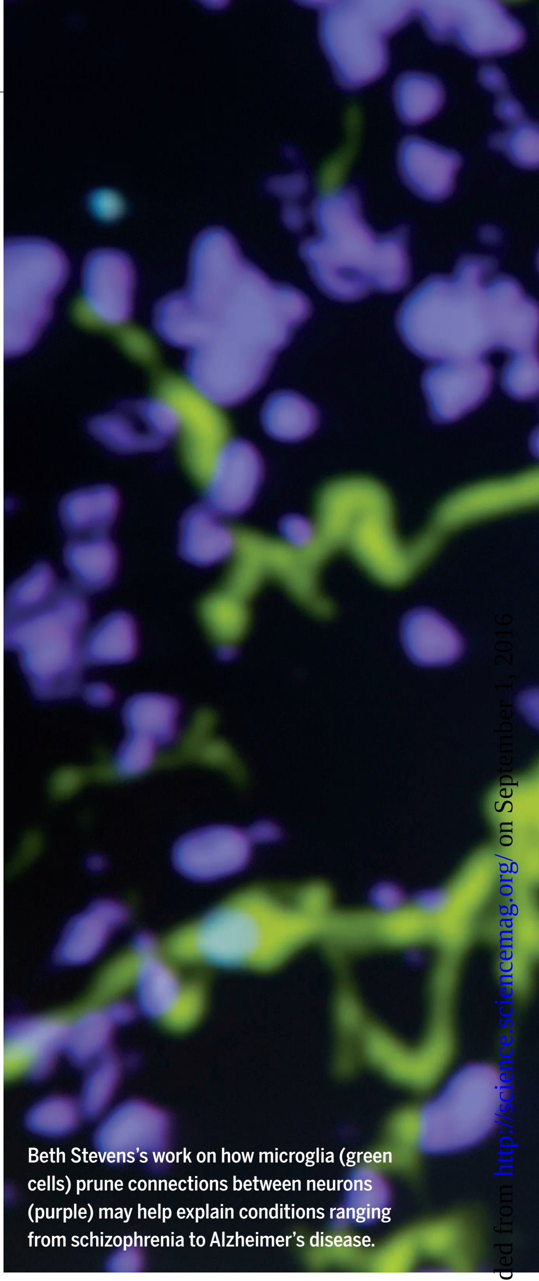

Beth Stevens's work on how microglia (green cells) prune connections between neurons (purple) may help explain conditions ranging from schizophrenia to Alzheimer's disease.

PHOTO: KEN RICHARDSON

In 2010, neurobiologist Beth Stevens had completed a remarkable rise from laboratory technician to star researcher. Then 40, she was in her second year as a principal investigator at Boston Children's Hospital with a joint faculty position at Harvard Medical School. She had a sleek, newly built lab and a team of eager postdoctoral investigators. Her credentials were impeccable, with high-profile collaborators and her name on an impressive number of papers in well-respected journals.

But like many young researchers, Stevens feared she was on the brink of scientific failure. Rather than choosing a small, manageable project, she had set her sights on tackling an ambitious, unifying hypothesis linking the brain and the immune system to explain both normal brain development and disease. Although the preliminary data she'd gathered as a postdoc at Stanford University in Palo Alto, California, were promising, their implications were still murky. "I thought, 'What if my model is just a model, and I let all these people down?'" she says.

Stevens, along with her mentor at Stanford, Ben Barres, had proposed that brain cells called microglia prune neuronal connections during embryonic and later development in response to a signal from a branch of the immune system known as the classical complement pathway. If a glitch in the complement system causes microglia to prune too many or too few connections, called synapses, they'd hypothesized, it could lead to both developmental and degenerative disorders.

Since then, finding after finding has shored up and extended this picture. This year alone, Stevens and her collaborators have published papers in *Science* and *Nature* linking the complement pathway and microglia to diseases such as schizophrenia, Alzheimer's, and cognitive problems from infection with West Nile virus. A study on Huntington disease is forthcoming, Stevens says. Although some scientists say that such research is unlikely to produce therapies any time soon, clinical trials of antibodies that block the complement system in the brain could start for glaucoma and other neurodegenerative diseases by the beginning of 2017. Stevens's decision to stick with her hypothesis, says neuroimmunologist Richard Ransohoff of the biotech company Biogen in Cambridge, Massachusetts, has "worked out spectacularly."

> ***"She's like a four-shot espresso."***
>
> **Cagla Eroglu**, Duke University

ATHLETIC, WITH A MOP OF BLOND CURLS, Stevens has piercing blue eyes that seem capable of knocking a glass off a table with sheer concentration. "She's like a four-shot espresso," says Cagla Eroglu, a neuroscientist at Duke University in Durham, North Carolina, who met Stevens at Stanford, where both completed their postdoctoral training.

Downing a Diet Coke in her office in the Center for Life Science at Boston Children's Hospital, Stevens gestures at a large whiteboard, where she has scribbled a list of projects and grant applications "to keep track of what's cooking" for her and the 14 postdocs, graduate students, and technicians in her lab. At any given point, one team in her lab may be looking for molecular triggers of the complement system while a second observes microglia in vivo and another investigates why certain types of synapses get pruned more often than others. Stevens's many-pronged strategy is a smart move that keeps her lab productive, and "can open up many new directions for the field," says Eric Huang, a neurobiologist at the University of California, San Francisco.

From her office window, Stevens can almost see her hometown of Brockton, Massachusetts, where she went to public school. Her father was a principal, her mom an elementary school teacher. "Even all their friends were teachers," she says. "I think my parents are still wondering what happened there."

Stevens didn't get interested in science until her senior year in high school, when

her Advanced Placement biology teacher told stories about his other job in a clinical microbiology lab. At Northeastern University in Boston, she followed his example and took a job in a hospital laboratory. Her favorite case involved an episode of food poisoning that she helped tie to a sausage contaminated with the *Listeria monocytogenes* bacterium. Although Stevens planned to be a physician, she realized then that she was more attracted to research. "I wasn't really interested in hanging out with the patients as much as figuring out what was wrong with them."

As Stevens approached graduation in 1993, her professors told her to go to the National Institutes of Health (NIH) for more research experience. When her new husband got a chance to work in Washington, D.C., she went with him, determined to get a job at the NIH campus in nearby Bethesda, Maryland.

Stevens trekked to NIH weekly to scan sheets of job postings—"This was before internet job listings," she says. She began waiting tables at a nearby Chili's so she could easily dash over to NIH to check for new jobs. Months passed; her CV languished. One day, neuroscientist Douglas Fields, who had a habit of leafing through the rejected CVs submitted to NIH, cold-called Stevens and offered the 22-year-old a job as a technician. Even though she was "totally green," she says, he soon made her the manager of his lab at the National Institute of Child Health and Human Development in Bethesda.

Fields was interested in how brain activity increases the expression of certain genes in neurons, including one encoding an adhesion protein called L1. This molecule helps cells called glia wrap the wirelike neuronal projections known as axons in layers of fatty insulation, or myelin. Stevens spent hours in the lab trying to model the process in a dish. Eventually, she succeeded. Fields listed her name as a coauthor on the resulting paper—a rare honor for a technician (*Science*, 24 March 2000, p. 2267). And Stevens was left with a passion for glia, cells that neuroscientists had long viewed as "housekeepers," passively providing neurons with nutrients and sponging up excess ions and neurotransmitters.

Stevens decided to get a Ph.D. in neuroscience at the University of Maryland, College Park, while continuing to work at NIH. Upon finishing, she returned to full-time work as Fields's technician and lab manager. By that point, she had caught the attention of Story Landis, then-director of the National Institute of Neurological Disorders and Stroke (NINDS) in Bethesda. The NINDS head told Stevens she was "crazy" not to pursue a career as an independent scientist, advising her to do a postdoctoral position elsewhere and offering help with contacts.

Barres, one of the world's leading glia researchers, ultimately invited Stevens to join his lab. She couldn't have landed in a better place to pursue ambitious, big-picture science, Ransohoff says. Although there are many ways to motivate people, he explains—"Love the hell out of them, scare the hell out of them, and work the hell out of them"—Barres "supports the hell out of them with resources, advice, and scientific direction when needed, then lets them go."

Stevens was "a force of nature," Barres recalls. "She was always working late at night, on holidays, nights, weekends." She also revved up the lab's social life, organizing happy hours and parties for everyone's birthdays, Eroglu says. "Some people are drawn to science because of the challenge—they prefer pain, and want to suffer. Beth really enjoys what she's doing, which makes her a joy to work with."

Barres and his team had long studied star-shaped glia in the brain called astrocytes, which secrete chemicals that can influence neuronal growth. Karen Christopherson, also a Barres postdoc, discovered another remarkable property of astrocytes: They appear to induce neurons to massively increase their production of a protein called C1q. Elsewhere in the body, C1q is known to trigger the complex molecular cascade of the classical complement pathway.

Among other roles, the complement system helps label pathogens and damaged cells as cellular trash throughout the body, affixing them with protein tags that serve as an "eat me" signal for immune cells called macrophages. Christopherson's finding led Barres and Stevens to wonder whether the complement system also plays a role in a key process as the brain develops in the womb and after birth: tagging and pruning back the thicket of newly formed synapses and leaving only functional connections. If C1q were necessary for proper pruning, they hypothesized, synapses in mice without the protein should be disrupted.

Stevens and Barres obtained mice in which the gene for C1q had been knocked out, then looked for alterations in a deep region of the brain's visual system called the visual thalamus. Before a newborn animal has even opened its eyes, neurons in this region undergo massive pruning of synapses, leaving a neatly organized system in which most cells receive inputs from only the right or left eye.

The mice lacking C1q didn't display any obvious visual abnormalities, Stevens says. But they had too many neural connections in a key relay center of the visual pathway, the lateral geniculate nucleus (LGN), showing that C1q was necessary for synaptic refinement. The protein is virtually absent in the neurons of healthy mice with mature brains, suggesting that it plays only a fleeting role early in brain development. In a mouse model of glaucoma, however—a disease in which neurons of the retina are destroyed—Stevens showed that C1q levels were much higher than normal. The findings, reported in *Cell* in 2007, "were really novel, and set the stage for the whole field" to take a closer look at the role of the complement in brain development and function, Huang says.

In later studies of the C1q knockout mice, Stanford neuroscientist David Prince, working in collaboration with Stevens and Barres, found that the animals' hyperconnected neural wiring in the cortex makes them prone to seizures, memory loss, and other cognitive deficits. Stevens and her colleagues focused next on what was doing the pruning in the postnatal brain. A movie clip created by a fellow Barres postdoc, Axel Nimmerjahn, recorded through a sheer window in a mouse's skull, hinted that microglia—which play the role of microphages in the brain—were responsible. The cells continuously extended and retracted slender protrusions as if actively exploring. Stevens had never seen any other cell move so purposefully. She was smitten. "I mean, I loved astrocytes, but they don't do that," she says.

Weeding out the weak

Two types of immune cells, plus complement proteins, work together to prune less active synapses in brain development—and this process may abnormally reactivate during some diseases.

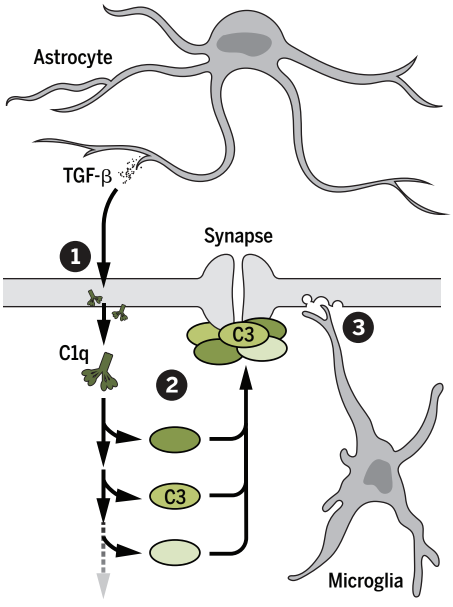

1 Signaling through TGF-β, astrocytes in the developing brain induce neurons to make C1q.

2 C1q initiates the complement cascade, which marks weak or superfluous synapses with C3 and other proteins.

3 Microglia ingest, or prune, complement-tagged synapses, leaving the strongest connections.

GRAPHIC: V. ALTOUNIAN/SCIENCE

Up to that point, Stevens and many others had ignored microglia because they were thought to arrive too late in the brain to affect neurodevelopment. A group led by Miriam Merad at Mount Sinai School of Medicine in New York City, however, demonstrated that microglia begin to populate the brain within days of gestation (*Science*, 5 November 2010, p. 841). That made them "perfect candidates" to conduct early synaptic pruning, Stevens says. Microglia were also the only known brain cells with a receptor for C3, a downstream product of the complement cascade.

AFTER COMPLETING HER POSTDOC position with Barres, Stevens accepted the job offer from Boston and headed back east, intent on putting together the pieces of the puzzle. Finding a way to test whether microglia actually were ingesting pieces of synapses in the living brain was her first challenge. It occurred to Dori Schafer, one of the first postdocs Stevens hired, to combine mice genetically engineered to make their microglia glow bright green under ultraviolet light with a system that Barres and Stevens had used to tease apart retinal projections in the LGN. The system made synapses connected to one eye appear red and those linked to the other eye blue. All Schafer had to do was look for bits of red and blue synapses inside the green microglia. One Saturday afternoon, the first results rolled in. "I still remember the first cell I saw with bits of presynaptic terminals inside of it," Schafer says.

Scientists had long known that neuronal activity strengthens synapses whereas less active synapses are eliminated, and Stevens and others had predicted that microglia would go after a neuron's weaker connections. To test that hypothesis, Schafer applied pharmacological agents to the eyes of developing mice to increase or decrease the firing activity of neurons in one eye, and found that the less active synaptic connections were more aggressively eaten and pruned by microglia. She also used mice that lacked the complement receptor in microglia, and discovered that this reduced the rate at which the cells devoured synapses. The mice also had more synapses than controls, similar to the C1q knockouts, she says.

While Schafer and Stevens were writing up these findings, a competing group led by Cornelius Gross of the European Molecular Biology Laboratory in Heidelberg, Germany, turned up the heat by publishing a conceptually similar paper in *Science*. The study suggested that microglia have a role in synaptic pruning in the hippocampus, but pointed to a different immune-related protein called fractalkine—which, among other roles, shepherds microglial migration around the brain—as a key player. In mice lacking a receptor for this protein, maturation of neuronal connections was delayed. Gross's work, however, didn't point to a clear mechanism for the pruning. Schafer and Stevens hastened to publish their complement work in *Neuron*. Their contribution was particularly provocative, Gross says, because the classical complement system had long been known to be involved in the ingestion of pathogens and dead or damaged cells. "It's really like a smoking gun."

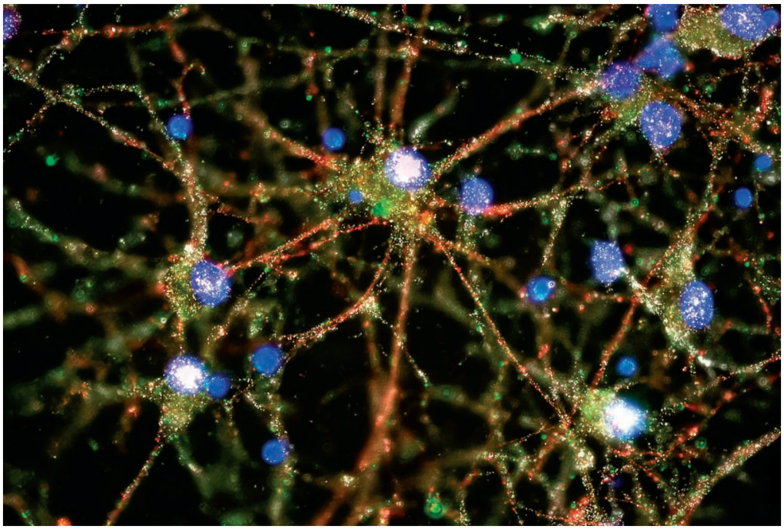
The complement protein C4 (green) often overlaps with synaptic markers (red and white dots) in this culture of neurons (blue marks main cell bodies), a sign of how it may flag synapses for pruning in brain development and disease.

IMAGE: HEATHER DE RIVERA/MCCARROLL LAB/HARVARD

Even now, however, no one has definitively shown that microglia eat synapses in a living animal's brain. The evidence is circumstantial, Gross notes—from before-and-after shots showing either microglia hovering near a synapse or microglia that have engulfed pieces of the synapse. It's not clear in those images whether the microglia actively ate the synapses or merely gobbled up pieces that had already weakened or fallen off. But Schafer, now an assistant professor at the University of Massachusetts Medical School in Worcester, thinks she may have a way to catch pruning in action. She is studying the mouse's barrel cortex, the part of the rodent brain that is wired to the animals' whiskers. "If we manipulate one whisker, we know exactly where to look" for synaptic changes, she says, which should increase the odds of capturing images of microglia in the act of eating synapses.

ALTHOUGH IT'S NOW WELL ACCEPTED that C1q is necessary for proper neuronal wiring early in life, evidence is mounting that the molecule can be detrimental later on. As mice and humans age, C1q levels rise in their brains up to 300-fold, Barres has found. Reducing its levels or blocking its ability to start the complement cascade limits cognitive and memory decline in aging mice compared with untreated controls, Stevens and others have further demonstrated.

Studies of human disease also hint that the complement can trigger harmful synapse loss. In January, geneticist Steven McCarroll at Harvard Medical School and the Broad Institute in Cambridge, Massachusetts, reported evidence that the *C4A* gene, which encodes a complement protein downstream of C1q, may contribute to the synapse loss and brain tissue thinning that characterizes schizophrenia. After analyzing genome data from more than 64,000 people, they found that a subset of those with the mental disorder were more likely than controls to have an overactive version of *C4A*. When McCarroll and Stevens teamed up with Harvard's Michael Carroll, who knocked out the mouse version of this gene, they found reduced synapse pruning during postnatal development in the altered rodents. Gross and others hailed the potential new schizophrenia mechanism, published in *Nature*, as a major advance.

The next month, in *Science*, Stevens described results suggesting that overhungry microglia are responsible for the early loss of synapses in Alzheimer's disease (*Science*, 6 May, p. 712). In several mouse strains bred to produce excessive amyloid, a protein that forms plaques in the brains of people with Alzheimer's, abnormally high levels of C1q set off a microglial feast, which destroyed functional synapses long before plaque formation and symptoms of cognitive impairment set in. That pattern of decline is consistent with observations that synapse loss is a more powerful predictor of Alzheimer's symptoms than amyloid plaques, and "brings into light what's happening in the early stage of the disease," says Jonathan Kipnis, a neuroscientist at the University of Virginia School of Medicine in Charlottesville.

Most recently, in *Nature*, a collaboration with Stevens's group led by neurobiologist Robyn Klein at Washington University in St. Louis in Missouri demonstrated in mice that the classical complement pathway also revs up during recovery from infection by West Nile virus, driving microglia to engulf synapses at a dangerous rate. That could help account for the chronic memory impairments that more than half of people experience after infection, says Huang, who calls the research "fascinating."

Such findings have piqued interest in targeting C1q clinically. Annexon Biosciences, a South San Francisco, California–based company, is leading the way. Co-founded by Barres back in 2011, after mouse data suggested blocking C1q could be beneficial for multiple neurodegenerative and autoimmune diseases, Annexon has developed several antibodies that can bind and block the action of the complement protein.

The company, in which Stevens is a shareholder, plans to launch human clinical trials of the drugs in people with Alzheimer's, Huntington, and glaucoma by next year, but Huang and others warn that the drugs may not make a dent in more complex disorders such as schizophrenia. Another challenge will be to show that the antibodies really are preserving synapses. One tool may grow from a study published last month in *Science Translational Medicine* in which a research team showed that it could use a positron emission tomography scan to quantify synapse numbers, and loss, in living people. That could be "really important," Stevens says.

Now past the crucible of starting her own lab, Stevens's anxieties of just a few years ago have dissipated. She's confident in her science and settling into a new role as a mentor, seeking to repeat what others once did for her. Stevens has "already transferred" the Barres-style incubator environment to Boston, and produced exceptional "scientific grandchildren," Ransohoff says.

Stevens recently started another happy hour—this one for other junior principal investigators in the Boston area. When people see other people launching their careers, and it looks effortless, "they don't know what you're really going through," the former Chili's waitress and lab technician says. "When you get a chance to get together and have a beer, you realize we're all going through the same thing." ■

REVIEW

Multifaceted interactions between adaptive immunity and the central nervous system

Jonathan Kipnis

Neuroimmunologists seek to understand the interactions between the central nervous system (CNS) and the immune system, both under homeostatic conditions and in diseases. Unanswered questions include those relating to the diversity and specificity of the meningeal T cell repertoire; the routes taken by immune cells that patrol the meninges under healthy conditions and invade the parenchyma during pathology; the opposing effects (beneficial or detrimental) of these cells on CNS function; the role of immune cells after CNS injury; and the evolutionary link between the two systems, resulting in their tight interaction and interdependence. This Review summarizes the current standing of and challenging questions related to interactions between adaptive immunity and the CNS and considers the possible directions in which these aspects of neuroimmunology will be heading over the next decade.

Although the initial experiments carried out by Medawar and colleagues (*1*), as well as others (*2*), have demonstrated that the immune response to the central nervous system (CNS) antigens does exist (although it is distinct from the response in other tissues), the CNS was traditionally viewed as an immune-privileged site. This depiction set a clear separation between the nervous and immune systems until quite recently (*3*, *4*). Therefore, the CNS was generally assumed to be largely devoid of immune entities, the microglia (a macrophage-like cell) being an acknowledged exception (*5*). Any sign of immune presence within the CNS parenchyma was perceived as a hallmark of pathology.

Numerous seminal works have investigated the interaction between innate immunity and the CNS under conditions such as stress, bulimia or anorexia, fever, and others (*6*–*8*). The development of an animal model [experimental allergic (or autoimmune) encephalomyelitis (EAE)] of a major neuroinflammatory disease [multiple sclerosis (MS)] led to closer scrutiny of the interactions between adaptive immunity and the CNS (*9*). For more than 80 years, studies with the EAE model resulted in many breakthrough findings in the fields of immunology and neuroscience (*10*–*20*).

For a long time, the immune system was commonly viewed solely as the body's defense mechanism against pathogens. In the early 1990s, however, Matzinger proposed the "danger" theory, in which the immune system responds not only to signals from pathogens but also to danger signals released from damaged tissues, even in the case of sterile injuries (*21*). Around the same time, Cohen advanced the idea of the "immunological homunculus" (*22*), assigning the immune system physiological roles in tissue maintenance and homeostasis. These studies broadened our understanding of what the immune system does and, in combination with other works on the role of adaptive immunity in the injured CNS (*23*, *24*), led to a wider understanding that the two systems may be more closely connected than was previously thought.

In this article, I will provide a brief overview of multifaceted interactions between adaptive immunity and the CNS as we see them today and will highlight critical questions currently confronting neuroimmunologists.

> ***"…the interface between pathogens and immunity influenced the evolution of our almost infinitely complex nervous system."***

Neuroimmune interactions in CNS disorders

In MS, immune cells in the brain and spinal cord attack the myelin sheath that encases nerves. EAE, the animal model of MS, has provided many insights into how the immune system interacts with the CNS in this disease [reviewed in (*25*–*28*)]. Briefly, the devastating effects of MS and EAE were initially ascribed primarily to autoimmune CD4$^+$ T cells [in EAE, the CD4$^+$ T cells were reactive to proteins found in the myelin, particularly myelin basic protein, proteolipid protein, and myelin oligodendrocyte glycoprotein (MOG) (*15*, *17*)]. Over the years, our understanding of the complexity of this disease has grown as a result of intensive research on its underlying mechanisms. The current consensus is that many other immune cells besides CD4$^+$ T cells—including CD8$^+$ T cells, B cells, neutrophils, natural killer cells, and monocytes and macrophages—are involved in MS pathology (*29*–*33*). This research also revealed that the damage incurred in EAE, and likely also in MS, is mediated by the immune system, and the overall outcome of the inflammatory process in this disease is unequivocally detrimental.

Many, if not all, neurodegenerative diseases also exhibit some sort of immune association. In Alzheimer's disease (AD), for example, phagocytes are thought to play an important role in disease progression, although the identity of the major phagocytes in AD brains remains unclear. More specifically, whether microglia or blood monocyte–derived macrophages that engraft the parenchyma contribute to disease pathology is unknown (*34*–*38*).

Peripheral myeloid cells are not the only cells involved in neurodegenerative diseases, as T lymphocytes were recently proposed to play a role in animal models of several neurodegenerative conditions, including AD and amyotrophic lateral sclerosis (ALS). For example, AD-susceptible mice progress to disease more rapidly when they lack an adaptive immune system (*39*). This suggests that T cells may be protecting the diseased brain, much as they do after CNS injury (*24*, *40*, *41*), as discussed in detail below. Aging is associated with T cell dysfunction; consequently, AD progression in mouse models is slowed down and its outcome improved by enhanced functioning of effector T cells (*42*). Likewise, mouse models of ALS on a T cell–deficient background show more rapid disease progression (*43*). Although the mechanism of immune-mediated neuroprotection is not fully understood, accumulating evidence from different neurological diseases points to a beneficial role for both peripheral (macrophage, T cell) and resident (microglial) immune cells.

Neuroimmune interactions after CNS injury

Acute injury to the CNS, such as a contusive spinal cord injury or optic nerve crush injury, results in global immune changes throughout the body (*44*), most prominently within the deep cervical lymph nodes, the meningeal spaces (including the cerebrospinal fluid), and the site of injury itself (*45*–*49*). The adaptive response at the site of injury is preceded by the innate immune response, in which the injured CNS promptly releases alarmins, such as interleukin (IL)–33, adenosine triphosphate, and HMGB1, which activate glia and recruit granulocytes and monocytes to the site of injury (*46*, *50*). IL-33 is particularly important for monocyte recruitment, and injury outcomes are worse in mice lacking alarmins or monocytes. Compared with other organs, the CNS expresses very high amounts of IL-33 (*51*). However, the reason for this is unclear. It might simply be that IL-33 also has other, as yet unknown, effects in the CNS or that IL-33 represents a mechanism that has evolved to recruit immune cells upon CNS injury, perhaps to fight pathogens invading the exposed nervous tissue and to help heal the wound. This

---

Center for Brain Immunology and Glia (BIG), Department of Neuroscience, School of Medicine, University of Virginia, Charlottesville, VA 22908, USA.
Email: kipnis@virginia.edu

mechanism might have been later adopted to also heal sterile CNS injuries.

In the case of infection, innate immunity leads to a pathogen-specific adaptive immune response. This, in turn, further regulates the innate response, skewing it (once the infection has cleared) from an antipathogenic to a tissue-building phenotype. The adaptive response then regulates itself by suppressing effector T cells and retaining a small population of memory clones that can be easily and rapidly reactivated upon subsequent exposure to the same infection. A similar scenario is likely to occur in response to CNS injury (*49*), although the antigenic specificity of T cells that respond to the injury is unknown. The T cell response may be specific to CNS-restricted antigens (*24*). However, depending on the experimental conditions, T cells may also be activated in a T cell receptor (TCR)–independent manner (*45*). If the response is activated as a result of drainage of CNS antigens into draining lymph nodes, T cells will likely mount a response to these self-antigens.

The above scenario raises a question: What prevents these potentially self-reactive T cells from attacking the brain? Because the failure of such putative mechanisms of tolerance within the CNS might result in the development of autoimmune diseases such as MS, it is of crucial importance to identify and understand these mechanisms. In most, if not all, experimental animal models of CNS injury, the net outcome of the spontaneous T cell response to injury is neuroprotective. However, an uncontrolled autoimmune T cell response may result in destructive outcomes. The regulation of the immune response after injury, therefore, is crucially important (*45*, *47*, *52*).

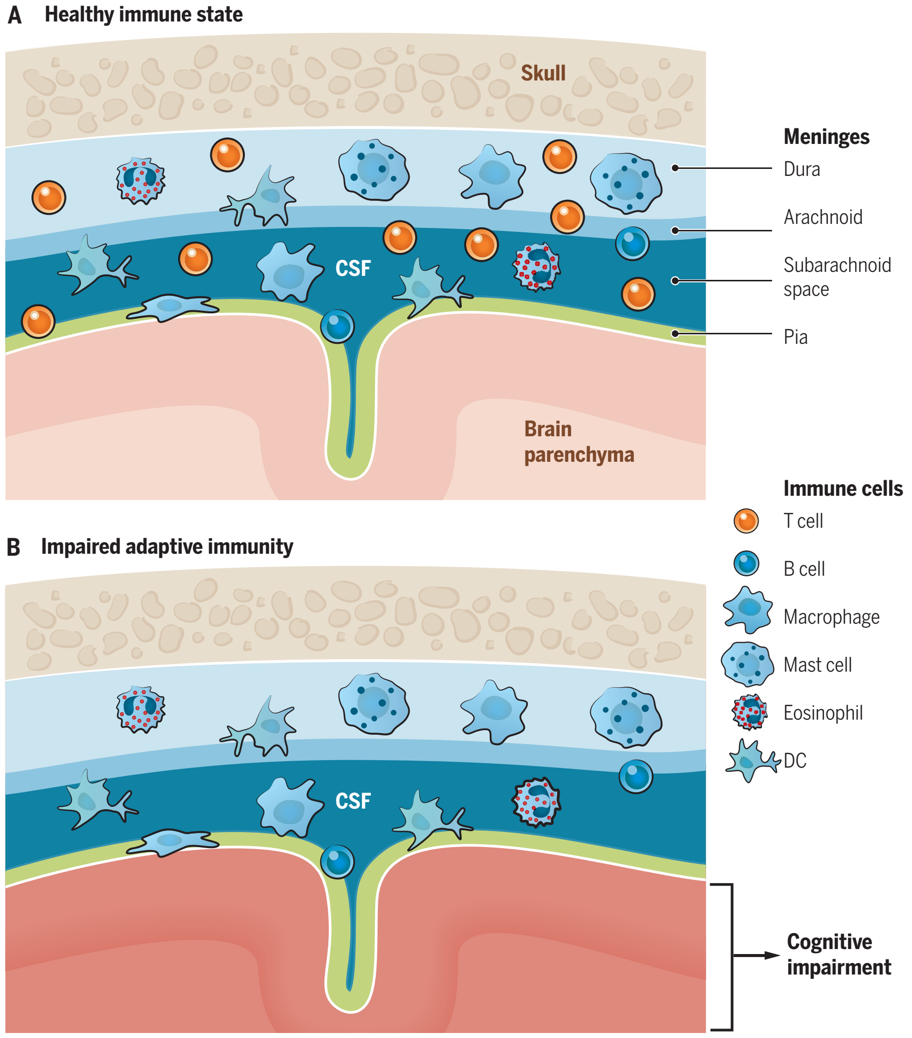

Fig. 1. Meningeal immunity in "surveillance" of brain function. (**A**) Representation of meninges (pia mater, lining the brain parenchyma; dura mater, attached to skull; arachnoid, attached to dura mater; subarachnoid space, space between arachnid and pia mater, where the CSF flows) and their coverage by the immune cells. Recent evidence suggests that meningeal immune cells, primarily T cells, affect brain function. (**B**) Elimination of meningeal T cells by using genetically modified mice, pharmacologically trapping T cells in the deep cervical lymph nodes, or preventing their migration to meningeal spaces results in impaired cognitive function. The precise mechanism of how meningeal T cells regulate cognitive function is still not fully understood. DC, dendritic cell.

CREDIT: FIGURES ADAPTED BY *SCIENCE* FROM A. IMPAGLIAZZO

Neuroimmune interactions in homeostasis

Whether the endogenous responses to CNS injury and neurodegeneration are exclusively autoimmune in nature requires further study. If responding T cells recognize self-antigens and are yet beneficial, what would be the evolutionary advantage of having a task force with the potential for attacking healthy tissue? After injury to the CNS, would the beneficial capacity of such T cells possess sufficient evolutionary force to favor such a trait? One plausible explanation that might accommodate this possibility is that the immune response to injury is an extreme manifestation of a CNS-specific immunity that is always present and whose role is to protect the healthy CNS in its daily functioning.

The above rationale led me and colleagues to examine the role of adaptive immunity in cognitive function (*53*). Unexpectedly, mice deficient in T lymphocytes exhibited cognitive impairment, and passive transfer of mature T cells improved their cognitive function. Further research on the effect of immunity on CNS function has yielded greater knowledge of the immune cell populations required for learning and memory (mainly $CD4^+$ T cells) and provided some initial insights into their antigenic specificity and the location from which their beneficial effects are mediated (*53*–*57*). The jury is still out with regard to the antigenic specificity of the T cells that is required for proper cognitive function. Our studies indicate that OTII mice (TCR transgenic mice, bearing ~90% of T cells with specificity to ovalbumin) exhibit cognitive impairment, whereas injecting them with MOG-reactive T cells (CNS protein–specific T cells) improves cognitive function, suggesting an autoimmune nature of procognitive T cells (*58*, *59*). T cells likely mediate their beneficial effects from the meningeal spaces—that is, the regions between the three membranes that make up the brain and the spinal cord–enveloping meninges (Fig. 1). Data supporting this notion are numerous, though not yet conclusive. For example, meningeal T cells demonstrate changes in phenotype and activation in mice undergoing cognitive tasks or exposed to stress (*55*). Moreover, treatment of mice with an antibody targeting the VLA-4 integrin, which attenuates the migration of immune cells (primarily T cells and monocytes) across the blood-brain barrier (BBB) and the blood-meningeal barrier (BMB) (as well as across gut barriers), results in cognitive impairment (*55*). Furthermore, elimination of the deep cervical lymph nodes that drain the CNS results in disturbed meningeal T cells (as well as meningeal myeloid cells) and is associated with impaired learning behavior (*58*, *59*). However, these findings are mainly correlative. Further investigation is needed to pinpoint the role of T cells within meningeal barriers on CNS function.

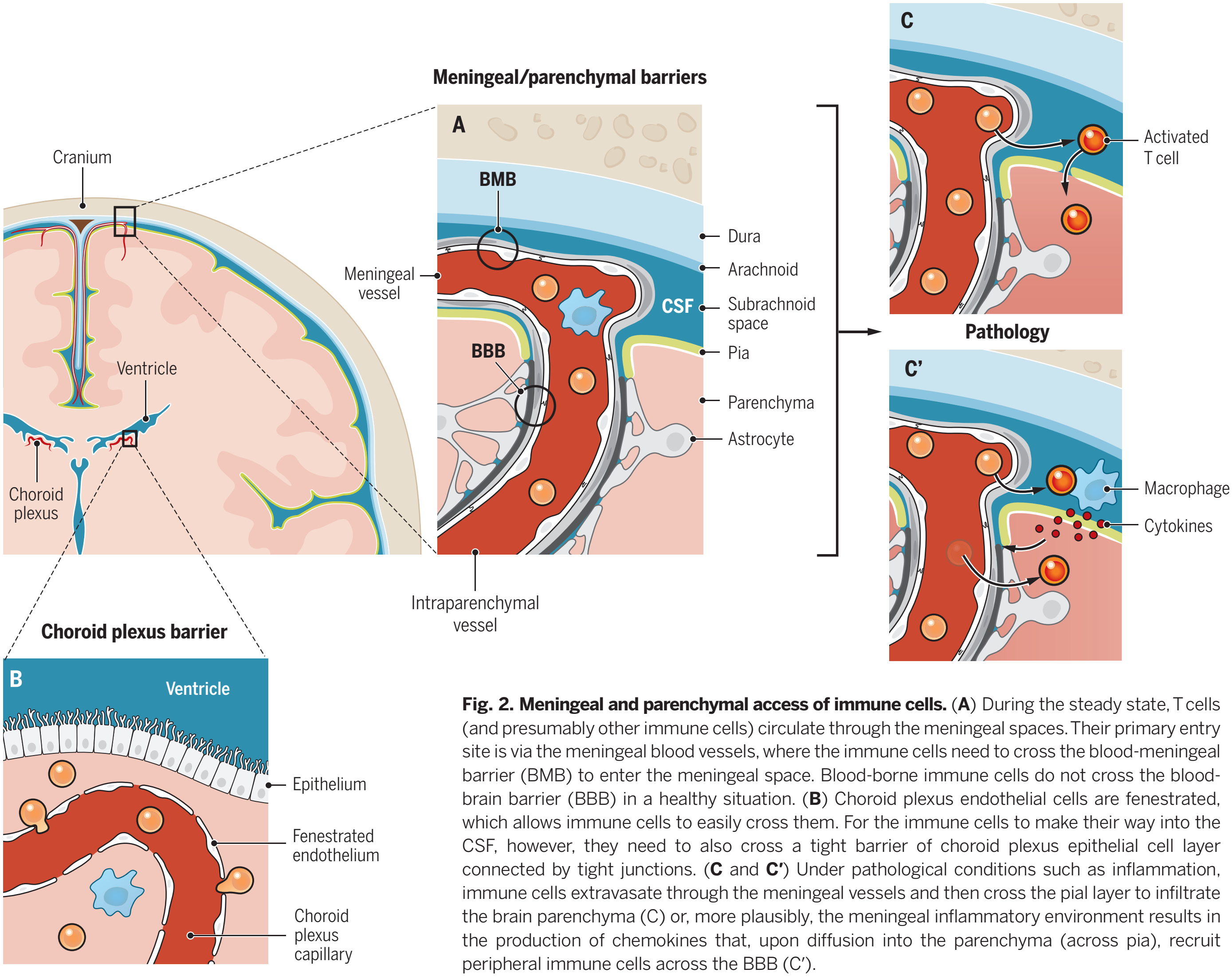

Fig. 2. Meningeal and parenchymal access of immune cells. (**A**) During the steady state, T cells (and presumably other immune cells) circulate through the meningeal spaces. Their primary entry site is via the meningeal blood vessels, where the immune cells need to cross the blood-meningeal barrier (BMB) to enter the meningeal space. Blood-borne immune cells do not cross the blood-brain barrier (BBB) in a healthy situation. (**B**) Choroid plexus endothelial cells are fenestrated, which allows immune cells to easily cross them. For the immune cells to make their way into the CSF, however, they need to also cross a tight barrier of choroid plexus epithelial cell layer connected by tight junctions. (**C** and **C′**) Under pathological conditions such as inflammation, immune cells extravasate through the meningeal vessels and then cross the pial layer to infiltrate the brain parenchyma (C) or, more plausibly, the meningeal inflammatory environment results in the production of chemokines that, upon diffusion into the parenchyma (across pia), recruit peripheral immune cells across the BBB (C′).

Although the role of meningeal immunity in CNS function is not yet fully understood, its composition and maintenance represent an interesting aspect of tissue immunology. The meningeal T cell population is dynamic: Treatment with FTY720 (a sphingosine 1-phosphate receptor-1 agonist that traps lymphocytes in lymph nodes) or VLA-4–targeting antibodies reduces the number of T cells and monocytes in the meninges (*55*, *58*, *59*). Moreover, removal of the deep cervical lymph nodes results in an increase in T cell number in meningeal spaces, pointing to their circulation between these anatomical locations. In parabiotic wild-type (WT) mice, lymphocyte exchange occurs in the meninges (suggesting that the immunity within meningeal barriers is dynamic), but the rate of exchange is lower than the 50:50 ratio seen in the blood. This ratio changes, however, when TCR transgenic mice are attached parabiotically to WT mice: The amount of WT cells entering the meninges of TCR transgenic mice is at least doubled relative to WT:WT parabionts (*59*). These results further indicate that meningeal immunity is dynamic and T cells are presumably enriched for a specifically selected repertoire. Despite the importance of meningeal immunity in neuroinflammatory diseases such as MS, as well in neuroviral infections, an understanding of immune cell trafficking into this compartment is only emerging (*60*–*62*). Also, migration of these cells out of the meninges was only vaguely understood until recently.

How do immune cells enter and exit the CNS?

Access of immune cells to the CNS parenchyma is likely secondary to their infiltration into the meninges during inflammation (*60*). It is therefore important to understand the routes through which immune cells find their way into and out of the meninges, as well as what keeps them in the meninges as opposed to freeing them to return to the periphery or infiltrate the parenchyma.

Two plausible routes might explain how immune cells access the meninges: through the meningeal blood vessels or, alternatively, via the choroid plexus. The choroid plexus is located within each ventricle of the brain and is composed of epithelial cells surrounding the capillaries and the stromal cells. The endothelial cells in the choroid plexus, unlike elsewhere in the CNS, are fenestrated (*63*). Because the role of choroid plexus epithelial cells is to produce cerebrospinal fluid (CSF) by filtering the blood, the choroid plexus is highly vascularized, allowing for the presence of many immune cells. However, this does not necessarily mean that cells are able to penetrate the epithelial layer and thus gain entry into the meningeal spaces/CSF. To access the meninges, immune cells from blood vessels supplying the choroid plexus would need to traverse the endothelial barrier (an explainable step) and then the choroid plexus epithelial cell barrier with tight gap junctions (an unusual step for lymphocytes) to enter the CSF. For a cell to penetrate the meningeal vessels and enter the CSF, it has to cross the BMB. The BMB differs from the BBB and lacks some of the latter's components, such as astrocyte endfeet

(*64*, *65*), making it easier for cells to penetrate (Fig. 2, A and B).

A recent study suggests that meningeal blood vessels recruit T cells into the meningeal spaces (*60*). Though activation of T cells in the meninges and their detachment are probably necessary for the cells to access the parenchyma, the route from the meningeal spaces/CSF to the parenchyma is not well understood. Meningeal cells have the capability to transmigrate across pia mater to reach parenchyma (*48*), but the mechanisms guiding such a process are still unclear. Under neuroinflammatory conditions, the gradient of chemokines produced and induced by meningeal immune cells might result in transmigration of immune cells across the BBB (*66*). Both routes might contribute to immune infiltration in patients with MS [particularly given the differential homing of encephalitogenic CD8$^+$ T cells (*67*)] and need to be studied further (Fig. 2C).

CNS drainage: New concepts for old

Much is still unclear about the entry of cells into the meningeal spaces and the CNS parenchyma. Until recently, the CNS routes by which immune cells and macromolecules exit the meninges and the CNS were even less clear. All bodily tissues are served by two kinds of vessels: (i) blood vessels that convey blood, oxygen, and nutrients to the tissue and (ii) lymphatic vessels that remove the tissue's waste products. These vascular routes are shared by immune cells, which use blood vessels as a means of accessing the tissue and lymphatic vessels as the main exit routes. It is therefore likely that immune cells surveying a tissue leave it by the same exit path as that taken by the tissue's waste products. If this is the case in the meninges, then we need to understand the drainage system of the brain (or, for that matter, of the entire CNS) to comprehend how immune cells exit the CSF/meninges. Because of the lack of lymphatic vessels in the CNS parenchyma, its drainage pathways have remained unclear. A new (or revised) hypothesis proposed that the perivascular space [formed between a blood vessel's endothelial cells and the astrocytic endfeet processes and termed as "glymphatic" (*68*)] serves as a channel that allows CSF to enter the parenchyma along the arteries (Fig. 3). Pulsation of the vessels allows perivascular fluid, along with its macromolecules (of a particular size range), to diffuse from the periarterial spaces into the parenchyma, from which it is subsequently reabsorbed at the perivenular space, owing to the expression of aquaporin 4 (a protein that conducts water through the cell membrane) by perivenular astrocytes. On the way from the periarterial to the perivenular space, the fluid "washes" the parenchyma, carrying tissue-generated waste products with it. Those waste products are then carried through the perivenular space back into the CSF (*69*) (Fig. 3). But what drains the CSF?

Humans produce about six times their CSF volume per day, most of which drains into venous sinuses through the arachnoid granulations. This path is unlikely to allow immune cells to traffic out because immune cells normally do not leave tissues through reverse transmigration into the blood vessels. An alternative pathway might be exiting via the cribriform plate, a porous plate on the skull that allows olfactory nerves to exit the brain and innervate the nasal cavity (*70*). Immune cells and CNS antigens and other macromolecules could leave the CNS along the olfactory nerves and enter the nasal mucosa, from which they are reabsorbed by the nasal mucosa lymphatics and drained into the deep cervical lymph nodes (*71*, *72*). The absence of classical lymphatics in the CNS was the distinctive trait that led to the proposal of this path (Fig. 4).

This hypothesis of drainage into the deep cervical lymph nodes was recently challenged when the reported existence of meningeal lymphatics was proposed as the direct migratory route for immune cells and macromolecules from the CSF into the deep cervical lymph nodes (*73*, *74*). A scrupulous search of the literature revealed that meningeal lymphatic vessels and CNS-draining lymphatic connections were suggested in the past (*75*–*77*) but were apparently overlooked by contemporary researchers (*70*, *71*). Markers that permit an unambiguous definition of lymphatic vessels have only recently been developed (*78*, *79*). Many organs—such as the eye (*80*) and, most recently, the CNS (*73*, *74*)—once believed to be devoid of lymphatic vessels appear to be drained by lymphatic vessels. Although meningeal lymphatic vessels drain macromolecules from within the brain parenchyma, their location is extraparenchymal. A study published nearly 40 years ago indicated that the brains of patients with MS harbor lymphatic vessels (*76*). Verifying these findings with modern tools would be an important achievement, because although the healthy parenchyma is not vascularized by lymphatic vessels but rather drained via lymphatic vessels in the meninges, it is plausible that in inflammatory conditions such as MS, the meningeal lymphatic vessels may extend, physiologically or pathologically, into the CNS parenchyma. Definitive proof that this happens is not easy to obtain because no exclusive markers of lymphatic endothelial cells currently exist, and many of the molecules expressed by lymphatic endothelial cells are also expressed by other cells in the CNS (*79*). Development of novel whole-organism imaging techniques will make it possible to conduct a closer examination of routes for the removal of waste material from the brain parenchyma and may even lead to the discovery of lymphatic vessels within the parenchyma itself. Such putative parenchymal vessels may not be fully functional and, in the healthy adult animal, may not even be organized into vessels. However, if they grow and form functional vessels during the course of inflammation, it might be possible to achieve more efficient drainage of immune cells. Similar mechanisms may apply to the generation of tertiary lymphatic structures associated with CNS inflammation in MS patients and in some animal models (*81*, *82*).

Why are the nervous and immune systems so important for each other's functioning?

This Review has focused on the adaptive immune system's effects on the brain. I did not attempt to review the recent works on the new roles of microglia in healthy and diseased CNS function (*83*–*88*), as the subject warrants a full analysis of its own. Space restrictions here also prohibit inclusion of another relevant topic in neuroimmunology: interaction between the immune system and the peripheral nervous system (*89*–*94*).

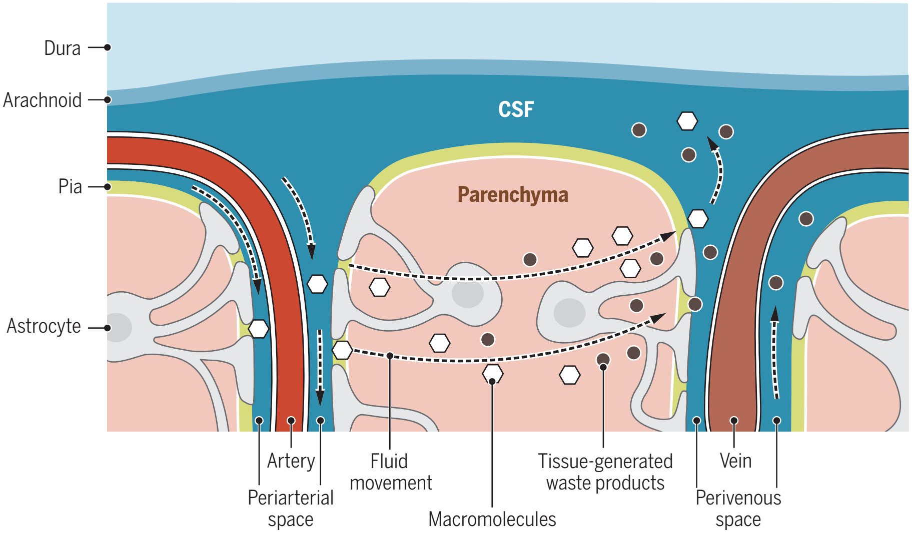

Fig. 3. Schematic representation of the glymphatic system. Periarterial space (formed between a blood vessel's endothelial cells and the astrocytic endfeet processes) allows CSF to follow the arteries into the parenchyma. CSF, along with macromolecules within it, diffuses from the periarterial spaces as an interstitial fluid into the parenchyma, "washes" the parenchyma, and is reabsorbed into perivenular space, to be then carried back and mixed with the CSF.

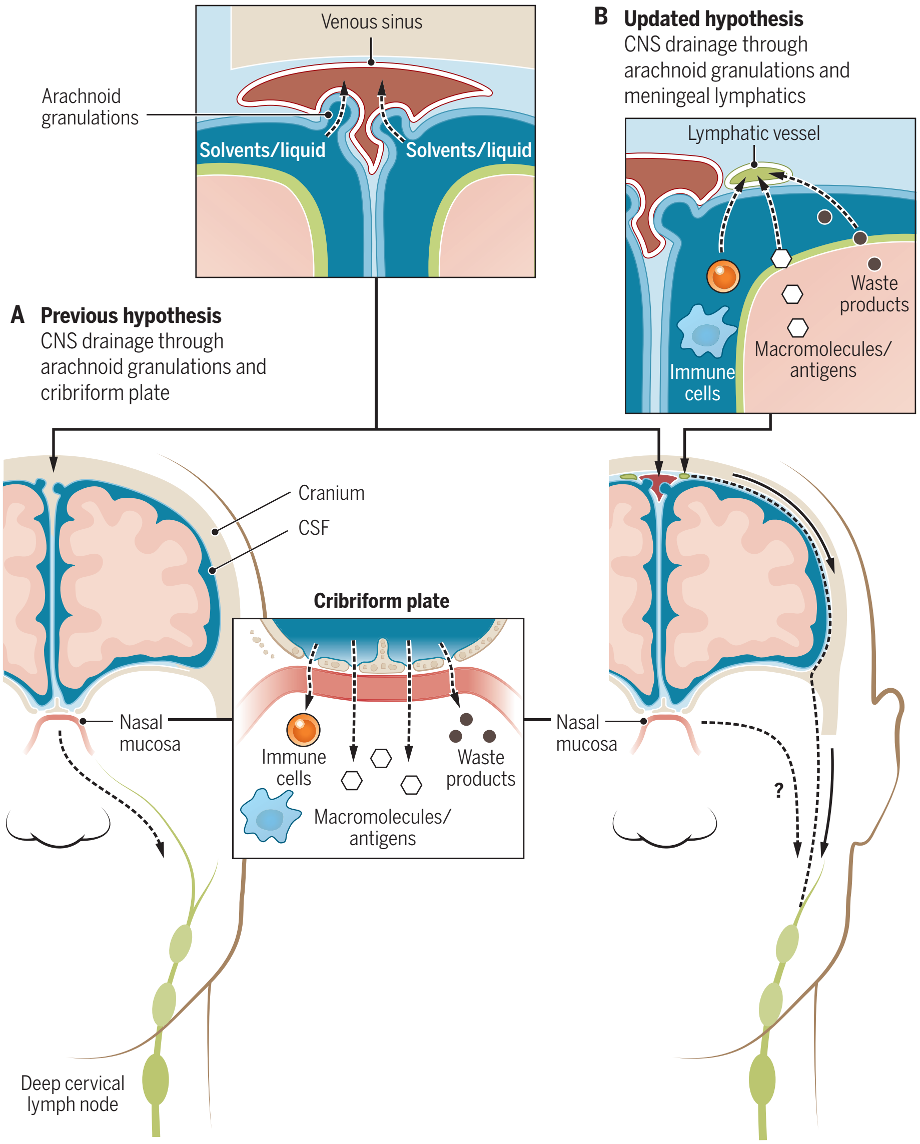

Fig. 4. CNS drainage: New concepts for old. (**A**) Before the discovery of meningeal lymphatic vessels, the old concept of CNS drainage was based on the fact that water from CSF is drained through arachnoid granulations, whereas macromolecules and immune cells from the CNS and the CSF are drained through the cribriform plate into nasal lymphatics and, from there, to CNS-draining deep cervical lymph nodes. (**B**) Discovery of the meningeal lymphatic vessels led to the hypothesis that they may drain meningeal immune cells and macromolecules from the parenchyma and the CSF, whereas the contribution of the cribriform plate as a drainage route for immune cells under homeostatic conditions needs to be reassessed. This route may be more active during neuroinflammatory conditions. Additional studies are needed to better characterize the contribution of each route of drainage for immune cells and macromolecules from the CNS and the CSF under homeostatic and pathological conditions.

Many molecules classically defined as "immune" are also crucial for CNS development and function (*95*–*98*). This fact further contributes to the growing appreciation that the two systems are molecularly and cellularly equipped for close communication. The interaction of the two systems, for so long considered to function separately, begs a fundamental question: Why are they so closely related, with each so capable of affecting the other?

The answer is to be found by looking into the evolutionary development of their coexistence (*99*). Assuming that pathogens represent a major driving force of evolution and that the counterforce is antipathogen immunity, it is plausible that the interface between pathogens and immunity influenced the evolution of our almost infinitely complex nervous system. Moreover, some behavioral traits may have evolved as a result of an "arms race" between the nervous and immune systems and the pathogens. As an example, because many of our ancestors died from infections, sickness behavior might have evolved to prevent the spread of the infective agent. This might have led to the evolvement of cytokine ability to affect the brain in a manner expressed as social withdrawal (*100*). On the other hand, the infective agent would favor social behavior on the part of the host so that the pathogen could spread. For example, mice infected with the parasite *Toxoplasma gondii* lose their fear response to cats, their predator and the parasite's natural host (*101*). The study indicated that this may occur by direct parasite infection of mouse neurons; however, it did not rule out that a loss of fear might have been mediated by cytokines produced by the immune system. If so, behavioral development might similarly have been shaped through interactions with pathogens. Recent work in my lab suggests that social behavior and an antipathogen response (for example, through an interferon-γ signaling pathway) might have coevolved (*102*). For the evolution of social behavior both within and between groups, an antipathogenic immune response would be needed to protect individuals from pathogen spread. Along similar lines, inability to fight an infection might have resulted in traits of self-isolation or other antisocial behavior.

Neuroimmunology: Quo vadis?

The major questions in neuroimmunology are too numerous to be listed in a few pages. However, since the emphasis of this Review is on the adaptive arm of the immune system and its effects on CNS function in physiology and pathology, it seems justifiable to discuss the unanswered questions of neuroimmunology from that perspective.

Recently discovered meningeal lymphatic vessels (*73*, *74*) seem to represent an important exit route for immune cells (and macromolecules) from the CNS and/or CSF. The way into the CNS and/or the CSF is still a matter of debate. Although the most-recent studies have convincingly demonstrated that meningeal blood vessels are the main route for immune cells into the CSF and meningeal spaces (*60*), how T cells access the parenchyma is not yet clear. One possibility is that meningeal T cells infiltrate the parenchyma when a regulatory mechanism fails. Another is that meningeal myeloid cells produce chemokines that allow peripheral T cells to migrate across the blood vessels into the parenchyma (Fig. 2).

A question closely related to the matter of entry and exit routes is the antigenic specificity of meningeal T cells affecting the brain. One plausible scenario might be that T cells in the meninges are largely specific for CNS self-antigens (autoimmune T cells). Interstitial fluid from the CNS drains, at least partially, into the CSF, where it is sampled by meningeal myeloid cells, which then present the acquired antigens to T cells. Such tonic activation allows autoimmune T cells to maintain a particular homeostatic cytokine profile that controls the phenotype of meningeal myeloid cells and thus allows the brain to function properly. When control mechanisms fail, these T cells may acquire an unfavorable phenotype and then invade the parenchyma.

Another possibility is that the meninges do not necessarily select for CNS self-reactive T cells but instead serve throughout the organism's lifetime as a reservoir for any and all specificities of memory T cells. Thus, for example, upon viral infection a representative memory T cell for a specific viral epitope may migrate and reside within the meninges to protect the CNS, via its barriers, from future encounters with that pathogen. Not yet clear in this scenario, however, is knowledge of the mechanism that would maintain those cells within the meninges or how their activity might affect brain function.

The current working model probably leans more toward the first scenario, where the establishment and maintenance of the meningeal T cell repertoire can conceivably be perceived and mechanistically understood. Preliminary findings suggest that meningeal immunity is prone to anti–self-antigen specificity (*50*, *76*). Ultimately, the way to address the question of antigenic specificity of meningeal T cells is likely to be via single-cell sequencing of the TCR, reconstruction of the transgenic TCR and its examination for recognition of self-antigens, and examination of cognitive function in mice transgenic for different TCRs retrieved from meningeal T cells.

Although we are far from a complete understanding of how meningeal immunity shapes CNS function, it is plausible to suggest that the CNS has pushed its immune activity to its borders (i.e., meningeal linings) to allow neural cells to function undisturbed. Therefore, another major challenge is to gain a more global understanding of how meningeal immunity affects the brain. So far, several cytokines are known to affect certain brain functions. A more comprehensive mapping of the presence and absence of different cytokines and immune cell subtypes, and how they affect signaling within the CNS, will be crucial. The use of reporter mice, combined with neuronal activation techniques such as optogenetics (*103*) or magnetogenetics (*104*), may allow mapping of neural ensembles that respond to the presence or absence of a particular molecular (immune-derived) player.

As our understanding of the interactions between these two complex systems advances, more questions will undoubtedly emerge. The field of neuroimmunology can be likened to an iceberg: We can perceive certain aspects (e.g., neuroinflammatory conditions) as a threat, but the huge undersurface (in this case, its therapeutic potential) has not been sufficiently explored. As we enter a new era of neuroimmunological research, equipped with an astonishing array of tools and technologies from the fields of neuroscience, immunology, genomics, and bioinformatics, we can look forward to some fascinating revelations and discoveries.

Science has made great progress in the fight against infectious agents, autoimmune diseases, and some types of cancers. However, apart from the fact that the U.S. Food and Drug Administration has approved 13 therapeutic modalities for MS, the treatment of neurological disorders is lagging behind. Perhaps the harnessing and targeting of the immune system as a therapy for neurological disorders should be moved to the frontlines as a crucial focus for the current and next generation of scientists.

REFERENCES AND NOTES

1. P. B. Medawar, *Br. J. Exp. Pathol.* **29**, 58–69 (1948).
2. M. Hašek, J. Chutna, M. Sládecek, Z. Lodin, *Nature* **268**, 68–69 (1977).
3. H. Wekerle, *Curr. Top. Microbiol. Immunol.* **305**, 25–50 (2006).
4. M. J. Carson, J. M. Doose, B. Melchior, C. D. Schmid, C. C. Ploix, *Immunol. Rev.* **213**, 48–65 (2006).
5. P. del Río-Hortega, in *Cytology and Cellular Pathology of the Nervous System*, W. Penfield, Ed. (Paul B. Hoebaer, New York, 1932), pp. 483–534.
6. F. S. Dhabhar, A. R. Satoskar, H. Bluethmann, J. R. David, B. S. McEwen, *Proc. Natl. Acad. Sci. U.S.A.* **97**, 2846–2851 (2000).
7. R. Ader, N. Cohen, *Science* **215**, 1534–1536 (1982).
8. R. Ader, N. Cohen, *Psychosom. Med.* **37**, 333–340 (1975).
9. L. Steinman, *J. Exp. Med.* **197**, 1065–1071 (2003).
10. S. S. Zamvil *et al*., *J. Exp. Med.* **162**, 2107–2124 (1985).
11. S. Zamvil *et al*., *Nature* **317**, 355–358 (1985).
12. L. Steinman *et al*., *Nature* **299**, 738–740 (1982).
13. T. A. Yednock *et al*., *Nature* **356**, 63–66 (1992).
14. V. K. Kuchroo *et al*., *Cell* **80**, 707–718 (1995).
15. Y. Chen, V. K. Kuchroo, J. Inobe, D. A. Hafler, H. L. Weiner, *Science* **265**, 1237–1240 (1994).
16. D. Chabas *et al*., *Science* **294**, 1731–1735 (2001).
17. O. Lider, T. Reshef, E. Beraud, A. Ben-Nun, I. R. Cohen, *Science* **239**, 181–183 (1988).
18. M. F. Farez *et al*., *Cell* **162**, 1338–1352 (2015).
19. L. Mayo *et al*., *Nat. Med.* **20**, 1147–1156 (2014).
20. I. D. Mascanfroni *et al*., *Nat. Immunol.* **14**, 1054–1063 (2013).
21. P. Matzinger, *Annu. Rev. Immunol.* **12**, 991–1045 (1994).
22. I. R. Cohen, *Immunol. Today* **13**, 490–494 (1992).
23. C. J. Serpe, A. P. Kohm, C. B. Huppenbauer, V. M. Sanders, K. J. Jones, *J. Neurosci.* **19**, RC7 (1999).
24. G. Moalem *et al*., *Nat. Med.* **5**, 49–55 (1999).
25. V. K. Kuchroo *et al*., *Annu. Rev. Immunol.* **20**, 101–123 (2002).
26. L. Steinman, *Annu. Rev. Immunol.* **32**, 257–281 (2014).
27. H. L. Weiner, *Ann. Neurol.* **65**, 239–248 (2009).
28. P. A. Gourraud *et al*., *Ann. Neurol.* **76**, 633–642 (2014).
29. A. L. Croxford, S. Spath, B. Becher, *Trends Immunol.* **36**, 651–662 (2015).
30. S. B. Simmons, E. R. Pierson, S. Y. Lee, J. M. Goverman, *Trends Immunol.* **34**, 410–422 (2013).
31. N. Pikor, J. L. Gommerman, *Mult. Scler. Relat. Disord.* **1**, 123–130 (2012).
32. E. Petrovich *et al*., *FASEB J.* **30**, 1767–1778 (2016).
33. B. Aubé *et al*., *J. Immunol.* **193**, 2438–2454 (2014).
34. A. R. Simard, D. Soulet, G. Gowing, J. P. Julien, S. Rivest, *Neuron* **49**, 489–502 (2006).
35. M. Colonna, Y. Wang, *Nat. Rev. Neurosci.* **17**, 201–207 (2016).
36. Y. Wang *et al*., *Cell* **160**, 1061–1071 (2015).
37. F. L. Heppner, R. M. Ransohoff, B. Becher, *Nat. Rev. Neurosci.* **16**, 358–372 (2015).
38. T. R. Jay *et al*., *J. Exp. Med.* **212**, 287–295 (2015).
39. S. E. Marsh *et al*., *Proc. Natl. Acad. Sci. U.S.A.* **113**, E1316–E1325 (2016).
40. J. Kipnis *et al*., *J. Neurosci.* **21**, 4564–4571 (2001).
41. J. Kipnis *et al*., *Proc. Natl. Acad. Sci. U.S.A.* **97**, 7446–7451 (2000).
42. K. Baruch *et al*., *Nat. Med.* **22**, 135–137 (2016).
43. D. R. Beers, J. S. Henkel, W. Zhao, J. Wang, S. H. Appel, *Proc. Natl. Acad. Sci. U.S.A.* **105**, 15558–15563 (2008).
44. J. Hazeldine, J. M. Lord, A. Belli, *Front. Neurol.* **6**, 235 (2015).
45. J. T. Walsh *et al*., *J. Clin. Invest.* **125**, 699–714 (2015).
46. S. P. Gadani, J. T. Walsh, I. Smirnov, J. Zheng, J. Kipnis, *Neuron* **85**, 703–709 (2015).
47. J. T. Walsh *et al*., *J. Immunol.* **193**, 5013–5022 (2014).
48. T. L. Roth *et al*., *Nature* **505**, 223–228 (2014).
49. M. V. Russo, D. B. McGavern, *Trends Immunol.* **36**, 637–650 (2015).
50. S. P. Gadani, J. T. Walsh, J. R. Lukens, J. Kipnis, *Neuron* **87**, 47–62 (2015).
51. J. Schmitz *et al*., *Immunity* **23**, 479–490 (2005).
52. J. Kipnis *et al*., *Proc. Natl. Acad. Sci. U.S.A.* **99**, 15620–15625 (2002).
53. J. Kipnis, H. Cohen, M. Cardon, Y. Ziv, M. Schwartz, *Proc. Natl. Acad. Sci. U.S.A.* **101**, 8180–8185 (2004).
54. J. Kipnis, S. Gadani, N. C. Derecki, *Nat. Rev. Immunol.* **12**, 663–669 (2012).
55. N. C. Derecki *et al*., *J. Exp. Med.* **207**, 1067–1080 (2010).
56. J. Kipnis, N. C. Derecki, C. Yang, H. Scrable, *Trends Immunol.* **29**, 455–463 (2008).
57. A. Brynskikh, T. Warren, J. Zhu, J. Kipnis, *Brain Behav. Immun.* **22**, 861–869 (2008).
58. A. Radjavi, I. Smirnov, J. Kipnis, *Brain Behav. Immun.* **35**, 58–63 (2014).
59. A. Radjavi, I. Smirnov, N. Derecki, J. Kipnis, *Mol. Psychiatry* **19**, 531–533 (2014).
60. C. Schläger *et al*., *Nature* **530**, 349–353 (2016).
61. P. Kivisäkk *et al*., *Ann. Neurol.* **65**, 457–469 (2009).
62. P. Kivisäkk *et al*., *Proc. Natl. Acad. Sci. U.S.A.* **100**, 8389–8394 (2003).
63. R. Shechter, A. London, M. Schwartz, *Nat. Rev. Immunol.* **13**, 206–218 (2013).
64. M. A. Lécuyer, H. Kebir, A. Prat, *Biochim. Biophys. Acta* **1862**, 472–482 (2016).
65. B. Broux, E. Gowing, A. Prat, *Semin. Immunopathol.* **37**, 577–590 (2015).
66. B. Engelhardt, R. M. Ransohoff, *Trends Immunol.* **26**, 485–495 (2005).
67. C. Larochelle *et al*., *Ann. Neurol.* **78**, 39–53 (2015).
68. M. Nedergaard, *Science* **340**, 1529–1530 (2013).
69. L. Xie *et al*., *Science* **342**, 373–377 (2013).
70. R. O. Weller, E. Djuanda, H. Y. Yow, R. O. Carare, *Acta Neuropathol.* **117**, 1–14 (2009).
71. J. Goldmann *et al*., *J. Leukoc. Biol.* **80**, 797–801 (2006).
72. M. G. Harris *et al*., *Sci. Rep.* **4**, 4422 (2014).
73. A. Louveau *et al*., *Nature* **523**, 337–341 (2015).
74. A. Aspelund *et al*., *J. Exp. Med.* **212**, 991–999 (2015).
75. K. H. Andres, M. von Düring, K. Muszynski, R. F. Schmidt, *Anat. Embryol.* **175**, 289–301 (1987).
76. J. W. Prineas, *Science* **203**, 1123–1125 (1979).
77. L. Varga, I. Piukovich, O. T. Zoltán, M. Gábor, M. Földi, *Acta Med. Acad. Sci. Hung.* **22**, 15–23 (1966).
78. K. Alitalo, *Nat. Med.* **17**, 1371–1380 (2011).
79. Y. Yang, G. Oliver, *J. Clin. Invest.* **124**, 888–897 (2014).
80. A. Aspelund *et al*., *J. Clin. Invest.* **124**, 3975–3986 (2014).
81. A. Peters *et al*., *Immunity* **35**, 986–996 (2011).
82. R. Magliozzi *et al*., *Brain* **130**, 1089–1104 (2007).
83. A. H. Stephan, B. A. Barres, B. Stevens, *Annu. Rev. Neurosci.* **35**, 369–389 (2012).
84. M. J. Vasek *et al*., *Nature* **534**, 538–543 (2016).
85. S. Hong *et al*., *Science* **352**, 712–716 (2016).
86. R. C. Paolicelli *et al*., *Science* **333**, 1456–1458 (2011).
87. H. Lui *et al*., *Cell* **165**, 921–935 (2016).
88. B. Stevens *et al*., *Cell* **131**, 1164–1178 (2007).
89. C. A. von Hehn, R. Baron, C. J. Woolf, *Neuron* **73**, 638–652 (2012).
90. M. Rosas-Ballina *et al*., *Science* **334**, 98–101 (2011).
91. S. Talbot *et al*., *Neuron* **87**, 341–354 (2015).
92. I. M. Chiu *et al*., *Nature* **501**, 52–57 (2013).
93. K. J. Tracey, *Cell* **164**, 343–344 (2016).
94. V. A. Pavlov, K. J. Tracey, *Immunol. Res.* **63**, 38–57 (2015).
95. C. J. Shatz, *Neuron* **64**, 40–45 (2009).
96. H. Lee *et al*., *Nature* **509**, 195–200 (2014).
97. A. Datwani *et al*., *Neuron* **64**, 463–470 (2009).
98. J. K. Atwal *et al*., *Science* **322**, 967–970 (2008).
99. D. Kioussis, V. Pachnis, *Immunity* **31**, 705–710 (2009).
100. R. Dantzer, J. C. O'Connor, G. G. Freund, R. W. Johnson, K. W. Kelley, *Nat. Rev. Neurosci.* **9**, 46–56 (2008).
101. W. M. Ingram, L. M. Goodrich, E. A. Robey, M. B. Eisen, *PLOS ONE* **8**, e75246 (2013).
102. A. J. Filiano *et al*., *Nature* **535**, 425–429 (2016).
103. P. Rajasethupathy, E. Ferenczi, K. Deisseroth, *Cell* **165**, 524–534 (2016).
104. M. A. Wheeler *et al*., *Nat. Neurosci.* **19**, 756–761 (2016).

ACKNOWLEDGMENTS

I thank S. Smith for editing the manuscript, A. Impagliazzo for the artwork, and all members of my lab for valuable comments during multiple discussions of this work. This work was supported by NIH grants AG034113 and NS096967.

10.1126/science.aag2638

REVIEW

Maternal immune activation: Implications for neuropsychiatric disorders

Myka L. Estes and A. Kimberley McAllister*

Epidemiological evidence implicates maternal infection as a risk factor for autism spectrum disorder and schizophrenia. Animal models corroborate this link and demonstrate that maternal immune activation (MIA) alone is sufficient to impart lifelong neuropathology and altered behaviors in offspring. This Review describes common principles revealed by these models, highlighting recent findings that strengthen their relevance for schizophrenia and autism and are starting to reveal the molecular mechanisms underlying the effects of MIA on offspring. The role of MIA as a primer for a much wider range of psychiatric and neurologic disorders is also discussed. Finally, the need for more research in this nascent field and the implications for identifying and developing new treatments for individuals at heightened risk for neuroimmune disorders are considered.

The Zika virus and its accompanying risk of microcephaly (*1*) have finally turned public attention to the detrimental effects of maternal infection. Although images of microcephalic newborns evoke outcry and require government action, the direct effects of Zika are only one part of a much larger global health hazard. An acute maternal immune response initiated by many common viruses is sufficient to cause lifelong changes in brain function and behavior of offspring in animal models (*2*). Although Zika and other pathogens may confer higher risk of specific disorders, growing evidence suggests that maternal immune activation (MIA) in the absence of a pathogen may increase the risk of a broad spectrum of central nervous system (CNS) disorders in humans (*3*) (Fig. 1).

Maternal infection and psychiatric disorders

The association between maternal infection and neurodevelopmental disorders is long-standing but not without controversy. After the 1964 rubella pandemic, the incidence of two neurodevelopmental disorders, autism (ASD) and schizophrenia (SZ), rose from less than 1% in the unexposed population to about 13 and 20%, respectively (*2*). Subsequent studies charting historic outbreaks of flu, measles, mumps, chickenpox, and polio revealed an association with ASD, SZ, and several mood disorders (*4*). However, not all ecological studies have replicated these associations (*5*). The differing conclusions may stem from differences in estimating the exposed population (*5*). Nevertheless, several prospective studies following birth cohorts (*3*, *6*) are consistent with an association between viral infection and psychiatric disorders in offspring and add other classes of pathogens to the list: namely, bacterial infections—including pneumonia, sinusitis, and tonsillitis—and the parasite *Toxoplasma gondii* (*2*, *3*).

How can such a diverse group of pathogens confer similar risks of neurodevelopmental disorders? Common to the implicated pathogens is the maternal immune response. In support of this possibility, enduring fevers above a certain threshold pose the greatest risk (*6*). It follows that immune system activation above that threshold due to any environmental insult or genetic predisposition would also increase risk. Indeed, maternal autoimmune disorders, allergies, asthma, acute stress, and exposure to environmental pollutants—all of which lead to elevated immune responses—have been linked to an enhanced risk of ASD and SZ (*3*, *6*). These findings may help to contextualize two recent prospective studies that failed to find a significant association between prenatal infection and SZ after adjusting for parental infection in general, parental psychiatric disorder, and socioeconomic status (*7*, *8*). For example, in one study, the modest association between prenatal infection and SZ was not significantly different from an association with a generalized familial liability to develop severe infection (*8*). This finding may again point to the importance of the maternal immune background. A paternal association implicates the immunogenetic background of the fetus. Thus, the immune status of both mother and child determines the vulnerability to MIA. A second study found a synergism between maternal infection and maternal psychiatric disorders (*7*). Since many individuals with SZ have immune abnormalities, this association could point to maternal immune status, as well as synergism with genetic risk factors. If MIA is a primer for a wide array of disorders, then further work is necessary to identify additive (*9*) and synergizing risk factors (*7*) that may be hidden in the adjusted models typically used in these studies.

Explosive growth in the human population, urbanization, and climate change combine to drive emerging infectious diseases like Zika (*10*). Simultaneously, pervasive poverty that limits access to childhood vaccinations, together with baseless fear of vaccinations within affluent groups, has led to a resurgence in infectious diseases of the past, like measles, mumps, rubella, whooping cough, and even polio (*11*). Increased exposure to new and old viruses heightens the risk of pregnant women contracting one of these diseases and thereby may increase the likelihood that their children will develop CNS disorders. Together, the increased presence of communicable diseases, combined with an uptick in autoimmune disorders (*6*), could account for a large proportion of the concerning recent increase in incidence of neurodevelopmental disorders (*12*).

Animal models of maternal infection

Evidence for these associations has been growing steadily more compelling, but epidemiology alone cannot establish a causal relationship between MIA and risk of neurodevelopmental disorders. Thus, this association in humans will likely remain controversial at least into the near future. Humans are genetically, ecologically, and behaviorally heterogeneous, all of which can influence susceptibility to disease and therefore complicate and undermine detection of causal relationships. Clinical research is also limited in its ability to identify the molecular pathways downstream of maternal infection because humans cannot be subject to invasive experimentation. Moreover, there is currently not an effective way to identify the at-risk pregnancies. The majority of pregnancies, even those at high risk, will lead to healthy offspring, and the resulting CNS disorders in offspring often do not appear for many years after birth and appear to be influenced by postnatal risk factors that synergize with genetic and prenatal risk to act as "second hits" (*3*, *13*–*15*). Clearly, there is a compelling need for long-term and large prospective studies to identify the specific aspects of infection during pregnancy (e.g., the type of pathogen, extent of fever, and timing of infection), as well as synergies with postnatal exposures, that lead to heightened risk of CNS disorders in offspring.

Because of these challenges of studying MIA in humans, animal research is therefore essential for identifying causal mechanisms and developing new diagnostic tools and therapeutics. Indeed, a causal relationship between maternal infection and ASD- and SZ-related behavioral abnormalities has been clearly demonstrated using rodent and, more recently, nonhuman primate (NHP) animal models. In these models, pregnant animals are exposed to an immunological manipulation at a specific gestational stage. The behavior and brain structure and function of MIA offspring are then compared with those of control offspring. The most common immunogens used in these studies include influenza infection and exposure to viral {polyinosinic:polycytidylic [poly(I:C)]} and bacterial [lipopolysaccharide (LPS)] mimics that cause MIA (*14*). These MIA animal models meet all of the criteria required for validity for a disease model: They mimic a known disease-related risk factor (construct validity), they exhibit a wide range

---

Center for Neuroscience, University of California Davis, One Shields Avenue, Davis, CA 95618, USA.
*Corresponding author. Email: kmcallister@ucdavis.edu

of disease-related symptoms (face validity), and they can be used to predict the efficacy of treatments (predictive validity). Each specific MIA model has important advantages and disadvantages. Differences in gestational age, immunogen, dose, and timing lead to overlapping and distinct phenotypic signatures that are critical factors in evaluating their use as preclinical models. The common principles revealed by these models are included in this overview of the field. See other recent reviews for details on each model (*4*, *14*), as well as additional maternal immune (*14*), maternal antibody (*16*), autoimmune (*17*), and stress (*18*) models.

Rodent MIA models

The rodent MIA models manifest a comprehensive range of SZ- and ASD-related behavioral abnormalities. Offspring from the poly(I:C) rodent model, in particular, exhibit most of the core behavioral symptoms of ASD—abnormal communication, abnormal social behaviors, and increased repetitive behaviors (*2*–*4*, *6*, *14*). Offspring from these MIA models also show many additional SZ- and ASD-related behaviors, including decreased sensorimotor gating (which measures the ability of the brain to filter out extraneous information), deficits in working memory and cognitive flexibility, increased anxiety, and enhanced sensitivity to amphetamines (*2*, *3*, *14*). Importantly, many of these behaviors can be alleviated by antipsychotic drugs, supporting the disease relevance of these models (*3*, *4*, *14*).

In addition to these aberrant behaviors, adult MIA offspring also exhibit neuropathologies emerging at specific developmental ages, especially SZ-associated reduced cortical thickness and hippocampal volume and increased ventricular size, as well as ASD-associated aberrations in Purkinje cells (*2*–*4*, *14*). Several studies have also recently reported deficits in dendritic spine density, levels of synaptic proteins, synaptic transmission, long-term plasticity, and cortical malformations (*4*, *19*–*24*). However, most of these measures have been studied in single brain regions from single models at a single age. So, although it is likely that MIA causes changes in synaptic connectivity, function, and plasticity, elucidating the details and common principles remains an important goal for the future.

Recent work has also uncovered neurochemical changes in adult MIA offspring that are characteristic of SZ and ASD (*3*, *4*, *14*, *25*) (Fig. 2).

> ***"…maternal autoimmune disorders, allergies, asthma, acute stress, and exposure to environmental pollutants… have been linked to an enhanced risk of [autism and schizophrenia]."***

Serotonin and dopaminergic signaling is altered in MIA offspring across models (*3*, *4*, *14*). Additionally, specific changes in inhibitory neurotransmission have been linked to both SZ and ASD (*26*), and similar reductions in several components of the γ-aminobutyric acid (GABA) system are present in the brains of MIA offspring (*3*, *4*, *14*, *25*, *27*–*29*). One of the most exciting recent advances in the MIA field is the discovery of deficits in the function of parvalbumin (PV) cells, known to be selectively altered in SZ, in the brains of adult MIA offspring (*3*, *14*, *22*, *30*). MIA causes a specific reduction in inhibition from PV cells onto pyramidal neurons that is sufficient to cause deficits in attentional set shifting and enhance anxiety-related behavior in offspring (*30*), similar to behavioral changes in SZ patients with confirmed evidence of gestational infection (*31*). Consistent with predictions from a loss of perisomatic inhibition of pyramidal cells in the prefrontal cortex (PFC) (*4*), MIA offspring exhibit increased power in the theta band (*32*) and reduced electroencephalogram coherence, specifically between the hippocampus (HC) and the medial PFC (*4*). These findings mirror reductions in long-range signaling in SZ (*33*).

NHP MIA models

Even though these rodent models have remarkably strong face, construct, and predictive validity for SZ and ASD, the potential of using rodents to tell us about psychiatric disorders that are so inherently human has remained controversial. To bridge the gap between rodents and humans, several groups have established rhesus macaque MIA models. Some of these NHP models display behavioral symptoms of ASD and SZ—increased repetitive behaviors, abnormal communication, and impaired social interactions—that start at weaning and increase in intensity with age (*4*, *14*, *34*). MIA also alters gray- and white-matter volume in an immunogen-specific manner (*4*) and causes subtle changes in dendritic arborization (*35*) in neonatal NHP offspring. An outstanding question that can be addressed uniquely by NHP models is whether molecular signatures of MIA identified in rodent models underlie phenotypes similar to ASD and SZ in humans. Answering this question in the future will be a major advantage for generating new therapies.

Considerations in interpreting MIA models

MIA models use a surprisingly wide range of protocols that vary in the type, as well as the timing, mode of delivery, and dose, of immunogen used. The type of immunogen dictates the nature of the immune response and downstream phenotypes. The timing of exposure is also key in determining the nature and severity of the outcomes (Fig. 3) (*14*). MIA in early versus late gestation causes distinct fetal brain cytokine responses and changes in neuropathology and behavior in

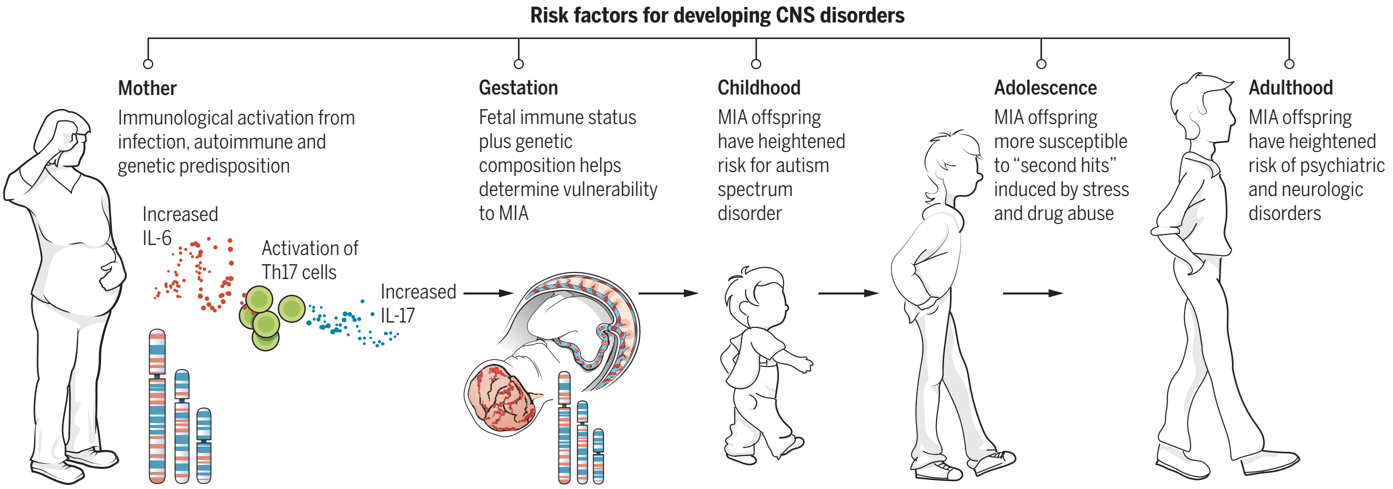

Fig. 1. MIA as a disease primer. This schematic depicts the current model for how MIA leads to psychiatric disorders in offspring. Infection leads to release of proinflammatory cytokines and activation of $\mathrm{T_H}$17 cells in the mother's bloodstream (*6*, *19*). A combination of genetic background, autoimmune status, and second hits during childhood and adolescence (including stress and drug abuse) combines with the consequences of maternal infection to increase the likelihood of offspring developing psychiatric disorders as adults (*3*, *6*, *14*, *37*).

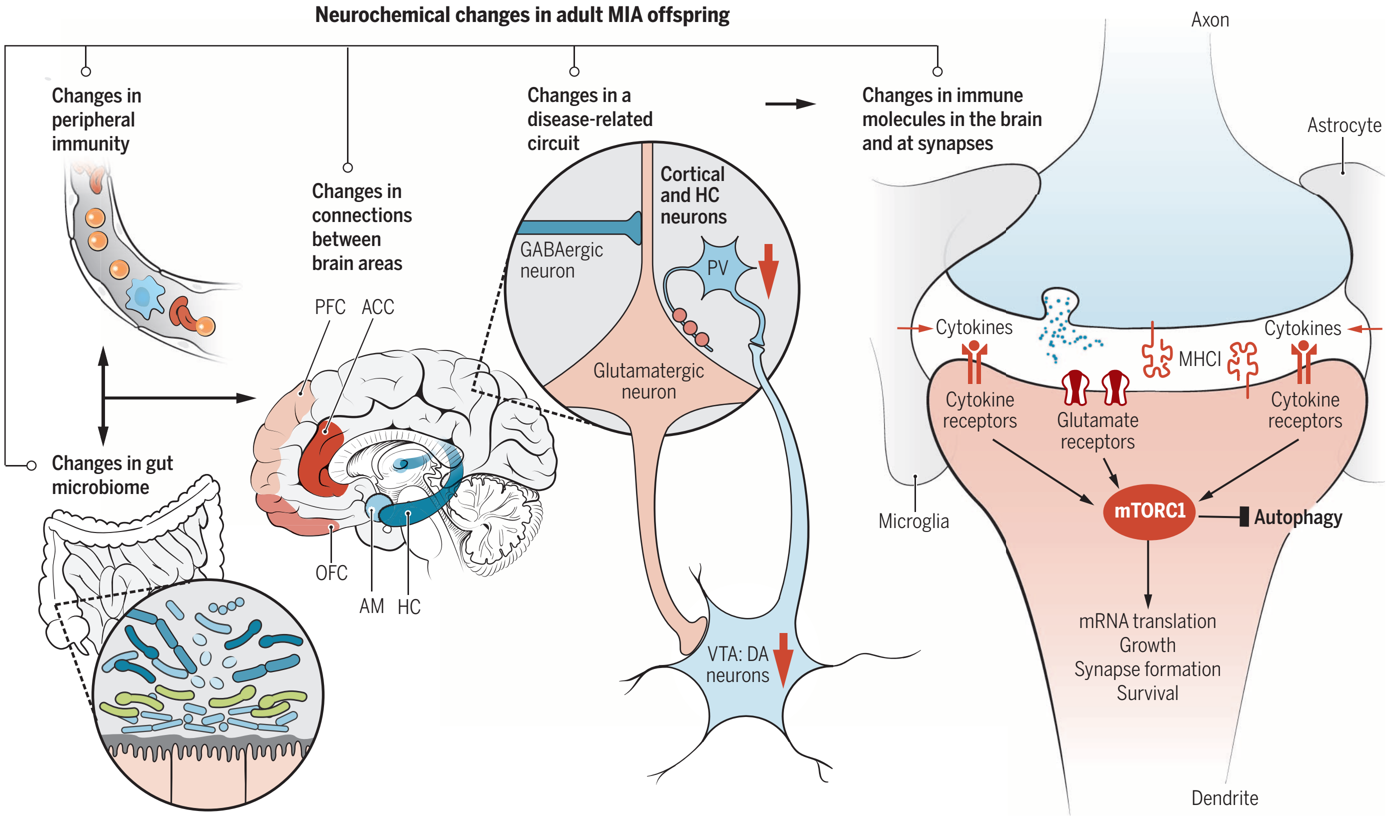

Fig. 2. Mechanisms underlying the effects of MIA on brain function. Aberrations in the microbiome after MIA can lead to altered development of peripheral immunity, both of which can alter brain development. Deficits in long-range connections between brain regions implicated in SZ and ASD, including the HC, PFC, anterior cingulate cortex (ACC), orbitofrontal cortex (OFC), and amygdala (AM), have been reported in MIA (*3*, *4*, *14*). Specific alterations in activity of glutamatergic neurons in the cortex caused by decreased function of dopaminergic (DA) neurons in the ventral tegmental area (VTA) and decreased GABAergic input also occur in SZ and ASD, as well as in the MIA models (*3*, *4*, *14*). Changes in expression of immune molecules in the brain and even at synapses, including cytokines and MHCI molecules, alter synaptic plasticity and function and contribute to the changes in circuitry and connectivity between brain regions that characterize these disorders (*6*). Finally, alterations in immune and neuronal signaling due to MIA may converge upon the mTOR pathway, which regulates synapse formation, growth, translation, survival, and autophagy (*68*). mTORC1, mTOR complex 1.

adult offspring (*14*, *36*), but whether the timing of exposure leads to distinct CNS disorders remains unknown. MIA outcomes can also be dependent on the mouse strain (*37*, *38*), individual differences in maternal immune responsiveness within a strain (*39*), and gender differences in offspring (*4*, *14*). Finally, the mode of delivery and dose of the immunogen also dictate the outcome in offspring after MIA, implying that there must be a threshold of MIA required to produce ASD- and SZ-like phenotypes in offspring (*14*, *30*). A key advance would be quantifying the threshold for MIA to induce disease-relevant phenotypes. This would allow better comparison between studies and more effective use of the model in the preclinical arena (*29*).

MIA as a disease primer

In humans, most maternal infections do not lead to SZ or ASD in offspring (*40*); thus, it is currently thought that multiple "hits" (exposure to more than one risk factor) may be required for disease induction (Fig. 1). MIA appears to act as a "disease primer" (*14*) to make an individual more susceptible to the effects of genetic mutations and environmental exposures in triggering disease-related symptoms later in life (*41*). Consistent with this idea, the incidence of both ASD and SZ is much higher in families with autoimmune disorders (*2*, *6*), and the effect of maternal infection in increasing SZ risk is greater in families with a history of SZ (*3*). Indeed, low-dose poly(I:C) MIA synergizes with mutations in SZ- and ASD-associated genes, including *DISC1*, *NRG1* (encodes Neuregulin-1), *NR4A2* (encodes Nurr1), and *TSC2*, to cause greater effects than either insult alone (*3*, *4*, *14*).

Although studies of interactions between MIA and environmental risk factors have only recently begun, the results thus far using animal models suggest that even subclinical maternal infection can make offspring much more vulnerable to second "hits" (Fig. 1). Subthreshold MIA increases the likelihood of environmental risk factors, such as stress and drug use, to cause SZ- and ASD-related phenotypes in offspring (*3*, *14*). Peripubertal stress causes synergistic effects in subclinical poly(I:C) MIA offspring on a wide range of SZ- and ASD-related behaviors and molecular phenotypes (*3*, *4*, *14*). Similarly, adolescent cannabis exposure causes synergistic effects in subclinical MIA mice (*4*, *42*). Combined insults can even change the nature of the phenotype. LPS MIA alone results in *N*-methyl-D-aspartate receptor hypofunction and a loss of hippocampal long-term plasticity in adolescent rats, but, when combined with restraint stress, the outcome switches to the opposite phenotypes (*4*). Although the molecular mechanism of MIA as a disease primer is unknown, brain region–specific alterations in epigenetic marks at several loci, including *DISC1*, could be a molecular signature of its priming effect (*43*, *44*).

There is also growing evidence that MIA is associated with a much wider array of psychiatric and neurologic disorders than just ASD and SZ. Recently, MIA has been linked to anxiety, major depressive disorder (MDD), and bipolar disorder (BPD) in people (*3*, *45*–*47*). These seemingly distinct disorders share a surprising number of genetic and environmental risk factors, behavioral abnormalities, and alterations in brain structure and function (*3*, *48*, *49*). MIA animal models also exhibit behavioral and neurochemical alterations consistent with depression and anxiety (*3*, *47*, *50*). MIA has even been shown recently to prime mice for degenerative diseases during aging, including Alzheimer's disease (*51*).

These links of MIA to an increasing array of diseases as diverse as neurodevelopmental disorders (e.g., ASD) and neurodegenerative diseases (e.g., Alzheimer's disease) that afflict individuals at nonoverlapping stages of life and result in distinct symptoms have been surprising. This conundrum is not an issue for MIA alone but rather has surfaced in the field of genetics as well, with increasing evidence for associations between specific genes and a similarly wide range of CNS disorders (*52*–*54*). How MIA or genetic mutations can cause such a wide range of disorders is unknown, but both may act to prime an individual for second hits, and the nature and timing of those second hits may determine when and which disease will result, if any (Fig. 1).

The fact that MIA is associated with such a broad range of disorders indicates that MIA animal models can be used to identify common molecular pathways that are shared among them. This is good news from a treatment perspective because it predicts that new therapies could have efficacy in a wide range of human diseases. When, where, and how the common pathways are disrupted may be critical to understanding disease-specific vulnerabilities and can be manipulated and identified using the MIA animal models. Perhaps most important, the larger the family of MIA-associated CNS disorders, the greater the public health implications for initiatives aimed at preventing maternal infection in high-risk populations.

How does MIA alter brain function and behavior in offspring?

Immune activation within the maternal compartment likely influences the developing fetal CNS through inflammatory mediators found in the blood and amniotic fluid of ASD and SZ mothers (*2*, *3*, *6*, *14*) (Fig. 1). Whether or not these proteins cross the placenta and act directly upon the fetal brain is unknown. MIA somehow induces alterations in multiple cytokines within the fetal brain in a matter of hours (*6*, *14*). Although MIA triggers unequivocal inflammation within the mother, the limited cytokine profiles that have been measured in the fetal brain do not by themselves signify a classic inflammatory response (*29*, *55*). Whether, and how, these changes in fetal brain cytokines are related to MIA neuropathologies are critical questions for the field. More research is needed to address these issues and to quantify the dynamic changes in a large number of immune molecules across brain regions and age, with the ultimate goal of identifying immune signatures associated with specific disease-related neuropathologies and behaviors.

Nevertheless, several maternal cytokines have already been identified as critical mediators of MIA on disease-related phenotypes in offspring (Fig. 1). Injection of a single inflammatory cytokine [interleukin (IL)–6, –17, or –2] is sufficient to induce several ASD- and SZ-like behaviors in offspring (*14*, *19*, *56*). Moreover, coadministration of poly(I:C) with an IL-6 or an IL-17 function blocking antibody, or with overexpression of the anti-inflammatory cytokine IL-10, partially prevents the effects of MIA in offspring (*3*, *19*). However, little is known about how these maternal cytokines alter brain development. One possibility is that MIA leads to long-lasting changes in expression of immune molecules known to regulate neural connectivity and function in offspring (*6*). Indeed, the levels of numerous cytokines are altered throughout development and into adulthood in the brain of MIA offspring in a region- and age-specific manner (*6*, *57*). These cytokines are likely to regulate the expression of other classes of immune molecules on neurons, including major histocompatibility complex I (MHCI) molecules (Fig. 2). In the immune system, MHCI levels are controlled by cytokines as an important early step in the immune response. In the healthy brain, MHCI is found on neurons, where it negatively regulates synapse formation and the synaptic plasticity required for activity-dependent synaptic pruning (*6*, *58*, *59*). Alterations in synaptogenesis and pruning are associated with a range of neurodevelopmental disorders and are thought to play a central role in the etiology of ASD and SZ (*60*, *61*). MIA causes a dramatic change in MHCI levels on neurons in the brains of neonatal offspring (*6*, *21*), and the resulting increase in MHCI at birth is required for the dramatic MIA-induced deficit in the ability of newborn neurons to form synapses (*62*). Outstanding questions for the field include determining whether these changes in cortical connectivity are long-lasting and causally related to the disease-related behaviors emerging at later stages of development.

MHCI is one of several immune proteins present at the synapse capable of mediating responses to infection while concurrently regulating activity-dependent plasticity and circuit formation. These versatile proteins—part immune defense, part

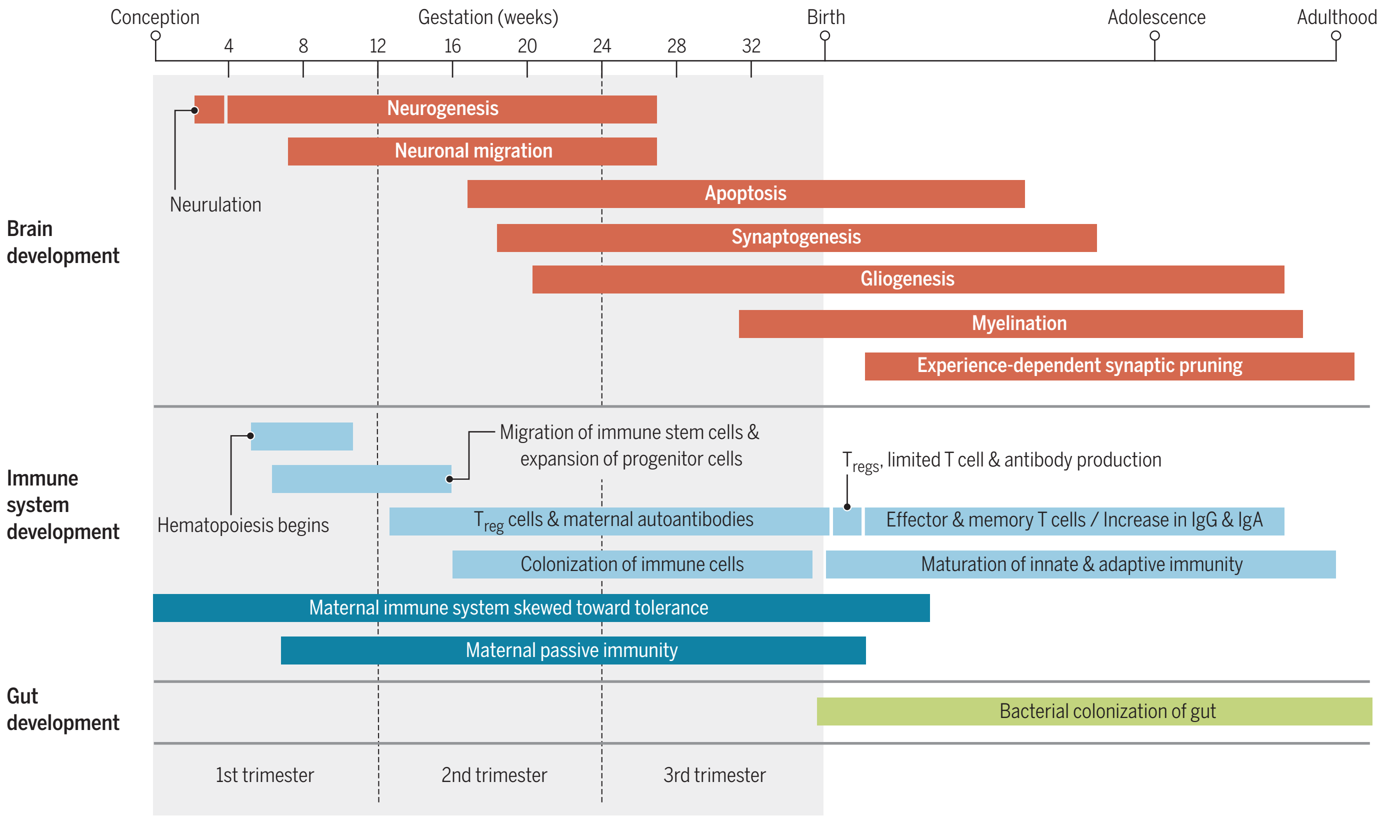

Fig. 3. Timeline of major events occurring in brain, immune system, and gut development from conception to adulthood (*83*–*85*).

synaptic structure—are the most likely suspects to bring about changes in brain development in response to maternal infection (*63*). Although studies on this topic are only just beginning, MIA presumably alters the expression and function of these immune proteins in the brain as it does for cytokines and MHCI. The alterations may be acute, reflecting the nature, intensity, and duration of infection, or chronic through epigenetic changes that may synergize with other risk factors at different stages of life. With such heterogeneity from onset to phenotype, could there be a unifying converging pathway underlying MIA's priming effect?

If immune molecules act through similar pathways in the brain (and the same intracellular machinery is present, which remains an open question), then it is possible that immune signaling in neurons may converge upon mammalian target of rapamycin (mTOR) signaling. In the immune system, mTOR acts as a regulatory hub integrating inputs from numerous upstream intracellular signaling pathways—including cytokines, trophic factors, and synaptic scaffolding proteins—many of which are altered in the brains of MIA offspring, as well as individuals with ASD, SZ, MDD, and AD (*64*–*68*). Dysregulation of protein synthesis due to alterations in the mTOR pathway has been implicated in several monogenetic forms of ASD, as well as the SZ-associated *DISC-1* mutation in animal models (*68*, *69*). Hyper- or hypoactivation of mTOR signaling imparts mutation-specific alterations in neuronal morphology and synaptic plasticity, as well as the synthesis of many synaptic proteins and glutamate receptors (*70*), which are common features of several MIA models. mTOR signaling also regulates macroautophagy, a homeostatic process leading to the breakdown of unused proteins and structures within cells that has been implicated in several neurodegenerative diseases and, recently, idiopathic forms of ASD (*61*). Although direct evidence for a role for mTOR dysfunction in MIA is lacking, this is a plausible exemplar of several potential signaling hubs that have been implicated in a similar wide range of disorders as MIA. These hubs could be altered by underlying genetic mutations or postnatal environmental risk factors to cause distinct responses in individuals after MIA, leading to the growing list of disorders associated with maternal infection.

The gut-immune-brain axis in MIA

Several intriguing studies indicate that some MIA-induced neuropathologies may emanate from outside the nervous system (Fig. 2). MIA mice exhibit peripheral immune abnormalities, including T and myeloid cell skewing to inflammatory phenotypes, mirroring some patient studies (*3*, *6*). These peripheral changes are likely to alter immune-brain communication, which has been demonstrated to modulate cognition (*71*). As such, reconstitution of MIA offspring with normal bone marrow ameliorates repetitive and anxiety-like behaviors, suggesting that some MIA phenotypes are causally related to ongoing immune imbalances (*3*).

As an essential nexus for nervous-immune-endocrine system interactions, the gut may also play an important role in MIA and, thus, may be an effective target for therapeutic interventions. During birth, the fetal gut is colonized by maternal microbiota (Fig. 3), and this formative colonization primes the developing immune system and directs immune homeostasis (Fig. 2). Like individuals with ASD and other disorders, MIA offspring display altered microbiota signatures. Restoring a more typical microbiome by treating MIA offspring with *Bacteroides fragilis* not only restores peripheral immune homeostasis but also ameliorates several aberrant behaviors (*72*). Exploiting the gut as a novel therapeutic route requires animal models of healthy and disease-relevant microbiota. Typical research rodents raised under sanitized conditions lack exposure to a wide variety of microbes, which can stunt immune system development (*73*). Exposure to specific microbiota due to housing conditions has recently been shown to drive T helper cell 17 (T_H17) T cell differentiation, a cell type that may be necessary for MIA but is absent in many mouse lines (*19*, *37*, *74*). These microbiota-induced differences in immunity have only recently become appreciated, and their contribution to variability in the MIA model and the presence, type, and severity of disease in humans remains to be determined.

Implications for treatment of psychiatric disorders

The great promise of the MIA model lies in its potential to lead to novel therapeutics and to determine when particular symptoms emerge and are sensitive to those new treatments. Currently, a handful of therapeutic manipulations rescue some MIA-induced phenotypes. Further work promises to identify new classes of therapies for psychiatric disorders. Importantly, some of these therapies can be used during the presumptive prodromal phase to prevent the emergence of SZ-related phenotypes. For example, treatment of adolescent MIA rats with a COX-2 inhibitor protects them from developing several SZ-related behavioral aberrations (*3*, *4*). Similarly, minocycline, a microglia (a type of macrophage-like cell in the brain) modulator, prevents the emergence of MIA-induced behaviors and changes in cytokines in the adult brain when given during exposure to peripubertal stress (*3*, *4*, *75*). Several SZ- and ASD-related phenotypes in MIA offspring can also be prevented with probiotics (*72*), antibodies to specific cytokines (*19*, *76*), environmental enrichment (*77*), or maternal dietary supplementation with zinc (*78*, *79*), *n-3* polyunsaturated fatty acids (*80*, *81*), or N-acetyl-cysteine (NAC) (*82*). Finally, one of the most exciting potential treatments is antipurinergic therapy, which completely reverses several ASD-related phenotypes in MIA offspring (*4*).

The future

If MIA is a disease primer for numerous CNS disorders, as mounting evidence suggests, then MIA animal models are critical for determining the molecular pathways that mediate the resulting neuropathology and abnormal behaviors. Although the field is in its infancy, newly identified convergent pathways are already starting to serve as targets for development of new therapeutics. The altered signaling in these molecular pathways is age-, region-, and gender-specific, a critical finding that helps explain the considerable individual differences in vulnerability to MIA-related disorders. Tailoring therapies to different stages of these disorders requires MIA animal models in which dynamic changes can be quantified and related to specific symptoms. Effective use of these new treatments in humans will depend in large part on new, as yet undiscovered, approaches to identify at-risk individuals. MIA models are already uncovering synergizing genetic and environmental risk factors that will help define these populations. The ultimate goal, which is now within sight, is to use new therapeutic interventions before deleterious symptoms appear, decreasing the incidence of, or even preventing the emergence of, immune-mediated psychiatric illness in adulthood.

REFERENCES AND NOTES

1. S. A. Rasmussen, D. J. Jamieson, M. A. Honein, L. R. Petersen, *N. Engl. J. Med.* **374**, 1981–1987 (2016).
2. P. H. Patterson, *Behav. Brain Res.* **204**, 313–321 (2009).
3. I. Knuesel *et al*., *Nat. Rev. Neurol.* **10**, 643–660 (2014).
4. S. Reisinger *et al*., *Pharmacol. Ther.* **149**, 213–226 (2015).
5. J. P. Selten, A. Frissen, G. Lensvelt-Mulders, V. A. Morgan, *Schizophr. Bull.* **36**, 219–228 (2010).
6. M. L. Estes, A. K. McAllister, *Nat. Rev. Neurosci.* **16**, 469–486 (2015).
7. Å. Blomström *et al*., *Schizophr. Bull.* **42**, 125–133 (2016).
8. P. R. Nielsen, T. M. Laursen, P. B. Mortensen, *Schizophr. Bull.* **39**, 230–237 (2013).
9. P. R. Nielsen, U. Meyer, P. B. Mortensen, *Schizophr. Res.* **172**, 35–40 (2016).
10. K. F. Smith *et al*., *J. R. Soc. Interface* **11**, 20140950 (2014).
11. E. Dubé, M. Vivion, N. E. MacDonald, *Expert Rev. Vaccines* **14**, 99–117 (2015).
12. C. A. Boyle *et al*., *Pediatrics* **127**, 1034–1042 (2011).
13. P. R. Nielsen, M. E. Benros, P. B. Mortensen, *Schizophr. Bull.* **40**, 1526–1532 (2014).
14. U. Meyer, *Biol. Psychiatry* **75**, 307–315 (2014).
15. J. P. Debost *et al*., *Schizophr. Bull.* **2016**, sbw083 (2016).
16. J. Camacho *et al*., *Behav. Brain Res.* **266**, 46–51 (2014).
17. L. Brimberg, A. Sadiq, P. K. Gregersen, B. Diamond, *Mol. Psychiatry* **18**, 1171–1177 (2013).
18. C. L. Howerton, T. L. Bale, *Horm. Behav.* **62**, 237–242 (2012).
19. G. B. Choi *et al*., *Science* **351**, 933–939 (2016).
20. U. Meyer, J. Feldon, S. H. Fatemi, *Neurosci. Biobehav. Rev.* **33**, 1061–1079 (2009).
21. P. Coiro *et al*., *Brain Behav. Immun.* **50**, 249–258 (2015).
22. Z. Zhang, H. van Praag, *Brain Behav. Immun.* **45**, 60–70 (2015).
23. S. Giovanoli *et al*., *J. Neuroinflammation* **12**, 221 (2015).
24. E. Patrich, Y. Piontkewitz, A. Peretz, I. Weiner, B. Attali, *Sci. Rep.* **6**, 19106 (2016).
25. J. Richetto, F. Calabrese, M. A. Riva, U. Meyer, *Schizophr. Bull.* **40**, 351–361 (2014).
26. R. Gao, P. Penzes, *Curr. Mol. Med.* **15**, 146–167 (2015).
27. G. D. Hoftman *et al*., *Schizophr. Bull.* **41**, 180–191 (2015).
28. M. J. Schmidt, K. Mirnics, *Neuropsychopharmacology* **40**, 190–206 (2015).
29. L. Harvey, P. Boksa, *Neuropharmacology* **62**, 1767–1776 (2012).
30. S. Canetta *et al*., *Mol. Psychiatry* **21**, 956–968 (2016).
31. A. S. Brown *et al*., *Am. J. Psychiatry* **166**, 683–690 (2009).
32. A. R. Wolff, D. K. Bilkey, *Brain Behav. Immun.* **48**, 232–243 (2015).
33. P. J. Uhlhaas, W. Singer, *Nat. Rev. Neurosci.* **11**, 100–113 (2010).
34. C. J. Machado, A. M. Whitaker, S. E. Smith, P. H. Patterson, M. D. Bauman, *Biol. Psychiatry* **77**, 823–832 (2015).
35. R. K. Weir *et al*., *Brain Behav. Immun.* **48**, 139–146 (2015).
36. D. Arsenault, I. St-Amour, G. Cisbani, L. S. Rousseau, F. Cicchetti, *Brain Behav. Immun.* **38**, 77–90 (2014).
37. M. L. Estes, A. K. McAllister, *Science* **351**, 919–920 (2016).
38. J. J. Schwartzer *et al*., *Transl. Psychiatry* **3**, e240 (2013).
39. S. L. Bronson, R. Ahlbrand, P. S. Horn, J. R. Kern, N. M. Richtand, *Behav. Brain Res.* **220**, 55–64 (2011).
40. J. P. Selten, V. A. Morgan, *Bipolar Disord.* **12**, 753–754 (2010).
41. Y. Ayhan, R. McFarland, M. V. Pletnikov, *Prog. Neurobiol.* **136**, 1–27 (2016).

42. S. L. Hollins, K. Zavitsanou, F. R. Walker, M. J. Cairns, *Brain Behav. Immun.* **56**, 187–196 (2016).
43. B. Tang, H. Jia, R. J. Kast, E. A. Thomas, *Brain Behav. Immun.* **30**, 168–175 (2013).
44. C. M. Connor *et al.*, *Schizophr. Res.* **140**, 175–184 (2012).
45. A. M. Simanek, H. C. Meier, *Curr. Probl. Pediatr. Adolesc. Health Care* **45**, 325–364 (2015).
46. R. Parboosing, Y. Bao, L. Shen, C. A. Schaefer, A. S. Brown, *JAMA Psychiatr.* **70**, 677–685 (2013).
47. M. Ronovsky, S. Berger, B. Molz, A. Berger, D. D. Pollak, *Curr. Neuropharmacol.* **14**, 1 (2015).
48. U. Meyer, J. Feldon, O. Dammann, *Pediatr. Res.* **69**, 26R–33R (2011).
49. S. H. Lee *et al.*, *Nat. Genet.* **45**, 984–994 (2013).
50. A. M. Depino, *Neuroscience* **299**, 56–65 (2015).
51. D. Krstic *et al.*, *J. Neuroinflammation* **9**, 151 (2012).
52. A. Malishkevich *et al.*, *Transl. Psychiatry* **5**, e501 (2015).
53. K. Lepeta *et al.*, *J. Neurochem.* (2016).
54. H. Wang, *Front. Cell. Neurosci.* **9**, 43 (2015).
55. M. L. Estes, A. K. McAllister, *Brain Pathol.* **24**, 623–630 (2014).
56. N. M. Ponzio, R. Servatius, K. Beck, A. Marzouk, T. Kreider, *Ann. N. Y. Acad. Sci.* **1107**, 118–128 (2007).
57. P. A. Garay, E. Y. Hsiao, P. H. Patterson, A. K. McAllister, *Brain Behav. Immun.* **31**, 54–68 (2013).
58. C. J. Shatz, *Neuron* **64**, 40–45 (2009).
59. M. W. Glynn *et al.*, *Nat. Neurosci.* **14**, 442–451 (2011).
60. A. Sekar *et al.*, *Nature* **530**, 177–183 (2016).
61. G. Tang *et al.*, *Neuron* **83**, 1131–1143 (2014).
62. B. M. Elmer, M. L. Estes, S. L. Barrow, A. K. McAllister, *J. Neurosci.* **33**, 13791–13804 (2013).
63. I. Voineagu, V. Eapen, *Front. Hum. Neurosci.* **7**, 738 (2013).
64. A. Caccamo, V. De Pinto, A. Messina, C. Branca, S. Oddo, *J. Neurosci.* **34**, 7988–7998 (2014).
65. Z. M. Ignácio *et al.*, *Br. J. Clin. Pharmacol.* **2016**, bcp.12845 (2016).
66. S. L. Hollins, K. Zavitsanou, F. R. Walker, M. J. Cairns, *Transl. Psychiatry* **4**, e452 (2014).
67. A. M. Hemmerle *et al.*, *Schizophr. Res.* **168**, 411–420 (2015).
68. M. Sahin, M. Sur, *Science* **350**, aab3897 (2015).
69. J. Y. Kim *et al.*, *Neuron* **63**, 761–773 (2009).
70. E. Santini, E. Klann, *Sci. Signal.* **7**, re10 (2014).
71. J. Kipnis, *Science* **353**, 766–771 (2016).
72. E. Y. Hsiao *et al.*, *Cell* **155**, 1451–1463 (2013).
73. L. K. Beura *et al.*, *Nature* **532**, 512–516 (2016).
74. Y. Yang *et al.*, *Nature* **510**, 152–156 (2014).
75. S. Giovanoli *et al.*, *Transl. Psychiatry* **6**, e772 (2016).
76. S. E. Smith, J. Li, K. Garbett, K. Mirnics, P. H. Patterson, *J. Neurosci.* **27**, 10695–10702 (2007).
77. E. J. Connors, A. N. Shaik, M. M. Migliore, A. C. Kentner, *Brain Behav. Immun.* **42**, 178–190 (2014).
78. J. S. Chua, C. J. Cowley, J. Manavis, A. M. Rofe, P. Coyle, *Brain Behav. Immun.* **26**, 326–336 (2012).
79. P. Coyle, N. Tran, J. N. Fung, B. L. Summers, A. M. Rofe, *Behav. Brain Res.* **197**, 210–218 (2009).
80. M. J. Weiser *et al.*, *Prostaglandins Leukot. Essent. Fatty Acids* **106**, 27–37 (2016).
81. Q. Li *et al.*, *Transl. Psychiatry* **5**, e641 (2015).
82. F. Lanté *et al.*, *Hippocampus* **18**, 602–609 (2008).
83. B. Clancy *et al.*, *Neuroinformatics* **5**, 79–94 (2007).
84. D. J. Dowling, O. Levy, *Trends Immunol.* **35**, 299–310 (2014).
85. A. K. Simon, G. A. Hollander, A. McMichael, *Proc. Biol. Sci.* **282**, 20143085 (2015).

ACKNOWLEDGMENTS

The authors thank members of the McAllister laboratory for ongoing discussions about the topics covered in this Review. Due to journal guidelines, we were not permitted to cite many of the original reports, and we apologize to those whose articles are not referenced. Please see referenced reviews for primary source articles. A.K.M. and M.L.E. are listed as inventors on a patent application (U.S. Patent Application 61/989,791) entitled "Methods for Diagnosing and Treating Neuroimmune-Based Psychiatric Disorders." M.L.E. has been supported by a Stanley and Jacqueline Schilling Neuroscience Postdoctoral Research Fellowship, a Dennis Weatherstone Predoctoral Fellowship from Autism Speaks (no. 7825), the Letty and James Callinan and Cathy and Andrew Moley Fellowship from the ARCS (Achievement Rewards for College Scientists) Foundation, and a Dissertation Year Fellowship from the University of California Office of the President. A.K.M. is supported by grants from the National Institute of Neurological Disorders and Stroke (R01-NS060125-05), the National Institute of Mental Health (P50-MH106438-01), the Simons Foundation (SFARI no. 321998), and the University of California Davis Research Investments in Science and Engineering Program.

10.1126/science.aag3194

REVIEW

How neuroinflammation contributes to neurodegeneration

Richard M. Ransohoff

Neurodegenerative diseases such as Alzheimer's disease, Parkinson's disease, amyotrophic lateral sclerosis, and frontotemporal lobar dementia are among the most pressing problems of developed societies with aging populations. Neurons carry out essential functions such as signal transmission and network integration in the central nervous system and are the main targets of neurodegenerative disease. In this Review, I address how the neuron's environment also contributes to neurodegeneration. Maintaining an optimal milieu for neuronal function rests with supportive cells termed glia and the blood-brain barrier. Accumulating evidence suggests that neurodegeneration occurs in part because the environment is affected during disease in a cascade of processes collectively termed neuroinflammation. These observations indicate that therapies targeting glial cells might provide benefit for those afflicted by neurodegenerative disorders.

The human central nervous system (CNS) might represent the most complex entity in existence, although conclusive evidence to support or falsify that hypothesis will probably forever be elusive. Nonetheless, the CNS is beyond question the most elaborate system of which we have daily experience. CNS disorders alter and often degrade the structure and function of this intricate organ. Neurodegeneration is a common (but not invariable) component of CNS disorders and includes processes by which previously established CNS functions such as mobility, memory and learning, judgment, and coordination are progressively lost. Neurodegenerative diseases primarily occur in the later stages of life, positioning time as an essential cofactor in pathogenesis of the major neurodegenerative disorders in a mechanism-driven fashion (*1*–*3*). The achievements of medicine and public health efforts in reducing early- and midlife mortality from certain cancers, infectious diseases, and cardiovascular disorders mean that a larger number of individuals are aging and therefore susceptible to neurodegenerative disease by virtue of their survival. The large cohort of aging people in the developed world threatens society with a substantial burden of care for those afflicted with neurodegeneration (*4*). Moreover and most poignantly, these diseases rob affected persons of those attributes that make long lives worth living: thinking, feeling, remembering, deciding, and moving. Here I consider neuroinflammation in neurodegeneration, a topic that comprises most of the nonneuronal contributors to the cause and progression of neurodegenerative disease. The study of this topic is animated by our hope that meaningful action, in the form of novel treatments, will follow understanding.

What is neurodegeneration?

Neurons are the primary cells of the CNS and endow it with its distinctive functions. Connections between neurons are enacted at synapses, where neurotransmitters are released in quanta to deliver an excitatory or inhibitory signal to the synaptic-target neuron. Cell processes that deliver these signals are termed axons, whereas dendrites receive synaptic inputs. Each of the ~10^{11} neurons in the human brain integrates many synaptic inputs from other neurons and, for each input received, may or may not initiate an axonal action potential and thereby provide synaptic input to its target neuron—a system comprising 10^{15} connections in all.

> ***"Neuroinflammation has been famously difficult to define in relation to neurodegenerative disease."***

Neurodegeneration by definition disturbs the properties of the CNS and therefore affects neuronal function, as well as the structure or survival of neurons. Unlike primary cells from skin, the liver, or muscle, neuronal cells of the CNS do not regenerate after damage by disease, ischemia (deprivation of oxygen, glucose, or blood flow), or physical trauma. Because the complexity of the human CNS is so great, neurodegenerative disorders that derange its function have been challenging to understand and treat: No therapeutics ameliorate the natural course of neurodegenerative disease.

Major neurodegenerative diseases include Alzheimer's disease (AD), frontotemporal lobar dementia (FTLD), Parkinson's disease (PD), and amyotrophic lateral sclerosis (ALS). Individuals diagnosed with multiple sclerosis (MS) are also at risk of developing a neurodegenerative course, typically at later stages of the disease; such cases are termed progressive MS (P-MS). One might consider that AD, PD, and ALS are primary neurodegenerative diseases, in which the initial

---

Biogen, 225 Binney Street, Cambridge, MA 02142, USA.
Email: richard.ransohoff@biogen.com

Table 1. Protein aggregates in neurodegenerative diseases. A-β, N-terminal amyloidogenic fragments of APP; MAPT, microtubule-associated protein tau; TDP-43, 43-kDa TAR DNA-binding protein.

Composition of aggregate	Associated disorders	Physiological localization	Localization in disease
A-β	AD, PDD	Membrane	Extracellular
MAPT	AD, FTLD-tau	Axonal	Cytoplasmic
α-synuclein	PD, PDD	Synaptic	Cytoplasmic
TDP-43	ALS, FTLD-TDP	Nuclear	Cytoplasmic

signs of pathology affect neurons. By comparison, neurodegeneration in P-MS appears to be secondary to the initiating events, which target CNS myelin.

Those studying neurodegenerative conditions rely on a shared set of research tools. Among many others, neurodegeneration researchers draw from neuropathology (analysis of affected tissue), genetics, and model systems. Most neurodegenerative disorders directly affect only the nervous system and specifically the CNS (brain, spinal cord, and optic nerve), as distinguished from the peripheral nervous system (PNS), which encompasses the nerves and muscles of the body and its internal organs. Over many decades of dedicated study, neuropathologists have found that discrete populations of neurons are lost or impaired in each of these diseases—for example, pigmented dopamine neurons in PD and neurons of the motor system in ALS. Additionally, AD, ALS, FTLD, and PD feature characteristic protein aggregates within neurons; representative instances are neurofibrillary tangles in AD and Lewy bodies in PD. A distinctive tissue change termed amyloidosis, in which extracellular proteins are arrayed in beta-pleated sheets, typifies the cortex and hippocampus in AD and in PD with dementia (PDD) (Table 1). In both AD and PDD, N-terminal fragments of amyloid precursor protein (APP) are the major constituents of the extracellular amyloid deposits. Discovering the neurons targeted by each disease and identifying disease-selective pathological protein aggregates has enabled substantial progress in understanding these disorders.

A small minority (<5%) of patients affected by AD, PD, ALS, or FTLD demonstrate Mendelian inheritance of their disease. Furthermore, for each disorder and each major constituent of the characteristic protein aggregate, rare mutations of the encoding genes validate a causal relation between mutant proteins and disease (*5*–*7*). For the most part, disease manifestations of the Mendelian forms of neurodegeneration phenocopy those of the sporadic cases, save only for earlier onset in the case of the former. For this reason, it is considered highly likely that a pathogenic relationship also holds between protein aggregates and disease for sporadic cases. Given their importance for categorizing distinct disorders, the protein aggregates are used in a new molecular nosology that includes synucleinopathies, tauopathies, and amyloidoses. Researchers have accumulated substantial evidence favoring the interlinked hypotheses that relate protein aggregates to sporadic neurodegenerative disease. Nonetheless, only successful therapeutic trials targeting protein aggregates, their upstream causes, or their downstream effects will confirm that these devastating diseases are indeed caused by processes related to protein aggregates.

The current paradigm for these major primary neurodegenerative diseases includes additional commonalities. First, neurodegenerative diseases including PD, AD, and FTLD demonstrate a predictable temporospatial pathological evolution, involving one brain region followed by another and then another. It has been proposed that this mode of progression is mediated at least in part by the transfer of pathogenic protein forms between adjacent cells (*8*, *9*). It is important, however, to emphasize that this intra-individual spreading of pathogenic protein, although reminiscent of prion disease, is not proposed to be associated with risk of exposure to affected persons or their tissues (*10*). Furthermore, although cell-to-cell spread of fibrillar forms of pathogenic proteins can be demonstrated experimentally, its

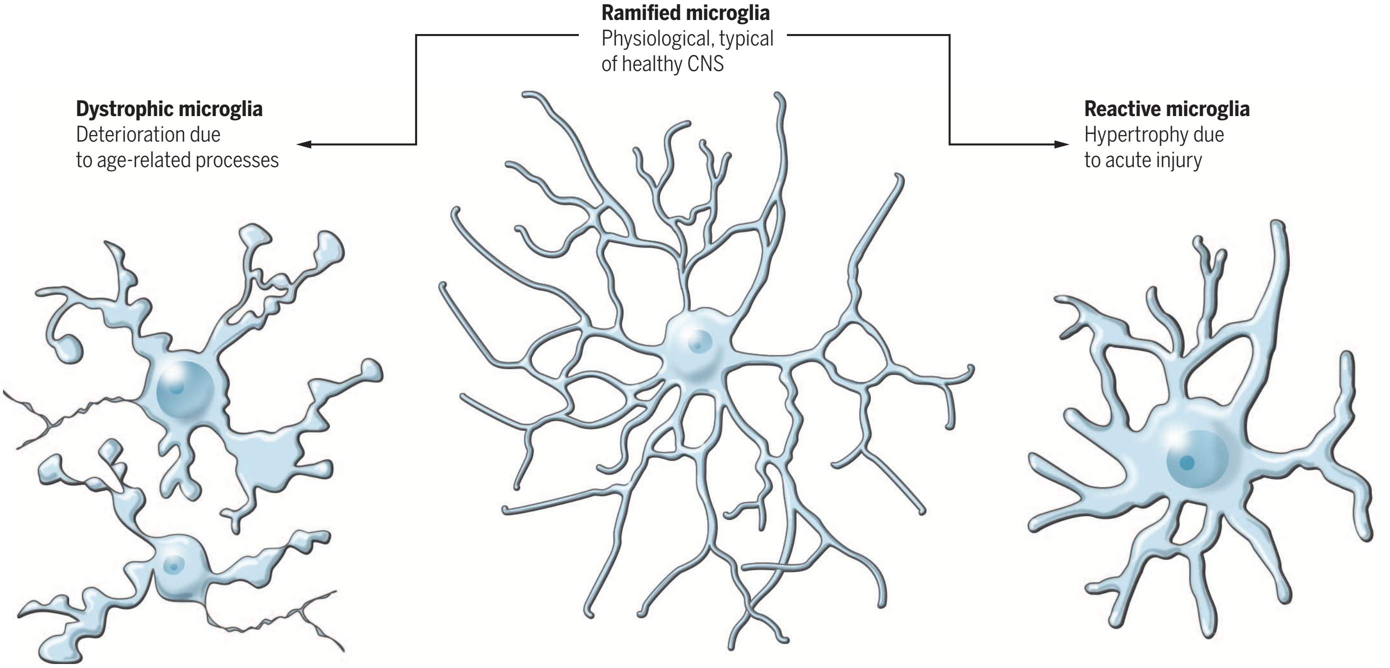

Fig. 1. Morphology of ramified (healthy CNS), reactive, and dystrophic microglia. Microglia reflect their response to the environment in part through their morphology. Morphology does not reliably reflect function, dysfunction, or RNA expression profile phenotype but only demonstrates that the cell is responding to altered homeostasis (*76*). The cartoon depicts three states of microglial morphology: ramified (physiological) microglia, typical of those observed in the healthy CNS; reactive microglia, characteristic of those seen after acute injury; and dystrophic microglia, as observed in the aging brain, particularly in the context of neurodegeneration.

Table 2. Selected elements of the CNS neuroinflammatory system.

Name	Category	Peripheral counterpart	Peripheral function	CNS function
Microglia	Myeloid cell	Circulating monocyte or tissue macrophage	Host defense, wound repair	Synapse formation (*58*), refinement (*59*), monitoring (*60*), and maintenance; inflammatory response; adult neurogenesis modulation (*61*, *62*)
Astrocyte	Glial cell	None	Not applicable	Glutamate reuptake, ionic buffering, water balance, energy substrate for neurons, BBB maintenance (*63*), inflammatory response (*64*, *65*)
Oligodendrocyte	Glial cell	Schwann cell	Myelination of peripheral axons	Myelination of CNS axons, trophic support for myelinated axons (*66*)
NG2$^+$ glia	Glial cell	None	Not applicable	Precursor to adult oligodendroglia (*67*, *68*), inflammatory response (*69*)
CX3CR1	Chemokine receptor	Same as CNS	Monocytes patrolling vessel walls, inflammatory response	Neuron-glia interactions (*50*, *70*, *71*)
C1q, C3, C4, CR3	Complement components	Same as CNS	Host defense	Synaptic pruning (*72*)
TNF-α	Cytokine	Same as CNS	Host defense, inflammation	Synaptic scaling (*73*), neuroprotection (*74*, *75*)

role in disease progression is not a matter of universal agreement. It remains plausible instead that pathology occurs serially in vulnerable neuronal populations, which are proposed to have increasing regionally restricted frequency in the aging brain (*11*). Second, it is hypothesized that protein aggregates, although visually striking when viewed in tissue sections, may not in all cases represent the crucial pathogenic alteration, but rather that their fibrillar or oligomeric precursors may have direct neurotoxicity (*11*). Third, it is widely held that defects in mitochondrial function and turnover (termed mitophagy), autophagy, and management of oxidative stress are involved in various ways in each of these disorders (*12*).

What is neuroinflammation?

Neuroinflammation has been famously difficult to define in relation to neurodegenerative disease. In contrast, neuroinflammation in multiple sclerosis (MS) is unambiguous, comprising often florid infiltration of the CNS parenchyma by blood-derived lymphocytes and monocyte-derived macrophages, accompanied by frank impairment of blood-brain barrier (BBB) function and intense glial reaction. Neuroinflammation in diseases such as AD, PD, and ALS is typified instead by a reactive morphology of glial cells, including both astrocytes and microglia (Fig. 1), accompanied by low to moderate levels of inflammatory mediators in the parenchyma. This reaction, both cellular and molecular, is not distinguishable between one disease and another or from other conditions such as stroke or traumatic injury. Given this lack of specificity, it is easy to conclude that the glial reaction is secondary to neuronal death or dysfunction and is accordingly unlikely to provide useful targets for therapeutic intervention or topics for intensive investigation.

It has been several decades since the detection of inflammatory mediators in AD and PD autopsy brain sections led to the proposal that neuroinflammation might promote progression of these disorders (*13*, *14*). Additional support came from a population-based prospective study that used pharmacological records and showed a dose-related negative correlation between the use of nonsteroidal anti-inflammatory drugs (NSAIDs) during midlife and the likelihood of later developing AD (*15*). However, subsequent AD treatment trials using NSAIDs, glucocorticosteroids, or selective cyclooxygenase-2 inhibitors failed to provide evidence for efficacy and imposed considerable adverse effects (*16*), leaving inflammation's part in neurodegenerative disease in doubt through the early years of the 21st century.

In this regard, it could until recently be argued that neurodegeneration was mainly a cell-autonomous process affecting neurons. Neurodegenerative disease research advanced the understanding of molecular pathogenesis by identifying selective neuron populations that are affected in each disease. Moreover, there was a potent prima facie plausibility relating the affected cell population with signs and symptoms of the disease, as with neuronal death in the motor system in ALS, in which patients suffer muscle atrophy and weakness. Incisive PD studies using in vitro systems, including the use of somatic cells reprogrammed to become (for example) dopamine neurons, provided support for this hypothesis (*17*).

Demonstrating a non–cell-autonomous neurodegenerative process would open new prospects for understanding how neurodegeneration might be promoted by local CNS inflammation, but it was unclear how to proceed until genetic bases for the Mendelian forms of neurodegeneration were identified and then used to develop in vivo disease models. Dramatic findings came from studying a mouse model of ALS in which the gene encoding mutant superoxide dismutase-1 (mSOD1) was expressed using a ubiquitous promoter, yielding a severe phenotype of motor neuron death with weakness and shortened life span, as observed in humans carrying the same gene variant (*18*). The question was deceptively simple: Did it matter whether the *mSOD1* transgene was expressed in cells other than neurons? Modifying this model to enable inducible deletion of *mSOD1* from all myeloid cells (represented in the CNS by microglia) produced an unexpected prolongation of life span without altering the timing of disease onset (*19*). A comparable effect was obtained by conditionally deleting *mSOD1* from astrocytes (*20*), and this manipulation also suppressed microglial acquisition of reactive morphology, suggesting a pathogenic scheme by which astrocyte-microglial interactions promoted mSOD1-related neurodegeneration (*21*, *22*). These results showed unequivocally that lack of transgene expression by glia altered the course in the mSOD1 model. Additional positive support for non–cell-autonomous neuronal degeneration came from expression of a mutant α-synuclein transgene selectively in astrocytes, which produced PD-like pathology and behavioral deficits in mice (*23*, *24*). Simultaneously, reports emerged that autopsy tissue sections from cases of PD, PDD, and other diseases associated with aggregated α-synuclein (collectively termed synucleinopathies) featured distinctive aggregates in astrocytes and oligodendrocytes, as well as neuronal Lewy bodies (*25*, *26*).

Unlike neurons, microglia and astrocytes are challenging to study in vitro, partially because they adopt a reactive nonphysiological phenotype upon explant culture, showing a gene expression profile that is markedly different from that of glia when isolated and analyzed immediately ex vivo (*27*). Additionally, the intrinsic functions of glia are exerted in support of neurons within a complex three-dimensional matrix, so that meaningful glial properties cannot be modeled in two-dimensional cultures (*28*). Given this difficulty of using reductionist experimental approaches to evaluate glial neuroinflammatory properties, and in view of the nonspecific nature of cardinal inflammatory changes in glia during neurodegenerative disease, it seems reasonable to propose an all-purpose definition of neuroinflammation in neurodegeneration: contributions by glial cells, elements of the BBB, or systemic inflammatory processes that are harmful or beneficial to the severity of neurodegenerative disease. This broad definition acknowledges the primacy of neurons in brain function and disease and further recognizes that the glial reaction to neuronal injury, dysfunction, or death may be helpful or harmful (or neutral). Additionally, it is proposed that neurodegeneration can progress in a fashion that is non–cell-autonomous with respect to neurons, suggesting that glial biology, the BBB, or the systemic environment all could offer legitimate targets for therapeutic intervention. Moreover, there is no implied similarity to peripheral inflammatory reactions, as demonstrated (for example) by skin or gut macrophages in response to pathogens, because applications of knowledge gleaned from studying peripheral host defense and wound repair have been misleading when applied incautiously to CNS glia (*29*).

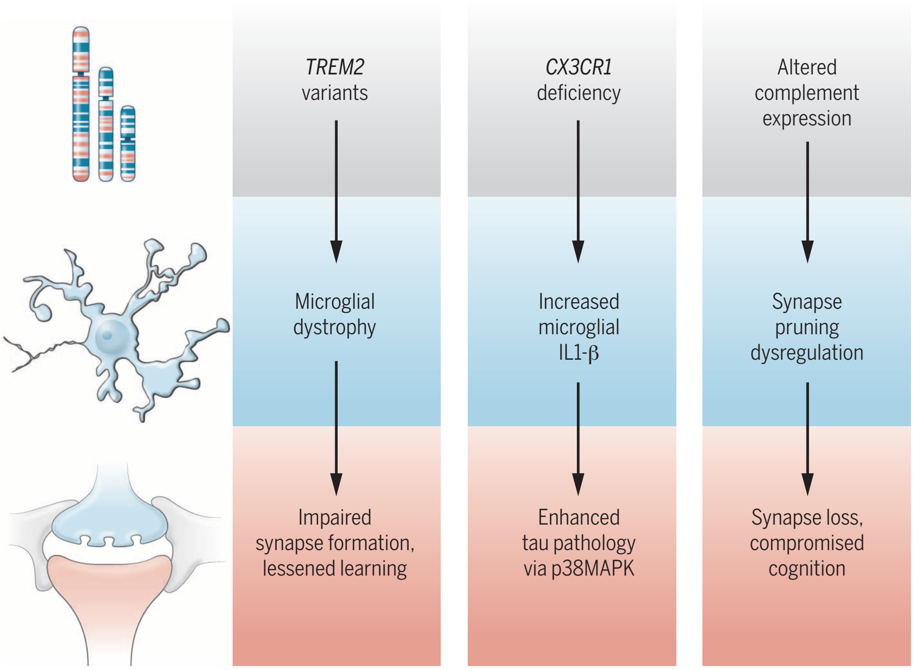

Fig. 2. Pathways from microglial gene variants or altered gene expression to neurodegeneration. *TREM2* variants (*31*), targeted deletion of *CX3CR1* (*70*), and altered complement expression (*77*) have all been associated with neurodegenerative phenotypes in the clinic or in animal models (top row). The middle and bottom rows show the downstream effects. The TREM2 phenotype of microglial dystrophy was studied by means of targeted gene deletion in mice (*78*); the behavioral effect, namely, cognitive deficit in heterozygous *TREM2* haploinsufficiency, was defined clinically (left column) (*79*). Also shown are the neurodegenerative effects of *CX3CR1* deficiency in hTau mice (middle column) (*70*) and complement dysregulation in a model of amyloid pathology (right column) (*77*).

Genetic clues associate neurodegeneration with neuroinflammation

Progress in every domain of biological science has been propelled by genome-level data, and neuroinflammation is no exception. CNS cells involved in neuroinflammatory reactions (microglia, astrocytes, and proteoglycan-NG2$^+$ glia; Table 2) were first identified by their altered morphologies, a descriptive analysis that was unavailing for deciphering whether the cellular reaction was advantageous or deleterious or whether the reaction made any meaningful contribution to pathogenesis. It was therefore a substantial advance to associate Nasu-Hakola disease with homozygous null mutations of *TREM2* (*30*), a gene expressed only by microglia among CNS cells. Despite the extreme rarity of this neurodegenerative disorder, its CNS manifestations of early midlife dementia were unambiguously referable to microglial dysfunction and represented the first evidence that intact microglial activities were essential for brain homeostasis. Relatively subtle *TREM2* genetic variants have now been associated with AD, FTLD, and possibly PD (*31*). Notwithstanding the wealth of *TREM2* coding variants with clinical phenotypes that we can investigate, a mechanistic understanding of why *TREM2* plays such a major role in the risk for neurodegeneration remains contentious and unresolved (*32*) (Fig. 2). Nonetheless, *TREM2* genetics have shown unmistakably that dysfunction of microglia or infiltrating myeloid cells could make a primary rather than a reactive contribution to neurodegeneration and thereby galvanized this field of research. The most salient effects have been found in AD research, where genome-wide association studies (GWAS), supplemented by examination of rare variants and identification of expression quantitative trait loci in microglia, have identified about 20 well-validated genes harboring risk alleles, of which about half are predominantly or only expressed in microglia (*33*). For example, *APOE*, the dominant risk-associated gene, is mainly expressed in astrocytes and reactive microglia (*34*). The availability of convenient, searchable, brain cell–specific databases of RNA-sequencing and microarray expression profiles enables the pursuit of this research direction (*34*–*36*).

In P-MS, inflammation begets neurodegeneration—but how?

MS is relatively common (prevalence of 1:1000) among susceptible populations. Onset occurs at about age 30, with two-thirds of affected individuals being women. Life is only modestly shortened by MS; the disease course is about 45 years. In its early phases of clinical presentation, MS is distinctive, which led to its characterization as a discrete disease entity more than 150 years ago. Patients experience abrupt (minutes to hours) or subacute (days to weeks) alterations in neurological function, termed attacks or relapses. In its early phase, MS remains a disturbing but not disabling disease for many patients, about 85% of whom present with the relapsing form of the disease. Relapses occur from time to time,

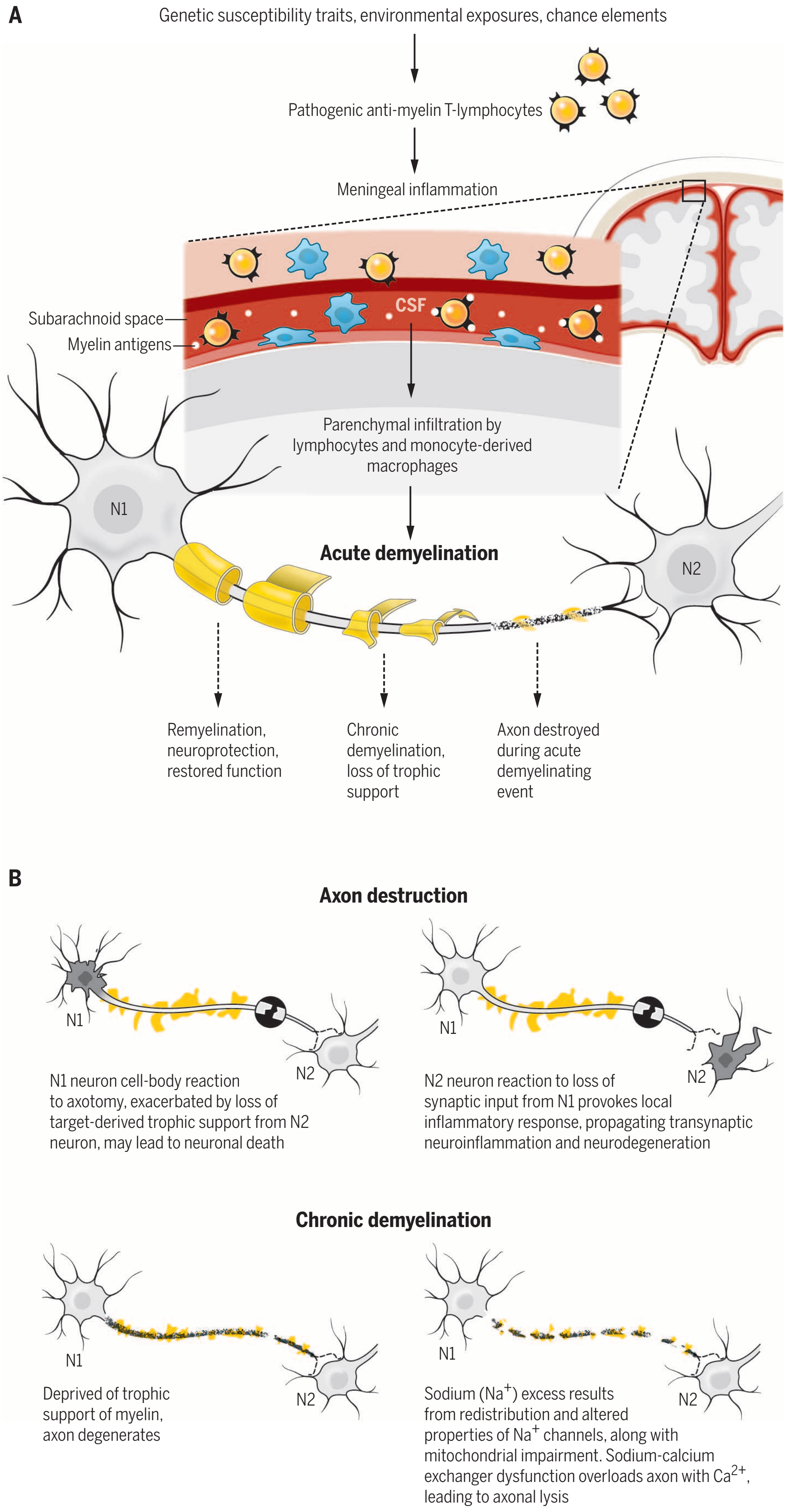

Fig. 3. Pathogenesis of neurodegeneration in P-MS. (**A**) Pathogenesis and short-term outcomes of acute demyelination. N1 is a neuron, shown extending an axon to synapse with neuron N2. The axon is myelinated (yellow shapes). In MS, generation of pathogenic antimyelin T cells results from gene-environment interactions, supplemented by yet-to-be-identified chance elements (*80–82*). Pathogenic T cells traffic through cerebrospinal fluid (CSF) and can be restimulated by myelin antigens in the subarachnoid space (*83*) to initiate meningeal inflammation (*41*); this is followed by parenchymal invasion by T cells and monocyte-derived macrophages, which mediate demyelination. Potential alternative outcomes of acute demyelination are shown at the bottom. (**B**) Outcomes of acute axotomy during demyelination and of chronic demyelination. Acute axotomy (top) causes a stereotyped cell-body reaction for neuron N1. Contingent on the proximity of the axotomy to the neuron cell body and the loss of trophic support from N2, this reaction may lead to the death of the N1 neuron. Additionally, removal of synaptic input can produce an intense local inflammatory reaction around the N2 target neuron (*84*) as glia sense the change in neuronal function. Chronic demyelination (bottom) deprives axons of essential trophic support, threatening their viability and producing susceptibility to axon degeneration (*85*). Furthermore, chronic demyelination causes redistribution of sodium (Na^+) channels away from nodes of Ranvier into the demyelinated segment, as well as altered channel expression (*86*), worsening the risk of Na^+ overload. Axonal conduction produces a Na^+ influx that is poorly balanced by Na^+- and K^+-dependent adenosine triphosphatase, which is impaired as a result of mitochondrial dysfunction (*87*). Sustained Na^+ overload reverses the Na^+-Ca^{2+} antiporter, and the resulting Ca^{2+} influx activates calcium-dependent enzymes, lysing the axon.

with substantial or complete resolution, and attacks leading to permanent disability are more the exception than the rule. MS patients exhibiting this disease pattern are said to have relapsing-remitting MS (RR-MS). Importantly, neurological function, as experienced by patients and assessed by neurologists, remains stable between relapses. Among all CNS diseases [except for neuromyelitis optica (NMO), an autoimmune astrocytopathy], MS is distinctive by virtue of its recurrent (multiphasic) and regionally diverse (multifocal) symptoms, punctuated by periods of symptomatic quiescence. The recurrent nature of MS is most likely due to cellular autoimmunity to myelin that drives the disease.

After a variable period of RR-MS, the disease appears to change its behavior. Attacks become much less common and may cease altogether, to be replaced by a progressive phase during which patients slowly and often relentlessly worsen, without periods of symptom reversal or improvement. This pattern of symptom evolution is designated secondary P-MS. In about 10% of cases, MS presents with progression from the onset, lacking the earlier phase of attacks and remissions. It seems most likely that this symptom pattern, termed primary P-MS, represents the sequelae of typical MS lesions that were clinically silent during the inflammatory phase of disease (*37*, *38*). However, recurrent longstanding neuroinflammation does not inevitably lead to neurodegeneration: In NMO, the other major inflammatory disease of the human CNS, which is caused by autoantibody-mediated astrocytopathy directed at aquaporin-4, there is no progressive phase for the vast majority of patients.

There is a coherent hypothesis to account for neurodegeneration after inflammatory demyelination in MS (Fig. 3). In this view, the sequelae of acute demyelination can lead to progressive loss of axons and neurons unless robust remyelination occurs, which happens in a subset of MS cases (*39*, *40*). In addition to these cellular sequelae of demyelination that produce neurodegeneration in MS, meningeal inflammatory infiltrates are established at the earliest stages of disease (*41*, *42*) and continue to be detectable during clinical progression (*43*), remaining readily observable at autopsy (*44*). Tissue studies (*41*, *44*) and magnetic resonance imaging–pathological correlations (*43*) support the likelihood that these intrathecal inflammatory foci drive ongoing demyelination of underlying cortical tissue.

Which neuroinflammatory treatment target for which disease?

The study of the neuroinflammatory aspects of neurodegeneration is now in a "good news–bad news" situation. Genetic, epidemiological, and descriptive research using brain tissue from patients—as well as results from model systems including genetically modified mice, zebrafish, flies, worms, and induced pluripotent stem cells (iPSCs), which harbor disease-associated genetic variants in the native genomic context—forcefully implicate inflammation in the neurodegenerative process. As one example, mice lacking progranulin, which is encoded by *Grn* and expressed predominantly in the microglia of both humans (*34*) and mice (*36*), showed substantial dysregulation of microglial complement gene expression and of lysosome maturation. These findings were associated with evidence of unexpectedly selective and regionally restricted loss of inhibitory vesicular GABA (γ-aminobutyric acid) transporter–labeled synapses of parvalbumin-positive neurons in the ventral thalamus, where complement deposition was observed on both excitatory and inhibitory synapses. In turn, aged $Grn^{-/-}$ mice exhibited altered thalamic excitability and excessive grooming. The relationship to complement gene expression was established by showing substantial phenotypic rescue in $Grn^{-/-}::C1qa^{-/-}$ mice (*45*). These findings are exciting because of the demonstration that a specific neuronal circuit can be functionally derailed through complement- and microglial-mediated synapse removal. At the same time, several issues were not addressed, including the relation of the phenotype to loss of progranulin as opposed to loss of granulin peptides (derived by proteolysis from progranulin); how complement dysregulation leads to selective synapse loss, given that deposition does not discriminate excitatory from inhibitory synapses; the role (if any) of lysosomal trafficking in the phenotype; and signaling pathways underlying altered microglial gene expression (*45*). Overall, this study advances our understanding of progranulin deficiency while standing in continuity with other studies showing that specific neuroinflammatory genes or pathways are plausibly associated with AD, PD, and ALS. Nonetheless, no therapeutics have emerged from this line of research. There are reasonable explanations for this circumstance, including the inherent complexity of neurodegenerative disease, challenges related to clinical trial design, and lack of actionable high-throughput screening platforms (particularly as regards cultured glial cells), among others. For now, the following strategic formulations to address these issues may be useful.

> ***"...neurodegeneration can progress in a fashion that is non-cell-autonomous with respect to neurons, suggesting that glial biology, the BBB, or the systemic environment all could offer legitimate targets for therapeutic intervention."***

Genetics are key

Target identification based on human-disease genetic validation enhances prospects for success. GWAS loci have proven to be robustly reproducible, and the initial threshold for genome-wide significance appears durable (*46*). Proceeding from loci to genes to pathways remains challenging, but methods for confirming "hits" are highly promising. Systems biology can make additional contributions to target prosecution.

Remain unbiased even after the omics are done

Confronted with an uncertain comprehension of neurodegenerative disease, it is tempting to rely on dogma. Deciphering inflammation has been challenging, even in the familiar context of adaptive-immune disorders such as rheumatoid arthritis. Innate immunity in the CNS is an unfamiliar landscape in which well-known actors and their properties may be upended. One example comes from considering neuroprotective properties of TNF-α (tumor necrosis factor–α) and the associated NF-κB (nuclear factor κB) signaling pathway (Table 2).

New models will be needed

In vitro cultures of glial cells have been poorly predictive of relevant activities and phenotypes in vivo (*28*). Novel systems including organotypic brain-slice cultures (*47*), zebrafish (*48*), and iPSCs (for astrocytes) (*49*) are required.

Consider the periphery

Glial cell phenotypes are modulated profoundly by peripheral inflammatory stimuli (*50*), including dysbiosis due to altered gut microbiota (*51*, *52*), findings which have been confirmed in clinical studies (*53*). Compared with direct manipulation of CNS cells or factors, manipulating the peripheral environment to modulate neurodegenerative disease would be manifestly less encumbered by concerns about safety, biomarker selection, or off-target effects. This consideration also pertains directly to the potential role of the BBB in neurodegeneration (*54*, *55*), which was highlighted by the finding that access of blood-borne pathogens to the CNS in the context of a compromised BBB might stimulate amyloid deposition (*56*).

Conclusions and future prospects

The study of neuroinflammation as a major contributor to neurodegeneration is, in some ways, fewer than two decades old, dating from the demonstration that altered microglia produce a neurodegenerative phenotype in humans (*57*). This line of research encompasses disease-related alterations in the environment in which neurons exist, including those coming from glial reaction to the disorder, as well as intra-CNS effects of peripheral inflammatory stimuli and the degradation of homeostasis caused by an impaired BBB. Available research resources such as genomic and epigenetic data sets, model organisms, and iPSC-derived cells enable an unprecedented scope of research attack. Given these circumstances, neuroinflammation researchers should be cognizant of the task's complexity and previous defeats, while approaching with cautious optimism the prospect of therapeutic success against these severe diseases.

REFERENCES AND NOTES

1. R. Madabhushi, L. Pan, L. H. Tsai, *Neuron* **83**, 266–282 (2014).
2. R. Lardenoije *et al.*, *Prog. Neurobiol.* **131**, 21–64 (2015).
3. G. G. Kovacs *et al.*, *Neuroscience* **269**, 152–172 (2014).
4. H. Leicht *et al.*, *PLOS ONE* **8**, e70018 (2013).
5. M. Goedert *et al.*, *Philos. Trans. R. Soc. Lond. B Biol. Sci.* **356**, 213–227 (2001).
6. S. Ajroud-Driss, T. Siddique, *Biochim. Biophys. Acta* **1852**, 679–684 (2015).
7. V. Chouraki, S. Seshadri, *Adv. Genet.* **87**, 245–294 (2014).
8. M. Jucker, L. C. Walker, *Nature* **501**, 45–51 (2013).
9. L. C. Walker, M. I. Diamond, K. E. Duff, B. T. Hyman, *JAMA Neurol.* **70**, 304–310 (2013).
10. J. Brettschneider, K. Del Tredici, V. M.-Y. Lee, J. Q. Trojanowski, *Nat. Rev. Neurosci.* **16**, 109–120 (2015).
11. D. J. Selkoe, J. Hardy, *EMBO Mol. Med.* **8**, 595–608 (2016).
12. M. Redmann, V. Darley-Usmar, J. Zhang, *Aging Dis.* **7**, 150–162 (2016).
13. P. L. McGeer, S. Itagaki, B. E. Boyes, E. G. McGeer, *Neurology* **38**, 1285–1291 (1988).
14. J. Rogers *et al.*, *Neurobiol. Aging* **17**, 681–686 (1996).
15. B. A. in 't Veld *et al.*, *N. Engl. J. Med.* **345**, 1515–1521 (2001).
16. D. Jaturapatporn, M. G. Isaac, J. McCleery, N. Tabet, *Cochrane Database Syst. Rev.* **2**, CD006378 (2012).
17. L. Qiang, R. Fujita, A. Abeliovich, *Neuron* **78**, 957–969 (2013).
18. D. L. Price *et al.*, *Ann. N. Y. Acad. Sci.* **920**, 179–191 (2000).
19. S. Boillée *et al.*, *Science* **312**, 1389–1392 (2006).
20. K. Yamanaka *et al.*, *Nat. Neurosci.* **11**, 251–253 (2008).
21. S. Boillée, C. Vande Velde, D. W. Cleveland, *Neuron* **52**, 39–59 (2006).
22. C. S. Lobsiger, D. W. Cleveland, *Nat. Neurosci.* **10**, 1355–1360 (2007).
23. X. L. Gu *et al.*, *Mol. Brain* **3**, 12 (2010).

24. J. C. McGann, D. T. Lioy, G. Mandel, *Curr. Opin. Neurobiol.* **22**, 850–858 (2012).
25. D. Brück, G. K. Wenning, N. Stefanova, L. Fellner, *Neurobiol. Dis.* **85**, 262–274 (2016).
26. L. Fellner, K. A. Jellinger, G. K. Wenning, N. Stefanova, *Acta Neuropathol.* **121**, 675–693 (2011).
27. O. Butovsky *et al.*, *Nat. Neurosci.* **17**, 131–143 (2014).
28. R. M. Ransohoff, V. H. Perry, *Annu. Rev. Immunol.* **27**, 119–145 (2009).
29. R. M. Ransohoff, *Nat. Neurosci.* **19**, 987–991 (2016).
30. M. M. Bianchin *et al.*, *Cell. Mol. Neurobiol.* **24**, 1–24 (2004).
31. J. Walter, *J. Biol. Chem.* **291**, 4334–4341 (2016).
32. R. E. Tanzi, *N. Engl. J. Med.* **372**, 2564–2565 (2015).
33. C. Villegas-Llerena, A. Phillips, P. Garcia-Reitboeck, J. Hardy, J. M. Pocock, *Curr. Opin. Neurobiol.* **36**, 74–81 (2016).
34. M. L. Bennett *et al.*, *Proc. Natl. Acad. Sci. U.S.A.* **113**, E1738–E1746 (2016).
35. I. R. Holtman *et al.*, *Glia* **63**, 1495–1506 (2015).
36. Y. Zhang *et al.*, *J. Neurosci.* **34**, 11929–11947 (2014).
37. O. H. Kantarci *et al.*, *Ann. Neurol.* **79**, 288–294 (2016).
38. B. A. Cree, *Handb. Clin. Neurol.* **122**, 211–230 (2014).
39. P. Patrikios *et al.*, *Brain* **129**, 3165–3172 (2006).
40. B. Kornek *et al.*, *Am. J. Pathol.* **157**, 267–276 (2000).
41. C. F. Lucchinetti *et al.*, *N. Engl. J. Med.* **365**, 2188–2197 (2011).
42. B. Obermeier *et al.*, *Nat. Med.* **14**, 688–693 (2008).
43. M. Absinta *et al.*, *Neurology* **85**, 18–28 (2015).
44. R. Magliozzi *et al.*, *Ann. Neurol.* **68**, 477–493 (2010).
45. H. Lui *et al.*, *Cell* **165**, 921–935 (2016).
46. J. R. Wendland, M. D. Ehlers, *Biol. Psychiatry* **79**, 650–656 (2016).
47. A. Masuch *et al.*, *Glia* **64**, 1285–1297 (2016).
48. D. A. Lyons, W. S. Talbot, *Cold Spring Harb. Perspect. Biol.* **7**, a020586 (2015).
49. P. W. Zhang *et al.*, *Glia* **64**, 63–75 (2016).
50. A. E. Cardona *et al.*, *Nat. Neurosci.* **9**, 917–924 (2006).
51. D. Erny *et al.*, *Nat. Neurosci.* **18**, 965–977 (2015).
52. V. Rothhammer *et al.*, *Nat. Med.* **22**, 586–597 (2016).
53. C. Holmes *et al.*, *Neurology* **73**, 768–774 (2009).
54. Z. Zhao, A. R. Nelson, C. Betsholtz, B. V. Zlokovic, *Cell* **163**, 1064–1078 (2015).
55. R. D. Bell *et al.*, *Neuron* **68**, 409–427 (2010).
56. D. K. Kumar *et al.*, *Sci. Transl. Med.* **8**, 340ra72 (2016).
57. H. H. Klünemann *et al.*, *Neurology* **64**, 1502–1507 (2005).
58. C. N. Parkhurst *et al.*, *Cell* **155**, 1596–1609 (2013).
59. D. P. Schafer *et al.*, *Neuron* **74**, 691–705 (2012).
60. M. E. Tremblay, R. L. Lowery, A. K. Majewska, *PLOS Biol.* **8**, e1000527 (2010).
61. L. Fourgeaud *et al.*, *Nature* **532**, 240–244 (2016).
62. R. M. Ransohoff, *Nature* **532**, 185–186 (2016).
63. B. Obermeier, A. Verma, R. M. Ransohoff, *Handb. Clin. Neurol.* **133**, 39–59 (2016).
64. M. Pekny *et al.*, *Acta Neuropathol.* **131**, 323–345 (2016).
65. M. V. Sofroniew, *Nat. Rev. Neurosci.* **16**, 249–263 (2015).
66. K. A. Nave, *Nature* **468**, 244–252 (2010).
67. M. O'Rourke, R. Gasperini, K. M. Young, *Neural Regen. Res.* **9**, 1261–1264 (2014).
68. A. Nishiyama, L. Boshans, C. M. Goncalves, J. Wegrzyn, K. D. Patel, *Brain Res.* **1638**, 116–128 (2016).
69. Z. Kang *et al.*, *Nat. Neurosci.* **16**, 1401–1408 (2013).
70. K. Bhaskar *et al.*, *Neuron* **68**, 19–31 (2010).
71. R. M. Ransohoff, A. E. Cardona, *Nature* **468**, 253–262 (2010).
72. A. H. Stephan, B. A. Barres, B. Stevens, *Annu. Rev. Neurosci.* **35**, 369–389 (2012).
73. D. Stellwagen, R. C. Malenka, *Nature* **440**, 1054–1059 (2006).
74. O. Watters, J. J. O'Connor, *J. Neuroinflammation* **8**, 87 (2011).
75. L. Marchetti, M. Klein, K. Schlett, K. Pfizenmaier, U. L. Eisel, *J. Biol. Chem.* **279**, 32869–32881 (2004).
76. V. H. Perry, *Acta Neuropathol.* **120**, 277–286 (2010).
77. S. Hong *et al.*, *Science* **352**, 712–716 (2016).
78. P. L. Poliani *et al.*, *J. Clin. Invest.* **125**, 2161–2170 (2015).
79. L. Montalbetti *et al.*, *Funct. Neurol.* **20**, 71–75 (2005).
80. S. Sawcer *et al.*, *Nature* **476**, 214–219 (2011).
81. R. M. Ransohoff, *Nat. Immunol.* **11**, 570–572 (2010).
82. K. L. Munger, A. Ascherio, *Expert Rev. Clin. Immunol.* **3**, 739–748 (2007).
83. R. M. Ransohoff, B. Engelhardt, *Nat. Rev. Immunol.* **12**, 623–635 (2012).
84. R. B. Banati *et al.*, *Brain* **123**, 2321–2337 (2000).
85. K. A. Nave, *Nat. Rev. Neurosci.* **11**, 275–283 (2010).
86. S. G. Waxman, *Trends Mol. Med.* **12**, 192–195 (2006).
87. R. J. Franklin, C. ffrench-Constant, J. M. Edgar, K. J. Smith, *Neurology* **8**, 624–634 (2012).

10.1126/science.aag2590

PERSPECTIVE

Inflammatory neuroprotection following traumatic brain injury

Matthew V. Russo and Dorian B. McGavern*

Traumatic brain injury (TBI) elicits an inflammatory response in the central nervous system (CNS) that involves both resident and peripheral immune cells. Neuroinflammation can persist for years following a single TBI and may contribute to neurodegeneration. However, administration of anti-inflammatory drugs shortly after injury was not effective in the treatment of TBI patients. Some components of the neuroinflammatory response seem to play a beneficial role in the acute phase of TBI. Indeed, following CNS injury, early inflammation can set the stage for proper tissue regeneration and recovery, which can, perhaps, explain why general immunosuppression in TBI patients is disadvantageous. Here, we discuss some positive attributes of neuroinflammation and propose that inflammation be therapeutically guided in TBI patients rather than globally suppressed.

Traumatic brain injuries (TBIs) cause many reactions; one of the most prominent is neuroinflammation. Damage to the CNS elicits inflammatory responses from resident microglia and macrophages, as well as peripheral immune cells, such as neutrophils, monocytes, and T cells. Microglia and resident macrophages immediately respond to injury after sensing damage-associated molecular patterns (DAMPs), such as the presence of adenosine triphosphate (ATP) or intracellular proteins that are released from damaged or dying cells. Signaling from DAMP receptors initiates local cytokine and chemokine production, which affects the immediate environment and provides a cue for peripheral immune infiltration (*1*). A major question in the field of TBI research is how the immune response influences the pathogenesis of brain injury and recovery. Although a number of studies suggest that neuroinflammation is detrimental and inhibitory to neural regeneration following TBI, the failure of anti-inflammatory drugs to achieve a therapeutic benefit in human clinical trials supports a growing need to more carefully interrogate the duality of TBI-induced immunity. Immune reactions do indeed have the means to cause damage, but they also play a critical role in promoting tissue repair and recovery following brain injury.

Pathogenic inflammation following TBI

Microglia are resident immune sentinels that respond to nearly all inflammatory events within the CNS. Their exact contribution to the pathogenesis of brain injuries is not entirely understood, but studies have shown that microglial activation can persist for years following TBI in humans (*2*). For example, analysis of microglia and associated pathology in TBI patients revealed clusters of activated microglia (evidenced by CR3 and CD68 immunoreactivity) in 28% of patients that survived for more than 1 year after a single brain injury (*2*). These patients also showed active signs of white matter degeneration, indicative of a chronic pathological process. However, it is unclear whether microglia are active participants in this prolonged degenerative process or are simply responding to the pathology induced by other mechanisms. Investigators have attempted to interrogate microglia in animal models of TBI, although the results are not definitive. Minocycline is an antibiotic with anti-inflammatory properties that is commonly used to suppress microglia and/or macrophage activation. This compound showed some therapeutic benefit (i.e., reduced microglia activation and brain lesion size) in a weight drop model of TBI (*3*), but the improvement cannot be linked exclusively to the effect of minocycline on microglia. Another study similarly concluded that microglia are pathogenic by studying cortical injury in the reduced form of nicotinamide adenine dinucleotide phosphate (NADPH) oxidase-2 (NOX2)$^{-/-}$ mice (*4*). NOX2 is a subunit of NADPH oxidase expressed by activated microglia and known to generate reactive oxygen species (ROS). Both ROS production and lesion sizes were reduced in injured NOX2$^{-/-}$ mice, which suggested that microglia-derived ROS exacerbates TBI damage (*4*). Because the mice in this study were globally deficient in NOX2, it will be important in future studies to link pathogenic NOX2 activity exclusively to microglia.

> ***"At least some inflammation may be necessary in the acute stage of CNS injury to clear damage and set the stage for remodeling efforts."***

Viral Immunology and Intravital Imaging Section, National Institutes of Neurological Disorders and Stroke, National Institutes of Health, Bethesda, MD 20852, USA.
*Corresponding author. Email: mcgavernd@mail.nih.gov

Peripherally derived myeloid cells have also been implicated in TBI pathogenesis. After CNS injury, blood-derived monocytes migrate to the site of damage, where they differentiate into macrophages and persist as needed until the inflammation subsides. Even though macrophages aid wound-healing responses, many studies have concluded that monocytes are inherently pathogenic after TBI. For example, a subset of circulating monocytes express C-C chemokine receptor type 2 (CCR2), and macrophage numbers were reduced by >80% following cortical injury of CCR2$^{-/-}$ mice. This resulted in improved hippocampal neuronal survival and functional recovery relative to wild-type controls (*5*). This study demonstrates that peripheral CCR2^{+} monocytes can contribute to hippocampal damage after direct cortical injury. Additional studies are needed to address whether all injured brain regions suffer the same fate after invasion by CCR2^{+} monocytes, as well as how other monocyte subsets contribute to TBI pathogenesis and recovery.

Immunosuppressive clinical trials

The association between neurodegeneration and neuroinflammation has stimulated a great deal of interest in using immunosuppressive treatments for CNS injuries. Many drugs with anti-inflammatory properties—such as corticosteroids, nonsteroidals, statins, and specific cytokine inhibitors—have been tested in different TBI animal models (*6*). Although many of these treatments were effective in lessening pathology and improving neurological function, the results varied according to the injury model and/or treatment window. On the basis of promising preclinical data, large phase III clinical trials were conducted to assess the efficacy of immunosuppressive treatments in the acute phase of TBI. Corticosteroids had been used for decades to treat head injuries without a substantial amount of clinical data to support their efficacy. In 2004, a definitive trial found that administration of methylprednisolone within 8 hours of injury increased the risk of death at 6 months post TBI (*7*). The treatment group was also less likely to have a favorable recovery (based on the Glasgow Outcome Scale) at 6 months. Another clinical trial examined the effects of treating TBI patients with progesterone, an anti-inflammatory neurosteroid, within 4 hours of head injury (*8*). Evaluation at 6 months post injury revealed no significant difference between progesterone and the placebo control groups in terms of mortality or favorable outcomes. These trials demonstrate that suppressing the immune response acutely after a head injury at best has no effect and at worst actually increases the risk of death 6 months later.

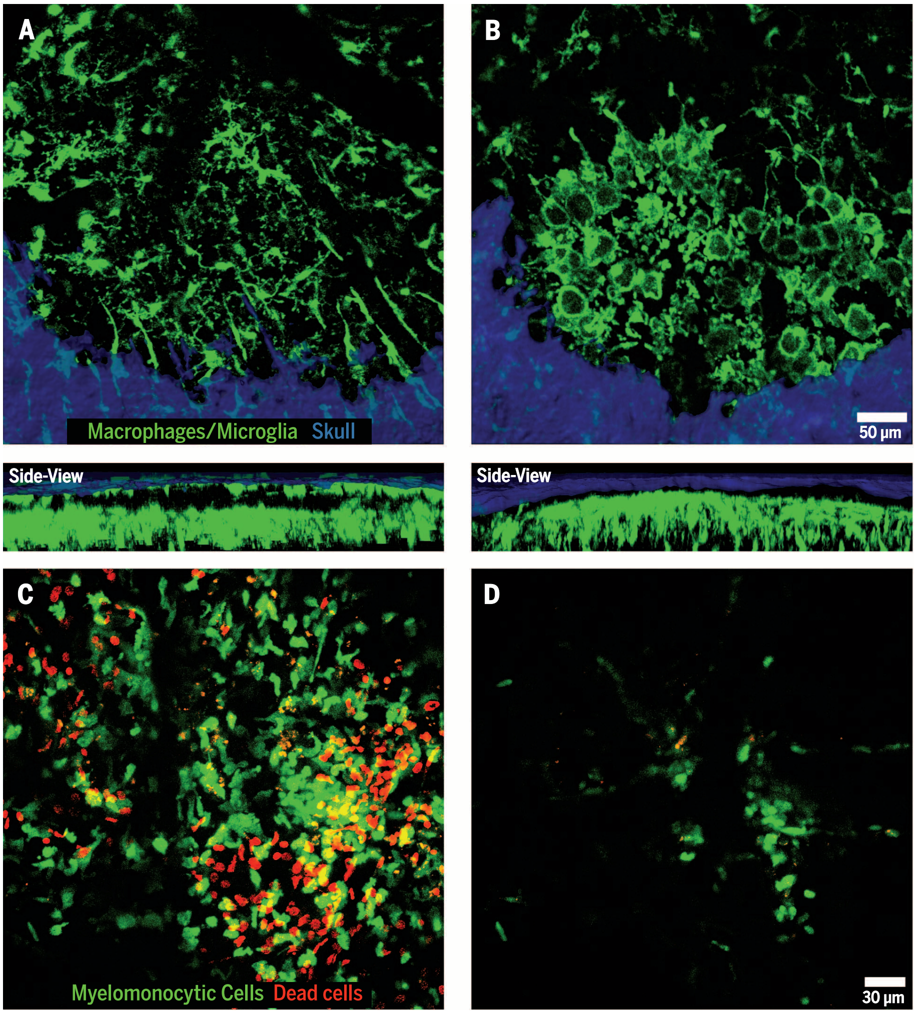

Fig. 1. Myeloid cell dynamics following brain injury. (**A** and **B**) Two-photon *z*-stacks captured through a thinned skull (blue) window of CX3CR1$^{gfp/+}$ mice show the morphology of macrophages and microglia (green) in the meninges and brain parenchyma, respectively. (A) Naïve microglia are ramified, whereas meningeal macrophages have a wormlike appearance. (B) Within minutes to hours after a meningeal contusion injury, meningeal macrophages rapidly disappear (die) and activated microglia migrate to the glia limitans and assume a "jellyfish" morphology that allows them to fill spaces previously occupied by dead astrocytes. These cells participate in phagocytosis and reduce leakage from the meninges into the underlying brain parenchyma. See corresponding movie S1. (**C** and **D**) Lysozyme-M$^{gfp/+}$ myelomonocytic cells (neutrophils/monocytes in green) are recruited to sites of meningeal cell death (red) beginning ~1 hour after TBI. A two-photon *z*-stack captured at 24 hours post injury demonstrates that nearly all the myelomonocytic cells responding to cell death are in the (C) meninges (top 30 μm of *z*-stack) as opposed to the (D) parenchyma (bottom 30 μm of the same *z*-stack). See corresponding movie S3.

The benefit of CNS inflammation

Why have potent immunosuppressive drugs failed to benefit TBI patients in phase III stage clinical trials? At least some inflammation may be necessary in the acute stage of CNS injury to clear damage and set the stage for remodeling efforts. Immunity promotes regeneration in peripheral tissues, so it is counterintuitive to think that neuroinflammation is universally neurodegenerative. The immune system is usually an active participant in wound healing. Within the CNS, positive aspects of immune cells that mobilize in response to damage include clearing dead cells, supporting the barrier system, and setting the stage for wound healing. Microglia, monocytes, macrophages, neutrophils, and T cells can collectively orchestrate a response that preserves neural tissue and fosters regeneration.

Because of their ubiquitous presence and abundant DAMP sensors, microglia are usually among the first responders to brain damage. For example, microglia express several purinergic receptors that allow them to quickly respond to extracellular purines, such as ATP. Detection of extracellular ATP causes microglia to project processes toward a site of damage within minutes. In a meningeal contusion model, ATP released by surface-associated astrocytes in the damaged glial limitans (a structure that separates the meninges and brain parenchyma) caused underlying microglia to shift into honeycomb- and jellyfish-like morphologies that provided

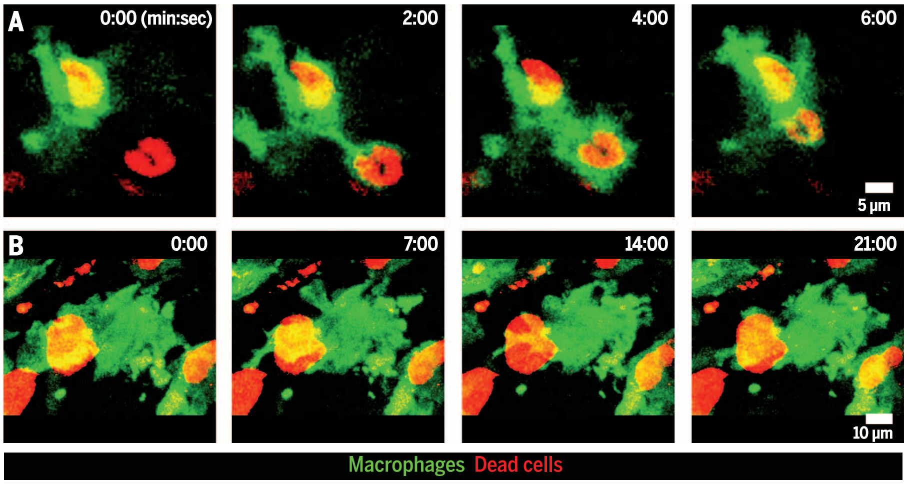

Fig. 2. Scavenging macrophages after brain injury. (**A** and **B**) Meningeal macrophages repopulate the meninges beginning ~2 days post injury, where they assume the role of scavengers. Time-lapse two-photon movies of the meningeal space show (A) a single macrophage that had previously engulfed a dead cell extending a process to phagocytose another cell at 2 days post injury and (B) a macrophage probing and sampling a dead cell at 4 days post injury. See corresponding movie S2.

barrier support and debris clearance, respectively (Fig. 1 and movie S1) (*1*, *9*). Acute inhibition of this response increased the amount of neural cell death in the parenchyma. Microglia also participate in immediate CNS barrier support following damage of cerebral capillaries (*10*). Capillary damage caused by focal laser injury induces a purinergic receptor–dependent extension of microglia processes toward the vascular wall in an effort to prevent leakage into the parenchyma. Inhibition of this response resulted in capillary leakage that lasted three times as long as that observed in control mice. In addition to providing barrier support, microglia and macrophages can also clear debris from the injured CNS (Fig. 2 and movie S2). After damage to the corpus callosum, impaired myelin clearance by microglia leads to a decreased recruitment of oligodendrocyte precursor cells, which results in disorganized and defective axonal remyelination (*11*). In general, microglia are critical participants in the acute phase of a CNS injury. Sealing barriers and clearing debris are just two benefits of having these cells involved in the response.

Despite the various protective layers separating the CNS from peripheral tissues, immune cells infiltrate the CNS in response to trauma. In a model of spinal cord injury, neutrophil recruitment was necessary for proper wound healing and repair (*12*). Mice treated with neutrophil-depleting antibodies exhibited decreased astrocyte reactivity at the injury site, larger lesions, and worse neurological outcomes. Neutrophils are also recruited to the meninges in a purinergic receptor–dependent manner following acute brain injury, and interference with this response actually increased the amount of meningeal cell death (Fig. 1 and movie S3) (*9*). It is presently unclear how neutrophils contribute to neuroprotective responses following CNS injury, but these cells do have the ability to recruit peripheral monocytes within a day or two. Spinal cord injury elicits a marked recruitment of proinflammatory macrophages that is followed several days later by wound-healing macrophages (*13*). When this wound-healing response was blocked, mice were unable to properly repair the lesion and recover motor skills (*13*). Similar to peripheral tissues, innate immune cells are essential for tissue remodeling and repair in the CNS. The challenge is to develop strategies that foster wound-healing responses while impeding maladaptive neuroinflammation.

The adaptive immune system is usually associated with the containment and clearance of pathogens, but T cells can also play a positive role in CNS injury responses. CNS damage can promote the nonspecific recruitment of CD4$^+$ T cells that produce interleukin-4 (IL-4) in a major histocompatibility complex II–independent manner (*14*). Release of IL-4 potentiates neurotrophin signaling that helps stimulate axonal regrowth after injury. Mice lacking T cells or IL-4 demonstrated increased neuronal loss and neurological dysfunction following CNS injury. During CNS tissue repair, effector and regulatory CD4$^+$ T cells work in tandem. Regulatory T cells (T_{regs}) often keep immune responses in check by modulating inflammatory mediators to promote wound healing and remodeling. Depletion of T_{regs} before CNS injury increased the recruitment of effector CD4$^+$ T cells and improved neurological recovery (*15*). By contrast, T_{reg} depletion several days after injury actually interfered with the tissue repair process. Similarly to the transition from proinflammatory to wound-healing macrophages, these T_{reg} data show that the neuroinflammatory response to injury changes as time progresses.

Concluding remarks

When preclinical and clinical data are combined, a clearer picture of TBI immunity emerges. Inflammation induced by a CNS injury should not be viewed as inherently maladaptive or neurotoxic. In general, neuroinflammatory responses during the acute phase of TBI have a lot of positive attributes that include barrier maintenance, debris clearance, cytokine and/or neurotrophin production, and immune regulation, among others. Inhibition of these responses will likely enhance neural damage and impede the wound-healing response to TBI. This conclusion is supported by the failure of immune-dampening drugs (e.g., methylprednisolone and progesterone) to achieve a clinical benefit in human TBI patients when administered shortly after injury. Nevertheless, neuroinflammation can become maladaptive over time. This might occur during the chronic stages of TBI, especially when macrophages and microglia remain in an inflammatory state in the CNS for months or years and acquire aberrant functions. Genetic predispositions, environment variables, and the location and severity of the injury are also likely to shape neuroinflammatory responses. Additional research is required to explore all of these variables and to better define the temporal aspects of CNS inflammation after TBI. It is incredibly important to identify the critical time window when inflammatory cells participate in tissue repair following TBI. Future therapies should focus on guiding CNS immunity toward a favorable outcome rather than suppressing it entirely.

REFERENCES AND NOTES

1. K. N. Corps, T. L. Roth, D. B. McGavern, *JAMA Neurol.* **72**, 355–362 (2015).
2. V. E. Johnson *et al.*, *Brain* **136**, 28–42 (2013).
3. S. Homsi *et al.*, *J. Neurotrauma* **27**, 911–921 (2010).
4. K. Dohi *et al.*, *J. Neuroinflammation* **7**, 41 (2010).
5. C. L. Hsieh *et al.*, *J. Neurotrauma* **31**, 1677–1688 (2014).
6. P. J. Bergold, *Exp. Neurol.* **275**, 367–380 (2016).
7. P. Edwards *et al.*, *Lancet* **365**, 1957–1959 (2005).
8. D. W. Wright *et al.*, *N. Engl. J. Med.* **371**, 2457–2466 (2014).
9. T. L. Roth *et al.*, *Nature* **505**, 223–228 (2014).
10. N. Lou *et al.*, *Proc. Natl. Acad. Sci. U.S.A.* **113**, 1074–1079 (2016).
11. A. Lampron *et al.*, *J. Exp. Med.* **212**, 481–495 (2015).
12. D. P. Stirling, S. Liu, P. Kubes, V. W. Yong, *J. Neurosci.* **29**, 753–764 (2009).
13. R. Shechter *et al.*, *Immunity* **38**, 555–569 (2013).
14. J. T. Walsh *et al.*, *J. Clin. Invest.* **125**, 699–714 (2015).
15. C. Raposo *et al.*, *J. Neurosci.* **34**, 10141–10155 (2014).

ACKNOWLEDGMENTS

This work was supported by the NIH intramural program.

SUPPLEMENTARY MATERIALS

www.sciencemag.org/content/353/6301/783/suppl/DC1
Movies S1 to S3

10.1126/science.aaf6260

RESEARCH

Microglia development follows a stepwise program

Matcovitch-Natan et al., *p. 789*

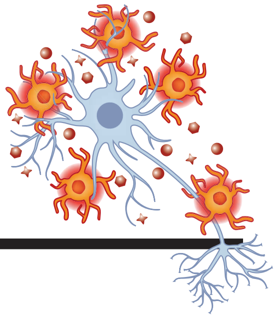

IN *SCIENCE* JOURNALS

Edited by **Caroline Ash**

The Parlung River in Eastern Tibet

GEOMORPHOLOGY

Unlinking erosion from uplift in Tibet

Conventional wisdom suggests that the locations of gorges or "knickpoints" along the edges of large plateaus remain fixed because erosion drives tectonic uplift. Nowhere should this be more evident than the rapidly uplifting and eroding Tibetan plateau. However, King *et al.* found evidence for slow migration of a major knickpoint along the Parlung River in eastern Tibet. They used a new method with exceptional time resolution for determining regional cooling rates called multi–OSL (optically stimulated luminescence) thermochronology. It appears that the Parlung knickpoint is steadily moving upstream as a response to tectonic uplift that is unrelated to the local erosion rates. —BG

Science, this issue p. 800

CRYSTALLOGRAPHY

Stop wiggling and hold that pose

X-ray crystallography can be the definitive method for determining the structure and chirality of small organic molecules, but orientational disorder in the crystal can limit its resolution. Lee *et al.* used a chiral metal-organic framework containing formate ligands that can bind and align molecules covalently to reduce this motion (see the Perspective by Öhrström). The structure and absolute configuration—i.e., which spatial arrangement of atoms is the *R* or *S* isomer—of several organic molecules can thus be measured. These range from small molecules, such as methanol, to complex plant hormones, such as gibberellins that have eight stereocenters or jasmonic acid, whose absolute configuration had not previously been directly established. —PDS

Science, this issue p. 808; see also p. 754

SEPARATION MEMBRANES

Carbon sieving to separate the similar

Separating organic molecules, particularly those with almost equal sizes and similar physical properties, can be challenging and may require energy-intensive techniques such as freeze fractionation. Taking inspiration from reverse osmosis of aqueous fluids, Koh *et al.* describe the synthesis, characterization, and mass transport performance of carbon molecular sieve membranes for the separation of liquid-phase organic molecules at room temperature. This technique is capable of separating very similar isomers, such as *ortho*- and *para*-xylene, on an industrial scale. —MSL

Science, this issue p. 804

HUMAN GENETICS

Genetic variation and coronary artery disease

Most genetic variants lie outside protein-coding genes, but their effects, especially in human health, are not well understood. Franzén *et al.* examined gene expression in tissues affected by coronary artery disease (CAD). They found that individuals with loci that have been associated with CAD in genome-wide analyses had different patterns of tissue-specific gene expression than individuals without these genetic variants. Similarly, tissues not associated with CAD did not have CAD-like expression patterns. Thus, tissue-specific data can be used to dissect the genetic effects that predispose individuals to CAD. —LMZ

Science, this issue p. 827

SYNTHETIC GENOMICS

Recoding and repurposing genetic codons

By recoding bacterial genomes, it is possible to create organisms that can potentially synthesize

PHOTO (FROM TOP): MATCOVITCH-NATAN *ET AL.*; ZHANGZHUGANG/WIKICOMMONS

products not commonly found in nature. By systematic replacement of seven codons with synonymous alternatives for all protein-coding genes, Ostrov *et al.* recoded the *Escherichia coli* genome. The number of codons in the *E. coli* genetic code was reduced from 64 to 57 by removing instances of the UAG stop codon and excising two arginine codons, two leucine codons, and two serine codons. Over 90% functionality was successfully retained. In 10 cases, reconstructed bacteria were not viable, but these few failures offered interesting insights into genome-design challenges and what is needed for a viable genome. —LMZ

Science, this issue p. 819

BEHAVIORAL ECOLOGY

Born prepared to be hot

Embryonic birds are sensitive to external sounds while in the egg, and information can be transmitted from parent to offspring acoustically. Mariette *et al.* show that zebra finch parents call to their eggs when temperatures rise. These calls influence how chicks grow after hatching and their tolerance of and preferences for higher temperatures. Thus, parents are able to prepare their offspring for the warming environment in which they must grow and reproduce. Such mechanisms, if more widely distributed, may help some species adapt to our warming world. —SNV

Science, this issue p. 812

Zebra finch calls can help their unhatched chicks adapt to hotter temperatures.

PHOTOS (FROM LEFT): GOLDEN-COLT/ISTOCK.COM; SIPPL SIPA USA/ASSOCIATED PRESS

PHYSIOLOGY

Sleeping with lower blood pressure

Individuals with sleep apnea periodically stop breathing or breathe more shallowly while sleeping. The resulting intermittent decreases in blood oxygen concentrations (hypoxia) activate an organ called the carotid body, which sends out signals to increase breathing but also increases blood pressure and can lead to hypertension. Using a rodent model of sleep apnea, Yuan *et al.* found that the carotid bodies of the rodents produced reactive oxygen species that stimulate the generation of hydrogen sulfide, a gasotransmitter that in turn stimulates carotid body activity. Inhibiting the enzyme that generates hydrogen sulfide prevented the rodents from developing high blood pressure. —WW

Sci. Signal. **9**, ra80 (2016).

CANCER

Photobombing T_{regs} during cancer

Regulatory T cells (T_{regs}) are immunosuppressive cells that reduce inflammation. But reducing inflammation interferes with cancer defenses. Sato *et al.* have found a way to selectively deplete T_{regs} in tumors to promote antitumor effects while minimizing the risk of excess inflammation and autoimmunity. Such selectivity can be achieved by deploying a method called near-infrared photoimmunotherapy. In this technique, part of an antibody that recognizes T_{regs} is fused to a light-sensitive dye. Shining near-infrared light on the tumor activates the antibody and triggers killing of the T_{regs}. In mice, this treatment not only killed the targeted tumor but also destroyed untreated tumors of the same type that were located in other parts of the body, indicating its potential for the treatment of metastatic disease. —YN

Sci. Transl. Med. **8**, 352ra110 (2016).

IN OTHER JOURNALS

Edited by **Sacha Vignieri**
and **Jesse Smith**

Climate deterioration may exacerbate conflict in war-torn, arid regions.

HUMAN CONFLICT

Climate disasters in conflict-prone regions

Does climate change have the potential to enhance the risks of conflict in human societies? Stroessner *et al.* studied patterns of conflict outbreaks and climate-related disasters in ethnically divided countries between 1980 and 2010. Almost one-quarter of conflicts coincided closely with climatic extremes, particularly drought. Affected regions included North Africa, the Levant, Syria, and Afghanistan. Although the patterns are largely correlational and the local and regional circumstances varied, the study suggests that climate deterioration may exacerbate societal instability in the affected regions. —AMS

Proc. Natl. Acad. Sci. U.S.A. 10.1073/pnas.1601611113 (2016).

VACCINE DEVELOPMENT

Single serotype for Zika

Zika virus strains are of either African or Asian genetic lineage, and Asian strains are the cause of the outbreak in Central and South America. Dowd *et al.* report that natural antibodies produced by individuals infected with the presently circulating Asian strains can neutralize viruses from either lineage. This indicates a single Zika viral serotype and suggests that a single-strain vaccine could be broadly protective against diverse strains of Zika.

ALSO IN *SCIENCE* JOURNALS

Edited by **Caroline Ash**

IMMUNOGENOMICS

Microglia development follows a stepwise program

Microglia are cells that defend the central nervous system. However, because they migrate into the brain during development, the changes that they undergo, including those that affect gene expression, have been difficult to document. Matcovitch-Natan *et al.* transcriptionally profiled gene expression and analyzed epigenetic signatures of microglia at the single-cell level in the early postnatal life of mice. They identified three stages of microglia development, which are characterized by gene expression and linked with chromatin changes, occurring in sync with the developing brain. Furthermore, they showed that the proper development of microglia is affected by the microbiome. —LMZ

Science, this issue p. 789

ECONOMICS

Measuring consumption and wealth remotely

Nighttime lighting is a rough proxy for economic wealth, and nighttime maps of the world show that many developing countries are sparsely illuminated. Jean *et al.* combined nighttime maps with high-resolution daytime satellite images (see the Perspective by Blumenstock). With a bit of machine-learning wizardry, the combined images can be converted into accurate estimates of household consumption and assets, both of which are hard to measure in poorer countries. Furthermore, the night- and daytime data are publicly available and nonproprietary. —GJC

Science, this issue p. 790; see also p. 753

STATISTICAL PHYSICS

To thermalize, or not to thermalize?

Intuition tells us that an isolated physical system subjected to a sudden change (i.e., quenching) will evolve in a way that maximizes its entropy. If the system is in a pure, zero-entropy quantum state, it is expected to remain so even after quenching. How do we then reconcile statistical mechanics with quantum laws? To address this question, Kaufman *et al.* used their quantum microscope to study strings of six rubidium atoms confined in the wells of an optical lattice (see the Perspective by Polkovnikov and Sels). When tunneling along the strings was suddenly switched on, the strings as a whole remained in a pure state, but smaller subsets of two or three atoms conformed to a thermal distribution. The force driving the thermalization was quantum entanglement. —JS

Science, this issue p. 794; see also p. 752

GENE REGULATION

Patterns of developmental regulation within tissues

Expression of a given gene at the RNA level does not always correlate with expression at the protein level for many organisms. Walley *et al.* have built an integrated atlas of gene expression and regulatory networks in developing maize, using the same tissue samples to measure the transcriptome, proteome, and phosphoproteome. Coexpression networks from the transcriptome and proteome showed little overlap with each other, even though they showed enrichment of similar pathways. Integration of mRNA, protein, and phosphoprotein data sets improved the predictive power of the gene regulatory networks. —BJ

Science, this issue p. 814

ZIKA VIRUS

Characterizing the Zika virus antibody response

Given the public health emergency that Zika virus poses, scientists are seeking to understand the Zika-specific immune response. Stettler *et al*. analyzed 119 monoclonal antibodies isolated from four donors that were infected with Zika virus during the present epidemic, including two individuals that had previously been infected with dengue virus, another member of the flavivirus family. Neutralizing antibodies primarily recognized the envelope protein domain III (EDIII) or quaternary epitopes on the intact virus, and an EDIII-targeted antibody protected mice against lethal infection. Some EDI/II-targeting antibodies cross-reacted with dengue virus in vitro and could enhance disease in dengue-infected mice. Whether dengue and Zika virus antibodies cross-react in humans remains to be tested. —KLM

Science, this issue p. 823

PLANT SCIENCE

Transferring a bioactive

Artemisinin, which is critical in defense against malaria, was originally found in tiny hairs on the surface of leaves of the plant *Artemisia annua.* But this source plant does not support a sufficiently stable supply of artemisinin for worldwide use. Fuentes *et al.* have developed a synthetic biology approach termed COSTREL (combinatorial supertransformation of transplastomic recipient lines) that produces the immediate precursor of artemisinin, artemisinic acid, in widely cultivated tobacco (*Nicotiana tabacum* cv. Petit Havana). The first stage of COSTREL involves transformation of tobacco chloroplasts with genes encoding the core enzymes of the artemisinin biosynthetic pathway. With that pathway established, the second stage involves combinatorial nuclear transformation to superimpose genes that regulate flux through the biosynthetic pathway. A transformation mix supports selection of the most optimal gene combination. The resulting tobacco plants produce artemisinic acid at up to ~4.8 kg per acre. —PJH

eLife 10.7554/eLife.13664 (2016).

Once only found in small hairs on sweet wormwood plants, artemisinin can now be produced by tobacco plants.

Antibodies elicited by Zika virus target the envelope protein of the virion, for which the two genetic lineages share >95% amino acid identity. —LDC

Cell Rep. 10.1016/j.celrep.2016.07.049 (2016).

MATERIALS SCIENCE

Tunable materials switching with light

Composite materials incorporate weak, stretchy, energy-absorbing materials between sheets of strong, brittle ones. Adaptive materials can locally repair or tune themselves in response to an external stimulus such as light. Zhu *et al.* combined these ideas into a nacre-mimetic nanocomposite built from a nanoclay, a polymer, and a small amount of reduced graphene oxide (rGO). The polymer includes thermally reversible hydrogen-bonding motifs, whose interlinking determines whether the nanocomposite is very stiff and strong or stiff and ductile. On irradiation with near-infrared light, the rGO controllable heats the polymer, making it possible to switch a single material between these states. —MSL

Nano Lett. 10.1021/acs.nanolett.6b02127 (2016).

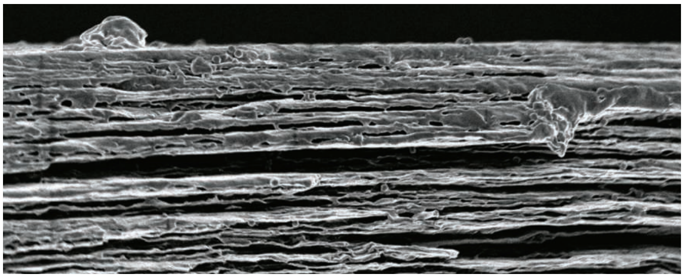

Scanning electron micrograph of a cross section of a nacre-mimetic nanocomposite

RNA EDITING

Selection may influence transcriptional variation

Posttranscriptional modifications, including changing an adenosine (A) to an inosine (I), may affect the translation of RNA transcripts into proteins. Yu *et al.* examined the extent and conservation or divergence of A-to-I editing across the genomes of seven *Drosophila* species. Editing occurred most commonly as nonconserved events observed only in a single gene from a gene family within a species. Positive selection was identified in cases where multiple genes within a gene family were edited across species; these also showed enrichment for function in the neural system. This suggests that editing may be selected for developmental variation. —LMZ

PLOS Genet. 10.1371/journal.pgen.1006191 (2016).

ORGANIC CHEMISTRY

A light approach to diverse amino acids

As the building blocks of all proteins, amino acids have long been a target of modification for chemists. Installing unnatural side chains can facilitate medicinal research, as well as fundamental studies of protein function and dynamics. Jiang *et al*. present a versatile method for replacing the natural side chains of aspartic and glutamic acid with a variety of ketones, esters, amides, and alkynes while preserving the original stereochemistry. A ruthenium catalyst excited by visible light spurs ejection of a phthalimide-activated acid group from the original side chain, leaving a reactive radical to bind the new substituent. —JSY

Sci. Rep. 10.1038/srep26161 (2016).

DIVERSITY

The physics of a gender gap

Women are underrepresented at all levels of physics, even though the number of girls taking physics classes in U.S. high schools is increasing. Lock and Hazari examined the relationship between gender narratives and who students believe can be a physicist. They analyzed documentation of the classes of one high school teacher who engaged students in discussions on the underrepresentation of women in physics, along with student and teacher interviews and relevant student work, for possible mechanisms connecting these discussions to an increase in physics identity for female students. They found that the discussions created an opportunity for students' views of professional and school science to change, which may subsequently enable a shift in physics identity development among female students. —MM

Phys. Rev. Phys. Educ. Res. 10.1103/PhysRevPhysEducRes.12.020101 (2016)

PHOTO (FROM TOP): MANFRED RUCKSZIO / ALAMY STOCK PHOTO

RESEARCH ARTICLE SUMMARY

IMMUNOGENOMICS

Microglia development follows a stepwise program to regulate brain homeostasis

Orit Matcovitch-Natan,* Deborah R. Winter,* Amir Giladi, Stephanie Vargas Aguilar, Amit Spinrad, Sandrine Sarrazin, Hila Ben-Yehuda, Eyal David, Fabiola Zelada González, Pierre Perrin, Hadas Keren-Shaul, Meital Gury, David Lara-Astaiso, Christoph A. Thaiss, Merav Cohen, Keren Bahar Halpern, Kuti Baruch, Aleksandra Deczkowska, Erika Lorenzo-Vivas, Shalev Itzkovitz, Eran Elinav, Michael H. Sieweke,†‡ Michal Schwartz,†‡ Ido Amit†‡

INTRODUCTION: Microglia, as the resident myeloid cells of the central nervous system, play an important role in life-long brain maintenance and in pathology. Microglia are derived from erythromyeloid progenitors that migrate to the brain starting at embryonic day 8.5 and continuing until the blood-brain barrier is formed; after this, self-renewal is the only source of new microglia in the healthy brain. As the brain develops, microglia must perform different functions to accommodate temporally changing needs: first, actively engaging in synapse pruning and neurogenesis, and later, maintaining homeostasis. Although the interactions of microglia with the brain environment at steady state and in response to immune challenges have been well studied, their dynamics during development have not been fully elucidated.

RATIONALE: We systematically studied the transcriptional and epigenomic regulation of microglia throughout brain development to decipher the dynamics of the chromatin state and gene networks governing the transformation from yolk sac progenitor to adult microglia. We used environmental and genetic perturbation models to investigate how timed disruptions to microglia impact their natural development.

RESULTS: Global profiles of transcriptional states indicated that microglia development proceeds through three distinct temporal stages, which we define as early microglia (until embryonic day 14), pre-microglia (from embryonic day 14 to a few weeks after birth), and adult microglia (from a few weeks after birth onward). ATAC-seq (assay for transposase-accessible chromatin followed by sequencing) for chromatin accessibility and ChIP-seq (chromatin immunoprecipitation followed by sequencing) for histone modifications further characterized the differential regulatory elements in each developmental phase. Single-cell transcriptome analysis revealed minor mixing of the gene expression programs across phases, suggesting that individual cells shift their regulatory networks during development in a coordinated manner. Specific markers and regulatory factors distinguish each phase: For example, we identified MAFB as an important transcription factor of the adult microglia program. Microglia-specific knockout of *MafB* led to disruption of homeostasis in adulthood and increased expression of interferon and inflammation pathways. We found that microglia from germ-free mice exhibited dysregulation of dozens of genes associated with the adult phase and immune response. In addition, maternal immune activation, which has been linked to behavioral disorders in adult offspring, had the greatest impact on pre-microglia, resulting in a transcriptional shift toward the more advanced developmental stage.

CONCLUSION: Our work identifies a stepwise developmental program of microglia in synchrony with the developing brain. Each stage of microglia development has evolved distinct pathways for processing the relevant signals from the environment to balance their time-dependent role in neurogenesis with regulation of immune responses that may cause collateral damage. Genetic or environmental perturbations of these pathways can disrupt stage-specific functions of microglia and lead to loss of brain homeostasis, which may be associated with neurodevelopmental disorders. ■

ON OUR WEBSITE

Read the full article at http://dx.doi.org/10.1126/science.aad8670

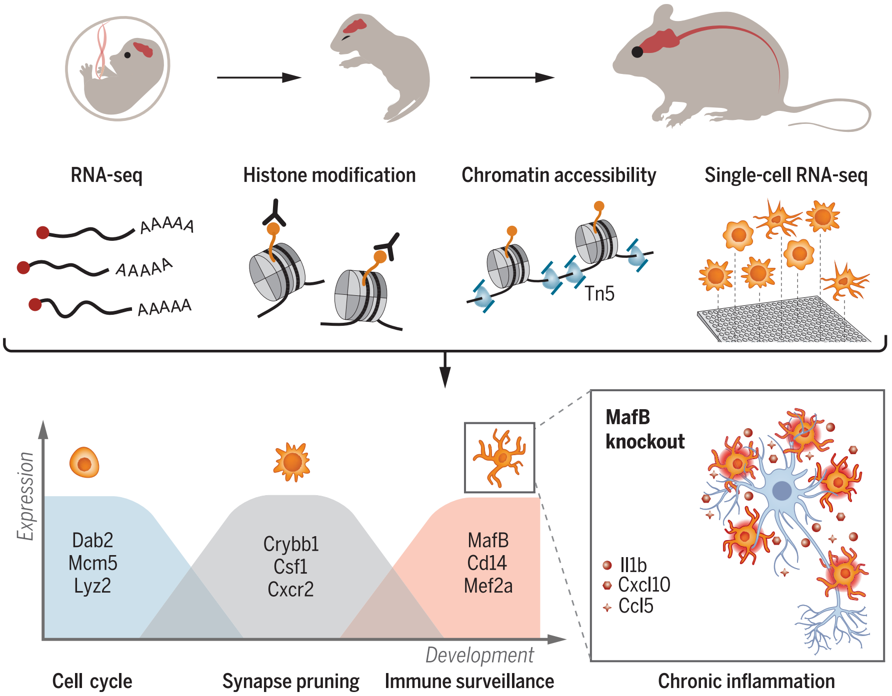

Microglia development proceeds in a stepwise manner. Microglia were isolated from mice throughout development from embryo to adult. Data from population-level RNA-seq, ChIP-seq, and ATAC-seq, as well as single-cell RNA-seq, show that microglia development proceeds through three distinct stages—early, pre-, and adult—with characteristic gene expression and functional states. Perturbations of this developmental process, such as from *MafB* knockout, lead to disrupted brain homeostasis by the dysregulation of adult and inflammatory genes. Tn5, transposase 5.

The list of author affiliations is available in the full article online.

*These authors contributed equally to this work.

†These authors contributed equally to this work.

‡Corresponding author. Email: sieweke@ciml.univ-mrs.fr (M.H.S.); michal.schwartz@weizmann.ac.il (M.S.); ido.amit@weizmann.ac.il. (I.A.)

Cite this article as O. Matcovitch-Natan *et al.*, *Science* **353**, aad8670 (2016). DOI: 10.1126/science.aad8670

RESEARCH ARTICLE

IMMUNOGENOMICS

Microglia development follows a stepwise program to regulate brain homeostasis

Orit Matcovitch-Natan,[1,2]* Deborah R. Winter,[1]* Amir Giladi,[1] Stephanie Vargas Aguilar,[3,4,5,6] Amit Spinrad,[1,2] Sandrine Sarrazin,[3,4,5] Hila Ben-Yehuda,[2] Eyal David,[1] Fabiola Zelada González,[3,4,5] Pierre Perrin,[3,4,5] Hadas Keren-Shaul,[1] Meital Gury,[1] David Lara-Astaiso,[1] Christoph A. Thaiss,[1] Merav Cohen,[2] Keren Bahar Halpern,[7] Kuti Baruch,[2] Aleksandra Deczkowska,[2] Erika Lorenzo-Vivas,[1] Shalev Itzkovitz,[7] Eran Elinav,[1] Michael H. Sieweke,[3,4,5,6]†‡ Michal Schwartz,[2]†‡ Ido Amit[1]†‡

Microglia, the resident myeloid cells of the central nervous system, play important roles in life-long brain maintenance and in pathology. Despite their importance, their regulatory dynamics during brain development have not been fully elucidated. Using genome-wide chromatin and expression profiling coupled with single-cell transcriptomic analysis throughout development, we found that microglia undergo three temporal stages of development in synchrony with the brain—early, pre-, and adult microglia—which are under distinct regulatory circuits. Knockout of the gene encoding the adult microglia transcription factor MAFB and environmental perturbations, such as those affecting the microbiome or prenatal immune activation, led to disruption of developmental genes and immune response pathways. Together, our work identifies a stepwise microglia developmental program integrating immune response pathways that may be associated with several neurodevelopmental disorders.

Microglia are the resident myeloid cells of the central nervous system (CNS) that control the patterning and wiring of the brain in early development and contribute to homeostasis throughout life (*1*–*3*). In the embryo, starting at day 8.5 postconception (E8.5), erythromyeloid progenitors (EMPs) develop in the yolk sac; these cells are $CD45^+$ $cKit^+$ and have the capacity to colonize the fetal liver and differentiate into erythrocytes and various myeloid cells, including tissue-resident macrophages (*4*). A subset of EMPs matures into CX_3CR1^+ cells in the yolk sac and becomes microglia progenitors (*5*, *6*). These progenitors migrate to the brain starting around days E9.5 to E10.5 and may continue to do so until the formation of the blood-brain barrier at day E13.5 to E14.5 (*4*, *7*). The microglia population proliferates locally within the brain and distributes spatially in the CNS (*8*, *9*). This original pool of cells is the only source of myeloid cells in the healthy brain (*10*, *11*). Other myeloid cells, such as bone marrow–derived monocytes, only infiltrate the brain under pathological circumstances (*6*, *12*–*14*).

Myeloid cells, particularly macrophages, are endowed with a higher plasticity than was previously appreciated. They engage in a bidirectional dialogue with their microenvironment, which both shapes their fate and is influenced by their activity (*15*–*18*). In the brain, exposure to TGFB1, which acts through the Smad and Irf7 pathways, has been shown to shape the chromatin landscape and influence the response and phenotype of microglia (*19*, *20*). In combination with environmental signals, general lineage-specific factors such as Pu.1 and Irf8 define the microglial regulatory network and distinguish it from other tissue-resident macrophages (*7*, *15*, *16*). The evolution of the microglial regulatory network may also be shaped by multiple tissue-specific signals, including protein aggregates, stress signals, and nutrients, as well as the communities of commensal microorganisms colonizing the skin, respiratory, gastrointestinal, and urogenital tract that are collectively termed the microbiota (*21*, *22*). The collection of physiological and pathological cues sensed by microglia, originating from within the brain or externally (*21*), may fluctuate spatially across the different brain regions and temporally with development of the brain. Thus, microglial programming must be complex enough to process dynamic environmental signals and execute the temporal functions necessary to accommodate the brain's needs throughout development and adulthood.

It is still unknown how one cell type can have the necessary functional diversity to meet the needs of both the developing brain and life-long maintenance. We hypothesized that microglia acquire specialized functions tailored to changes in the developing brain by a combination of gene regulation and response to environmental signals. Although microglia share many circuits with monocytes, they must maintain tight control of inflammatory and antiviral pathways to prevent neuronal damage, particularly under the various stress conditions that may influence the fetus during pregnancy (*23*). Thus far, the expression programs and regulatory networks have only been documented for early yolk sac progenitors and adult microglia (*2*, *7*, *15*, *16*, *19*, *24*). Microglia modulate synaptic transmission, formation, and elimination and shape embryonic and postnatal brain circuits (*25*–*31*). However, many of these processes, such as synaptic pruning and neuronal maturation, peak in mice during the first week after birth—a period that has not previously been profiled in microglia (*27*–*31*)—and may be important to understanding the circuits and etiology of many neurodevelopmental diseases.

Perturbation of the microglial environment during development may alter the strict timing of developmental programs, leading to misplaced expression of gene pathways such as inflammation, disrupting neuronal development, and causing brain disorders at later stages in life (*30*). For example, prenatal exposure to viral infection has been correlated with an increased risk of schizophrenia and autism in mouse and human offspring (*32*, *33*). The precise effects of perturbations on development are highly dependent on the timing of infection, suggesting interference with specific processes (*34*, *35*).

Results

Temporal expression profiles during microglia development

To study the dynamics of the gene programs involved in microglia development, we performed RNA sequencing (RNA-seq) to measure the global gene expression of myeloid progenitors from the yolk sac (*5*) and microglia from embryonic, postnatal, and adult brains (*36*) for a total of nine time points throughout microglia development (Fig. 1A and fig. S1). Biological replicates were highly correlated ($r > 0.98$, Pearson's correlation), and few transcriptional changes were noted across adjacent time points (fig. S2A). Unexpectedly, we found a large number of genes that were differentially expressed across developmental time points (Fig. 1B). Early microglia were associated with genes involved in cell cycling and differentiation, such as *Mcm5* and *Dab2* (*37*). In contrast, *Csf1*, *Cxcr2*, and other genes involved in neuronal development peaked in expression a

---

[1]Department of Immunology, Weizmann Institute of Science, Rehovot, Israel. [2]Department of Neurobiology, Weizmann Institute of Science, Rehovot, Israel. [3]Centre d'Immunologie de Marseille-Luminy (CIML), Université Aix-Marseille, UM2, Campus de Luminy, Marseille, France. [4]Institut National de la Santé et de la Recherche Médicale (INSERM), U1104, Marseille, France. [5]Centre National de la Recherche Scientifique (CNRS), UMR7280, Marseille, France. [6]Max-Delbrück-Centrum für Molekulare Medizin in der Helmholtz-Gemeinschaft (MDC), Robert-Rössle-Straß 10, 13125 Berlin, Germany. [7]Department of Cell Biology, Weizmann Institute of Science, Rehovot, Israel.
*These authors contributed equally to this work. †These authors contributed equally to this work. **‡Corresponding author. Email: sieweke@ciml.univ-mrs.fr (M.H.S.); michal.schwartz@weizmann.ac.il (M.S.); ido.amit@weizmann.ac.il (I.A.)**

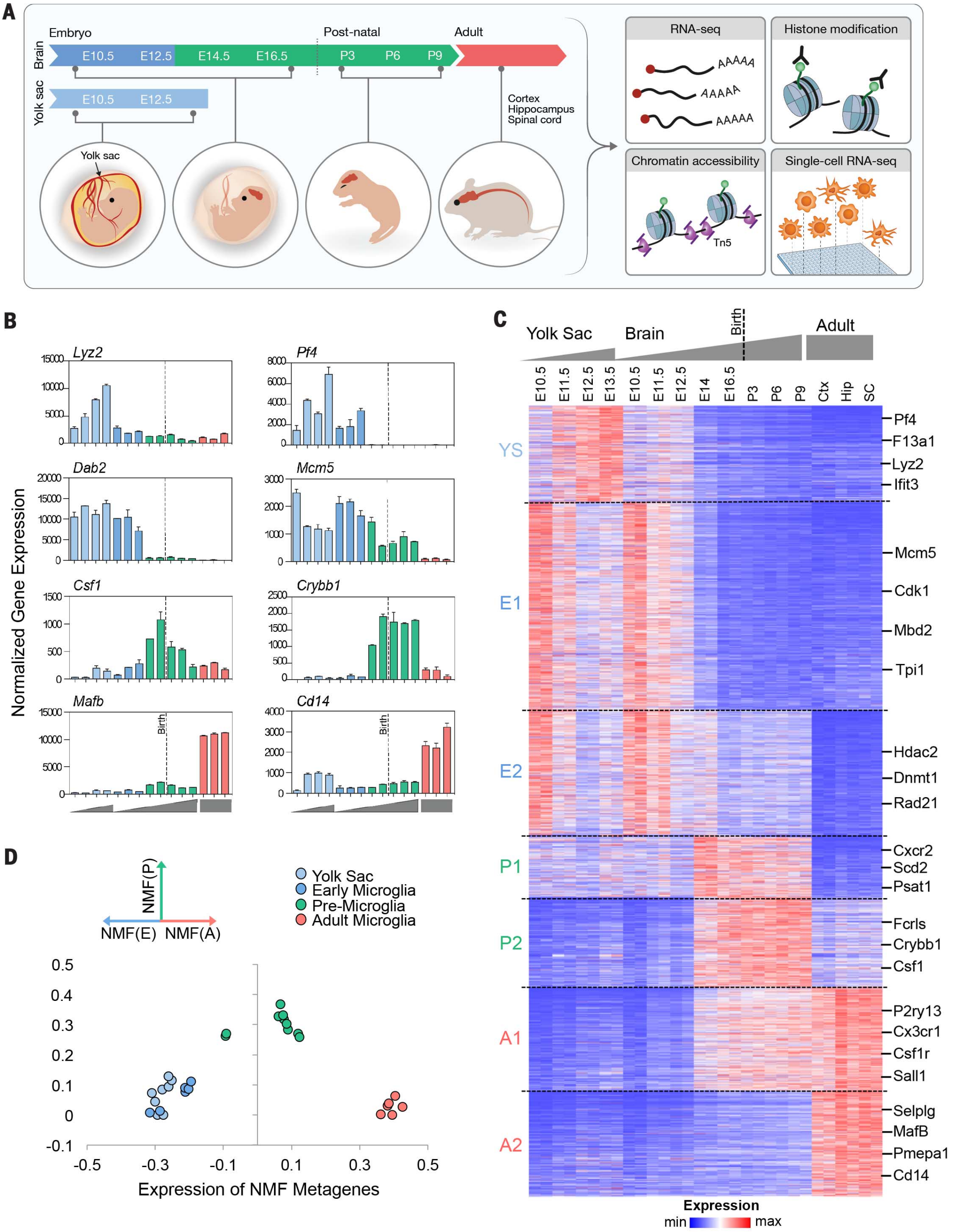

Fig. 1. Global gene expression patterns reveal distinct microglia developmental phases. (**A**) Schematic showing the multidimensional data collected throughout microglia development (Tn5, transposase 5). (**B**) Bar graphs of expression of a representative set of gene markers across the course of microglia development, as determined by RNA-seq. Error bars indicate SEM. Units on the *y* axes are arbitrary. Gray polygons below the *x* axes correspond to the stages shown at the top of (C). (**C**) *K* means clustering ($k = 7$) (38) of 3059 genes with differential expression across the course of microglia development (Ctx, cortex; Hip, hippocampus; SC, spinal cord). Clusters are indicated on the left. (**D**) NMF analysis of gene expression revealed three metagenes representing distinct transcriptional programs. Samples are color-coded by tissue and program (light blue, yolk sac; blue, early microglia; green, pre-microglia; red, adult microglia). The *y* axis shows the NMF values for the "pre" metagene (P); the *x* axis shows the maximum NMF values between the "adult" metagene (A, positive) or the "early" metagene (E, negative).

few days before birth and decreased by adulthood. Canonical adult microglia genes, including *Cd14* and *Pmepa1*, were primarily expressed only in adult microglia.

Microglia development demonstrates discrete transcriptional phases

To identify global patterns of gene expression, we performed k-means clustering ($k = 7$) that divided the data into four main categories on the basis of the developmental location and timing of gene expression (Fig. 1C; fig. S2, B and C; and table S1). We focused on 3059 of the most highly and differentially expressed genes throughout development (38). We defined these stages as early microglia (1289 genes, clusters E1 and E2, day E10.5 to E14), pre-microglia [589 genes, clusters P1 and P2, day E14 to postnatal day 9 (P9)], and adult microglia (808 genes, clusters A1 and A2, 4 weeks and onward). Adult microglia exhibited only a small number of differentially expressed genes (76 genes; table S2) (38) across different CNS regions including the cortex, hippocampus, and spinal cord. In addition, a group of genes was most highly expressed in the yolk sac (373 genes, cluster YS). Comparison of gene ontologies (GOs) indicated that yolk sac–specific genes were associated with defense response and multiple hematopoietic fates [e.g., *Lyz2* (39) and *Pf4* (40)], whereas shared clusters between the yolk sac and early brain were enriched for genes associated with proliferation and cell cycle (fig. S2B). The yolk sac and early brain microglia showed high correlation at the transcriptional level over time, despite differences in microenvironment (fig. S2A). This observation suggests either that microglia newly arrived to the brain are not immediately adapting upon encountering the neural environment, or alternatively that the first stage of microglia development commences in the yolk sac.

We observed that the pre-microglia stage reflects a distinct phenotype of characteristic genes. Because previous studies have focused on cells from more mature developmental stages, many of these genes have not been annotated with microglia function. However, we found that a subset of the genes that were expressed at this stage was related to the GO categories of neural migration, neurogenesis, and cytokine secretion (fig. S2B). Based on the timing of the pre-microglia program, this phase probably represents when microglia adopt a role in synaptic pruning and neural maturation; later, when the brain matures, they enter a surveillance and homeostatic phase, where they acquire functions associated with tissue maintenance and signaling (41) and express canonical microglia genes (fig. S2B).

To confirm and strengthen the reproducibility of these microglia transcriptional stages, we applied dimension reduction analyses to the RNA-seq data, including nonnegative matrix factorization (NMF) (38, 42) and principal component analysis (PCA). NMF, which deconstructs the data into a given number of metagenes, robustly uncovered three discrete expression programs coinciding with the three microglia stages (Fig. 1D and fig. S2, D to F). Similar results were obtained with PCA (fig. S1G). This partitioning suggests that the temporal expression profile of microglia development in the brain consists primarily of two major transition events: (i) early microglia to pre-microglia around day E13.5 to E14.5 and (ii) pre-microglia to adult microglia a few weeks after birth.

Microglia developmental phases are linked with changes in the chromatin landscape

The changing chromatin landscape across developmental time points can provide information about the regulatory mechanisms underlying gene expression profiles. Accessible or "open" chromatin regions contain regulatory elements that influence transcription in a cell type–specific or condition-specific manner (43–45). Thus, for each transcriptional stage (yolk sac, early microglia, pre-microglia, and adult microglia), we performed an assay for transposase accessible chromatin followed by sequencing [ATAC-seq (46)] and used a recently developed, highly sensitive method called iChIP (47) for chromatin immunoprecipitation followed by sequencing (ChIP-seq). Unlike what we observed in the RNA-seq data, the chromatin landscape of early microglia was more closely related to that of pre-microglia than to that of the yolk sac stage (fig. S3A), suggesting that chromatin changes precede changes in RNA (47). ATAC-seq identifies accessible regions within promoters ($H3K4me3^+$ regions near the transcription start site of genes), enhancers [distal regions associated with higher H3K4me1 and -2 (48, 49)], and other regulatory elements, such as CTCF binding sites (46). As observed previously (16), the accessibility of promoter regions was largely conserved over time (fig. S2B). Thus, we focused on candidate enhancers marked by distal ATAC-seq regions with high levels of H3K4me2, as assayed by iChIP (47). These enhancer regions could be divided into four major categories, similar to the gene expression profiles (Fig. 2, A and B; fig. S3, C and D; and table S3). The first category was composed of enhancers marked only in the yolk sac (e.g., F13a1) and may reflect regions that are active in cells not migrating to the brain. A second category comprised enhancers accessible in both the early and pre-microglia, but not in adult microglia. The final two categories consisted of enhancers that are most prominent in adult microglia and are distinguished by whether they are open (e.g., Sall1 and MafB) or closed (e.g., Irf8) earlier in development. Notably, no category was found solely in pre-microglia. This suggests that that the pre-microglia phase does not undergo unique chromatin remodeling, but rather exhibits differential usage of the epigenomic landscape established early in microglia development.

To confirm that the observed chromatin changes were related to transitions in microglia development, we assessed whether different enhancer dynamics were associated with the global expression patterns (Figs. 1C and 2B). We linked enhancers to genes by their proximity to the transcription start site (Fig. 2C and table S4) (38). Genomic regions close to genes expressed in the early stage tended to be in the first two enhancer categories (clusters YS, E1, and E2; Fig. 1C). Similarly, the latter two categories were enriched for genes from the adult microglia transcriptional profile (clusters A1 and A2; Fig. 1C). The dynamics of the microglia enhancer repertoire confirm that the microglia gene expression across developmental stages reflects shifts in the underlying chromatin landscape. However, it is important to note that with bulk data, such as from the RNA expression and chromatin profiling described above, it is unclear whether the transcriptional signal represents the average profile of a heterogeneous mixture of cells from different phases or homogenous populations where each cell exhibits the relevant temporal profile.

Single-cell transcriptome analysis reveals coordinated shifts between phases

To assess the heterogeneity at each temporal phase in microglia development, we performed massively parallel single-cell RNA-seq [MARS-seq (50)] on a representative time point from each phase. Then we combined the data for cells from all phases and clustered them on the basis of their gene expression profiles (51). To correct for batch effects, each sample was normalized separately before clustering across time points (38). Clustering analysis of 2831 single-cell profiles (696 from the yolk sac stage, 734 from the early microglia stage, 705 from the pre-microglia stage, and 696 from the adult microglia stage) created a detailed map of 2071 differentially expressed genes across 16 transcriptionally homogeneous subpopulations (Fig. 3, A and B). The expression of key marker genes (Fig. 3B and fig. S4A) was combined with global correlation analysis (fig. S4B) to examine the intercluster relationships of transcriptional subpopulations. We determined that each cluster originated almost entirely from a specific stage, confirming that the temporal dynamics of microglia development are the most dominant discriminative feature, even at the single-cell level (Fig. 3C). The exceptions were two subpopulations to which both the yolk sac and early brain time points contributed (VII and VIII; fig. S4C). It is possible that these subpopulations were composed of cells that were on the verge of or had just completed migration to the brain. Moreover, there was additional variation in the yolk sac–specific subpopulation VI and, to a lesser degree, subpopulations II, III, and IV (Fig. 3, A and B, and fig. S4A), which displayed high expression of monocytic genes. When the single-cell subpopulations were compared with the bulk RNA-seq time points (Fig. 1), we found that several of the yolk sac subpopulations (IV to VIII) were best matched to early microglia expression (fig. S4D). This suggests that the yolk sac population is heterogeneous and may include cells with other hematopoietic fates as well as cells with varying levels of commitment to the microglia fate. Once in the brain, their further development occurs in a discrete stepwise fashion that is temporally regulated by environmental cues.

In general, the temporal gene markers that we identified from the bulk RNA-seq analysis exhibited equivalent expression in the single-cell data (Fig. 3B and fig. S4A). To confirm the stage-specific expression of marker genes (Fig. 3, D to F, upper left panels) in the intact brain, we imaged individual mRNA molecules using single-molecule fluorescent in situ hybridization (smFISH) in frozen brain sections from the early, pre-, and adult stages (Fig. 3, D to F, and fig. S5A) (52–54). We found that *Mcm5*, *Csf1*, and *MafB* were enriched in CX_3CR1^+ microglia cells from the early-, pre-, and adult-stage brain, respectively. Immunohistochemistry confirmed that DAB2, a protein that has not been previously associated with microglia, was specifically expressed in early microglia (E12.5), but not at later time points (fig. S5, B and C). Further, *Csf1R* and *Selplg* were expressed in adult microglia, which is consistent with the Allen Brain Atlas (55) (fig. S5D). Taken together, these results indicate that coordinated transcriptional events control the transitions through microglia development and are probably due to changes in the microenvironment of the CNS.

Distinct transcription factors regulate microglia developmental phases

Transcription factors play important roles in regulating the chromatin state and gene expression

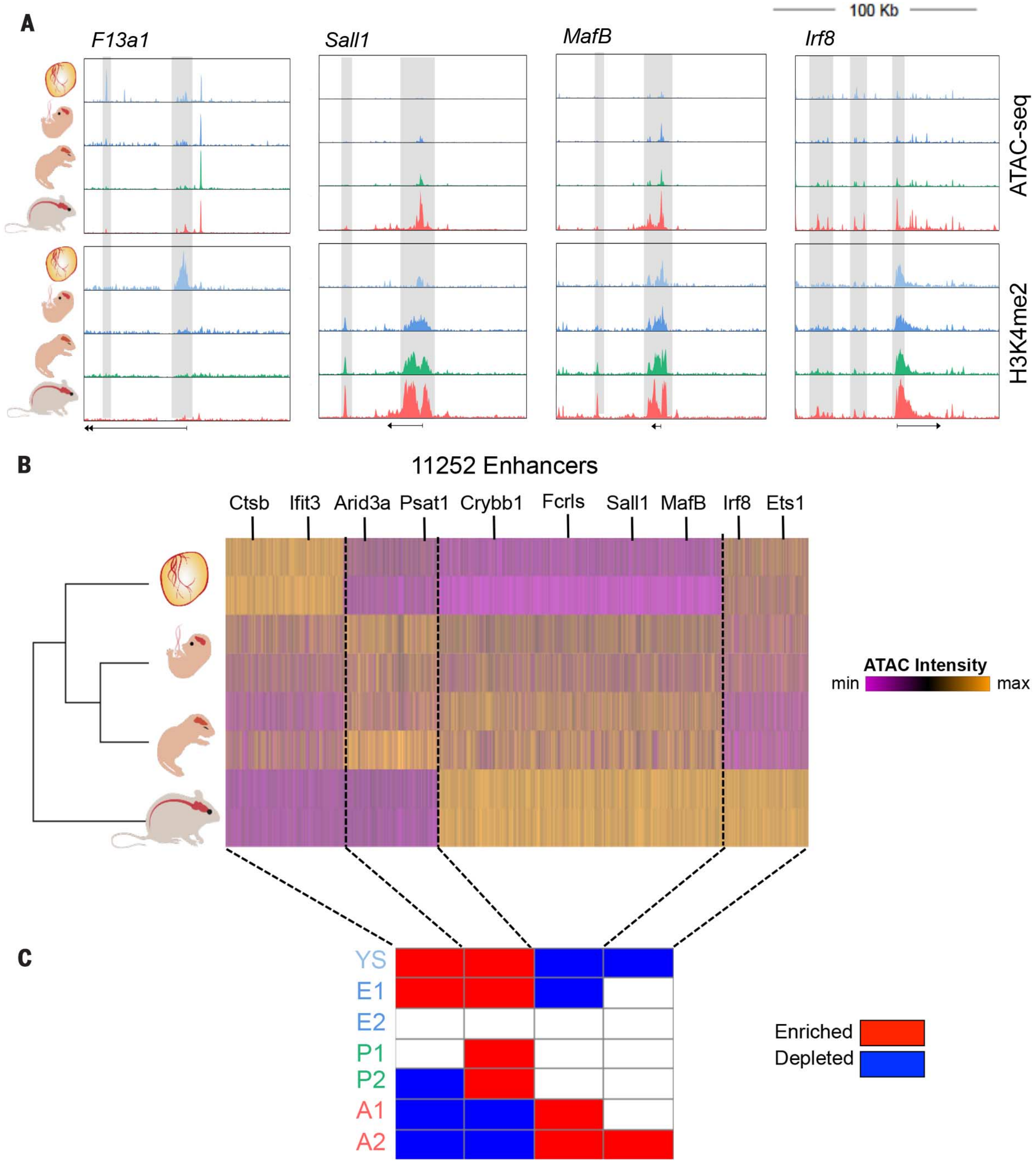

YS	🟥	🟥	🟦	🟦
E1	🟥	🟥	🟦	
E2				
P1		🟥		
P2	🟦	🟥		
A1	🟦	🟦	🟥	
A2	🟦	🟦	🟥	🟥

Enriched 🟥
Depleted 🟦

Fig. 2. Chromatin dynamics reflect distinct phases of microglia development. (**A**) Normalized profiles of H3K4me2 and ATAC-seq signals in 100–kilobase (kb) regions from yolk sac progenitors (E12.5; light blue), early microglia (E12.5; blue), pre-microglia (P1; green), and adult microglia (8 weeks; red). Arrows beneath each panel indicate gene location. Gray shading highlights differential chromatin regions. (**B**) *K* means clustering ($k = 4$) of ATAC-seq intensity in distal H3 K4me2 regions reveals four main categories of candidate enhancers. (**C**) Overlap between enhancer dynamics and gene expression clusters from Fig. 1C (boxes marked as enriched or depleted: $P < 0.05$, hypergeometric distribution).

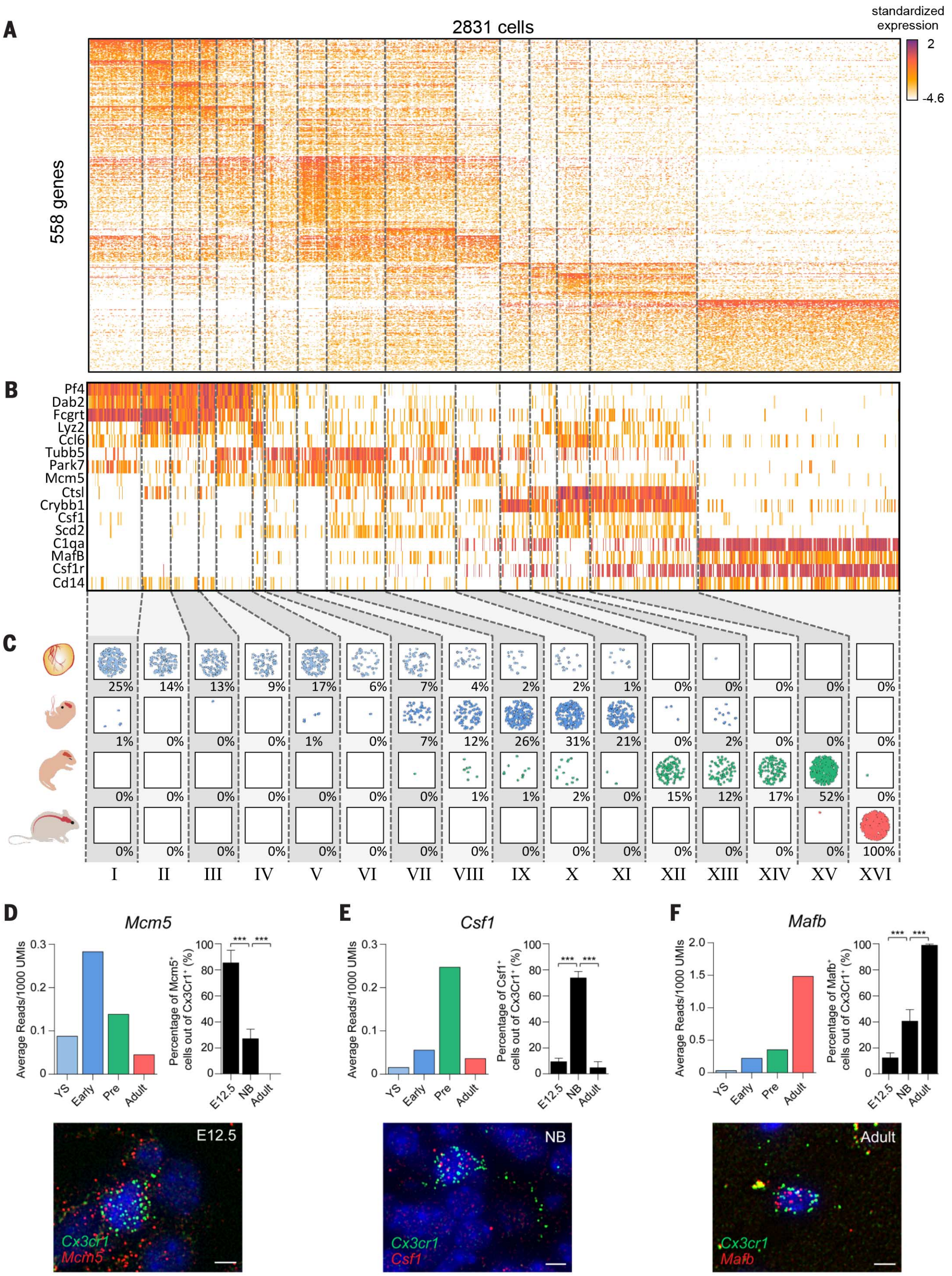

Fig. 3. Single-cell RNA-seq shows distinct phases of development. (**A**) Heatmap showing the 558 most variable genes, organized into clusters (k = 16) based on 2071 total differential genes (Materials and methods) in 2831 individual cells isolated from among yolk sac progenitors (E12.5), early microglia (E12.5), pre-microglia (E18.5), and adult microglia (8 weeks). (**B**) Representative set of marker genes differentially expressed between the different developmental stages. (**C**) Illustration of the number of sorted cells from each stage (top to bottom: yolk sac, early, pre-, and adult) that were assigned to a given subpopulation defined by the clustering in (A). The percent of cells out of the total in the stage is given below each box. (**D**) smFISH of mRNA molecules for *Mcm5*, a marker for early microglia, in intact brain tissue. The top left panel shows the average expression of *Mcm5* across single cells from subpopulations associated with each developmental stage. The top right panel shows the percent of CX$_3$CR1–GFP (green fluorescent protein–tagged) cells that overlap *Mcm5* RNA molecules (red). The bottom panel is a representative image of smFISH in an early brain section. (**E**) Same as (D), but for *Csf1*, a marker for pre-microglia (NB, newborn). (**F**) Same as (D), but for *MafB*, a marker for adult microglia. Scale bars, 5 μm. ***$P < 0.001$.

of a cell (56, 57). To investigate regulatory factors defining the temporal stages of microglia development, we focused on the expression of genes known to have a DNA binding or chromatin remodeling function and found candidate regulators for each stage (Fig. 4, A and B; fig. S6A; and table S5). In particular, cell cycle factors and chromatin remodelers were highly expressed in the early microglia stage. Canonical microglia transcription factors, such as EGR1 and SALL1, began to be expressed in the pre-microglia stage and were further induced in adulthood. In contrast, we observed several regulators, including JUN, FOS, MEF2A, and MAFB, that were specific to the adult stage and are therefore likely to be involved in establishing microglia homeostatic functions or in terminating developmental functions of pre-microglia (Fig. 4B and fig. S6A).

Motif analysis of the promoters associated with genes from the expression clusters (Fig. 1C) highlighted the differential occurrence of motifs for multiple transcription factors across microglia development (Fig. 4C, fig. S6B, and table S6), which coincided with the clusters exhibiting the highest expression of the genes encoding these factors. For example, the MEF2A motif was found to be enriched only in the regulatory regions of adult microglia genes. Previous work focusing on the mechanisms of tissue-resident macrophage specification has also suggested that the MEF2 family is important in microglia identity and may play a role in shaping the epigenomic landscape (16). Thus, changes in microglia function throughout development are probably linked to synchronized changes in the underlying regulatory networks.

MAFB regulates adult microglia homeostasis

We further focused on the functional role of MAFB, one of the principal transcription factors that was highly elevated at the shift from pre- to adult microglia (Figs. 1B, 3B, and 3F). Using immunohistochemistry, we confirmed that MAFB was induced in the transition from pre- to adult microglia (Fig. 5A and fig. S7, A and B). MAFB has previously been shown to be critical for terminal differentiation of monocytes and tissue-resident macrophages and for restricting their self-renewal capacity (58–60). In addition, the MAF motif has been found to be enriched in macrophage-specific enhancer regions, suggesting that it has the capacity to alter the chromatin landscape in a lineage-specific manner (16). However, the role of MAFB in microglia development and homeostasis has not yet been established.

To address the functional role of MAFB in microglia development, we generated *MafB*$^{flox/flox}$ *Csf1R*$^{Cre/+}$ transgenic mice that exhibited loss of *MafB* expression in the macrophage lineage (Fig. 5B and fig. S7, C to E), including microglia, but not in other cells in the CNS. We collected microglia from newborn (pre-microglia) and adult mice and compared their transcriptional profiles with those of control mice (*MafB*$^{flox/flox}$*Csf1R*$^{+/+}$) of the same age. Successful knockout was confirmed by analyzing *MafB* expression levels (Fig. 5C). Consistent with the strong up-regulation of *MafB* in adult microglia, we observed a greater number of expression changes at the adult stage than at the

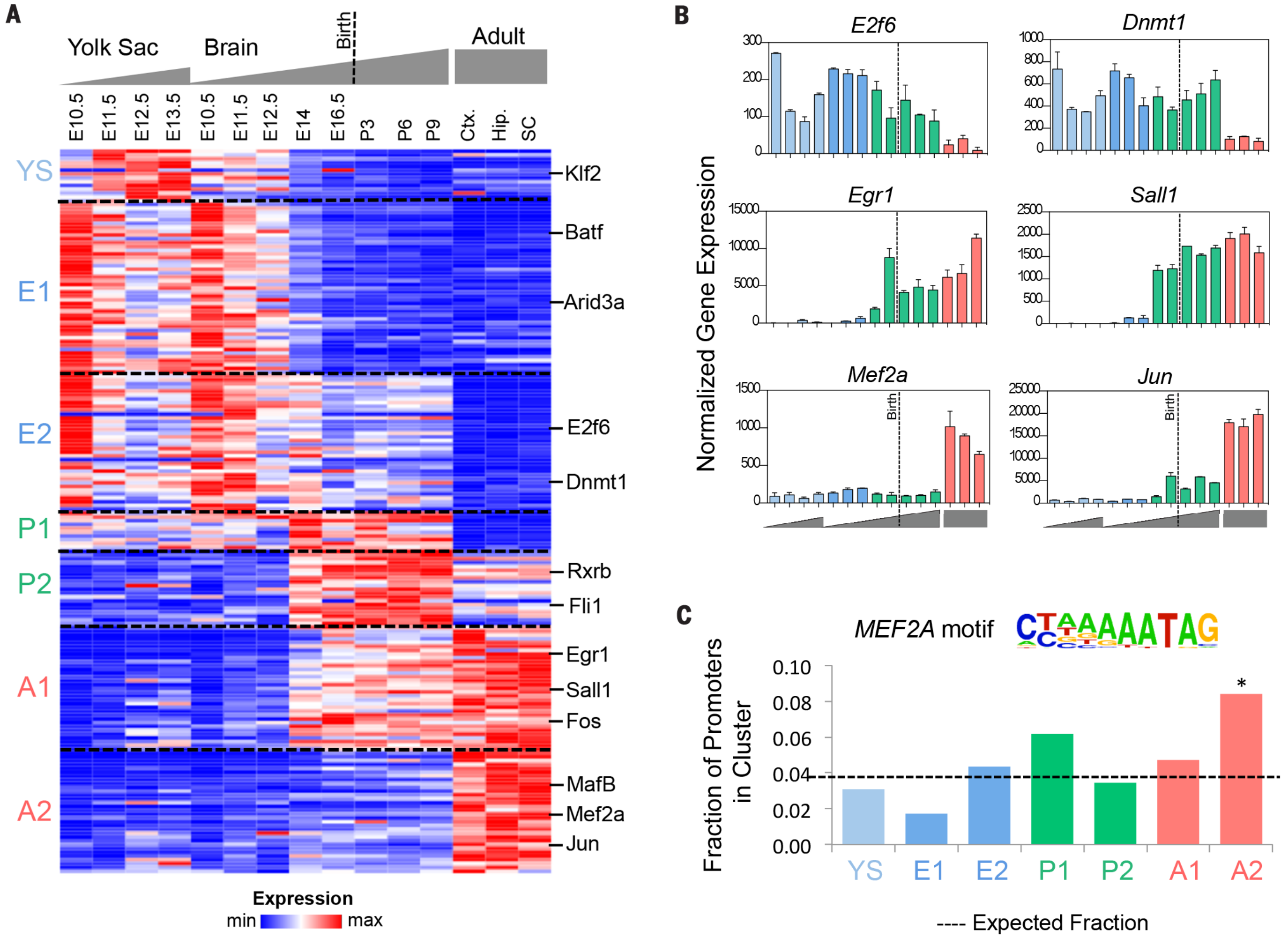

Fig. 4. Regulatory factors involved in each phase of microglia development. (**A**) Heatmap of gene expression of 190 transcription factors and chromatin modifiers from the clusters in Fig. 1C. (**B**) Bar graphs of expression of representative regulators across microglia development. Error bars indicate SEM. (**C**) Fraction of promoters associated with genes in each expression cluster (Fig. 1C) containing the sequence motif for MEF2A (logo shown). The dashed line indicates the expected distribution of promoters. *$P < 0.05$, hypergeometric distribution, for the significance of enrichment.

pre-microglia stage (Fig. 5, C to E; fig. S7F; and tables S7 and S10). Moreover, all categories of genes regulated by MAFB were significantly enriched for genes expressed in the late adult stage of microglia development, such as *Ctsh* and *Pmepa1* (cluster A2; $P < 0.05$, hypergeometric distribution; Fig. 5, C and D, and fig. S7, G and H). Notably, genes that were up-regulated in both pre- and adult microglia included genes in the interferon-STAT pathway, such as *Oas2*, *Mx1*, *Ifit3*, *Cxcl10*, and *Il1b* (Fig. 5, C and D), and were associated with immune and viral GO terms (fig. S7I). Together, these results reveal a role for MAFB in suppressing antiviral response pathways and confirm its functional importance in regulating adult microglia homeostasis.

Germ-free mice contain microglia with an underdeveloped adult phenotype

To further substantiate the importance of the stepwise microglia development program, we assessed how environmental perturbations in specific stages might differentially affect microglia development and the associated genes. To this end, we chose the models of germ-free (GF) conditions and maternal immune activation (MIA). Studies have shown that changes in the microbiome affect the immune system as well as the brain (*61*, *62*), and mice with dysbiosis have defects in their microglia population (*21*). To test whether the microbiome contributes to the environmental signals controlling microglia development, we sorted microglia from GF mice at the pre- (newborn) and adult stages and compared them with those of control mice of the same age housed in a conventional pathogen-free environment. We observed a greater number of genes that were

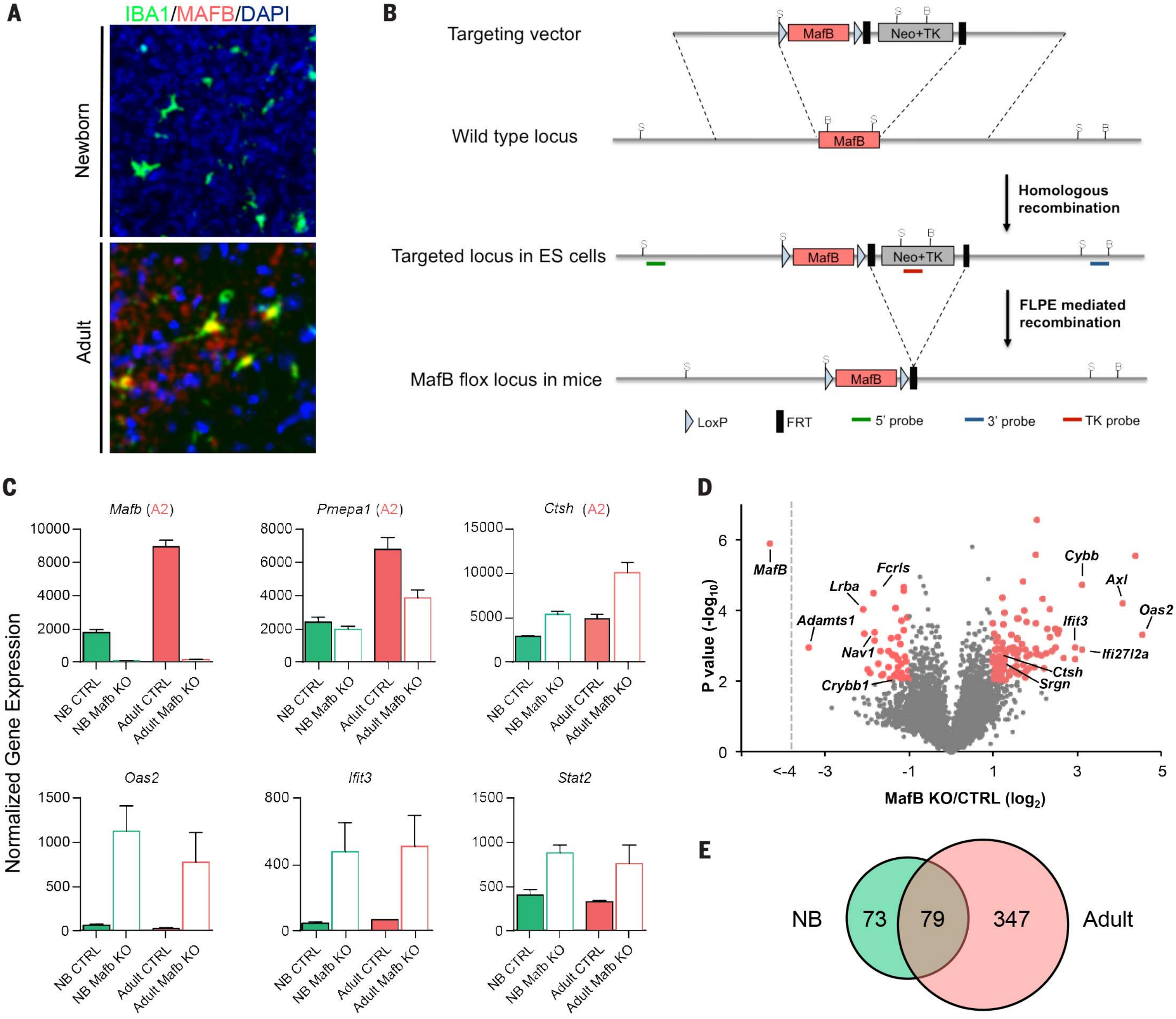

Fig. 5. MAFB is critical for regulation of homeostasis in adult microglia. (**A**) Representative images of coronal sections from whole brains of mice, showing overlap of immunostaining for Hoechst (blue; DAPI, 4′,6-diamidino-2-phenylindole), IBA-1 (green), and MAFB (red) (scale bar, 50 μm). Sections taken from adult mice (8 weeks) demonstrate the coexpression of the microglia marker IBA-1 and the protein MAFB, whereas coexpression was not observed in pre-microglia (newborn mice). (**B**) Diagram of *MafB* knockout mouse generation (Neo, neomycin; TK, thymidine kinase; ES, embryonic stem cells; FLPE, enhanced Flp recombinase; FRT, flippase recognition target). (**C**) Expression of representative genes that are dysregulated in either pre- or adult microglia from *MafB* knockout (KO) mice (CTRL, control). Error bars indicate SEM. (**D**) Volcano plot showing the fold change of genes between *MafB* knockout and control microglia from adult mice on the *x* axis, with significance of the fold change on the *y* axis. *P* values were determined by a two-tailed *t* test. (**E**) Overlap of differentially regulated genes from pre- (green) and adult (red) microglia.

down-regulated, and down-regulated to a higher degree, in adult microglia compared with those of newborns (322 versus 240) (Fig. 6, A and B; fig. S8, A to C; and tables S8 and S10), which may be explained by the change in microbiome composition at weaning (*63*, *64*). In line with previous reports (*21*), microglia from GF mice exhibited decreased expression of genes associated with inflammation and defense responses (Fig. 6, B and C, and fig. S8, B and C). Importantly, genes associated with adult microglia (Fig. 6, A and B, and fig. S8C) were also perturbed in adult GF mice: Of the down-regulated developmental genes, a significant fraction were part of the late adult microglia signature (cluster A2, 20 genes; $P = 1.1 \times 10^{-2}$, hypergeometric distribution). These results link the microbiome to the transition of microglia from the pre- to adult phenotype and suggest that microglia development is sensitive to perturbations influencing immune signals.

Microglia development is perturbed by immune activation during pregnancy

MIA by viral infection has been shown to cause neurodevelopmental defects in adult offspring, as well as behavioral deficits (*32*). Functional abnormalities in the brains of the progeny range from autism to schizophrenia, depending on the timing and conditions of the maternal infection (*35*). Transient exposure of pregnant mice to polyriboinosinic-polyribocytidilic acid (poly I:C) serves as an animal model that reproduces the human disease. Viral infection or poly I:C injection at different stages of the pregnancy leads to distinct neurodevelopmental disease in adulthood, which implicates the specific brain developmental process being executed at the time of intervention (*33*–*35*, *65*). To examine the effect of MIA on microglia development, we injected pregnant mice with poly I:C at day E14.5 (initiation of the pre-microglia stage) and collected independent samples of microglia from the newborn and adult offspring of at least two mothers for RNA-seq analysis (fig. S8D and table S9).

In pre-microglia, 174 and 68 developmental genes exhibited at least twofold increased and decreased expression, respectively, in poly I:C offspring compared with phosphate-buffered saline (PBS)–injected controls (Fig. 6, D and E; fig. S8, E and F; and table S10) (*38*). Within this set, there was significant overlap between genes with increased expression in newborn offspring of mothers injected with poly I:C and those from clusters expressed primarily in adult microglia (clusters A1 and A2; Fig. 1C), whereas depleted genes overlapped with clusters associated with early microglia (clusters E1 and E2; Fig. 1C). Similar results were observed in a comparable experiment with poly I:C injection at E12.5 (fig. S8G). We observed far fewer examples of differential expression in developmental genes at the adult stage compared

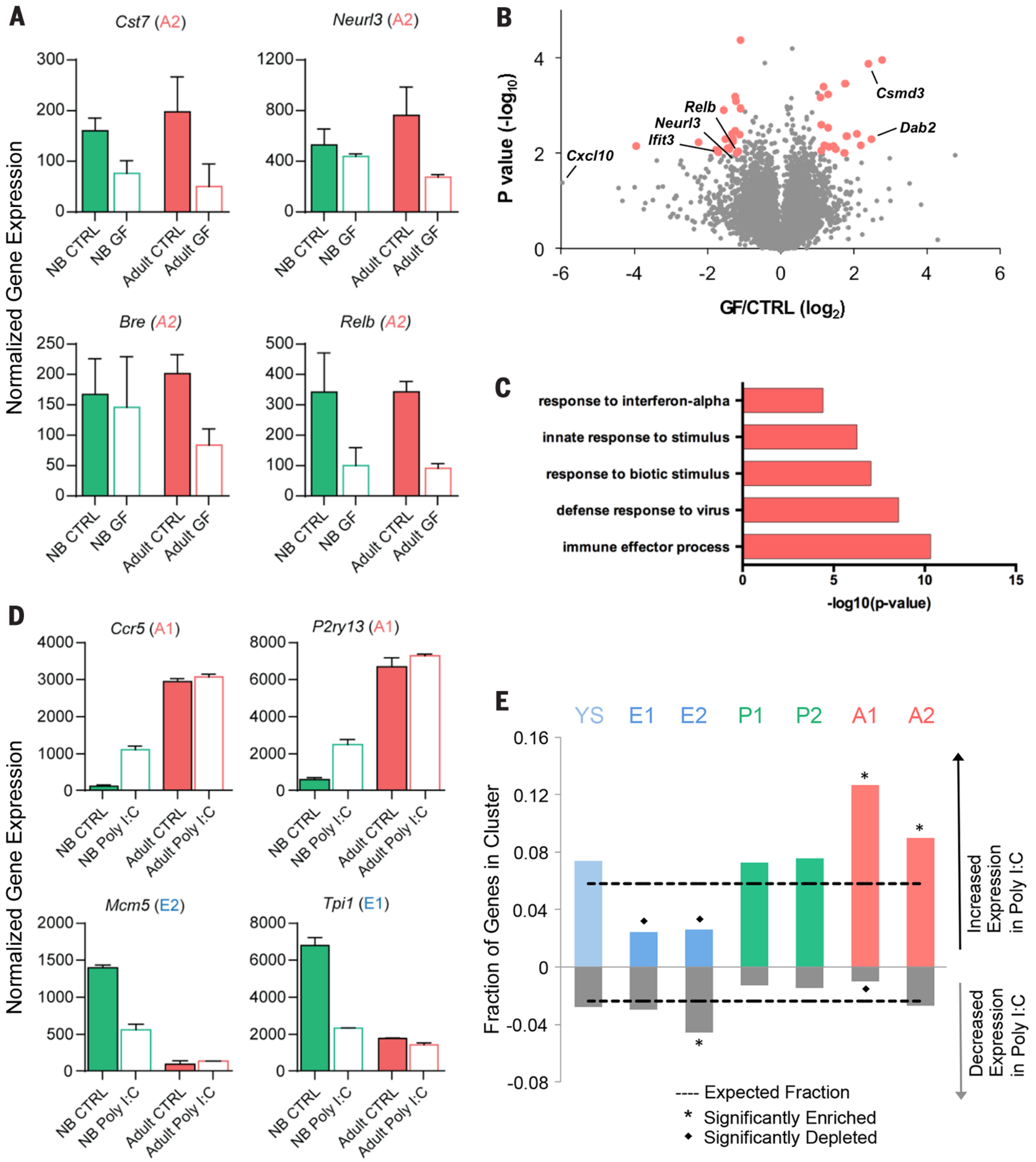

Fig. 6. Perturbations of immune signals shift microglia expression patterns. (**A**) Expression levels in microglia from newborn and adult GF mice compared with those of control mice. Shown are representative genes that are down-regulated in adult microglia. The associated expression cluster from Fig. 1C is indicated. Error bars indicate SEM. (**B**) Volcano plot showing the fold change between GF and control microglia from adult mice on the *x* axis, with significance of the fold change on the *y* axis. *P* values were determined by a two-tailed *t* test. (**C**) Enrichment of GO terms in adult down-regulated genes. (**D**) Expression levels in microglia from newborn and adult offspring of poly I:C–injected (E14.5) mice compared with those from offspring of control mice (PBS-injected). Shown are representative genes that are differentially regulated in pre-microglia. The associated expression cluster from Fig. 1C is indicated. Error bars indicate SEM. (**E**) Fraction of genes in each expression cluster from Fig. 1C that were differentially regulated (at least a twofold change) in pre-microglia from offspring of poly I:C–injected mice relative to those from offspring of control mice (PBS-injected). The dashed line indicates the expected distribution of genes. *$P < 0.05$, hypergeometric distribution, for the significance of enrichment or depletion.

with the pre-microglia stage (fig. S8, E and F), suggesting that the overall expression program of poly I:C mice was realigned with the normal phenotype at adulthood. This may explain why previous studies of adult microglia in MIA did not uncover microglia perturbations (66) and emphasizes that a transient perturbation in microglia development might have far-reaching implications on the brain in adulthood. Overall, microglia from mice subjected to MIA and analyzed at the pre-microglia stage were transcriptionally shifted toward a more advanced developmental stage. We propose that such disruptions in the precise timing of microglia development may perturb their physiological functions in the developing brain and may explain neurodevelopmental diseases in later stages of development, long after the microglia phenotype is restored.

Discussion

Tissue-resident cells of the immune system must exhibit plasticity in the face of a multitude of signals while still maintaining tight regulation of tissue homeostatic functions. Microglia, as resident myeloid cells in an immune-privileged tissue, provide an ideal model for studying the cross-talk of immune cells with the surrounding environment during development. Once the blood-brain barrier is formed early in development, entry of other immune cells from the periphery is negligible, so the developmental effects on microglia can be solely attributed to the processes that they undergo within the brain (9, 24). Microglia are not only pivotal during CNS development but are also responsible for brain homeostasis throughout life while restricting deviation such as aggressive inflammation. Here we identify three distinct phases of regulatory networks in microglia and demonstrate how perturbation of this tight regulation leads to distinct functional effects.

On the basis of the present findings, we propose that the expression program of each phase has evolved to support the parallel development of the brain, while keeping in check local innate immune functions that may cause collateral damage. We might expect to see similar transitions in the resident myeloid cells of other tissues, for example, in Kupffer cells, the resident macrophages of the liver (24, 67). Moreover, resident cells also receive changing signals from their environment as the tissue ages (e.g., increased apoptotic cells); these signals must also be controlled to avoid dangerous responses. Our research highlights the importance of resident myeloid cell adaptation to the changing microenvironment throughout development and the potential for pathologies associated with perturbation of the regulatory circuitry through environmental signals, such as from the microbiome or MIA.

Each stage in microglia development was found to be associated with different signals and functions; thus, the transitions between stages may represent a source of fragility in the system. Perturbations that target these transitions are likely to disrupt different processes depending on the timing and may have an impact on the homeostasis of the adult brain, as indicated by the dysregulation of the developmental expression patterns of immune response genes. For example, previous research has suggested that the immune system is adapted to natural changes in the microbiota composition related to weaning, which occurs in the first weeks after birth, around the time of the pre- to adult microglia shift (61, 63, 64, 68). Our results suggest that in mice lacking these microbiome signals, microglia maturity is disrupted with down-regulation of genes associated with inflammation. These signals may reach the brain either directly through certain metabolites (21) or, more likely, indirectly through the effect of systemic immunity on the barriers of the blood-brain interface (69–71). On the other hand, a transient MIA at E14.5 has the greatest effect on the pre-microglia stage and is accompanied by an up-regulation of inflammatory genes. Nevertheless, the resulting behavioral disorders are observed in the offspring at adulthood and may reflect the impact of the stage-specific microglia response on neurogenesis and synaptic pruning. Such perturbations probably act through distinct regulatory factors in each developmental phase.

MAFB controls cell cycle arrest during terminal macrophage differentiation, whereas its absence is required for macrophage proliferation (58–60). In this work, we identified the critical influence of MAFB on the ability of microglia to express the adult gene program and its role in inflammatory regulation. Thus, MAFB may represent an important "off-state" factor for regulating the response of microglia under various stress conditions (1). In its absence, dozens of developmental genes are dysregulated, and microglia adopt a dramatic antiviral response state. The role attributed here to MAFB in microglia homeostasis was only detectable in the context of distinct stages of microglia development. The relationship between MAFB and the immune response pathway has yet to be fully described, but previous work suggests that MAFB may have an antagonistic relationship with the interferon pathway (72). This suggests that microglia-specific *MafB* knockout mice could have an altered interferon response affecting penetrance of neurodevelopmental disease and aging phenotype (69). Further work on MAFB and identification of other signals and factors that contribute to microglia transitions and homeostasis will allow us to better understand the cross-talk between microglia and the CNS in both normal development and pathology.

In light of our results, as well as those emerging with respect to inhibitory factors such as programmed cell death protein 1 (PD-1), it is becoming clear that the immune system has developed at least as many inhibitory pathways as activating pathways for immune modulation (73). Further, these immune inhibitory pathways have probably evolved in a tissue-specific manner to curb immune activation and collateral damage in sensitive tissues such as the brain. These modulation pathways can be intrinsic (e.g., MAFB) or extrinsic (PD-1) to the cell. A more thorough understanding of the cross-talk between microglia and other cells within the CNS, as well as the signals and pathways that are involved during development and aging, is essential to developing new approaches for intervention and improved diagnostics.

Materials and methods

Animals

$CX_3CR1^{GFP/+}$ (74) and wild-type C57/Bl6 mice were taken throughout development as indicated in the text with two replicates at each time point (with the exception of brain E14, which combines samples from E13.5 and E14.5). Timed pregnancy was performed to obtain the embryos at defined time points after conception. Pregnant females with vaginal plugs were determined as 0.5 dpc. Adult mice were taken at 8 weeks. Animals were supplied by the Animal Breeding Center of the Weizmann Institute of Science. All animals were handled according to the regulations formulated by the Institutional Animal Care and Use Committee.

Isolation of hematopoietic cells from yolk sacs

Yolk sacs were dissected from staged embryos. Single-cell suspensions were achieved using a software-controlled sealed homogenization system (Dispomix; www.biocellisolation.com) in PBS. Cell suspensions were first blocked with Fc-block CD16/32 (BD Biosciences, San Jose, CA), and then stained for $CD45^+$ (1:150; 30-F11, BioLegend, San Diego, CA), $CD11b^+$ (1:150; M1/70, BioLegend, San Diego, CA) and gated for CX_3CR1-GFP positive. Cell populations were sorted with SORP-aria.

Microglia harvesting

Naïve C57BL/6J female mice were bred overnight with $CX_3CR1^{GFP/GFP}$ males (74). Vaginal plugs were checked the next morning and were referred to as embryonic day 0.5 (E0.5). Mice were taken at different time points as indicated in the text; adult mice cortex, hippocampus, and spinal cords were taken at age of 8 weeks. Prenatal brains were dissected and stripped of meninges. Adult and postnatal mice were perfused with PBS transcardially; brains were dissected and stripped of meninges and choroid plexus. Single-cell suspensions were achieved using a software-controlled sealed homogenization system (Dispomix; www.biocellisolation.com) in PBS, followed by density gradient separation; pellet was mixed with 40% percoll and centrifuged at 800*g* for 20 min at room temperature. Supernatant was discarded and pellet taken further for antibody staining. Samples were first blocked with Fc-block CD16/32 (BD Biosciences, San Jose, CA) and then gated for $CD45^{int}$ (1:150; 30-F11, BioLegend), $CD11b^{int}$ (1:150; M1/70, BioLegend), and CX_3CR1-GFP^+. Cell populations were sorted with SORP-aria (BD Biosciences, San Jose, CA).

Germ-free mice

Wild-type C57/Bl6 mice were born and raised in sterile isolators in the absence of any microbial colonization as described previously (75). Sterility was routinely monitored by PCR- and culture-based methods. Brains from GF mice and SPF controls were taken at day 1 and week 4. Microglia from whole brains were harvested as described above and gated for CD45^{int} and CD11b^{int}, as we and others have carefully confirmed these cells to be similar to the populations collected from the CX$_3$CR1-GFP$^+$ microglia populations (see fig. S1C). Cell populations were sorted with SORP-aria (BD Biosciences, San Jose, CA).

Maternal immune activation by poly I:C

Naïve female mice were bred overnight with C57BL/6J males. Vaginal plugs were checked the next morning and were referred to as embryonic day 0.5 (E0.5). On E12.5 or E14.5, pregnant females were injected intravenously (i.v.) with a single dose of 5 mg/kg poly I:C (Sigma-Aldrich, Rehovot, Israel) dissolved in PBS, or an equivalent volume of PBS as a control. The dose of poly I:C was determined according to Meyer *et al.* (*76*). The injection volume was 5 ml/kg. Pups from injected animals were taken at postnatal day 1 and at age of 4 weeks. Microglia were harvested from whole brains as described above, and gated by CD45^{int} and CD11b^{int}, as we and others have carefully confirmed these cells to be similar to the populations collected from the CX$_3$CR1-GFP$^+$ microglia populations (see fig. S1C). Cell populations were sorted with SORP-aria (BD Biosciences, San Jose, CA).

MafB *knockout mice*

Female MafB$^{flox/+}$Csf1R$^{+/+}$ or MafB$^{flox/flox}$Csf1RCre$^{+/+}$ were bred with male MafB$^{flox/flox}$Csf1R-Cre$^{Cre/+}$ (refer to the supplementary materials for description of knockout generation). Vaginal plugs were checked the next morning and were referred to as embryonic day 0.5 (E0.5). Postnatal mice were taken at P2 and adults at age of 5 weeks; animals were perfused with PBS transcardially; brains were dissected and stripped of meninges and choroid plexus. Microglia were harvested from whole brains. Single-cell suspension was achieved by mechanical dissociation, followed by density gradient separation; pellet was mixed with 70% percoll and overlayied on 37% percoll underlaid by 30% percoll, centrifuged at 800*g* for 30 min at 4°C. 37%/70% interface was collected for antibody staining. Samples were pre-gated using Zombie Violet fixable viability kit (BioLegend, France) and Ly6C$^-$ (HK1.4, BioLegend, France) and then gated for CD45.2^{int} (104, BD Biosciences, France) and CD11b^{int} (1:150; M1/70, BD Biosciences, France). Cell populations were sorted with SORP-ariaBD FACSAria III (BD Biosciences, France).

Single-molecule fluorescent in situ hybridization

CX$_3$CR1$^{GFP/+}$ were perfused, brain tissues were harvested and fixed in 4% paraformaldehyde for 3 hours, incubated overnight with 30% sucrose in 4% paraformaldehyde, and then embedded in OCT. 7-μm cryosections were used for hybridization. Probe libraries were designed and constructed as previously described (*53*). Single-molecule FISH probe libraries consisted of 48 probes of length 20 bps and were coupled to cy5 or alexa594. Hybridizations were performed overnight in 30°C. DAPI dye for nuclear staining was added during the washes. To detect microglia, CX$_3$CR1$^{GFP/+}$ mice were used and cells were detected by their GFP fluorescent signal. Images were taken with a Nikon Ti-E inverted fluorescence microscope equipped with a ×100 oil-immersion objective and a Photometrics Pixis 1024 charge-coupled device camera using MetaMorph software (Molecular Devices, Downington, PA). The image-plane pixel dimension was 0.13 μm. *P* values were calculated by Fisher exact test (*77*).

RNA sequencing

Cells were harvested at different time points into Lysis/Binding buffer (Invitrogen). mRNA was captured with 12 μl of Dynabeads oli-go(dT) (Life Technologies), washed, and eluted at 70°C with 10 μl of 10 mM Tris-Cl (pH 7.5). RNA-seq was performed as previously described (*50*), and DNA libraries were sequenced on an Illumina NextSeq 500 or HiSeq with an average of 4 million aligned reads per sample.

RNA processing and analysis

We aligned the RNA-seq reads to the mouse reference genome (NCBI 37, mm9) using TopHat v2.0.13 with default parameters (*78*). Duplicate reads were filtered if they aligned to the same base and had identical UMIs. Expression levels were calculated and normalized for each sample to the total number of reads using HOMER software (http://homer.salk.edu) with the command "*analyzeRepeats.pl rna mm9 -d [sample files] -count 3utr -condenseGenes*" (*79*). For the RNA-seq analysis in Fig. 1, we focused on highly expressed genes with twofold differential over the noise (set at 100) between the means of at least two time points (3059 genes). The value of *k* for the *k* means clustering (Matlab function *kmeans*) was chosen by assessing the average silhouette (Matlab function *evalclusters*; higher score means more cohesive clusters) for a range of possible values with correlation as the distance metric (fig. S1C). GO associations for each cluster were determined using GOrilla (http://cbl-gorilla.cs.technion.ac.il/) (*80*, *81*). The overlap with microglia-specific genes was determined by comparison with genes from the brain-specific macrophage expression cluster in (*16*) and the significance of enrichment was calculated using a hypergeometric distribution. The subset of genes that were differential across CNS regions was determined based on a greater than twofold differential between any two of the three regions (cortex, hippocampus, and spinal cord) and the highest expression of the three falling within twofold of the maximum expression across microglia development. NMF and PCA were performed using built-in Matlab functions *nnmf* and *pca*, respectively. The value of *k* for the NMF was chosen by assessing the plot of root mean square residuals for a range of values (fig. S1F).

iChIP

Naïve C57BL/6J female mice were bred overnight with CX$_3$CR1$^{GFP/GFP}$ males (*74*). Vaginal plugs were checked the next morning and were referred to as embryonic day 0.5 (E0.5). Mice were taken at E12.5, day 1, and 8 weeks. Microglia were harvested from whole brains and sorted as indicated above. iChIP was prepared as previously described (*47*).

ATAC-seq

Naïve C57BL/6J female mice were bred overnight with CX$_3$CR1$^{GFP/GFP}$ males (*74*). Vaginal plugs were checked the next morning and were referred to as embryonic day 0.5 (E0.5). Mice were taken at E12.5, day 3, and 8 weeks. Microglia were harvested from whole brains and sorted as indicated above. To profile for open chromatin, we used an adaptation of the ATAC-seq protocol (*46*, *82*) as previously described (*16*).

Processing of ChIP-seq and ATAC-seq

Reads were aligned to the mouse reference genome (mm9, NCBI 37) using Bowtie2 aligner version 2.2.5 (*83*) with default parameters. The Picard tool *MarkDuplicates* from the Broad Institute (http://broadinstitute.github.io/picard/) was used to remove PCR duplicates. To identify regions of enrichment (peaks) from ChIP-seq reads of H3K4me2 and ATAC-seq, we used the HOMER package *makeTagDirectory* followed by *findPeaks* command with the histone parameter or 500-bp centered regions, respectively (*79*). Union peaks file were generated for ATAC by combining and merging overlapping peaks in all samples.

Chromatin analysis

The read density (number of reads in 10 million total reads per 1000 bp) for H3K4me2 and ATAC was calculated in each region from the union ATAC peaks files. We consider promoters to be within ± 2000 bp of a TSS (n = 12930). We defined 11,252 high-confidence distal enhancers based on their presence in at least two replicates of the same ATAC-seq population, the distal location of the regions (i.e., excluding promoters), and the average H3 K4me2 read density. The region intensity was given in log-base2 of the normalized density [$\log2(x + 1)$]. The value of *k* for the *k*-means clustering (Matlab function *kmeans*) was chosen by assessing the average silhouette (Matlab function *evalclusters*) for a range of possible values with correlation as the distance metric (fig. S3D). The significance of the overlap between chromatin categories and expression clusters was determined using the hypergeometric distribution ($P < 0.05$; table S4).

Gene tracks and normalization

All gene tracks were visualized as *bigWig* files of the combined replicates normalized to 10,000,000 reads and created by the HOMER algorithm *makeUCSCfile* (*79*). For visualization, the tracks were smoothed by averaging over a sliding window of 500 bases and all tracks for a given region were scaled to the highest overall peak.

Single-cell sorting

Naïve C57BL/6J female mice were bred overnight with CX$_3$CR1$^{GFP/GFP}$ males (*74*). Vaginal plugs were checked the next morning and were referred to as embryonic day 0.5 (E0.5). Mice were taken at E12.5, E18.5, and 8 weeks. Microglia were harvested and sorted from whole brains as indicated above into 384-well cell capture plates containing 2 μl of lysis solution and barcoded poly(T) reverse-transcription (RT) primers for single-cell RNA-seq (*50*). Barcoded single-cell capture plates were prepared with a Bravo automated liquid handling platform (Agilent) as described previously (*50*). Four empty wells were kept in each 384-well plate as a no-cell control during data analysis. Immediately after sorting, each plate was spun down to ensure cell immersion into the lysis solution, snap frozen on dry ice, and stored at –80°C until processed.

Single-cell libraries and analysis

Single-cell libraries were prepared using the MARS-seq protocol and processed as described previously (*50*). In order to assess the heterogeneity of the previously defined phases in microglia development, we used a recently published batch-aware multinomial mixture-model clustering algorithm (*51*). Since samples derive from different spatial and temporal points, we devised an approach that would reduce batch effect within each sample but preserve genuine gene expression differences between samples. Each sample, consisting of four batches, was clustered separately. This preliminary clustering was used to infer optimum batch correction coefficients for each gene. A new debatched UMI data set was created, implementing the inferred corrections on the UMI count. The debatched data set was then used to jointly cluster all samples using the same algorithm with no debatching (all batch correction coefficients were set to 1).

This two-step clustering approach proved to increase likelihood score and significantly reduce intra-cluster gene variance when compared with clustering each sample separately, allowing debatching between samples or disallowing debatching completely.

Immunohistochemistry

Mice were transcardially perfused with PBS before brain tissue fixation. The following primary antibodies were used: mouse anti-Dab2 (1:100; BD Bioscience, San Jose, CA), Rabbit anti-GFP (1:100; MBL, Woburn, MA), Goat anti-GFP (1:100; Abcam, Cambridge, MA), Goat anti-IBA1 (1:100; Abcam, Cambridge, MA), Rabbit anti-MAFB (1:100; Bethyl Laboratories, Montgomery, TX). Secondary antibodies were Cy3/Cy2 conjugated donkey anti-mouse/goat antibodies (1:200; Jackson ImmunoResearch, West Grove, PA). The slides were exposed to Hoechst nuclear staining (1:4000; Invitrogen Probes, Carlsbad, CA) for 1 min before their sealing. Two negative controls were used in immunostaining procedures: staining with isotype control antibody followed by secondary antibody, or staining with secondary antibody alone.

For DAB2 staining, microglia from CX$_3$CR1$^{GFP/+}$ mice underwent tissue processing and immunohistochemistry on paraffin embedded sectioned (6 μm thick). Microscopic analysis was performed using a fluorescence microscope (E800; Nikon).

For MAFB staining, microglia from wild-type mice underwent tissue processing and immunohistochemistry on floating sections (30 μm thick). Microscopic analysis was performed using confocal microscopy (Zeiss, LSM880).

Motif analysis

For motif finding, we used the sets of genes from each expression cluster (Fig. 1C) individually as input for the HOMER package motif finder algorithm *findMotifGenome.pl* (*79*). By parsing the known motif list, we compiled the occurrences of the sequence motifs for the transcription factors of interest within the promoters of each expression cluster. A hypergeometric distribution was used to calculate the significance of the overlap between motif occurrences in our set and the expression clusters from Fig. 1C.

Statistical methods

In general, two replicates (in some cases, averaged over offspring from same mother) per sample from independent mice were used for the analyses, so that expression differences would be comparable between time points. In the poly I:C experiment, replicates originated from different mothers. The *MafB* knockout experiment used three replicates from independent mice for both newborn and adult. Genes were considered to have increased or decreased in expression if the log fold change was greater than 1 between the mean of replicates. Genes with normalized log expression value less than 6 were not used for this comparison because of the noise at these low expression levels. *P* values for expression changes used in the volcano plots were calculated using a two-tailed *t* test on the log expression values. A hypergeometric distribution was used to calculate the significance of the overlap between differentially expressed genes, motifs, chromatin clusters, and the expression clusters from Fig. 1C. GO associations and related *P* values were determined using GOrilla (http://cbl-gorilla.cs.technion.ac.il/) (*80*, *81*). Pairwise similarity between replicates or samples was given as the Pearson's correlation.

Further details are included in the supplementary materials.

REFERENCES AND NOTES

1. U.-K. Hanisch, H. Kettenmann, Microglia: Active sensor and versatile effector cells in the normal and pathologic brain. *Nat. Neurosci.* **10**, 1387–1394 (2007). doi: 10.1038/nn1997; pmid: 17965659
2. A. Nimmerjahn, F. Kirchhoff, F. Helmchen, Resting microglial cells are highly dynamic surveillants of brain parenchyma in vivo. *Science* **308**, 1314–1318 (2005). doi: 10.1126/science.1110647; pmid: 15831717
3. M. Prinz, J. Priller, S. S. Sisodia, R. M. Ransohoff, Heterogeneity of CNS myeloid cells and their roles in neurodegeneration. *Nat. Neurosci.* **14**, 1227–1235 (2011). doi: 10.1038/nn.2923; pmid: 21952260
4. E. Gomez Perdiguero *et al.*, Tissue-resident macrophages originate from yolk-sac-derived erythro-myeloid progenitors. *Nature* **518**, 547–551 (2015). doi: 10.1038/nature13989; pmid: 25470051
5. F. Ginhoux *et al.*, Fate mapping analysis reveals that adult microglia derive from primitive macrophages. *Science* **330**, 841–845 (2010). doi: 10.1126/science.1194637; pmid: 20966214
6. C. Schulz *et al.*, A lineage of myeloid cells independent of Myb and hematopoietic stem cells. *Science* **336**, 86–90 (2012). doi: 10.1126/science.1219179; pmid: 22442384
7. K. Kierdorf *et al.*, Microglia emerge from erythromyeloid precursors via Pu.1- and Irf8-dependent pathways. *Nat. Neurosci.* **16**, 273–280 (2013). pmid: 23334579
8. J. Bruttger *et al.*, Genetic cell ablation reveals clusters of local self-renewing microglia in the mammalian central nervous system. *Immunity* **43**, 92–106 (2015). doi: 10.1016/j.immuni.2015.06.012; pmid: 26163371
9. B. Ajami, J. L. Bennett, C. Krieger, W. Tetzlaff, F. M. V. Rossi, Local self-renewal can sustain CNS microglia maintenance and function throughout adult life. *Nat. Neurosci.* **10**, 1538–1543 (2007). doi: 10.1038/nn2014; pmid: 18026097
10. D. Hashimoto *et al.*, Tissue-resident macrophages self-maintain locally throughout adult life with minimal contribution from circulating monocytes. *Immunity* **38**, 792–804 (2013). doi: 10.1016/j.immuni.2013.04.004; pmid: 23601688
11. J. Sheng, C. Ruedl, K. Karjalainen, Most tissue-resident macrophages except microglia are derived from fetal hematopoietic stem cells. *Immunity* **43**, 382–393 (2015). doi: 10.1016/j.immuni.2015.07.016; pmid: 26287683
12. A. Mildner *et al.*, Microglia in the adult brain arise from Ly-6C^{hi}CCR2^{+} monocytes only under defined host conditions. *Nat. Neurosci.* **10**, 1544–1553 (2007). doi: 10.1038/nn2015; pmid: 18026096
13. R. Shechter *et al.*, Infiltrating blood-derived macrophages are vital cells playing an anti-inflammatory role in recovery from spinal cord injury in mice. *PLOS Med.* **6**, e1000113 (2009). doi: 10.1371/journal.pmed.1000113; pmid: 19636355
14. R. Shechter *et al.*, Recruitment of beneficial M2 macrophages to injured spinal cord is orchestrated by remote brain choroid plexus. *Immunity* **38**, 555–569 (2013). pmid: 23477737
15. D. Gosselin *et al.*, Environment drives selection and function of enhancers controlling tissue-specific macrophage identities. *Cell* **159**, 1327–1340 (2014). doi: 10.1016/j.cell.2014.11.023; pmid: 25480297
16. Y. Lavin *et al.*, Tissue-resident macrophage enhancer landscapes are shaped by the local microenvironment. *Cell* **159**, 1312–1326 (2014). doi: 10.1016/j.cell.2014.11.018; pmid: 25480296
17. M. Greter *et al.*, Stroma-derived interleukin-34 controls the development and maintenance of Langerhans cells and the maintenance of microglia. *Immunity* **37**, 1050–1060 (2012). doi: 10.1016/j.immuni.2012.11.001; pmid: 23177320
18. Y. Wang *et al.*, IL-34 is a tissue-restricted ligand of CSF1R required for the development of Langerhans cells and microglia. *Nat. Immunol.* **13**, 753–760 (2012). doi: 10.1038/ni.2360; pmid: 22729249
19. O. Butovsky *et al.*, Identification of a unique TGF-β–dependent molecular and functional signature in microglia. *Nat. Neurosci.* **17**, 131–143 (2014). doi: 10.1038/nn.3599; pmid: 24316888
20. M. Cohen *et al.*, Chronic exposure to TGFβ1 regulates myeloid cell inflammatory response in an IRF7-dependent manner. *EMBO J.* **33**, 2906–2921 (2014). doi: 10.15252/embj.201489293; pmid: 25385836
21. D. Erny *et al.*, Host microbiota constantly control maturation and function of microglia in the CNS. *Nat. Neurosci.* **18**, 965–977 (2015). doi: 10.1038/nn.4030; pmid: 26030851
22. S. Sawa *et al.*, RORγt^{+} innate lymphoid cells regulate intestinal homeostasis by integrating negative signals from the symbiotic microbiota. *Nat. Immunol.* **12**, 320–326 (2011). doi: 10.1038/ni.2002; pmid: 21336274
23. P. H. Patterson, Immune involvement in schizophrenia and autism: Etiology, pathology and animal models. *Behav. Brain Res.* **204**, 313–321 (2009). doi: 10.1016/j.bbr.2008.12.016; pmid: 19136031
24. G. Hoeffel *et al.*, C-Myb^{+} erythro-myeloid progenitor-derived fetal monocytes give rise to adult tissue-resident macrophages. *Immunity* **42**, 665–678 (2015). doi: 10.1016/j.immuni.2015.03.011; pmid: 25902481
25. S. Wakselman *et al.*, Developmental neuronal death in hippocampus requires the microglial CD11b integrin and DAP12 immunoreceptor. *J. Neurosci.* **28**, 8138–8143 (2008). doi: 10.1523/JNEUROSCI.1006-08.2008; pmid: 18685038
26. A. Sierra *et al.*, Microglia shape adult hippocampal neurogenesis through apoptosis-coupled phagocytosis. *Cell Stem Cell* **7**, 483–495 (2010). doi: 10.1016/j.stem.2010.08.014; pmid: 20887954
27. R. C. Paolicelli *et al.*, Synaptic pruning by microglia is necessary for normal brain development. *Science* **333**, 1456–1458 (2011). doi: 10.1126/science.1202529; pmid: 21778362

28. D. P. Schafer *et al*., Microglia sculpt postnatal neural circuits in an activity and complement-dependent manner. *Neuron* **74**, 691–705 (2012). doi: 10.1016/j.neuron.2012.03.026; pmid: 22632727
29. D. P. Schafer, E. K. Lehrman, B. Stevens, The "quad-partite" synapse: Microglia-synapse interactions in the developing and mature CNS. *Glia* **61**, 24–36 (2013). doi: 10.1002/glia.22389; pmid: 22829357
30. H. Kettenmann, F. Kirchhoff, A. Verkhratsky, Microglia: New roles for the synaptic stripper. *Neuron* **77**, 10–18 (2013). doi: 10.1016/j.neuron.2012.12.023; pmid: 23312512
31. Y. Zhan *et al*., Deficient neuron-microglia signaling results in impaired functional brain connectivity and social behavior. *Nat. Neurosci.* **17**, 400–406 (2014). doi: 10.1038/nn.3641; pmid: 24487234
32. A. S. Brown, E. J. Derkits, Prenatal infection and schizophrenia: A review of epidemiologic and translational studies. *Am. J. Psychiatry* **167**, 261–280 (2010). doi: 10.1176/appi.ajp.2009.09030361; pmid: 20123911
33. K. A. Garbett, E. Y. Hsiao, S. Kálmán, P. H. Patterson, K. Mirnics, Effects of maternal immune activation on gene expression patterns in the fetal brain. *Transl. Psychiatry* **2**, e98 (2012). doi: 10.1038/tp.2012.24; pmid: 22832908
34. U. Meyer, J. Feldon, M. Schedlowski, B. K. Yee, Immunological stress at the maternal-foetal interface: A link between neurodevelopment and adult psychopathology. *Brain Behav. Immun.* **20**, 378–388 (2006). doi: 10.1016/j.bbi.2005.11.003; pmid: 16378711
35. U. Meyer *et al*., The time of prenatal immune challenge determines the specificity of inflammation-mediated brain and behavioral pathology. *J. Neurosci.* **26**, 4752–4762 (2006). doi: 10.1523/JNEUROSCI.0099-06.2006; pmid: 16672647
36. D. Gate, K. Rezai-Zadeh, D. Jodry, A. Rentsendorj, T. Town, Macrophages in Alzheimer's disease: The blood-borne identity. *J Neural Transm.* **117**, 961–970 (2010). doi: 10.1007/s00702-010-0422-7; pmid: 20517700
37. C. Prunier, P. H. Howe, Disabled-2 (Dab2) is required for transforming growth factor β-induced epithelial to mesenchymal transition (EMT). *J. Biol. Chem.* **280**, 17540–17548 (2005). doi: 10.1074/jbc.M500974200; pmid: 15734730
38. Materials and methods are available as supplementary materials on *Science* Online.
39. G. Brady *et al*., Analysis of gene expression in a complex differentiation hierarchy by global amplification of cDNA from single cells. *Curr. Biol.* **5**, 909–922 (1995). doi: 10.1016/S0960-9822(95)00181-3; pmid: 7583149
40. S. D. J. Calaminus *et al*., Lineage tracing of Pf4-Cre marks hematopoietic stem cells and their progeny. *PLOS ONE* **7**, e51361 (2012). doi: 10.1371/journal.pone.0051361; pmid: 23300543
41. I. Amit, D. R. Winter, S. Jung, The role of the local environment and epigenetics in shaping macrophage identity and their effect on tissue homeostasis. *Nat. Immunol.* **17**, 18–25 (2016). doi: 10.1038/ni.3325; pmid: 26681458
42. D. D. Lee, H. S. Seung, Learning the parts of objects by non-negative matrix factorization. *Nature* **401**, 788–791 (1999). doi: 10.1038/44565; pmid: 10548103
43. D. S. Gross, W. T. Garrard, Nuclease hypersensitive sites in chromatin. *Annu. Rev. Biochem.* **57**, 159–197 (1988). doi: 10.1146/annurev.bi.57.070188.001111; pmid: 3052270
44. G. Felsenfeld, M. Groudine, Controlling the double helix. *Nature* **421**, 448–453 (2003). doi: 10.1038/nature01411; pmid: 12540921
45. D. R. Winter, I. Amit, The role of chromatin dynamics in immune cell development. *Immunol. Rev.* **261**, 9–22 (2014). doi: 10.1111/imr.12200; pmid: 25123274
46. J. D. Buenrostro, P. G. Giresi, L. C. Zaba, H. Y. Chang, W. J. Greenleaf, Transposition of native chromatin for fast and sensitive epigenomic profiling of open chromatin, DNA-binding proteins and nucleosome position. *Nat. Methods* **10**, 1213–1218 (2013). doi: 10.1038/nmeth.2688; pmid: 24097267
47. D. Lara-Astiaso *et al*., Chromatin state dynamics during blood formation. *Science* **345**, 943–949 (2014). doi: 10.1126/science.1256271; pmid: 25103404
48. A. Barski *et al*., High-resolution profiling of histone methylations in the human genome. *Cell* **129**, 823–837 (2007). doi: 10.1016/j.cell.2007.05.009; pmid: 17512414
49. N. D. Heintzman *et al*., Distinct and predictive chromatin signatures of transcriptional promoters and enhancers in the human genome. *Nat. Genet.* **39**, 311–318 (2007). doi: 10.1038/ng1966; pmid: 17277777
50. D. A. Jaitin *et al*., Massively parallel single-cell RNA-seq for marker-free decomposition of tissues into cell types. *Science* **343**, 776–779 (2014). doi: 10.1126/science.1247651; pmid: 24531970
51. F. Paul *et al*., Transcriptional heterogeneity and lineage commitment in myeloid progenitors. *Cell* **163**, 1663–1677 (2015). doi: 10.1016/j.cell.2015.11.013; pmid: 26627738
52. K. Bahar Halpern *et al*., Bursty gene expression in the intact mammalian liver. *Mol. Cell* **58**, 147–156 (2015). doi: 10.1016/j.molcel.2015.01.027; pmid: 25728770
53. S. Itzkovitz, I. C. Blat, T. Jacks, H. Clevers, A. van Oudenaarden, Optimality in the development of intestinal crypts. *Cell* **148**, 608–619 (2012). doi: 10.1016/j.cell.2011.12.025; pmid: 22304925
54. A. Lyubimova *et al*., Single-molecule mRNA detection and counting in mammalian tissue. *Nat. Protoc.* **8**, 1743–1758 (2013). doi: 10.1038/nprot.2013.109; pmid: 23949380
55. E. S. Lein *et al*., Genome-wide atlas of gene expression in the adult mouse brain. *Nature* **445**, 168–176 (2007). doi: 10.1038/nature05453; pmid: 17151600
56. L. A. Cirillo, K. S. Zaret, An early developmental transcription factor complex that is more stable on nucleosome core particles than on free DNA. *Mol. Cell* **4**, 961–969 (1999). doi: 10.1016/S1097-2765(00)80225-7; pmid: 10635321
57. M. Garber *et al*., A high-throughput chromatin immunoprecipitation approach reveals principles of dynamic gene regulation in mammals. *Mol. Cell* **47**, 810–822 (2012). doi: 10.1016/j.molcel.2012.07.030; pmid: 22940246
58. A. Aziz, E. Soucie, S. Sarrazin, M. H. Sieweke, MafB/c-Maf deficiency enables self-renewal of differentiated functional macrophages. *Science* **326**, 867–871 (2009). doi: 10.1126/science.1176056; pmid: 19892988
59. L. M. Kelly, U. Englmeier, I. Lafon, M. H. Sieweke, T. Graf, MafB is an inducer of monocytic differentiation. *EMBO J.* **19**, 1987–1997 (2000). doi: 10.1093/emboj/19.9.1987; pmid: 10790365
60. E. L. Soucie *et al*., Lineage-specific enhancers activate self-renewal genes in macrophages and embryonic stem cells. *Science* **351**, aad5510 (2016). doi: 10.1126/science.aad5510; pmid: 26797145
61. E. Y. Hsiao *et al*., Microbiota modulate behavioral and physiological abnormalities associated with neurodevelopmental disorders. *Cell* **155**, 1451–1463 (2013). doi: 10.1016/j.cell.2013.11.024; pmid: 24315484
62. L. V. Hooper, D. R. Littman, A. J. Macpherson, Interactions between the microbiota and the immune system. *Science* **336**, 1268–1273 (2012). doi: 10.1126/science.1223490; pmid: 22674334
63. J. E. Koenig *et al*., Succession of microbial consortia in the developing infant gut microbiome. *Proc. Natl. Acad. Sci. U.S.A.* **108**, 4578–4585 (2011). doi: 10.1073/pnas.1000081107; pmid: 20668239
64. M.-C. Arrieta, L. T. Stiemsma, N. Amenyogbe, E. M. Brown, B. Finlay, The intestinal microbiome in early life: Health and disease. *Front. Immunol.* **5**, 427 (2014). pmid: 25250028
65. P. H. Patterson, Maternal infection and immune involvement in autism. *Trends Mol. Med.* **17**, 389–394 (2011). doi: 10.1016/j.molmed.2011.03.001; pmid: 21482187
66. S. Giovanoli, U. Weber-Stadlbauer, M. Schedlowski, U. Meyer, H. Engler, Prenatal immune activation causes hippocampal synaptic deficits in the absence of overt microglia anomalies. *Brain Behav. Immun.* **55**, 25–38 (2015). doi: 10.1016/j.bbi.2015.09015; pmid: 26408796
67. S. Yona *et al*., Fate mapping reveals origins and dynamics of monocytes and tissue macrophages under homeostasis. *Immunity* **38**, 79–91 (2013). doi: 10.1016/j.immuni.2012.12.001; pmid: 23273845
68. I. G. Pantoja-Feliciano *et al*., Biphasic assembly of the murine intestinal microbiota during early development. *ISME J.* **7**, 1112–1115 (2013). doi: 10.1038/ismej.2013.15; pmid: 23535917
69. K. Baruch *et al*., Aging-induced type I interferon response at the choroid plexus negatively affects brain function. *Science* **346**, 89–93 (2014). doi: 10.1126/science.1252945; pmid: 25147279
70. Y. Ziv *et al*., Immune cells contribute to the maintenance of neurogenesis and spatial learning abilities in adulthood. *Nat. Neurosci.* **9**, 268–275 (2006). doi: 10.1038/nn1629; pmid: 16415867
71. N. C. Derecki *et al*., Regulation of learning and memory by meningeal immunity: A key role for IL-4. *J. Exp. Med.* **207**, 1067–1080 (2010). doi: 10.1084/jem.20091419; pmid: 20439540
72. H. Kim, B. Seed, The transcription factor MafB antagonizes antiviral responses by blocking recruitment of coactivators to the transcription factor IRF3. *Nat. Immunol.* **11**, 743–750 (2010). doi: 10.1038/ni.1897; pmid: 20581830
73. C. J. Nirschl, C. G. Drake, Molecular pathways: Coexpression of immune checkpoint molecules: Signaling pathways and implications for cancer immunotherapy. *Clin. Cancer Res.* **19**, 4917–4924 (2013). doi: 10.1158/1078-0432.CCR-12-1972; pmid: 23868869
74. S. Jung *et al*., Analysis of fractalkine receptor CX$_3$CR1 function by targeted deletion and green fluorescent protein reporter gene insertion. *Mol. Cell. Biol.* **20**, 4106–4114 (2000). doi: 10.1128/MCB.20.11.4106-4114.2000; pmid: 10805752
75. C. A. Thaiss *et al*., Transkingdom control of microbiota diurnal oscillations promotes metabolic homeostasis. *Cell* **159**, 514–529 (2014). doi: 10.1016/j.cell.2014.09.048; pmid: 25417104
76. U. Meyer *et al*., Relative prenatal and postnatal maternal contributions to schizophrenia-related neurochemical dysfunction after in utero immune challenge. *Neuropsychopharmacology* **33**, 441–456 (2008). doi: 10.1038/sj.npp.1301413; pmid: 17443130
77. A. Agresti, A survey of exact inference for contingency tables. *Stat. Sci.* **7**, 131–153 (1992). doi: 10.1214/ss/1177011454
78. C. Trapnell, L. Pachter, S. L. Salzberg, TopHat: Discovering splice junctions with RNA-seq. *Bioinformatics* **25**, 1105–1111 (2009). doi: 10.1093/bioinformatics/btp120; pmid: 19289445
79. S. Heinz *et al*., Simple combinations of lineage-determining transcription factors prime cis-regulatory elements required for macrophage and B cell identities. *Mol. Cell* **38**, 576–589 (2010). doi: 10.1016/j.molcel.2010.05.004; pmid: 20513432
80. E. Eden, D. Lipson, S. Yogev, Z. Yakhini, Discovering motifs in ranked lists of DNA sequences. *PLOS Comput. Biol.* **3**, e39 (2007). doi: 10.1371/journal.pcbi.0030039; pmid: 17381235
81. E. Eden, R. Navon, I. Steinfeld, D. Lipson, Z. Yakhini, GOrilla: A tool for discovery and visualization of enriched GO terms in ranked gene lists. *BMC Bioinformatics* **10**, 48 (2009). doi: 10.1186/1471-2105-10-48; pmid: 19192299
82. S. Picelli *et al*., Tn5 transposase and tagmentation procedures for massively scaled sequencing projects. *Genome Res.* **24**, 2033–2040 (2014). doi: 10.1101/gr.177881.114; pmid: 25079858
83. B. Langmead, C. Trapnell, M. Pop, S. L. Salzberg, Ultrafast and memory-efficient alignment of short DNA sequences to the human genome. *Genome Biol.* **10**, R25 (2009). doi: 10.1186/gb-2009-10-3-r25; pmid: 19261174

ACKNOWLEDGMENTS

We thank members of the I.A. and M.S. laboratories for discussions, T. Wiesel for artwork, M. Barad from the CIML flow cytometry platform for assistance with microglia sorting, and M. Azoulay and O. Rozenberg for animal handling. Research in the I.A. laboratory is supported by the European Research Council (grant 309788); the Israeli Science Foundation (grant 1782/11); the European Commission Seventh Framework Programme (EC FP7) BLUEPRINT consortium; the Ernest and Bonnie Beutler Research Program of Excellence in Genomic Medicine; a Minerva Stiftung research grant; the Israeli Ministry of Science, Technology and Space; the David and Fela Shapell Family Foundation; and the National Human Genome Research Institute Center for Excellence in Genome Science (grant 1P50HG006193). I.A. holds the Alan and Laraine Fischer Career Development Chair. Research in the M.S. laboratory is supported by the Advanced European Research Council (grant 232835) and by the EC FP7 HEALTH-2011 program (grant 279017). M.S. holds the Maurice and Ilse Katz Professorial Chair in Neuroimmunology. M.H.S. was supported by grants from the Agence Nationale de la Recherche (grants ANR BLAN07-1_205752 and ANR-11-BSV3-026-01), the Fondation pour la Recherche Médicale (DEq. 20071210559 and DEq. 20110421320), and InCA (French National Cancer Institute; grant 13-10/405/AB-LC-HS). M.H.S. is a Berlin Institute of Health Einstein fellow and an INSERM-Helmholtz group leader. D.R.W. is supported by the European Molecular Biology Organization (EMBO; ALT766-2014) and the EC FP7 (Marie Curie Actions, EMBOCOFUND2012, GA-2012-600394). ATAC-seq, ChIP-seq, bulk RNA-seq, and single-cell RNA-seq data are deposited in the Genome Expression Omnibus under accession number GSE79819.

SUPPLEMENTARY MATERIALS

www.sciencemag.org/content/353/6301/aad8670/suppl/DC1
Materials and Methods
Figs. S1 to S8
Tables S1 to S10

14 November 2015; accepted 10 June 2016
Published online 23 June 2016
10.1126/science.aad8670

RESEARCH ARTICLES

ECONOMICS

Combining satellite imagery and machine learning to predict poverty

Neal Jean,[1,2]* Marshall Burke,[3,4,5]*† Michael Xie,[1] W. Matthew Davis,[4]
David B. Lobell,[3,4] Stefano Ermon[1]

Reliable data on economic livelihoods remain scarce in the developing world, hampering efforts to study these outcomes and to design policies that improve them. Here we demonstrate an accurate, inexpensive, and scalable method for estimating consumption expenditure and asset wealth from high-resolution satellite imagery. Using survey and satellite data from five African countries—Nigeria, Tanzania, Uganda, Malawi, and Rwanda—we show how a convolutional neural network can be trained to identify image features that can explain up to 75% of the variation in local-level economic outcomes. Our method, which requires only publicly available data, could transform efforts to track and target poverty in developing countries. It also demonstrates how powerful machine learning techniques can be applied in a setting with limited training data, suggesting broad potential application across many scientific domains.

Accurate measurements of the economic characteristics of populations critically influence both research and policy. Such measurements shape decisions by individual governments about how to allocate scarce resources and provide the foundation for global efforts to understand and track progress toward improving human livelihoods. Although the quantity and quality of economic data available in developing countries have improved in recent years, data on key measures of economic development are still lacking for much of the developing world (*1*). This data gap is hampering efforts to identify and understand variation in these outcomes and to target intervention effectively to areas of greatest need (*2*, *3*).

Data gaps on the African continent are particularly constraining. According to World Bank data, during the years 2000 to 2010, 39 of 59 African countries conducted fewer than two surveys from which nationally representative poverty measures could be constructed. Of these countries, 14 conducted no such surveys during this period (*4*) (Fig. 1A), and most of the data from conducted surveys are not in the public domain. Coverage is similarly limited for the Demographic and Health Surveys (DHS), the primary source for population-level health statistics in most developing countries as well as for internationally comparable data on household assets—a common measure of wealth (Fig. 1B). For the same 11-year period, 20 of the 59 countries had no DHS asset-based surveys taken, and an additional 19 had only one. These shortcomings have prompted calls for a "data revolution" to sharply scale up data collection efforts within Africa and elsewhere (*1*). But closing these data gaps with more frequent household surveys is likely to be both prohibitively costly—perhaps costing hundreds of billions of U.S. dollars to measure every target of the United Nations Sustainable Development Goals in every country over a 15-year period (*5*)—and institutionally difficult, as some governments see little benefit in having their lackluster performance documented (*2*, *6*).

Given the difficulties of scaling up traditional data collection efforts, an alternative path to measuring these outcomes might use novel sources of passively collected data, such as data from social media, mobile phone networks, or satellites. A popular recent approach leverages satellite images of luminosity at night ("nightlights") to estimate economic activity (*7*–*10*). While this particular technique has shown promise in improving existing country-level economic production statistics (*7*, *10*), it appears less capable of distinguishing differences in economic activity in areas with populations living near and below the international poverty line ($1.90 per capita per day). In these impoverished areas, luminosity levels are generally also very low and show little variation (Fig. 1, C to F, and fig. S1), making nightlights potentially less useful for studying and tracking the livelihoods of the very poor. Other recent approaches using mobile phone data to estimate poverty (*11*, *12*) show promise, but could be difficult to scale across countries given their reliance on disparate proprietary data sets.

Here we demonstrate a novel machine learning approach for extracting socioeconomic data from high-resolution daytime satellite imagery. We then validate this approach in five African countries for which recent georeferenced local-level data on economic outcomes are available. In contrast to existing methods, ours can produce fine-grained poverty and wealth estimates using only data available in the public domain.

Transfer learning

High-resolution satellite imagery is increasingly available at the global scale and contains an abundance of information about landscape features that could be correlated with economic activity. Unfortunately, such data are highly unstructured and thus challenging to extract meaningful insights from at scale, even with intensive manual analysis. Recent applications of deep learning techniques to large-scale image data sets have led to marked improvements in fundamental computer vision tasks such as object detection and classification, but these techniques are generally most effective in supervised learning regimes where labeled training data are abundant (*13*). In our setting, however, labeled data are scarce. Even in the instances where detailed household surveys do exist (Fig. 1, A and B), individual surveys typically only contain information for hundreds of locations, yielding data sets many orders of magnitude smaller than those typically used in deep learning applications. Thus, although deep learning models such as convolutional neural networks could in principle be trained to directly estimate economic outcomes from satellite imagery, the scarcity of training data on these outcomes makes the application of these techniques challenging.

We overcome this challenge through a multistep "transfer learning" (*14*) approach (see supplementary materials section 1), whereby a noisy but easily obtained proxy for poverty is used to train a deep learning model (*15*). The model is then used to estimate either average household expenditures or average household wealth at the "cluster" level (roughly equivalent to villages in rural areas or wards in urban areas), the lowest level of geographic aggregation for which latitude and longitude data are available in the public-domain surveys that we use (see supplementary materials 1.4). Household expenditures, where available, are the standard basis from which national poverty statistics are calculated in poor countries, and we use expenditure data from the World Bank's Living Standards Measurement Study (LSMS) surveys. To measure wealth, we use an asset index drawn from the DHS, computed as the first principal component of survey responses to multiple questions about asset ownership. Although the asset index cannot be used directly to construct benchmark measures of poverty, asset-based measures are thought to better capture households' longer-run economic status (*16*, *17*), with the added advantage that many of the enumerated assets are directly observable to the surveyor and therefore are measured with relatively little error.

To estimate these outcomes, our transfer learning pipeline involves three main steps. First, we start with a convolutional neural network (CNN) model that has been pretrained on ImageNet, a large image classification data set that consists of labeled images

---

[1]Department of Computer Science, Stanford University, Stanford, CA, USA. [2]Department of Electrical Engineering, Stanford University, Stanford, CA, USA. [3]Department of Earth System Science, Stanford University, Stanford, CA, USA. [4]Center on Food Security and the Environment, Stanford University, Stanford, CA, USA. [5]National Bureau of Economic Research, Boston, MA, USA.
*These authors contributed equally to this work. †Corresponding author. Email: mburke@stanford.edu

from 1000 different categories (*18*). In learning to classify each image correctly (e.g., "hamster" versus "weasel"), the model learns to identify low-level image features such as edges and corners that are common to many vision tasks (*19*).

Next, we build on the knowledge gained from this image classification task and fine-tune the CNN on a new task, training it to predict the nighttime light intensities corresponding to input daytime satellite imagery. Here we use the word "predict" to mean estimation of some property that is not directly observed, rather than its common meaning of inferring something about the future. Nightlights are a noisy but globally consistent—and globally available—proxy for economic activity. In this second step, the model learns to "summarize" the high-dimensional input daytime satellite images as a lower-dimensional set of image features that are predictive of the variation in nightlights (see Fig. 2). The trained CNN can be treated as a feature extractor that has learned a nonlinear mapping from each input image to a concise feature vector representation (supplementary materials 1.1). Both daytime imagery (drawn here from the Google Static Maps API) and nightlights (*20*) are available at relatively high resolutions for the entire global land surface, providing a very large labeled training data set.

Finally, we use mean cluster-level values from the survey data along with the corresponding image features extracted from daytime imagery by the CNN to train ridge regression models that can estimate cluster-level expenditures or assets. Regularization in the ridge model guards against overfitting, a potential challenge given the high dimensionality of the extracted features and the relatively small survey data sets. Intuitively, we expect that some subset of the features that explain variation in nightlights is also predictive of economic outcomes.

How might a model partially trained on an imperfect proxy for economic well-being—in this case, the nightlights used in the second training step above—improve upon the direct use of this proxy as an estimator of well-being? Although nightlights display little variation at lower expenditure levels (Fig. 1, C to F), the survey data indicate that other features visible in daytime satellite imagery, such as roofing material and distance to urban areas, vary roughly linearly with expenditure (fig. S2) and thus better capture variation among poorer clusters. Because both nightlights and these features show variation at higher income levels, training on nightlights can help the CNN learn to extract features like these that more capably capture variation across the entire consumption distribution.

Nightlights also have difficulty distinguishing between poor, densely populated areas and wealthy, sparsely populated areas, an added motivation for not using nightlights to estimate per capita consumption. Our approach does not depend on nightlights being able to make this distinction, and instead uses nightlights only as intermediate labels to learn image features that are correlated with economic well-being. The final step of our analysis, in which we train a model to directly estimate local per capita outcomes from daytime image features, does not rely on nightlights.

Visualization of the extracted image features suggests that the model learns to identify some livelihood-relevant characteristics of the landscape (Fig. 2). The model is clearly able to discern semantically meaningful features such as urban areas, roads, bodies of water, and agricultural areas, even though there is no direct supervision—that is, the model is told neither to look for such features, nor that they could be correlated with economic outcomes of interest. It learns on its own that these features are useful for estimating nighttime light intensities. This is in contrast to existing efforts to extract features from satellite imagery, which have relied heavily on human-annotated data (*21*).

Results

Our transfer learning model is strongly predictive of both average household consumption expenditure and asset wealth as measured at the cluster level across multiple African countries. Cross-validated predictions based on models trained separately for each country explain 37 to 55% of the variation in average household consumption

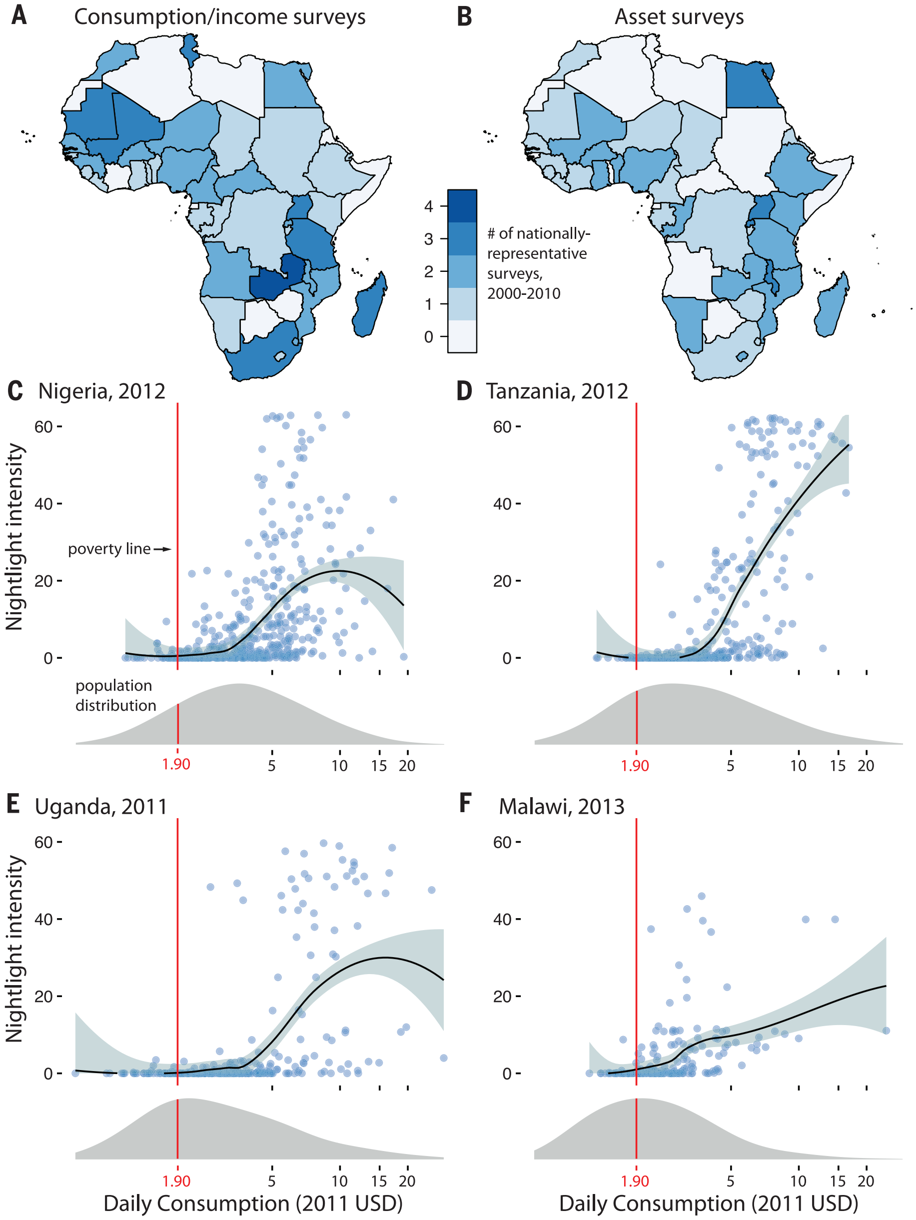

Fig. 1. Poverty data gaps. (**A**) Number of nationally representative consumption surveys occurring in each African country between 2000 and 2010. (**B**) Same as (A), for DHS surveys measuring assets. (**C** to **F**) Relationship between per capita consumption expenditure (measured in U.S. dollars) and nightlight intensity at the cluster level for four African countries, based on household surveys. Nationally representative share of households at each point in the consumption distribution is shown beneath each panel in gray. Vertical red lines show the official international extreme poverty line ($1.90 per person per day), and black lines are fits to the data with corresponding 95% confidence intervals in light blue.

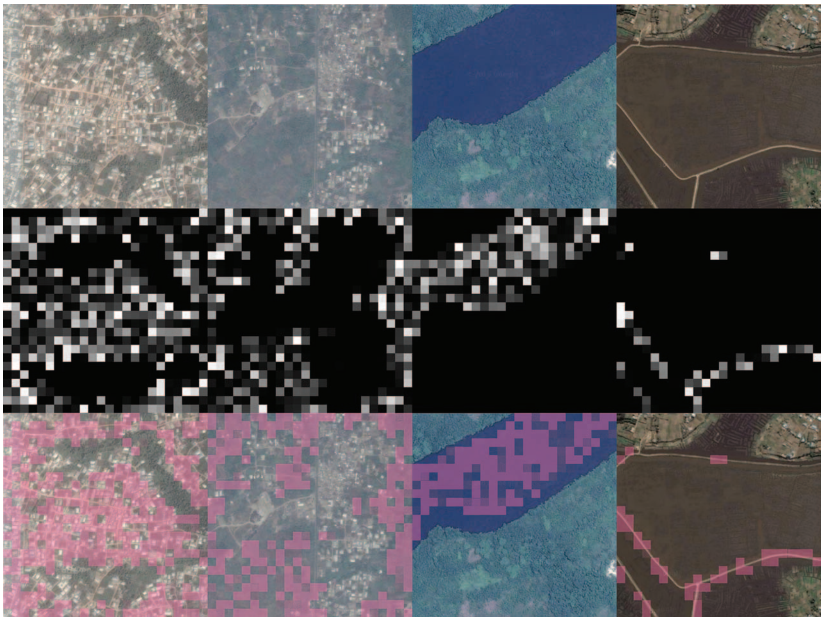

Fig. 2. Visualization of features. By column: Four different convolutional filters (which identify, from left to right, features corresponding to urban areas, nonurban areas, water, and roads) in the convolutional neural network model used for extracting features. Each filter "highlights" the parts of the image that activate it, shown in pink. By row: Original daytime satellite images from Google Static Maps, filter activation maps, and overlay of activation maps onto original images

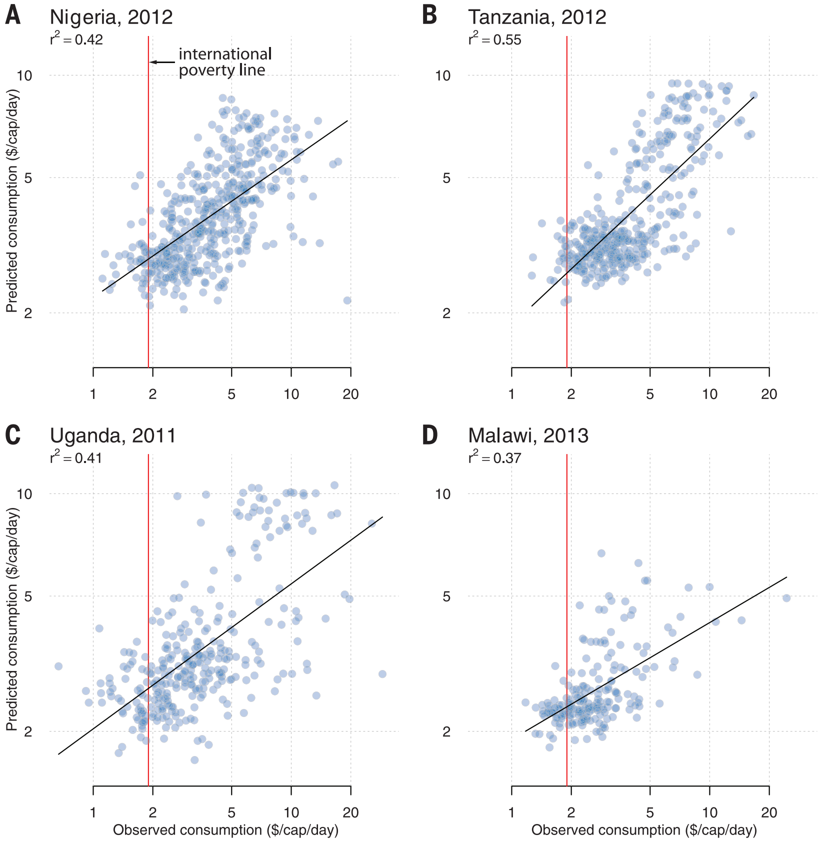

Fig. 3. Predicted cluster-level consumption from transfer learning approach (*y* axis) compared to survey-measured consumption (*x* axis). Results are shown for Nigeria (**A**), Tanzania (**B**), Uganda (**C**), and Malawi (**D**). Predictions and reported r^2 values in each panel are from fivefold cross-validation. Black line is the best fit line, and red line is international poverty line of $1.90 per person per day. Both axes are shown in logarithmic scale. Countries are ordered by population size.

across four countries for which recent survey data are available (Fig. 3), and 55 to 75% of the variation in average household asset wealth across five countries with recent survey data (fig. S3). Models trained on pooled consumption or asset observations across all countries (hereafter "pooled model") perform similarly, with cross-validated predictions explaining 44 to 59% of the overall variation in these outcomes (fig. S4).

This high overall predictive power is achieved despite a lack of temporal labels for the daytime imagery (i.e., the exact date of each image is unknown), as well as imperfect knowledge of the location of the clusters, as up to 10 km of random noise was added to cluster coordinates by the data collection agencies to protect the privacy of survey respondents. Predictive power for assets is nearly uniformly higher than for consumption, perhaps reflecting the larger sample sizes available in the asset surveys; that the asset index is thought to serve as a better proxy for households' longer-run economic status (*16*, *17*) (which could be better correlated with landscape features that change slowly over time); and/or the possibility that certain assets in the index (such as roof type) are directly identified in extracted features (see supplementary materials 2.1). We investigate these potential explanations by constructing our own asset index from variables available in the Uganda LSMS and comparing predictive performance for that index relative to performance for consumption measured in the same survey. We find that differences in the outcome being measured, rather than differences in survey design or direct identification of key assets in daytime imagery, likely explain these performance differences (see supplementary materials 2.1 and fig. S5). Finally, asset-estimation performance of our model in Rwanda surpasses performance in a recent study using cell phone data to estimate identical outcomes (*11*) (cluster-level r^2 = 0.62 in that study, and r^2 = 0.75 in our study; r^2 is the coefficient of determination), again with the added advantage that our predictions can be constructed entirely from publicly available data, obviating the need to obtain and evaluate proprietary data sets when scaling across countries.

To test whether our transfer learning model improves upon the direct use of nightlights to estimate livelihoods, we ran 100 trials of 10-fold cross-validation separately for each country and for the pooled model, each time comparing the predictive power of our transfer learning model to that of nightlights alone. To understand relative performance on different subsets of the consumption distribution, trials were run separately with the sample of clusters restricted to those whose average consumption fell below each quintile of the consumption distribution. The same procedure was repeated for assets.

Despite being trained partially on nightlights, our model is on average substantially more predictive of variation in consumption and assets than nightlights alone. For expenditures, our model outperforms nightlights at nearly all points in the consumption distribution, for both the pooled model and for countries run independently (Fig. 4A and fig. S6). In the pooled setting, for clusters below the international poverty line, our model outperforms nightlights in 81.3% of trials, with an average increase in r^2 of 0.04. For clusters below two times the poverty line, our model outperforms nightlights in 98.5% of trials, with an average increase in r^2 of 0.10, an 81.2% increase in explanatory power. For clusters below three times the poverty line, our model outperforms nightlights in 99.5% of trials, with an average increase in r^2 of 0.12, corresponding to a 54.2% increase in explanatory power. Results for individual countries are similar, with the predictive power of our model outperforming nightlights for all countries at nearly all parts of the consumption distribution (fig. S6). Our model's relative performance against nightlights is even better for assets than for consumption (Fig. 4B), particularly for clusters with low average asset levels. Using more information in nightlights beyond mean luminosity leads to some improvement in nightlights performance, but this improved use of nightlights is still outperformed by our model (see supplementary materials 2.2 and fig S7).

We also study whether our approach improves upon other simpler approaches to extracting information from daytime imagery and predicting economic outcomes using available survey data. We find that our CNN feature extractor far outperforms common general-purpose image features such as color histograms and histograms of oriented gradients (see supplementary materials 2.3 and fig. S8). Our approach also performs as well as or better than an intuitive approach of using data from past surveys to predict outcomes in more recent surveys (see supplementary materials 2.4 and table S2).

To further quantify the statistical significance of our results, we perform an experiment in which we randomly reassign daytime imagery to survey locations and retrain the model on these incorrect images (see supplementary materials 1.7). We repeat this experiment 1000 times within each country and for the pooled model, then compare the predictive power when daytime images were assigned to their correct locations (as in Fig. 3) to the distribution of r^2 values obtained from the 1000 placebo trials. As shown in Fig. 4, C and D, the r^2 values obtained using "correct" daytime imagery are much higher than any of the r^2 values obtained from the reshuffled images, for both consumption and assets, indicating that our model's level of predictive performance is unlikely to have arisen by chance.

Finally, capitalizing on our survey-based measures of consumption and assets in multiple countries, we study the extent to which a model trained using data and satellite image features from one country can estimate livelihoods in other countries. Examining whether a particular model generalizes across borders is useful for understanding whether accurate predictions can be made from imagery alone in areas with no survey data—an important practical concern given the paucity of existing survey data in many African countries (see Fig. 1)—as well as for gaining insight about commonalities in the determinants of livelihoods across countries.

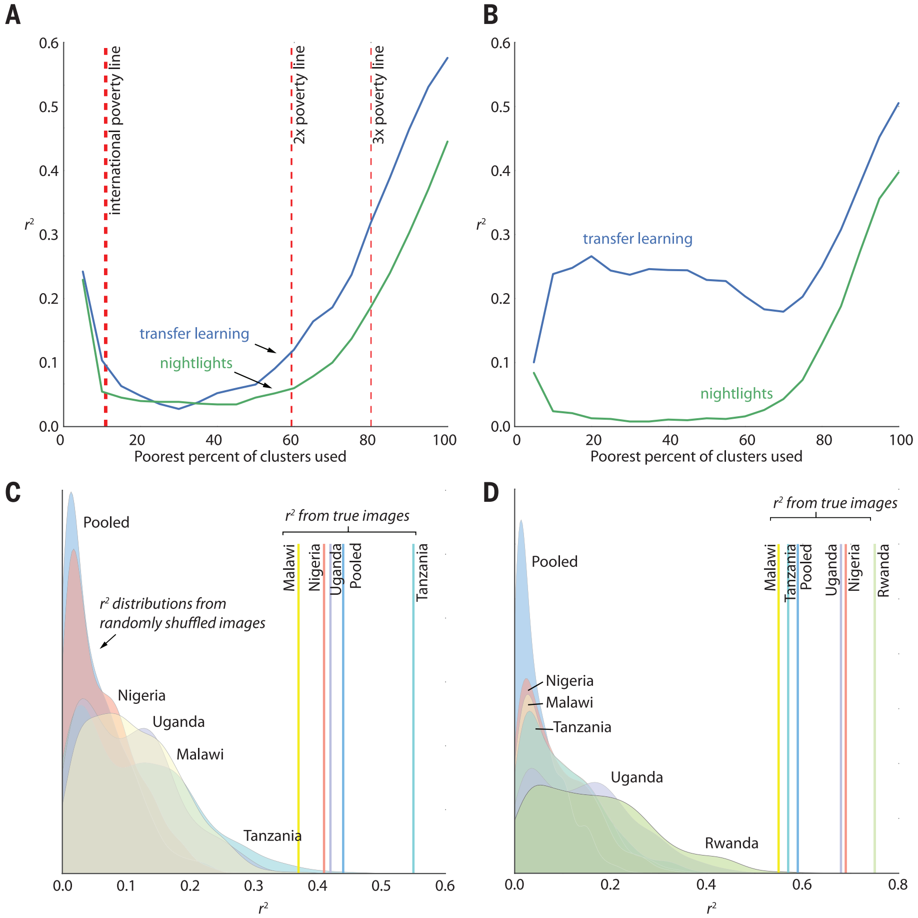

Fig. 4. Evaluation of model performance. (**A**) Performance of transfer learning model relative to nightlights for estimating consumption, using pooled observations across the four LSMS countries. Trials were run separately for increasing percentages of the available clusters (e.g., x-axis value of 40 indicates that all clusters below 40th percentile in consumption were included). Vertical red lines indicate various multiples of the international poverty line. Image features reduced to 100 dimensions using principal component analysis. (**B**) Same as (A), but for assets. (**C**) Comparison of r^2 of models trained on correctly assigned images in each country (vertical lines) to the distribution of r^2 values obtained from trials in which the model was trained on randomly shuffled images (1000 trials per country). (**D**) Same as (C), but for assets. Cross-validated r^2 values are reported in all panels.

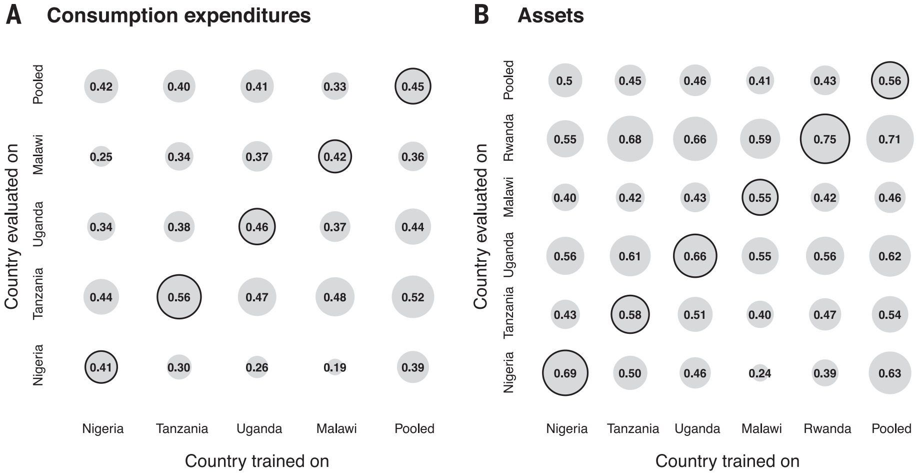

A Consumption expenditures

Country evaluated on	Nigeria	Tanzania	Uganda	Malawi	Pooled
Pooled	0.42	0.40	0.41	0.33	0.45
Malawi	0.25	0.34	0.37	0.42	0.36
Uganda	0.34	0.38	0.46	0.37	0.44
Tanzania	0.44	0.56	0.47	0.48	0.52
Nigeria	0.41	0.30	0.26	0.19	0.39

Country trained on

B Assets

Country evaluated on	Nigeria	Tanzania	Uganda	Malawi	Rwanda	Pooled
Pooled	0.5	0.45	0.46	0.41	0.43	0.56
Rwanda	0.55	0.68	0.66	0.59	0.75	0.71
Malawi	0.40	0.42	0.43	0.55	0.42	0.46
Uganda	0.56	0.61	0.66	0.55	0.56	0.62
Tanzania	0.43	0.58	0.51	0.40	0.47	0.54
Nigeria	0.69	0.50	0.46	0.24	0.39	0.63

Country trained on

Fig. 5. Cross-border model generalization. (**A**) Cross-validated r^2 values for consumption predictions for models trained in one country and applied in other countries. Countries on x axis indicate where model was trained, countries on y axis where model was evaluated. Reported r^2 values are averaged over 100 folds (10 trials, 10 folds each). (**B**) Same as in (A), but for assets.

We find that for both consumption and assets, models trained in-country uniformly outperform models trained out-of-country (Fig. 5), as would be expected. But we also find that models appear to "travel well" across borders, with out-of-country predictions often approaching the accuracy of in-country predictions. Pooled models trained on all four consumption surveys or all five asset surveys very nearly approach the predictive power of in-country models in almost all countries for both outcomes. These results indicate that, at least for our sample of countries, common determinants of livelihoods are revealed in imagery, and these commonalities can be leveraged to estimate consumption and asset outcomes with reasonable accuracy in countries where survey outcomes are unobserved.

Discussion

Our approach demonstrates that existing high-resolution daytime satellite imagery can be used to make fairly accurate predictions about the spatial distribution of economic well-being across five African countries. Our model performs well despite inexact data on both the timing of the daytime imagery and the location of clusters in the training data, and more precise data in either of these dimensions are likely to further improve model performance.

Notably, we show that our model's predictive power declines only modestly when a model trained in one of our sample countries is used to estimate consumption or assets in another country. Despite differences in economic and political institutions across countries, model-derived features appear to identify fundamental commonalities in the determinants of livelihoods across settings, suggesting that our approach could be used to fill in the large data gaps resulting from poor survey coverage in many African countries. In contrast to other recent approaches that rely on proprietary commercial data sets, our method uses only publicly available data and so is straightforward and nearly costless to scale across countries.

Although our model outperforms other sources of passively collected data (e.g., cellphone data, nightlights) in estimating economic well-being at the cluster level, we are currently unable to assess its ability to discern differences within clusters, as public-domain survey data assign identical coordinates to all households in a given cluster to preserve respondent privacy. In principle, our model can make predictions at any resolution for which daytime satellite imagery is available, though predictions on finer scales would likely be noisier. New sources of ground truth data, whether from more disaggregated surveys or novel crowdsourced channels, could enable evaluation of our model at the household level. Combining our extracted features with other passively collected data, in locations where such data are available, could also increase both household- and cluster-level predictive power.

Given the limited availability of high-resolution time series of daytime imagery, we also have not yet been able to evaluate the ability of our transfer learning approach to predict changes in economic well-being over time at particular locations. Such predictions would be very helpful to both researchers and policy-makers and should be enabled in the near future as increasing amounts of high-resolution satellite imagery become available (*22*).

Our transfer learning strategy of using a plentiful but noisy proxy shows how powerful machine learning tools, which typically thrive in data-rich settings, can be productively employed even when data on key outcomes of interest are scarce. Our approach could have broad application across many scientific domains and may be immediately useful for inexpensively producing granular data on other socioeconomic outcomes of interest to the international community, such as the large set of indicators proposed for the United Nations Sustainable Development Goals (*5*).

REFERENCES AND NOTES

1. United Nations, "A World That Counts: Mobilising the Data Revolution for Sustainable Development" (2014).
2. S. Devarajan, *Rev. Income Wealth* **59**, S9–S15 (2013).
3. M. Jerven, *Poor Numbers: How We Are Misled by African Development Statistics and What to Do About It* (Cornell Univ. Press, 2013).
4. World Bank, PovcalNet online poverty analysis tool, http://iresearch.worldbank.org/povcalnet/ (2015).
5. M. Jerven, "Benefits and costs of the data for development targets for the Post-2015 Development Agenda," Data for Development Assessment Paper Working Paper, September (Copenhagen Consensus Center, Copenhagen, 2014).
6. J. Sandefur, A. Glassman, *J. Dev. Stud.* **51**, 116–132 (2015).
7. J. V. Henderson, A. Storeygard, D. N. Weil, *Am. Econ. Rev.* **102**, 994–1028 (2012).
8. X. Chen, W. D. Nordhaus, *Proc. Natl. Acad. Sci. U.S.A.* **108**, 8589–8594 (2011).
9. S. Michalopoulos, E. Papaioannou, *Q. J. Econ.* **129**, 151–213 (2013).
10. M. Pinkovskiy, X. Sala-i-Martin, *Q. J. Econ.* **131**, 579–631 (2016).
11. J. Blumenstock, G. Cadamuro, R. On, *Science* **350**, 1073–1076 (2015).
12. L. Hong, E. Frias-Martinez, V. Frias-Martinez, "Topic models to infer socioeconomic maps," AAAI Conference on Artificial Intelligence (2016).
13. Y. LeCun, Y. Bengio, G. Hinton, *Nature* **521**, 436–444 (2015).
14. S. J. Pan, Q. Yang, *IEEE Trans. Knowl. Data Eng.* **22**, 1345–1359 (2010).
15. M. Xie, N. Jean, M. Burke, D. Lobell, S. Ermon, "Transfer learning from deep features for remote sensing and poverty mapping," AAAI Conference on Artificial Intelligence (2016).
16. D. Filmer, L. H. Pritchett, *Demography* **38**, 115–132 (2001).
17. D. E. Sahn, D. Stifel, *Rev. Income Wealth* **49**, 463–489 (2003).
18. O. Russakovsky *et al.*, *Int. J. Comput. Vis.* **115**, 211–252 (2014).
19. A. Krizhevsky, I. Sutskever, G. E. Hinton, *Adv. Neural Inf. Process. Syst.* **25**, 1097–1105 (2012).
20. National Geophysical Data Center, Version 4 DMSP-OLS Nighttime Lights Time Series (2010).
21. V. Mnih, G. E. Hinton, in *11th European Conference on Computer Vision, Heraklion, Crete, Greece, 5 to 11 September 2010* (Springer, 2010), pp. 210–223.
22. E. Hand, *Science* **348**, 172–177 (2015).

ACKNOWLEDGMENTS

We gratefully acknowledge support from NVIDIA Corporation through an NVIDIA Academic Hardware Grant, from Stanford's Global Development and Poverty Initiative, and from the AidData Project at the College of William & Mary. N.J. acknowledges support from the National Defense Science and Engineering Graduate Fellowship Program. S.E. is partially supported by NSF grant 1522054 through subcontract 72954-10597. We declare no conflicts of interest. All data and code needed to replicate these results are available at http://purl.stanford.edu/cz134jc5378.

SUPPLEMENTARY MATERIALS

www.sciencemag.org/content/353/6301/790/suppl/DC1
Materials and Methods
Figs. S1 to S22
Tables S1 to S3
References (*23*–*27*)

30 March 2016; accepted 6 July 2016
10.1126/science.aaf7894

STATISTICAL PHYSICS

Quantum thermalization through entanglement in an isolated many-body system

Adam M. Kaufman, M. Eric Tai, Alexander Lukin, Matthew Rispoli, Robert Schittko, Philipp M. Preiss, Markus Greiner*

Statistical mechanics relies on the maximization of entropy in a system at thermal equilibrium. However, an isolated quantum many-body system initialized in a pure state remains pure during Schrödinger evolution, and in this sense it has static, zero entropy. We experimentally studied the emergence of statistical mechanics in a quantum state and observed the fundamental role of quantum entanglement in facilitating this emergence. Microscopy of an evolving quantum system indicates that the full quantum state remains pure, whereas thermalization occurs on a local scale. We directly measured entanglement entropy, which assumes the role of the thermal entropy in thermalization. The entanglement creates local entropy that validates the use of statistical physics for local observables. Our measurements are consistent with the eigenstate thermalization hypothesis.

When an isolated quantum system is perturbed—for instance, owing to a sudden change in the Hamiltonian (a so-called quench)—the ensuing dynamics are determined by an eigenstate distribution that is induced by the quench (*1*). At any given time, the evolving quantum state will have amplitudes that depend on the eigenstates populated by the quench and the energy eigenvalues of the Hamiltonian. In many cases, however,

---

Department of Physics, Harvard University, Cambridge, MA 02138, USA.
*Corresponding author. Email: greiner@physics.harvard.edu

such a system can be difficult to simulate, often because the resulting dynamics entail a large amount of entanglement (*2–5*). Yet, remarkably, this same isolated quantum system can thermalize under its own dynamics, unaided by a reservoir (Fig. 1) (*6–8*), so that the tools of statistical mechanics apply and challenging simulations are no longer required. In this case, most observables of a quantum state coherently evolving according to the Schrödinger equation can be predicted from a thermal ensemble and thermodynamic quantities. Even with infinitely many copies of this quantum state, these same observables are fundamentally unable to reveal whether this is a single quantum state or a thermal ensemble. In other words, a globally pure quantum state is apparently indistinguishable from a mixed, globally entropic thermal ensemble (*6*, *7*, *9*, *10*). Ostensibly, the coherent quantum amplitudes that define the quantum state in Hilbert space are no longer relevant, even though they evolve in time and determine the expectation values of observables. The dynamic convergence of the measurements of a pure quantum state with the predictions of a thermal ensemble, and the physical process by which this convergence occurs, are the experimental focus of this work.

Theoretical studies have, in many regards, clarified the role of quantum mechanics in statistical physics (*6*, *7*, *9–13*). The conundrum surrounding the agreement of pure states with extensively entropic thermal states is resolved by the counterintuitive effects of quantum entanglement. A canonical example of this point is the Bell state of two spatially separated spins: Although the full quantum state is pure, local measurements of just one of the spins reveals a statistical mixture with reduced purity. This local statistical mixture is distinct from a superposition because no operation on the single spin can remove these fluctuations or restore its quantum purity. In such a way, the spin's entanglement with another spin creates local entropy, which is called entanglement entropy. Entanglement entropy is not a phenomenon that is restricted to spins but exists in all quantum systems that exhibit entanglement. And although probing entanglement is a notoriously difficult experimental problem, this loss of local purity or, equivalently, the development of local entropy, establishes the presence of entanglement when it can be shown that the full quantum state is pure.

We directly observed a globally pure quantum state dynamically lose local purity to entanglement and, in parallel, become locally thermal. Recent experiments have demonstrated analogies between classical chaotic dynamics and the role of entanglement in few-qubit spin systems (*14*), as well as the dynamics of thermalization within an ion system (*15*). In addition, studies of bulk gases have shown the emergence of thermal ensembles and the effects of conserved quantities in isolated quantum systems through macroscopic observables and correlation functions (*16–19*). We are able to directly measure the global purity as thermalization occurs through single-particle resolved quantum many-body interference. In turn, we show that we can observe microscopically the role of entanglement in producing local entropy in a thermalizing system of itinerant particles, which is paradigmatic of the systems studied in statistical mechanics.

Below, we explore the equivalence between the entanglement entropy that we measured and the expected thermal entropy of an ensemble (*11*, *12*). We further address how this equivalence is linked to the eigenstate thermalization hypothesis (ETH), which provides an explanation for thermalization in closed quantum systems (*6*, *7*, *9*, *10*). The ETH is typically framed in terms of the small variation of observables (expectation values) associated with eigenstates that are close in energy (*6*, *7*, *10*), but the role of entanglement in these eigenstates is paramount (*12*). Fundamentally, the ETH implies an equivalence of the local reduced density matrix of a single excited energy eigenstate and the local reduced density matrix of a globally thermal state (*20*), an equivalence which is made possible only by entanglement and the impurity that it produces locally within a globally pure state. The equivalence ensures thermalization of most observable quantities after a quantum quench. Through parallel measurements of the entanglement entropy and local observables within a many-body Bose-Hubbard system, we were able to experimentally study this equivalence that lies at the heart of quantum thermalization.

Experimental protocol

For our experiments, we used a Bose-Einstein condensate of ^{87}Rb atoms loaded into a two-dimensional optical lattice positioned at the focus of a high-resolution imaging system (*21*, *22*). The system is described by the Bose-Hubbard Hamiltonian

$$\hat{H} = -(J_x \sum_{x,y} \hat{a}^\dagger_{x,y}\,\hat{a}_{x+1,y} + J_y \sum_{x,y} \hat{a}^\dagger_{x,y}\,\hat{a}_{x,y+1} + h.c.) + \frac{U}{2}\sum_{x,y} \hat{n}_{x,y}(\hat{n}_{x,y} - 1) \qquad (1)$$

where $\hat{a}^\dagger_{x,y}$, $\hat{a}_{x,y}$, and $\hat{n}_{x,y} = \hat{a}^\dagger_{x,y}\hat{a}_{x,y}$ are the bosonic creation, annihilation, and number operators at the site located at $\{x,y\}$, respectively (*h.c.*, hermitian conjugate). Atoms can tunnel between neighboring lattice sites at a rate J_i (where i indicates the direction of tunneling) and experience a pairwise interaction energy U when multiple atoms occupy a site. We had independent control over the tunneling amplitudes J_x and J_y through the lattice depth, which could be tuned to yield from $J/U \ll 1$ to $J/U \gg 1$. In addition to the optical lattice, we were able to superimpose arbitrary potentials by using a digital micromirror device placed in the Fourier plane of our imaging system (*23*).

To initiate the experiment, we isolated a plaquette of 2 × 6 sites from a larger low-entropy Mott insulator with unity filling (Fig. 2A) (*24*), which produced two copies of a six-site Bose-Hubbard chain. At this point, each copy was in a product state of single-atom Fock states on each of the constituent sites. We then suddenly switched on tunneling in the x direction, whereas tunneling in the y direction was suppressed. Each chain was restricted to the original six sites by introducing a barrier at the ends of the chains to prevent tunneling out of the system. These combined steps quenched the six-site chains into a Hamiltonian for which the initial state represents a highly excited state that has substantial overlap with an appreciable number of energy eigenstates. Each chain represents an identical but independent copy of a quenched system of six particles on six sites, which evolves in the quenched Hamiltonian for a controllable duration.

We then measured the quantum purity or on-site number statistics (Fig. 2C). For the former, we appended to the quench evolution a beam splitter operation that interferes the two identical copies by freezing dynamics along the chain and allowing for tunneling in a projected double-well potential for a prescribed time (*25*). In the last step for both measurements, a potential barrier was raised between the two copies, and a one-dimensional time-of-flight in the direction transverse to the chain was performed to measure the resulting occupation on each site of each copy.

The ability to measure quantum purity is crucial to assessing the role of entanglement in our system. Tomography of the full quantum state would typically be required to extract the

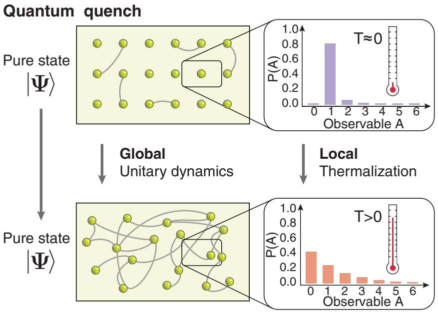

Fig. 1. Schematic of thermalization dynamics in closed systems. An isolated quantum system at zero temperature can be described by a single pure wavefunction $|\Psi\rangle$. Subsystems of the full quantum state are pure, as long as the entanglement between subsystems (indicated by the gray lines between the particles) vanishes (upper panels). If suddenly perturbed, the full system evolves unitarily, developing considerable entanglement between all parts of the system (lower panels). The bar graphs show the probability of an observable before and after perturbation of the system. Although the full system remains in a pure and in this sense zero-entropy state, the entropy of entanglement causes the subsystems to equilibrate, and local thermal mixed states appear to emerge within a globally pure quantum state.

global purity, which is particularly challenging in the full 462-dimensional Hilbert space defined by the itinerant particles in our system. Furthermore, whereas in spin systems global rotations can be used for tomography (*26*), there is no known analogous scheme for extracting the full density matrix of a many-body state of itinerant particles. The many-body interference described here, however, allows us to extract quantities that are quadratic in the density matrix, such as the purity (*25*). After performing the beam splitter operation, we were able to obtain the quantum purity of the full system and any subsystem simply by counting the number of atoms on each site of one of the six-site chains (Fig. 2C).

Each run of the experiment yielded the parity $P^{(k)} = \Pi_i p_i^{(k)}$, where i is iterated over a set of sites of interest in copy k. The single-site parity operator $p_i^{(k)}$ returns 1 (–1) when the atom number on site i is even (odd). It has been shown that the beam splitter operation yields $\langle P^{(1)} \rangle = \langle P^{(2)} \rangle = \mathrm{Tr}(\rho_1 \rho_2)$, where ρ_i is the density matrix on the set of sites considered for each copy (*4*, *25*, *27*). Because the preparation and quench dynamics for each copy are identical, yielding $\rho_1 = \rho_2 \equiv \rho$, the average parity reduces to the purity: $\langle P^{(k)} \rangle = \mathrm{Tr}(\rho^2)$. When the set of sites considered constitutes the full six-site chain, the expectation value of this quantity returns the global many-body purity, whereas for smaller sets it provides the local purity of the respective subsystem.

Comparing measurements taken with and without the beam splitter, our data immediately illustrate the contrast between the global and local behaviors and how thermalization is manifest (Fig. 2B). Our observations show that the global many-body state retains its quantum purity over time, affirming the unitarity of its evolution after the quench. This global measurement also clearly distinguishes the quantum state that we produced from a canonical thermal ensemble with a purity that is orders of magnitude smaller. Yet the number statistics locally converge to a distribution of thermal character, which can be faithfully modeled by that same thermal ensemble. We next experimentally explored the question suggested by this observation: How does a pure state that appears globally distinct from a thermal ensemble possess local properties that mirror this thermal state?

The growth of entanglement after a quench is key to understanding how entropy forms within the subsystems of a pure quantum state, thereby facilitating thermalization (*2*, *4*, *5*, *28*). When two parts of a system are entangled, the full quantum state ρ cannot be written in a separable fashion with respect to the Hilbert spaces of the subsystems (*29*, *30*). As has been shown theoretically (*4*, *27*) and recently observed experimentally (*25*), this causes the subsystems ρ_A and ρ_B to be in an entropic mixed state even though the full many-body quantum state is pure (*30*). The mixedness of the subsystem can be quantified by the second-order Rényi entropy $S_A = -\log[\mathrm{Tr}(\rho_A^2)]$, which is the natural logarithm of the purity of the subsystem density matrix. Although the von Neumann entropy is typically used in the context of statistical mechanics, both quantities grow as a subsystem density matrix becomes mixed and increasingly entropic. In the Rényi case, the purity in the logarithm quantifies the number of states contributing to the statistical mixture described by the density matrix.

Entanglement entropy dynamics and saturation

We first studied the dynamics of the entanglement entropy immediately after the quench for varying subsystem sizes (Fig. 3). Initially, we observed an approximately linear rise in the entropy with time, with a similar slope among the subsystems considered (Fig. 3, inset) (*2*). After an amount of time that depended on the subsystem size, the entanglement entropy saturated to a steady-state value, about which there were small residual temporal fluctuations. The presence of residual fluctuations is attributable in part to the finite size of our system. An exact numerical calculation of the dynamics with no free parameters shows excellent agreement with our experimental measurements. Crucially, the data indicate that whereas the subsystems acquire entropy with time (Fig. 3, A to C), the entropy of the full system remains constant and is small throughout the dynamics (Fig. 3D) (*24*). The high purity of the full

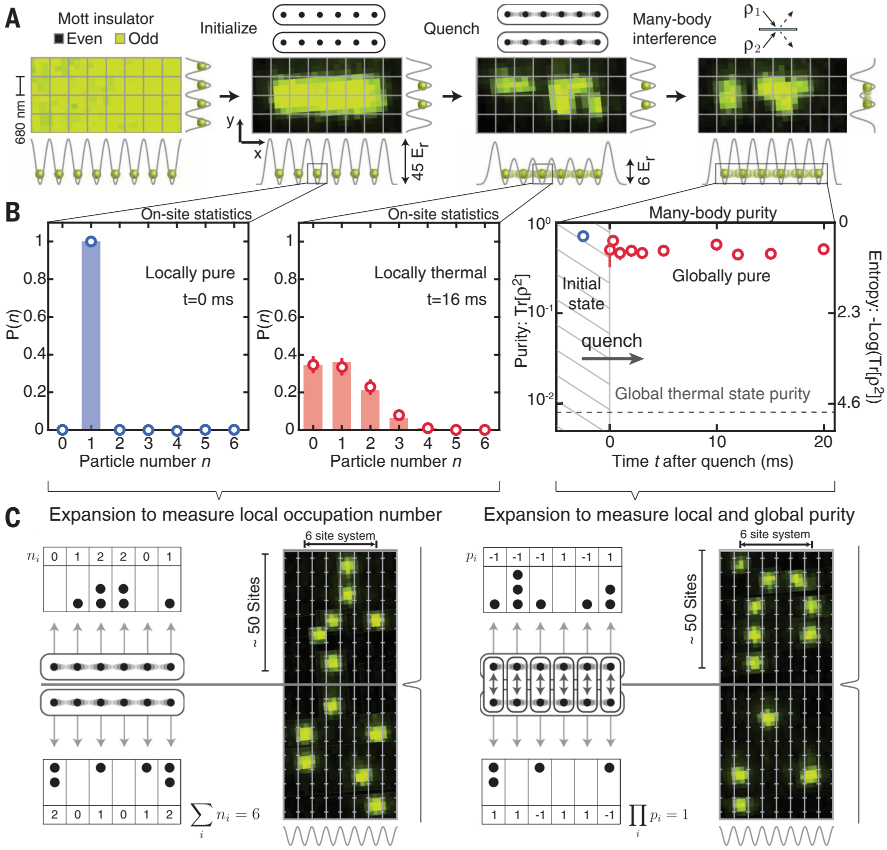

Fig. 2. Experimental sequence. (**A**) Using tailored optical potentials superimposed on an optical lattice, we deterministically prepared two copies of a six-site Bose-Hubbard system, where each lattice site is initialized with a single atom. We reduced the lattice depth along x (specified in units of the lattice recoil energy E_r) to enable tunneling and obtained either the ground state (adiabatic melt) or a highly excited state (sudden quench) in each six-site copy. After a variable evolution time, we froze the evolution and characterized the final quantum state by either acquiring number statistics or the local and global purity. Even and odd refer to the atom number parity. (**B**) Site-resolved number statistics of the initial distribution (left panel, showing a strong peak at one atom with vanishing fluctuations) and the distribution at later times (middle panel), compared with the predictions of a canonical thermal ensemble (red bars) of the same average energy as the quenched quantum state [$J/(2\pi)$ = 66 Hz; $U/(2\pi)$ = 103 Hz]. Error bars are SEM. Measurements of the global many-body purity show that it is static and high (right panel). This is in contrast to the vanishing global purity of the canonical thermal ensemble, yet this same ensemble accurately describes the local number distribution that we observed. (**C**) To measure the atom number locally, we allowed the atoms to expand in half-tubes along the y direction while pinning the atoms along x. In separate experiments, we applied a many-body beam splitter by allowing the atoms in each column to tunnel in a projected double-well potential. The resulting atom number parity (even or odd) on each site encodes the global and local purity.

system allows us to conclude that the dynamical increase in entropy in the subsystems originates in the propagation of entanglement between the system's constituents. The approximately linear rise at early times (Fig. 3, inset) is related to the spreading of entanglement in the system within an effective light cone (*2*, *31*, *32*). Furthermore, in analogy to the growth of thermodynamic entropy in an equilibrating classical mechanical system, such as a gas in a closed container, we observed the growth of local entropy in a closed quantum mechanical system. In the quantum mechanical case, however, the mechanism responsible for the entropy is entanglement, which is absent from a system modeled by classical mechanics.

When a system thermalizes, we expect that the saturated values of local observables should correspond to the predictions of a statistical ensemble. By analogy, if the entanglement entropy plays the role of thermal entropy, then in a thermalized pure state, we expect extensive growth in the entanglement entropy with subsystem volume. When the entanglement entropy in a quantum state grows linearly with the size of the subsystem considered, it is known as a volume law. Theoretical work using conformal field theory has shown that indeed, at long times, a volume law is expected for a quenched, infinite, continuous system, whereas only an area law with a logarithmic correction is expected for the ground state (*2*, *33*, *34*). Characterizing the large amount of entanglement associated with a volume law is particularly challenging because it results in nearly every entry of the density matrix having a small but, importantly, nonzero magnitude.

Using the techniques outlined here, we obtained measurements showing a near-volume law in the entanglement entropy (Fig. 4A). A linear growth with volume in the entanglement entropy occurs when each subsystem incoherently populates a number of states that scales with the size of the subsystem Hilbert space. This is because, for the Bose-Hubbard model, the Hilbert space is approximately exponential in the lattice size, which results in a linear growth in $S_A = -\log[\mathrm{Tr}(\rho_A^2)]$. The exact slope of the entanglement entropy versus subsystem volume depends on the average energy of the thermalized pure state (*35*). In contrast, we can prepare the ground

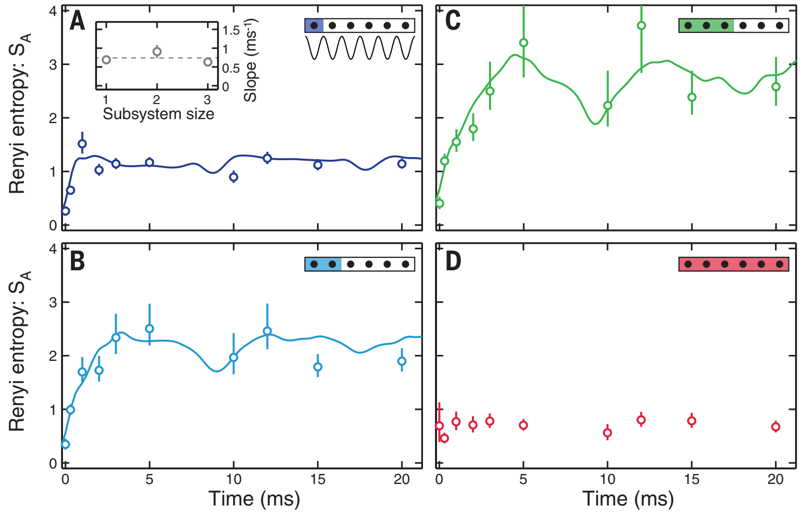

Fig. 3. Dynamics of entanglement entropy. Starting from a low-entanglement ground state, a global quantum quench leads to the development of large-scale entanglement between all subsystems. We quenched a six-site system from the Mott insulating product state ($J/U \ll 1$) with one atom per site to the weakly interacting regime of $J/U = 0.64$ [$J/(2\pi) = 66$ Hz] and measured the dynamics of the entanglement entropy. Shown are the dynamics for (**A**) one-, (**B**) two-, and (**C**) three-site subsystems and (**D**) the full system. As it equilibrates, a subsystem acquires local entropy, whereas the entropy of the full system remains constant and at a value given by measurement imperfections (D). The measured dynamics are consistent with exact numerical simulations (*24*) with no free parameters (solid lines). Error bars are SEM. For the largest entropies encountered in the three-site subsystem shown in (C), the large number of populated microstates leads to a significant statistical uncertainty in the entropy, which is reflected in the upper error bar extending to large entropies or being unbounded (*24*). The inset in (A) shows the slope of the early time dynamics, extracted from (A) to (C) with a piecewise linear fit (*24*). The dashed line is the mean of these measurements.

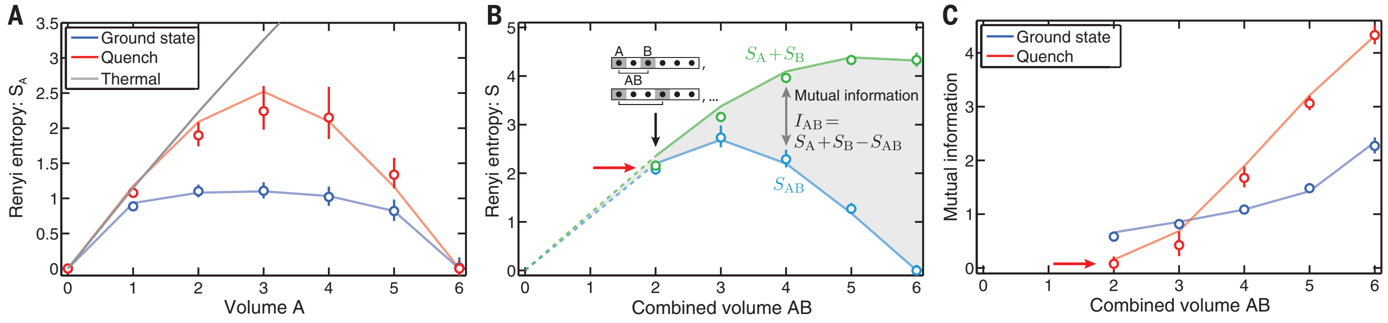

Fig. 4. Thermalized many-body systems. After the quench, the many-body state reaches a thermalized regime with saturated entanglement entropy. (**A**) In contrast to the ground state, for which the Rényi entropy only weakly depends on subsystem size, the entanglement entropy of the saturated quenched state grows almost linearly with size. As the subsystem size becomes comparable to the full system size, the subsystem entropy bends back to near zero, reflecting the globally pure zero-entropy state. For small subsystems, the Rényi entropy in the quenched state is nearly equal to the corresponding thermal entropy from the canonical thermal ensemble density matrix. (**B**) The mutual information $I_{AB} = S_A + S_B - S_{AB}$ quantifies the amount of classical (statistical) and quantum correlations between subsystems A and B (gray region). For small subsystems, the thermalized quantum state has $S_A + S_B \approx S_{AB}$, thanks to the near-volume law scaling (red arrow), leading to vanishing mutual information. When the volume of AB approaches the system size, the mutual information will grow because $S_A + S_B$ exceeds S_{AB}. (**C**) Mutual information I_{AB} versus the volume of AB for the ground state and the thermalized quenched state. For small system sizes, the quenched state exhibits smaller correlations than the adiabatically prepared ground state, and the mutual information is nearly vanishing (red arrow). When probed on a scale near the system size, the highly entangled quenched state exhibits much stronger correlations than the ground state. Throughout this figure, the entanglement entropies from the last time point in Fig. 3 are averaged over all relevant partitionings with the same subsystem volume; we have also corrected for the extensive entropy unrelated to entanglement (*24*). All solid lines represent numerical calculations with no free parameters (*24*).

state of the quenched Hamiltonian by adiabatically reducing the lattice depth. In this case, the superfluid ground state of the Bose-Hubbard model has suppressed entanglement, which is predicted to incur slow logarithmic growth in the entanglement entropy with subsystem volume (*33*). Our measurements clearly distinguish the two cases. The back-bending of the entanglement entropy as the subsystem surpasses half the system size indicates that the state is globally pure. In the quenched state, the high global purity is striking in a state that locally appears to be completely dephased, which is behavior often associated with environmentally induced decoherence or other noise sources.

We further observed near-quantitative agreement between the measured dependence of the entanglement entropy on subsystem volume and the prediction of a thermal ensemble. We made this comparison by computing a canonical thermal ensemble ρ^T (where T is temperature) with an average energy equal to that of the quenched quantum state that we produced experimentally (*35*). The gray line in Fig. 4A is the Rényi (thermal) entropy as a function of subsystem size for this calculated thermal state. Although our limited system size prevents comparison over a large range of subsystem sizes, the initial rise of the entanglement entropy with subsystem volume mimics that of the thermal entropy. Despite their similarity, it is worth emphasizing the disparate character of the thermal and entanglement entropies. The entanglement entropy (either Rényi or von Neumann) is instantaneously present in the pure quantum state after coherent unitary evolution, arising from the nonseparability of the quantum state between the subsystem and traced-out degrees of freedom. On the other hand, the von Neumann thermal entropy within a subsystem of a mixed thermal state is the thermodynamic entropy in statistical mechanics, which could be extracted from irreversible heat flow experiments on the subsystem (*12*). Therefore, the similarity of the Rényi entropies that we determined points to an experimental equivalence between the entanglement and thermodynamic entropies (*35*, *36*).

The behavior of the entanglement entropy provides a clean framework for understanding the entropy within thermalizing closed quantum systems. However, one of the most well-known features of entanglement, the presence of nonlocal correlations, appears inconsistent with what one expects of thermalized systems. In particular, the massive amount of entanglement implied by a volume law suggests high correlation between disparate parts of the system, whereas a key feature of a thermal state is the absence of such long-range correlations. A useful metric for correlations, both classical (statistical) and quantum, between two subsystems A and B is the mutual information $I_{AB} = S_A + S_B - S_{AB}$ (*25*, *37*). The mutual information demonstrates that the amount of correlation in the presence of a volume law is vanishing for subsystem volumes that sample less than half the full system, which is where the entropy growth is nearly linear (Fig. 4B). Furthermore, even though the thermalized quantum state carries more entanglement entropy than the ground state, small subsystems display smaller correlations in the thermalized quantum state than they do in the superfluid ground state (Fig. 4C). Once the subsystem volume is comparable to the system size, which is where the entanglement entropy deviates from the volume law, the quantum correlations entailed by the purity of the full system become apparent. The mutual information therefore illustrates how the volume law in the entanglement entropy yields an absence of correlations between sufficiently local observables, even though the quantum state retains a large amount of entanglement.

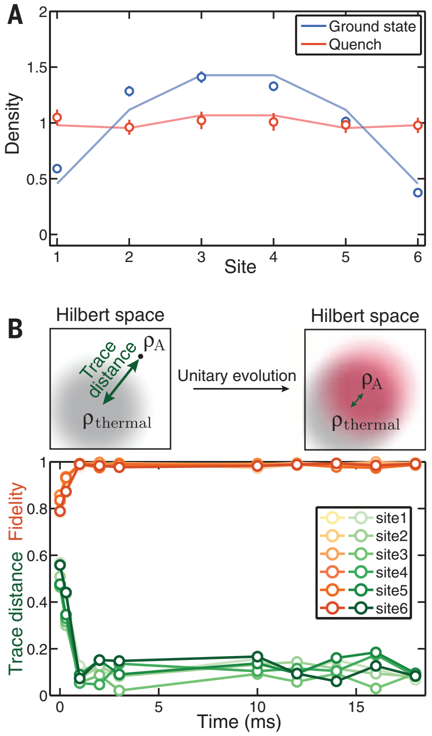

Fig. 5. Observation of local thermalization. (**A**) After quenching to $J/U = 2.6$, the saturated average particle number on each site (density) is nearly equal among the sites of the system, which resembles a system at thermal equilibrium. By comparison, the ground state for the same Bose-Hubbard parameters has appreciable curvature. (**B**) In measuring the probabilities of observing a given particle number on a single site, we can obtain the local single-site density matrix and observe the approach to thermalization. Using two different metrics—trace distance and fidelity—we compare the observed state to the mixed state derived from the subsystem of a canonical thermal ensemble after a quench to $J/U = 0.64$. The trace distance provides an effective distance between the mixed states in Hilbert space, whereas the fidelity is an overlap measure for mixed states. The two metrics illustrate how the pure state subsystem approaches the thermal ensemble subsystem shortly after the quench. The starting value of these quantities is given by the overlap of the initial pure state with the thermal mixed state. Solid lines connect the data points.

Local observables in the thermalized pure state

Our comparisons between the entanglement entropy and the thermal entropy suggest that the pure quantum state that we studied has thermalized properties. We further examined the presence of thermalization by performing a series of measurements of local observables with which we can compare the predictions of various thermal ensembles. As with the entanglement entropy, we can also contrast our observations of the quenched thermalized state with the adiabatically prepared ground state. In Fig. 5A, we show the in situ number density distribution on the six sites for the saturated quenched state and the (superfluid) ground state. Whereas the ground state exhibits considerable curvature, the quenched state exhibits a flat density distribution. This flat density distribution is consistent with a situation in which the constituents of the many-body system collectively thermalize, so that each site is in equilibrium with its neighbors and physically similar.

We can perform a more rigorous test of single-site thermalization by comparing the measured density matrix of each site with the reduced density matrix of a canonical thermal ensemble ρ_A^T (Fig. 5B). Our measurements of the probabilities of observing a given particle number on a site completely characterize that single-site density matrix because there are no coherences between different number states, thanks to superselection rules. With this measured density matrix, we can perform a quantitative comparison with a thermal ensemble by using the trace distance $\left(\frac{1}{2}\text{Tr}(|\rho_A^T - \rho_A|)\right)$ and quantum fidelity $\left(\text{Tr}\left(\sqrt{\sqrt{\rho_A^T}\rho_A\sqrt{\rho_A^T}}\right)\right)$, both of which quantify the similarity of two mixed quantum states. After a short time, these quantities show a quantum fidelity exceeding 99% and a trace distance that fluctuates between 0 and 0.1, indicating the similarity between the local density matrix of a verified pure state and the local density matrix of a thermal state. The correspondence between the observables of a pure state and a thermal state depends on the equivalence of their reduced density matrices within the Hilbert space sampled by the observable. The measurement in Fig. 5B therefore shows that observables for the single-site Hilbert space should agree with the predictions of thermal ensembles.

We now focus on direct comparisons of observables with various thermal ensembles and the theoretical justification for such comparisons. So far, we have focused on the role of entanglement entropy in producing thermal characteristics, but it is the eigenstate distribution resulting from a quench (Fig. 6A) that determines the dynamics of observables, as well as their subsequent saturated values. Therefore, these populated eigenstates should clarify the origin of thermalization, which is the goal of the ETH. The underlying explanation for the ETH is that thermalizing, nonintegrable systems have excited eigenstates that look like nearly random vectors or, equivalently, are described by a Hamiltonian that approximately conforms to random matrix theory (*6*, *13*)—that is, for most bases, each eigenvector projects onto each basis vector with random quantum amplitude. The diffuse probability distribution of the eigenstates in most bases, such as the Fock state basis, is analogous to the chaotic dynamics of a closed classical mechanical system passing through every allowed point of phase space, and in the quantum case this has several consequences. Remarkably, this chaotic eigenstate assumption can be adapted to explain the saturation of measurement observables, the agreement of these saturated observables with thermal ensembles, and the presence of a volume law in the entanglement entropy (*6*, *13*, *38*, *39*). So, whereas in classical mechanical systems, it is the chaos in the temporal dynamics that leads to entropy maximization and thermalization within thermodynamic constraints, in quantum thermalizing systems, it is chaos in the energy eigenstates that generates the analogous behavior in the entanglement entropy and, in turn, causes thermalization.

In Fig. 6, C and D, we compare our measurements to the predictions of thermal ensembles that are illustrated in Fig. 6B. We also compare our results to a grand-canonical ensemble truncated to our total atom number (*24*); this ensemble perhaps most closely models how well the many-body state can act as a reservoir for its constituent subsystems. For each single-site and three-site observable, we show the atom number distributions for two different effective temperatures of $3.8J$ and $11J$, which are achieved by quenching to $J/U = 0.64$ and $J/U = 2.6$, respectively. The data are averaged in the saturated regime over times between 10 and 20 ms, and the error bars are the standard deviation in the measured probabilities. The agreement within the error bars indicates that in this temporal range, our observations remain near the thermal predictions, despite the presence of temporal fluctuations. For the single-site subsystem, the data are in good agreement with all the ensembles considered. Despite the fact that the quenched state is in a large distribution of eigenstates, our data show agreement for the case of a single eigenstate ensemble; this illustrates a key principle of the ETH, which holds that the reduced density matrix and associated observables vary slowly from eigenstate to eigenstate and are therefore relatively insensitive to the breadth of the distribution of populated states from the quench. We show the same comparisons for the three-site case in the bottom two panels. In this case, there is also agreement with most ensembles, though there is relatively less agreement with the single eigenstate and grand-canonical ensembles, particularly for the lower-temperature quench. This variation in agreement may indicate that these ensembles are more sensitive to how the size of the traced-out reservoir compares with the size of the subsystem, which suggests directions for further experiments (*11*, *40*).

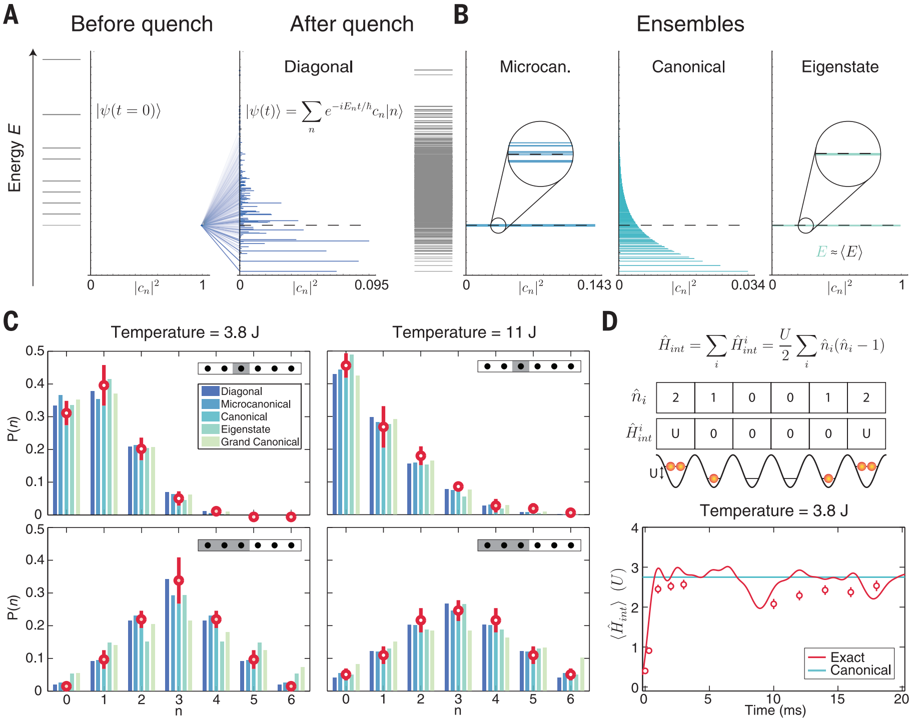

Fig. 6. Local observables in a globally pure quenched state. (**A**) In a quench, the ground state $|g\rangle$ of the initial Hamiltonian (represented in its eigenbasis in the first panel) is projected onto many eigenstates $|n\rangle$ of the new Hamiltonian. The full quantum state undergoes unitary evolution according to the eigenstate amplitudes and energies, c_n and E_n, respectively. $\langle E\rangle$ denotes the full system energy expectation value; $\hbar$ is the reduced Planck's constant. According to the ETH, the expectation value of observables at long times can be obtained from a diagonal ensemble (illustrated by the probability weights in the eigenstates of the quenched Hamiltonian), as well as from a microcanonical ensemble. (**B**) Along with the microcanonical ensemble, several other closely related ensembles (colored lines) are compared to the data. The dashed line indicates the expectation value of the full system energy. (**C**) Thermalization of local observables. For the different temperatures and subsystems shown, the measured number statistics are in excellent agreement with microcanonical and canonical thermal ensembles, verifying the thermal character of the local density matrix (*24*). A grand-canonical ensemble reproduces the data very well, as long as the subsystem is small compared with the full system. The error bars are the standard deviation of our observations over times between 10 and 20 ms. (**D**) Thermalization occurs even for global quantities such as the full-system interaction energy $\langle\hat{H}_{\text{int}}\rangle$. The thermalization dynamics as calculated from our number-resolved images are in close agreement with exact numerical simulation and a canonical prediction (*24*). Error bars are SEM.

The above measurements were performed on specific subsystems, but this technique allows extraction of the average global interaction energy (Fig. 6D). Because the interaction term in Eq. 1 is diagonal in the Fock state basis, we can use our measurements of the final particle configurations to compute the expectation value $\langle\hat{H}_{\text{int}}\rangle$. For the $T = 3.8J$ data, we show a time series of the initial growth in this quantity, which starts at zero because the initial state has a single particle per site. At long times, these observations are in near agreement with the canonical prediction. This measurement is sensitive to the entire six-site system as opposed to some subset of sites, which might suggest that it is global and unlikely to thermalize. Yet $\langle\hat{H}_{\text{int}}\rangle$ undergoes thermalization because it is a sum of local operators, each of which thermalizes and is insensitive to the global purity of the full system. The observed agreement is consistent with the idea that only a small set of operators, such as the global purity that we measured or other specific fine-tuned state projectors, can truly distinguish the pure state that we produced from a thermal state.

Discussion

Our observations speak to a natural mapping between thermalizing quantum mechanical systems and classical mechanical systems composed of itinerant particles. Classical statistical mechanics relies on a fundamental assumption: A system in thermal equilibrium can be found in any microstate that is compatible with the thermodynamic constraints imposed on the system and, as such, is described by an ensemble of maximal entropy (*41*, *42*). Although it is vastly successful, classical statistical mechanics does not itself justify this entropy maximization for closed systems (*13*, *41*), and an open-systems approach only defers the question of thermalization to the union of the bath and the system (*6*). Although ergodicity and time-averaging can provide a justification for entropy maximization in closed classical mechanical systems, ergodicity is not applicable on the same scale at which statistical mechanics is successful, and time-averaging can require exponentially long times (*13*, *41*, *42*). The latter also obscures the fact that there is in reality only one system, which, nevertheless, is well modeled by an entropic ensemble (*41*). Our study, as well as recent theoretical work (*11*, *12*, *35*), hint at a microscopic origin for entropy maximization in a single quantum state, namely, that which is induced by the entanglement that we have measured. Quantum mechanics does not require time-averaging; a single quantum state yields thermalized local observables, and these observables cannot distinguish this thermalized pure state from a mixed thermal ensemble of the same thermodynamic character.

Our measurements open up several avenues for further investigation. Instead of operating with a fixed total system size, it is possible to study how thermalization and fluctuations depend on the size of the system considered (*40*). Conversely, studying integrable Hamiltonians where thermalization fails (*43*), as well as the structure of the associated eigenstate spectrum of such systems, could allow direct tests of the relationship between conserved quantities and thermalization of a quantum state. Lastly, the application of these tools for characterizing the presence of thermalization and entanglement entropy could be powerful in studies of many-body localization, where one of the key experimental signatures is the logarithmic growth of entanglement entropy at long times and the suppression of precisely the thermalization that we have measured in this work (*20*, *44*–*47*).

REFERENCES AND NOTES

1. J. J. Sakurai, *Modern Quantum Mechanics* (Addison Wesley Longman, 1993).
2. P. Calabrese, J. Cardy, *J. Stat. Mech.* **2005**, P04010 (2005).
3. L. Amico, R. Fazio, A. Osterloh, V. Vedral, *Rev. Mod. Phys.* **80**, 517–576 (2008).
4. A. J. Daley, H. Pichler, J. Schachenmayer, P. Zoller, *Phys. Rev. Lett.* **109**, 020505 (2012).
5. J. Schachenmayer, B. P. Lanyon, C. F. Roos, A. J. Daley, *Phys. Rev. X* **3**, 031015 (2013).
6. J. M. Deutsch, *Phys. Rev. A* **43**, 2046–2049 (1991).
7. M. Rigol, V. Dunjko, M. Olshanii, *Nature* **452**, 854–858 (2008).
8. J. Eisert, M. Friesdorf, C. Gogolin, *Nat. Phys.* **11**, 124–130 (2015).
9. R. V. Jensen, R. Shankar, *Phys. Rev. Lett.* **54**, 1879–1882 (1985).
10. M. Srednicki, *Phys. Rev. E* **50**, 888–901 (1994).
11. L. F. Santos, A. Polkovnikov, M. Rigol, *Phys. Rev. E* **86**, 010102 (2012).
12. J. M. Deutsch, H. Li, A. Sharma, *Phys. Rev. E* **87**, 042135 (2013).
13. L. D'Alessio, Y. Kafri, A. Polkovnikov, M. Rigol, https://arxiv.org/abs/1509.06411v1 (2015).
14. C. Neill *et al.*, https://arxiv.org/abs/1601.00600 (2016).
15. G. Clos, D. Porras, U. Warring, T. Schaetz, http://arxiv.org/abs/1509.07712 (2015).
16. S. Trotzky *et al.*, *Nat. Phys.* **8**, 325–330 (2012).
17. T. Langen, R. Geiger, M. Kuhnert, B. Rauer, J. Schmiedmayer, *Nat. Phys.* **9**, 640–643 (2013).
18. R. Geiger, T. Langen, I. E. Mazets, J. Schmiedmayer, *New J. Phys.* **16**, 053034 (2014).
19. T. Langen *et al.*, *Science* **348**, 207–211 (2015).
20. R. Nandkishore, D. A. Huse, *Annu. Rev. Condens. Matter Phys.* **6**, 15–38 (2015).
21. W. S. Bakr *et al.*, *Science* **329**, 547–550 (2010).
22. J. F. Sherson *et al.*, *Nature* **467**, 68–72 (2010).
23. P. Zupancic *et al.*, *Opt. Express* **24**, 13881–13893 (2016).
24. Materials and methods are available as supplementary materials on *Science* Online.
25. R. Islam *et al.*, *Nature* **528**, 77–83 (2015).
26. C. A. Sackett *et al.*, *Nature* **404**, 256–259 (2000).
27. R. N. Palmer, C. Moura Alves, D. Jaksch, *Phys. Rev. A* **72**, 042335 (2005).
28. K. R. A. Hazzard *et al.*, *Phys. Rev. A* **90**, 063622 (2014).
29. R. Horodecki, P. Horodecki, M. Horodecki, K. Horodecki, *Rev. Mod. Phys.* **81**, 865–942 (2009).
30. R. Horodecki, M. Horodecki, *Phys. Rev. A* **54**, 1838–1843 (1996).
31. M. Cheneau *et al.*, *Nature* **481**, 484–487 (2012).
32. P. Richerme *et al.*, *Nature* **511**, 198–201 (2014).
33. P. Calabrese, J. Cardy, *J. Stat. Mech.* **2004**, P06002 (2004).
34. J. Eisert, M. Cramer, M. B. Plenio, *Rev. Mod. Phys.* **82**, 277–306 (2010).
35. J. R. Garrison, T. Grover, https://arxiv.org/abs/1503.00729 (2015).
36. T. Grover, M. P. A. Fisher, *Phys. Rev. A* **92**, 042308 (2015).
37. M. M. Wolf, F. Verstraete, M. B. Hastings, J. I. Cirac, *Phys. Rev. Lett.* **100**, 070502 (2008).
38. D. N. Page, *Phys. Rev. Lett.* **71**, 1291–1294 (1993).
39. K. Hyungwon, "Quantum nonequilibrium dynamics: Transport, entanglement, and thermalization," thesis, Princeton University (2014).
40. V. Yurovsky, A. Ben-Reuven, M. Olshanii, *J. Phys. Chem. B* **115**, 5340–5346 (2011).
41. S. K. Ma, *Statistical Mechanics* (World Scientific, 1985).
42. K. Huang, *Statistical Mechanics* (John Wiley and Sons, 1963).
43. T. Kinoshita, T. Wenger, D. S. Weiss, *Nature* **440**, 900–903 (2006).
44. M. Žnidarič, T. Prosen, P. Prelovšek, *Phys. Rev. B* **77**, 064426 (2008).
45. J. H. Bardarson, F. Pollmann, J. E. Moore, *Phys. Rev. Lett.* **109**, 017202 (2012).
46. M. Serbyn, Z. Papić, D. A. Abanin, *Phys. Rev. Lett.* **110**, 260601 (2013).
47. M. Schreiber *et al.*, *Science* **349**, 842–845 (2015).

ACKNOWLEDGMENTS

We acknowledge helpful discussions with S. Choi, S. Dickerson, J. Eisert, M. Foss-Feig, D. Greif, M. Headrick, D. Huse, M. Olshanii, C. Regal, J. Schachenmayer, and M. Wall. We are supported by grants from the NSF, including an NSF Graduate Research Fellowship (to M.R.); the Gordon and Betty Moore Foundation's Emergent Phenomena in Quantum Systems initiative (grant GBMF3795); and the Multidisciplinary University Research Initiative programs of the Air Force Office of Scientific Research and the Army Research Office.

SUPPLEMENTARY MATERIALS

www.sciencemag.org/content/353/6301/794/suppl/DC1
Materials and Methods
Figs. S1 to S3
Tables S1 and S2

11 March 2016; accepted 11 July 2016
10.1126/science.aaf6725

REPORTS

GEOMORPHOLOGY

Northward migration of the eastern Himalayan syntaxis revealed by OSL thermochronometry

Georgina E. King,[1,2]* Frédéric Herman,[1] Benny Guralnik[3]

Erosion influences the dynamical evolution of mountains. However, evidence for the impact of surface processes on tectonics mostly relies on the circumstantial coincidence of rugged topography, high stream power, erosion, and rock uplift. Using the optically stimulated luminescence (OSL) thermochronometry technique, we quantified the spatial and temporal exhumation of the eastern Himalayan syntaxis. We found increasing exhumation rates within the past million years at the northeast end of the Namche Barwa–Gyala Peri dome. These observations imply headward propagation of erosion in the Parlung River, suggesting that the locus of high exhumation has migrated northward. Although surface processes influence exhumation rates, they do not necessarily engage in a feedback that sets the location of tectonic deformation.

The topography of mountain ranges results from the interplay between climate, tectonics, and surface processes (*1*). A key aspect of this interplay is considered to be that surface processes may influence the dynamics of actively deforming mountain ranges through a system of positive feedbacks involving tectonics and erosion [reviewed in (*2*)]. The efficacy of such a system has been emphasized in analog and numerical experiments (*3*–*5*), which predict that erosion, rather than tectonics, can control the locus of deformation and exhumation of rocks toward Earth's surface (*6*). However, field evidence that supports such models is mostly circumstantial (*5*–*13*) and is based on the observation of a spatial coincidence between rugged topography, high rates of rock uplift, high precipitation, high stream

---

[1] Institute of Earth Surface Dynamics, University of Lausanne, CH-1015 Lausanne, Switzerland. [2] Institute of Geography, University of Cologne, 50923 Cologne, Germany. [3] Netherlands Centre for Luminescence Dating and Soil Geography and Landscape group, Wageningen University, Post Office Box 47, 6700 AA Wageningen, Netherlands.
***Corresponding author. Email: georgina.king@gmail.com**

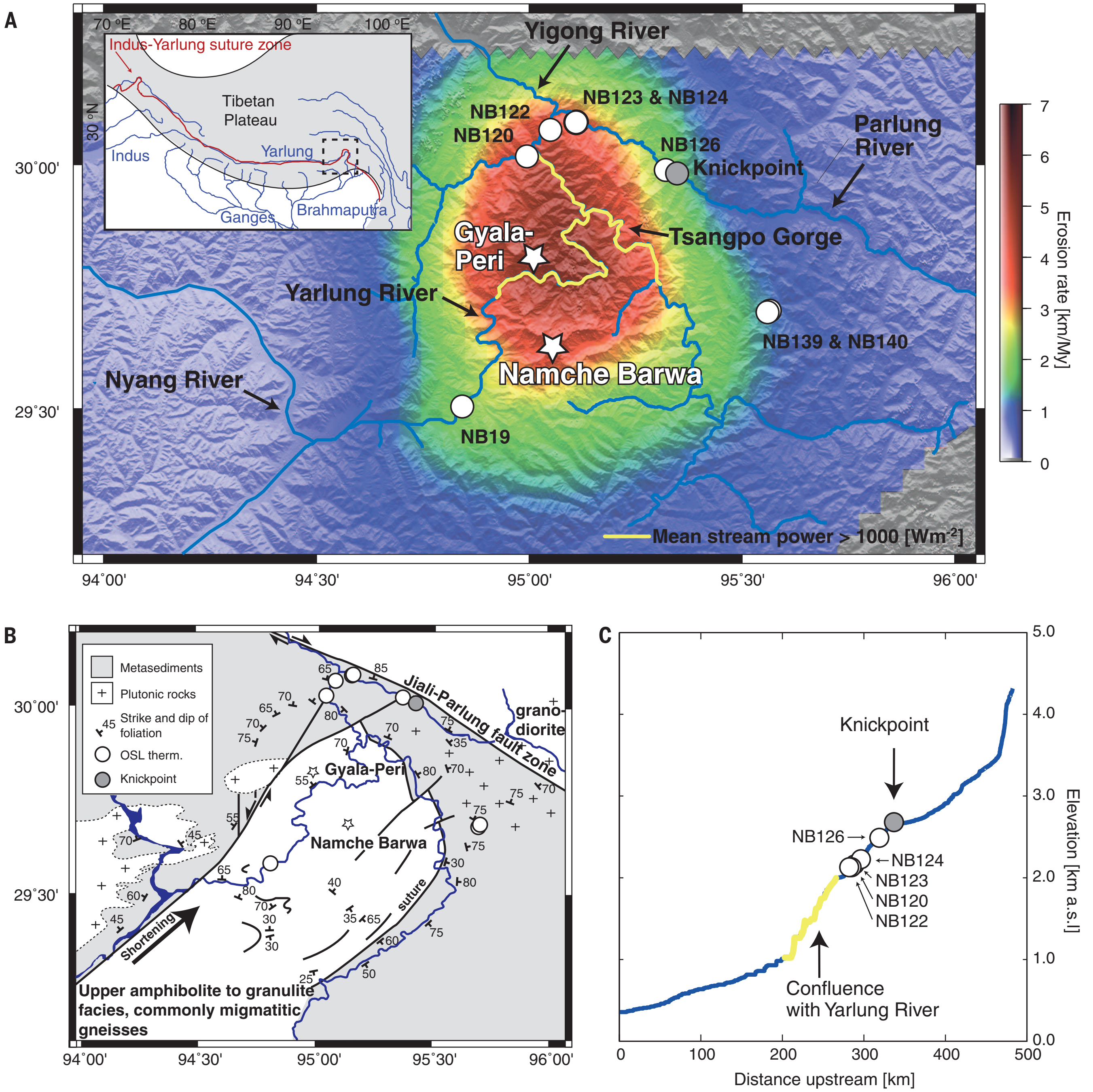

Fig. 1. Quaternary exhumation of Namche Barwa. (**A**) Erosion rates inferred from thermochronometric data (*12*, *22*, *43*–*45*) for the Namche Barwa massif and the neighboring Gyala Peri massif (marked with stars), integrated over the past 2 million years [further details are given in (*20*)]. The high-stream-power zone (>1000 Wm^{-2}), that has been previously identified as coincident with high rates of exhumation (*6*) is indicated in yellow. The locations of the multi-OSL thermochronometry samples for this study are indicated (white circles, not included in the inversion shown in Fig. 2). The inset shows the location of the eastern Himalayan syntaxis. My, million years. (**B**) Key tectonic structures that define the Namche Barwa massif (*21*), relative to sampling locations. The orientation of the north-plunging antiform is clearly defined by the faults and suture zone; the main direction of shortening is indicated. (**C**) Stream profile of the Parlung River along the transect shown in fig. S1, with the multi-OSL thermochronometry sample locations indicated. a.s.l., above sea level.

power, and high erosion rates in several mountain ranges (*7*–*9*). Whether such relationships can be extrapolated back over geological time and whether surface processes are responsible for patterns of tectonic deformation are highly disputed questions (*14*–*16*). If surface processes can dictate tectonics, of all places on Earth they must do so at the eastern Himalayan syntaxis of Namche Barwa. This region hosts some of the most extreme topography and highest erosion rates (>5 mm/year) worldwide and has been cited as one of the most striking examples of a tectonic response to erosion (*6*, *12*).

Exhumation resulting from feedbacks between surface processes and tectonics can be investigated through the determination of spatial and temporal changes in the exhumation rate. Low-temperature thermochronometry measures the cooling histories of rocks as they are exhumed toward Earth's surface in response to erosion (*17*). Measuring cooling ages with high precision on the sub-Quaternary time scale is challenging

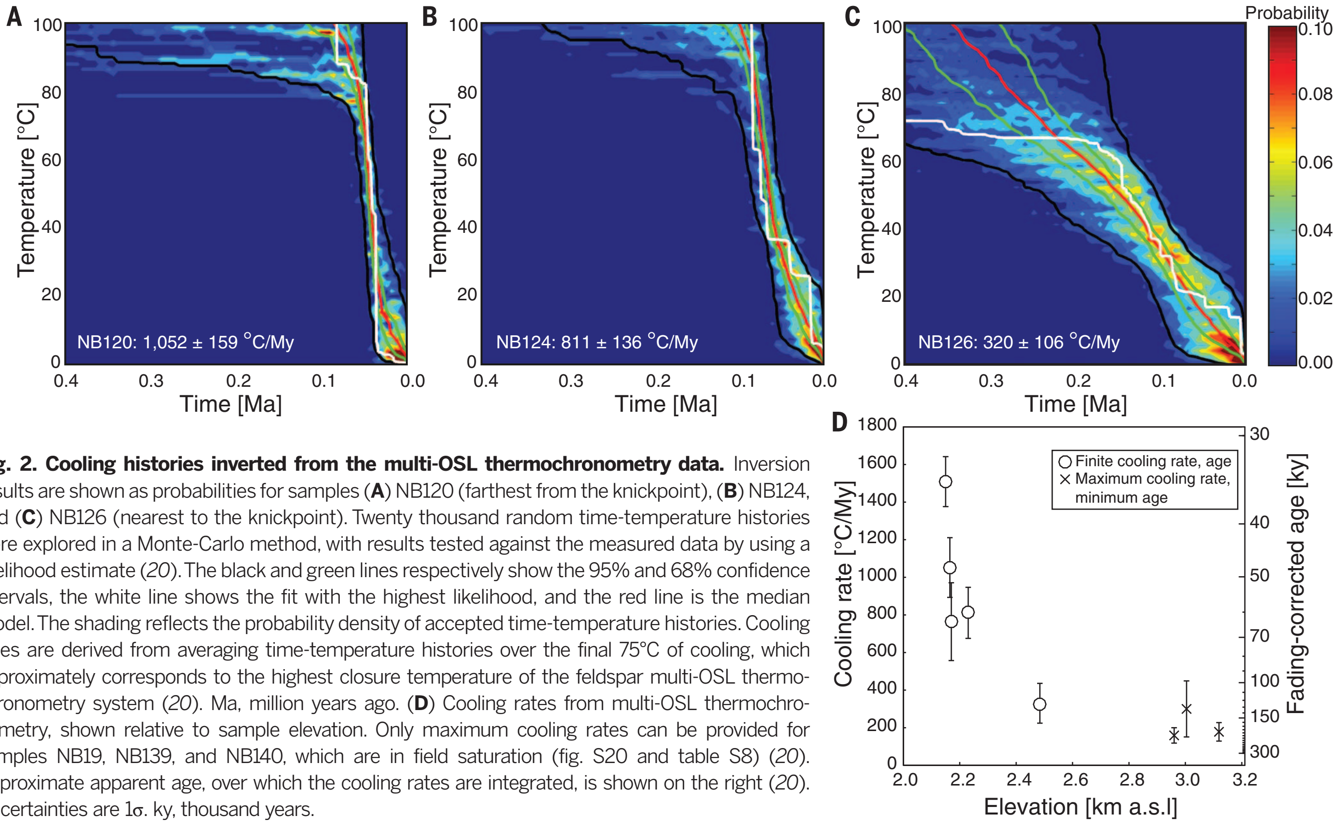

Fig. 2. Cooling histories inverted from the multi-OSL thermochronometry data. Inversion results are shown as probabilities for samples (**A**) NB120 (farthest from the knickpoint), (**B**) NB124, and (**C**) NB126 (nearest to the knickpoint). Twenty thousand random time-temperature histories were explored in a Monte-Carlo method, with results tested against the measured data by using a likelihood estimate (*20*). The black and green lines respectively show the 95% and 68% confidence intervals, the white line shows the fit with the highest likelihood, and the red line is the median model. The shading reflects the probability density of accepted time-temperature histories. Cooling rates are derived from averaging time-temperature histories over the final 75°C of cooling, which approximately corresponds to the highest closure temperature of the feldspar multi-OSL thermochronometry system (*20*). Ma, million years ago. (**D**) Cooling rates from multi-OSL thermochronometry, shown relative to sample elevation. Only maximum cooling rates can be provided for samples NB19, NB139, and NB140, which are in field saturation (fig. S20 and table S8) (*20*). Approximate apparent age, over which the cooling rates are integrated, is shown on the right (*20*). Uncertainties are 1σ. ky, thousand years.

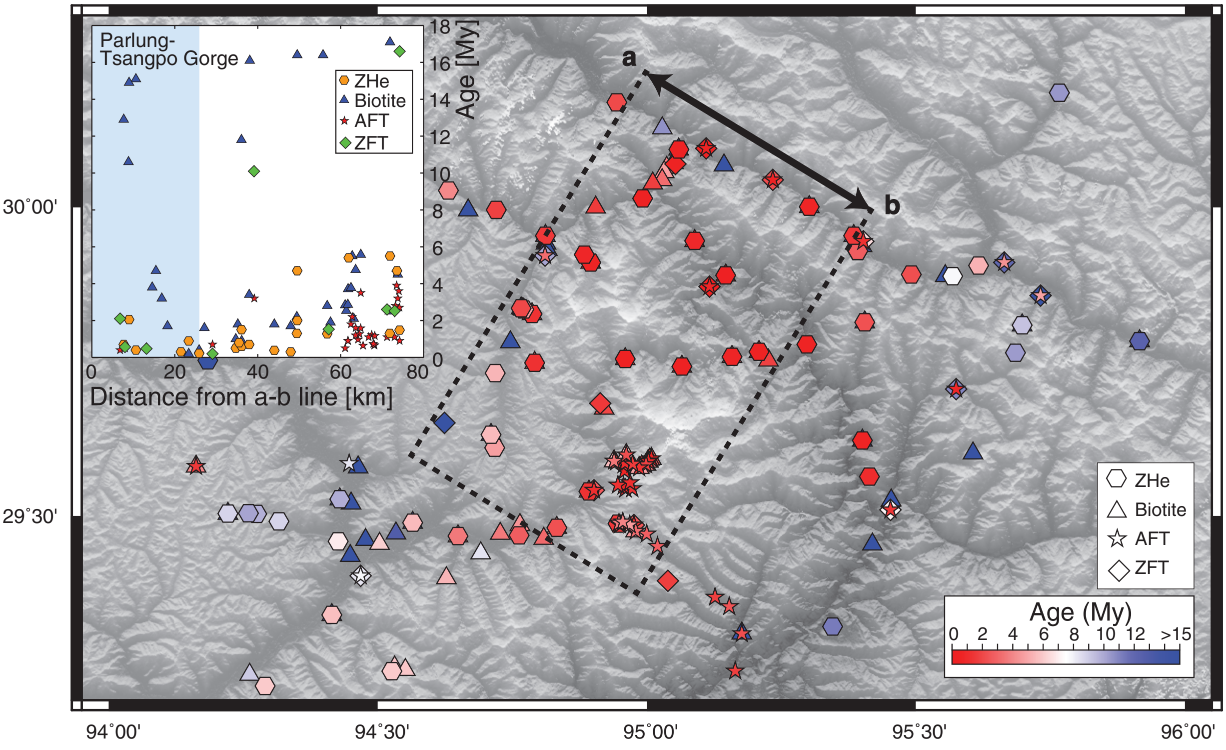

Fig. 3. Thermochronometric data across the massif. (U-Th)/He zircon (ZHe), ^{40}Ar/^{39}Ar in biotite (Biotite), apatite fission track (AFT), and zircon fission track (ZFT) ages are shown (*12*, *22*, *43*–*45*). The inset shows thermochronometric ages from within the black box, plotted along the main axial plane of the antiform (Fig. 1B). Distances are calculated perpendicular to the a–b transect. The blue shaded area in the inset highlights the zone of young AFT, ZHe, and ZFT ages in the northern end of the massif, which is the region of interest in Fig. 4.

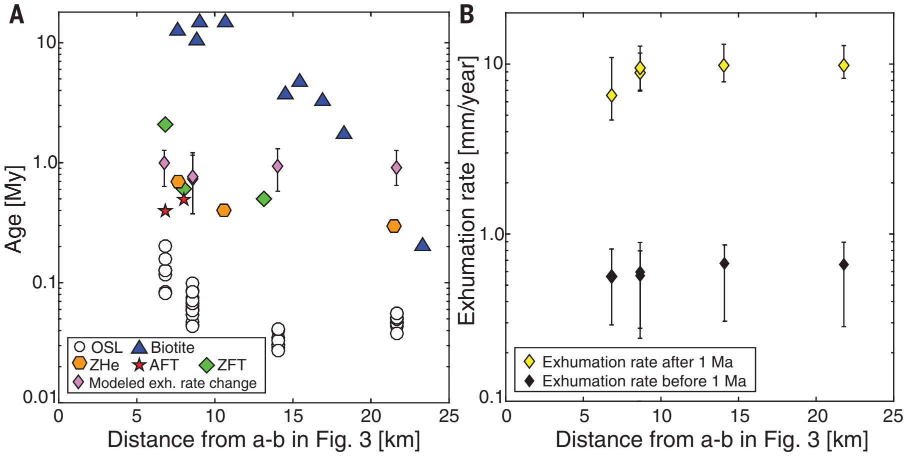

Fig. 4. Thermochronometric ages and timing of exhumation onset. (**A**) The multi-OSL thermochronometry data were inverted together with thermochronometric data obtained nearby (*20*) to determine the timing of the change in the exhumation rate (pink diamonds). (**B**) Inverting the data reveals that exhumation rates have increased by an order of magnitude in the Parlung catchment, from ~0.4 (black symbols) to 5 to 9 mm/year (yellow symbols) within the past ~1 million years [pink diamonds in (A)]. Distances are perpendicular to the a–b transect shown in Fig. 3. Uncertainties are 1σ.

for all established thermochronometric systems. However, the newly developed feldspar optically stimulated luminescence (OSL) thermochronometry system (*18*) and its extension to multiple OSL signals (multi-OSL) (*19*) allows us to constrain cooling histories at high resolution over time scales of 10^4 to 10^5 years in rapidly eroding terrains. OSL thermochronometry involves translating the abundance of trapped electrons in the crystalline lattice of common minerals (quartz and feldspar) into corresponding time-temperature histories (*18–20*).

The Namche Barwa massif is dominated by a north-plunging antiform (*21*), which began growing between 10 (*12*) and less than 4 million years ago (*14*, *22*) and which is characterized by a focused "bullseye" of high exhumation inferred from young thermochronometric ages (*12*, *21–23*). The massif is incised by two major rivers, the Yarlung and Parlung, that flow from the west and northeast, respectively, and drop by about 3 km through the Tsangpo Gorge to connect with the Brahmaputra River downstream (Fig. 1A). The zone of high exhumation is spatially coincident with a zone of high incision and therefore high erosion potential, as indicated by stream power values >1000 Wm^{-2} (Fig. 1A) (*6*). This coincidence forms the foundation of the "tectonic aneurysm" model (*13*), which predicts positive feedbacks between tectonic, rheological, thermal, and surface processes (*5*, *6*, *12*, *13*, *16*) that result in focused exhumation of a thermally weakened zone. Thus, it has been argued that the high exhumation zone has remained spatially stationary and coincident with the high stream power zone for at least 2 million years (*12*, *14*, *16*). However, a limited number of thermochronometric ages (*12*, *22*) of less than 0.7 million years suggests a more recent transition to high erosion rates to the north, upstream of the high-stream-power zone that is now observed in the Parlung River. Such a spatial mismatch means that the rates of erosion might result from a recent northward migration of the high exhumation rates associated with the Namche Barwa antiform (*22*).

The Parlung River exhibits a well-defined knickpoint at ~2700 m elevation, more than 50 km upstream of the high-stream-power zone (Fig. 1C). River knickpoints can be indicative of a change in the rate of rock uplift (*24*) or a drop in base level resulting (for example) from river capture (*22*, *25*). Either of these events initiates a wave of erosion that propagates upstream with time. Therefore, the morphology of the Parlung River may be a consequence of a recent tectonic change and/or drainage reorganization. Rapid incision and high rock uplift rates might not be limited to the Tsangpo Gorge, Namche Barwa, and Gyala Peri massifs (Fig. 1A) and thus may not be spatially stable.

To constrain cooling and exhumation rates in the past 1 million years (Fig. 2), we sampled five locations along the Parlung River across the northern end of the rapidly exhuming area and three locations farther south (Fig. 1). The Parlung River samples, taken from the northern end of the antiform where young thermochronometric ages (<1 million years) have been previously observed (Figs. 1B and 3), yielded feldspar OSL ages in the range of 30 to 150 thousand years. In contrast, the three locations farther south yielded minimum ages of 200 thousand years (Fig. 1). Inverting the finite OSL ages together with other nearby thermochronometric data (*12*, *16*, *22*) using a one-dimensional thermokinematic model (*20*) revealed an order-of-magnitude increase in the exhumation rate in the Parlung River during the past 1 million years (Fig. 4). This increase in exhumation rate is more recent than the ~10- to 4-million-year-old onset of uplift along the Yarlung Tsangpo to the southwest (*12*, *14*, *22*). When we consider the sample locations relative to the Parlung longitudinal profile, the rate of exhumation determined from the multi-OSL thermochronometry data is ~9 km per million years, with the exception of one sample immediately below the knickpoint (NB126), which yielded an exhumation rate of ~6 km per million years (Figs. 1C and 4B).

River drainages can deform in response to tectonic shortening (*26–28*) and, in particular, reorganize themselves in rapidly uplifting areas (*27*, *28*). The propagation of erosion along the Parlung River revealed by our data is possibly associated with drainage reorganization. The Parlung River currently flows from east to west, sharply turns into the Tsangpo Gorge, and links with the Yarlung-Brahmaputra system to the south (Fig. 1A). The Yarlung-Brahmaputra has been established since the early Miocene, 20 million years ago (*29*, *30*), and the peculiar river pattern reflects the capture of a formerly west-to-east flowing Parlung by the Yarlung-Brahmaputra system (*13*, *22*, *31–32*). Our data and modeling results suggest that the capture of the Parlung by the Yarlung-Brahmaputra may have happened in the past 1 million years.

The confluence of the Parlung River and the Yarlung-Brahmaputra system coincides with the main axial plane of the antiform (Fig. 1B), where rock uplift rates are highest (*21*, *22*, *33*). Continued northward migration of the dome along this plane has been predicted by a range of mechanical models (*34–36*) and corresponds to the main shortening direction observed in geodetic data for the area (*37*). When the thermochronometric data are plotted along this plane (*21*, *22*), one can clearly see the zone of young fission track and (U-Th)/He ages that persist in the north (Fig. 3). These observations, combined with our new OSL thermochronometry results, therefore suggest that the combination of river capture and high uplift rates have probably caused the increase in the exhumation rate in the northeastern end of the massif (Fig. 4).

Climate and its variation through time influence the erosion of mountains. Although subject to debate, an increase in erosion related to Cenozoic cooling has been documented (*38*, *39*), and Quaternary cooling has been suggested to have influenced the capture of the Parlung River (*29*). Changes in climate lead to changes in geomorphic processes, and the latitude and therefore climate of mountain ranges has been argued to determine both mountain height and volume (*1*, *40*). The dominance of glacial morphologies at high elevations and well-documented glaciations during the past 1 million years testifies to the presence of large glaciers above 4000 m in the eastern Himalaya syntaxis (*41*), but we cannot explain the feldspar multi-OSL thermochronometry data through a climatic influence alone. An intensification in Quaternary glaciations over the past 1 million years would result in higher rates of erosion at high elevations and would produce a flat river profile similar to that of the Parlung River (*42*). A trend of decreasing exhumation rate with increasing altitude has been reported from other thermochronometric data from Namche Barwa (*22*). Similarly, the feldspar multi-OSL thermochronometry data show lower cooling rates at high elevations (Fig. 2D), implying that glacial erosion is not the key process responsible for the increase in erosion in this area. Instead, increased frequency and extent of glacially dammed lakes (*11*) may inhibit exhumation and therefore cooling rates, potentially explaining this inverse trend.

Although the effect of climate cooling on surface processes during the Quaternary has been documented, validation of an influence of surface processes on tectonics remains elusive. Using multi-OSL thermochronometry of feldspar, we modeled sub-Quaternary cooling rates of the Namche Barwa massif. The data are inconsistent with a spatially stationary model of exhumation for the massif, which has been proposed to reflect feedbacks between river incision and tectonics (*6*). Instead, our data support a continued northeastern migration of exhumation (*22*). These results demonstrate that although surface processes and tectonics may appear to be tightly coupled, stream power has not necessarily engaged in a positive feedback with tectonics in pinning the locus of exhumation within the core of the eastern Himalayan syntaxis.

REFERENCES AND NOTES

1. J. D. Champagnac, P. Molnar, C. Sue, F. Herman, *J. Geophys. Res. Solid Earth* **117**, B02403 (2012).
2. K. X. Whipple, *Nat. Geosci.* **2**, 97–104 (2009).
3. F. Dahlen, J. Suppe, *Geol. Soc. Amer. Spec. Pap.* **218**, 161–178 (1988).
4. C. Beaumont, R. A. Jamieson, M. H. Nguyen, B. Lee, *Nature* **414**, 738–742 (2001).
5. P. O. Koons, P. K. Zeitler, C. P. Chamberlain, D. Craw, A. S. Meltzer, *Am. J. Sci.* **302**, 749–773 (2002).
6. N. J. Finnegan *et al.*, *Geol. Soc. Am. Bull.* **120**, 142–155 (2008).
7. R. C. Thiede, B. Bookhagen, J. R. Arrowsmith, E. R. Sobel, M. R. Strecker, *Earth Planet. Sci. Lett.* **222**, 791–806 (2004).
8. S. J. Dadson *et al.*, *Nature* **426**, 648–651 (2003).
9. P. O. Koons, R. J. Norris, D. Craw, A. F. Cooper, *Geology* **31**, 3–6 (2003).
10. A. L. Berger *et al.*, *Earth Planet. Sci. Lett.* **270**, 13–24 (2008).
11. O. Korup, D. R. Montgomery, *Nature* **455**, 786–789 (2008).
12. P. K. Zeitler, A. S. Meltzer, L. Brown, *Geol. Soc. Amer. Spec. Pap.* **507**, 23–58 (2014).
13. P. K. Zeitler *et al.*, *GSA Today* **11**, 4–9 (2001).
14. P. Wang *et al.*, *Science* **346**, 978–981 (2014).
15. P. Wang *et al.*, *Science* **349**, 799 (2015).
16. P. K. Zeitler, P. O. Koons, B. Hallet, A. S. Meltzer, *Science* **349**, 799 (2015).
17. J. Braun, P. van der Beek, G. Batt, *Quantitative Thermochronology: Numerical Methods for the Interpretation of Thermochronological Data* (Cambridge Univ. Press, 2006).
18. B. Guralnik *et al.*, *Earth Planet. Sci. Lett.* **423**, 232–243 (2015).
19. G. E. King, F. Herman, R. Lambert, P. G. Valla, B. Guralnik, *Quat. Geochronol.* **33**, 76–87 (2016).
20. Materials and methods are available as supplementary materials on *Science* Online.
21. J.-P. Burg *et al.*, *Terra Nova* **9**, 53–56 (1997).
22. D. Seward, J.-P. Burg, *Tectonophysics* **451**, 282–289 (2008).
23. E. Enkelmann, T. A. Ehlers, P. K. Zeitler, B. Hallet, *Earth Planet. Sci. Lett.* **307**, 323–333 (2011).
24. K. X. Whipple, G. E. Tucker, *J. Geophys. Res. Solid Earth* **104**, 17661–17674 (1999).
25. J. L. Schmidt *et al.*, *Earth Planet. Sci. Lett.* **430**, 448–457 (2015).
26. B. Hallet, P. Molnar, *J. Geophys. Res. Solid Earth* **106**, 13697–13709 (2001).
27. S. Castelltort *et al.*, *Nat. Geosci.* **5**, 744–748 (2012).
28. S. D. Willett, S. W. McCoy, J. T. Perron, L. Goren, C. Y. Chen, *Science* **343**, 1248765 (2014).
29. K. Lang, K. W. Huntington, *Earth Planet. Sci. Lett.* **397**, 145–158 (2014).
30. L. Bracciali, Y. Najman, R. R. Parrish, S. H. Akhter, I. Millar, *Earth Planet. Sci. Lett.* **415**, 25–37 (2015).
31. L. Seeber, V. Gornitz, *Tectonophysics* **92**, 335–367 (1983).
32. M. Clark *et al.*, *Tectonics* **23**, TC1006 (2004).
33. J. P. Burg *et al.*, *J. Asian Earth Sci.* **16**, 239–252 (1998).
34. J. P. Burg, Y. Podladchikov, *Int. J. Earth Sci.* **88**, 190–200 (1999).
35. R. Bendick, T. A. Ehlers, *Geophys. Res. Lett.* **41**, 5861–5867 (2014).
36. D. M. Whipp Jr., C. Beaumont, J. Braun, *J. Geophys. Res. Solid Earth* **119**, 5077–5096 (2014).
37. T. D. Gupta *et al.*, *Tectonophysics* **655**, 15–26 (2015).
38. P. Molnar, *Annu. Rev. Earth Planet. Sci.* **32**, 67–89 (2004).
39. F. Herman *et al.*, *Nature* **504**, 423–426 (2013).
40. D. L. Egholm, S. B. Nielsen, V. K. Pedersen, J. E. Lesemann, *Nature* **460**, 884–887 (2009).
41. L. A. Owen, M. W. Caffee, R. C. Finkel, Y. B. Seong, *J. Quaternary Sci.* **23**, 513–531 (2008).
42. N. Brozović, D. W. Burbank, A. J. Meigs, *Science* **276**, 571–574 (1997).
43. X. J. Yu *et al.*, *Chin. Sci. Bull.* **56**, 1123–1130 (2011).
44. Y. L. Lei, D. L. Zhong, J. Q. Ji, C. Z. Jia, J. Zhang, *Quat. Sci.* **28**, 584–590 (2008).
45. J.-Y. Tu *et al.*, *J. Asian Earth Sci.* **105**, 223–233 (2015).

ACKNOWLEDGMENTS

This research was funded by Swiss National Fund grants PP00P2-38956 and 200021-127127 and Netherlands Organisation for Scientific Research (NWO) Veni grant 863.15.026. R. Lambert, P. Valla, S. Willett, and O. Korup are thanked for insightful discussions. J.-P. Burg is thanked for providing samples and feedback. All of the raw data are available in the supplementary materials. The comments of three anonymous reviewers substantially improved the manuscript.

SUPPLEMENTARY MATERIALS

www.sciencemag.org/content/353/6301/800/suppl/DC1
Materials and Methods
Figs. S1 to S22
Tables S1 to S10
References (*46*–*79*)
Databases S1 to S64

15 January 2016; accepted 28 July 2016
10.1126/science.aaf2637

SEPARATION MEMBRANES

Reverse osmosis molecular differentiation of organic liquids using carbon molecular sieve membranes

Dong-Yeun Koh,[1] Benjamin A. McCool,[2] Harry W. Deckman,[2] Ryan P. Lively[1]*

Liquid-phase separations of similarly sized organic molecules using membranes is a major challenge for energy-intensive industrial separation processes. We created free-standing carbon molecular sieve membranes that translate the advantages of reverse osmosis for aqueous separations to the separation of organic liquids. Polymer precursors were cross-linked with a one-pot technique that protected the porous morphology of the membranes from thermally induced structural rearrangement during carbonization. Permeation studies using benzene derivatives whose kinetic diameters differ by less than an angstrom show kinetically selective organic liquid reverse osmosis. Ratios of single-component fluxes for *para*- and *ortho*-xylene exceeding 25 were observed and *para*- and *ortho*- liquid mixtures were efficiently separated, with an equimolar feed enriched to 81 mole % *para*-xylene, without phase change and at ambient temperature.

Molecular separation processes are essential in the production of clean water, pharmaceuticals, commodity and specialty chemicals, and fuels. Approximately 40 to 60% of the energy used in the production of these materials is spent on separation and purification processes (*1*). In downstream chemical processes, selective removal of high-value alkyl-aromatics is required for the production of synthetic fibers, solvents, and films and is performed with energy-intensive techniques such as crystallization and simulated moving bed adsorption (*2*). The separation of xylene isomers is especially challenging because of the similarities in physical properties [i.e., boiling point, molecular weight, and kinetic diameters (*3*)]. Membrane-based processes may reduce the energy intensity of these separations if effective separation materials can be developed.

Organic solvent nanofiltration has emerged as a separation process for purification of liquid organic solvents from high-value products such as pharmaceuticals (*4*). However, organic solvent nanofiltration membrane materials do not have the necessary molecular specificity to efficiently separate molecules of similar size. Thus, we explore the potential for organic solvent reverse osmosis (OSRO) using asymmetric carbon molecular sieve (CMS) hollow fiber membranes.

CMS membranes possess molecularly sized slit-like transport pathways that are provided by the disordered two-dimensional (2D), sp^2-hybridized carbon structure (figs. S1 and S2 and table S1). These result in higher productivity than that of cage-like zeolite structures while providing similar molecular selectivities (*5*–*8*). Selectivity is the driving-force–normalized relative ratio of the mass transport rates of different molecules permeating through the membrane (see eqs. S1 to S16 for discussion on the development of the selectivity eq. S17) and is considered to be an intrinsic property of the membrane. The term “separation factor” is an engineering parameter often used in membrane separation processes and is the ratio of permeate composition over the feed composition (eq. S18) (*9*). CMS membranes have proved effective at reducing energy

---

[1] School of Chemical and Biomolecular Engineering, Georgia Institute of Technology, Atlanta, GA 30332, USA. [2] Separations and Process Chemistry, Corporate Strategic Research, ExxonMobil Research and Engineering, Annandale, NJ 08801, USA.
*Corresponding author. Email: ryan.lively@chbe.gatech.edu

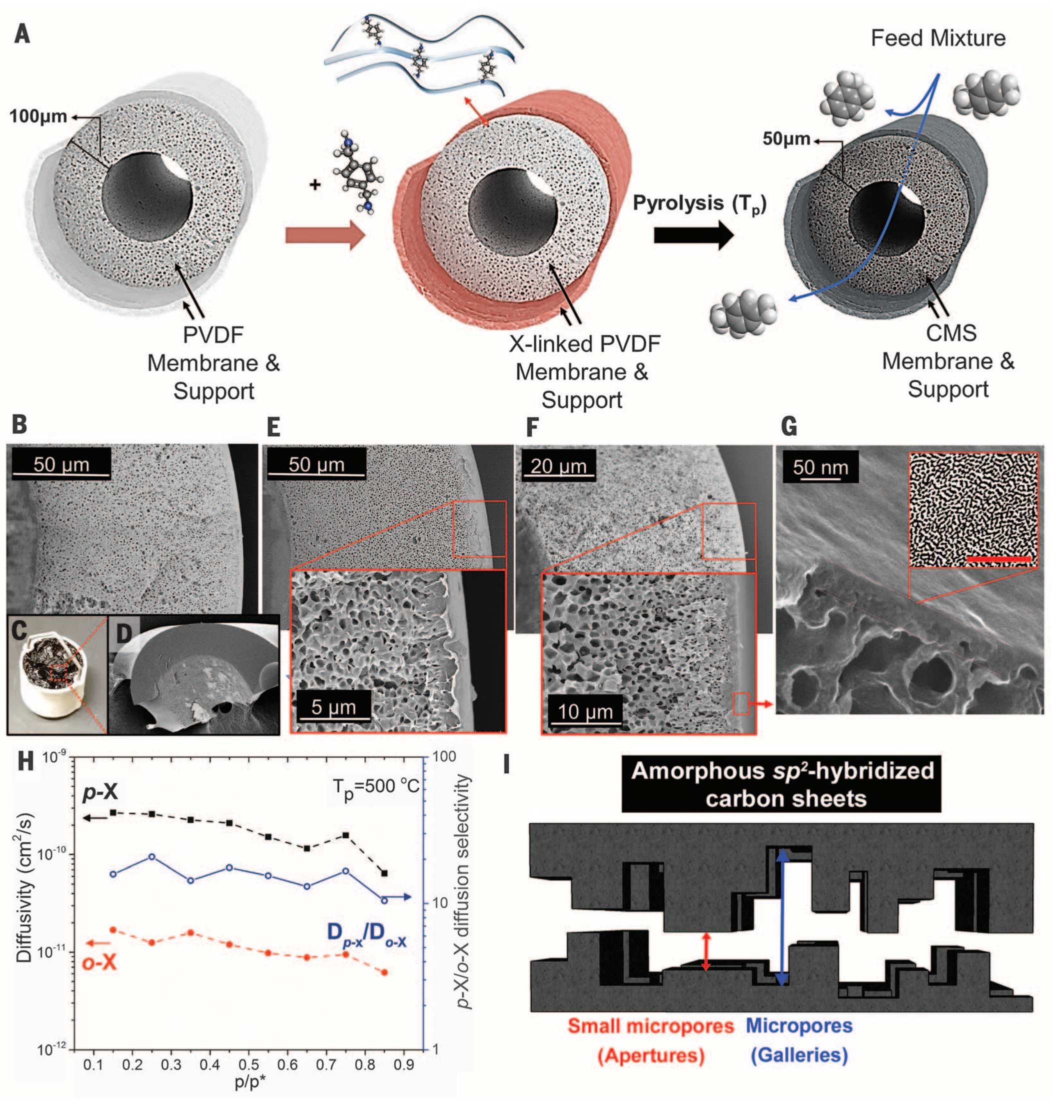

Fig. 1. Formation process, morphology, and diffusion characterization of asymmetrically porous CMS hollow fiber membranes. (**A**) Schematic of the formation process. Separation of liquid feeds of *p*-X and *o*-X isomers occurs via pressure-driven reverse osmosis. (**B**) Scanning electron microscopy (SEM) image of asymmetrically porous PVDF hollow fiber with thin-membrane layer. (**C**) CMS cake formed after the pyrolysis of PVDF hollow fiber precursor. (**D**) SEM image of pyrolysis product of PVDF hollow fiber precursor. The porous morphology is lost, and a dense carbon molecular sieve is obtained. (**E** and **F**) SEM images of cross-linked PVDF hollow fiber precursor and asymmetric CMS fiber membrane, respectively. Inset figures show magnified images of outer skin layer and the porous substructure that supports the membrane. (**G**) HeIM image of the CMS membrane formed from cross-linked PVDF. Inset figure shows enhanced TEM image visualizing bimodal micropore size distribution in the CMS membrane. Inset scale bar represents 5 nm. (**H**) Diffusion coefficients and corresponding diffusion selectivity between *p*-X and *o*-X in CMS film with T_p = 500°C. (**I**) An idealized schematic of the slit-like CMS microstructure, exhibiting small micropores (apertures, molecular sieving dimension) and micropores (galleries).

demands in a variety of gas separation processes such as olefin/paraffin separations (*10*, *11*), natural gas purification (*12*, *13*), and air separations (*14*) with high–glass transition temperature glassy polymers (typically polyimides) as precursors.

A schematic illustrating the synthesis and formation process for our CMS membranes is shown in Fig. 1A, fig. S3, and table S2. Non–cross-linked asymmetrically porous poly(vinylidene fluoride) (PVDF) hollow fiber membranes were found to undergo an irreversible loss of meso- and macroporosity during pyrolysis (Fig. 1, B to D). The resulting fibers were fused together to form a highly dense CMS sample that is not useful for separations owing to prohibitively slow mass transfer rates. Differential scanning calorimetry and dynamic mechanical analysis (DSC-DMA) (fig. S4) on neat PVDF films shows that the PVDF loses storage modulus when heated above room temperature and eventually yields at around 100°C, which is below its melting point of 165°C. The loss of meso- and macroporosity in the hollow fiber membrane is caused by the complete loss of PVDF storage modulus near the melting temperature of the polymer. Densification of the meso- and macroporous substructure of the hollow fiber results in substantial loss of molecular flux through the membrane owing to an increase in effective membrane thickness. Bhuwania *et al.* (*15*) introduced sol-gel cross-linking via organic-alkoxy silanes (vinyltrimethoxysilane) to partially restrict the substructure collapse of polyimide fibers during pyrolysis. We hypothesized that cross-linking polymer precursors will result in the retention of storage modulus in hollow fiber membranes, thereby maintaining the critical meso- and macroporosity of the substructure during pyrolysis. We developed a one-pot postspinning cross-linking technique for a variety of PVDF morphologies (i.e., dense flat sheet, porous flat sheet, and asymmetric hollow fibers; fig. S5). This technique is based on the dehydroflourination of PVDF at room temperature by base treatment (NaOH + MeOH) and subsequent nucleophilic attack (i.e., Michael addition) by *para*-xylylenediamine to form covalent bonds between PVDF chains (table S3 and fig. S6). In contrast to neat PVDF, cross-linked PVDF fibers gain storage modulus when heated and maintain a high storage modulus (>450 MPa) above 300°C (fig. S4). Notably, the cross-linked PVDF fibers are resistant to the porous substructure collapse during pyrolytic treatments >500°C; i.e., the asymmetrically porous structure of the hollow fiber membranes were maintained after pyrolysis (Fig. 1, E and F). The cross-linked PVDF continuously evolves –CF radicals at temperatures >150°C and thus likely initiates the formation of a microporous carbon-enriched structure at relatively low temperatures without losing meso- or macroscale morphology (figs. S7 to S10). As confirmed by electron microscopy, helium ion microscopy (HeIM), and membrane permeation, cross-linking the as-spun PVDF hollow fibers "locked in" the asymmetrically porous fiber structure, and the fiber morphology remained unchanged after the cross-linking process. A continuous CMS layer (as confirmed by gas permeation experiments, table S4) with a sub–100 nm thickness can be observed (Fig. 1G) on the outer layer of the meso- and macroporous hollow fiber, and subsequent experiments quantitatively support this HeIM observation (eqs. S19 and S20). Current state-of-the-art gas separation CMS membranes based on glassy

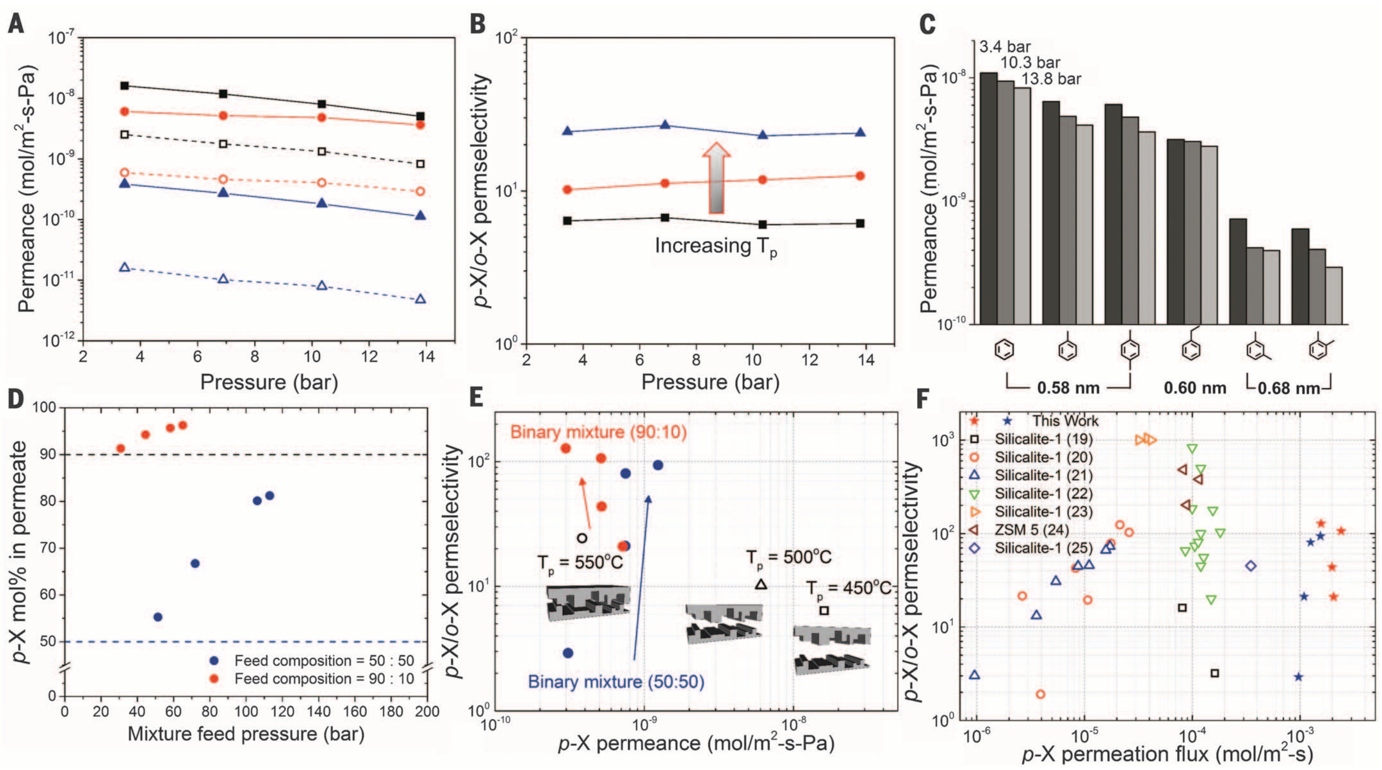

Fig. 2. Transport properties of CMS hollow fiber membranes. (**A**) Room-temperature single-component permeation of *p*-X (closed symbol solid lines) and *o*-X (open symbol dashed lines) through membranes with different T_p = 450° (black square), 500s° (red circles), and 550°C (blue triangles). (**B**) *p*-X/*o*-X ideal permselectivities (eq. S17) of CMS membranes with different T_p = 450° (black squares), 500° (red circles), and 550°C (blue triangles). (**C**) Single-component permeation of benzene, toluene, ethylbenzene, and xylene isomers with different transmembrane pressure in membranes pyrolyzed at 500°C. (**D**) Room-temperature mixture permeation (OSRO) with CMS membranes pyrolyzed at 550°C. *Para*-xylene compositions in permeate when using equimolar mixture (50:50 mol/mol) and a 90:10 (mol/mol) mixture of *p*-X/*o*-X are shown as blue circles and red circles, respectively. (**E**) Ideal selectivity (measured from single-component hydraulic permeances) of *p*-X/*o*-X in CMS membrane with varying pyrolysis temperatures (T_p) of 450° (open square), 500° (open triangle), and 550°C (open circle). Mixture selectivity of *p*-X/*o*-X permeating through asymmetric CMS hollow fiber membranes pyrolyzed at 550°C with different feed composition; 50/50 (blue circles) and 90/10 (red circles). Blue and red arrows indicate increasing transmembrane pressure (*N* = 2 membrane modules). (**F**) *p*-X/*o*-X permselectivities of different advanced membranes as a function of permeation flux (mol m^{-2} s^{-1}). Silicalite-1 membranes (black square) at 100° to 390°C and 2.7 × 10^{-3} bar of *p*-X (*19*). RTP (rapid thermal processing)-treated *c*-oriented MFI (red circle) at 50° to 200°C and 3 × 10^{-3} bar of *p*-X (*20*). *c*-Oriented MFI membranes (blue triangle) at 50° to 200°C and 4.5 × 10^{-3} bar of *p*-X (*21*). *a*- and *b*-Oriented silicalite-1 membranes (green down-triangle) at 200°C and 3.2 × 10^{-3} bar of *p*-X (*22*). *b*-Out-of-plane–oriented silicalite-1 membranes (orange right-triangle) at 100° to 200°C and 5.0 × 10^{-3} bar of *p*-X (*23*). *b*- and *c*-oriented ZSM-5 membranes (brown left-triangle) at 100° to 200°C and 4.5 × 10^{-3} bar of *p*-X (*24*). Pervaporation result for template-free secondary grown silicalite-1 membranes (purple diamond) at 50°C and 1 bar of *p*-X (*25*).

polyimides have membrane thicknesses of ~1 μm (*14*). An HeIM image of a CMS membrane derived from cross-linked PVDF reveals the nanoscopic membrane layer, and a transmission electron microscopy (TEM) image qualitatively reveals the bimodal distribution of micropore sizes in the carbon (Fig. 1G, inset). Additional electron and helium-ion micrographs are available in the supplementary materials (figs. S11 to S13). The CMS hollow fiber membranes are somewhat more brittle than their PVDF or cross-linked PVDF precursors. The CMS hollow fibers can be bent to a radius of curvature of ~45 mm (fig. S5), exhibit an ultimate yield stress of 6.5 MPa at 0.4% strain during a tensile strength test (fig. S14), have sufficient mechanical integrity to be assembled into hollow fiber membrane modules, and can withstand transmembrane pressures >100 bar without failure (eq. S21).

Nitrogen physisorption was used to quantify the microporous dimensions of the CMS membranes created at different pyrolysis temperatures (T_P) and to further elucidate the molecular separation capability of the CMS fibers (fig. S15). CMS fibers derived from cross-linked PVDF (T_p = 550°C) exhibit a 3900% greater surface area than both neat and cross-linked fibers owing to the creation of a microporous structure during pyrolysis (table S5). Pore-size calculations based on the experimental isotherms reveal an extremely narrow bimodal distribution of pores, with a micropore population ranging from 6.0 to 6.3 Å in size and another population ranging from 8.0 to 8.4 Å in size (fig. S16). The kinetic diameter of benzene derivatives produced from petrochemical processes falls into this range.

The OSRO concept is enabled almost entirely by the diffusive selectivity of the CMS membrane for a small molecule over a larger molecule. Diffusion rates of *p*-xylene (*p*-X, 5.8 Å) and *o*-xylene (*o*-X, 6.8 Å) in CMS films (fig. S17) were measured in vapor uptake experiments at 25° to 45°C. The micropore dimensions of the films were confirmed to be very similar to those of the fibers (fig. S18). *Ortho*-xylene showed substantially slower uptake compared to that of *p*-X regardless of the pyrolysis temperature (figs. S19 to S22). The diffusion coefficients of *p*-X in CMS flat sheets are 5 to 25 times higher than that of *o*-X, depending on the pyrolysis temperature. Diffusion coefficients of these isomers and the diffusion selectivity (i.e., $D_{p\text{-X}}/D_{o\text{-X}}$) as a function of the vapor relative pressure (p/p_0) are shown in Fig. 1H. The diffusion selectivity decreases slightly with the relative pressure, and the selectivity near vapor saturation is in the range of 10 to 15 for the films pyrolyzed at 500°C. The diffusion selectivity increased to 25 to 30 for the films pyrolyzed at 550°C. As expected, the total mass uptake at each relative pressure for *p*-X and *o*-X in CMS flat sheet exhibits only small differences as shown in the full sorption isotherms (figs. S23 to S25), confirming that the dominant source of membrane selectivity is kinetics. The actual OSRO permeation process is quite different from that of simple vapor diffusion experiments. Indeed, there are many nonidealities that influence the transport rates in the OSRO experiments, such as pore flow contributions, large transmembrane pressures, ambiguity in mass transfer barrier thickness (in the case of asymmetric fibers), changes in diffusion rates near unit activity, and nonideal isotherm shapes at pressures greater than the molecule's vapor pressure.

We characterized the ideal selectivity between *p*-X and *o*-X on the basis of their permeance ratios through the CMS fiber as a function of transmembrane pressure (experimental setup shown in fig. S26). The CMS fibers exhibited molecular sieving properties with relatively high *p*-X permeances at room temperature (Fig. 2, A and B); moreover, the single-component permselectivities closely matched the kinetic selectivities measured in the independent vapor diffusion experiments. CMS fibers prepared at higher final pyrolysis temperature showed much higher ideal *p*-X/*o*-X selectivities—up to ~26 at T_p = 550°C. Figure 2C highlights the molecular sieving characteristics of the CMS membrane (T_P = 500°C) in single-component permeation experiments of a series of benzene derivatives. The substantial permeance decrease observed for molecules with kinetic diameters larger than 5.8 to 5.9 Å agree with the pore-size calculations (fig. S16) and the vapor diffusion rate experiments. *Para*-xylene permeance decreased by a factor of 20 when the pyrolysis temperature was changed from 450° to 550°C, indicating the formation of more narrow—yet more selective—transport channels at higher pyrolysis temperature in the microporous carbon materials; similar changes in CMS transport properties have been observed in gas separations (*16*). The asymmetrically porous structure of the CMS hollow fibers remained unchanged after testing, as seen from the electron and HeIM micrographs (figs. S12 and S27), which highlights the good mechanical and chemical resistance of these CMS membranes.

The ultimate arbiter of novel membrane processes is performance when challenged with realistic feed conditions. *Para*-xylene/*ortho*-xylene feed mixtures were supplied to the shell side of hollow fiber membrane modules at high pressures (50 to 120 bar). The OSRO process occurs without any phase change of the permeating compounds; i.e., a liquid feed is supplied to the membrane, and liquid permeate and retentate are extracted from the membrane. OSRO is a pressure-driven process that must overcome the osmotic pressure difference across the membrane to achieve useful fluxes and molecular selectivities. A 50:50 and a 90:10 (mol/mol) mixture of *p*-X/*o*-X were used as feed mixtures for the membranes formed via 550°C pyrolysis of cross-linked PVDF hollow fibers. Each membrane was tested for 1 week on stream at each feed condition and transmembrane pressure. The CMS hollow fiber membranes rejected *o*-X from the mixture feed upon pressurization beyond the osmotic gradient (Fig. 2D and table S6) at room temperature, and the rejection increased sigmoidally with increasing pressure. Liquid permeances and selectivities of the membrane are shown as filled symbols in Fig. 2E and in figs. S28 to S30. For both sets of OSRO experiments, the selectivity of the membrane measured with the mixture feed becomes higher than the "ideal" selectivity based on the single-component permeation results. The real permselectivity (eq. S17 and table S7) of the membrane is expected to deviate from the ideal permselectivity of the membrane because of complex nonideal mixture diffusion effects of liquid molecules in highly loaded microporous spaces. Similar *p*-X purity enhancements are found for a ternary *p*-X/*o*-X/*m*-X mixture (table S6), although the separation factor decreases by ~30%. It is interesting that in some cases, zeolite membranes fail to efficiently separate aromatic hydrocarbons from binary and ternary mixture feeds when vapor permeation (100° to 200°C) and pervaporation (25° to 75°C) are used, because the slowest species determine the permeation rates in uniform micropores at highly loaded conditions (*17*, *18*). However, in the pressure-driven OSRO process, especially in amorphous microporous membranes with many different slit-like transport routes available for penetrant permeation, the faster species in both the ideal single-component and nonideal mixture permeation experiments is the same. Figure 2F shows the comparison of *p*-X permeation flux with *p*-X/*o*-X selectivity from this work versus state-of-the-art MFI-type zeolite membranes as listed in the figure caption. The uniform micropores of MFI provide excellent permselectivities for the high-temperature (100° to 400°C) *p*-X/*o*-X vapors. The OSRO membranes exhibit order-of-magnitude increases in flux relative to these zeolite membranes while still maintaining high molecular selectivities of ~100 (separation factors approaching 4.3, table S8). It is important to note that the zeolite membranes are typically tested at low-pressure (~10^{-3} bar) and much-higher-temperature (100° to 300°C) xylene vapors, as opposed to the room-temperature, high-pressure liquids that are used in the CMS OSRO membranes. High-temperature, low-pressure operation keeps the xylene loading in the zeolites within the dilute regime, which increases permeance. At these conditions, the *p*-X permeance in MFI is an order of magnitude or greater than the CMS OSRO membranes. There is considerable evidence that the zeolite membrane permeance and selectivity decrease substantially at higher xylene loadings and driving forces (*19*); moreover, increasing downstream xylene partial pressures will further decrease the separation factor relative to the selectivity (figs. S31 and S32). Our calculations indicate (eqs. S22 to S24) that when operated at low temperature and high *p*-X loadings, the *p*-X permeance of the MFI membranes is on the same order of magnitude as the CMS OSRO membranes. Indeed, increasing the *p*-X driving force in MFI membranes can only result in decreasing *p*-X permeance. Notably, the overall energy intensity for pumping fluids (the primary energy cost in OSRO separations) is substantially lower than for separation processes that require phase change, such as pervaporation.

We have demonstrated the efficacy of OSRO for the separation of xylene isomers and provide a potential candidate for energy-efficient small-molecule (<1 nm in size) separations that are prevalent in the supply chains of a variety of industries. The CMS-enabled OSRO devices discussed here exhibited more than 10 times higher xylene isomer fluxes relative to state-of-the-art zeolite membrane materials and excellent mechanical resistance, with the ability to withstand more than 100 bar of transmembrane pressure. In addition, they performed a bulk separation of xylene isomers, while achieving major reductions in operating temperature and removing the necessity for energy-intensive phase change.

REFERENCES AND NOTES

1. J. L. Humphrey, G. E. Keller, *Separation Process Technology* (McGraw-Hill, 1997).
2. M. A. Fahim, T. A. Alsahhaf, A. Elkilani, in *Fundamentals of Petroleum Refining* (Elsevier, Amsterdam, 2010).
3. R. Szostak, *Handbook Of Molecular Sieves: Structures* (Springer, 1992).
4. P. Marchetti, M. F. Jimenez Solomon, G. Szekely, A. G. Livingston, *Chem. Rev.* **114**, 10735–10806 (2014).
5. P. S. Tin, H. Y. Lin, R. C. Ong, T.-S. Chung, *Carbon* **49**, 369–375 (2011).
6. T. A. Centeno, A. B. Fuertes, *J. Membr. Sci.* **160**, 201–211 (1999).
7. H. Suda, K. Haraya, *J. Phys. Chem. B* **101**, 3988–3994 (1997).
8. K. M. Steel, W. J. Koros, *Carbon* **41**, 253–266 (2003).
9. R. W. Baker, J. G. Wijmans, Y. Huang, *J. Membr. Sci.* **348**, 346–352 (2010).
10. L. Xu *et al.*, *J. Membr. Sci.* **423-424**, 314–323 (2012).
11. M. Rungta, L. Xu, W. J. Koros, *Carbon* **50**, 1488–1502 (2012).
12. H. Wang, L. Zhang, G. R. Gavalas, *J. Membr. Sci.* **177**, 25–31 (2000).
13. M. Ogawa, Y. Nakano, *J. Membr. Sci.* **162**, 189–198 (1999).
14. Y. K. Kim, H. B. Park, Y. M. Lee, *J. Membr. Sci.* **243**, 9–17 (2004).
15. N. Bhuwania *et al.*, *Carbon* **76**, 417–434 (2014).
16. M. Rungta, L. Xu, W. J. Koros, *Carbon* **85**, 429–442 (2015).
17. C. D. Baertsch, H. H. Funke, J. L. Falconer, R. D. Noble, *J. Phys. Chem.* **100**, 7676–7679 (1996).
18. K. Wegner, J. Dong, Y. S. Lin, *J. Membr. Sci.* **158**, 17–27 (1999).
19. J. Hedlund *et al.*, *Microporous Mesoporous Mater.* **52**, 179–189 (2002).
20. J. Choi *et al.*, *Science* **325**, 590–593 (2009).
21. G. Xomeritakis, Z. Lai, M. Tsapatsis, *Ind. Eng. Chem. Res.* **40**, 544–552 (2001).
22. T. C. T. Pham, T. H. Nguyen, K. B. Yoon, *Angew. Chem. Int. Ed.* **52**, 8693–8698 (2013).
23. K. V. Agrawal *et al.*, *Adv. Mater.* **27**, 3243–3249 (2015).
24. Z. Lai *et al.*, *Science* **300**, 456–460 (2003).
25. W. Yuan, Y. S. Lin, W. Yang, *J. Am. Chem. Soc.* **126**, 4776–4777 (2004).

ACKNOWLEDGMENTS

Supported by ExxonMobil Research and Engineering. Membrane fabrication, characterization, and testing were carried out by D.-Y.K. Mass transport analysis was conducted by B.A.M. and H.W.D. R.P.L. conceived the research. We thank R. J. Colby (ExxonMobil Corporate Strategic Research) for assistance with the helium ion microscopy images. We thank S. H. Pang (Georgia Institute of Technology) for assistance with the TEM images and F. Zhang (Georgia Institute of Technology) for assistance with the dynamic mechanical analysis. Detailed descriptions of materials and methods, membrane fabrication protocols, membrane spectroscopic characterization, mass transport experiments, OSRO experiments, and mass transport analysis are in the supplementary materials. D.-Y.K., B.A.M., H.W.D., and R.P.L. are inventors on a provisional patent application (62/254792) submitted by ExxonMobil Research and Engineering that covers hydrocarbon reverse osmosis membranes and applications.

SUPPLEMENTARY MATERIALS

www.sciencemag.org/content/353/6301/804/suppl/DC1
Materials and Methods
Figs. S1 to S32
Tables S1 to S8
Supplementary Text
References (*26–37*)

4 January 2016; accepted 29 July 2016
10.1126/science.aaf1343

CRYSTALLOGRAPHY

Coordinative alignment of molecules in chiral metal-organic frameworks

Seungkyu Lee,[1,2,3,4] Eugene A. Kapustin,[1,2,3,4] Omar M. Yaghi[1,2,3,4,5]*

A chiral metal-organic framework, MOF-520, was used to coordinatively bind and align molecules of varying size, complexity, and functionality. The reduced motional degrees of freedom obtained with this coordinative alignment method allowed the structures of molecules to be determined by single-crystal x-ray diffraction techniques. The chirality of the MOF backbone also served as a reference in the structure solution for an unambiguous assignment of the absolute configuration of bound molecules. Sixteen molecules representing four common functional groups (primary alcohol, phenol, vicinal diol, and carboxylic acid), ranging in complexity from methanol to plant hormones (gibberellins, containing eight stereocenters), were crystallized and had their precise structure determined. We distinguished single and double bonds in gibberellins, and we enantioselectively crystallized racemic jasmonic acid, whose absolute configuration had only been inferred from derivatives.

Single-crystal x-ray diffraction is a powerful technique for the definitive identification of chemical structures. Although most molecules and molecular complexes can be crystallized, often enthalpic and entropic factors introduce orientational disorder that prevents determination of a high-resolution structure (*1*). Several strategies based on the inclusion of guests in a host framework (*2*–*4*) that helps maintain molecular orientation have been used to overcome this challenge. However, most of these methods rely primarily on weak interactions to induce crystalline order of the included molecules.

Here, we demonstrate a strategy for crystallization of molecules within the pores of chiral metal-organic frameworks (MOFs) (*5*). This strategy provides the following advantages: (i) The molecules make covalent bonds to well-defined metal sites of the MOF; these bonds anchor them and lower their motional degrees of freedom, thereby promoting their alignment into an ordered pattern across the interior of the crystalline framework. (ii) The absolute structure of the chiral MOF serves as a reference for the direct determination of the absolute configuration of bound chiral molecules (*6*). This latter feature avoids the reported pseudosymmetry problems that have obscured the absolute structures that specify the enantiomorph in achiral host framework systems (*7*–*9*).

Specifically, we used this coordinative alignment (CAL) method to successfully crystallize 16 different molecules in the interior of MOF-520 [$Al_8(\mu\text{-}OH)_8(HCOO)_4(BTB)_4$; BTB = 1,3,5-benzenetribenzoate] (*10*). These molecules represent a range of functionality, flexibility, and complexity. The first 12 are relatively simple molecules: benzoic acid **1**, methanol **2**, ethylene glycol **3**, 3-nitrophenol **4**, heptanoic acid **5**, 3-hydroxybenzoic acid **6**, 3,5-diaminobenzoic acid **7**, trimesic acid **8**, 4-bromophenol **9**, 2-(2,6-dichloranilino)phenylacetic acid (diclofenac) **10**, 5,7-dihydroxy-3-(4-hydroxyphenyl)chromen-4-one (genistein) **11**, and *tert*-butyloxycarbonyl-(*RS*)-3-amino-1,2-propanediol **12**. In addition, this method led us to successfully crystallize two different plant hormone types within the MOF: gibberellins (form A_1, **13**, and form A_3, **14**) with eight stereocenters, and (±)-jasmonic acid (**15**, **16**). The precision of the crystal structures with only 30% occupancy of the bound gibberellins enabled us to distinguish the single bond in **13** from the double bond in **14**, this being the only difference between the two complex molecules. The crystal structure of (±)-jasmonic acid, whose absolute configuration had only been inferred from derivatives, was obtained enantioselectively, with each enantiomorph of the MOF binding only one enantiomer of jasmonic acid.

We chose MOF-520 as the framework for implementing the CAL method of crystallization because of its high crystallinity, robustness, and chirality (Fig. 1). Its secondary building units (SBUs) are rings of eight aluminum octahedra sharing corners through eight μ-OHs and four formate ligands. Each of these SBUs is linked by 12 BTB units, and each BTB is linked to three SBUs to make a three-dimensional, extended porous framework. Two types of ellipsoidal pores are formed from elongated arrangements of SBUs that are octahedral (10.01 Å × 10.01 Å × 23.23 Å) and tetrahedral (5.89 Å × 5.89 Å × 6.21 Å). The framework of MOF-520 crystallizes in the noncentrosymmetric space group $P4_22_12$, with a chiral atomic arrangement. The absolute

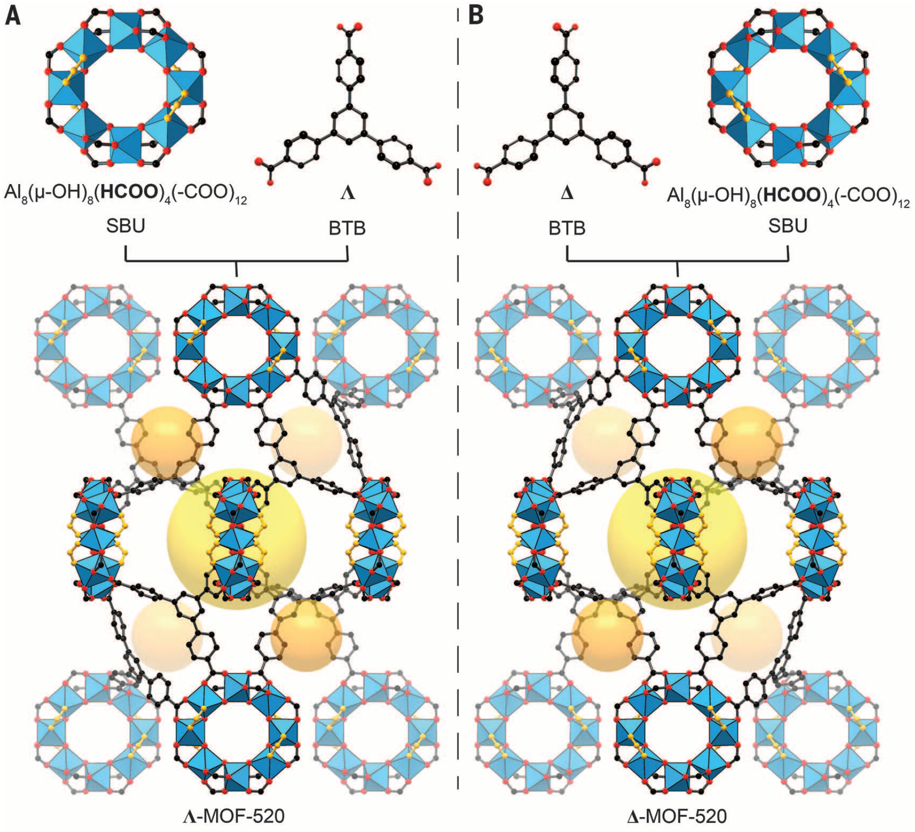

Fig. 1. Structures of MOF-520 enantiomorphs and their building units. MOF-520 comprises the SBU, $Al_8(\mu\text{-}OH)_8(HCOO)_4(\text{-}COO)_{12}$, and BTB linker. Each SBU is coordinated by 16 carboxylates, 12 from BTB linkers and 4 from formate ligands (highlighted in yellow on the SBU). The absolute structure descriptors Λ-MOF-520 (**A**) and Δ-MOF-520 (**B**) are assigned on the basis of absolute configuration of the BTB linker. The large yellow and small orange balls represent the octahedral and tetrahedral pores, respectively. Color code: black, C; red, O; blue polyhedra, Al.

---

[1] Department of Chemistry, University of California, Berkeley, CA 94720, USA. [2] Materials Sciences Division, Lawrence Berkeley National Laboratory, Berkeley, CA 94720, USA. [3] Kavli Energy NanoSciences Institute, Berkeley, CA 94720, USA. [4] Berkeley Global Science Institute, Berkeley, CA 94720, USA. [5] King Abdulaziz City for Science and Technology, Riyadh 11442, Saudi Arabia.
*Corresponding author. Email: yaghi@berkeley.edu

structure of each enantiomorph is designated as Λ or Δ according to the chirality of the BTB linker in the respective crystal structure (Fig. 1, A and B). Although each single crystal is nearly enantiomorphically pure according to the Flack parameters of the refined structures—0.049(17) for Λ and 0.031(11) for Δ (*11*)—the overall bulk sample is a racemic conglomerate containing both enantiomorphs (tables S1 to S3).

The distinctive nature of this MOF lies in each of the aluminum SBUs having four formate ligands in addition to 12 carboxyl units from BTB linkers to complete the octahedral coordination sites of the aluminum centers (Fig. 1). These formate ligands occupy two sites on each face of the SBU in a chiral tetrahedral arrangement with D_2 symmetry. We anticipated that through acid-base chemistry, we could substitute these formates with incoming organic molecules such as carboxylates, alkoxides, and phenolates (Fig. 2A). Given that the interior of the MOF has large octahedral pores, it is reasonable to expect molecules of varying size and complexity to diffuse into this space and covalently bind to the metal sites (Fig. 2B), thereby aligning themselves within the MOF to be amenable to x-ray structure determination (see below).

Before examining the incorporation of molecules into the pores of MOF-520, we used single-crystal x-ray diffraction (SXRD) techniques (*10*, *12*) to ensure full characterization of the structure of the MOF. We confirmed the chemical composition of the evacuated MOF-520 by ^{1}H nuclear magnetic resonance (NMR) of digested samples (calculated formate/BTB ratio, 1:1; found, 1:0.93) and by elemental analysis [calculated weight percent (wt %), C 58.81, H 3.14, N 0.0; found wt %, C 59.20, H 3.19, N < 0.2]. The porosity of MOF-520 was confirmed by measurement of N_2 type I isotherm at 77 K, which led to a final uptake of 770 cm^3 g^{-1} at 1 atm, similar to a calculated uptake, 821 cm^3 g^{-1}, based on the structure obtained from the SXRD data (both values at standard temperature and pressure). The MOF-520 samples were also characterized by infrared spectroscopy to ensure the absence of solvent in the pores, thermal gravimetric analysis to confirm the thermal stability of the MOF, and powder x-ray diffraction to confirm the bulk purity of the crystals (*12*).

Molecules **1** to **16** have functionalities that include primary alcohol, phenol, vicinal diol, and carboxylic acid (Fig. 2A). These molecules were covalently bonded to the MOF by immersion of single crystals of MOF-520 in a concentrated solution of the respective molecule followed by heating (40° to 100°C) for at least 12 hours (*12*). One of the single crystals in the resulting racemic conglomerate batch was chosen and SXRD data were collected. The architectural robustness and high chemical stability of MOF-520 enabled the substitution of the symmetrically equivalent four formates in the SBU with the carboxylates of incoming molecules and their covalent binding to the SBUs with full retention of crystallinity. In the case of alkoxides and phenolates, only two formates on the same face of the SBU were replaced in addition to μ-OHs (Fig. 2B). This substitution pattern led to a doubling of the unit cell in the *c*-direction without affecting the connectivity of the MOF backbone. Consecutive SBUs along *c* were substituted strictly on the opposite face of the ring, leading to a change in the space groups of the Λ- and Δ-frameworks, $P4_22_12$, to an enantiomorphic pair, $P4_32_12$ (Λ) and $P4_12_12$ (Δ), respectively.

Relatively small achiral molecules were chosen to describe in detail the four different binding modes in Δ-MOF-520 for all incoming molecules: benzoic acid **1** as a carboxylic acid, methanol **2** as a primary alcohol, ethylene glycol **3** as a vicinal diol, and 3-nitrophenol **4** as a phenol. Benzoic acid shared the same binding mode as formate, where for **2**, two methoxides replaced two formates on the same face of the ring and doubly bridged the Al in a μ^2 manner, thus changing the corner-sharing Al octahedra to edge-sharing. This geometry change induced further substitution of two μ-OHs with the methoxides. Overall, four alkoxides replaced two formates and two μ-OHs, with two coordinated formates remaining on the C_2 symmetric SBU. The binding mode of **3** was similar to that of **2**, where the formates and μ-OHs were substituted and the same geometry change of the SBU occurred. The main difference is that the remaining two formates are now bonded to the SBU as terminal ligands, which had previously been bridging ligands on the SBU of Δ-MOF-520. In the case of **4**, two different binding modes were observed with positional disorder; one is similar to that of **2**, and the other is shown in Fig. 2B (two of four phenolic oxygen atoms are bridging).

The resulting substituted frameworks, MOF-520-**2** and MOF-520-**3**, have a larger pore width relative to the original MOF-520 [distance between the Al atoms of adjacent SBUs = 14.70 ± 0.04 Å and 14.13 ± 0.05 Å, respectively, versus 13.73 ± 0.04 Å for MOF-520] (fig. S16). Thus, we used MOF-520 for the crystallization of incoming molecules **1** to **10**, **12**, **15**, and **16**; MOF-520-**2** for **11**; and MOF-520-**3** for **13** and **14**.

The crystal structures of all molecules bound to the MOF were determined by SXRD and show the binding modes outlined above. All of the structures were refined anisotropically (Fig. 3). In general, the value of anisotropic displacement parameters of the incorporated molecules increased with their distance from the binding sites; this was as expected, because the orientations of the bound

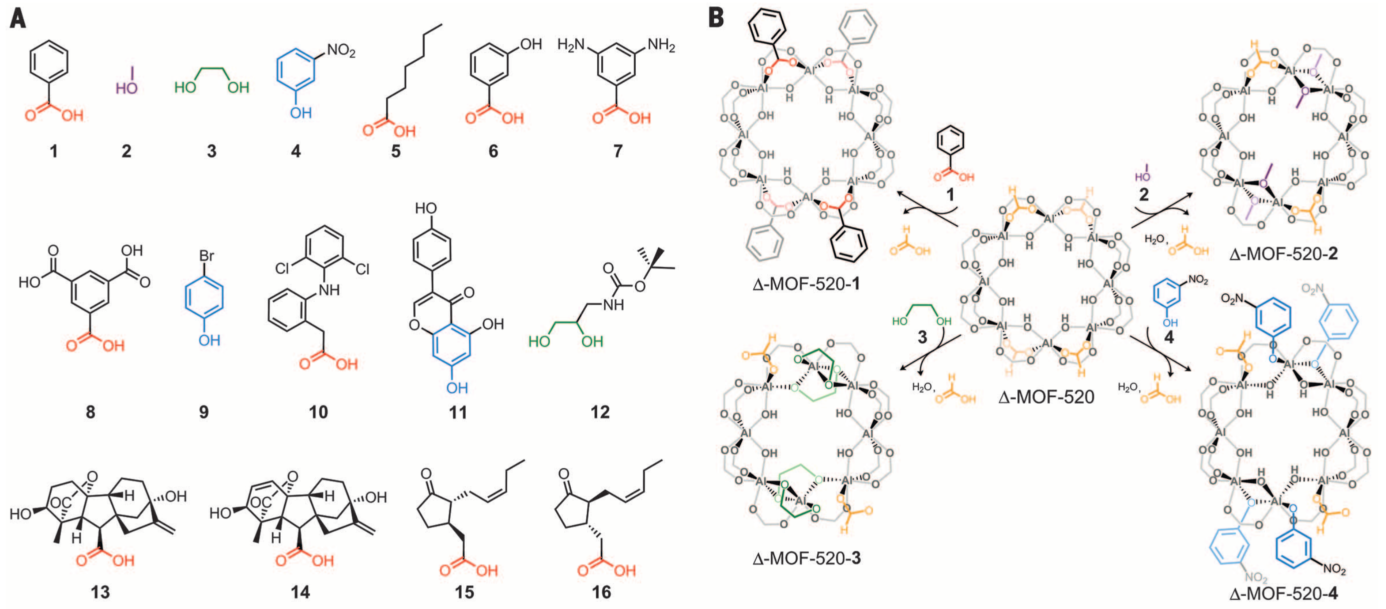

Fig. 2. Structures of incoming molecules (1 to 16) and coordination modes of their deprotonated forms on the SBU of Δ-MOF-520. (**A**) The structures of **1** to **16** represent the molecules binding to the SBU, where their functionalities are highlighted with colors: red, carboxylic acid; purple, primary alcohol; green, vicinal diol; blue, phenol. (**B**) The SBU of Δ-MOF-520 is shown in the center, with the four formate ligands (yellow) highlighted. The deprotonated forms of **1** to **4** replace all (**1**) or some (**2** to **4**) of the formate ligands and μ-OH on the SBU; the resulting coordination modes and the functionalities of the molecules are colored. For clarity, the chiralities of Λ-MOF-520-**2** and -**4** are converted to Δ configuration.

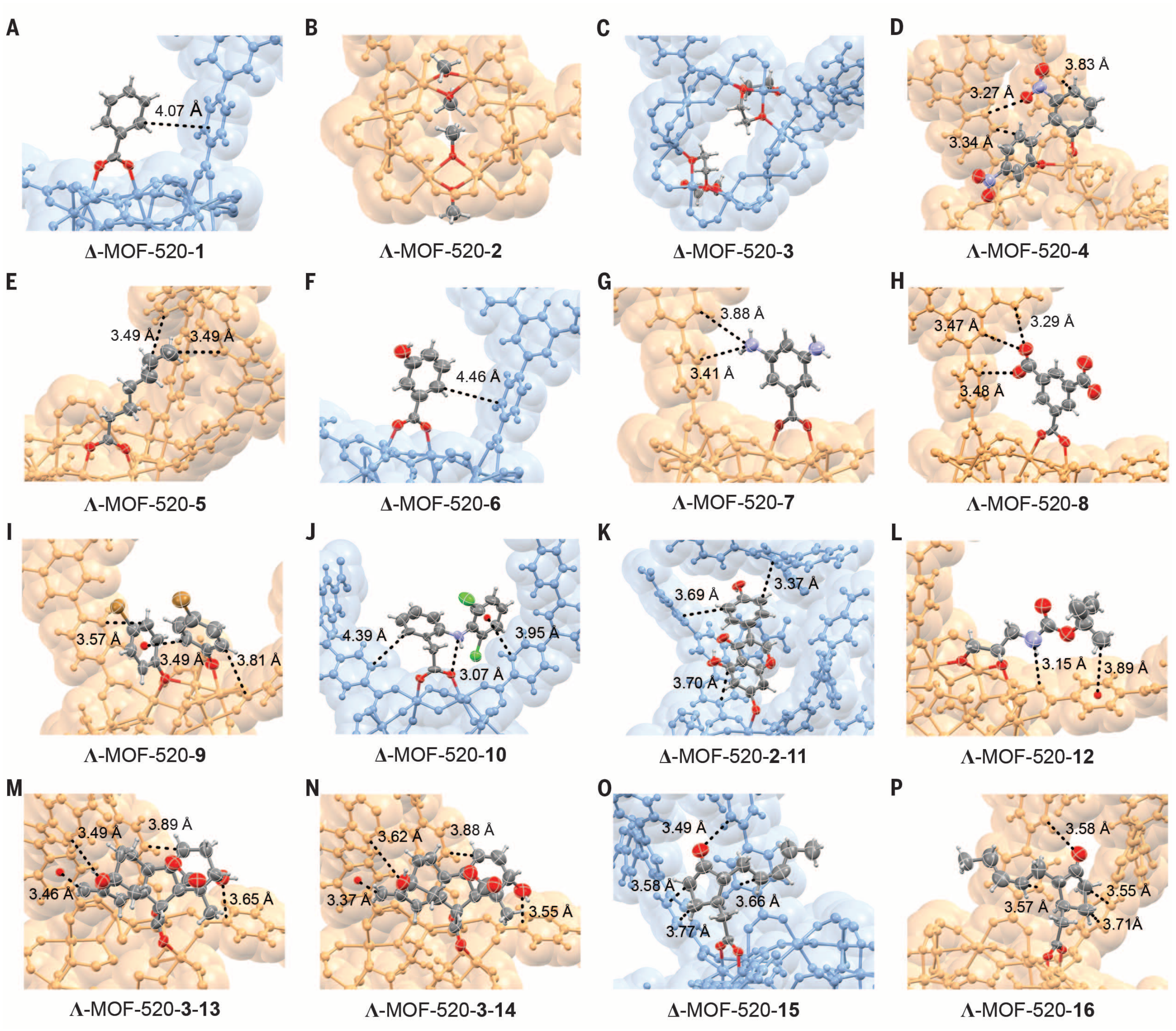

Fig. 3. Refined structures of 1 to 16 crystallized in Λ- or Δ-MOF-520. (**A** to **P**) The refined structures of the molecules obtained from SXRD data are indicated with 50% probability thermal ellipsoids. The surroundings of the coordination sites of Λ- and Δ-MOF-520 are shown with orange and blue space-filling models, respectively. Intramolecular interactions [except for (A) and (F)] between the moieties of the molecules and the surroundings of the coordination sites are indicated with dotted lines and distances (Å). In the case of positional disorder, only one conformation of bound molecules is shown for clarity. Color code: gray, C; red, O; white, H; pale violet, N; green, Cl; brown, Br.

molecules are mainly governed by a single site of covalent attachment. Those parts of the bound molecules that are far from the binding sites are stabilized by noncovalent interactions such as π-π interactions and weak hydrogen bonds with the aromatic rings and carboxylates of the framework (Fig. 3 and table S4).

The bound molecules **1**, **2**, **3**, and **6** are simple and small in their structure; their ordering within the MOF is sustained only by covalent bonds to aluminum, with no weak interactions with the framework observed (Fig. 3, A, B, C, and F). The covalent binding is sufficient to anchor these molecules and lower their degrees of freedom, an aspect that is present in all crystal structures of **1** to **16**; weak interactions play a role for some molecules but not all. For example, in Δ-MOF-520-**6**, the closest distance from the covalent bond **6** to the framework is 4.46 Å, which corresponds to the distance between the *ortho*-carbon of **6** and the adjacent aromatic ring of the MOF; this indicates that there are no contributing secondary interactions with the framework (Fig. 3F). However, the entire structure of **6** was solved without ambiguity. The OH group of **6** is pointing away from the framework, which suggests a possible repulsive interaction with the adjacent aromatic ring of the linker. No detectable residual electron density was observed in the structure refinement for the second OH group at the other *meta* position.

Within the MOF, molecules **10** and **11** were also ordered by anchoring through covalent bonding to aluminum, but their order was further enhanced by the presence of π-π (T-shaped for **10** and parallel-displaced for **11**) and hydrogen bonding (N–H···O for **10** and O–H···π for **11**) interactions to the framework (Fig. 3, J and K). Similar interactions were also observed for the molecules **4**, **5**, **7** to **9**, and **12** to **16**. Details of the structural information (including the covalent bond distances, the types of closest noncovalent interactions between the bound molecules and

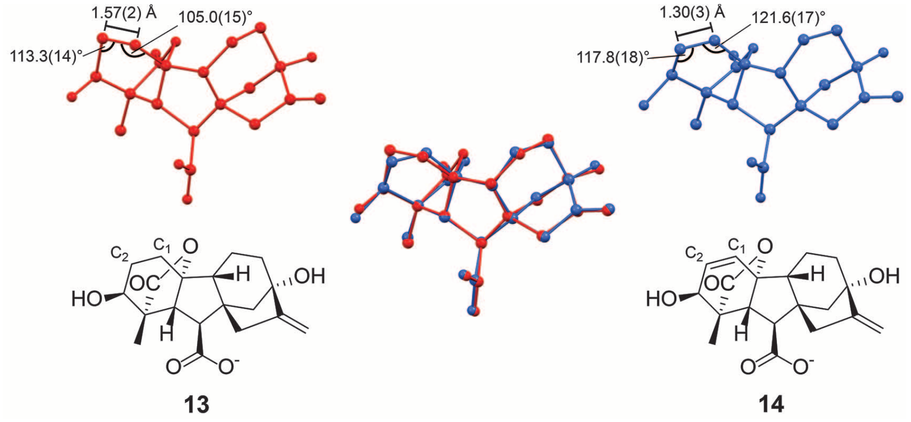

Fig. 4. Comparison of the molecular geometries of 13 and 14. Ball-and-stick models of the structures of **13** and **14** crystallized in Λ-MOF-520-**3** are shown in red and blue, respectively. Their conformations are overlaid in the middle. The structural difference, a single bond between C_1 and C_2 for **13** and a double bond for **14**, can be distinguished from the distances and the angles indicated on the models. For clarity, only atoms C_1 and C_2 are labeled.

the framework, and refinement parameters) are given in table S4.

Because the CAL method yields highly ordered arrangements for molecules within the MOF, their structure can be determined even with low occupancy at the binding sites. This feature makes it possible to obtain structures of larger and more complex molecules with high accuracy and to determine the absolute configuration of chiral molecules with high certainty. The structures of gibberellins **13** and **14**, two derivatives of a natural plant hormone, illustrate the power of the CAL method (Fig. 3, M and N, and Fig. 4). All nonhydrogen atoms of these complex molecules with eight stereocenters could be assigned from an occupancy of only 30%. The final structures were refined without any geometrical constraints or restraints applied on the gibberellin molecules (tables S17 and S18). The accuracy of our method is documented by the characterization of the subtle structure difference between **13** and **14**, where we find C_1–C_2 to be a single bond (1.57 ± 0.02 Å) in **13** and a double bond (1.30 ± 0.03 Å) in **14**. The C–C–C bond angles at C_1 and C_2 are 105.0° ± 1.5° and 113.3° ± 1.4° in **13** and 121.6° ± 1.7° and 117.8° ± 1.8° in **14**, indicative of sp^3 and sp^2 hybridization, respectively. Ball-and-stick representations of the structures are superimposed for direct comparison in Fig. 4.

The absolute structures of Λ-MOF-520-**3**-**13** and -**14** were assigned on the basis of their Flack parameters—0.063(9) and 0.05(2), respectively—despite the low occupancies of the molecules. In previous reports, the absolute configurations of the guests were determined in achiral host frameworks (*7–9*, *13*). In those methods, pseudocentrosymmetry problems were reported and the absolute structure determinations were obscured, even though the structures of the guests were identified in the structure solution. This problem may be caused by several factors, such as low guest occupancy (*7*, *9*), lack of high-angle reflections because of disorder of the guest (*9*, *14*), and the nearly centrosymmetric nature of the guest (*8*, *9*, *15*). The chiral MOFs show anomalous scattering from the framework itself, regardless of any included chiral molecules (*15*, *16*). The strong enantiomorph-distinguishing power originates mainly from the scattering of the chiral framework and is enhanced by chiral and achiral bound molecules. It is sufficient for determining the absolute structure of the resulting crystal, including the absolute configuration of the bound molecule, even when the occupancy of the latter is low.

One advantage of the CAL method for the determination of the absolute configuration of molecules is that it may reduce dependence on the absolute structure parameters of the inclusion crystal data. For example, when a single crystal with absolute structure Λ has been determined by SXRD and subsequently used in the inclusion, the absolute configuration of the incorporated molecule can be directly deduced from the predetermined Λ structure. In this case, the correctness of the absolute configuration of incorporated molecules is highly dependent on the predetermined absolute structure and the knowledge of the enantiopurity of the single crystal used for the inclusion (*6*).

Finally, to demonstrate that the chirality of the binding sites of MOF-520 can separate enantiomers when one of them interacts more favorably with the binding site of one of the enantiomorphs of the MOF, we determined the absolute configuration of another plant hormone, jasmonic acid, for which a crystal structure has heretofore not been reported. A solution of a racemic mixture of (–)-jasmonic acid **15** and (+)-jasmonic acid **16** was reacted with a racemic conglomerate of MOF-520, and SXRD data for two enantiomorphic crystals were collected after the reaction. The molecules **15** and **16** selectively attached to Δ-MOF-520 and Λ-MOF-520, respectively (Fig. 3, O and P). The positions of the last three carbons were not clearly defined, presumably because of their conformational flexibility, the low occupancy of 33%, and the ensuing overlap with the electron density of residual disordered solvent. However, the atoms defining the stereocenters of **15** and their absolute configurations, *R* for C_3 and *R* for C_7, were observed unambiguously with a Flack parameter of 0.037(8). This result corresponds to that deduced from the absolute configurations of a derivative of **15**, (–)-methyl jasmonate, which were determined by a synthetic approach (*17*). The enantiomer **16** attached to Λ-MOF-520 showed the opposite absolute configuration, as indicated by a refined Flack parameter of 0.040(8). We note that the enantiomerically pure molecules **13** and **14** had an occupancy that was sufficiently high for unambiguous structure and absolute configuration determination only in one of the two enantiomorphs. This enantioselective binding can potentially be applied to the absolute configuration determination of samples that contain a minor enantiomer, without the need for chiral high-performance liquid chromatography separation before carrying out the inclusion procedure (*7*).

REFERENCES AND NOTES

1. A. Holden, P. Morrison, *Crystals and Crystal Growing* (MIT Press, 1982).
2. J. L. Atwood, J. E. D. Davies, D. D. MacNicol, *Inclusion Compounds: Structural Aspects of Inclusion Compounds Formed by Inorganic and Organometallic Host Lattices* (Academic Press, 1984).
3. Y.-M. Legrand, A. van der Lee, M. Barboiu, *Science* **329**, 299–302 (2010).
4. Y. Inokuma *et al.*, *Nature* **495**, 461–466 (2013).
5. H. Furukawa, K. E. Cordova, M. O'Keeffe, O. M. Yaghi, *Science* **341**, 1230444 (2013).
6. H. D. Flack, G. Bernardinelli, *Acta Crystallogr. A* **55**, 908–915 (1999).
7. S. Yoshioka, Y. Inokuma, M. Hoshino, T. Sato, M. Fujita, *Chem. Sci.* **6**, 3765–3768 (2015).
8. E. Sanna *et al.*, *Chem. Sci.* **6**, 5466–5472 (2015).
9. M. Hoshino, A. Khutia, H. Xing, Y. Inokuma, M. Fujita, *IUCrJ* **3**, 139–151 (2016).
10. F. Gándara, H. Furukawa, S. Lee, O. M. Yaghi, *J. Am. Chem. Soc.* **136**, 5271–5274 (2014).
11. H. D. Flack, G. Bernardinelli, *J. Appl. Crystallogr.* **33**, 1143–1148 (2000).
12. See supplementary materials on *Science* Online.
13. T. R. Ramadhar, S.-L. Zheng, Y.-S. Chen, J. Clardy, *Acta Crystallogr. A* **71**, 46–58 (2015).
14. H. D. Flack, G. Bernardinelli, D. A. Clemente, A. Linden, A. L. Spek, *Acta Crystallogr. B* **62**, 695–701 (2006).
15. H. D. Flack, U. Shmueli, *Acta Crystallogr. A* **63**, 257–265 (2007).
16. J. M. Bijvoet, A. F. Peerdeman, A. J. van Bommel, *Nature* **168**, 271–272 (1951).
17. R. K. Hill, A. G. Edwards, *Tetrahedron* **21**, 1501–1507 (1965).

ACKNOWLEDGMENTS

Supported by BASF SE (Ludwigshafen, Germany) for the synthesis, and by King Abdulaziz City for Science and Technology (Center of Excellence for Nanomaterials and Clean Energy Applications) for the characterization of compounds. We thank S. Teat for synchrotron x-ray diffraction data acquisition support at beamline 11.3.1 [Advanced Light Source (ALS), Lawrence Berkeley National Laboratory (LBNL)]; K. Gagnon for discussion of structure refinement; and H.-B. Bürgi for invaluable discussions of structure refinement and editing of this manuscript. NMR data were acquired at the Molecular Foundry, LBNL. Work performed at ALS and the Molecular Foundry is supported by the Office of Science, Office of Basic Energy Sciences, of the U.S. Department of Energy under contract DE-AC02-05CH11231 (ALS and Foundry). Use of CheXray facility at the College of Chemistry (UC Berkeley) is supported by NIH Shared Instrumentation grant S10-RR027172. Data reported in this paper are tabulated in the supplementary materials and archived at the Cambridge Crystallographic Data Centre under reference numbers CCDC 1488938 to 1488955.

SUPPLEMENTARY MATERIALS

www.sciencemag.org/content/353/6301/808/suppl/DC1
Materials and Methods
Figs. S1 to S29
Tables S1 to S20
References (*18–22*)

19 April 2016; accepted 7 July 2016
10.1126/science.aaf9135

BEHAVIORAL ECOLOGY

Prenatal acoustic communication programs offspring for high posthatching temperatures in a songbird

Mylene M. Mariette* and Katherine L. Buchanan

In many species, embryos can perceive and learn external sounds. Yet, the possibility that parents may use these embryonic capacities to alter their offspring's developmental trajectories has not been considered. Here, we demonstrate that zebra finch parents acoustically signal high ambient temperatures (above 26°C) to their embryos. We show that exposure of embryos to these acoustic cues alone adaptively alters subsequent nestling begging and growth in response to nest temperature and influences individuals' reproductive success and thermal preferences as adults. These findings have implications for our understanding of maternal effects, phenotypic plasticity, developmental programming, and the adaptation of endothermic species to a warming world.

By shaping offspring phenotype to the environment experienced by the mother, maternal effects have the capacity to alter population dynamics in fluctuating environments (*1*–*3*). Maternal effects, as other forms of phenotypic plasticity, may therefore provide a mechanism for species' persistence under global warming (*4*, *5*). In particular, parental effects may improve offspring thermal acclimation (*6*) and optimize offspring growth in current temperature regimes, as demonstrated in invertebrates (*7*) and recently in ectothermic vertebrates (*8*). Whether parents in endothermic species can program their offspring for current climatic conditions is currently unknown.

Here, we investigated whether avian parents can signal environmental conditions to their embryos, allowing them to adaptively modulate their growth in response to temperature. Because, in birds, mothers can no longer affect the biochemical environment of their embryos after laying, we tested the possibility that parents signal current climatic conditions via acoustic cues. Indeed, parents call to their eggs during incubation in several bird species (*9*–*11*), and late-stage avian embryos can perceive, and even produce, sound (*12*–*15*). Prenatal acoustic communication, mostly in precocial birds, has been found to synchronize hatching (*14*), allow embryos to solicit parental incubation (*12*, *15*), and improve imprinting, perceptual learning, and brain functions (*16*–*18*), although the direct fitness impact of these effects has not been quantified. Recent studies in two species of fairy wrens (*Malurus* spp.) showed that nestlings imitate the call of their foster incubating mother, and provisioning mothers tend to discriminate against foreign-sounding nestlings (*10*, *11*). Therefore, by altering nestling begging, incubation calling may have the potential to function similarly to other avian maternal effects, such as yolk hormone content that modifies nestling begging and growth (*3*, *19*, *20*). Yet, whether parents signal environmental conditions and alter the developmental trajectory of their offspring using prenatal acoustic communication is unknown.

The Australian zebra finch (*Taeniopygia guttata*) is an arid-adapted songbird that breeds opportunistically in fluctuating temperature regimes (*21*) and in which nestling mass before fledging varies by up to 30%, depending on nesting density (*22*) and parental care coordination (*23*). We identified that, in outdoor aviaries, wild-derived zebra finches produced an "incubation call" while alone with their eggs (real or dummy) with their partner away from the nest (*24*) (fig. S1). This call was exclusively uttered toward the end of the incubation period, within 5 days of hatching (Fig. 1A) (time to expected hatch date: linear: $Z = 2.19$, $P = 0.03$; quadratic: $Z = -2.38$, $P = 0.02$, $n = 266$ recordings) (table S1), and calling rate per hour increased closer to expected hatch date (table S1). In addition, incubation calling was very clearly associated with elevated ambient temperatures, occurring only when maximal daily temperature rose above 26°C ($Z = 2.81$, $P = 0.005$, $n = 266$) (Fig. 1B), regardless of seasonal variation (fig. S2 and table S1). Therefore, as suggested in fairy wrens (*10*, *11*, *25*), zebra finch parents appear to control the production of incubation calls to signal environmental conditions to their embryos, because calling only occurred close to hatching, rather than as a spontaneous reaction to heat.

To investigate experimentally whether this calling behavior may prepare offspring for high ambient temperatures, eggs were artificially incubated at a standard temperature (37.7°C) and exposed to acoustic playback of either incubation calls ("treatment") or control contact calls in the last 5 days of incubation (fig. S1) (*24*). Nestlings hatched in the incubators were then returned to the aviary to be raised in nest boxes with naturally contrasting temperature profiles, depending on sun exposure throughout the day. Nestlings exposed to incubation calls as embryos followed a different growth pattern in response to nest temperature than did control nestlings: Treatment nestling mass (and to a lesser extent tarsus length) on day 13 decreased with nest temperature, whereas it increased in control nestlings (Fig. 2) (mass: $t = -3.30$, $P = 0.001$, $n = 130$ nestlings from 45 broods) (tables S2 and S3). This effect at the end of the nestling period (day 13) was already arising just 1 day

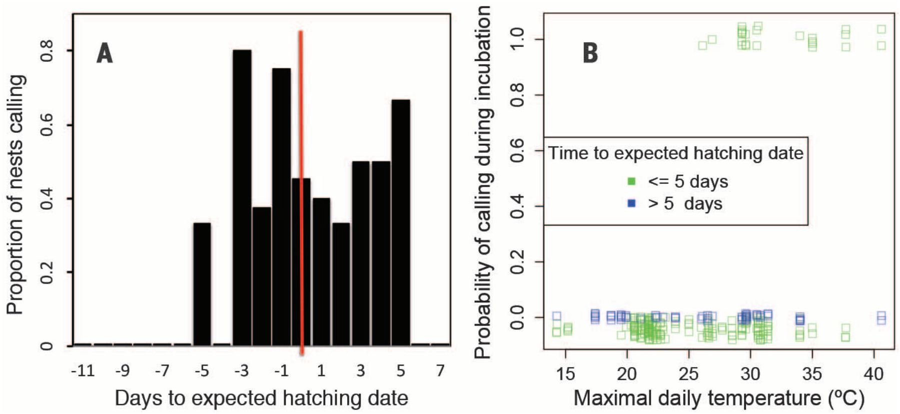

Fig. 1. Incubation calling behavior in relation to incubation stage and ambient temperatures. (**A**) Proportion of nests producing incubation calls on hot days (maximal daily temperature ≥26°C) in relation to the number of days before or after expected hatching date (vertical red line). (**B**) Probability of pairs emitting incubation calls in relation to maximal daily temperature on the day of recording for nests within 5 days of hatching (green) or either before or after this period (blue). Each data point represents one nest in a recording session.

Centre for Integrative Ecology, School of Life and Environmental Sciences, Deakin University, Waurn Ponds Campus, 75 Pigdons Road, Waurn Ponds VIC 3216, Australia.
*Corresponding author. Email: m.mariette@deakin.edu.au

after hatching [linear mixed model (LMM) on mass at day 1: t = –2.18, P = 0.032, n = 125 nestlings from 45 broods] and was observed throughout nestling development (same interaction on two random subsamples: 2 days post-hatching: t = –2.20, P = 0.0037, n = 61 nestlings from 30 broods; and 10 days: t = –2.91, P = 0.0094, n = 44 nestlings from 22 broods). This interaction was, however, not present at hatching (LMM: playback by future nest temperature: t = –1.03, P = 0.31; playback alone: t = –0.13, P = 0.89, n = 130 nestlings from 45 broods) and was not due to differential nestling mortality (Cox proportional hazard regression: playback by nest temperature: Z = 0.25, P = 0.80, n = 166 nestlings in 52 broods; nest temperature in treatment: Z = –0.43, P = 0.67, n = 79 nestlings in 35 broods; nest temperature in control: Z = –0.38, P = 0.70, n = 87 nestlings in 37 broods).

In birds, maternal effects on nestling growth induced by differential hormone concentrations in the egg are partly mediated posthatching by their effects on nestling begging (*19*, *20*). Therefore, and because incubation calling altered nestling begging in fairy wrens (*10*, *11*), we investigated whether differences in nestling begging could underlie the differential growth patterns followed by experimental nestlings in response to nest temperatures (*24*). Accordingly, in the first 3 days after hatching, treatment nestlings (i.e., incubation call playback) were more likely to call while begging when they had experienced high temperatures in the nest since hatching, whereas control nestlings called less, independently of temperature (Fig. 3) (generalized LMM: playback by temperature in nest: Z = 2.23, P = 0.026, n = 77 recordings for 59 chicks from 19 broods). Nestling mass and satiation at the time of recording had no effect on the probability of calling while begging (mass: Z = –0.71, P = 0.48; presence of seeds in crop: Z = 0.86, P = 0.39), which suggests that this call might signal thermal state (*12*, *15*) rather than hunger level or body condition.

The decrease in mass with increasing nest temperatures that we found in treatment nestlings (compared with control nestlings) (Fig. 2) is consistent with the current pattern observed in many wild bird species worldwide (*26*). Although this environmentally driven size reduction is generally expected to have negative effects on offspring fitness [e.g., (*27*, *28*)], reducing mass gain at high temperature might be beneficial if it reduces oxidative damage associated with growth in such an environment or if small body size facilitates heat loss (*26*, *29*, *30*). Therefore, to determine whether such a pattern is adaptive, we measured the reproductive success of our experimental birds at adulthood (*24*). Resembling the pattern in treatment nestlings, females that as nestlings had low body mass under hot conditions during development or greater body mass in cold rearing conditions produced more fledglings in their first breeding season (Fig. 4A) [generalized linear model (GLM): Z = –2.66, P = 0.0078, n = 39 females]. This effect applied to both treatment and control

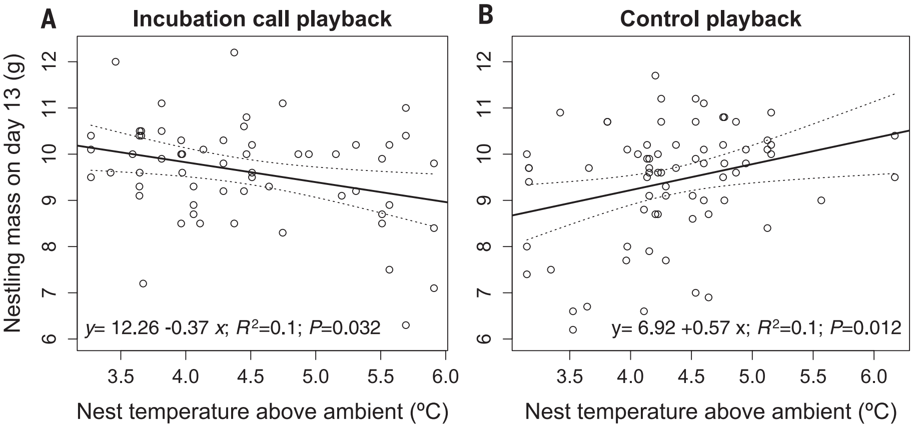

Fig. 2. Nestling mass on day 13 (i.e., at the end of the nestling phase) in relation to nest temperature above ambient. (**A**) Treatment nestlings exposed to incubation calls. (**B**) Control nestlings exposed to parental contact calls. Raw data are shown, with one data point per nestling. The lines depict the regression line (full) and 95% confidence intervals (dotted).

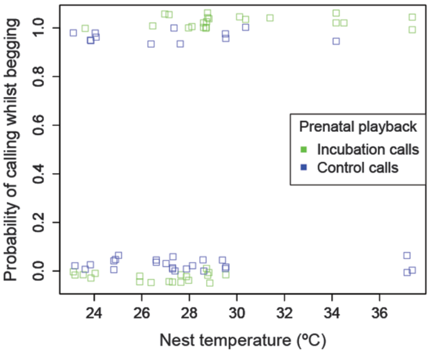

Fig. 3. Probability of calling while begging in relation to nest temperature experienced since hatching (nest temperature above ambient + mean daily maximum temperature) for nestlings that heard incubation calls (green) or control calls (blue) as embryos. Each data point represents one nestling.

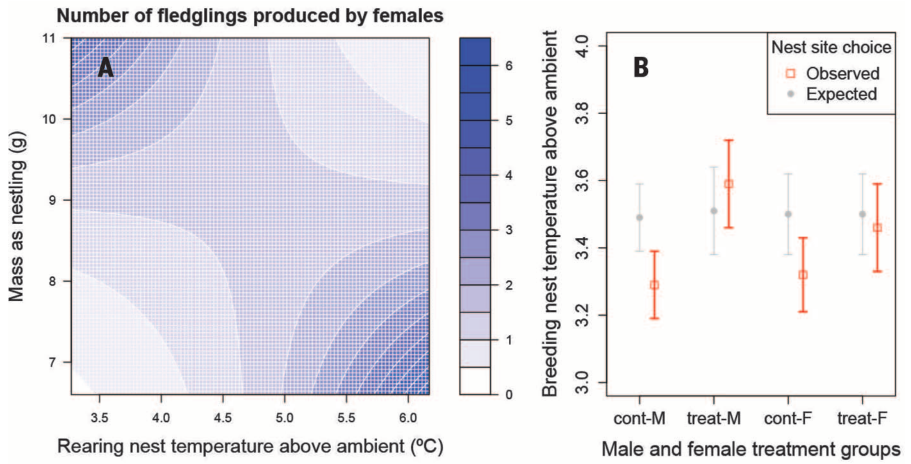

Fig. 4. Effect of incubation calling as late-stage embryos on individuals' reproductive success and thermal preferences in their first year. (**A**) The number of fledglings produced by females (predicted values from GLM) in relation to the nest temperature (above ambient) that they experienced as nestlings and their mass as 13-day-old nestlings. (**B**) Observed (red) mean (±SE) temperature above ambient of breeding nest boxes used at adulthood by treatment ("treat") and control ("cont") males and females, compared with values expected by chance (gray) given nest box availability and pair composition (two treatment, two control, or mixed partners).

females (no additional effect of playback treatment: $Z = 0.39$, $P = 0.69$) after controlling for female mass as adult ($Z = 2.83$, $P = 0.005$). Furthermore, this fitness effect of early mass and thermal conditions persisted in females' second year of life despite repairing (GLM: $Z = -2.31$, $P = 0.021$; repairing: $Z = 1.17$, $P = 0.24$; adult mass: $Z = 2.82$, $P = 0.005$, $n = 36$ females, including 25 with a new partner). Males followed a similar trend to females in their first year [GLM with temperature in nest (i.e., ambient temperature + nest differential): $Z = -1.97$, $P = 0.049$, $n = 36$ males] but not their second year (GLM: $Z = 1.65$, $P = 0.10$, $n = 38$ males).

Last, the evolutionary advantage of maternal effects has been questioned in unpredictable environments, where environmental conditions during development do not predict those encountered later in life (*31*). However, individuals may partly compensate for this by seeking microhabitats that best suit their phenotype. Accordingly, treatment individuals exposed to incubation calls in the egg went on to consistently breed in hotter nest boxes than control birds, because control males used cooler boxes and treatment males used warmer boxes than expected by chance in the first and second years, respectively (Fig. 4B) (Monte-Carlo simulations: first-year control males: $P = 0.024$, $n = 22$, and females: $P = 0.075$, $n = 15$; second-year treatment males: $P = 0.046$, $n = 10$; all others: $P > 0.05$) (*24*).

Overall, we have demonstrated experimentally that by acoustically signaling high ambient temperatures to their embryos before hatching, zebra finch parents can program the developmental trajectories of their offspring in response to this key environmental variable. Our findings therefore provide both an adaptive function for prenatal communication and a type of maternal effect where parental control over signal production can be unambiguously tested. By uncovering a mechanism for a transgenerational effect of temperature on development in endotherms, our study also advances our understanding of the acclimatization capacities of organisms to rising temperatures.

REFERENCES AND NOTES

1. B. Dantzer *et al.*, *Science* **340**, 1215–1217 (2013).
2. R. A. Duckworth, V. Belloni, S. R. Anderson, *Science* **347**, 875–877 (2015).
3. T. A. Mousseau, C. W. Fox, *Trends Ecol. Evol.* **13**, 403–407 (1998).
4. C. Teplitsky, J. A. Mills, J. S. Alho, J. W. Yarrall, J. Merilä, *Proc. Natl. Acad. Sci. U.S.A.* **105**, 13492–13496 (2008).
5. O. Vedder, S. Bouwhuis, B. C. Sheldon, *PLOS Biol.* **11**, e1001605 (2013).
6. J. M. Donelson, P. L. Munday, M. I. McCormick, C. R. Pitcher, *Nat. Clim. Chg.* **2**, 30–32 (2012).
7. F. R. Groeters, H. Dingle, *J. Evol. Biol.* **1**, 317–333 (1988).
8. S. Salinas, S. B. Munch, *Ecol. Lett.* **15**, 159–163 (2012).
9. D. B. Miller, G. Gottlieb, *Anim. Behav.* **26**, 1178–1194 (1978).
10. D. Colombelli-Négrel *et al.*, *Curr. Biol.* **22**, 2155–2160 (2012).
11. D. Colombelli-Négrel, M. S. Webster, J. L. Dowling, M. E. Hauber, S. Kleindorfer, *Auk* **133**, 273–285 (2016).
12. R. B. Brua, G. L. Nuechterlein, D. Buitron, *Auk* **113**, 525–533 (1996).
13. G. Gottlieb, *Science* **147**, 1596–1598 (1965).
14. N. K. Woolf, J. L. Bixby, R. R. Capranica, *Science* **194**, 959–960 (1976).
15. R. M. Evans, A. Whitaker, M. O. Wiebe, *Auk* **111**, 596–604 (1994).
16. J. J. Bolhuis, *Biol. Rev. Camb. Philos. Soc.* **66**, 303–345 (1991).
17. R. Lickliter, T. B. Hellewell, *Dev. Psychobiol.* **25**, 17–31 (1992).
18. T. Sanyal *et al.*, *PLOS ONE* **8**, e67347 (2013).
19. G. Boncoraglio, D. Rubolini, M. Romano, R. Martinelli, N. Saino, *Horm. Behav.* **50**, 442–447 (2006).
20. J. L. Lipar, E. D. Ketterson, *Proc. Biol. Sci.* **267**, 2005–2010 (2000).
21. R. A. Zann, *The Zebra Finch* (Oxford Univ. Press, New York, 1996).
22. M. M. Mariette, S. C. Griffith, *Ecology* **94**, 325–335 (2013).
23. M. M. Mariette, S. C. Griffith, *Am. Nat.* **185**, 270–280 (2015).
24. Materials and methods are available as supplementary materials on *Science* Online.
25. S. Kleindorfer, C. Evans, D. Colombelli-Négrel, *Biol. Lett.* **10**, 20140046 (2014).
26. J. L. Gardner, A. Peters, M. R. Kearney, L. Joseph, R. Heinsohn, *Trends Ecol. Evol.* **26**, 285–291 (2011).
27. S. J. Cunningham, R. O. Martin, C. L. Hojem, P. A. R. Hockey, *PLOS ONE* **8**, e74613 (2013).
28. J. A. van Gils *et al.*, *Science* **352**, 819–821 (2016).
29. M. E. Hall, J. D. Blount, S. Forbes, N. J. Royle, *Funct. Ecol.* **24**, 365–373 (2010).
30. C. Selman, J. D. Blount, D. H. Nussey, J. R. Speakman, *Trends Ecol. Evol.* **27**, 570–577 (2012).
31. M. J. Sheriff, O. P. Love, *Ecol. Lett.* **16**, 271–280 (2013).

ACKNOWLEDGMENTS

This project was supported by Australian Research Council grants DP130100417 and LP140100691 and Future Fellowship FT140100131 to K.L.B. and a research fellowship from Deakin University to M.M.M. We have no conflict of interest. We thank I. Goedegebuur, K. Pinch, B. Oliver, and N. Wells for assistance with data collection and processing and W. Buttemer, J. Endler, S. Kleindorfer, M. Klaassen, M. Ramenofsky, J. Wingfield, the Centre for Integrative Ecology discussion group, and three anonymous reviewers for providing comments on the manuscript. Data have been deposited in the Dryad Digital Repository (accession number doi:10.5061/dryad.v8969).

SUPPLEMENTARY MATERIALS

www.sciencemag.org/content/353/6301/812/suppl/DC1
Materials and Methods
Figs. S1 and S2
Tables S1 to S3
References (*32–40*)

17 March 2016; accepted 14 July 2016
10.1126/science.aaf7049

GENE REGULATION

Integration of omic networks in a developmental atlas of maize

Justin W. Walley,[1,2]* Ryan C. Sartor,[1]* Zhouxin Shen,[1] Robert J. Schmitz,[3,4]† Kevin J. Wu,[1] Mark A. Urich,[3,4] Joseph R. Nery,[4] Laurie G. Smith,[1] James C. Schnable,[5] Joseph R. Ecker,[3,4,6] Steven P. Briggs[1]‡

Coexpression networks and gene regulatory networks (GRNs) are emerging as important tools for predicting functional roles of individual genes at a system-wide scale. To enable network reconstructions, we built a large-scale gene expression atlas composed of 62,547 messenger RNAs (mRNAs), 17,862 nonmodified proteins, and 6227 phosphoproteins harboring 31,595 phosphorylation sites quantified across maize development. Networks in which nodes are genes connected on the basis of highly correlated expression patterns of mRNAs were very different from networks that were based on coexpression of proteins. Roughly 85% of highly interconnected hubs were not conserved in expression between RNA and protein networks. However, networks from either data type were enriched in similar ontological categories and were effective in predicting known regulatory relationships. Integration of mRNA, protein, and phosphoprotein data sets greatly improved the predictive power of GRNs.

Predicting the functional roles of individual genes at a system-wide scale is a complex challenge in biology. Transcriptome data have been used to generate genome-wide gene regulatory networks (GRNs) (*1–4*) and coexpression networks (*5–7*), the design of which was based on the presumption that mRNA measurements are a proxy for protein abundance measurements. However, genome-wide correlations between the levels of proteins and mRNAs are weakly positive (*8–15*), which indicates that cellular networks built solely on transcriptome data may be enhanced by

---

[1]Division of Biological Sciences, University of California San Diego, La Jolla, CA 92093, USA. [2]Department of Plant Pathology and Microbiology, Iowa State University, Ames, IA 50011, USA. [3]Plant Biology Laboratory, The Salk Institute for Biological Studies, La Jolla, CA 92037, USA. [4]Genomic Analysis Laboratory, The Salk Institute for Biological Studies, La Jolla, CA 92037, USA. [5]Department of Agronomy and Horticulture, University of Nebraska, Lincoln, NE 68583, USA. [6]Howard Hughes Medical Institute, The Salk Institute for Biological Studies, 10010 North Torrey Pines Road, La Jolla, CA 92037, USA.
*These authors contributed equally to this work. †Present address: Department of Genetics, Davison Life Sciences, 120 East Green Street, Athens, GA 30602, USA. ‡**Corresponding author. Email: sbriggs@ucsd.edu**

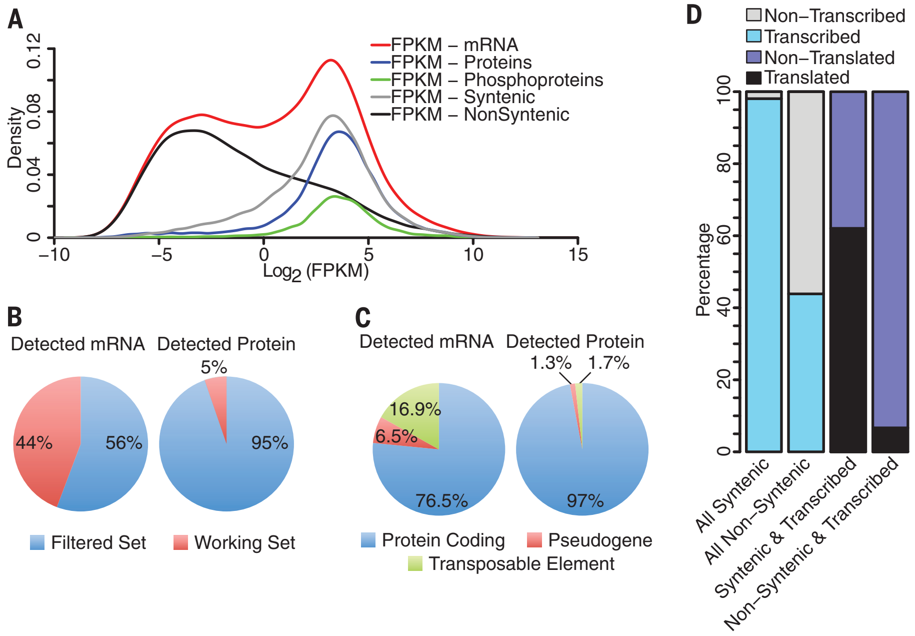

Fig. 1. Comparison of transcriptome and proteome data sets. (**A**) FPKM distribution of mRNA abundance (red). FPKM values of transcripts corresponding to quantified proteins (blue), phosphopeptides (green), syntenic genes conserved between maize and sorghum (gray), and nonsyntenic genes (black) are shown. Data are the average expression from the 23 tissues profiled. (**B**) Percentage of quantified mRNA and proteins in the annotated filtered (high-confidence gene models) and working (all gene models) gene sets. (**C**) Breakdown of detected mRNA and proteins, based on annotations. (**D**) Percentages of all annotated genes that are transcribed and percentages of all transcribed genes that are translated, for both the syntenic and nonsyntenic gene sets.

integration with proteomics data. We generated an integrated developmental atlas of the transcriptome, proteome, and phosphoproteome of the model organism *Zea mays* (maize) and then used these three different cellular descriptions to generate transcriptome- and proteome-based networks.

We profiled 23 tissues spanning vegetative and reproductive stages of maize development to generate a comprehensive and integrated gene expression atlas. Specifically, transcriptome profiling by mRNA sequencing (mRNA-seq) (three biological replicates, 23 tissues) was carried out on a subset of the samples used for proteome profiling (three to seven biological replicates, 33 tissues) by electrospray ionization tandem mass spectrometry (*14*, *16*–*19*) (tables S1 to S3). We assessed reproducibility of the biological replicates by calculating Pearson correlations and found an average of 0.9, 0.84, and 0.7 for the transcriptome, proteome, and phosphoproteome data sets, respectively (table S4). Transcripts were observed from 62,547 genes. Proteins and phosphoproteins were observed from 16,946 and 5587 genes, respectively. The RNA-seq data were bimodal, as reported for mouse and human (*20*, *21*), with nearly all proteins and phosphoproteins arising from the 34,455 transcripts in the high-abundance population (right peak), with an average FPKM (fragments per kilobase of exon per million fragments mapped) greater than 1 (Fig. 1A). Proteins were observed from 46% of these transcripts (right peak). To determine whether coverage of the transcriptome by the proteome was constrained by the diversity of tissues sampled, we generated proteomics data from an additional 10 tissue types yielding proteins from a total of 18,522 genes (proteins from 17,862 genes and phosphoproteins from 6185 genes), but this only increased coverage of the high-abundance transcriptome to 48%.

There are a variety of possible technical and biological explanations for why we detect proteins from less than half of the high-abundance transcript-producing genes and why we do not observe corresponding mRNA for 245 quantified proteins. Previously, we found evidence for multiple mechanisms that may explain the detection of proteins but not mRNA. These mechanisms include (i) differential stability of mRNA and proteins; (ii) transport of proteins between tissues; and (iii) diurnal, out-of-phase accumulation of mRNAs and cognate proteins (*14*). The heightened sensitivity of transcriptomics relative to proteomics likely provides a partial explanation for why we detect proteins corresponding to less than half of the transcript-producing genes. Additionally, we observed a greater percentage of proteins arising from the annotated filtered gene set, which consists of 39,656 high-confidence gene models that exclude transposons, pseudogenes, and other low-confidence members present in the working gene set (Fig. 1B). Furthermore, a higher proportion of proteins than transcripts arise from genes annotated as protein coding (Fig. 1C), which suggests that transcripts from many genes may not produce proteins. Genes conserved at syntenic orthologous locations between maize and sorghum exhibited a unimodal, high-expression pattern, in contrast to genes in nonsyntenic locales (Fig. 1A). Considering all genes that expressed mRNAs, syntenic genes were nine times more likely than nonsyntenic genes to express proteins (Fig. 1D). To show that this observation is not due to the higher average transcript expression level of syntenic genes, we examined a range of transcript abundance cutoffs and obtained similar results, even when looking at the highest-abundance syntenic and nonsyntenic transcripts (fig. S1). A greater frequency of protein expression is a possible mechanistic explanation for the eightfold enrichment of genes responsible for visible mutant phenotypes among syntenically conserved genes in maize (*22*).

We next examined how genes and biological processes change throughout development. Initially, we focused on transcription factors (TFs), as they are key regulators of development, growth, and cell fate. Of the 2732 annotated TFs and transcriptional co-regulators, we detected 2627 as mRNA (23 tissues), 1026 as protein (33 tissues), and 559 as phosphoprotein (33 tissues). We used hierarchical clustering to identify 712 (mRNA), 469 (protein), and 419 (phosphoprotein) TFs that exhibited tissue-specific enrichment (figs. S2 to S4 and table S5). We also examined expression trends at the TF family level. First, we used traditional overrepresentation analysis to identify TF families whose members are detected in a given tissue at a greater frequency than chance (figs. S5A, S6A, and S7A). To augment the overrepresentation analysis, we also examined TF family–level expression profiles by quantifying the total amount of each TF family's mRNA, protein, and/or phosphoprotein present in given tissue (figs. S5B, S6B, and S7B). Taken together, these data describe the spatiotemporal expression pattern of individual TFs and TF families across development.

We expanded our analyses to examine the patterns of all gene types across maize development. We used the weighted gene coexpression network analysis (WGCNA) R package (*23*) to group similarly expressed genes—detected as mRNA (23 tissues), protein (33 tissues), or phosphoprotein (33 tissues) in at least four tissues—into modules (clusters). This approach enabled us to group 31,447 mRNAs, 13,175 proteins, and 4267 phosphoproteins into coexpression modules (fig. S8 and table S6). We next plotted the eigengene profile for each module in order to assign the tissue(s) in which each module is highly expressed (figs. S9 to S12). We observed that 36 well-characterized genes required for maize development—including the homeobox TFs Knotted1 [KN1, Maize Genetics and Genomics Database (MGGD) accession number GRMZM2G017087] (*24*) and Rough Sheath 1 (RS1, MGGD accession number GRMZM2G028041) (*25*), as well as the transcriptional co-repressor Ramosa1 Enhancer Locus2 (REL2, MGGD accession number GRMZM2G042992) (*26*) (table S6)—are present in mRNA, protein, and phosphoprotein modules that correspond to dividing and meristematic tissues. The phosphorylation pattern of these proteins is similar to their mRNA profile and occurs in tissues known to have altered developmental phenotypes in mutant plants, which suggests that phosphorylation of these proteins might positively regulate their function. Finally, we determined overrepresentation of MapMan functional categories in each module (table S6). As expected, we found that genes involved in photosynthetic light reactions have mRNA and protein that are enriched predominantly in the mature leaf. We did not detect an enrichment of light-reaction phosphoproteins in the mature leaf module, which suggests that phosphorylation is not a major regulator of the light reactions (fig. S11 and table S6).

Biological networks can be constructed based on many different types of data and serve to elucidate the structure underlying complex systems. Typically, transcript profiling data are used to generate various types of gene expression networks. However, we observed a weakly positive correlation between mRNA and protein levels in our data set (supplementary text, figs. S13 to S17, and table S7), in agreement with research done in a range of organisms (*8*–*15*). Although the modest correlation between mRNA and protein levels is well documented, a major outstanding question is whether transcriptome-based networks predict the same relationships as proteome-based networks. Given our extensive developmental gene expression atlas, we addressed this question by generating two different types of networks: coexpression networks and GRNs. We first generated coexpression networks (table S8), which are undirected networks where nodes are genes connected on the basis of highly correlated expression patterns (Fig. 2A) (*5*–*7*). For these network reconstructions, we used 10,979 genes that were detected as both transcripts and proteins in at least 5 of the 23 developmental gene expression atlas tissues in which we profiled both mRNA and protein. Pairwise mRNA-to-mRNA and protein-to-protein coexpression networks were built with Spearman correlations using WGCNA (fig. S18 and table S8). The biweight midcorrelation yielded similar results (figs. S19 and S20). To directly compare the mRNA- and protein-based coexpression networks and compile a high-confidence coexpression data set, each network was constrained to include only edges with a correlation score >0.75 (top 1 million edges), which is a frequently used correlation threshold for coexpression networks (table S8). As a measure of similarity, we calculated edge conservation by dividing the set intersect by the union (known as the Jaccard index) and reported this as a percentage. We found that 122,029 of the combined 2 million edges (6.1%) were conserved in both networks (Fig. 2B). Though this edge overlap is greater than the 0.8% expected by chance (*P* value = 0), the majority of relationships between genes were specific to each network, even when we expanded the network size to 10 million edges (fig. S20).

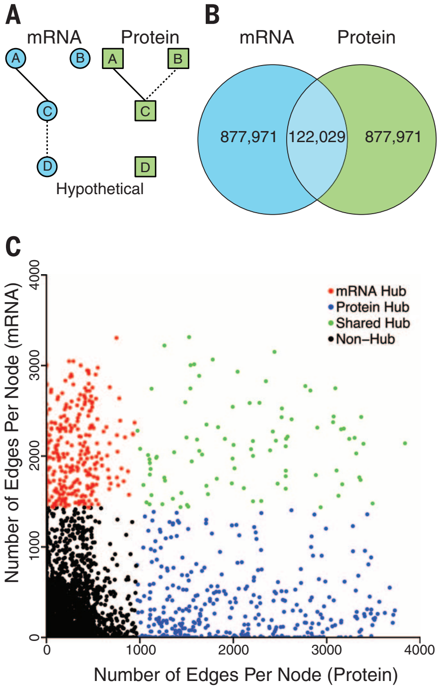

Fig. 2. Coexpression network analyses. (**A**) Hypothetical undirected coexpression subnetwork showing conserved (solid lines) and nonconserved (dotted lines) coexpression edges between mRNA and protein networks. (**B**) Venn diagram depicting edge conservation (solid lines in Fig. 2A) between the two coexpression networks. (**C**) Number of edges a given gene (node) has in the protein (*x* axis) and mRNA (*y* axis) coexpression networks. Nodes above the 90th percentile for the number of edges are considered hubs and are colored according to whether they are hubs in the protein (blue) or mRNA (red) network or both (green). Black dots represent nonhub nodes.

To examine whether the lack of edge overlap was due to experimental noise, we used single biological replicates (three mRNA and three protein networks) to create six new coexpression networks. Pairwise comparisons revealed a similar low level of edge conservation (5%) between the mRNA and protein coexpression networks. However, 46% of mRNA-to-mRNA edges and 36% of protein-to-protein edges were conserved between replicate coexpression networks (fig. S21). These data suggest that biological phenomena underpin the observed lack of edge conservation between transcriptome- and proteome-derived coexpression networks.

A key feature of scale-free networks is a small number of highly interconnected hubs. Because hubs are more likely than nonhubs to be required for network integrity and organism survival, the identification of so-called "hub genes" is of interest (*23*, *27*–*30*). We therefore determined the highly interconnected hub genes in each coexpression network, which we categorized as nodes in the top 10th percentile for most edges (Fig. 2C and fig. S22A). When we compared the hub genes from each network, we found that the majority (85%) were not shared between the mRNA and protein coexpression networks (Fig. 2C and fig. S22).

Groups of coexpressed genes (modules) were derived from the two networks. Each module was examined for over- or underrepresentation of MapMan categories (table S9). The majority of modules from each network (mRNA: 17 of 19; protein: 18 of 25) showed significant enrichment for one or more categories (adjusted *P* value < 0.05). Overall, we observed similar enrichment of categories between the two coexpression networks (fig. S23). Whereas the overall degree of enrichment was very similar for most categories in both coexpression networks, the actual genes that accounted for the significantly enriched categories were mostly specific to one network (35% protein-specific, 27% mRNA-specific, and 38% shared) (Fig. 3). Taken together, these results demonstrate that transcript- and protein-based coexpression networks yield differing predictions of gene relatedness and function. Presumably, the discrepancy between transcriptome and proteome coexpression networks arises from the limited correlation between mRNA and protein abundance, which has been attributed to a range of factors that include differing stabilities of mRNA and protein, translational control, and protein movement from the tissue of synthesis (*8*, *14*, *31*).

To further explore the regulatory patterns of gene expression across maize development, we generated GRNs, which are directed networks of TFs and their target genes (Fig. 4A) (*1*). Unsupervised GRNs were created using GENIE3, which takes advantage of the random forest machine learning algorithm and was the top-performing method in the DREAM4 and -5 GRN reconstruction challenges (*32*, *33*). Three independent GRNs were generated from the 23 tissues in which we profiled both mRNA and protein. To construct these networks, we varied whether the TFs (termed "regulators") were quantified as mRNAs (2200 TFs), proteins (545 TFs), or phosphopeptides (441 TFs) and used a common set of 41,021 quantified mRNAs (termed "target genes") (table S10). We evaluated the GRNs by using published data for two classical maize TFs, the homeobox TF KN1 and the bZIP TF Opaque2 (O2). These TFs were chosen as benchmarks because they have been the subject of high-quality RNA-seq and chromatin immunoprecipitation (ChIP)–seq studies in both wild-type and null mutant backgrounds, and they represent two distinct types of TFs with key developmental roles (*24*, *34*). Target genes are bound by their TF in a ChIP-seq assay, and their mRNA levels change when their TF is knocked out. Using the published direct targets of KN1 and O2, we generated receiver operating characteristic (ROC) and precision-versus-recall curves, which are two methods commonly used to evaluate the power of a predictive model (*35*). These curves showed that the overall qualities of all three GRNs were similar (fig. S24). However, when we looked at the top 500 scoring GENIE3 predictions for KN1 and O2 in each GRN, we observed a performance advantage for the two protein-based GRNs in accurately predicting target genes (Fig. 4B and fig. S25A). Specifically, the KN1 subnetworks accurately predicted 108 (mRNA), 129 (protein), and 125 (phosphopeptide) targets, with the O2 subnetworks performing similarly. Additionally, 44% (KN1) and 31% (O2) of

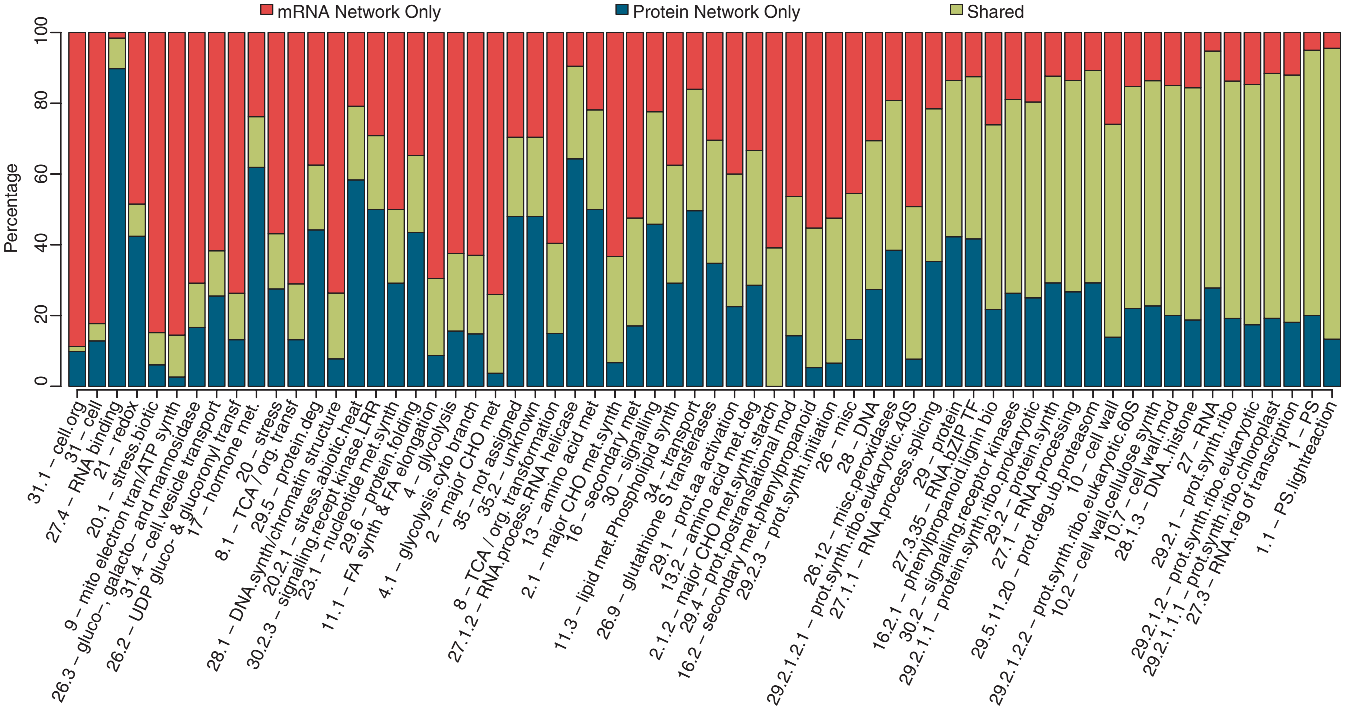

Fig. 3. Categorical enrichment analysis of coexpression modules. Coexpression modules were determined by WGCNA and functionally annotated using MapMan categories. Categories enriched (Benjamini-Hochberg adjusted *P* value ≤ 0.05) in one or more modules are represented by vertical bars and labeled with the bin number and name. For each category, the genes accounting for the enrichment were extracted separately from mRNA and protein modules. Only functional categories with at least 20 genes are shown. Colored bars represent the proportion of genes in each enriched category that are specific to one network (mRNA, red; protein, blue) or shared between the networks (green).

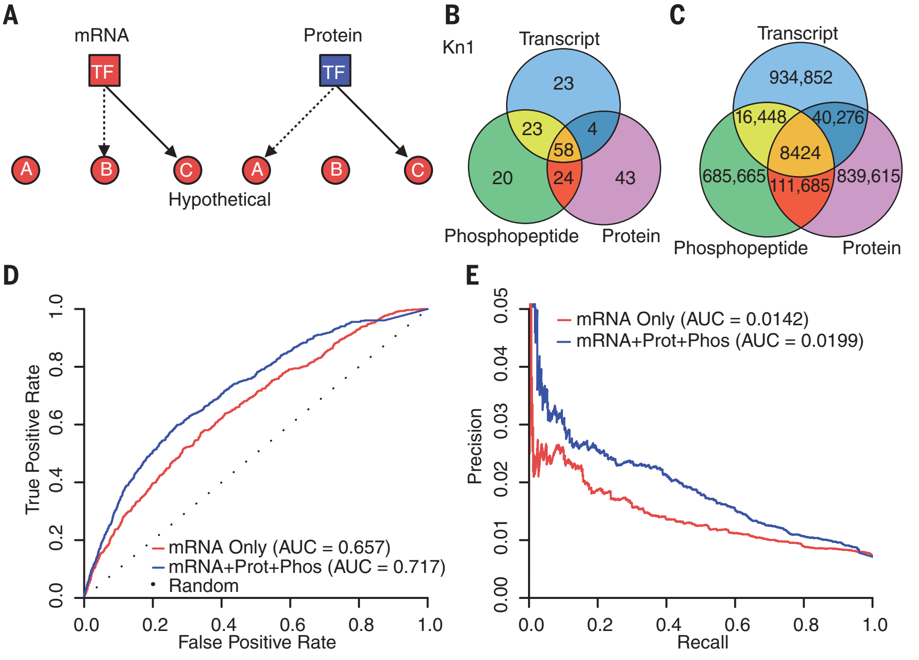

Fig. 4. Unsupervised GRN analyses. (**A**) Hypothetical GRN subnetwork depicting a TF regulator (square) and potential target genes (circle) quantified as mRNA (red) or protein (blue). GRN-specific and -conserved predictions are depicted by dotted and solid lines, respectively. (**B**) Overlap of the true-positive predictions from the top 500 true GRN predictions for KN1 quantified as mRNA, protein, or phosphopeptide. True KN1 targets were identified by Bolduc *et al*. (*24*). (**C**) Overlap of the top 1 million TF target predictions between the GRNs reconstructed using TF abundance quantified at the mRNA, protein, or phosphopeptide level. (**D**) ROC curves and (**E**) precision-recall curves generated using known Kn1 and O2 target genes for a mRNA-only GRN (red) and a fully integrated GRN built by combining mRNA, protein, and phosphoprotein data into a single GRN (blue).

all correctly predicted targets were specific to a single type of GRN (Fig. 4B and fig. S25A). These results indicated that predictions made by all three GRNs were largely complementary to each other.

We expanded our analyses to examine all TFs in the three GRNs. Again, we found that there was low edge conservation between the GRNs, with the vast majority of edges being present in a single GRN (fig. S26). Specifically, when considering one million edges, 93% were present in a single GRN (Fig. 4C). This amount increased to 96% for the 200,000 highest-confidence predictions, which we determined using KN1 precision data as the cutoff (fig. S25, B and C). This finding illustrates that the different accumulation patterns of mRNA, protein, and phosphorylation for a given TF (fig. S27) result in disparate GRN predictions.

The three preceding GRNs were constructed using different-sized sets of TF regulators, which complicated direct comparisons of networks constructed using TF abundance measurements at the mRNA or protein level. Therefore, we used 539 TFs quantified as both mRNAs and proteins to reconstruct GRNs. Evaluation of these GRNs using the KN1 and O2 data indicated quality and accuracy similar to those of the full-sized networks (fig. S28). We still observed a performance advantage for the protein GRN, as well as limited edge conservation between the mRNA- and protein-based GRNs, with only 6% of the top 200,000 edges being shared (figs. S28 and S29). We examined several possible features of the TF regulators to help further our understanding of the limited overlap in TF target predictions. The TFs connected by edges that were present only in the transcript GRN had lower and more variable protein abundance than the TFs connected by edges that were shared with or specific to the protein GRN (fig. S30, A to D). As expected, the mRNA-to-protein correlations were higher for targets of edges present in both GRNs (fig. S30E).

To further validate GRN predictions and test whether network relationships were consistent between different maize varieties, we took advantage of natural variation in regulator abundance arising from the natural genetic variation present in another inbred line, Mo17. Specifically, we compared mRNA and protein abundance in primary roots of Mo17 to B73. Whereas most TFs and target genes were expressed at similar levels in B73 and Mo17, we identified 149 (mRNA), 26 (protein), and 16 (phosphopeptide) regulatory TFs that were expressed at significantly different levels. We found, with high confidence, that for many of these differentially expressed TFs, their GRN predicted target groups were also significantly enriched for differentially expressed transcripts (figs. S31 to S33). Thus, elements of the GRN structure were preserved, and quantitative changes in regulator abundance levels are associated with altered network output and gene expression patterns. Additionally, these findings validated the GRN approaches used in this study and demonstrated the utility of applying this method to examine dynamics of gene regulation.

After analyzing separate mRNA- and protein-based GRNs, we considered integrating the data sets to determine whether the resulting single GRN would have improved inference over the individual GRNs. Specifically, we constructed four additional GRNs, each consisting of combinations of TF regulators quantified as mRNA, protein, and/or phosphopeptides (table S10). Details of how the combined mRNA, protein, and phosphopeptide GRNs were made are described in the supplementary materials. We examined the performance of the resulting networks using the validation set of KN1 and O2 published targets (Fig. 4 and fig. S24). All GRNs reconstructed with combinations of TF regulators performed better than single-input GRNs. This finding demonstrates that integrating readouts of gene expression quantified at different levels results in improved GRN inference. Our use of TF mRNA levels to infer TF activity had provided good GRN predictive power. The area under the ROC curve (AUC) was 0.657, compared with 0.500 for random predictions. When the mRNA measurements were combined with protein abundance and phosphorylation levels to infer TF activity, the AUC increased to 0.717. Thus, if an investigator wished to use network predictions with a false-positive rate of 20%, the mRNA-only network would predict 40% of the true positives, compared with 50% for the combined network (Fig. 4D and fig. S24A). Likewise, examination of Fig. 4E and fig. S24B reveals that if an investigator wished to use network predictions with a precision of 0.021 (which is three times higher than expected at random), then 16% of the true positives would be recalled from the mRNA-only network versus 41% for the combined network.

By quantitatively measuring mRNAs, proteins, and phosphoproteins in parallel in a tissue-specific manner, we discovered unexpected relationships among these cellular readouts across maize development. In particular, our comparison of transcriptome- to proteome-based dendrograms and coexpression networks showed little overlap at the gene level, even though the samples were classified similarly and had similar ontological enrichments. The discovery that most protein-expressing genes are conserved and syntenic also was unexpected. The coexpression networks and GRNs provide a conceptual framework for future detailed studies in a model organism that is central to food security and bioenergy. Our findings highlight the importance of studying gene regulation at multiple levels.

REFERENCES AND NOTES

1. G. Krouk, J. Lingeman, A. M. Colon, G. Coruzzi, D. Shasha, *Genome Biol.* **14**, 123 (2013).
2. T. S. Gardner, J. J. Faith, *Phys. Life Rev.* **2**, 65–88 (2005).
3. Z. Bar-Joseph *et al.*, *Nat. Biotechnol.* **21**, 1337–1342 (2003).
4. R. De Smet, K. Marchal, *Nat. Rev. Microbiol.* **8**, 717–729 (2010).
5. V. van Noort, B. Snel, M. A. Huynen, *Trends Genet.* **19**, 238–242 (2003).
6. J. M. Stuart, E. Segal, D. Koller, S. K. Kim, *Science* **302**, 249–255 (2003).
7. S. Horvath, J. Dong, *PLOS Comput. Biol.* **4**, e1000117 (2008).
8. B. Schwanhäusser *et al.*, *Nature* **473**, 337–342 (2011).
9. C. Vogel *et al.*, *Mol. Syst. Biol.* **6**, 400 (2010).
10. S. Ghaemmaghami *et al.*, *Nature* **425**, 737–741 (2003).
11. K. Baerenfaller *et al.*, *Science* **320**, 938–941 (2008).
12. A. Ghazalpour *et al.*, *PLOS Genet.* **7**, e1001393 (2011).
13. L. Ponnala, Y. Wang, Q. Sun, K. J. van Wijk, *Plant J.* **78**, 424–440 (2014).
14. J. W. Walley *et al.*, *Proc. Natl. Acad. Sci. U.S.A.* **110**, E4808–E4817 (2013).
15. M. P. Washburn *et al.*, *Proc. Natl. Acad. Sci. U.S.A.* **100**, 3107–3112 (2003).
16. H. Qiao *et al.*, *Science* **338**, 390–393 (2012).
17. K. N. Chang *et al.*, *eLife* **2**, e00675 (2013).
18. M. R. Facette, Z. Shen, F. R. Björnsdóttir, S. P. Briggs, L. G. Smith, *Plant Cell* **25**, 2798–2812 (2013).
19. C. Marcon *et al.*, *Plant Physiol.* **168**, 233–246 (2015).
20. D. Hebenstreit *et al.*, *Mol. Syst. Biol.* **7**, 497 (2011).
21. N. Nagaraj *et al.*, *Mol. Syst. Biol.* **7**, 548 (2011).
22. J. C. Schnable, M. Freeling, *PLOS ONE* **6**, e17855 (2011).
23. P. Langfelder, S. Horvath, *BMC Bioinformatics* **9**, 559 (2008).
24. N. Bolduc *et al.*, *Genes Dev.* **26**, 1685–1690 (2012).
25. R. G. Schneeberger, P. W. Becraft, S. Hake, M. Freeling, *Genes Dev.* **9**, 2292–2304 (1995).
26. A. Gallavotti *et al.*, *Development* **137**, 2849–2856 (2010).
27. M. S. Mukhtar *et al.*, *Science* **333**, 596–601 (2011).
28. R. Albert, H. Jeong, A. L. Barabasi, *Nature* **406**, 378–382 (2000).
29. M. A. Calderwood *et al.*, *Proc. Natl. Acad. Sci. U.S.A.* **104**, 7606–7611 (2007).
30. H. Jeong, S. P. Mason, A. L. Barabási, Z. N. Oltvai, *Nature* **411**, 41–42 (2001).
31. K. Baerenfaller *et al.*, *Mol. Syst. Biol.* **8**, 606 (2012).
32. V. A. Huynh-Thu, A. Irrthum, L. Wehenkel, P. Geurts, *PLOS ONE* **5**, e12776 (2010).
33. D. Marbach *et al.*, *Nat. Methods* **9**, 796–804 (2012).
34. C. Li *et al.*, *Plant Cell* 10.1105/tpc.114.134858 (2015).
35. M. Schrynemackers, R. Küffner, P. Geurts, *Front. Genet.* **4**, 262 (2013).

ACKNOWLEDGMENTS

We thank V. Walbot for tassel and anther tissues, F. Hochholdinger for root tissues, and J. Fowler for pollen tissues. This work was supported by the NSF (grant 0924023 to S.P.B. and grants MCB-0929402 and MCB1122246 to J.R.E.), an NIH National Research Service Award Postdoctoral Fellowship (F32GM096707 to J.W.W.), and the Howard Hughes Medical Institute and the Gordon and Betty Moore Foundation (grant GBMF3034 to J.R.E.). Sequence data can be downloaded from the National Center for Biotechnology Information's Sequence Read Archive (accession number GSE50191). Raw mass spectra have been deposited at the Mass Spectrometry Interactive Virtual Environment (MassIVE) repository (accession numbers MSV000079290 and MSV000079303). Normalized expression data have been integrated into the genome browser and individual gene model pages at the central Maize Genetics and Genomics Database (www.maizegdb.org/).

SUPPLEMENTARY MATERIALS

www.sciencemag.org/content/353/6301/814/suppl/DC1
Materials and Methods
Supplementary Text
Figs. S1 to S33
Tables S1 to S10
References (*36*–*45*)

10 May 2016; accepted 25 July 2016
10.1126/science.aag1125

SYNTHETIC GENOMICS

Design, synthesis, and testing toward a 57-codon genome

Nili Ostrov,[1]* Matthieu Landon,[1,2,3]* Marc Guell,[1,4]* Gleb Kuznetsov,[1,5]*
Jun Teramoto,[1,6] Natalie Cervantes,[1] Minerva Zhou,[7] Kerry Singh,[7]
Michael G. Napolitano,[1,8] Mark Moosburner,[1] Ellen Shrock,[1] Benjamin W. Pruitt,[4]
Nicholas Conway,[4] Daniel B. Goodman,[1,4] Cameron L. Gardner,[1] Gary Tyree,[1]
Alexandra Gonzales,[1] Barry L. Wanner,[1,9] Julie E. Norville,[1]
Marc J. Lajoie,[1]† George M. Church[1,4]†

Recoding—the repurposing of genetic codons—is a powerful strategy for enhancing genomes with functions not commonly found in nature. Here, we report computational design, synthesis, and progress toward assembly of a 3.97-megabase, 57-codon *Escherichia coli* genome in which all 62,214 instances of seven codons were replaced with synonymous alternatives across all protein-coding genes. We have validated 63% of recoded genes by individually testing 55 segments of 50 kilobases each. We observed that 91% of tested essential genes retained functionality with limited fitness effect. We demonstrate identification and correction of lethal design exceptions, only 13 of which were found in 2229 genes. This work underscores the feasibility of rewriting genomes and establishes a framework for large-scale design, assembly, troubleshooting, and phenotypic analysis of synthetic organisms.

The degeneracy of the canonical genetic code allows the same amino acid to be encoded by multiple synonymous codons (*1*). Although most organisms follow a common 64-codon template for translation of cellular proteins, deviations from this universal code found in several prokaryotic and eukaryotic genomes (*2*–*6*) have spurred the exploration of synthetic cells with expanded genetic codes.

Whole-genome synonymous codon replacement provides a mechanism to construct unique organisms exhibiting genetic isolation and enhanced biological functions. Once a codon is replaced genome-wide and its cognate transfer RNA (tRNA) is eliminated, the genomically recoded organism (GRO) can no longer translate the missing codon (*7*). Genetic isolation is achieved because DNA acquired from viruses, plasmids, and other cells would be improperly translated, which would render GROs insensitive to infection and horizontal gene transfer (fig. S1).

In addition, proteins with novel chemical properties can be explored by reassigning replaced codons to incorporate nonstandard amino acids (nsAAs), which function as chemical handles for bioorthogonal reactivity and enable biocontainment of GROs (*8*–*11*). Building on previous work that demonstrated single–stop codon replacement (*7*), we set out to explore the feasibility of multiple codon replacements genome-wide, with the aim of producing a virus-resistant, biocontained bacterium for industrial applications.

We present computational design of an *Escherichia coli* genome in which all 62,214 instances of seven different codons (5.4% of all *E. coli* codons) have been synonymously replaced, and experimental validation of 2.5 Mb (63%) of this synthetic genome (Fig. 1 and data file S1). Once completely assembled, the resulting strain ("*rE.coli-57*") would use only 57 of the canonical 64 codons (fig. S2). Although several synthetic genomes have been previously reported (*12*–*19*), a functionally

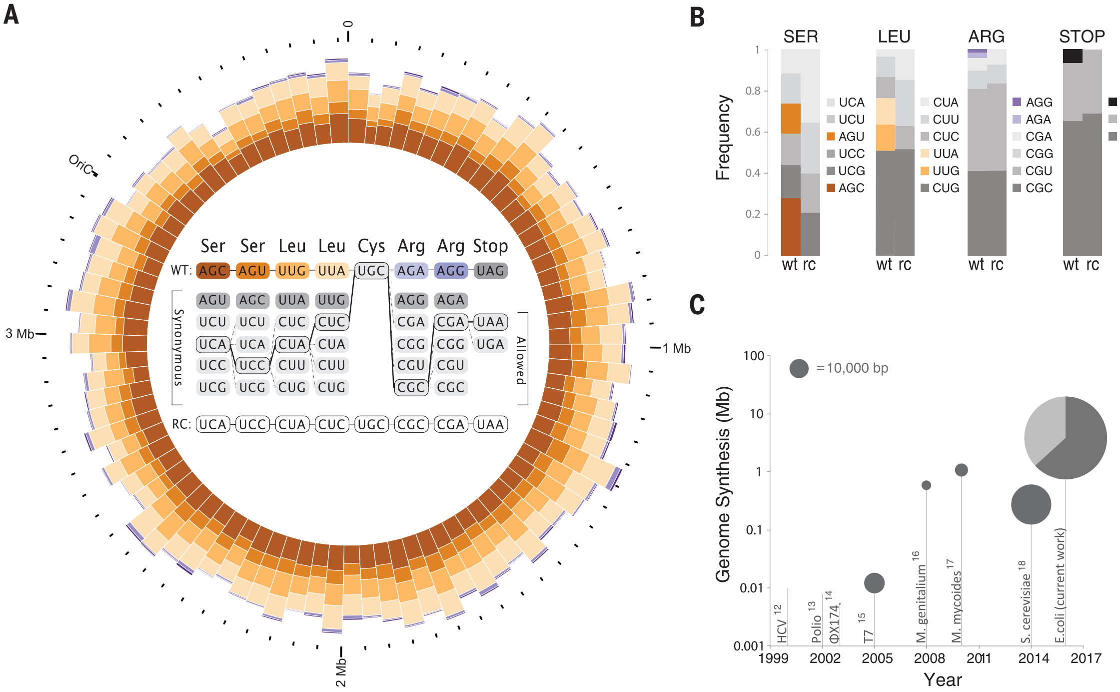

Fig. 1. A 57-codon *E. coli* genome. (**A**) The recoded genome was divided into 87 segments of ~50 kb. Codons AGA, AGG, AGC, AGU, UUA, UUG, and UAG were computationally replaced by synonymous alternatives (center). Other codons (e.g., UGC) remain unchanged. Color-coded histograms represent the abundance of the seven forbidden codons in each segment. (**B**) Codon frequencies in nonrecoded [wild-type (wt), *E. coli* MDS42] versus recoded [(rc), *rE.coli-57*] genome. Forbidden codons are colored. (**C**) The scale of DNA editing in genomes constructed by de novo synthesis. Plot area represents the number of modified base pairs compared with the parent genome. For the current work, dark gray represents percent of genome validated in vivo at time of publication (63%). HCV, hepatitis C virus; T7, bacteriophage T7; *M. genitalium*, *Mycoplasma genitalium*; and *M. mycoides*, *Mycoplasma mycoides*.

---

[1]Department of Genetics, Harvard Medical School, Boston, MA 02115, USA. [2]Program in Systems Biology, Harvard University, Cambridge, MA 02138, USA. [3]Ecole des Mines de Paris, Mines Paristech, Paris 75272, France. [4]Wyss Institute for Biologically Inspired Engineering, Boston, MA 02115, USA. [5]Program in Biophysics, Harvard University, Boston, MA 02115, USA. [6]Department of Biological Sciences, Purdue University, West Lafayette, IN 47907, USA. [7]Department of Biological Engineering, Massachusetts Institute of Technology, Cambridge, MA 02139, USA. [8]Program in Biological and Biomedical Sciences, Harvard University, Cambridge, MA 02138, USA. [9]Department of Microbiology and Immunobiology, Harvard Medical School, Boston, MA 02115, USA.
*These authors contributed equally to this work. †Corresponding author. Email: mlajoie@uw.edu (M.J.L.); gchurch@genetics.med.harvard.edu (G.M.C.)

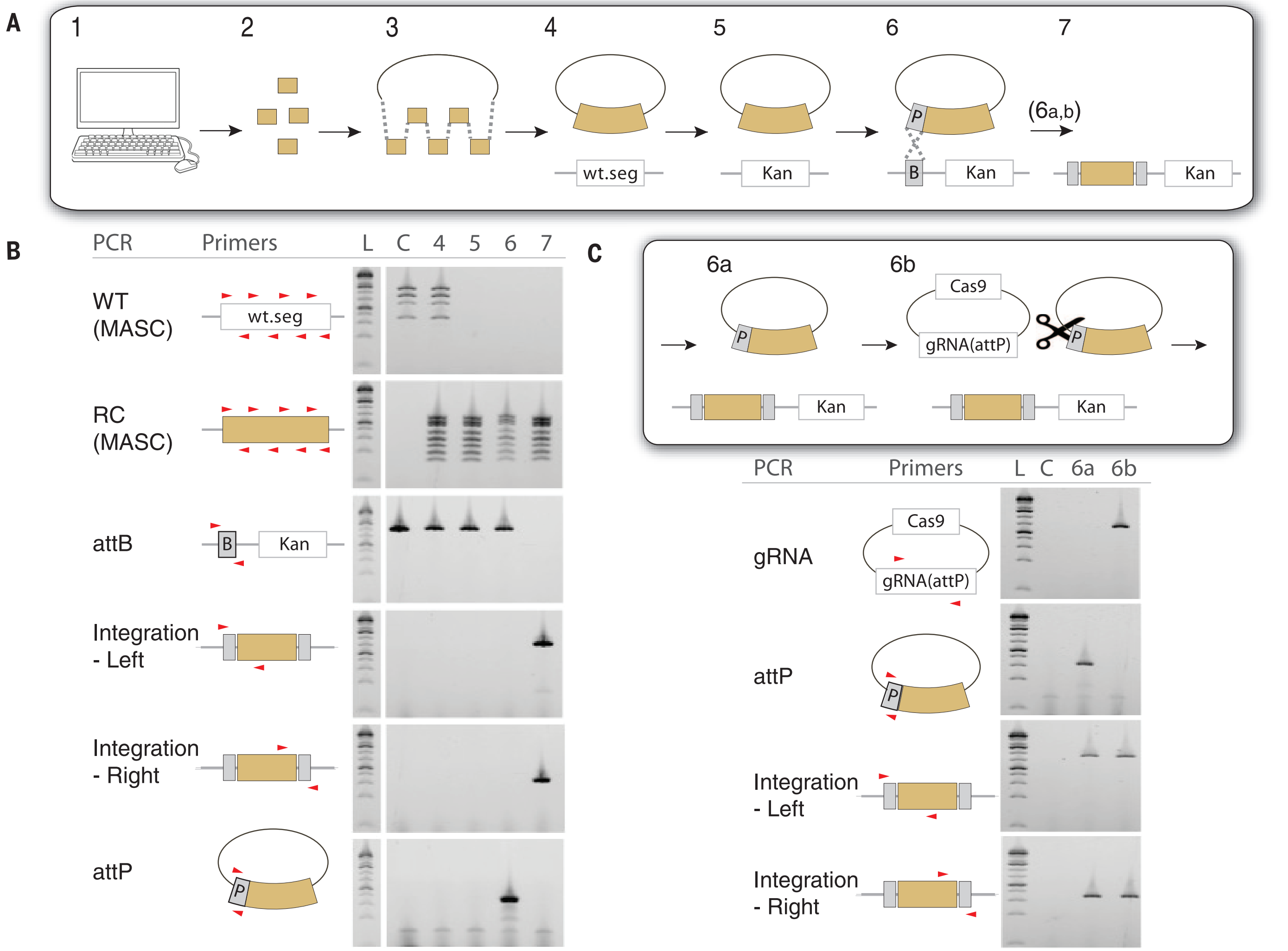

Fig. 2. Experimental strategy for recoded genome validation. (**A**) Pipeline schematics: 1) computational design; 2) de novo synthesis of 2- to 4-kb recoded fragments with 50–base pair overlap; 3) assembly of 50-kb segment (orange) in *S. cerevisiae* on a low-copy plasmid; 4) plasmid electroporation in *E. coli* (*wt.seg* is a nonrecoded chromosomal segment); 5) *wt.seg* is replaced by kanamycin cassette (Kan), such that cell viability depends solely on recoded gene expression; 6) λ-Integrase–mediated recombination of *attP* and *attB* sequences (P, episomal; B, chromosomal); 6a,b) elimination of residual vectors [see (C)]; and 7) single-copy integrated recoded segment. *attL-attR* sites shown in gray. Chromosomal deletions were performed in *E. coli* TOP10. (**B**) Polymerase chain reaction (PCR) analysis of steps 4 to 7 (L, GeneRuler 1 kb plus ladder; C, TOP10 control). Numbers correspond to schematics in (A). PCR primers shown in red (table S3). (**C**) Cas9-mediated vector elimination: Residual vector carrying recoded segment is targeted for digestion by Cas9 using *attP*-specific guide RNA (gRNA).

altered genome of this scale has not yet been explored (Fig. 1C).

Previous work suggests that codon usage alterations can affect gene expression and cellular fitness in multiple ways (*20*–*26*). However, parsing the individual impact of each codon remains difficult. Moreover, the number of modifications required to replace all instances of seven codons throughout the genome is far beyond the capabilities of current single-codon–editing strategies (*7*, *27*). Although it is possible to simultaneously edit multiple alleles using MAGE (*28*) or Cas9 (*29*), these strategies would require extensive screening with numerous oligos and likely would introduce off-target mutations (*7*, *30*). With plummeting costs of DNA synthesis, financial barriers for synthesizing entire genomes are greatly reduced, which allows for an almost unlimited number of modifications independent of biological template. Here, we developed computational and experimental tools to rapidly design and prototype synthetic organisms.

In choosing codons for replacement, UAG (stop) was selected because it was previously replaced genome-wide (*7*). AGG and AGA (Arg) are among the rarest codons in the genome, so selecting them minimizes the number of changes required. Other codons [AGC (Ser), AGU (Ser), UUG (Leu), and UUA (Leu)] were chosen such that their anticodon is not recognized as a tRNA identity element by endogenous aminoacyl-tRNA synthetases. We also considered mischarging of newly introduced tRNA by endogenous aminoacyl-tRNA synthetases upon codon reassignment. Last, we confirmed that all chosen codons are recognized by a tRNA different from that of their synonymous codons so that both codons and cognate tRNA could be eliminated (Fig. 1 and figs. S2 and S3).

In order to minimize synthesis costs and improve genome stability, we based our 57-codon genome on the reduced genome *E. coli* MDS42 (*31*). Our computational tool automated synonymous replacement of all forbidden codon occurrences in protein-coding genes while satisfying biological and technical constraints (figs. S4 and S5 and table S1). Primarily, we preserved amino acid sequences of all coding genes and adjusted DNA sequences to meet synthesis requirements (e.g., removing restriction sites, normalizing regions of extreme GC content, and reducing repetitive sequences). Alternative codons were selected to minimize disruption of biological motifs, such as ribosome binding sites (RBS) and mRNA secondary structure (*30*), and relative codon usage was conserved in order to meet translational demand (*32*, *33*). If no acceptable synonymous codon was found, the constraints were relaxed until an alternative was identified.

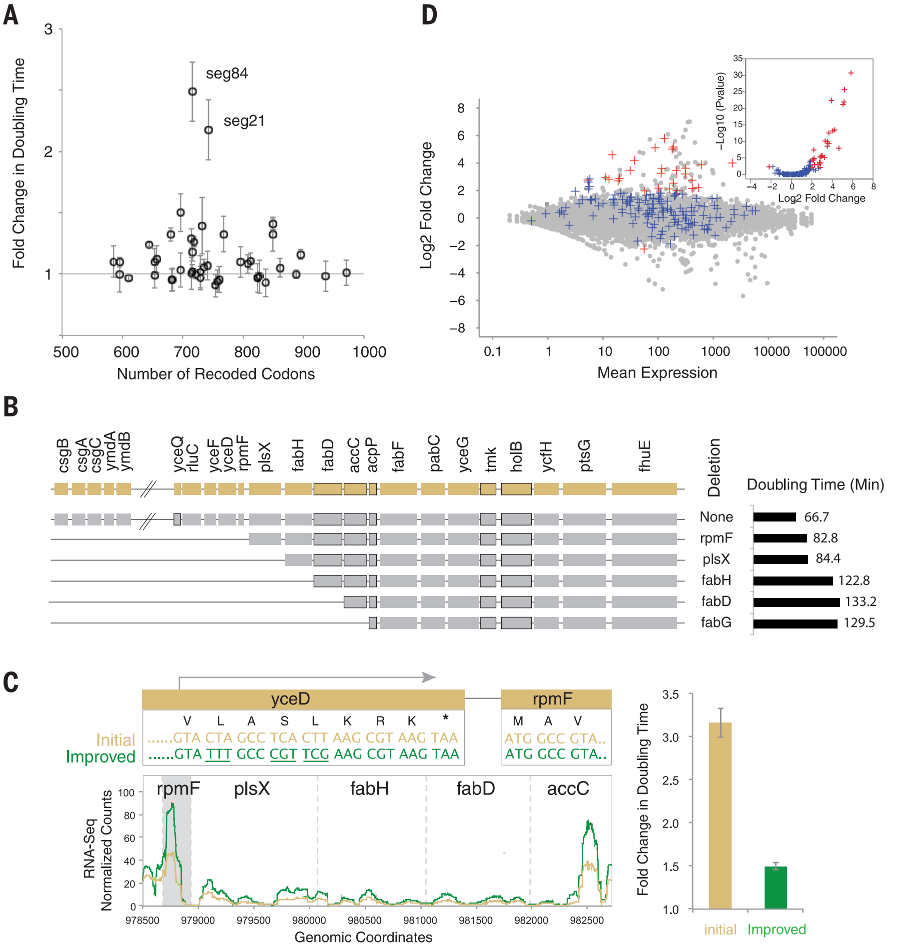

Fig. 3. Phenotypic analysis of recoded strains. (**A**) Recoded segments were episomally expressed in the absence of corresponding wild-type genes. Doubling time shown relative to nonrecoded parent strain (*35*). (**B**) Localization of fitness impairment in segment 21. Chromosomal genes (gray) were deleted to test for functional complementation by recoded genes (orange). Decrease in doubling time was observed upon deletion of *rpmF-accC* operon. Essential genes are framed. (**C**) Fine-tuning of *rpmF-accC* operon promoter resulted in increased gene expression and decrease in doubling time (normalized counts represent mean scaled sequencing depth). Orange, initial promoter; green, improved promoter. (**D**) RNA-seq analysis of 208 recoded genes (blue, segments 21, 38, 44, 46, 70). Wild-type gene expression shown in gray. Differentially expressed recoded genes shown in red (absolute log2 fold-change >2, adjusted $P < 0.01$). Fold-changes represent the difference between expression of each gene in a given strain and the average expression of the same gene in all other strains. (Inset) *P*-value distribution of recoded genes.

Forbidden codons were uniformly distributed throughout the genome and averaged ~17 codon changes per gene. Essential genes (*34*), which provide a stringent test for successful codon replacement, contained ~6.3% of all forbidden codons (3,903 of 62,214). Altogether, the recoded genome required a total of 148,955 changes to remove all instances of forbidden codons and to adjust the primary DNA sequence.

We parsed the recoded genome into 1256 synthesis-compatible overlapping fragments of 2 to 4 kb. These were used to construct 87 segments of ~50 kb each, which are convenient for yeast assembly and shuttling. Notably, intermediate 50-kb segments are also easier to troubleshoot than a full-size recoded genome or 3548 individual genes. We estimated that each segment would contain, on average, only ~1 potentially lethal recoding exception (*7*, *30*, *35*).

Carrying on average ~40 genes and ~3 essential genes, each segment was then individually tested for recoded gene functionality (fig. S4). Each segment was assembled in *Saccharomyces cerevisiae* and electroporated directly into *E. coli* on a low-copy plasmid. Subsequent deletion of the corresponding chromosomal sequence provided a stringent test for functionality of the recoded genes because errors in essential genes would be lethal (Fig. 2 and table S2).

Thus far, we performed chromosomal deletions for 2229 recoded genes (55 segments), which accounted for 63% of the genome and 53% of essential genes (fig. S6 and table S4). We thought it encouraging that 99.5% of recoded genes were found to complement wild-type genes without requiring any optimization. Moreover, the majority of chromosomally deleted strains exhibited limited fitness impairment (<10% doubling-time increase) (Fig. 3A and fig. S7).

Severe fitness impairment (>1.5-fold increase) was observed in only two strains. The causal genes were mapped by systematically removing wild-type genes, followed by measurement of strain fitness (Fig. 3, B and C, and fig. S8). We found fitness impairment in segment 21 was caused by insufficient expression of the recoded fatty acid biosynthesis operon *rpmF-accC*. Specifically, codon changes in upstream *yceD* were found to disrupt the operon promoter. Fitness was improved when *yceD* codons were altered via MAGE to preserve the overlapping promoter (Fig. 3C) (*35*). In segment 84, analysis suggested that three genes caused impairment of fitness (fig. S8), including the recoded gene *ytfP*, which contained a large deletion. Finally, RNA-sequencing (RNA-seq) analysis of 208 recoded genes suggested that the majority of genes exhibit limited change in transcription level (Fig. 3D and fig. S9) (*35*), and only 28 genes were found to be significantly differentially transcribed.

When a recoded segment failed to complement wild-type genes, it was diagnosed by making small chromosomal deletions. Notably, only 13 recoded essential genes ("design exceptions") were found that failed to support cell viability because of synonymous codon replacement (which corresponded to 9 segments) (table S4).

We chose gene *accD* as a test case to develop our troubleshooting pipeline for design exceptions (Fig. 4). First, RBS strength and mRNA folding were analyzed to pinpoint the cause of expression disruption (*22*, *23*, *26*). We further used degenerate oligos to prototype viable alternative codons (fig. S10). On the basis of these insights, a new recoded sequence was computationally generated (Fig. 4 and fig. S11) and introduced into the recoded segment via lambda Red recombineering. Viable clones were selected upon chromosomal deletion (*35*).

To further confirm adequate chromosomal expression, we integrated 11 recoded segments into the chromosome. We used *attP*-specific Cas9-mediated DNA cleavage to ablate all nonintegrated plasmids, which left a single recoded segment copy per cell. For all but one of 11 segments tested, a single copy was found to support cell viability (fig. S7). Nevertheless, we were unable to achieve a single copy of segment 32. Preliminary analysis suggested impairment of the recoded *pheMST* operon (fig. S12).

Finally, DNA sequence analysis was performed for all validated segments, showing some degree of in vivo mutations that are expected during strain engineering (table S4). Nevertheless, the average mutation rate was much lower than expected from using DNA editing methods (0.01 versus 1 mutation per codon change) (*7*). Moreover, the infrequent occurrence of reversions (25 instances in nonessential genes) speaks to the stability of the recoded genome.

It is well appreciated that without proper selection, substantial modifications to codon usage and tRNA anticodons can lead to genome instability. This could be circumvented by creating dependence on the recoded state, which also

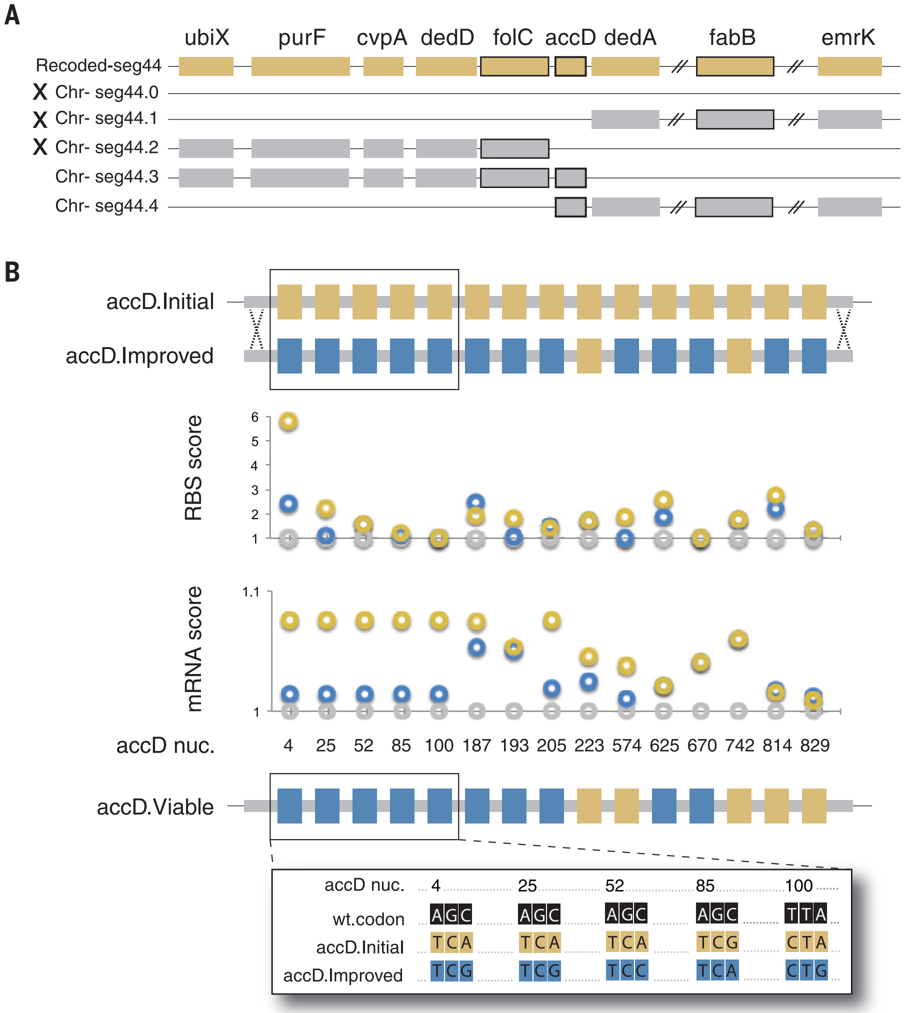

Fig. 4. Troubleshooting lethal design exceptions. (**A**) Recoded segment 44 (orange) did not support cell viability upon deletion of the corresponding chromosomal sequence (*Chr-seg44.0*). The causative recoded gene *accD* was identified by successive chromosomal deletions (*Chr-seg44.1-4*; "X," nonviable). Essential genes are framed. (**B**) λ-Red recombination was used to exchange lethal *accD* sequence (*accD.Initial*, recoded codons in orange) with an alternative recoded *accD* sequence (*accD. Improved,* alternative codons in blue). mRNA structure and RBS motif strength were calculated for both sequences. Wild type shown in gray. *accD nuc* is the first position in each recoded codon. The resulting viable sequence (*accD.Viable*) carried codons from both designs. Full sequences are provided in fig. S11. *mRNA* and RBS scores are the ratio between predicted mRNA folding energy (kcal/mol) (*37*) or predicted RBS strength (*38*) of recoded and nonrecoded codon.

provides stringent biocontainment (*9*, *36*). We previously developed a biocontained strain in which two essential genes, *adk* and *tyrS*, were altered to depend on nsAAs (*10*). Here, we confirmed that 57-codon versions of *adk* and *tyrS* were functional in vivo and that recoded and nsAA-dependent *adk* maintained fitness and provided extremely low escape rates as previously reported (fig. S13). These results suggest that the final *rE.coli-57* strain could support a similar biocontainment strategy.

As we continue toward creating a fully recoded organism, progress described herein provides crucial insights into the challenges we may encounter. The *rE.coli-57* genetic code will remain unchanged until both codons and respective tRNAs and release factors are removed (e.g., tRNAs genes *argU*, *argW*, *serV*, *leuX*, and *leuZ*, and release factor *prfA*). Only then could it be tested for novel properties, and up to four orthogonal nsAAs could be introduced.

Taken together, our results demonstrate the feasibility of radically changing the genetic code and the tractability of large-scale synthetic genome construction. A hierarchical, in vivo validation approach supported by robust design software brings the estimated total cost of constructing *rE.coli-57* to ~$1 million (table S5). Once complete, a genetically isolated *rE.coli-57* will offer a unique chassis with expanded synthetic functionality that will be broadly applicable for biotechnology.

REFERENCES AND NOTES

1. F. H. Crick, *Science* **139**, 461–464 (1963).
2. A. Ambrogelly, S. Palioura, D. Söll, *Nat. Chem. Biol.* **3**, 29–35 (2007).
3. A. Kano, Y. Andachi, T. Ohama, S. Osawa, *J. Mol. Biol.* **221**, 387–401 (1991).
4. T. Oba, Y. Andachi, A. Muto, S. Osawa, *Proc. Natl. Acad. Sci. U.S.A.* **88**, 921–925 (1991).
5. G. Macino, G. Coruzzi, F. G. Nobrega, M. Li, A. Tzagoloff, *Proc. Natl. Acad. Sci. U.S.A.* **76**, 3784–3785 (1979).
6. J. Ling, P. O'Donoghue, D. Söll, *Nat. Rev. Microbiol.* **13**, 707–721 (2015).
7. M. J. Lajoie *et al.*, *Science* **342**, 357–360 (2013).
8. C. C. Liu, P. G. Schultz, *Annu. Rev. Biochem.* **79**, 413–444 (2010).
9. P. Marliere, *Syst. Synth. Biol.* **3**, 77–84 (2009).
10. D. J. Mandell *et al.*, *Nature* **518**, 55–60 (2015).
11. A. J. Rovner *et al.*, *Nature* **518**, 89–93 (2015).
12. K. J. Blight, A. A. Kolykhalov, C. M. Rice, *Science* **290**, 1972–1974 (2000).
13. J. Cello, A. V. Paul, E. Wimmer, *Science* **297**, 1016–1018 (2002).
14. H. O. Smith, C. A. Hutchison 3rd, C. Pfannkoch, J. C. Venter, *Proc. Natl. Acad. Sci. U.S.A.* **100**, 15440–15445 (2003).
15. L. Y. Chan, S. Kosuri, D. Endy, *Mol. Syst. Biol.* **1**, 0018 (2005).
16. D. G. Gibson *et al.*, *Science* **319**, 1215–1220 (2008).
17. D. G. Gibson *et al.*, *Science* **329**, 52–56 (2010).
18. N. Annaluru *et al.*, *Science* **344**, 55–58 (2014).
19. C. A. Hutchison 3rd *et al.*, *Science* **351**, aad6253 (2016).
20. G. Kudla, A. W. Murray, D. Tollervey, J. B. Plotkin, *Science* **324**, 255–258 (2009).
21. T. Tuller, Y. Y. Waldman, M. Kupiec, E. Ruppin, *Proc. Natl. Acad. Sci. U.S.A.* **107**, 3645–3650 (2010).
22. J. B. Plotkin, G. Kudla, *Nat. Rev. Genet.* **12**, 32–42 (2011).
23. D. B. Goodman, G. M. Church, S. Kosuri, *Science* **342**, 475–479 (2013).
24. M. Zhou *et al.*, *Nature* **495**, 111–115 (2013).
25. T. E. F. Quax, N. J. Claassens, D. Söll, J. van der Oost, *Mol. Cell* **59**, 149–161 (2015).
26. G. Boël *et al.*, *Nature* **529**, 358–363 (2016).
27. F. J. Isaacs *et al.*, *Science* **333**, 348–353 (2011).
28. H. H. Wang *et al.*, *Nature* **460**, 894–898 (2009).
29. K. M. Esvelt *et al.*, *Nat. Methods* **10**, 1116–1121 (2013).
30. M. J. Lajoie *et al.*, *Science* **342**, 361–363 (2013).
31. G. Pósfai *et al.*, *Science* **312**, 1044–1046 (2006).
32. K. Temme, D. Zhao, C. A. Voigt, *Proc. Natl. Acad. Sci. U.S.A.* **109**, 7085–7090 (2012).
33. A. H. Yona *et al.*, *Elife* **2**, e01339 (2013).
34. Y. Yamazaki, H. Niki, J. Kato, *Methods Mol. Biol.* **416**, 385–389 (2008).
35. Materials and methods are available as supplementary materials at the *Science* website.
36. S. Osawa, T. H. Jukes, *J. Mol. Evol.* **28**, 271–278 (1989).
37. N. R. Markham, M. Zuker, *Nucleic Acids Res.* **33** (Web Server), W577-W581 (2005).
38. H. M. Salis, *Methods Enzymol.* **498**, 19–42 (2011).

ACKNOWLEDGMENTS

Funding for this work was provided by U.S Department of Energy grant DE-FG02-02ER63445 and Defense Advanced Research Projects Agency grant BAA-12-64. B.L.W. was supported by NSF grant 106394; G.K. was supported by DOD NDSEG Fellowship; D.B.G. was supported by NSF Graduate Research Fellowship; E.S. was supported by the Origins of Life Initiative at Harvard University. We thank Gen9 (D. Leake, I. Saaem, and E. Nickerson), SGI-DNA (D. Gibson), and Twist (E. Leprout) for DNA synthesis and J. Aach for insightful comments. G.K., M.J.L., M.L., M.G.N., D.B.G., and G.M.C. are inventors on patent application #62350468 submitted by the President and Fellows of Harvard College. The authors declare competing financial interests: Details are available in the supplementary documents of the paper. All FASTQ sequence files have been submitted to the Sequence Read Archive (SRA) at National Center for Biotechnology Information submission number SUB1484507. Plasmids will be available under a materials transfer agreement with Addgene.

SUPPLEMENTARY MATERIALS

www.sciencemag.org/content/353/6301/819/suppl/DC1
Materials and Methods
Supplementary Text
Figs. S1 to S13
Tables S1 to S5
References (*39*–*58*)
Data File S1

29 January 2016; accepted 21 July 2016
10.1126/science.aaf3639

ZIKA VIRUS

Specificity, cross-reactivity, and function of antibodies elicited by Zika virus infection

Karin Stettler,[1]* Martina Beltramello,[1]* Diego A. Espinosa,[2]† Victoria Graham,[3]† Antonino Cassotta,[4,5]† Siro Bianchi,[1]† Fabrizia Vanzetta,[1]† Andrea Minola,[1] Stefano Jaconi,[1] Federico Mele,[4] Mathilde Foglierini,[4] Mattia Pedotti,[4] Luca Simonelli,[4] Stuart Dowall,[3] Barry Atkinson,[3] Elena Percivalle,[6] Cameron P. Simmons,[7,8,9] Luca Varani,[4] Johannes Blum,[10,11] Fausto Baldanti,[6] Elisabetta Cameroni,[1] Roger Hewson,[3] Eva Harris,[2] Antonio Lanzavecchia,[4,5] Federica Sallusto,[4]‡§ Davide Corti[1]‡§

Zika virus (ZIKV), a mosquito-borne flavivirus with homology to Dengue virus (DENV), has become a public health emergency. By characterizing memory lymphocytes from ZIKV-infected patients, we dissected ZIKV-specific and DENV–cross-reactive immune responses. Antibodies to nonstructural protein 1 (NS1) were largely ZIKV-specific and were used to develop a serological diagnostic tool. In contrast, antibodies against E protein domain I/II (EDI/II) were cross-reactive and, although poorly neutralizing, potently enhanced ZIKV and DENV infection in vitro and lethally enhanced DENV disease in mice. Memory T cells against NS1 or E proteins were poorly cross-reactive, even in donors preexposed to DENV. The most potent neutralizing antibodies were ZIKV-specific and targeted EDIII or quaternary epitopes on infectious virus. An EDIII-specific antibody protected mice from lethal ZIKV infection, illustrating the potential for antibody-based therapy.

After its introduction into Brazil in 2015, Zika virus (ZIKV) has spread rapidly, and in February 2016, the World Health Organization (WHO) declared it a Public Health Emergency of International Concern (*1*–*3*). The main route of ZIKV infection is through bites by *Aedes* mosquitos, but the virus may also be sexually (*4*) and vertically transmitted (*5*). Although most of the ZIKV infections are asymptomatic or cause only mild symptoms, there is evidence that ZIKV infection can lead to neurological complications, such as Guillain-Barré syndrome in adults (*6*) and congenital birth defects, including microcephaly in the developing fetus (*5*, *7*, *8*), likely through its ability to infect human neural progenitor cells (*9*).

Whereas flavivirus envelope (E) proteins mediate fusion and are the main target of neutralizing antibodies, the nonstructural protein 1 (NS1) is secreted by infected cells and is involved in immune evasion and pathogenesis (*10*). Two recent studies showed a high level of structural similarity between the E protein of ZIKV and that of other flaviviruses—such as dengue virus (DENV), yellow fever virus (YFV), and West Nile virus (WNV)—but also revealed distinct features that may be related to the ZIKV neurotropism (*11*, *12*). Similarly, the structural analysis of ZIKV NS1 revealed conserved features with NS1 of other flaviviruses, although with different electrostatic characteristics (*13*).

A phenomenon that is characteristic of certain flaviviruses is the disease-enhancing activity of cross-reactive antibodies elicited by previous infections by heterologous viruses, termed antibody-dependent enhancement (ADE). In the case of DENV, for which four serotypes are known, there is epidemiological evidence that a primary infection protects from reinfection with the same serotype but represents a risk factor for the development of severe disease upon reinfection with a different serotype (*14*). The exacerbated disease is triggered by E- and prM-specific antibodies that fail to neutralize the incoming virus but instead enhance its capture by Fc receptor–expressing (FcR$^+$) cells, leading to enhanced viral replication and activation of cross-reactive memory T cells. The resulting cytokine storm is thought to be the basis of the most severe form of disease, known as dengue hemorragic fever/dengue shock syndrome (*15*, *16*). The role of antibodies in severe dengue is supported by studies showing that waning levels of maternal antibodies in infants represent a higher risk for development of severe dengue disease (*16*–*19*). Whether individuals with antibodies induced by previous DENV infections can develop a more severe ZIKV infection or have higher risk of fetal transmission is unknown. Similarly, it is unclear whether ZIKV antibodies may affect subsequent DENV infection. Therefore, it is important to dissect the level of cross-reactive immunity at the B cell and T cell level in response to ZIKV infection.

To understand the role of antibodies in ZIKV neutralization and heterologous enhancement of flavivirus infection, we isolated a panel of 119 monoclonal antibodies (mAbs) from four ZIKV-infected donors from the current epidemic, of which two were DENV-naïve (ZA and ZD) and two had serological records of DENV infection (ZB and ZC) (table S1) (*20*). These mAbs were selected from Epstein-Barr virus–immortalized memory B cells on the basis of their binding to ZIKV NS1 or E proteins and for their ability to neutralize ZIKV infection, and were compared, side by side, with a panel of mAbs previously isolated from DENV-infected donors (*21*). The mAbs were primarily immunoglobulin G (IgG), were highly polyclonal, and carried a lower level of somatic mutations as compared with that of other acute or recurrent infections (fig. S1 and table S2).

Out of the 119 ZIKV-reactive mAbs isolated, 41 bound to NS1. ZIKV and DENV NS1 share 51 to 53% of amino acid identity (Fig. 1, A and B, and fig. S2). The mAbs isolated from ZIKV-infected, DENV-naïve donors were to a large extent ZIKV-specific and did not cross-react to DENV NS1, whereas those isolated from ZIKV-infected, DENV-immune donors showed, as expected, a higher degree of cross-reactivity (Fig. 1C, fig. S3, and table S3). The limited cross-reactivity of NS1-reactive mAbs from ZIKV-infected, DENV-naïve donors was corroborated by the lack of reactivity to DENV1-4 NS1 proteins of plasma from ZIKV-infected, DENV-naïve donors (fig. S4). Conversely, the plasma of the ZIKV-infected, DENV-immune donors reacted strongly to DENV1-4 NS1 proteins, which is consistent with a recall response to NS1 dominated by cross-reactive antibodies. Reciprocally, NS1-reactive mAbs isolated from DENV-immune, ZIKV-naïve donors showed variable patterns of cross-reactivity between DENV serotypes but, with the exception of a single mAb, did not cross-react with ZIKV NS1 (Fig. 1D, fig. S5, and table S4).

Given the interest in developing a diagnostic tool that would discriminate ZIKV-specific from DENV-specific antibodies, we identified antigenic sites (figs. S1 and S2) on NS1 targeted by ZIKV-specific but not by cross-reactive mAbs (fig. S6, A to D). MAbs reacting to two distinct sites on ZIKV NS1 were used in a two-determinant immunoassay so as to detect circulating NS1 protein in body fluids during acute infection (fig. S6E). In addition, mAb ZKA35 binding to the antigenic site S2 was used as a probe in a blockade-of-binding assay (*22*) so as to detect ZIKV-specific, but not DENV-specific, serum antibodies to NS1 (Fig. 1E) and has a potential to be developed in a serological assay in order to detect clinical and subclinical ZIKV infections at the population level.

---

[1]Humabs BioMed SA, Via Mirasole 1, 6500 Bellinzona, Switzerland. [2]Division of Infectious Diseases and Vaccinology, School of Public Health, University of California, Berkeley, Berkeley, CA, USA. [3]National Infection Service, Public Health England, Porton Down, Salisbury, Wiltshire, UK. [4]Institute for Research in Biomedicine, Università della Svizzera italiana, Via Vincenzo Vela 6, 6500 Bellinzona, Switzerland. [5]Institute for Microbiology, ETH Zurich, Wolfgang-Pauli-Strasse 10, 8093 Zurich, Switzerland. [6]Molecular Virology Unit, Microbiology and Virology Department, Fondazione Istituto di Ricovero e Cura a Carattere Scientifico (IRCCS) Policlinico San Matteo, Pavia, Italy. [7]Centre for Tropical Medicine, Nuffield Department of Medicine, University of Oxford, UK. [8]Oxford University Clinical Research Unit, Center for Tropical Medicine, Ho Chi Minh City, Vietnam. [9]Department of Microbiology and Immunology, University of Melbourne, Peter Doherty Institute, 792 Elizabeth Street, Melbourne VIC 3000, Australia. [10]Swiss Tropical and Public Health Institute, Socinstrasse 57, 4002 Basel, Switzerland. [11]University of Basel, Petersgraben 4, 4031 Basel, Switzerland.
*These authors contributed equally to this work. †These authors contributed equally to this work. ‡These authors contributed equally to this work. **§Corresponding author. Email: davide.corti@humabs.ch (D.C.); federica.sallusto@irb.usi.ch (F.S.)**

Given the role of T cells in antibody production and in immunopathology, we also investigated the specificity and cross-reactivity of CD4$^+$ memory T cells from the same donors using the T cell library method (Fig. 1, F and G) (*23*). NS1-specific memory CD4$^+$ T cells were present in the CXCR3$^+$ T helper 1 (T$_H$1) compartment and, with variable frequencies, in the CXCR3$^-$ T$_H$ compartment. With a few exceptions, these T$_H$ cells were specific for either ZIKV or DENV NS1 (Fig. 1, F and G, and fig. S7A), which is consistent with a low level of T cell cross-reactivity, even in subjects who were already exposed to DENV.

The E protein is formed by three domains: EDI, which is involved in the conformational changes required for viral entry; EDII, which contains the fusion loop; and EDIII, which may be involved in binding to cellular receptors (*24*). DI, DII, and DIII of ZIKV and DENV share 35, 51, and 29% amino acid identity, respectively (Fig. 2A). According to the structure of the ZIKV E protein dimer (*11*, *12*), the majority of the ZIKV- and DENV-conserved solvent-accessible residues are located in EDII, particularly in the fusion loop and the neighboring region (Fig. 2B and fig. S8). Strikingly, the majority of ZIKV EDI/II–specific mAbs isolated from the four ZIKV donors (65%; 24 of 37) cross-reacted with the E protein of all four DENV serotypes (Fig. 2C, fig. S9, and table S5). Similarly, a large proportion (67%; 31 of 46) of DENV EDI/II–reactive mAbs isolated from DENV donors were also cross-reactive with ZIKV E protein (Fig. 2D, fig. S10, and table S6). These data indicate that the human antibody response to the E protein and in particular to EDI/II is cross-reactive between ZIKV and DENV, which is consistent with previous reports on mAbs from mice immunized with flavivirus antigens (*11*, *25*). ZIKV-immune plasma was also found to cross-react with ZIKV and DENV1-4 E proteins (fig. S11), possibly because of the abundant EDI/II cross-reactive antibody response (*21*, *26*–*28*).

In contrast, most of the EDIII-reactive mAbs (90%; 27 of 30) isolated from ZIKV or DENV donors were specific for either ZIKV or DENV E protein (Fig. 2, C and D; figs. S9 and S10; and tables S5 and S6). In addition, whereas the EDI/II mAbs showed only modest or even no neutralizing activity against ZIKV infection, the EDIII-reactive antibodies were overall more highly neutralizing than EDI/II–reactive antibodies (table S5). By screening for ZIKV neutralization, we also isolated several highly potent neutralizing antibodies that failed to bind to ZIKV E and EDIII proteins (Fig. 2C). These mAbs, that we define as neutralizing non-E-binding (NNB), could recognize quaternary epitopes that are displayed on the infectious virions but not on soluble proteins, as recently demonstrated for DENV (*29*–*31*). E-specific CD4$^+$ T cells were primarily detected in the CXCR3$^+$ T$_H$ cell subset and, with only a few exceptions, were specific for ZIKV E protein (Fig. 2, E and F, and fig. S7B). Furthermore, E-reactive T cells directly isolated from ex vivo cultures of memory CD4$^+$ T cells of ZIKV- or DENV-infected donors (fig. S12) did not cross-react upon secondary stimulation with heterologous E proteins (Fig. 2G). These findings indicate an overall low level of T cell cross-reactivity between ZIKV and DENV E proteins.

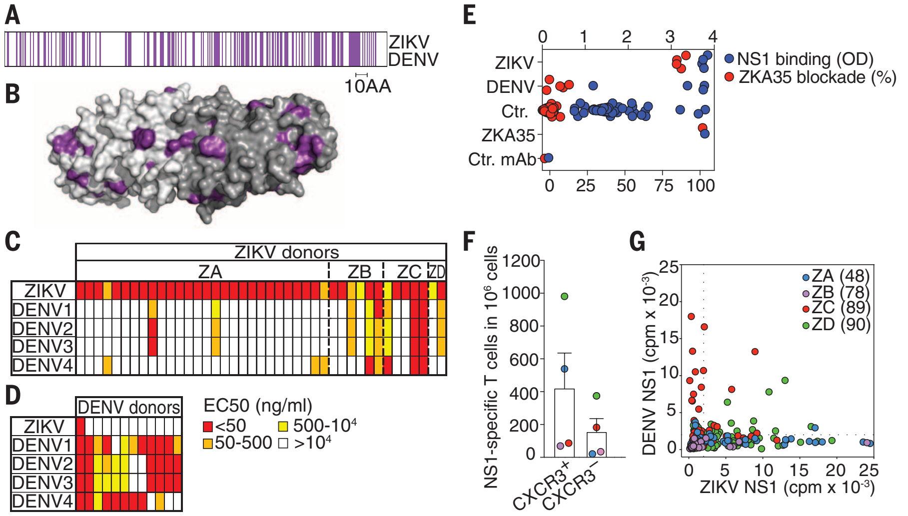

Fig. 1. Specificity and cross-reactivity of NS1-reactive mAbs and T cells derived from ZIKV- and DENV-infected donors. (**A**) Sequence conservation of NS1 proteins as determined by the alignments shown in fig. S2. Conserved residues in NS1 are in purple. (**B**) Structure of the ZIKV NS1 dimer [Protein Data Bank (PDB) 5IY3]. The two monomers are shown with different shades of gray. The surface residues of each protomer that are conserved between ZIKV and DENV are colored as in (A). (**C** and **D**) Heat map of the reactivity of (C) 41 mAbs derived from four ZIKV-infected donors (ZA-ZD) and (D) 12 mAbs derived from two DENV-infected donors. The mAbs were tested for binding to NS1 proteins of ZIKV and DENV1-4 [median effective concentration (EC$_{50}$), nanograms per milliliter]. A description of the immune status of the donors and the mAbs codes is provided in table S1. The binding curves of NS1-reactive mAbs are shown in figs. S3 and S5, and EC$_{50}$ values are reported in tables S3 and S4. Data are representative of at least two independent experiments. (**E**) Plasma from ZIKV-infected (n = 4 donors), DENV-infected (n = 5 donors), and control donors (n = 48 donors) (1/10 dilution) were tested for their capacity to bind NS1 (blue dots) and to inhibit the binding of the biotinylated mAb ZKA35 to NS1 (red dots). (**F** and **G**) T cell libraries were generated from CXCR3$^+$ and CXCR3$^-$ memory CD4$^+$ T cells of the four ZIKV-infected donors and screened for reactivity against ZIKV or DENV1-4 NS1 proteins by use of ^{3}H-thymidine incorporation. Shown is the estimated number of ZIKV NS1–specific T cells per 10^6 cells [mean + SEM and color-coded values for individual donors (F)]. Shown is also the proliferation [counts per minute (cpm)] of individual cultures to either ZIKV or DENV1-4 NS1 proteins (G). The cultures from different donors are color-coded, and their numbers are shown in parentheses. Dotted lines represent the cut-off value.

To address the biological properties of ZIKV and DENV antibodies, we used a selected mAb panel and measured in parallel their binding (Fig. 3A), neutralizing, and ADE activity (Fig. 3, B and C). This panel also contained Fc mutant versions of mAbs that do not bind to FcγR and complement [LALA mutants; leucine (L) to alanine (A) substitution at the position 234 and 235] (*21*, *32*). The EDIII-specific mAbs ZKA64 and ZKA190 and the NNB mAb ZKA230 were highly potent in ZIKV neutralization, with median inhibitory concentration (IC$_{50}$) values of 93, 9, and 10 ng/ml, respectively. Furthermore, all these mAbs enhanced infection of ZIKV in the non-permissive K562 human erythroleukemic cell line at a broad range of concentrations, including those that fully neutralized ZIKV infection on Vero cell line. Whereas EDIII mAbs ZKA64 and ZKA190 did not enhance ZIKV infections of K562 cells above 1 μg/ml, the NNB mAb ZKA230 failed to do so, a result that might be due to the different mechanisms of neutralization of free viruses versus FcγR-internalized viruses. In contrast, the cross-reactive EDI/II–specific mAbs ZKA3 and ZKA78 only partially neutralized ZIKV infectivity, while effectively enhancing infection of K562 cells. Consistent with their cross-reactivity, these EDI/II–specific mAbs also neutralized and enhanced DENV1 infection.

The above results suggest that cross-reactive antibodies elicited by either ZIKV or DENV infection and primarily directed to EDI/II can mediate heterologous ADE. We therefore asked whether ADE could be also induced with immune sera and whether this could be blocked by neutralizing mAbs delivered in a LALA format (Fig. 3, D and E). In a homologous setting, four ZIKV-immune plasma collected from convalescent patients showed similar capacity to enhance ZIKV infection of K562 cells, and this ADE effect was completely blocked by the EDIII-specific ZKA64-LALA mAb, but only partially inhibited by the cross-reactive EDI/II DV82-LALA mAb (Fig. 3D). In a heterologous setting, the four ZIKV-immune plasma strongly enhanced infection by DENV1 to levels comparable with those observed with DENV3 plasma. The enhancement of DENV1 infection by both ZIKV and DENV3 plasma was completely inhibited by DV82-LALA, but not by ZKA64-LALA because of its lack of cross-reactivity to DENV1 (Fig. 3E).

The ADE-blocking ability of a single EDIII-specific LALA mAb could be related not only to its capacity to out-compete serum-enhancing antibodies but also to neutralize virus once internalized into endosomes, similarly to what has been reported for the WNV-neutralizing antibody E16 (*33*). Conversely, the lack of ADE-blocking ability of DV82-LALA might be explained by the inability of antibodies to EDI/II to effectively neutralize endocytosed virus.

The above results suggest that previous ZIKV and DENV immunity may pose a risk of a more severe disease upon exposure to heterologous virus through ADE. To address this possibility in vivo, we selected two EDI/II cross-reactive mAbs elicited by ZIKV (ZKA78) or DENV (DV82) and tested them for their capacity to enhance infection by DENV or ZIKV in animal models. Preadministration of ZKA78 or DV82, but not their LALA versions, to DENV2-infected AG129 mice led to severe symptoms and lethality by day 5 (Fig. 4A), suggesting that ZIKV immunity could predispose to enhanced DENV pathology in vivo. Given the high lethality of ZIKV infection in immunodeficient mice (*34*–*36*), we investigated a possible ZIKV disease–enhancing activity of the DENV cross-reactive mAb DV82 in 129Sv/ev immunocompetent mice that are not permissive for productive ZIKV infection. However, in this mouse model we did not observe signs of enhanced disease or infection (fig. S13).

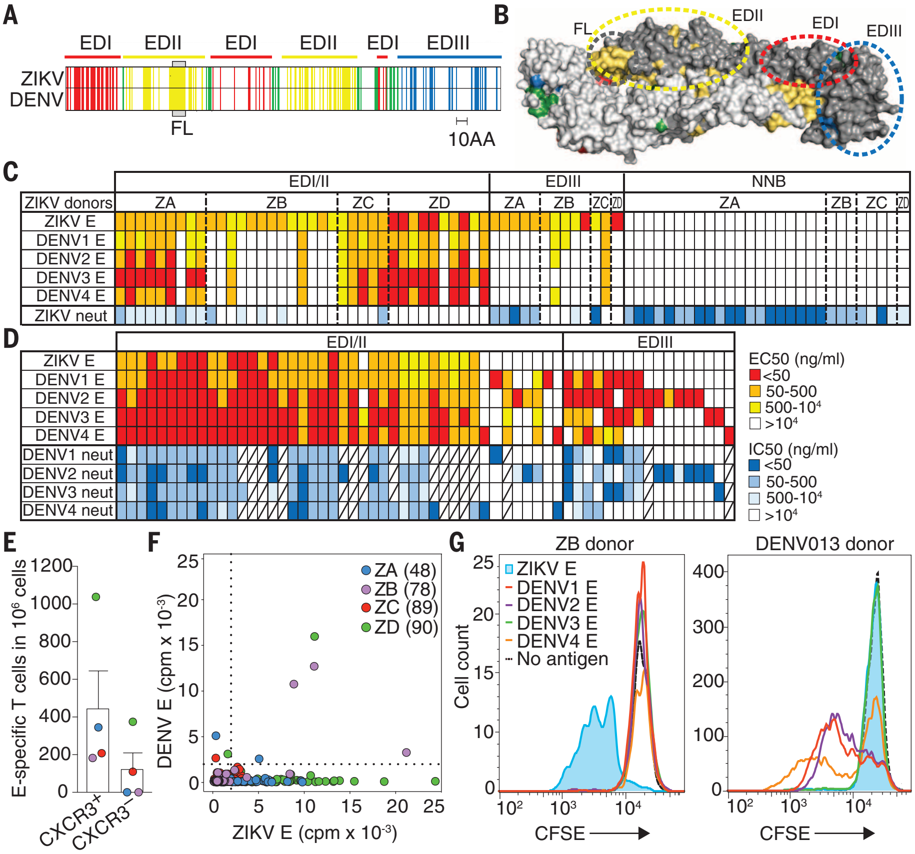

Fig. 2. Specificity and cross-reactivity of E-reactive mAbs and T cells derived from ZIKV- and DENV-infected donors. (**A**) Sequence conservation of E proteins as determined by the alignments of ZIKV isolates and DENV1-4 reference strains, as shown in fig. S8. Conserved residues in EDI, EDII, EDIII, and the hinge regions of the E protein are colored in red, yellow, blue, and green, respectively. FL, fusion loop. (**B**) Structure of the ZIKV E protein dimer (PDB 5JHM). The two monomers are shown with different shades of gray, and the residues conserved between ZIKV and DENV are colored as in (A). (**C** and **D**) Heat map of the reactivity of (C) 78 mAbs derived from four ZIKV donors and (D) 61 mAbs derived from nine DENV donors. NNB, neutralizing non-E-binding mAbs. The mAbs were tested for binding to E-recombinant proteins of ZIKV and DENV1-4 (EC_{50}, nanograms per milliliter). Also shown is the virus-neutralizing activity (IC_{50}, nanograms per milliliter). Strikethrough cells indicate not tested. Binding curves of E-reactive mAbs are shown in figs. S9 and S10. The EC_{50} and IC_{50} values of E-reactive and NNB mAbs are shown in tables S5 and S6. Data are representative of at least two independent experiments. (**E** and **F**) T cell libraries were generated from $CXCR3^+$ and $CXCR3^-$ memory $CD4^+$ T cells of the four ZIKV-infected donors and screened for reactivity against ZIKV or DENV1-4 E proteins by using ^{3}H-thymidine incorporation. Shown is the estimated number of ZIKV E–specific T cells per 10^6 cells [mean + SEM and color-coded values for individual donors (E)]. Also shown is the proliferation (cpm) of individual cultures to either ZIKV E or DENV1-4 E proteins (F). The cultures from different donors are color-coded, and their numbers are shown in parentheses. Dotted lines represent the cut-off value. (**G**) $CD4^+$ $CXCR3^+$ T cells from peripheral blood mononuclear cells of a ZIKV-infected (ZB) or DENV-infected (DENV013) donor were labeled with carboxyfluorescein succinimidyl ester (CFSE) and stimulated with ZIKV or DENV1-4 E proteins, respectively. Proliferating T cells were isolated by means of cell sorting, relabeled with CFSE, and stimulated with the indicated proteins. Shown are the CFSE profiles on day 5.

To develop a therapeutic approach to ZIKV infection, we tested the LALA form of the potently neutralizing EDIII-specific mAb ZKA64 in prophylactic and therapeutic settings. ZKA64-LALA completely protected A129 mice challenged with a lethal dose of ZIKV from body weight loss and lethality when given 1 day before or 1 day after ZIKV challenge (Fig. 4B).

This study reports the first characterization of the human immune response to ZIKV infection. The highly cross-reactive antibodies to EDI/II elicited by ZIKV or DENV infection that are poorly neutralizing but potently enhancing may pose a risk for heterologous ADE. We have shown in vitro and in a relevant animal model that an EDI/II cross-reactive mAb raised by ZIKV can induce lethal DENV infection. However, enhancement of ZIKV infection by DENV-elicited cross-reactive antibodies could be observed in vitro but not in vivo, a finding that may be due to the tropism of the virus or to the limitation of the mouse model. It will be important to address this issue in clinical and epidemiological studies, which may be facilitated by the development of serological diagnostics, such as the blockade-of-binding assay described in this study.

T cells in flavivirus infections play a complex role in both protection and pathogenesis (*15*). The low degree of $CD4^+$ T cell cross-reactivity between DENV and ZIKV, which we observed even in individuals who are immune to both viruses, suggests that in ZIKV infection original antigenic sin may not play a pathogenic role. Our findings also suggest that the risk of cytokine storm and consequent severe disease after enhanced heterologous infection of DENV by antibodies to ZIKV may be mitigated by the poor T cell cross-reactivity.

Our study describes two classes of potent neutralizing antibodies that are specific for ZIKV and directed either against EDIII or quaternary epitopes present on infectious virus, the latter being particularly frequent, similar to what has been described in DENV (*30*). Given the high potency and in vivo efficacy shown in this study, these antibodies, developed in wild type or their LALA versions produced in wild-type version or in LALA version so as to avoid possible enhancement, could be used in prophylactic or therapeutic settings to prevent congenital ZIKV infection in pregnant women living in high-risk areas (*37*).

REFERENCES AND NOTES

1. L. R. Petersen, D. J. Jamieson, A. M. Powers, M. A. Honein, *N. Engl. J. Med.* **374**, 1552–1563 (2016).
2. A. S. Fauci, D. M. Morens, *N. Engl. J. Med.* **374**, 601–604 (2016).
3. D. L. Heymann *et al.*, *Lancet* **387**, 719–721 (2016).
4. D. Musso *et al.*, *Emerg. Infect. Dis.* **21**, 359–361 (2015).
5. J. Mlakar *et al.*, *N. Engl. J. Med.* **374**, 951–958 (2016).

6. V.-M. Cao-Lormeau *et al*., *Lancet* **387**, 1531–1539 (2016).
7. E. J. Rubin, M. F. Greene, L. R. Baden, *N. Engl. J. Med.* **374**, 984–985 (2016).
8. G. Calvet *et al*., *Lancet Infect. Dis.* **16**, 653–660 (2016).
9. H. Tang *et al*., *Cell Stem Cell* **18**, 587–590 (2016).
10. D. A. Muller, P. R. Young, *Antiviral Res.* **98**, 192–208 (2013).
11. L. Dai *et al*., *Cell Host Microbe* **19**, 696–704 (2016).
12. D. Sirohi *et al*., *Science* **352**, 467–470 (2016).
13. H. Song, J. Qi, J. Haywood, Y. Shi, G. F. Gao, *Nat. Struct. Mol. Biol.* **23**, 456–458 (2016).
14. S. B. Halstead, *Microbiol. Spectr.* **2**, 249–271 (2014).
15. G. Screaton, J. Mongkolsapaya, S. Yacoub, C. Roberts, *Nat. Rev. Immunol.* **15**, 745–759 (2015).
16. S. B. Halstead, *Adv. Virus Res.* **60**, 421–467 (2003).
17. S. B. Halstead *et al*., *Emerg. Infect. Dis.* **8**, 1474–1479 (2002).
18. T. H. Nguyen *et al*., *J. Infect. Dis.* **189**, 221–232 (2004).
19. A. L. Rothman, *J. Clin. Invest.* **113**, 946–951 (2004).
20. M. Ginier, A. Neumayr, S. Günther, J. Schmidt-Chanasit, J. Blum, *Travel Med. Infect. Dis.* **14**, 16–20 (2016).
21. M. Beltramello *et al*., *Cell Host Microbe* **8**, 271–283 (2010).
22. B. Ohana *et al*., *Clin. Diagn. Lab. Immunol.* **7**, 904–908 (2000).
23. R. Geiger, T. Duhen, A. Lanzavecchia, F. Sallusto, *J. Exp. Med.* **206**, 1525–1534 (2009).
24. Y. Modis, S. Ogata, D. Clements, S. C. Harrison, *Proc. Natl. Acad. Sci. U.S.A.* **100**, 6986–6991 (2003).
25. T. P. Monath, J. J. Schlesinger, M. W. Brandriss, C. B. Cropp, W. C. Prange, *Am. J. Trop. Med. Hyg.* **33**, 695–698 (1984).
26. S. A. Smith *et al*., *J. Virol.* **86**, 2665–2675 (2012).
27. C.-Y. Lai *et al*., *J. Virol.* **82**, 6631–6643 (2008).
28. H.-E. Lin *et al*., *PLOS Negl. Trop. Dis.* **6**, e1447 (2012).
29. E. P. Teoh *et al*., *Sci. Transl. Med.* **4**, 139ra83 (2012).
30. W. Dejnirattisai *et al*., *Nat. Immunol.* **16**, 170–177 (2015).
31. A. Rouvinski *et al*., *Nature* **520**, 109–113 (2015).
32. A. J. Hessell *et al*., *Nature* **449**, 101–104 (2007).
33. B. S. Thompson *et al*., *PLOS Pathog.* **5**, e1000453 (2009).
34. S. D. Dowall *et al*., *PLOS Negl. Trop. Dis.* **10**, e0004658–e13 (2016).
35. H. M. Lazear *et al*., *Cell Host Microbe* **19**, 720–730 (2016).
36. M. T. Aliota *et al*., *PLOS Negl. Trop. Dis.* **10**, e0004682–e11 (2016).
37. M. A. Johansson, L. Mier-Y-Teran-Romero, J. Reefhuis, S. M. Gilboa, S. L. Hills, *N. Engl. J. Med.* **375**, 1–4 (2016).
38. S. Orozco *et al*., *J. Gen. Virol.* **93**, 2152–2157 (2012).

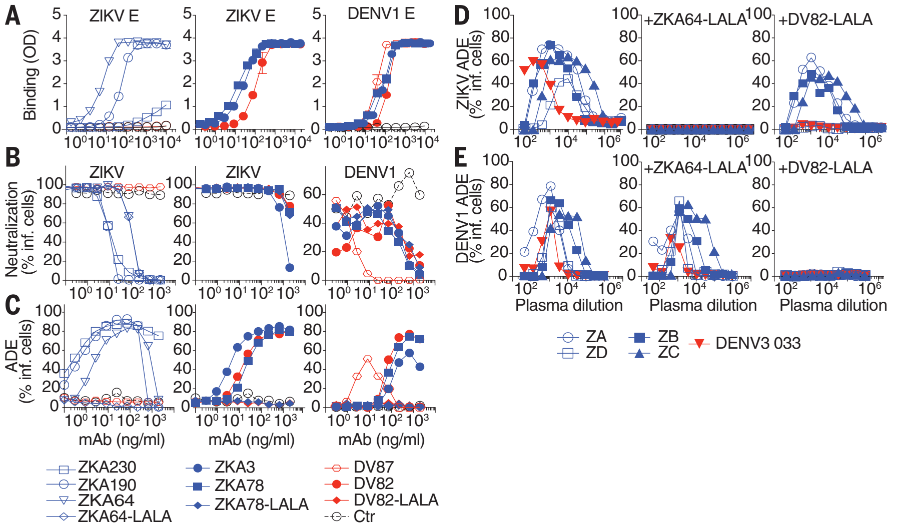

Fig. 3. Neutralization and enhancement of ZIKV and DENV infection by mAbs and immune plasma. (**A**) Binding of mAbs isolated from ZIKV-infected donors (blue) or from DENV-infected donors (red) to (left and middle) recombinant ZIKV E and (right) to DENV1 E protein. Open and solid symbols indicate mAbs specific or cross-reactive for ZIKV and DENV, respectively. (**B**) Neutralization of ZIKV and DENV1 as determined by the percentage of infected Vero cells. (**C**) ADE of ZIKV and DENV1 infection of nonpermissive K562 cells, as determined by the percentage of infected cells on day 5. (**D** and **E**) Inhibition of ADE by LALA mutant mAbs. Serial dilutions of ZIKV- and DENV3-immune plasma were incubated with ZIKV or DENV1 before addition to K562 cells in the absence or presence of a fixed amount (50 μg/ml) of ZKA64-LALA or DV82-LALA mAb. Shown is the percentage of infected K562 cells on day 4. Blue and red symbols indicate plasma derived from ZIKV- or DENV-infected donors, respectively. Data are representative of two independent experiments.

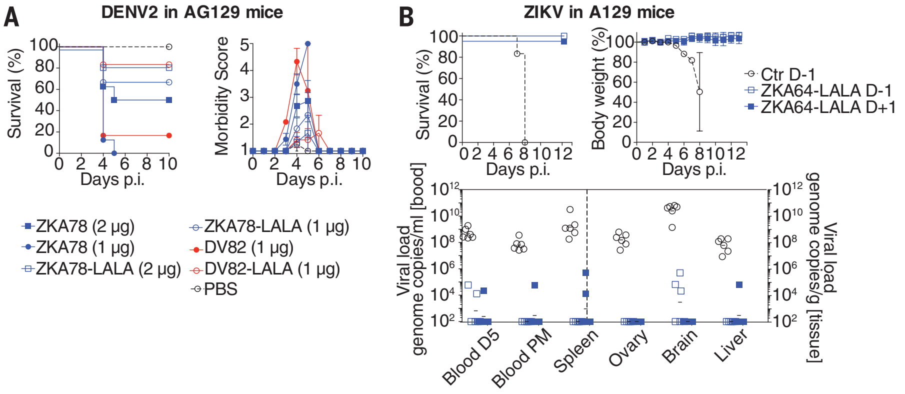

Fig. 4. In vivo enhancement of DENV2 infection by an anti-ZIKV cross-reactive mAb and ZIKV therapeutic efficacy of a potent anti-ZIKV EDIII-specific mAb. (**A**) In vivo ADE. MAbs were administered intraperitoneally to AG129 mice 20 to 24 hours before intravenous inoculation with 2.5 × 10^5 plaque-forming units (PFU) of DENV2 D2S10. Results are representative of two independent experiments, with $n = 8$ mice for the ZKA78 1 and 2-μg groups; $n = 6$ for the DV82 and all LALA mAb groups; and $n = 4$ for phosphate-buffered saline (PBS) group. (Left) A Kaplan-Meier survival curve is shown; significance was determined by using the Mantel-Cox log-rank test. ZKA78 versus PBS, $P = 0.0008$; ZKA78 versus ZKA78-LALA, $P = 0.0081$; DV82 versus PBS, $P = 0.0187$; and DV82 versus DV82-LALA, $P = 0.0255$. (Right) Mice were monitored over a 10-day period and scored for morbidity and mortality by using a standardized 5-point system (*38*). (**B**) Prophylaxis and therapy of ZIKV infection. MAbs (15 mg/kg) were administered intraperitoneally to A129 mice ($n = 6$ mice) 24 hours before or after subcutaneous inoculation with 10^2 PFU of ZIKV MP1751. (Top left) A Kaplan-Meier survival curve is shown. (Top right) Mice were monitored over a 13-day period for body weight loss. (Bottom) Viral loads were measured on day 5 in blood of all animals and in blood and indicated tissues when animals were culled at the end of the study or when the humane end points were met. Lines indicate geometric means.

ACKNOWLEDGMENTS

The data presented in this manuscript are tabulated in the main paper and in the supplementary materials. The views expressed are those of the authors and not necessarily those of the funding bodies. This work was supported by grants from the European Union (HEALTH-F3-2011-281803-Project IDAMS, "International Research Consortium on Dengue Risk Assessment, Management, and Surveillance" to F.S.), the European Research Council (grant 323183 PREDICT to F.S.), the Swiss National Science Foundation (grant 160279 to A.L.), the U.S. National Institutes of Health (grant R01 AI24493 to E.H.), and the Ministero della Salute, Fondazione IRCCS Policlinico San Matteo, Ricerca Corrente grant 8020615 (to E.P. and F.B.). A.L. is supported by the Helmut Horten Foundation. A.L. is the scientific founder of Humabs BioMed. D.C., A.L., and F.S. hold shares in Humabs BioMed. F.S. and F.B. are a scientific advisor and a consultant at Humabs BioMed, respectively. The MAbs described in this study are available under a materials transfer agreement with Humabs BioMed SA. L.V. is grateful for financial support by SNF grant 310030_166445 and Lions Club Monteceneri. A.L. is an inventor on a patent related to DENV mAbs described in this study: PCT/IB2009/007372 (Dengue virus neutralizing antibodies and uses thereof). D.C. is an inventor on a patent application held by Humabs BioMed SA related to ZIKV mAbs described in this study: PCT/EP2016/066684 (Novel antibodies specifically binding to Zika virus epitopes and uses thereof). Antibody nucleotide and amino acid sequences for the 68 mAbs described in table S2 have been deposited in GenBank (accession nos. KX496807 to KX496874).

SUPPLEMENTARY MATERIALS

www.sciencemag.org/content/353/6301/823/suppl/DC1
Figs. S1 to S13
Tables S1 to S6
References (*39–52*)

10 April 2016; accepted 5 July 2016
Published online 14 July 2016
10.1126/science.aaf8505

HUMAN GENETICS

Cardiometabolic risk loci share downstream cis- and trans-gene regulation across tissues and diseases

Oscar Franzén,[1,2]* Raili Ermel,[3,4]* Ariella Cohain,[1]* Nicholas K. Akers,[1] Antonio Di Narzo,[1] Husain A. Talukdar,[5] Hassan Foroughi-Asl,[5] Claudia Giambartolomei,[6] John F. Fullard,[6] Katyayani Sukhavasi,[3] Sulev Köks,[3] Li-Ming Gan,[7] Chiara Giannarelli,[1,8] Jason C. Kovacic,[8] Christer Betsholtz,[9,10] Bojan Losic,[1] Tom Michoel,[11] Ke Hao,[1] Panos Roussos,[1,6,12] Josefin Skogsberg,[5] Arno Ruusalepp,[2,3,4] Eric E. Schadt,[1] Johan L. M. Björkegren[1,2,3,5]†

Genome-wide association studies (GWAS) have identified hundreds of cardiometabolic disease (CMD) risk loci. However, they contribute little to genetic variance, and most downstream gene-regulatory mechanisms are unknown. We genotyped and RNA-sequenced vascular and metabolic tissues from 600 coronary artery disease patients in the Stockholm-Tartu Atherosclerosis Reverse Networks Engineering Task study (STARNET). Gene expression traits associated with CMD risk single-nucleotide polymorphism (SNPs) identified by GWAS were more extensively found in STARNET than in tissue- and disease-unspecific gene-tissue expression studies, indicating sharing of downstream cis-/trans-gene regulation across tissues and CMDs. In contrast, the regulatory effects of other GWAS risk SNPs were tissue-specific; abdominal fat emerged as an important gene-regulatory site for blood lipids, such as for the low-density lipoprotein cholesterol and coronary artery disease risk gene *PCSK9*. STARNET provides insights into gene-regulatory mechanisms for CMD risk loci, facilitating their translation into opportunities for diagnosis, therapy, and prevention.

In 2012, cardiovascular disease accounted for 17.5 million deaths, nearly one-third of all deaths worldwide, and >80% (14.1 million) were from coronary artery disease (CAD) and stroke. CAD is preceded by cardiometabolic diseases (CMDs) such as hypertension, impaired lipid and glucose metabolism, and systemic inflammation (*1*, *2*). Genome-wide association studies (GWAS) have identified hundreds of DNA variants associated with risk for CAD (*3*), hypertension (*4*), blood lipid levels (*5*), markers of plasma glucose metabolism (*6*–*10*), type 2 diabetes (*6*, *11*), body mass index (*12*), rheumatoid arthritis (*13*), systemic lupus erythematosus (SLE) (*14*), ulcerative colitis (*15*), and Crohn's disease (*16*). However, identifying susceptibility genes responsible for these loci has proven difficult.

GWAS loci typically span large, noncoding, intergenic regions with numerous single-nucleotide polymorphisms (SNPs) in strong linkage disequilibrium. These regions are enriched in cis-regulatory elements (*17*) and expression quantitative trait loci (eQTLs) (*18*–*20*), suggesting that gene regulation is the principal mechanism by which risk loci affect complex disease etiology. However, it is largely unknown whether this gene-regulatory effect includes one or several genes acting in one or multiple tissues and whether risk loci for different diseases share cis- and trans-gene regulation. A better understanding of gene regulation may also shed light on why known GWAS risk loci explain only ~10% of expected heritable variance in CMD risk (*21*). Possibly, multiple risk loci, acting through common cis- and trans-genes, contribute synergistically to heritability (*22*, *23*).

In the Stockholm-Tartu Atherosclerosis Reverse Networks Engineering Task study (STARNET) (fig. S1), we recruited 600 well-characterized (table S1 and fig. S2) CAD patients; genotyped DNA (6,245,505 DNA variant calls with minor allele frequency >5%) (fig. S3); and sequenced RNA isolated from blood, atherosclerotic-lesion-free internal mammary artery (MAM), atherosclerotic aortic root (AOR), subcutaneous fat (SF), visceral abdominal fat (VAF), skeletal muscle (SKLM), and liver (LIV) (15 to 30 million reads per sample) (figs. S4 to S11 and table S2).

In total, ~8 million cis-eQTLs were identified, and nearly half were unique SNP-gene pairs (figs. S12 to S26 and tables S3 to S7). The STARNET cis-eQTLs were enriched in genetic associations established by GWAS for CAD, CMDs, and Alzheimer's disease (AD) (*3*–*16*, *24*) (figs. S27 to S33) and were further enriched after epigenetic filtering (figs. S34 to S39). Of 3326 genome-wide significant-risk SNPs identified by GWAS to date (*25*), 2,047 (61%) had a matching cis-QTL in STARNET (Fig. 1A). Of the 54 lead risk SNPs verified in meta-analyses of CAD GWAS (*3*), 38 cis-eQTLs with a regulatory trait concordance score (RTC) >0.9 and at least one candidate gene were identified in STARNET (table S8 and fig. S27). Compared with large data sets of cis-eQTL isolated only from blood, cis-eQTLs across all tissues in STARNET matched >10-fold more CAD and CMD-related GWAS risk SNPs (Fig. 1B). STARNET cis-eQTLs isolated from CAD-affected tissues also matched several-fold more CAD and CMD-related GWAS risk SNPs than cis-eQTLs from corresponding tissues isolated from predominantly healthy individuals in the Genotype Tissue Expression (GTEx) study (*18*) (Fig. 1C). Thus, not all gene-regulatory effects of disease-risk SNPs are identifiable in blood or healthy tissues. This notion was further underscored by comparing the statistical significances of cis-eQTLs for GWAS risk SNPs in STARNET with corresponding associations in GTEx (Fig. 1D). In STARNET, gene fusions (table S9) and CAD-related loss of function mutations (table S10) were also detected.

The cis effects of disease-associated risk loci identified by GWAS are central for understanding downstream molecular mechanisms of disease. However, these cis-genes likely also affect downstream trans-genes. To identify possible trans effects, we ran a targeted analysis to call both cis- and trans-genes for lead risk SNPs identified by GWAS. After assigning cis-eQTLs for 562 risk SNPs for CAD, CMDs, and AD (*3*–*16*, *24*), we used a causal inference test (*26*) to conservatively call causal correlations between the cis-genes and trans-genes by assessing the probability that an interaction was causal [SNP→cis-gene→trans-gene; false discovery rate (FDR) $< 1\%$] and not reactive (SNP→trans-gene→cis-gene; $P > 0.05$) (*26*) (table S11). We found extensive sharing of cis- and trans-gene regulation by GWAS risk loci across tissues and CMDs. In CAD, 28 risk loci with at least one causal interaction (FDR $< 1\%$, $P > 0.05$) had a total of 51 cis-genes and 1040 trans-genes. Of these, 26 risk loci, 37 cis-genes [including 27 key drivers (*27*)], and 994 trans-genes were connected in a main CAD regulatory gene network acting across all seven tissues

---

[1]Department of Genetics and Genomic Sciences, The Icahn Institute for Genomics and Multiscale Biology Icahn School of Medicine at Mount Sinai, One Gustave L. Levy Place, New York, NY 10029, USA. [2]Clinical Gene Networks AB, Jungfrugatan 10, 114 44 Stockholm, Sweden. [3]Department of Pathophysiology, Institute of Biomedicine and Translation Medicine, University of Tartu, Biomeedikum, Ravila 19, 50411, Tartu, Estonia. [4]Department of Cardiac Surgery, Tartu University Hospital, 1a Ludwig Puusepa Street, 50406 Tartu, Estonia. [5]Division of Vascular Biology, Department of Medical Biochemistry and Biophysics, Karolinska Institutet, Scheeles Väg 2, 171 77 Stockholm, Sweden. [6]Division of Psychiatric Genomics, Department of Psychiatry and Friedman Brain Institute, Icahn School of Medicine at Mount Sinai, One Gustave L. Levy Place, New York, NY 10029, USA. [7]Cardiovascular and Metabolic Diseases, Innovative Medicines and Early Development Biotech Unit, AstraZeneca, Pepparedsleden 1, Mölndal, 431 83, Sweden. [8]Cardiovascular Research Center Icahn School of Medicine at Mount Sinai, One Gustave L. Levy Place, New York, NY 10029, USA. [9]AstraZeneca-Karolinska Integrated CardioMetabolic Centre (ICMC), Karolinska Institutet, Novum, Blickagången 6, 141 57 Huddinge, Sweden. [10]Department of Immunology, Genetics and Pathology Dag Hammarskjölds Väg 20, 751 85 Uppsala, Sweden. [11]Division of Genetics and Genomics, The Roslin Institute, University of Edinburgh, Old College, South Bridge, Edinburgh EH8 9YL, UK. [12]Department of Psychiatry, J. J. Peters VA Medical Center, Mental Illness Research Education and Clinical Center (MIRECC), 130 West Kingsbridge Road, Bronx, NY 10468, USA.
*These authors contributed equally to this work. **†Corresponding author. Email: johan.bjorkegren@mssm.edu**

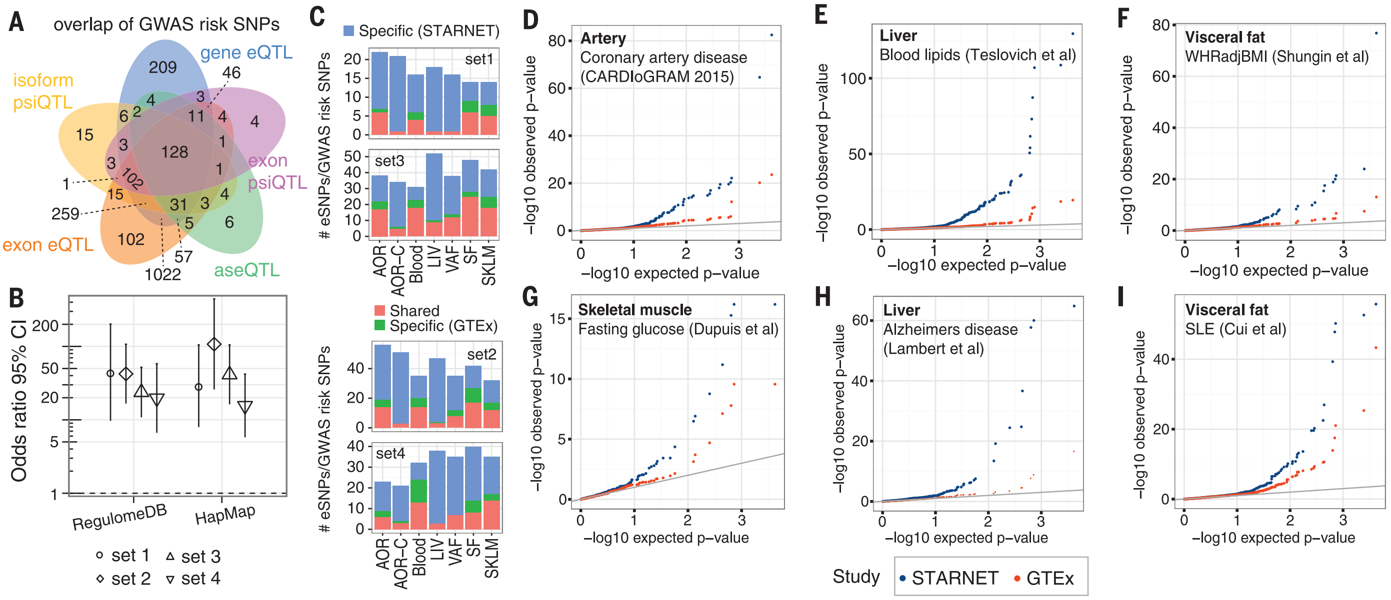

Fig. 1. QTLs and disease-associated risk SNPs identified by GWAS. (**A**) Venn diagram showing 2047 of 3326 disease-associated risk SNPs from the National Human Genome Research Institute GWAS catalog overlapping with at least one form of STARNET e/psi/aseQTLs. (**B**) Odds ratios that STARNET eQTLs coincide with CAD-associated risk SNPs (set 1, CARDIoGRAM-C4D, *n* = 53; set 2, CARDIoGRAM extended, *n* = 150) (*3*), blood lipids (set 3, *n* = 35) (*5*), and metabolic traits (set 4, *n* = 132) (*6*, *8*, *10*, *12*) versus blood eQTLs from RegulomeDB and HapMap. The *y* axis shows odds ratios. Error bars, 95% confidence intervals. (**C**) Stacked bar plots comparing tissue-specific eQTLs from STARNET and GTEx (*18*) coinciding with disease-associated risk SNPs in the same sets 1 to 4 as in (B). (**D** to **I**). Q-Q plots showing associations of tissue-specific STARNET (blue) and GTEx (*18*) (red) cis-eQTLs of disease-associated risk SNPs identified by GWAS for CAD (*3*) (D), blood lipids (*5*) (E), waist-hip ratio (*12*) (F), fasting glucose (*6*) (G), AD (*24*) (H), and SLE (*14*) (I).

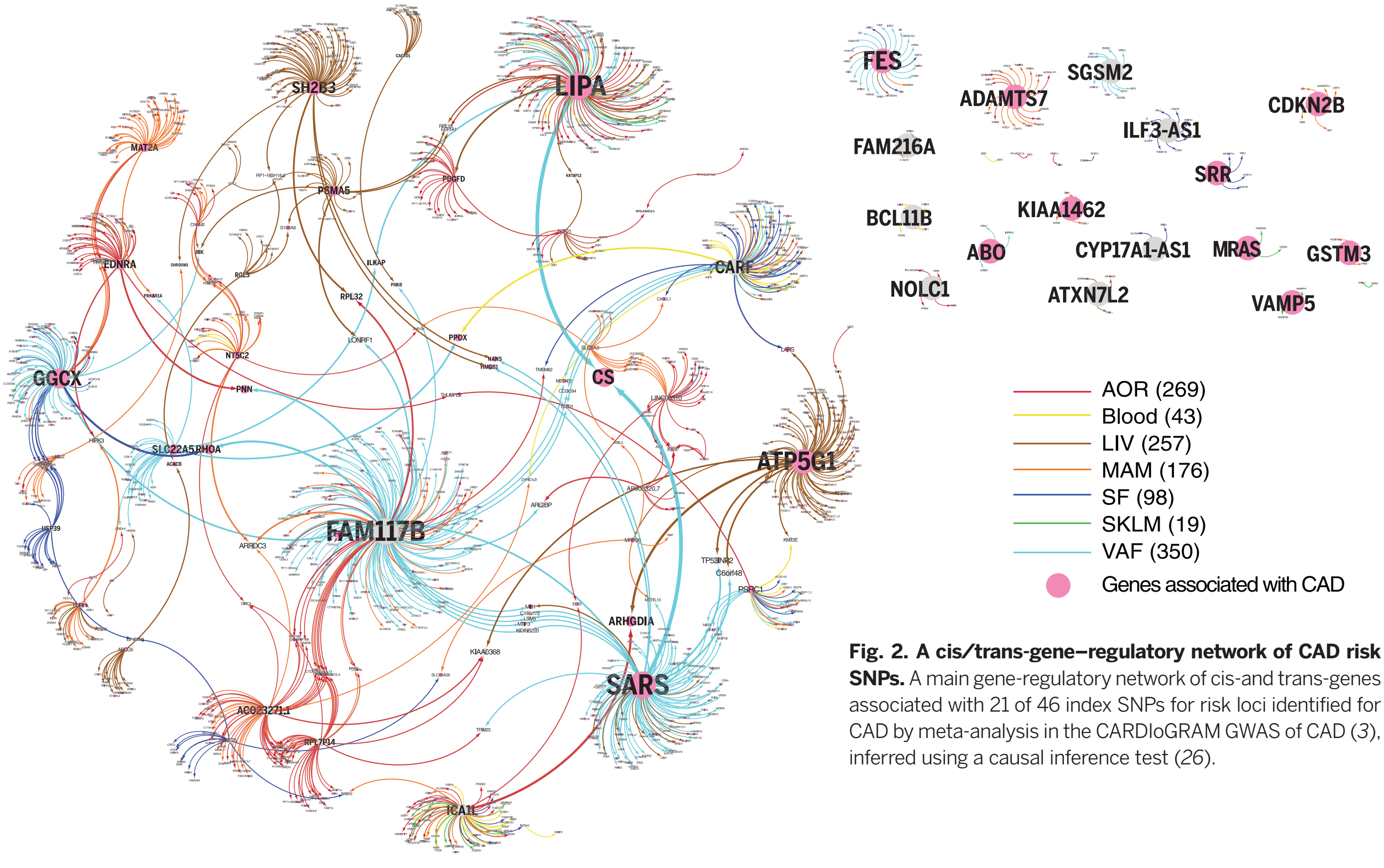

Fig. 2. A cis/trans-gene–regulatory network of CAD risk SNPs. A main gene-regulatory network of cis-and trans-genes associated with 21 of 46 index SNPs for risk loci identified for CAD by meta-analysis in the CARDIoGRAM GWAS of CAD (*3*), inferred using a causal inference test (*26*).

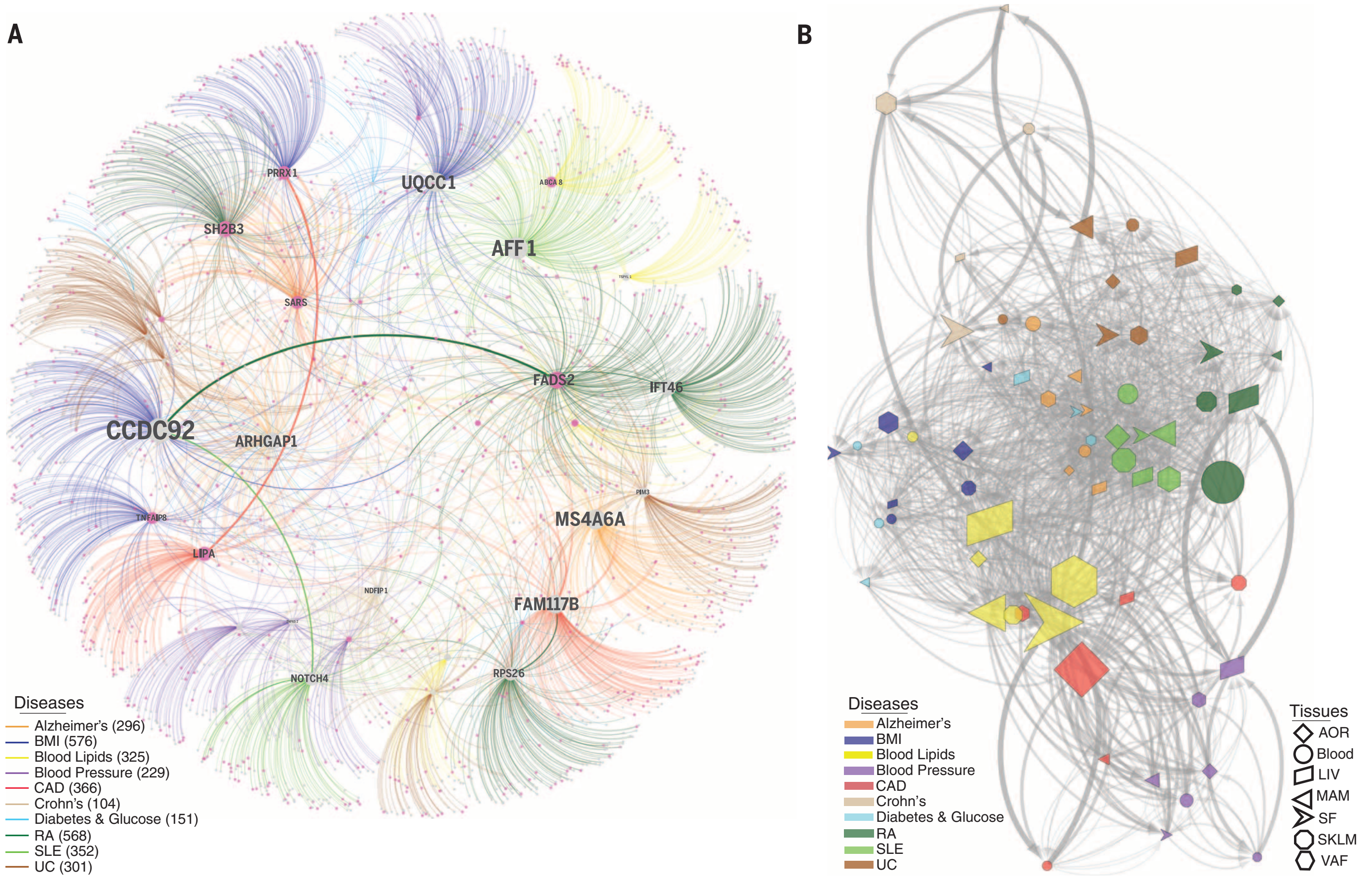

Fig. 3. Cis- and trans-gene regulation across CMDs and Alzheimer's disease. (**A**) A pan-disease risk SNP cis/trans-gene regulatory network. Thirty-six top key disease drivers, including 33 cis-genes for risk SNPs identified for CMDs including CAD and AD by GWAS (*3–16*, *24*), were identified as having >100 downstream genes in any disease-specific network or belonging to the top five key drivers in the main regulatory gene network for each disease (table S11). Edge thickness reflects how frequent an edge is part of the shortest path between all pairs of network nodes. Node size reflects the number of downstream nodes in the network. RA, rheumatoid arthritis; UC, ulcerative colitis. (**B**) Cis- and trans-gene regulation across disease-tissue pairs. Nodes represent unique disease-tissue pairs. Edges occur when a cis-gene in one node has downstream trans-genes present also in another node. Edge thickness defined as in (A). Node size reflects its centrality in the network: The position of the nodes in the network (i.e., layout) was derived from an edge-weighted spring layout algorithm. The "weight" is defined as the number of trans-genes that have a connection from the upstream node's cis-genes, normalized by the total number of trans-genes between two connecting nodes, with the result that highly connected nodes are positioned in the center of the network.

(Fig. 2). The trans-genes in this network were enriched with genes previously associated with CAD and atherosclerosis (Fisher's test, 1.54-fold; $P = 8 \times 10^{-10}$) (table S11). Sharing of cis/trans-genes downstream of complex disease risk loci also emerged for other CMDs and AD (*3–16*, *24*) (fig. S40). In fact, we identified 33 cis-genes regulated by risk SNPs across all CMDs, including CAD and AD, acting as key drivers in a pan-disease cis/trans-gene regulatory network (Fig. 3A).

Among CMDs, cis/trans-genes of GWAS risk SNPs for blood lipid levels (*5*) emerged as central (Fig. 3B) where tissue-specific downstream effects were, besides LIV (46 cis- and 150 trans-genes), observed in the fat tissues (SF, 45 cis- and 372 trans-genes; VAF, 38 cis- and 465 trans-genes) (fig. S41 and table S11). Visceral abdominal fat examples included *ABCA8/ABCA5* (rs4148008) associated with 36 downstream trans-genes in VAF and HDL (high-density lipoprotein); *EVI5* (rs7515577) associated with 32 VAF trans-genes and total cholesterol; and *STARD3* (rs11869286) associated with 7 VAF trans-genes and HDL. In addition, the cis-gene *TMEM258* (rs174546) with 22 trans-genes in abdominal fat surfaced as a parallel/alternative regulatory site of plasma low-density lipoprotein (LDL) to the proposed *FADS*-1,2,3 in LIV (*5*) (fig. S41). Other risk SNPs with VAF-specific cis-genes had few or even no trans-genes (fig. S41). For example, two risk SNPs—rs11206510 for CAD and rs12046679 for LDL cholesterol level (*3*, *5*)—regulate *PCSK9* in VAF, not in LIV (Fig. 4, A and B). The VAF specificity of these eQTLs *PCSK9* was confirmed in an independent gene expression data set from morbidly obese patients (*28*) (Fig. 4C and fig. S30), suggesting that PCSK9 is secreted from VAF into the portal vein to affect hepatic LDL receptor degradation, LDL plasma levels, and risk for CAD (*29*). Interestingly, and as previously suggested (*30*), we observed that STARNET patients in the upper, compared to the lower, 5th to 20th percentiles of waist-hip ratio (i.e., patients with and without "male fat") had higher levels of circulating PCSK9 (Fig. 4D) and LDL/HDL ratio (Fig. 4E).

STARNET provides new insights into tissue-specific gene-regulatory effects of disease-associated risk SNPs identified by GWAS, as exemplified by abdominal fat for blood lipids, and will be a complementary resource for exploring GWAS findings moving forward. Furthermore, STARNET also revealed unexpected sharing of cis- and trans-genes downstream of risk loci for CMDs across both tissues and diseases. We anticipate that the identified cis/trans-gene regulatory networks will help elucidate the complex downstream effects of risk loci for common complex diseases, including possible epistatic effects that could shed light on the missing heritability of CMD risk. Given the detailed phenotypic data on STARNET patients, we can begin to identify how genetic variability interacts with environmental perturbations across tissues to cause pathophysiological alterations and complex diseases.

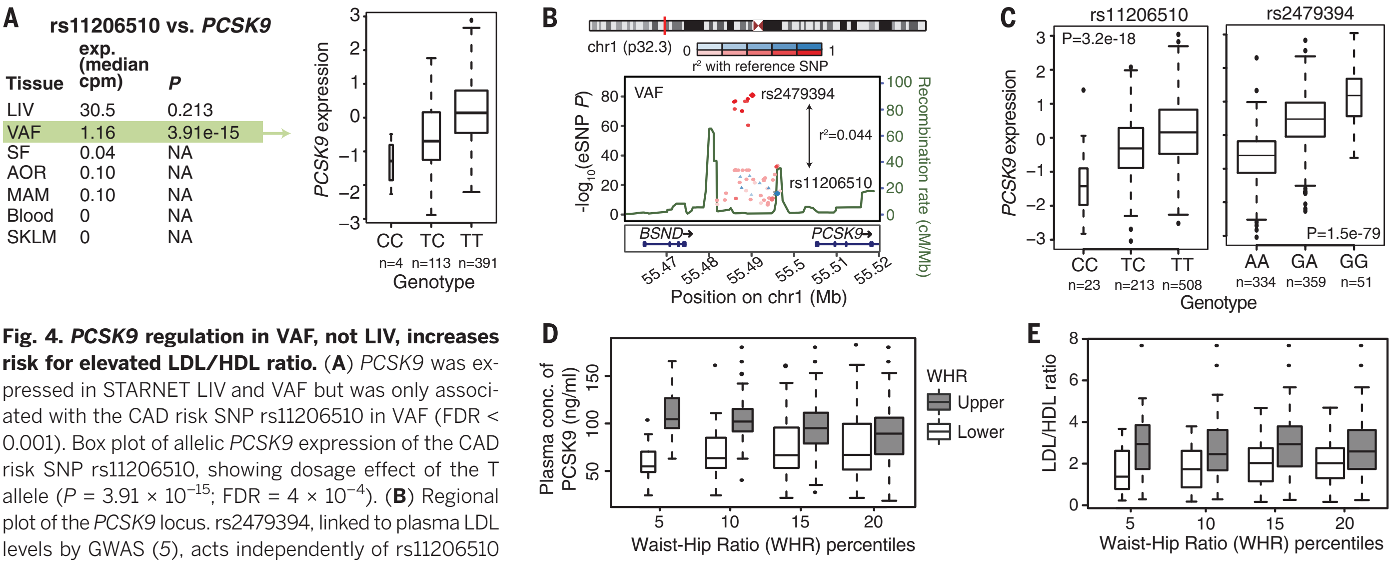

Tissue	exp. (median cpm)	*P*
LIV	30.5	0.213
VAF	1.16	3.91e-15
SF	0.04	NA
AOR	0.10	NA
MAM	0.10	NA
Blood	0	NA
SKLM	0	NA

Fig. 4. *PCSK9* regulation in VAF, not LIV, increases risk for elevated LDL/HDL ratio. (**A**) *PCSK9* was expressed in STARNET LIV and VAF but was only associated with the CAD risk SNP rs11206510 in VAF (FDR < 0.001). Box plot of allelic *PCSK9* expression of the CAD risk SNP rs11206510, showing dosage effect of the T allele ($P = 3.91 \times 10^{-15}$; FDR = 4×10^{-4}). (**B**) Regional plot of the *PCSK9* locus. rs2479394, linked to plasma LDL levels by GWAS (*5*), acts independently of rs11206510 as the lead eQTL of *PCSK9* expression in VAF. rs2479394 was not an eQTL of *PCSK9* in STARNET LIV. (**C**) Box plots of allelic *PCSK9* expression in VAF of rs11206510 and rs2479394 in a gene-tissue expression study of morbidly obese patients (fig. S29) (*28*). (**D** and **E**) Box plots of PCSK9 levels (D) and ratios of LDL/HDL (E) in plasma isolated from the STARNET patients within the upper and lower 5th to 20th percentiles of waist-hip ratio (WHR) (PCSK9: 5th, $P = 8.0 \times 10^{-11}$; 10th, $P = 1.9 \times 10^{-11}$; 15th, $P = 5.9 \times 10^{-5}$; 20th, $P = 0.004$. LDL/HDL ratio: 5th, $P = 0{,}007$; 10th, $P = 0.001$; 15th, $P = 0.0005$; 20th, $P = 0.0009$.

REFERENCES AND NOTES

1. G. K. Hansson, *N. Engl. J. Med.* **352**, 1685–1695 (2005).
2. G. I. Shulman, *N. Engl. J. Med.* **371**, 2237–2238 (2014).
3. M. Nikpay *et al.*, *Nat. Genet.* **47**, 1121–1130 (2015).
4. G. B. Ehret *et al.*, *Nature* **478**, 103–109 (2011).
5. T. M. Teslovich *et al.*, *Nature* **466**, 707–713 (2010).
6. J. Dupuis *et al.*, *Nat. Genet.* **42**, 105–116 (2010).
7. N. Soranzo *et al.*, *Diabetes* **59**, 3229–3239 (2010).
8. R. J. Strawbridge *et al.*, *Diabetes* **60**, 2624–2634 (2011).
9. A. K. Manning *et al.*, *Nat. Genet.* **44**, 659–669 (2012).
10. P. An *et al.*, *Metabolism* **63**, 461–468 (2014).
11. E. Zeggini *et al.*, *Nat. Genet.* **40**, 638–645 (2008).
12. D. Shungin *et al.*, *Nature* **518**, 187–196 (2015).
13. E. A. Stahl *et al.*, *Nat. Genet.* **42**, 508–514 (2010).
14. Y. Cui, Y. Sheng, X. Zhang, *J. Autoimmun.* **41**, 25–33 (2013).
15. C. A. Anderson *et al.*, *Nat. Genet.* **43**, 246–252 (2011).
16. A. Franke *et al.*, *Nat. Genet.* **42**, 1118–1125 (2010).
17. K. Musunuru *et al.*, *Nature* **466**, 714–719 (2010).
18. K. G. Ardlie *et al.*, *Science* **348**, 648–660 (2015).
19. H. Foroughi Asl *et al.*, *Circ Cardiovasc Genet* **8**, 305–315 (2015).
20. H. A. Talukdar *et al.*, *Cross-Tissue Regulatory Gene Networks in Coronary Artery Disease Cell Syst* **2**, 196–208 (2016).
21. P. M. Visscher, M. A. Brown, M. I. McCarthy, J. Yang, *Am. J. Hum. Genet.* **90**, 7–24 (2012).
22. W. H. Wei, G. Hemani, C. S. Haley, *Nat. Rev. Genet.* **15**, 722–733 (2014).
23. P. C. Phillips, *Nat. Rev. Genet.* **9**, 855–867 (2008).
24. J. C. Lambert *et al.*, *Nat. Genet.* **45**, 1452–1458 (2013).
25. D. Welter *et al.*, *Nucleic Acids Res.* **42**, D1001–D1006 (2014).
26. J. Millstein, B. Zhang, J. Zhu, E. E. Schadt, *BMC Genet.* **10**, 23 (2009).
27. I. M. Wang *et al.*, *Mol. Syst. Biol.* **8**, 594 (2012).
28. D. M. Greenawalt *et al.*, *Genome Res.* **21**, 1008–1016 (2011).
29. K. Leander *et al.*, *Circulation* **133**, 1230–1239 (2016).
30. S. Yusuf *et al.*, *Lancet* **366**, 1640–1649 (2005).

ACKNOWLEDGMENTS

The STARNET study was supported by the University of Tartu (SP1GVARENG to J.L.M.B.), the Estonian Research Council (ETF grant 8853 to A.R. and J.L.M.B.), the Astra-Zeneca Translational Science Centre-Karolinska Institutet (a joint research program in translational science, to J.L.M.B.), Clinical Gene Networks AB (CGN) as an SME of the FP6/FP7 EU-funded integrated project CVgenes@target (HEALTH-F2-2013-601456), the Leducq transatlantic networks, CAD Genomics (C.G., E.E.S., and J.L.M.B.), Sphingonet (C.B.), the Torsten and Ragnar Söderberg Foundation (C.B.), the Knut and Alice Wallenberg Foundation (C.B.), the American Heart Association (A14SFRN20840000 to J.C.K., E.E.S., and J.L.M.B.), the National Institutes of Health (NIH NHLBI R01HL125863 to J.L.M.B.; NIH NHLBI R01HL71207 to E.E.S.; R01AG050986 to P.R.; NIH NHLBI K23HL111339 to C.G.; NIH NHLBI K08HL111330 to J.C.K.), and the Veterans Affairs (Merit grant BX002395 to P.R.). The DNA genotyping and RNA sequencing were in part performed by the SNP&SEQ technology platform at Science for Life Laboratory the National Genomics Infrastructure (NGI) in Uppsala and Stockholm supported by the Swedish Research Council (VR-RF1), the Knut and Alice Wallenberg Foundation, and Uppsala Multidisciplinary Center for Advanced Computational Science (UPPMAX). CGN has financially contributed to the STARNET study. J.L.M.B. is the founder and chairman of CGN. J.L.M.B., E.E.S., and A.R. are on the board of directors for CGN. J.L.M.B., T.M., and A.R. own equity in CGN and receive financial compensation from CGN. This work was supported in part through the computational resources and staff expertise provided by Scientific Computing at the Icahn School of Medicine at Mount Sinai. The STARNET data is accessible through the Database of Genotypes and Phenotypes (dbGAP).

SUPPLEMENTARY MATERIALS

www.sciencemag.org/content/353/6301/827/suppl/DC1
Materials and Methods
Figs. S1 to S41
Tables S1 to S11
References (*31*–*89*)

25 October 2015; accepted 22 July 2016
10.1126/science.aad6970

ICP-OES Spectrometer Software

Neo software for inductively coupled plasma-optical emission spectroscopy (ICP-OES) spectrometers is designed to facilitate method development, samples measurements, and results management. A high dynamic range detection mode is integrated for standard measurement, advanced quality control protocols, and retrospective analysis with respect to the integrity of raw results to match with good laboratory practices requirements. For ease of use, ICP Neo displays all information on a single screen. Method development features include a visual display of interference-free lines using the S^3 wavelengths database. Full automation is possible with a Smart Rinse feature for rinse efficiency monitoring between two samples, limits on correlation coefficient and recalculated concentrations, and quality control procedures that are fully EPA compliant. ICP Neo is Microsoft Windows compatible; CPU05 electronics are required. Basic training is performed by a trained service engineer. Researchers can use the software and perform samples analysis as soon as installation is completed.

Horiba Scientific
For info: 732-494-8660
www.horiba.com/scientific

Pulsed Flame Photometric Detector

The OI Analytical 5383 Pulsed Flame Photometric Detector (PFPD) is ideal for petrochemical, environmental lab, and food and beverage applications. Now in its second generation, the detector features improvements in electronics and signal processing, delivering higher selectivity and higher sensitivity. When mounted in a gas chromatograph (GC) or GC/MS, the 5383 gives chemists the ability to specifically determine and selectively analyze low levels of sulfur, phosphorus, and 26 other analytes of interest. New, intuitive, easy-to-use software provides a powerful tool for configuration, optimization, and analysis. The 5383 offers greater ease of use, improved analysis capabilities, and a compact, modular design that saves bench space while maintaining the specificity, reliable technology, and cost-efficient, time-saving features that distinguished its predecessor.

Xylem
For info: 978-778-1010
www.xylem.com

Controlled Laboratory Reactor

Designed by chemists, Asynt ReactoMate Controlled Laboratory Reactor (CLR) systems enable precise control of reaction variables, simple manipulation of vessels and connected apparatus, and the safest possible working conditions. ReactoMate CLR systems accommodate reaction vessels from benchtop to pilot plant scale. The Mettler Toledo RX-10 automation system connects any type and volume of ReactoMate CLR to circulating thermostats, stirrer motors, and sensors. This connectivity allows researchers precision automation, control, and monitoring of chemical reactions and processes in the lab or kilo-lab environment. The intuitive RX-10 touchscreen automates the most commonly used unit operations, and data acquisition utilizing the RX-10 enables scientists to perform more successful experiments and make informed decisions quickly. Reactomate CLR systems are compatible with all leading brands of overhead stirrers. Built to operate from –70°C to +220°C, ReactoMate CLR systems use a PT100 temperature probe linked to the heating/cooling circulator to ensure accurate solution temperature control.

Asynt
For info: +44-(0)-1638-781709
www.asynt.com

Constitutional Array

The addition of research-validated single nucleotide polymorphism (SNP) probes to the CytoSure Constitutional v3 array enables it to do exon-level copy number variation (CNV) and loss of heterozygosity (LOH) detection for comprehensive genetic analysis of developmental delay disorders. The CytoSure Constitutional v3 array content covers 502 targeted genes, with high probe density across the most biologically relevant regions, enabling the detection of single-exon aberrations. With the addition of SNP probes on the new CytoSure Constitutional v3 +LOH array, a broader range of copy-neutral genetic factors can be investigated on a single array, including LOH and uniparental disomy. The SNP probe coverage also functions as an additional validation of CNVs, reducing the need to perform follow-up investigations. Powerful data analysis and interpretation of these advanced arrays is also streamlined with CytoSure Interpret Software, which is provided with each array alongside full on-site training.

Oxford Gene Technology
For info: +44-(0)-1865-856826
www.ogt.com

Biosimilar Assays

A range of ready-to-use assays now exists for testing Actemra, Stelara, and Lucentis biosimilars. The new assays allow biopharma manufacturers to generate accurate comparability results rapidly and cost-effectively. The new assays available include Actemra IL-6R Neutralization Bioassays; an Actemra IL-6R Binding ELISA; Stelara IL-12/IL-23 Binding Assays; a Stelara C1q Binding Assay; a Stelara Neutralization Bioassay; as well as Lucentis VEGF Binding Assays and a Lucentis VEGF Neutralization Bioassay. The availability of prequalified, off-the-shelf assays provides biosimilar developers the opportunity to test a wide range of biosimilars quickly and economically, utilizing assays from just one trusted supplier. Sartorius Stedim BioOutsource, which launched these assays, has its own in-house R&D department and is continually adding to its portfolio of assays. If an assay is not listed, scientists can contact the firm to discuss its availability or use the company's expert services to configure an assay to meet their specific requirements.

Sartorius Stedim Biotech
For info: +44-(0)-141-946-4222
www.sartorius.com

Electronically submit your new product description or product literature information! Go to www.sciencemag.org/about/new-products-section for more information.

Cell Signaling
TECHNOLOGY®

ADVERTISEMENT

The time is now for the scientific community to come together to respond to the challenges of reproducibility and to be part of the solution.

It takes the ingenuity and hard work of the entire research community to move science forward. We build on the ideas and results of our peers to discover new avenues of investigation that in turn inspire ideas for others to advance.

In this way, every new publication acts as a stepping stone, paving the way to a clear and reliable path towards solving a particular scientific problem. Countless diseases have yielded to this approach over the past 100 years, which is a testament both to the expertise and resourcefulness of the community and the strength of its methodology.

Recently, however, there have been reports in journals such as *Nature* and *Science*, stating that the published literature is becoming less reproducible. These reports suggest that the methods that have served us well in the past may now be failing to faithfully guide us.

As a company rooted in science, we are troubled by these reports. Our mission has always been to produce and rigorously validate our products in-house, so they will work dependably in your experiments and be useful to the important experiments they support. Our approach to product development was affirmed by our peers who ranked us as the number one company for reproducibility, sensitivity, specificity and technical support in 2015*. We were honored to be so recognized, and we feel strongly that this recognition comes with a responsibility to act as a leader in addressing the growing reproducibility crisis.

To this end, Cell Signaling Technology is partnering with the Global Biological Standards Institute (GBSI) as well as representatives from industry and the manufacturing, publishing and academic fields. This group is hosting an online discussion with the community, this summer, to generate as many opinions and ideas from the community as it can. The group will then convene this September to review the fruits of the online discussion, draft consensus definitions of reproducibility and its underlying causes, and offer technological and process-oriented solutions.

The reproducibility crisis is undoubtedly a complicated problem, but the challenge is not insurmountable. This is especially true if we address the problem the way we would any other: head-on and as a community.

Together, we can create a means to do better; we can strengthen our faith in the published literature and be confident in our ability to advance biomedical science.

We invite you to join the discussion
www.cellsignal.com/GBSI

Sincerely,

Roberto Polakiewicz

Roberto Polakiewicz, Ph.D.
Chief Scientific Officer
Cell Signaling Technology

*2015 Biocompare Antibody Market Report

ADVERTISER RETAINS SOLE RESPONSIBILITY FOR CONTENT

16PADSCORP0091ENG

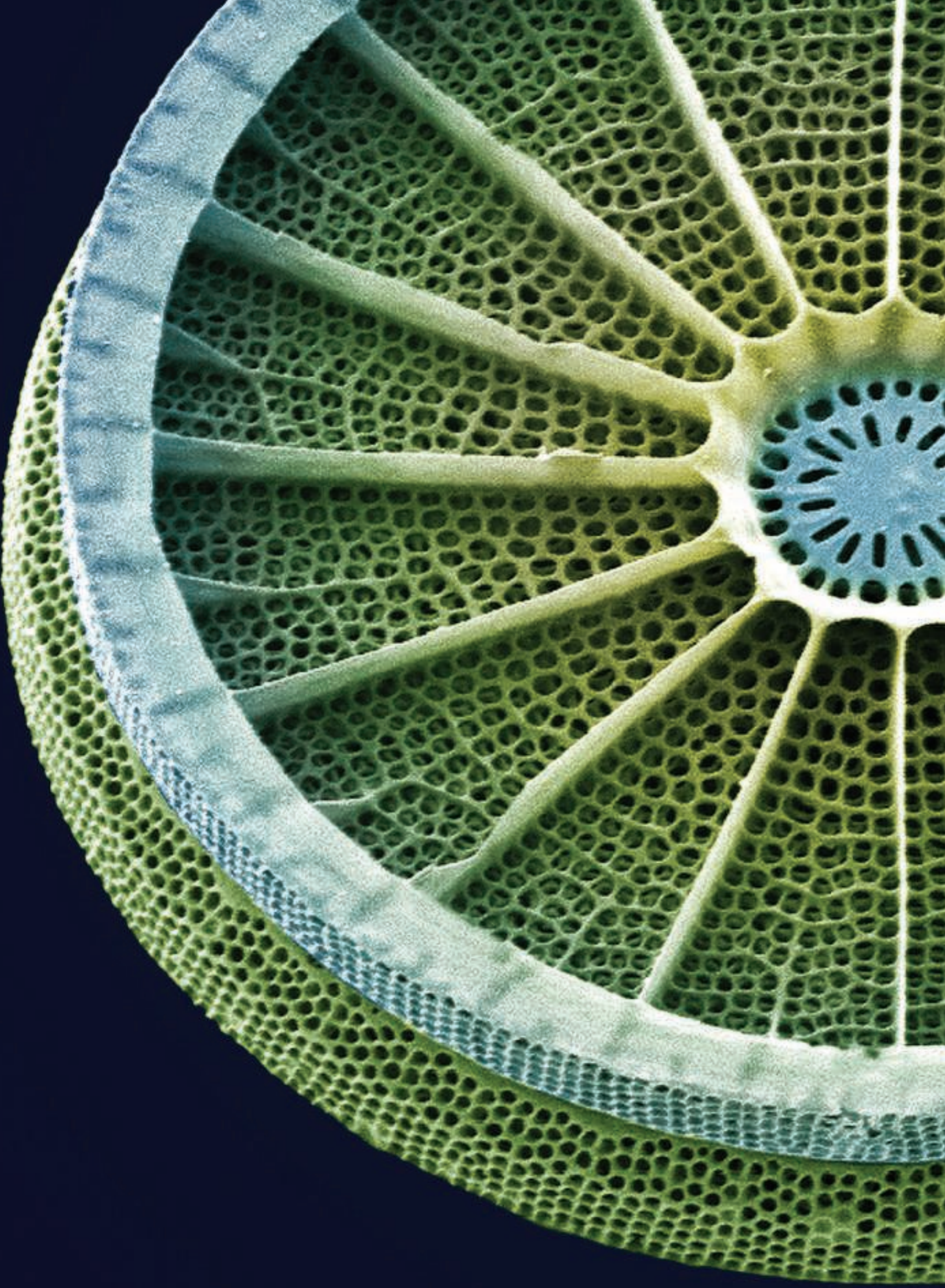

NEW ENGLAND
BioLabs® Inc.

Target with precision.

Introducing the NEBNext Direct™ Cancer HotSpot Panel

Using a unique approach, the NEBNext Direct Cancer HotSpot Panel enriches for 190 common cancer targets from 50 genes prior to next generation sequencing. Combining a novel method for hybridization-based target enrichment with library preparation, the NEBNext Direct technology reduces processing time and minimizes sample loss. Ideal for automation, NEBNext Direct enables highly-specific deep sequencing of genomic regions of interest for the discovery and identification of low frequency variants from challenging sample types.

Visit **NEBNextDirect.com** to learn more and to inquire about sampling this product.

TARGETS INCLUDE REGIONS FROM THE FOLLOWING CANCER-RELATED GENES, INCLUDING >18,000 COSMIC FEATURES:

ABL1
AKT1
ALK
APC
ATM
BRAF
CDH1
CDKN2A
CSF1R
CTNNB1
EGFR
ERBB2
ERBB4
EZH2
FBXW7
FGFR1
FGFR2
FGFR3
FLT3
GNA11
GNAQ
GNAS
HNF1A
HRAS
IDH1
IDH2
JAK2
JAK3
KDR
KIT
KRAS
MET
MLH1
MPL
NOTCH1
NPM1
NRAS
PDGFRA
PIK3CA
PTEN
PTPN11
RB1
RET
SMAD4
SMARCB1
SMO
SRC
STK11
TP53
VHL

For research use only; not intended for diagnostic use.

NEW ENGLAND BIOLABS® and NEB® are registered trademarks of New England Biolabs, Inc.
NEBNEXT DIRECT™ is a trademark of New England Biolabs, Inc.

Image: jim / AdobeStock

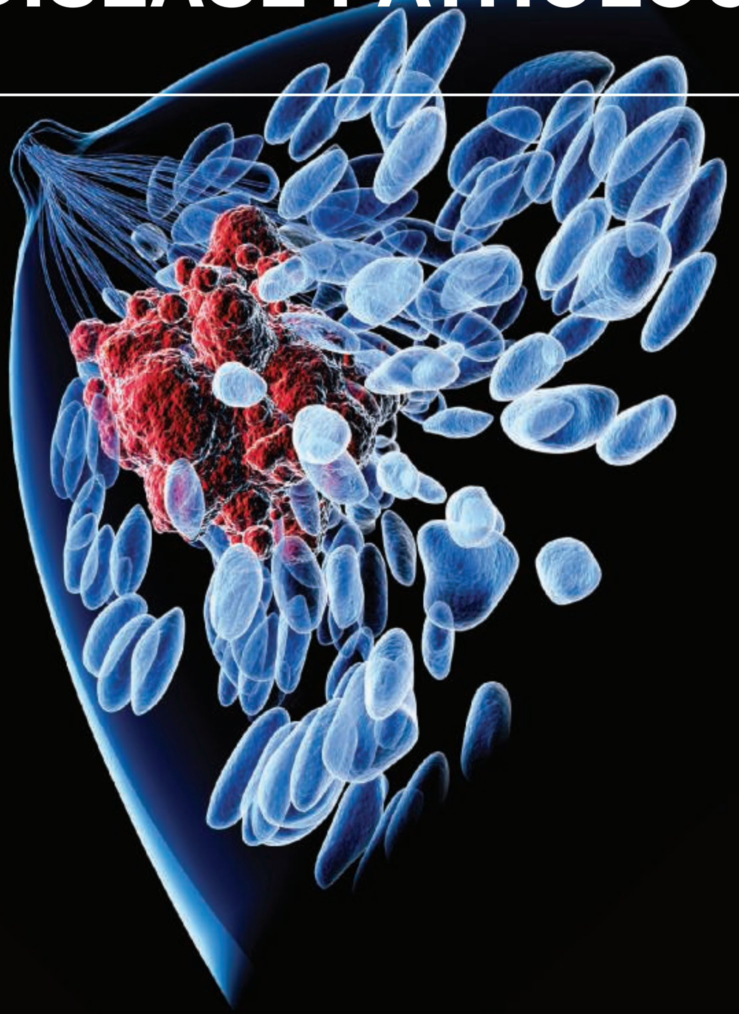

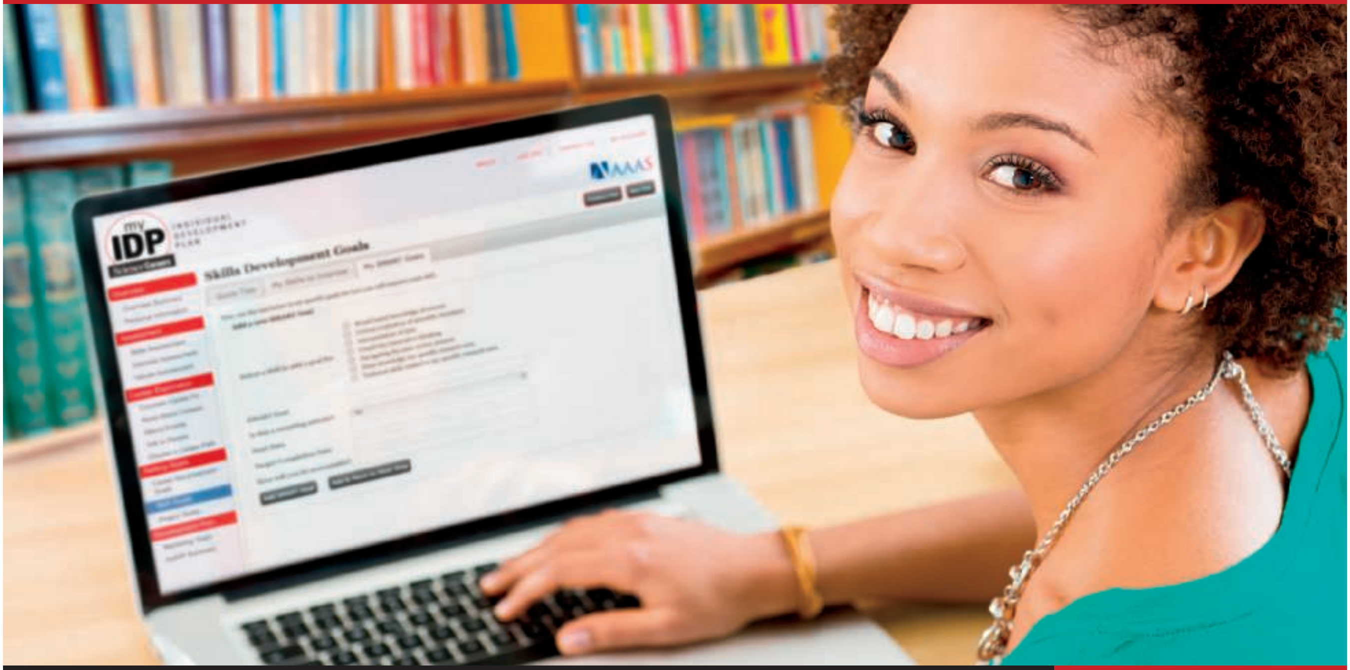

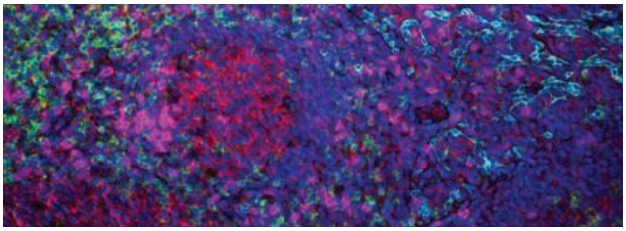

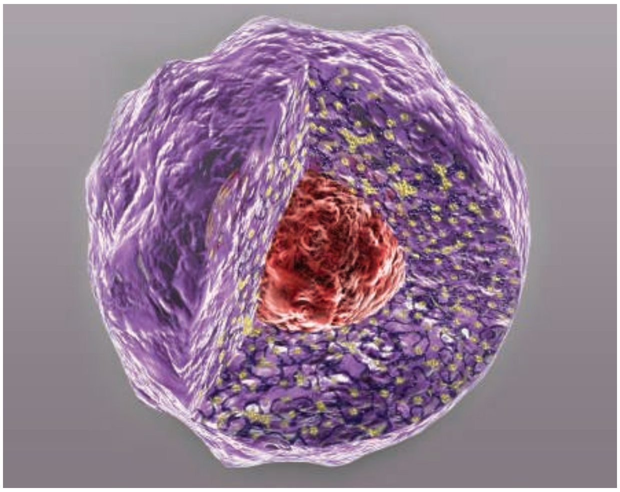


Cell Signaling Technology
CellSimple
Mar 14 13:33:56
CellSimple
System is Ready...
Touch Assay Icon to Begin
Apoptosis (Annexin V - FITC, PI)
Cell Cycle
Fluorescence Only
Multiplex Bead Assay
Open Flow Cytometry
Viability PI
Cell Health (Calcein-AM, PI)
Help
CST
CellSimple Cell Analyzer

WORKING LIFE

By **Amar M. Singh**

Choosing the nontenure track

“Isn’t this just a glorified postdoc position? Won’t taking this offer hurt my chances of landing a tenure-track professor position?” These were the questions I asked my adviser when he offered me a promotion from postdoc to assistant research scientist, the title given to non–tenure-track research faculty members at my institution. I was about to hit my 5-year mark, which was the maximum amount of time the university allowed for postdoc appointments, so we needed to figure out what my next move would be. I was grateful for my adviser’s help and pleased that he wanted to keep me around. At the same time, though, I had just started applying to tenure-track faculty positions and didn’t want to do anything to jeopardize my chances.

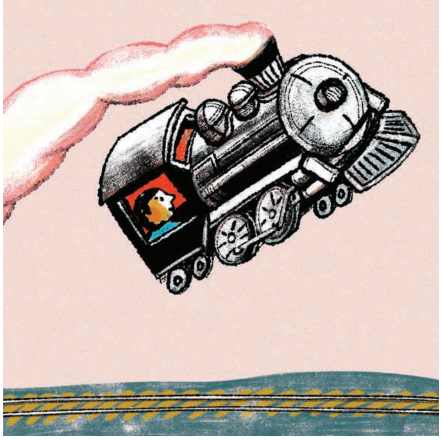

“I finally decided that I needed to go in a different direction.”

My adviser said that we could request an extension for my postdoc appointment if I preferred—which I did. I spent 2 more years as a postdoc and continued to apply for tenure-track faculty positions. After being shortlisted three times but only getting one interview, I finally decided that I needed to go in a different direction.

The time seemed right to explore options in industry, which I had been interested in since my early days as a master’s student but had never pursued because I enjoyed my academic research. Happily, I landed a senior scientist position at a small biotech company that was doing exciting gene-editing work—an area that is scorching hot thanks to the development of CRISPR-Cas9 technology. I had hit the jackpot! After a few months of adjusting to life in the biotech world, I was pleased to find that I enjoyed the team-oriented atmosphere and the focus on completing projects based on firm milestones.

But 1 year in, I realized that the fit wasn’t right for me. At the company, we had to stay completely focused on the product we were developing, and I missed the opportunity to pursue creative new ideas. I just didn’t find the work very intellectually stimulating. I was also surprised to find that the position was in some ways even less stable than a grant-funded one in academia. In industry, even if you perform well, your job can be threatened by factors that are completely out of your control, such as weak company revenue. The lack of job security, together with poor job satisfaction, led me to re-evaluate my decision to leave academia.

I got in touch with my former postdoc adviser for advice, and to see whether he knew of any opportunities for me. I was thrilled when he quickly brought up the non–tenure-track position he had previously offered me. At the same time, recruiters for two biotech companies also approached me. This time the choice was easy: I returned to what I love, academic research.

I’ve only been back in academia for 2 months now, but I’m confident that I made the right decision. I don’t feel at all like a glorified postdoc. I’m lucky to be in a supportive environment, where I will have the opportunity to write my own grants, do exciting research, and teach undergraduate courses. In some ways, I feel that my current position is better than starting out as a brand new tenure-track assistant professor, because I get to do the research I enjoy without the pressures of fully funding a lab. The grants I write need only support myself and my ideas, which may allow me to take on more high-risk, high-reward projects.

Even so, I think my desire to be completely independent and run my own research group will never completely fade. Only time will tell if I eventually decide to apply for a tenure-track job, but I no longer believe that my current position will hurt my chances if I do. I know several researchers who have made the jump from nontenure to tenure track, and I think that the opportunities a nontenure job offers to land independent grants and publish papers as a corresponding author can actually strengthen applications, not weaken them. Regardless, I’m happy to have the freedom to develop and pursue my own ideas, and I’ve learned to not be afraid of switching tracks to find my right fit. ■

Amar M. Singh is an assistant research scientist at the University of Georgia, Athens. Send your career story to SciCareerEditor@aaas.org.

ILLUSTRATION: ROBERT NEUBECKER

Published by AAAS

Science Careers Advertising

For full advertising details, go to ScienceCareers.org and click For Employers, or call one of our representatives.

Tracy Holmes
Worldwide Associate Director
Science Careers
Phone: +44 (0) 1223 326525

THE AMERICAS

E-mail: advertise@sciencecareers.org
Fax: +1 (202) 289 6742

Tina Burks
Phone: +1 (202) 326 6577

Nancy Toema
Phone: +1 (202) 326 6578

Online Job Posting Questions
Phone: +1 (202) 312 6375

EUROPE / INDIA / AUSTRALIA / NEW ZEALAND / REST OF WORLD

E-mail: ads@science-int.co.uk
Fax: +44 (0) 1223 326532

Sarah Lelarge
Phone: +44 (0) 1223 326527

Kelly Grace
Phone: +44 (0) 1223 326528

Online Job Posting Questions
Phone: +44 (0) 1223 326528

JAPAN

Katsuyoshi Fukamizu (Tokyo)
E-mail: kfukamizu@aaas.org
Phone: +81 3 3219 5777

Hiroyuki Mashiki (Kyoto)
E-mail: hmashiki@aaas.org
Phone: +81 75 823 1109

CHINA / KOREA / SINGAPORE / TAIWAN / THAILAND

Ruolei Wu
E-mail: rwu@aaas.org
Phone: +86 186 0082 9345

Danny Zhao
E-mail: dzhao@aaas.org
Phone: +86 131 4114 0012

All ads submitted for publication must comply with applicable U.S. and non-U.S. laws. *Science* reserves the right to refuse any advertisement at its sole discretion for any reason, including without limitation for offensive language or inappropriate content, and all advertising is subject to publisher approval. *Science* encourages our readers to alert us to any ads that they feel may be discriminatory or offensive.

ScienceCareers
FROM THE JOURNAL SCIENCE AAAS

ScienceCareers.org

Dartmouth

Faculty Position in Ecosystem Ecology
Department of Biological Sciences
Hanover, NH USA

The Department of Biological Sciences at **Dartmouth College** seeks applicants for a tenure-track Assistant Professor position in **Ecosystem Ecology**. We seek highly qualified candidates who investigate ecosystem processes to address broadly relevant conceptual issues in ecology. We welcome applicants who study any group of organisms in any type of ecosystem (terrestrial, freshwater, and marine), and who could include local field sites as part of their research and teaching programs. Candidates must have a Ph.D. or equivalent degree. We seek a colleague who will supervise an independent, extramurally funded research program; provide research training for graduate and undergraduate students; teach introductory ecology and other courses at the undergraduate and graduate levels; and contribute to our recently expanded cross-departmental graduate program in Ecology, Evolution, Ecosystems and Society. Dartmouth also offers many opportunities to interact with faculty in other departments and programs, including the Environmental Studies Program and the Department of Earth Sciences. Application materials should include a cover letter, curriculum vitae, three representative publications, statements of research and teaching interests, and the names and contact information for three references. Please submit materials electronically to: **https://apply.interfolio.com/36642**

Application review will begin on **15 September 2016** and continue until the position is filled. For further information about the department and graduate programs, see http://biology.dartmouth.edu

Dartmouth College is an Equal Opportunity/Affirmative Action Employer with a strong commitment to diversity and inclusion. We prohibit discrimination on the basis of race, color, religion, sex, age, national origin, sexual orientation, gender identity or expression, disability, veteran status, marital status, or any other legally protected status. Applications by members of all underrepresented groups are encouraged.

UNIVERSITY OF MICHIGAN

BIOLOGICAL SCIENCES SCHOLARS PROGRAM
For Junior, Tenure Track Faculty

The University of Michigan Medical School announces recruitment for the Biological Sciences Scholars Program (BSSP) to enhance the institution's strengths in the biological and biomedical research areas.

Now entering its 18th year, the BSSP has led recruitment of outstanding scientists pursuing research in genetics, microbiology, immunology, virology, structural biology, biochemistry, molecular pharmacology, stem cell biology, cancer biology, physiology, cell and developmental biology, bioinformatics, and the neurosciences. The Program seeks individuals with PhD, MD, or MD/PhD degrees, at least two years of postdoctoral research experience, and who have not previously held a tenure-track faculty position. Candidates will show evidence of superlative scientific accomplishment and scholarly promise. Successful candidates will be expected to establish a vigorous, externally-funded research program, and to become leaders in departmental and program activities, including teaching at the medical, graduate, and/or undergraduate levels. Primary departmental affiliation(s) will be determined by the applicant's qualifications and by relevance of the applicant's research program to departmental initiatives and themes. All faculty recruited via the BSSP will be appointed at the Assistant Professor level.

APPLICATION INSTRUCTIONS: Please apply to the Scholars Program through the BSSP website at: **http://bssp.med.umich.edu**. A curriculum vitae (including bibliography), a three page research plan, an NIH biosketch, and three original letters of support should all be submitted through the BSSP website. More information about the Scholars Program, instructions for applicants and those submitting letters of recommendation, and how to contact us is located on the BSSP web site: **http://bssp.med.umich.edu**. The deadline for applications is **Friday, September 30, 2016**.

The University of Michigan is an Affirmative Action/Equal Opportunity Employer.

Dartmouth

Faculty Position in Cell and Molecular Biology
Department of Biological Sciences
Hanover, NH USA

The Department of Biological Sciences at **Dartmouth** invites applications for a tenure-track position in the broadly defined area of **Cell and Molecular Biology** at the Assistant, Associate, or Full Professor rank. We seek highly qualified candidates who are addressing fundamental research questions in any biological system. The successful candidate will be expected to direct an independent research program that will attract extramural funding, to provide research training for graduate and undergraduate students, and to teach at the undergraduate and graduate levels. The candidate will join the university-wide Molecular and Cellular Biology graduate program that includes investigators in Arts and Sciences, Geisel School of Medicine, and Thayer School of Engineering. The Dartmouth life sciences research community is highly collaborative and utilizes a diverse array of interdisciplinary approaches to investigate key processes at the molecular, cellular and organismal levels. Dartmouth provides a highly competitive start-up package as well as access to state of the art multi-user research facilities. Applicants must have a Ph.D. or equivalent degree in Biology or a related discipline. Application materials should include a cover letter, curriculum vitae, three representative publications, statements of research and teaching interests, and at least three confidential letters of reference. Please upload application materials electronically to: **https://apply.interfolio.com/36586**

Application review will begin on **October 1, 2016** and continue until the position is filled. Further information about the department http://biology.dartmouth.edu/ and MCB graduate program http://www.dartmouth.edu/~mcb/ can be found at the indicated links.

Dartmouth is an Equal Opportunity/Affirmative Action Employer with a strong commitment to diversity and inclusion. We prohibit discrimination on the basis of race, color, religion, sex, age, national origin, disability, veteran status, marital status, or any other legally protected status. Application by members of any underrepresented group is encouraged.

Dartmouth

Faculty Position in Microbial Ecology
Department of Biological Sciences
Hanover, NH USA

The Department of Biological Sciences at **Dartmouth College** seeks applicants for a tenure-track Assistant Professor position in **Microbial Ecology**. We seek highly qualified candidates who investigate important questions relating to the ecology of microbes and their interactions with other organisms. Candidates must have a Ph.D. or equivalent degree. We seek a colleague who will supervise an independent, extramurally funded research program; provide research training for graduate and undergraduate students; teach introductory ecology and other courses at the undergraduate and graduate levels; and contribute to Dartmouth's recently expanded cross-departmental graduate program in Ecology, Evolution, Ecosystems and Society. Dartmouth also offers many other relevant opportunities for research and graduate training, including the Molecular and Cellular Biology Graduate Program and the Microbiology & Molecular Pathogenesis Program. Application materials should include a cover letter, curriculum vitae, three representative publications, statements of research and teaching interests, and contact information for three references. Please submit materials electronically to: **https://apply.interfolio.com/36648**

Application review will begin on **15 September 2016** and continue until the position is filled. For further information about the department and graduate programs, see http://biology.dartmouth.edu

Dartmouth College is an Equal Opportunity/Affirmative Action Employer with a strong commitment to diversity and inclusion. We prohibit discrimination on the basis of race, color, religion, sex, age, national origin, sexual orientation, gender identity or expression, disability, veteran status, marital status, or any other legally protected status. Applications by members of all underrepresented groups are encouraged.

ScienceCareers online @sciencecareers.org

For recruitment in science, there's only one *Science*.

Faculty Careers

Issue date: September 16
Book ad by August 30
Ads accepted until Sept 9 if space allows

Issue date: October 7
Book ad by September 20
Ads accepted until Sept 30 if space allows

Hiring Faculty? Whatever your timing, we've got two special features for your faculty ads this fall! The September 16 feature offers advice on how to develop skills for reviewing grants and papers. The October 7 feature covers business principles for researchers. Reach *Science* readers and share opportunities at your university.

What makes *Science* the best choice for recruiting?

- Read and respected by 400,000 readers around the globe
- 62% of our weekly readers work in academia and 65% are Ph.D.s. *Science* connects you with more scientists in academia
- Your ad dollars support AAAS and its programs, which strengthens the global scientific community.

Why choose these Faculty Features for your advertisement?

- Relevant ads lead off these career sections with a special Faculty banner
- October 7 issue will be distributed at the American Society of Human Genetics meeting, 18–22 October, Vancouver.

Expand your exposure by posting your print ad online:

- Link on the job board homepage directly to Faculty jobs
- Dedicated landing page for faculty positions.

Deliver your message to a global audience of targeted, qualified scientists.

129,574
subscribers in print every week

352,966
monthly unique browsers on ScienceCareers.org

65%
of our weekly readers are Ph.D.s

Produced by the *Science*/AAAS Custom Publishing Office.

SCIENCECAREERS.ORG

ScienceCareers
FROM THE JOURNAL SCIENCE AAAS

To book your ad: **advertise@sciencecareers.org**

The Americas
+202 326 6582
Japan
+81 3 3219 5777

Europe/RoW
+44(0)1223 326500
China/Korea/Singapore/Taiwan
+86 186 0082 9345

UNIVERSITY OF
CAMBRIDGE

www.jobs.cam.ac.uk

Professorship in the Department of Physiology, Development and Neuroscience (Professorship of Anatomy, established in 1707)

Department of Physiology, Development and Neuroscience

Upon the retirement of Professor Bill Harris, the Board of Electors to the Professorship of Anatomy (an historic title which does not restrict the research interests) invite applications for this Professorship from persons whose research falls within the diverse and multifaceted fields encompassed by the Department of Physiology, Development and Neuroscience. The appointment will be made from 1 October 2018 or as soon as possible thereafter.

Candidates will have an outstanding research record of international stature within a relevant field and will have the vision, leadership, experience and enthusiasm to build on current strengths in maintaining and developing a leading research presence. They will hold a PhD or equivalent postgraduate qualification.

Besides research, standard professorial duties include teaching and teaching-related activities, such as examining and supervisions, and appropriate administrative responsibilities. The Professor will be based in Cambridge. A competitive salary will be offered.

To apply online for this vacancy and to view further information about the role, please visit: http://www.jobs.cam.ac.uk/job/11099.

Closing date: 31 October 2016

Further information is available at: www.admin.cam.ac.uk/offices/academic/secretary/professorships/ or contact the Human Resources Division, University Offices, The Old Schools, Cambridge, CB2 1TT, (email: ibise@admin.cam.ac.uk).

Applications, consisting of a letter of application, a statement of current and future research plans, a curriculum vitae and a publications list, along with details of three referees should be made online no later than 31 October 2016.

Informal enquiries may be directed to Professor Ole Paulsen, Professor of Physiology and Acting Head of Department of Physiology, Development and Neuroscience (2016/17), telephone: +44 (0)1223) 333804 or email: op210@cam.ac.uk.

Please quote reference PM09807 on your application and in any correspondence about this vacancy.

The University values diversity and is committed to equality of opportunity.

The University has a responsibility to ensure that all employees are eligible to live and work in the UK.

Director Position

Institute of Cellular and Organismic Biology
Academia Sinica, Taiwan

Academia Sinica, Taiwan, invites applications and nominations for the position of Director of the Institute of Cellular and Organismic Biology (ICOB). The initial appointment is for a period of three years (renewable for a second term), and will also carry the title of Research Fellow.

As the pre-eminent academic research institution in Taiwan, Academia Sinica is devoted to fundamental and applied research in life sciences, mathematics and physical sciences, and humanities and social sciences. ICOB currently consists of 22 laboratories engaging in the following five focal areas of research: “Aquabiology and Marine Biotechnology,” “Cellular Structural and Organismic Functional Analysis,” “Molecular Basis of Organismic Dysfunctions and Diseases,” “Neuroscience,” and “Molecular Basis and Translational Application of Stem Cells.” ICOB is well funded and equipped with modern research facilities managed by experienced research specialists. ICOB maintains a high research standard with a high-quality publication record. For more information about Academia Sinica and ICOB, please visit **http://www.sinica.edu.tw** and **http://icob.sinica.edu.tw/index_en.php**.

Interested candidates should have a PhD, MD or equivalent degree, with outstanding research accomplishments and demonstrated leadership ability. Besides pursuing a rigorous research program at ICOB, the successful candidate is expected to build on the existing strengths of ICOB, develop new research thrusts, and provide intellectual leadership in cellular and organismic biology research in Taiwan.

Applications including a complete curriculum vitae, a publication list, research accomplishments, or nominations with a brief rationale for recommendation and contact information, should be submitted to Chair of the Search Committee, ICOB, Academia Sinica, 128 Academia Road, Section 2, Nankang, Taipei 115, Taiwan or by Email to **charity@gate.sinica.edu.tw** before **September 30, 2016**. Letters of recommendation will be requested on the applicant’s behalf.

Yale University

School of Medicine

FACULTY POSITION AT THE ASSISTANT PROFESSOR LEVEL

DEPARTMENT OF CELLULAR AND MOLECULAR PHYSIOLOGY

The Department of Cellular and Molecular Physiology is conducting a search for new faculty members at the assistant professor level.

The search seeks candidates whose research connects the properties of molecules to the properties of physiological systems.

Excellent opportunities are available for collaborative research, as well as for graduate and medical student teaching. Candidates must hold a Ph.D., M.D., or equivalent degree. Applicants should include a curriculum vitae, a statement of research interests and goals, and should arrange to have three letters of reference sent. Applicants should apply at the following website: **apply.interfolio.com/36676**

Application Deadline: **October 14, 2016**

Yale University is an Affirmative Action/Equal Opportunity Employer and welcomes applications from women, persons with disabilities, covered veterans, and members of minority groups.

INDIANA UNIVERSITY
BLOOMINGTON

Tenured Faculty Position in Virology

The Microbiology Program in the Indiana University Department of Biology (http://www.bio.indiana.edu) invites applications for the **Lawrence M. Blatt Chair**, an endowed faculty position in Virology at the level of **Associate Professor with Tenure**. More senior candidates with exceptional credentials will also be considered.

We are particularly interested in scientists examining the interaction between viruses and host cells at the molecular and cellular level. Applicants working on virus structure and assembly, and virus evolution will also be considered. This position is part of a significant, continuing expansion in the life sciences at IU Bloomington and represents an exceptional opportunity to join a strong Microbiology Program and new interdisciplinary initiatives linked with Programs in Molecular and Cellular Biochemistry, Cell and Developmental Biology, Biotechnology, the Medical Sciences and a Precision Health Initiative. The successful candidate will be provided with a generous startup package and salary and will have access to outstanding research resources, including state-of-the-art facilities for genomics and bioinformatics, light and electron microscopy, flow cytometry, protein analysis, analytical chemistry, biophysical instrumentation, and crystallography.

Successful candidates must hold a PhD and have demonstrated exceptional leadership roles and scholarly success in their field, will have an outstanding track record in research including peer-reviewed publications and external funding, and will have excellent teaching credentials at the undergraduate and graduate levels.

Applications received by **October 7, 2016** will be assured of full consideration. Applicants should submit a cover letter, a CV, a research statement (5 page limit emphasizing current and planned research, and contributions to their research field), a list of three (or more) references, and up to 3 pdfs of published and/or submitted manuscripts using the submissions link at **http://indiana.peopleadmin.com/postings/2541**. For questions about the application procedure please contact **Jennifer Tarter** (**jenjones@indiana.edu**) or by mail at **1001 E. Third Street, Bloomington, IN 47405-7005** and for all other questions please contact Pranav Danthi (pdanthi@indiana.edu).

Indiana University is an Equal Employment and Affirmative Action Employer and a provider of ADA services. All qualified applicants will receive consideration for employment without regard to age, ethnicity, color, race, religion, sex, sexual orientation or identity, national origin, disability status or protected veteran status.

10 ways that *Science* Careers can help advance your career

1. Register for a free online account on **ScienceCareers.org**.
2. Search thousands of job postings and find your perfect job.
3. Sign up to receive e-mail alerts about job postings that match your criteria.
4. Upload your resume into our database and connect with employers.
5. Watch one of our many webinars on different career topics such as job searching, networking, and more.
6. Download our career booklets, including Career Basics, Careers Beyond the Bench, and Developing Your Skills.
7. Complete an interactive, personalized career plan at “my IDP.”
8. Visit our Career Forum and get advice from career experts and your peers.
9. Research graduate program information and find a program right for you.
10. Read relevant career advice articles from our library of thousands.

Visit **ScienceCareers.org**
today — all resources are free

Science Careers

FROM THE JOURNAL SCIENCE AAAS

SCIENCECAREERS.ORG

THE UNIVERSITY OF TENNESSEE
HEALTH SCIENCE CENTER
COLLEGE *of* NURSING

Associate Dean for Interprofessional Research

The University of Tennessee Health Science Center (UTHSC), the flagship, statewide, academic health system, invites nominations and applications for the position of **Associate Dean for Interprofessional Research** located in the **College of Nursing (CON)**. UTHSC seeks a dynamic leader to facilitate research and scholarship. The successful applicant should have a Doctoral degree with experience and knowledge in clinical research, a track record of NIH like funding, a history of working successfully with diverse colleagues, and a demonstrated ability to foster the research career of others. An earned nursing degree is not required for this position. The Associate Dean reports to the Dean of the College of Nursing and will be part of the leadership team.

Complete details on this research leadership opportunity are available in the Search Profile at **http://tinyurl.com/MM-UTHSC2016**

Review of candidates is underway. The search is open until the position is filled. *EOE/AA*

Kenny Daugherty
Myers McRae Executive Search and Consulting
Cell: (478) 747-0528
WWW.MYERSMCRAE.COM

MYERS MCRAE
EXECUTIVE SEARCH AND CONSULTING

FACULTY POSITIONS IN CHEMISTRY
Department of Chemistry
ARTS AND SCIENCE

The Department of Chemistry at New York University (NYU) invites applications for several tenure-track faculty positions in all areas of Chemistry, subject to final administrative approval. Candidates should have a Ph.D. in chemistry or related field, an outstanding record of research accomplishments, and a strong commitment to teaching at the undergraduate and graduate levels. The hires are anticipated to be at the junior level, although exceptional senior level candidates will be considered.

Candidates should submit a curriculum vita, a detailed description of research plans and interests, and a statement of teaching experience and interests. The application should include three references. To ensure full consideration, applications should be received by October 1, 2016. The anticipated start date is September 1, 2017, pending budgetary and administrative approval. Please submit applications through our web portal using the following link: ***http://chemistry.fas.nyu.edu/object/chem.nyufacultypositions.*** Questions about this position can be sent by Email to ***chemistry.search@nyu.edu***.

The Faculty of Arts and Science at NYU is at the heart of a leading research university that spans the globe. We seek scholars of the highest caliber, who embody the diversity of the United States as well as the global society in which we live. We strongly encourage applications from women, racial and ethnic minorities, and other individuals who are under-represented in the profession, across color, creed, race, ethnic and national origin, physical ability, gender and sexual identity, or any other legally protected basis. NYU affirms the value of differing perspectives on the world as we strive to build the strongest possible university with the widest reach. To learn more about the FAS commitment to diversity, equality and inclusion, please read ***http://as.nyu.edu/page/diversityinitiative.***

NEW YORK UNIVERSITY

EOE/Affirmative Action/Minorities/Females/Vet/Disabled/Sexual Orientation/Gender Identity

---

SAN DIEGO STATE UNIVERSITY
Leadership Starts Here

Assistant Professor: Immunology

THE DEPARTMENT OF BIOLOGY AT SAN DIEGO STATE UNIVERSITY invites applications for a tenure-track faculty position in IMMUNOLOGY at the Assistant Professor level. We are seeking a candidate whose research is at the forefront of cell and molecular biology in the field of immunology. We strongly encourage applications from candidates using non-mammalian model organisms to investigate the evolution of immunity, innate and adaptive immunity in host-microbe or parasitic interactions, or the role of the immune system in wound healing and tissue regeneration. The successful candidate will be expected to develop an externally funded, independent research program involving students. Contribution in the teaching mission of the Department of Biology, and service to the University and/or community is also expected. Applicants must hold a Ph.D. or equivalent degree and have postdoctoral experience.

Apply via Interfolio at **https://apply.interfolio.com/36734**. Review of applications will begin **October 1, 2016**, and will continue until the position is filled.

SDSU is a Title IX, Equal Opportunity Employer.